Physics of the Solid State, Vol. 42, No. 10, 2000, pp. 1775–1801. Translated from Fizika Tverdogo Tela, Vol. 42, No. 10, 2000, pp. 1729–1756.

REVIEW

Migration of Triplet Excitations of Complex Molecules in Disordered Media and in Systems with a Confined Geometry

S. A. Bagnich

Institute of Molecular and Atomic Physics, Belarussian Academy of Sciences, ul. F. Skoriny 70, Minsk, 220072 Belarus
e-mail: bagnich@imaph.bas-net.by

Received January 24, 2000; in final form, March 27, 2000

Abstract—The paper presents the results of analysis of migration of a triplet excitation in inhomogeneous media such as mixed molecular crystals, solid solutions of organic compounds in low-molecular solvents and polymers, as well as porous matrices activated by complex molecules. The experimental data obtained under conditions of steady-state excitation and time resolution are analyzed within different approaches used for describing the energy transport in disordered systems. © *2000 MAIK "Nauka/Interperiodica".*

INTRODUCTION

The study of disordered systems is one of the main problems in physics of condensed state. The interest in such systems is primarily provoked by the variety of their physical properties and by their ample potential for practical applications [1, 2].

Most photophysical processes and photochemical reactions occur directly at the molecular level. However, the rate and efficiency of these processes depend to a considerable extent on the energy transport to reaction centers and, hence, on the supramolecular organization of the system. In this connection, the problem of excitation transfer between molecules in condensed media became long ago a classical problem in solid state physics and luminescence [3, 4]. At a low concentration of an activator in the medium, molecules are independent. With increasing concentration, the molecules of the activator start interacting with one another, which leads to a nonradiative excitation transfer. The energy transfer from excited atoms, ions, or molecules to unexcited ones is a common natural phenomenon. It is often encountered when the concentration of interacting particles and the lifetime of an excited state are large enough. The transfer of excitation can take place between different and identical centers. In the latter case, the term "migration" is used for the energy transport. The simplest and most visual manifestation of energy transport between centers of different origin is the quenching of luminescence of excited particles (donors) as a result of their interaction with unexcited particles (acceptor) or luminescence sensitization, i.e., the formation of luminescence centers that have not been excited before.

One of the most important problems in spectroscopy of condensed media is associated with the study and the development of the method for controlling photophysical and photochemical processes occurring in molecular systems. The knowledge of the mechanisms of transformation of the electron excitation energy both in individual molecules and in organized molecular ensembles makes it possible to obtain promising materials for creating functional units in optoelectronics, recording and storing information, and optical sensors for physicochemical analysis. However, the solution of applied problems using noncrystalline solid-state molecular systems involves difficulties in predicting the dynamics of photoinduced processes. The rate of exchange-resonant processes in liquid solutions and molecular crystals is determined by the diffusion of interacting molecules and the migration of excitons, while in solid-state systems with an irregular structure the efficiency of exchange of excitation energy depends on the form of the distribution of the activator molecules. As a rule, activator molecules form a spatially disordered system in the medium. The molecules have different nearest neighbors, and the energy of their interaction with the surrounding molecules is a random quantity varying from center to center. Inhomogeneous broadening of spectral lines is a well-known manifestation of these differences. For this reason, the laws of dynamics of electron excitations in disordered systems such as mixed molecular crystals, glasses, gels, polymers, or films on the solid surface can differ significantly from model concepts developed for similar processes in homogeneous media. In this connection, it is important to study the main regularities of energy migration in microscopic inhomogeneous media characterized by geometrical and energetic disorders.

This review is devoted to an analysis of experimental data on the migration of electron excitation energy over triplet energy levels of complex molecules in various disordered media. The choice of the triplet excitation was dictated by the high sensitivity of the process of its migration over activator molecules to structural properties of the system, since the exchange-resonant interaction providing the basis of these reactions is a very short-range process and takes place on a small spatial scale [3].

1063-7834/00/4210-1775$20.00

1. MIGRATION OF ELECTRON EXCITATION ENERGY IN INHOMOGENEOUS SYSTEMS

The classical theory of energy transport was developed by Galanin and Frank [5, 6]. In 1947, Forster [7] developed a quantum-mechanical theory of nonradiative energy transfer between molecules in solutions. Dexter [8] generalized the transport theory to the case of exchange-resonant interaction between molecules. Various theoretical methods worked out on the basis of this theory were used in luminescence for describing the energy transport in disordered media. A comparative analysis of these methods is given in reviews [9, 10].

An analysis of the transport of excitation in highly doped mixed crystals revealed phenomena that could not be imagined before, i.e., the phenomena associated with the critical behavior. The results of investigations proved that the energy transport in a highly doped mixed crystal differs drastically from the transport in perfect or weakly doped crystals. The strong microscopic inhomogeneity (associated with clusters) existing in such a crystal determines the main parameters of energy transport. Interesting relations between obviously complex physical phenomena and simple mathematical models, viz., cluster statistics and percolation theory, were discovered. These models form the basis of the most important approaches in statistical thermodynamics.

1.1. Energy Transport in Mixed Molecular Crystals

Experimental results on exciton transport in isotopically mixed molecular crystals of naphthalene have been studied most comprehensively from the standpoint of the percolation theory. The detailed results of experiments under steady-state conditions of excitation are presented in [11–16].

From the phenomenological viewpoint, the most interesting effect, which is observed during energy transport in mixed molecular crystals, is the existence of a critical dependence on the concentration of substituted molecules when the efficiency of migration rapidly increases near the critical concentration. Such a behavior was predicted by Hong and Kopelman [17] on the basis of the percolation theory [18–21]. In [14], a triplet exciton transition in isotopically mixed naphthalene crystals was observed at a content of 10 mol % $C_{10}H_8$ in $C_{10}D_8$. The dependence of the migration efficiency of triplet excitations on the $C_{10}H_8$ concentration was successfully described in the framework of the cluster formalism [22] based on the concepts of the percolation theory. However, the critical concentration for triplet excitations was found to be considerably smaller than the 60 mol % (square lattice) predicted by the percolation theory. This effect was explained by the fact that dynamic percolation takes place for triplet excitations [12, 13, 23]. On the other hand, the critical concentration itself can be varied by changing other parameters such as trap concentration, temperature, and the energy barrier between the molecules of the donor band and the matrix band (Fig. 1). The strong dependence of the critical concentration on trap concentration and temperature, as well as the fact that the critical transition is not smeared upon an increase in these parameters, can be explained within the percolation model. Similar effects were observed for isotopically mixed benzene crystals [24–26] and for chemically mixed molecular crystals [27, 28] characterized by not only geometrical, but also energetic disorder, i.e., the spread in the energies of the excited states of molecules due to the energy fluctuation of their interaction with nearest neighbors.

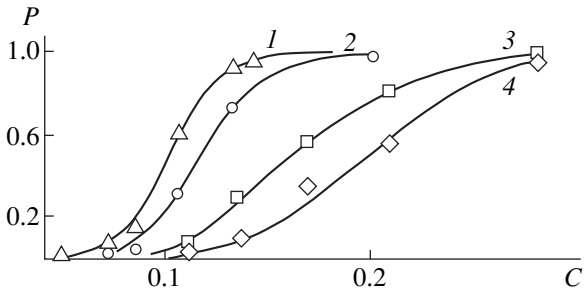

Fig. 1. Dependence of the probability of excitation capture by a trap on the fraction of naphthalene in a $C_{10}H_8/C_{10}D_8$ crystal. Relative concentration of acceptor (betamethyl naphthalene): (*1*, *2*) 10^{-3} and (*3*, *4*) 10^{-4}. Temperature, K: (*1*, *3*) 4.2 and (*2*, *4*) 1.7 [16].

In order to explain the effects observed in mixed molecular crystals, Klafter and Jortner [29–31] made an attempt to interpret the critical transition as the Anderson–Mott transition. They proposed that the limit of a detached band [32], when the excitation is located only in the quasi-lattice of one of the components, is applicable in the case of a disordered binary alloy. In the zeroth approximation, this leads to the exciton impurity band, which is transformed to the exciton band of a pure crystal in the limit $X = 1$. The shape and width of the band are determined by short-range interactions J_n of excitons, where n is the difference in the coordinates of interacting lattice sites. Another characteristic of the model is the energy associated with a disorder in the local random deformation energy W. The main simple idea put forth by Klafter and Jortner is that the value of $\langle J_n \rangle$ decreases monotonically with X, and that there exists a certain critical concentration X_c at which the Anderson criterion holds, i.e., $J_c \approx W/K$, where $J_c \equiv \langle J_n(X_c) \rangle$ and K is a numerical constant of the order of 10, which depends on the connectivity of the lattice. Below X_c, all exciton states are localized ("Anderson localization" [33]). Above X_c, there exist extended (band) states with localized states on their wings (Anderson–Mott model [33]). Thus, the exciton transfer, which is "nonmetallic" at concentrations lower than the critical value, becomes "metallic" at concentrations exceeding this value. Consequently, the critical concentration for an exciton transition plays the

role of an exciton mobility threshold by analogy with the Mott electron mobility threshold [33]. However, subsequent discussions [33–37] revealed the futility of such an approach in explaining the entire body of the observed results. Moreover, some experimental data are in complete contradiction with the model described above [11].

According to the authors of cluster formalism, three basic methods widely used in the theory of luminescence, viz., the continuous-time random walk method [38–41], the method of coherent potential [42–45], and the self-consistent graphic method [46, 47], cannot provide an adequate description of the observed results. It was shown that these models account only for first-order effects which take place in randomly disordered systems, e.g., the change in the mean distance between molecules of a donor upon a change in its concentration [32, 48, 49]. A higher-order effect, viz., the influence of surroundings of the donor and the acceptor on the individual pair rate of energy transfer, is disregarded in these approximate methods. However, these effects become significant near the critical concentration of the activator in the system.

Nevertheless, Blumen and Silbey [50] proposed a simple but comprehensive dynamical model for describing a sharp increase in the efficiency of transport for a certain ("critical") concentration of the donor. This model disregards the clusterization of molecules and the structure of the system, but, in the opinion of its authors, gives good agreement between the theoretical results and the results of experiments on the migration of triplet excitations in isotopically mixed crystals of naphthalene and benzene. This conclusion provoked many authors to disregard the effect of molecular clusterization in highly concentrated systems (see, for example, [51]) even despite the fact that the presence of clusters of activator molecules in these media is confirmed by the conclusions of the percolation theory as well as by the results of direct spectroscopic investigations [52–54]. At the same time, it was found [55, 56] that a good agreement between the theory and experiments is observed in the Blumen–Silbey model only for inductive-resonant interaction between molecules. In the case of exchange-resonant and superexchange mechanisms of interaction, the cluster model and the Blumen–Silbey model significantly differ when used for describing energy transport in inhomogeneous media.

1.2. Analysis of Migration of Electron Excitation Energy in Inhomogeneous Systems in the Cluster Model and in the Blumen–Silbey Model

The cluster model developed by Kopelman in [22, 23, 57] is based on the following assumptions: (1) an excitation is localized in a cluster containing m molecules; (2) the probability of creating an excitation in a given cluster is proportional to the number m of molecules in the cluster; (3) the probability that a given site in the cluster is occupied by a trap (acceptor) is equal to S, viz., the fraction of acceptors among activator molecules; and (4) the quantum-mechanical probability $\pi_m(t)$ of capturing an excitation in a trap (acceptor with a unit capture cross-section) inside the cluster containing m molecules does not depend on the cluster shape.

In the case of a finite lattice containing G substituted lattice sites (i.e., those occupied by donor or acceptor molecules), the probability of capture of an excitation by a trap for $S \ll 1$ is given by

$$P = G^{-1}\sum_m i_m m[1-(1-\pi_m m/G)^{\chi SG}], \qquad (1)$$

where $i_m(C)$ is the number of clusters with m sites, which depends on the concentration C of substituted sites; and χ is the capture efficiency ($\chi = 1$ for a trap with a unit capture cross-section). The capture probability P depends on the concentration C of substituted molecules, the time t, and the concentration S of traps.

Unfortunately, the cluster model does not provide an analytical expression describing the dependence of the probability of capture of an excitation by a trap on the donor concentration in the system. At the same time, the following expressions were derived for supertransfer, which give an idea of the efficiency of excitation transfer to a trap. In the range of concentrations lower than the critical value C_c, the capture probability is determined by the average number of molecules in a cluster, I_{AV}:

$$P = SI_{AV}, \quad C \ll C_c. \qquad (2)$$

In the range of concentrations higher than critical, the capture probability is determined by the power P_∞ of an infinite cluster:

$$P = P_\infty, \quad C \gg C_c. \qquad (3)$$

In turn, the dependence of I_{AV} and P_∞ on the activator concentration in the system is characterized by the following scaling expressions [58, 59]:

$$I_{AV} \propto |1 - C/C_c|^{-\gamma}, \quad C/C_c \ll 1, \qquad (4)$$

$$P_\infty \propto |1 - C/C_c|^{\beta}, \quad C/C_c \gg 1, \qquad (5)$$

where γ and β are the critical indices depending only on the dimensionality of space and having the following values: $\gamma = 2.2$ and $\beta = 0.14$ for $d = 2$, and $\gamma = 1.6$ and $\beta = 0.41$ for $d = 3$. Near the percolation threshold, we have

$$P = S^{1/\delta}, \quad C = C_c, \qquad (6)$$

where δ is the critical index which obeys the relationship $\delta = 1 + \gamma/\beta$. The value of δ is equal to 5 for the three-dimensional space and 17 for two dimensions.

Thus, the cluster model of energy migration is based on the mathematical functions I_{AV} and P_∞. The concentration dependence of these functions is determined by the connectivity of molecules in a cluster, which sets

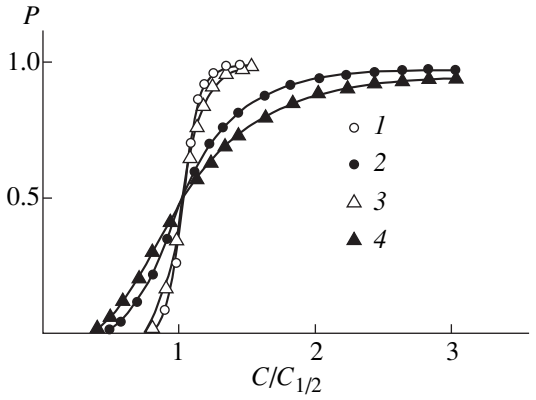

Fig. 2. Dependence of the probability of excitation capture by a trap on the reduced donor concentration for (*1*, *2*) two-dimensional and (*3*, *4*) three-dimensional spaces in the case of the exchange-resonant mechanism of interaction for two values of ϕ: (*1*, *3*) 40 and (*2*, *4*) 10 [55].

the effective topology of the system and, hence, the critical concentration. From the viewpoint of energy transport, the connectivity is the maximum separation between nearest molecules in a cluster for which the effective energy transport is still possible between them. In real systems for which dynamic percolation is observed, the connectivity and, hence, C_c, I_{AV}, and P_∞ are functions of time, trap concentration, and temperature. The variation in the latter quantities can change the cluster connectivity and, hence, the dependence of P on C. However, Kopelman [11] proved that the model of a cluster with leakage can provide a universal description of the dependence of P on C with the help of a reduced concentration defined as the ratio C/C_c of the absolute concentration to the critical one. In this case, according to the result of computer simulation of percolation processes on a square lattice [60], the shape of the curves $I_{AV}(C/C_c)$ and $P_\infty(C/C_c)$ does not depend on the connection provided that the lattice remains unchanged, and its spatial dimensionality does not change either.

The probability of excitation capture in a trap can be related to the time of energy transport to the trap through the following expression:

$$P = 1/(1 + \tau_{tr}/\tau_0), \tag{7}$$

where τ_0 is the lifetime of the excitation of a donor in the absence of an acceptor, and τ_{tr} is the time of energy transfer to the trap. Here, P corresponds to the probability that the excitation finds the trap during its lifetime. By using this approach, Blumen and Silbey derived an expression for τ_{tr} in the case of an exchange-resonant interaction between molecules, whose rate constant is defined as follows [61]:

$$k(r) = 1/\tau_0 \exp[2/L(R_0 - r)]. \tag{8}$$

Here R_0 is the critical radius of energy transfer, L is the effective Bohr radius, r is the separation between molecules, and τ_0 is the lifetime of triplet excitation.

Since for a comparative analysis, it is more convenient to use not the absolute donor concentration, but the reduced concentration as in the cluster model, the role of a "critical" concentration in this model can be played by the concentration $C_{1/2}$ defined from the relationship $P(C_{1/2}) = 0.5$. In [55, 56], the following relationships were obtained for the dependence of τ_{tr} on the reduced concentration $C/C_{1/2}$:

$$\tau_{tr}^d = \tau_0 \exp[\phi((C/C_{1/2}^d)^{-1/d} - 1)], \tag{9}$$

$$C_{1/2}^d = 2d/\pi(L\phi)^{-d}, \tag{10}$$

$$\phi = 2/L(R_0 + L/2\ln S + L/2\Delta E/kT), \tag{11}$$

where $C_{1/2}$ is the "critical" concentration determined from the relationship $P(C_{1/2}) = 1/2$, and ΔE is the activation energy of excitation transfer to the trap as a result of migration over donor molecules.

Using these relations, we can compare the results obtained in the Blumen–Silbey model and in the cluster model. The cluster model is based on the concept of clusters, their size distribution, and the dependence of this distribution on the molecular concentration. It was noted above that when the reduced concentration is used, we can expect a universal behavior of the curves describing the dependence of the probability of excitation capture in a trap on the donor concentration.

A completely different situation is observed in the Blumen–Silbey model. It follows from formula (9) that, in the case of exchange-resonant interaction, the value of τ_{tr} depends on ϕ even when the reduced concentration is used. The value of ϕ can be varied in experiments by changing the trap concentration and temperature. Figure 2 shows the dependences of the excitation capture probability on the reduced donor concentration, which were obtained by using formulas (7) and (9) for two values of ϕ. It should be noted that the calculations made by Loring and Fayer [62], who employed the self-consistent graphic approach, lead to the dependences of P on $C/C_{1/2}$, which are virtually similar to those obtained in the Blumen–Silbey model.

The universal nature of the dependences of excitation capture probability on the molecular concentration is not the only difference between the models described above. One more important difference also exists. It can be seen from Fig. 2 that a transition from two-dimensional to three-dimensional migration in the Blumen–Silbey model practically does not change the form of the dependence of P on $C/C_{1/2}$. At the same time, an entirely different behavior can be expected in the cluster model. It is generally accepted in the percolation theory that the dependence of P_∞ on C is described by a relationship of the type (5). Since the values of the critical index β for two- and three-dimensional spaces

differ considerably, the dependences of P on C/C_c should be different.

Thus, a comparison of the cluster model of energy migration in disordered systems with the Blumen–Silbey model shows that these models do have some common features in the description of energy transport under steady-state excitation, but are also characterized by considerable differences. The existence of these differences enables us to draw the conclusion about the ability of a model to correctly describe energy transport in disordered systems from an analysis of experimental data obtained for real two- and three-dimensional systems.

Isotopically mixed molecular crystals of naphthalene are among the best studied systems in which the two-dimensional topology is manifested effectively. It was mentioned above that the transport of triplet energy between molecules in this system occurs as a result of superexchange interaction. Gentry and Kopelman [48] showed that, as in the case of the exchange-resonant interaction, the dependence of the transfer rate constant on the distance for the superexchange interaction can be described by the exponential law

$$K_{tr}(r) = 1/\tau \exp[-\nu(r/a_0 - 1)], \qquad (12)$$

where τ is the time of energy transfer between nearest neighbors in the crystal, a_0 is the separation between them, and ν is a constant equal to 8.6. Hence, it follows that the curves presented in Fig. 2 correctly describe the dependences of capture probability on the donor concentration in the framework of the Blumen–Silbey model and for the superexchange interaction also. Figures 3 and 4 show the universal and scaling curves for energy transport in isotopically mixed naphthalene crystals [16]. It can be clearly seen that the dependences obtained for different temperatures and trap concentrations (the critical concentration was varied by 100%) are universal (i.e., almost coincide) in the entire range of reduced concentration investigated in experiments. The critical indices obtained as a result of scaling analysis coincide with the theoretical values obtained for a two-dimensional space.

Molecular crystals are generally anisotropic. For this reason, there are many effectively low-dimensional (relative to energy transport) crystals, i.e., two-dimensional crystals, like naphthalene or pyrazoline [63], or even one-dimensional crystals (e.g., isotopically mixed phenazine crystals [64]). Moreover, as a result of strong anisotropy of interaction, an effective two-dimensional energy transport is observed even in chemically mixed molecular crystals [28] and binary solids [65], which exhibit not only translational, but also orientational disordering.

The most suitable objects for studying three-dimensional energy transport are solid solutions of organic compounds in low-molecular solvents. However, such systems differ significantly from isotopically mixed crystals: apart from spatial disorder, these media pos-

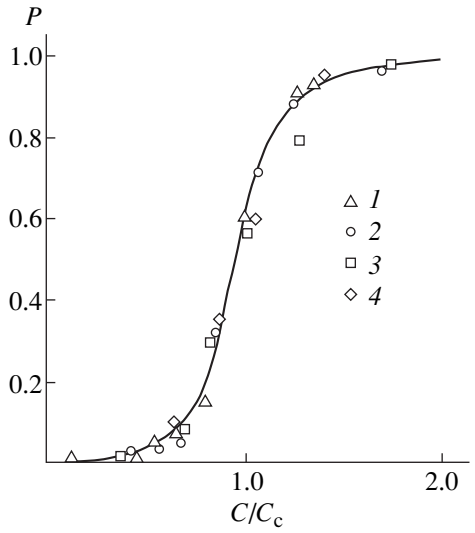

Fig. 3. Universal dependences for energy migration. The notation is the same as in Fig. 1 [16].

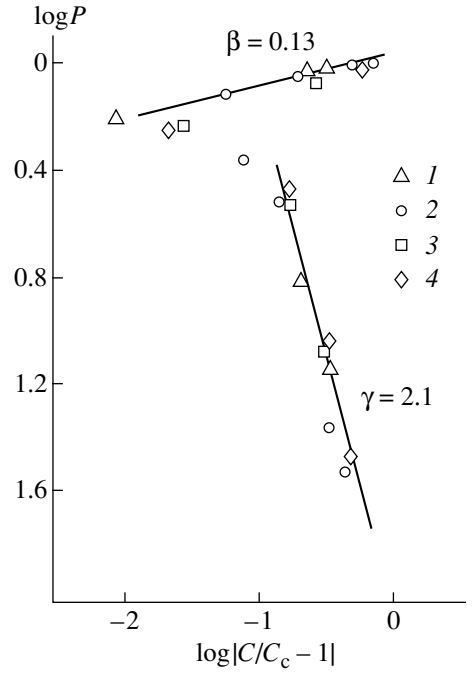

Fig. 4. Scaling dependences for energy migration. The notation is the same as in Fig. 1 [16].

sess a considerable energetic disorder, i.e., the spread in the energies of an excited state of molecules (several hundred cm^{-1}) due to fluctuations of the energy of their interaction with nearest neighbors. For this reason, Lange *et al.* [66] believe that the approaches used for describing the energy transport in isotopically mixed molecular crystals are inapplicable to such strongly disordered systems. Indeed, the crystal ordering in isotopically mixed molecular crystals leads to an insignifi-

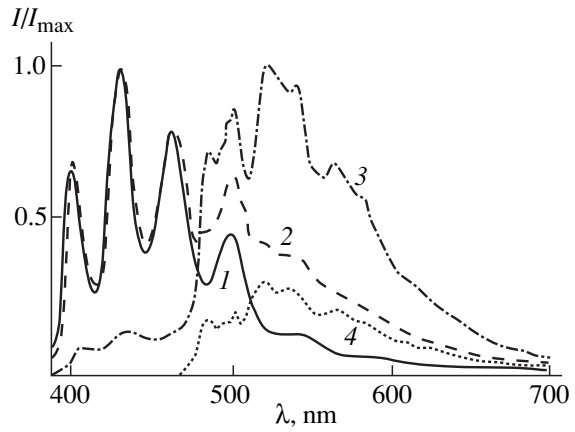

Fig. 5. Luminescence spectra of benzaldehyde-1-bromonaphthalene in ethanol at $T = 77$ K. Relative concentration of 1-bromonaphthalene is $S = 10^{-2}$. Benzaldehyde concentration, mol/l: (*1*) 1, (*2*) 2.5, and (*3*) 5. Spectrum *4* is the difference between spectra *2* and *1* [67].

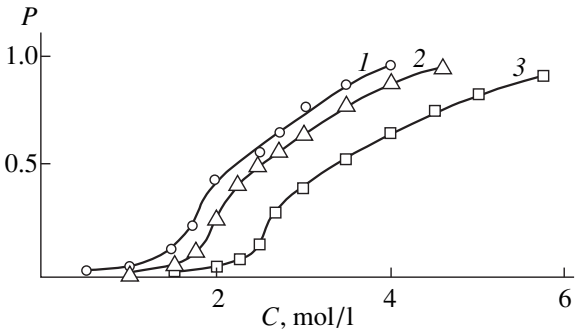

Fig. 6. Dependence of the probability of excitation capture by a trap on the concentration of benzaldehyde in ethanol. Relative concentration of 1-bromonaphthalene: (*1*, *2*) 10^{-2} and (*3*) 10^{-3}. Temperature, K: (*1*, *3*) 100 and (*2*) 77 [67].

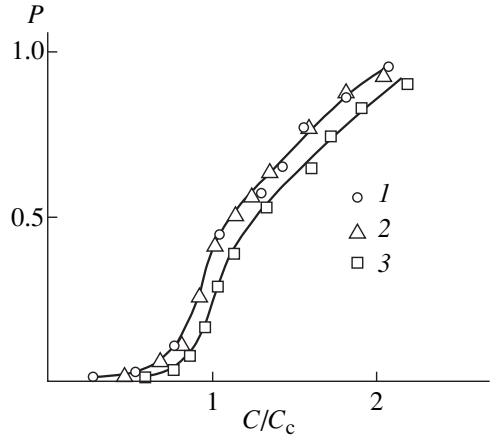

Fig. 7. Universal dependences for energy migration. The notation is the same as in Fig. 6 [67].

cant inhomogeneous broadening of triplet energy levels of donor molecules. However, the percolation model was successfully used for describing the migration of triplet excitations in chemically mixed molecular crystals in which the inhomogeneous broadening of energy levels of impurity molecules is an order of magnitude larger than that in isotopically mixed crystals [27, 28]. Moreover, a still stronger energetic disorder is observed in isotopically mixed molecular crystals of naphthalene for singlet excitations whose migration is due to the superexchange interaction, as in the case of triplet excitations. At the same time, Gentry and Kopelman [48] demonstrated that the observed percolation nature of the transport of singlet excitations in isotopically mixed molecular crystals of naphthalene at temperatures of a few degrees Kelvin are due only to such a strong energetic disorder.

An analysis of the three-dimensional migration of triplet excitations was carried out in [67] for a solid solution of benzaldehyde in ethanol.

1.3. Three-Dimensional Migration of Triplet Excitations of Organic Compounds in Solid Solutions

Considering that the exchange-resonant interaction has a short range, the system used for investigations should provide highly concentrated solutions. An example of such a system is a solution of benzaldehyde in ethanol. Using this system, one can obtain solid solutions of any concentration. Besides, the mechanism of triplet energy transport for carbonyl compounds has been studied comprehensively [3]. Figure 5 shows the luminescence spectra of benzaldehyde-1-bromonaphthalene for various concentrations of benzaldehyde at $T = 77$ K. According to Kopelman *et al.* [12], the value of probability can be determined in terms of the donor and acceptor luminescence intensities as follows:

$$P = \frac{I_A}{I_A + \alpha I_D}, \qquad (13)$$

where $\alpha = q_A/q_D$; $q_A$and q_D are quantum yields; and I_A and I_D are the acceptor and donor luminescence intensities, respectively, integrated over the spectrum.

Figure 6 shows the dependences of the probability of the excitation capture by a trap on the donor concentration for two temperatures and two relative concentrations of the acceptor. The universal and scaling dependences for energy migration over triplet levels of benzaldehyde in ethanol are presented in Figs. 7 and 8. While plotting these dependences, we chose the critical concentration with the help of formula (6) under the assumption that energy migration in the given system is three-dimensional. It can be seen from the figure that the dependences are similar, i.e., exhibit a universal behavior. All the scaling dependences have linear segments with identical slopes for concentrations much larger and much smaller than the critical value. The

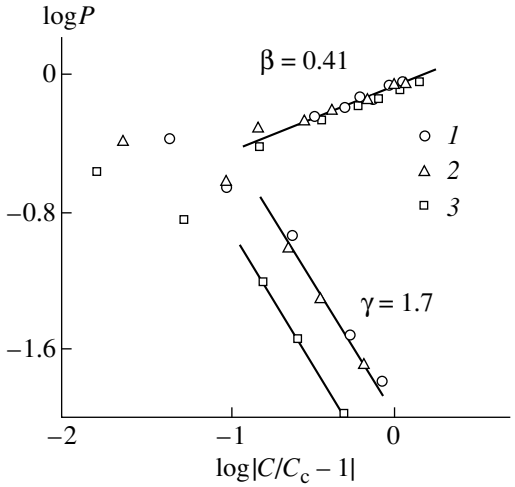

Fig. 8. Scaling dependences for energy migration. Notation is the same as in Fig. 6 [67].

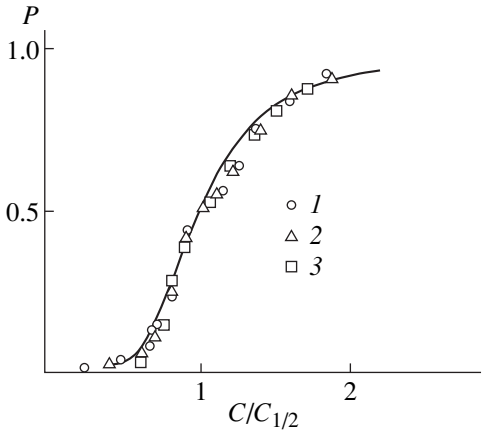

Fig. 9. Dependence of the probability of excitation capture by a trap on the reduced donor concentration $C/C_{1/2}$. Notation is the same as in Fig. 6. The solid line is the result of fitting of the theoretical dependence to the experimental curve by varying the parameter ϕ; ϕ = 13.4 [56].

critical indices obtained from the slopes of the linear segments by the least-squares method coincide with the theoretical values for a three-dimensional space. All that has been said above indicates that the experimental data obtained for the solid solution of benzaldehyde in ethanol agree with the cluster model of energy migration in disordered systems.

Let us now consider these experimental results from the viewpoint of the Blumen–Silbey model. Figure 9 shows the experimental dependences of P on $C/C_{1/2}$ and the theoretical curve, which is defined by formulas (7) and (9) and plotted as a result of fitting to experimental dependences by varying the parameter ϕ. It can be seen from the figure that the experimental curves exhibit a universal behavior. At the same time, the opposite result should be expected for the Blumen–Silbey model. The value of ϕ, for which the best matching between the theoretical and experimental dependences is attained, amounts to 13.4. In this case, however, the discrepancy between the theory and experiments is much stronger than in the cluster model.

Using formulas (10) and (11) in the Blumen–Silbey model, we can derive an expression relating the critical concentration to the parameters determining the efficiency of energy transport in the system:

$$1 = 4/3\pi C_{1/2}(T, S) \times [R_0(T) + L/2\ln S - L/2\Delta E/kT]^3. \quad (14)$$

A similar relationship was also obtained in the cluster model [68, 69].

One of the most important concepts in the percolation theory is that of connectivity, i.e., the maximum distance between particles for which an effective interaction leading to energy transport is still possible. The connectivity determines both the size distribution of clusters for any impurity concentration and the critical concentration for which percolation takes place. Energy transport in disordered systems is possible when the time of hopping between molecules is smaller than the excitation lifetime. It is just the finite excitation lifetime that determines the maximum length of a jump and, hence, the effective topology of the system. Consequently, we will apply the term "cluster" to an aggregate of molecules between which an effective energy transport is possible. Thus, in the case of energy migration over donor molecules, the connectivity condition for two donor molecules can be written in the form

$$t_{ij} \ll \tau_0, \quad (15)$$

where t_{ij} is the time of hopping between the ith and jth molecules, and τ_0 is the excitation lifetime. This connectivity condition for supertransfer (taking into account energetic disordering of the electron energy levels of activator molecules) was used [68, 69] to derive the following expression for the radius of molecular connectivity in a cluster:

$$R(T, S) = R_0(T) + L/2\ln S - L/2\Delta E/kT. \quad (16)$$

The quantity $R(T, S)$ is the maximum separation between nearest molecules in an infinite cluster for which the supertransfer limit is still realized.

In mixed molecular crystals, activator molecules can only be located at crystal lattice sites. Consequently, the problem of energy migration in these systems is similar to the lattice site problem in the percolation theory, and the process can be simulated on a lattice of a certain topology depending on the structure of the crystal matrix and the parameters of interaction between molecules. Unlike mixed molecular crystals, the distribution of activator molecules in low-molecular solvents can be arbitrary or almost arbitrary. Consequently, the problem of energy migration in these systems is close just to the problem of percolation over

random sites. The simplest problem in this class is the problem of spheres [70]. The application of the problem of enveloping spheres in the percolation theory has made it possible to derive the following expression relating the radius of molecular connectivity in a cluster to the critical concentration of molecules in the system:

$$2.7 = 4/3\pi C_c(T, S)R(T, S)^3. \quad (17)$$

A comparison of formulas (14) and (17) indicates that the relation between the critical concentration and the parameters determining the efficiency of energy transport in the system in the cluster model and in the Blumen–Silbey model are qualitatively identical, but differ quantitatively.

Using expressions (14), (16), and (17), the following values of parameters L, R_0, and ΔE were obtained from the experimental data: 0.71, 12.8 Å, and 493 cm^{-1} in the cluster model, and 0.66, 9.6 Å, and 426 cm^{-1} in the Blumen–Silbey model, respectively. It can be seen that the quantities determined differ significantly (especially for R_0). The results obtained in [71, 72] were used in [55] to determine the values $R_0 = 12.3$ Å and $L = 0.77$ Å for benzaldehyde in ethanol at 77 K. It can be seen that these values agree better with the results obtained in the cluster model. At first glance, the difference in the values of R_0 obtained in the cluster model and in the Blumen–Silbey model is not very striking. However, this is not quite true. The lifetimes for the triplet state of benzaldehyde that correspond to the obtained values of R_0 show that the difference is quite large. The cluster model gives the value of $\tau_0 \approx 7$ ms, which is slightly higher than the actual value. Nevertheless, this difference is incomparable to that observed in the Blumen–Silbey model, in which $\tau_0 \approx 2$ μs.

One more important result is worth noting. The processing of experimental curves for benzaldehyde in ethanol on the basis of the Blumen–Silbey model led to the parameter $\phi = 13.4$. A close value of ϕ is obtained by formula (10) taking into account the experimental data. Considering that the critical behavior for triplet excitations in naphthalene is observed for an activator concentration of the order of 10% (the average distance between molecules in this case is 25 Å), we can easily use formulas (10) and (11) to obtain the corresponding value of the parameter ϕ for isotopically mixed molecular crystal of naphthalene as well, which is approximately equal to 50. Consequently, in accordance with the results presented in Fig. 2, we should expect a steeper dependence of P on $C/C_{1/2}$ in the Blumen–Silbey model for benzaldehyde in ethanol than that for mixed naphthalene crystal, which contradicts the experimental data.

These facts convincingly prove the necessity to include the effect of clusterization of molecules for obtaining a correct description of energy transport in disordered systems in the case of exchange interaction between molecules.

An analysis of transport of electron excitation energy of organic compounds in low-molecular solvents is of fundamental rather than practical importance, since the application of such systems is limited by the glass transition temperature of the solvent used. For example, the low solubility of benzophenone in a solid solution of ethanol (<1 mol/l) made it impossible to study the energy migration at liquid nitrogen temperature [73]. The experiments made at 125 K led to the value of connectivity radius $R_{exp} = 18.5$ Å, which is much larger than the theoretical value $R_{theor} = 10$ Å obtained by using formula (16) on the basis of the benzophenone phosphorescence data. The dependence of the probability of excitation capture in a trap on the benzophenone concentration strongly differs from analogous dependences obtained for benzaldehyde at temperatures ranging from 77 to 100 K. It was shown [73] that this effect is due to diffusion of benzophenone molecules themselves in a liquid with viscosity $\eta = 100$ Pa s, such as ethanol at 125 K [74], since the glass transition temperature for the amorphous matrix is approximately equal to 67% of its melting temperature [75].

From the viewpoint of possible applications, the most convenient objects are solid solutions of organic compounds in polymer matrices.

2. PERCOLATION OF TRIPLET EXCITATIONS OF CARBONYL COMPOUNDS IN SYSTEMS WITH A CONFINED GEOMETRY

2.1. Effect of Microscopic Structure of an Amorphous Polymer on Percolation of Triplet Excitations of the Activator

One of the main advantages of such systems is that they can be used at room temperature. At the same time, specific properties of a polymer as the matrix (namely, the peculiarities of its microscopic structure), the existence of free volume and regions with different viscosities (which, in turn, leads to a locally inhomogeneous intercalation of molecules in the matrix), and the fractal properties of macromolecules themselves should obviously affect the percolation of electron excitation energy over activator molecules.

The luminescence spectra of the benzophenone–1-bromonaphthalene system in PMMA were used in [76] to obtain the dependences of the probability of excitation capture by a trap on the benzophenone concentration for various values of the relative concentration of 1-bromonaphthalene. The form of these dependences generally agrees with the theoretical results and experimental data obtained for a solid solution of benzaldehyde in ethanol. Nevertheless, these dependences possess a very important feature: the probability of excitation capture by a trap does not become equal to unity even for a donor concentration much higher than the critical value. From the results of numerical simulation [13], we can conclude that there is no supertransfer in the studied system under the given conditions. How-

ever, expression (3) is valid only in the limit of supertransfer. For high donor concentrations in the absence of supertransfer, the probability of excitation capture by a trap is defined as

$$P = P_\infty F_n, \quad C \gg C_c. \tag{18}$$

According to this expression, the capture probability differs from unity and is determined by the capture probability F_n for an infinitely large cluster even in the limit of high concentrations when the power of this cluster is equal to unity. The supertransfer limit can be attained [22] under the following conditions: the long lifetime of an excitation and/or a strong interaction between molecules, and/or effective capture of an excitation by a trap. The character of the interaction between molecules obviously does not change with temperature. The efficiency of excitation capture in 1-bromonaphthalene should not significantly depend on temperature either. However, the results obtained by Fraser *et al.* [77] show that, as we go from liquid nitrogen temperature to room temperature, the lifetime of a triplet excitation of benzophenone in PMMA decreases sharply. This decrease weakly affects the capture probability at donor concentrations smaller than the critical value, for which only finite clusters can exist, but reduces the excitation capture probability in an infinitely large cluster.

The temperature dependences of the probability of excitation capture by a trap were obtained in [78] for samples with various concentrations of the donor and the acceptor (Fig. 10). As the temperature increases, the capture probability first increases, thus indicating an increase in the efficiency of energy migration over triplet energy levels in benzophenone. However, at temperatures $T > 260$ K, the curves exhibit a decrease in the capture probability upon heating. A similar behavior was observed by Brown *et al.* [79] for isotopically mixed naphthalene crystals under selective excitation of the triplet energy level of the donor. The authors explained this effect by the formation of an additional channel of deactivation of triplet donor excitations, which can compete with their capture in a trap. In the case of benzophenone in PMMA, the rate constant of intramolecular nonradiative energy deactivation increases with temperature [77].

Proceeding from formula (13) and using the system of equations describing the number of excited donor and acceptor molecules under steady-state excitations, we can determine the probability of excitation capture by a trap in terms of the kinetic parameters describing the deactivation of a donor triplet excitation:

$$P = \frac{k_{tr}}{k_D^r + k_D^{nr} + k_{tr}}, \tag{19}$$

where k_D^r and k_D^{nr} are the rate constants of radiative and nonradiative deactivations of the triplet state of the donor, and k_{tr} is the rate constant of energy transfer to the acceptor. The rate constant of energy transfer to a trap under inhomogeneous broadening of the electron energy levels can be written in the form

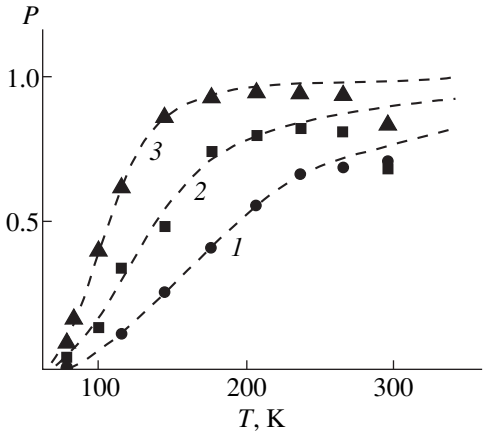

Fig. 10. Temperature dependences of the probability of excitation capture by a trap. Benzophenone concentration, mol/l: (*1*) 0.9 and (*2*, *3*) 1.5. 1-Bromonaphthalene concentration, mol/l: (*1*, *3*) 10^{-2} and (*2*) 10^{-3} [78].

$$k_{tr} = k_{tr}^0 e^{-\Delta E/kT}. \tag{20}$$

The rate constant of nonradiative deactivation of the triplet state is also a function of temperature and has the form [77]

$$k_D^{nr} = k_D^0 + k_D'(T), \tag{21}$$

where k_D^0 is a constant and $k_D'(T)$ is a certain function of temperature, the value of $k_D'(T)$ increasing with temperature, and $k_D'(0) = 0$. Substituting the expressions (20) and (21) into formula (19), we obtain

$$P = \frac{1}{k_1 e^{\Delta E/kT} + k_2 e^{\Delta E/kT} k_D'(T) + 1}, \qquad k_1 = \frac{k_D^r + k_D^0}{k_{tr}^0}, \quad k_2 = \frac{1}{k_{tr}^0}. \tag{22}$$

The first term in the denominator in formula (22) decreases with increasing temperature. Let us analyze the behavior of the second term. It is well known that the phosphorescence lifetime for all polyatomic hydrocarbons in PMMA virtually remains unchanged as the temperature varies from 4 to 77 K. This means that the value of $k_D'(T)$ is equal to zero in the given temperature range. For benzophenone in PMMA, such a weak dependence of τ_{ph} on T is observed up to 230 K [80]. The decisive role in the temperature dependence of the excitation capture probability in this temperature range is obviously played by the first term. For this reason, the capture probability will increase with heating. At temperatures higher than 230 K, the rate constant of

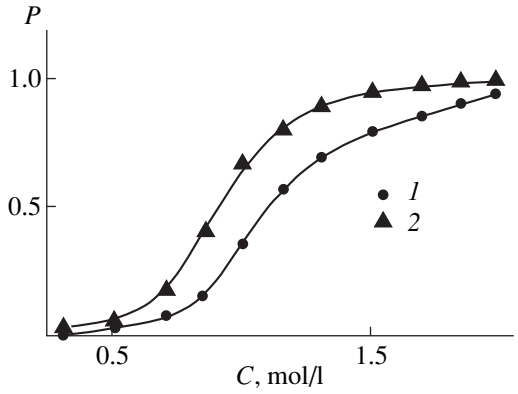

Fig. 11. Dependences of the probability of excitation capture by a trap on the benzophenone concentration in PMMA. Relative concentration of 1-bromonaphthalene $S = 10^{-2}$; T, K: (*1*) 125 and (*2*) 200 [82].

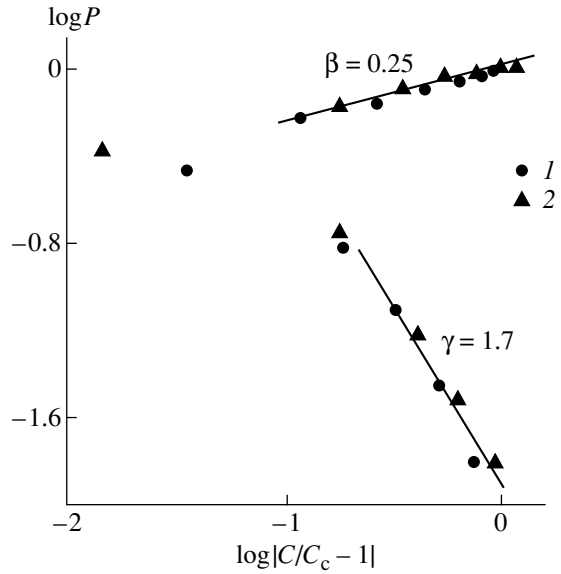

Fig. 12. Scaling dependences for energy transport. Notation is the same as in Fig. 11 [82].

nonradiative deactivation starts increasing rapidly [79]. If this process is quite rapid, the second term will also increase as a whole, thus leading to a decrease in the capture probability. When the second term in the denominator in formula (22) starts dominating, the capture probability decreases upon heating, which is actually observed in experiments (see Fig. 10).

In the low-temperature range, where the contribution from the second term is small, formula (22) can be written in the form

$$P = \frac{1}{k_1 e^{\Delta E/kT} + 1}. \quad (23)$$

This formula was used in [81] for processing experimental dependences in the temperature range in which $P < P_{max}$. The dashed curves (see Fig. 10) were obtained theoretically as a result of fitting. It follows from the obtained results that the dispersion of energy level for benzophenone molecules over which the electron excitation energy migrates amounts approximately to 450 cm^{-1}.

The temperature dependence of the efficiency of energy transport over triplet energy levels of benzophenone in PMMA was used in [82] to obtain the probability of excitation capture by a trap as a function of the benzophenone concentration in the temperature range where the supertransfer limit can be attained (Fig. 11). Figure 12 shows the scaling dependences. These dependences exhibit a universal behavior in the entire concentration range, which is predicted by the cluster model. However, the slope of the linear segment of the scaling curve in the range of concentrations much higher than the critical value corresponds to the critical index $\beta = 0.25$, which is considerably smaller than the theoretical value of 0.41 for a three-dimensional space. Using a model with limited percolation, Parris [83] showed that the anisotropy in the interaction of molecules in three-dimensional translationally disordered systems, in which the orientational order is preserved, limits the efficiency of energy transfer in one of the directions and can lead to energy migration with an intermediate dimensionality $2 < d < 3$. In this case, one can expect intermediate values of critical indices. The realization of such a situation in a three-dimensional system requires an orientational ordering of donor molecules. In the case of mixed molecular crystals, such an ordering is ensured by the crystal matrix with impurity molecules at the lattice sites. This ordering becomes possible in the system under investigation only if benzophenone molecules in concentrated samples form a crystalline structure, which is quite possible for highly concentrated samples.

In order to eliminate completely the effects associated with the orientational ordering of molecules, experiments were made in which benzaldehyde molecules served as the donor. Unlike benzophenone, whose melting point is 48°C (and, hence, the formation of its solid phase in highly concentrated samples occurs during their cooling to room temperature after polymerization), benzaldehyde at room temperature is the liquid (T_m = –26°C). For this reason, the formation of a solid structure in samples containing benzaldehyde in PMMA occurs when they are immersed in liquid nitrogen. On the contrary, pure benzaldehyde immersed in liquid nitrogen forms a transparent glass, i.e., an amorphous structure without any orientational or translational order. The dependences of the probability of excitation capture by a trap on the benzaldehyde concentration in PMMA were obtained in [84] in the temperature range 77–250 K. The universality and scaling tests revealed that the dependences obtained for benzaldehyde in PMMA perfectly coincide not only with one another, but also with similar dependences for benzophenone. The critical indices obtained for benzalde-

hyde from the scaling dependence are close to those for benzophenone in PMMA.

The difference between the critical index β obtained in a polymer matrix and the theoretical value for a three-dimensional space can be explained taking into account the microscopic structure of the amorphous polymer. The ideas concerning the universal nature of critical indices are based on the fact that their values are determined by the structure of clusters in the vicinity of the percolation threshold. The major role in this case is played by geometrical parameters of clusters, which are manifested at large distances (of the order of correlation radius). These distances are much larger than the lattice period (for lattice systems). Consequently, the geometry of a cluster does not depend on the lattice type for which the problem is formulated. In the general case, the problem can be formulated for lattice sites located in space at random, which does not affect the geometry of large clusters. However, the theoretical values of critical indices in the percolation theory were obtained by computer simulation of percolation processes in a Euclidean homogeneous space of a certain dimensionality. A similar situation is indeed encountered in the case of mixed molecular crystals and solutions in low-molecular solvents, which form a homogeneous glass upon freezing, i.e., in the case when a homogeneous matrix exists. For this reason, such systems exhibit perfect coincidence of experimental and theoretical values of critical indices. For amorphous polymers, a completely different situation can be expected.

Amorphous polymers, including PMMA, are strongly inhomogeneous matrices. According to the Yeh model [85], an amorphous polymer consists of interconnected grains (domains) having a diameter of 4–10 nm. Ordered regions with more or less parallel segments of chains having a size of 2–4 nm are located at the center of a grain. The ordered region is surrounded by the boundary region including the ends, loops and folds of the chains. The space between grains is filled with disordered globules of macromolecules. Impurity molecules in an amorphous polymer are concentrated predominantly in disordered regions having the largest free volume. In the low-concentration range, in which the cluster size is not large, the geometry of this free space in the polymer virtually does not affect the geometry and growth dynamics of finite clusters. As a result, the critical index γ determined in the concentration range $C \ll C_c$ is the same for a solid solution in ethanol and for the PMMA solution, and coincides with the theoretical value. A quite different situation takes place in the donor concentration range $C \gg C_c$, in which the critical index β is determined. This index defines the growth dynamics for an infinitely large cluster. In the case of an amorphous polymer, the topology of free space in which this process predominantly occurs necessarily affects the geometry of a percolation cluster and the rate of increase in its density. Consequently, the critical index β for a solution in an amorphous polymer differs from the theoretical value obtained for a homogeneous space.

An attempt to create an inhomogeneous matrix by introducing Al_2O_3 particles of size 1 μm into ethanol was made in [56]. When the concentration of such particles attained 10 vol %, a variation in critical indices (although less significant than for PMMA) was observed, which confirms the above assumption concerning the possible effect of microscopic organization of the matrix on the percolation processes occurring in these materials. The final conclusion could be drawn only by carrying out similar investigations in matrices whose topology is well known. Such matrices include, for example, porous glasses.

2.2. Percolation of Electron Excitation Energy in Solid Solution of Benzaldehyde in Porous Silicate Matrices

Several hypotheses were put forth concerning the effective topology of energy transport in porous glasses (PG). In some publications, e.g., in [86], a system of pores is treated as a percolation cluster with a fractal dimension of the order of two. Schaefer *et al.* [87] proposed that pores should be treated as one-dimensional formations. It is known from the percolation theory that the critical concentration at which an infinitely large cluster is formed for the first time increases with decreasing dimensionality of space. Consequently, in experiments on the capture of an excitation by a trap in the case of one-dimensional migration, one can expect a strong increase in the donor concentration for which an effective energy transport takes place in the system.

In order to carry out experiments on excitation capture by a trap under steady-state excitation, we chose a solution of benzaldehyde in ethanol in a porous sodium silicate glass with an average pore diameter of the order of 70 Å [88].

An analysis of the luminescence parameters of solid solutions of carbonyl compounds in porous silicate glasses revealed a number of effects associated with the interaction of molecules with pore walls. The results concerning the effect of porous silicate glass on the spectral and kinetic characteristics of solid solutions of carbonyl compounds were described in detail in [89–94]. Here, we only note the following points. An analysis of luminescence of porous glasses activated by organic molecules indicates that the porous matrix affects phosphorescence of solid solutions of carbonyl compounds introduced into it. The nature of this effect is determined by the interaction of molecules with absorption centers of the matrix, which are silanol (Si–OH) and siloxane (Si–O–Si) groups in the case of carbonyl compounds. The efficiency of the interaction decreases upon an increase in the size of molecules. Three types of solvents were discovered, whose use leads to various changes in the spectral and kinetic characteristics of the activator: (1) aprotic solvents

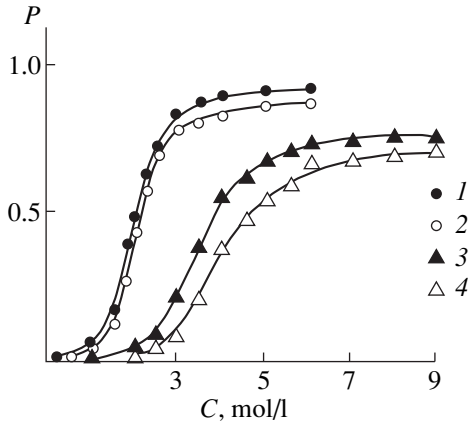

Fig. 13. Dependences of the probability of excitation capture by a trap on the benzaldehyde concentration in ethanol in sodium borosilicate glass. Relative concentration of 1-bromonaphthalene: (*1*, *2*) 10^{-2} and (*3*, *4*) 10^{-3}; *T*, K: (*1*, *3*) 77 and (*2*, *4*) 100 [88].

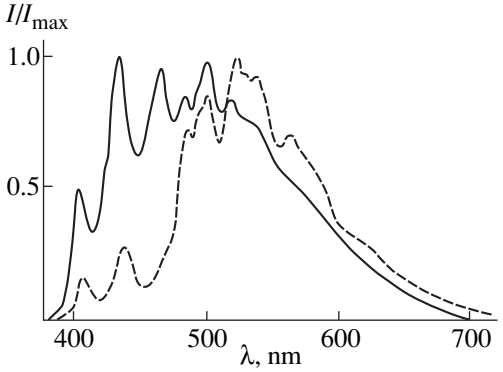

Fig. 14. Luminescence spectra for benzaldehyde-1-bromonaphthalene (dashed line) in PMMA and the same compound in the sodium borosilicate glass–PMMA matrix (solid line) at $T = 77$ K. Concentration of 1-bromonaphthalene is $S = 10^{-2}$, and the benzaldehyde concentration is 5 mol/l [97].

which weakly interact with carbonyl compounds, (2) alcohols forming a hydrogen bond with activators, and (3) solvents containing carbonyl groups. Two mechanisms of variation in spectral and kinetic parameters of phosphorescence were revealed for solid solutions of organic compounds in porous glasses. The first mechanism is associated with direct interaction of activator molecules with pore walls. The second mechanism involves the interaction with the adsorption centers of solvent molecules. The interaction of solvent molecules with the matrix changes their orientation in the solvate shell of the activator, which in turn is manifested in the change of spectral and kinetic characteristics of luminescence of the activator.

Figure 13 shows the dependences of the probability of excitation capture by a trap on the benzaldehyde concentration in the matrix, which were obtained from the luminescence spectra of samples for two concentrations of 1-bromonaphthalene at two temperatures. It can be seen from the figure that the probability of excitation capture by a trap for the system under investigation tends to a certain value of $P_{max} < 1$ upon an increase in the donor concentration, and the value of P_{max} decreases with a decrease in the acceptor concentration. Such a behavior can be attributed to the presence of donor molecules which serve as traps for the migrating excitation. These can be molecules either with a lower energy level or with a shorter lifetime of the excited state. Both situations can take place for the molecules which interact with the siloxane surface of the matrix.

The scaling dependences have linear segments with identical slopes for concentrations much higher and much lower than the critical value. However, the critical indices obtained from the slopes of the linear segments differ noticeably from the theoretical and experimental values obtained for a solid solution in ethanol. At the same time, they virtually coincide with the values obtained for benzaldehyde and benzophenone solutions in the amorphous polymer PMMA. This result confirms the above assumption concerning the effect of the matrix topology on percolation processes occurring in it and, hence, on the critical indices determining the formation and growth of clusters in the system. Similar results were also obtained when the sol–gel glass with an average pore diameter of 50 Å was used as the matrix [95]. In general, the dependences obtained for the two types of glasses coincide. However, some differences are also observed. In contrast to the sol–gel glass and the solid solution in ethanol, for which a decrease in the critical concentration upon an increase in temperature to 100 K was established, the concentration increases in sodium borosilicate glass. A similar behavior was also observed for benzaldehyde in PMMA in the range of temperatures higher than 200 K [84]. It was proven [88, 95] that this difference is associated with different effects produced by these porous glasses on the temperature dependence of the rate constant for intramolecular deactivation of the triplet state of benzaldehyde.

An analysis of the concentration dependence of the spectral and kinetic characteristics of phosphorescence of benzaldehyde in the PG–PMMA matrix and a comparison of the obtained results with similar data obtained for benzaldehyde in PMMA led to the conclusion [96] that, in the course of polymerization of methyl methacrylate in porous glass in highly concentrated samples, activator molecules are expelled from the polymer to pore walls. Consequently, an increase in the local concentration of the activator in the PG–PMMA matrix with its total concentration in solution is much faster than in PMMA. At the same time, an analysis of the migration of the electron excitation energy for benzaldehyde in these matrices [97, 98] revealed a considerable decrease in the probability of excitation capture by the acceptor (Fig. 14) and an increase in the critical

concentration of benzaldehyde upon a transition from the PMMA to the PG–PMMA matrix. These results seem to be quite unexpected if we take into account the effect of expulsion of the activator to pore walls during the polymerization of methyl methacrylate, since the local concentration should increase in this case, and, hence, the conditions for effective migration of triplet excitation should be created. It can be easily shown on the basis of the data on porous glass that, in order to cover the entire surface of pores with a monomolecular layer of benzaldehyde, it is sufficient to use a solution with a concentration of the order of 2 mol/l, assuming that all molecules will precipitate on pore walls in the course of polymerization. Even if we take into account the fact that a fraction of molecules remains in the polymer, the concentrations used are sufficient for covering the entire surface with benzaldehyde molecules. In the cluster model of energy migration, this means that we are dealing with a two-dimensional energy migration over an infinitely large cluster whose power is equal to unity. If the supertransfer limit is attained in the system, which is indeed the case for the given concentration of traps, the probability of excitation capture by a trap at such a cluster would be equal to unity. It was proven [97] that this contradiction can be removed in the problem of percolation in a two-dimensional potential [99], taking into account the microscopic structure of the porous surface of glass and peculiarities of adsorption of carbonyl compounds in the pores of silicate matrices.

3. KINETICS OF DELAYED LUMINESCENCE OF ORGANIC COMPOUNDS IN INHOMOGENEOUS MEDIA WITH ENERGY MIGRATION

The experiments made under the conditions of steady-state excitation provide rich information on the efficiency of energy transport in the system, but give no idea on the dynamics of this process. In this connection, an analysis of the kinetics of activator luminescence decay in systems with energy migration becomes essential. An analysis of random percolation, which is in fact microscopic diffusion in a microscopically inhomogeneous medium, leads to results that are similar, to a certain extent, to common results on diffusion. The relation between random motion (Brownian movement) and diffusion was established long ago by Einstein [100]. The relation between random motion (Brownian movement) and rate constants has also been established (although not quite reliably). Brownian movement of an individual particle in homogeneous media, together with a similar movement of another particle, leads to a constant collision probability per unit time. However, random migrations of an excitation over a fixed lattice with fixed but randomly distributed traps lead to a time-varying probability of their capture in the traps. As a result, the rate coefficients cannot be treated as rate constants any longer. A nontrivial kinetics of motion is also observed for a connectivity that does not change with time. However, the results of investigations prove that real systems with the exchange-resonant interaction between molecules exhibit dynamic percolation, i.e., the situation when the connectivity itself is a function of time. In this case, the cluster structure also varies with time, and, hence, the percolation dynamics depends on time in a more complicated manner than in a standard situation. This leads to the concepts of dynamic clusters, "leakage" from clusters, the formation of conglomerates similar to clusters formed by clusters, and the effect of all these factors on the kinetics. Consequently, the dynamics of excitations in microscopically inhomogeneous media is a very complex process.

For this reason, an analysis of phosphorescence decay kinetics for solid solutions of organic compounds, for which the applicability of the cluster model and the percolation theory was demonstrated in the first part of this review, is very important in establishing the main mechanisms responsible for the kinetics of energy transport in microscopically inhomogeneous media.

3.1. Dispersive Nature of Energy Transport in Inhomogeneous Media

In Section 1.1, we presented the expression for the probability of excitation capture by a trap, which was derived within the cluster formalism applied to steady-state excitation. It is obvious, however, that the excitation capture probability is a function of time. Let us define the probability of excitation capture by a trap during the time t as $P(t)$, where $0 < P(t) < 1$. We also introduce the quantity $q(t)$ equal to the average number of various lattice sites attended by an excitation during the time t. In a connected lattice, $q(t)$ and $P(t)$ increase with time monotonically. According to Kopelman and Argyrakis [101], the general formula describing the probability of excitation capture by a trap in a random lattice has the form

$$P(t) = P_\infty(1 - e^{S\chi q(t)}) + SI_{AV}. \quad (24)$$

If the number of excitations at the initial instant of time is ρ_0, their number at any instant is determined by the following expression [101]:

$$\partial \ln \rho / \partial t = -k - (1 - P)^{-1}(\partial P / \partial t). \quad (25)$$

Defining the rate coefficient for the excitation trapping as

$$K(t) = (1 - P)^{-1}(\partial P / \partial t), \quad (26)$$

we can obtain the following "rate equation:"

$$\partial \rho / \partial t = -k\rho - K(t)\rho. \quad (27)$$

The general expression for the rate coefficient derived in [101] is very cumbersome. However, in the limit of concentrations higher than the critical value, it

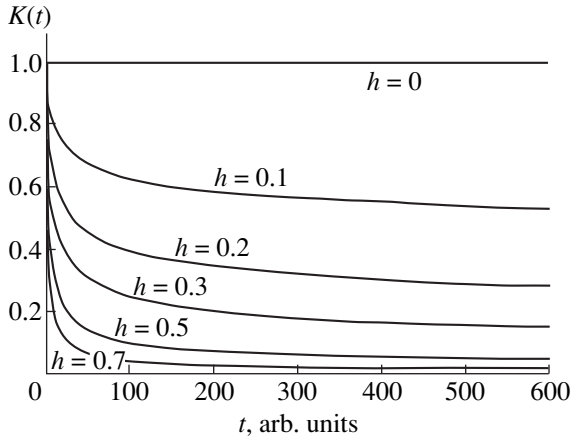

Fig. 15. Time dependences of the rate coefficient defined by formula (31) at different parameters h [105].

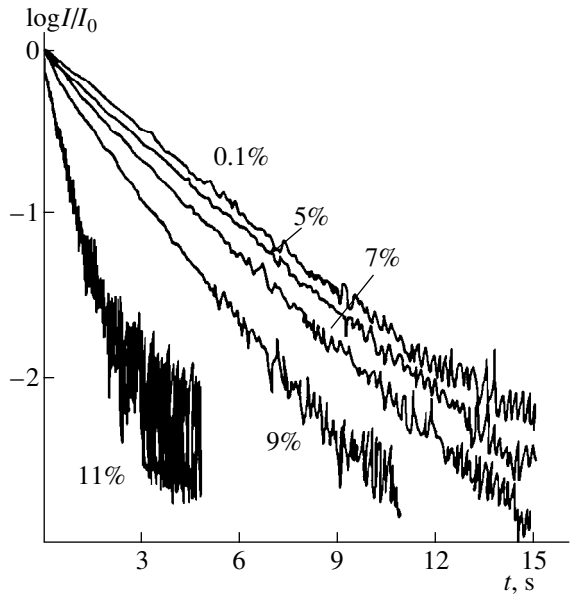

Fig. 16. Phosphorescence decay kinetics for naphthalene in isotopically mixed molecular crystals at its different concentrations. T = 1.7 K [108].

assumes the form

$$K(t) = S\chi(\partial q/\partial t). \quad (28)$$

It was shown [102, 103] that the time dependence of the average number q of different sites attended by an excitation for the critical and higher concentrations can be defined as

$$q(t) \propto t^{d_s/2}, \quad (29)$$

where d_s is the spectral dimensionality of the system [102, 103]. In this case, we have

$$K(t) \propto t^{d_s/2-1}. \quad (30)$$

Klymko and Kopelman [104] proposed that such a time dependence for the rate coefficient can be used as a rough approximation in the range of concentrations lower than the critical value. Consequently, we can write

$$K(t) = K_0 t^{-h}, \quad 0 \le h \le 1, \quad h = 1 - d_s'/2, \quad (31)$$

where K_0 is a constant and the parameter h characterizes the degree of local inhomogeneity of the medium. The lower limit $h = 0$ corresponds to the limit of a homogeneous medium, while the upper limit $h = 1$ corresponds to motion in systems with zero dimensionality, i.e., miniclusters. Figure 15 taken from [105] presents the $K(t)$ dependence for various values of h. It can be seen that, for nonzero values of h, the $K(t)$ dependence decreases rapidly for small values of time.

According to Klymko and Kopelman [104], the general expression for donor decay can be reduced to

$$I(t) = I_0 \exp\left[-\left(\frac{t}{\tau}\right)^{\frac{d_s'}{2}} - \frac{t}{\tau_0}\right], \qquad \tau = \left(\frac{2K_0}{d_s'}\right)^{\frac{-2}{d_s'}}. \quad (32)$$

It was proven [106, 107] on the basis of the model of continuous-time random walks that, in the case of capture of an excitation migrating over a percolation cluster by a trap, the luminescence decay over small time intervals can be described by a relationship similar to Eq. (32). According to Kopelman in Argyrakis [101], an exponential decay of donor luminescence can be expected only for a homogeneous three-dimensional space. In other cases, the decay is not exponential. The departure of decay from the exponential dependence is the larger, the stronger the inhomogeneity of the medium.

In spite of such a comprehensive theoretical analysis of this problem, the results of experimental investigations of donor phosphorescence decay in isotopically [108] and chemically [28] mixed molecular crystals are contradictory and prove that the decay law is determined, to a considerable extent, by the properties of the medium. It can be seen from Fig. 16 that isotopically mixed naphthalene crystals exhibit an exponential decay at the initial stage with an insignificant deviation for long time intervals [108], which contradicts the results of the theoretical analysis [101]. A chemically mixed crystal of dichlorobenzene in dibromobenzene exhibits a nonexponential decay for short time intervals, which becomes exponential in the limit of long time intervals (Fig. 17) [28].

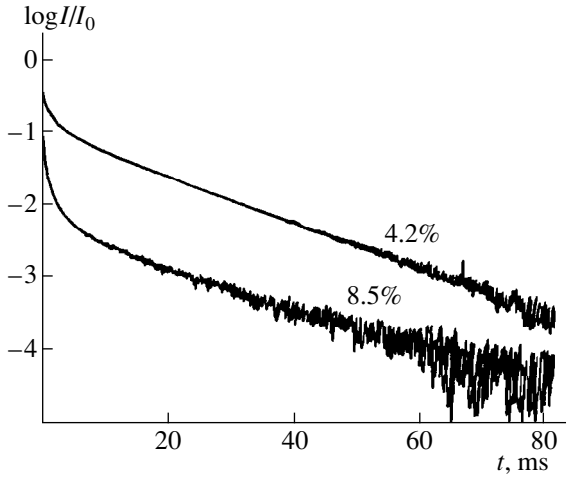

Fig. 17. Phosphorescence decay kinetics for dichlorobenzene in a molecular crystal of dibromobenzene at its different concentrations. T = 4.2 K [28].

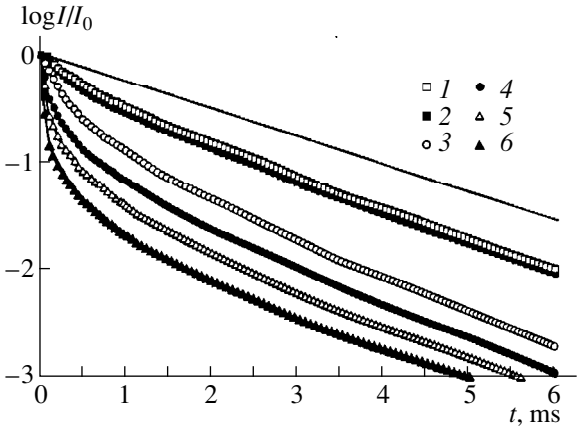

Fig. 18. Phosphorescence decay kinetics for benzaldehyde in ethanol at T = 77 K. Benzaldehyde concentration, mol/l: (solid line) 0.02, (*1*, 2) 2, (*3*, *4*) 3.5, and (*5*, *6*) 5. Relative concentration of 1-bromonaphthalene: (*1*, *3*, *5*) 0 and (*2*, *4*, *6*) 10^{-2} [109].

3.2. Kinetics of Phosphorescence Decay in Disordered Media

Taking into account the fact that the migration of electron excitation energy in a solid solution of benzaldehyde in ethanol under steady-state excitation is correctly described within the cluster formalism and the concepts of the percolation theory, this system was chosen in [109] for experiments with a time resolution aimed at studying the kinetics of energy transport in inhomogeneous media.

The decay of phosphorescence of benzaldehyde in samples with a low ($\sim 10^{-2}$ mol/l) concentration at 77 K follows an exponential law with a lifetime τ_0 = 1.7 ms (Fig. 18). Highly concentrated samples exhibit a departure of the donor decay kinetics from the exponential law. This departure and the decay rate increase with a rise in the benzaldehyde concentration. In order to analyze the experimental curves describing the decay in the model presented above and to determine the values of d_s and τ, we used the graphical method, which was proposed in [28] and involved the plotting of the dependence of $\log(-\ln I(t)/I_0)$ on $\log t$. Figure 19 shows such dependences for several samples. The values of d_s and τ obtained in this way for all the samples are presented in Table 1. An increase in the concentration of donors or acceptors reduces the value of τ. This fact indicates an increase in the efficiency of excitation capture by a trap. At the same time, this leads to a decrease in the parameter d_s. However, the cluster model of energy migration predicts the opposite dependence of the effective spectral dimensionality on the donor concentration. Indeed, the simulation of random walks over a random lattice in the range of concentrations above the critical value revealed a transition from fractal to uniform properties upon an increase in the concentration [110, 111]. This means that the effective spectral dimensionality increases and tends to the limiting value equal to 2.

Borczyskowski and Kirski [28] observed a similar situation for the transport of triplet excitations in chemically mixed molecular crystals. These authors assumed that an increase in the activator concentration leads to an increase in the system disorder. This approach can be described as follows. It was mentioned above that the method of continuous-time random walks as applied to the donor luminescence decay kinetics in the case of migration over a percolation cluster led to an expression similar to Eq. (32). However, this expression took into account only the geometrical parameters of the system. In real systems, the energy factor is as important as the geometrical factor. Klafter and Blumen [112] carried out a theoretical analysis taking into account both these fac-

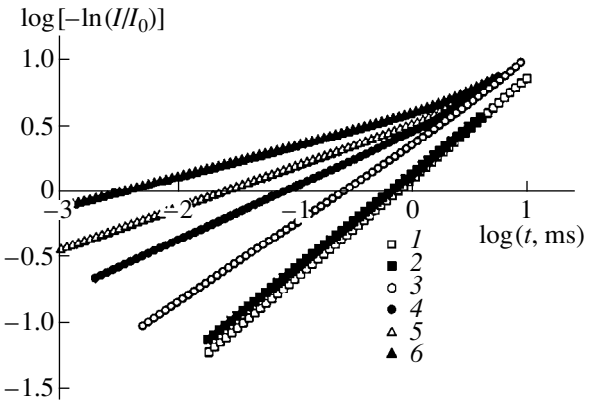

Fig. 19. Dependence of $\log[-\ln(I(t)/I_0)]$ on $\log t$ for benzaldehyde-1-bromonaphthalene in ethanol. Notation is the same as in Fig. 18 [109].

Table 1. Parameters d_s and τ obtained from processing of experimental data by formula (32)

C_D, mol/l	τ, 10^{-6} s		d_s	
	$S = 0$	$S = 10^{-2}$	$S = 0$	$S = 10^{-2}$
1.5	1120	1000	1.56	1.48
2.0	794	759	1.52	1.4
2.5	631	479	1.32	1.28
3.0	447	263	1.22	1.02
3.5	289	87	1.18	0.8
4.0	200	38	1.04	0.68
5.0	29	4	0.62	0.5

tors and found that formula (32) in this case assumes the form

$$I(t) = I_0 \exp\left[-\left(\frac{t}{\tau}\right)^{Y\frac{d_s'}{2}} - \frac{t}{\tau_0}\right], \quad 0 < Y < 1, \tag{33}$$

where Y is a parameter of the hopping time distribution associated with the energetic disorder in the system [113]. In chemically mixed crystals of dichlorobenzene in dibromobenzene, the inhomogeneous broadening strongly depends on the concentration of the activator (dichlorobenzene) and increases with a rise in the concentration from 10 cm^{-1} in diluted solutions to 100 cm^{-1} in concentrated solutions [27]. Such a strong increase in energetic disorder in the system decreases the parameter Y. This effect is only responsible for a decrease in the effective spectral dimensionality (which is determined from the experimental curves describing the donor luminescence decay) upon an increase in the concentration. Unfortunately, this approach is inapplicable to the system under investigation, since it does not exhibit such a strong dependence of inhomogeneous broadening of energy levels on the benzaldehyde concentration.

Apart from chemically mixed molecular crystals, such a situation was also observed in an analysis of the dynamics of a triplet excitation in binary organic glasses (benzophenone in methyl tetrahydrofuran or durane) [66]. Since the spread of the energy levels in these systems is much larger than the thermal activation energy for the triplet excitation transfer between benzophenone molecules, Lange *et al.* [66] proposed that the dynamics of triplet donor excitation should be regarded as a pure energy relaxation. In this case, the rate coefficient for the capture of an excitation by a trap is also a function of time and can be represented in the form [114]

$$K(t) = K_0 t^{\alpha - 1}, \quad \alpha = [(\sigma/4kT) + 1]^{-1}, \tag{34}$$

where σ is the width of the Gaussian density distribution for the excited state. A comparison of this formula with relationships (31) shows that the donor luminescence decay in this case can also be described by a relationship of the type (32), but the parameter $d_s/2$ should be replaced by the parameter α. An analysis of experimental results for benzaldehyde in ethanol and the results obtained in [66] by using the model under investigation leads to the following conclusions. According to Table 1, a change in the benzaldehyde concentration from 2.5 to 5 mol/l should be accompanied by a doubling of the inhomogeneous broadening. At the same time, spectroscopic data for the given sample disagree with these results. The same pattern was observed in [66]. Next, an increase in the acceptor concentration in both systems leads to a decrease in the parameter α, which corresponds to an increase in inhomogeneous broadening in the system. This conclusion contradicts the actually observed situation, since the introduction of acceptors into the system with such a low acceptor concentration weakly affects the distribution of the donor energy levels. Finally, according to formula (34), the dependence of the parameter α on the activator concentration in the system is associated only with a change in the inhomogeneous broadening of energy levels. At the same time, the results obtained by Ries and Bassler [115] by using the Monte Carlo method indicate that the geometrical properties of the system, which vary with the concentration, also significantly affect the value of α.

In systems with a large inhomogeneous broadening of energy levels at low temperatures, the kinetics of donor luminescence decay under the conditions of energy migration can be described by the following expression [116]:

$$I(t) = a_1 F_1(t) + a_2 F_2(t) + a_3 F_3(t). \tag{35}$$

Here, the function $F_1(t)$ describes the decay of molecules (characterized by a high energy of the excited state), from which a directed energy transfer takes place. The existence of this process and its influence on the kinetics are confirmed by the dependence of the decay rate on the luminescence wavelength over short intervals of time. The existence of a directed transfer in the samples used in the experiments is also confirmed by the evolution of the luminescence spectrum with time. Concentrated samples display a red shift in the phosphorescence spectrum of benzaldehyde with time. The magnitude of this shift increases with the activator concentration and amounts to 220 cm^{-1} for a sample with a benzaldehyde concentration of 4 mol/l. The function $F_2(t)$ describes the decay for molecules forming the subsystem over which the energy migration actually takes place. The results of experiments under the conditions of steady-state excitation show that the power of this subsystem increases with the concentration. The function $F_3(t)$ describes the decay for molecules with low energies of the excited state. These molecules themselves are traps at liquid nitrogen tempera-

ture and display a monomolecular decay. In the general case, the parameters a_i are functions of time, temperature, and the concentrations of the donor and the acceptor.

The cluster model of energy migration and all the conclusions following from it obviously pertain only to the fraction of molecules whose decay is described by the function $F_2(t)$. Consequently, we can expect an increase in the parameter d_s with a rise in the concentration only when $F_2(t)$ can be described by formula (32). However, the experimentally observed decay of $I(t)$ is determined by the functions $F_1(t)$ and $F_2(t)$ over short periods of time and by the function $F_3(t)$ over long time intervals. Even if we assume that $F_2(t)$ follows an exponential law with $\tau < \tau_0$, $I(t)$ will still be described by a nonexponential function. Consequently, using formula (32), we obtain a value of $d_s < 2$. The rate of directed transfer increases with the concentration. The rate of excitation capture by a trap also increases in this case. As a result, the decay rate $I(t)$ should increase with the donor concentration over small periods of time. At the same time, in the limit of long time intervals, the function $I(t)$ remains close to an exponential function with the decay time τ_0, which is actually observed in experiments. A similar behavior can also be expected for an increase in the trap concentration. Obviously, the contributions from the processes described above cannot be separated in an analysis of donor phosphorescence decay.

Thus, the observed contradiction between the experimental data and the cluster model of energy migration is due to a large inhomogeneous broadening of triplet energy levels of the donor in the system under investigation. This contradiction can be diminished if we go over to higher temperatures at which a decrease in the contribution from the functions $F_1(t)$ and $F_3(t)$ to the overall kinetics of luminescence decay of the system can be expected.

In [117, 118], we chose a solution of diacetyl in PMMA as an object of investigations in the high-temperature range, because diacetyl is known to be virtually the only exception in the family of ketone molecules which displays an exponential phosphorescence decay in PMMA at room temperature. Figure 20 shows that phosphorescence quenching in diacetyl in the presence of an acceptor of the triplet energy at room temperature is characterized by a critical dependence on the donor concentration in the system.

The processing of the experimental curves describing phosphorescence decay for diacetyl in PMMA [119] at room temperature led to the effective spectral dimensionality ranging from 0.9 to 1.16, which agrees with the theoretical value of the effective spectral dimensionality of the system at the critical point of the three-dimensional space. The value of d_s increases in this case with both the donor and acceptor concentrations, which is in accord with the predictions of the theory for dynamic percolation in the system.

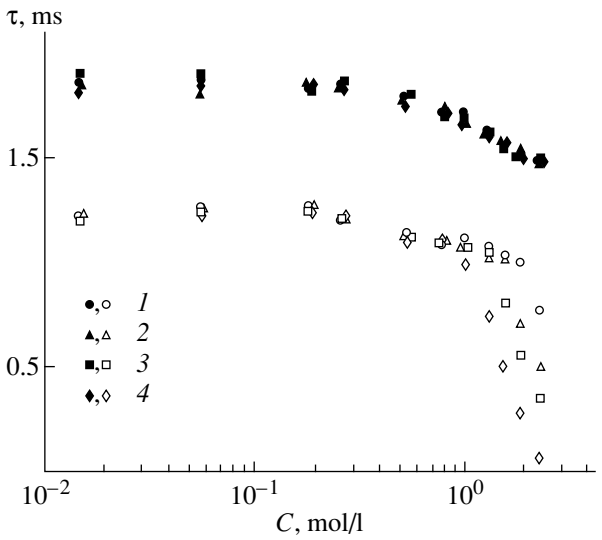

Fig. 20. Dependence of phosphorescence decay time for diacetyl on its concentration in PMMA. Concentration of anthracene, mol/l: (*1*) 0, (*2*) 3×10^{-4}, (*3*) 1.8×10^{-3}, and (*4*) 8.3×10^{-3}. Dark symbols correspond to $T = 77$ K, and light symbols, to 293 K [118].

The results of experiments also proved that the kinetics of phosphorescence decay in diacetyl becomes close to exponential over time intervals much longer than the lifetime of a triplet excitation. The decay rate increases with both donor and acceptor concentrations for long time intervals, which significantly differs from the situation observed for benzaldehyde in ethanol at 77 K. Havlin *et al.* [120] proved that the average value of the diffusion coefficient $D(t, C) \equiv \langle R^2(t)\rangle/t$ for random walks $R(t)$ at concentrations $C > C_c$ does not depend on time in the limit of long time intervals, and its value is defined as

$$D(t \longrightarrow \infty, C) \propto (C - C_c)^{\mu}, \quad C < C_c, \tag{36}$$

where μ is the critical index determined only by the dimensionality of space [58]: $\mu = 1.1$–1.3 in the two-dimensional case and $\mu = 1.5$–1.7 for three dimensions. It should be noted that relationship (36) is valid only for concentrations only slightly exceeding the critical value. On the other hand, the coherent potential method and the self-consistent graphical method lead to another expression for the dependence of the diffusion coefficient for an excitation in disordered media on the activator concentration in the limit of long time intervals in the case of the exchange-resonant interaction between molecules [9]:

$$D(t \longrightarrow \infty, C) \propto C^{-2/3}\exp\left(-\frac{2A}{C^{1/3}L}\right), \tag{37}$$

where L is the effective Bohr radius appearing in formula (8), and A is the constant equal to 0.83 in the method of coherent potential and 0.78 in the case of the self-consistent graphical approach. The validity of this

formula is substantiated in [9] by the fact that a similar relationship was derived in the percolation theory for the dependence of the electron conductivity of strongly inhomogeneous media on the concentration of impurity centers. In the two expressions, even the values of the coefficient A virtually coincide (according to the percolation theory, $A = 0.87$ [121]). However, in spite of the fact that the dependence of electron transport rate (in the case of electron conductivity) on the separation between donor centers virtually coincides with an analogous relationship for energy transport in the case of the exchange-resonant interaction, a considerable difference exists between these two processes. The lifetime of an electron is not limited. For this reason, the electron can jump over any distance with a nonzero probability. However, the excitation lifetime is limited, which is manifested in the existence of the maximum distance over which a jump can occur. Jumps over larger distances are ruled out. The expression for the dependence of the conductivity of the medium on the impurity concentration was obtained in the percolation theory for the case when the transport rate $k(r) = \text{const}$ over distances shorter than r_0 and $k(r) = 0$ over distances larger than r_0. In this case, the dependence of the system conductivity on the concentration of impurity centers is described by a relationship similar to expression (36) [121]. At the same time, the results of simulation of random walks over a percolation cluster above the percolation threshold for different-type dependences of the hopping time on distance (const, r, e^r, and 10^r) show [122] that the nature of transport in the limit of long time intervals is virtually independent of the formula describing the hopping time if the maximum distance beyond which the jumps cannot occur is set. All that has been said above suggests that relationship (36) is more suitable for describing the concentration dependence of the diffusion coefficient for an electron excitation in inhomogeneous media. In order to verify this assumption, the phosphorescence decay curves for diacetyl in PMMA in the range from 3 to 7 ms were approximated in [123] by an exponential law. Using the obtained values of decay time and the Stern–Volmer formula

$$\frac{1}{\tau} = \frac{1}{\tau_0} + K_d C_A, \tag{38}$$

we obtained the quenching rate constants K_d for various concentrations of diacetyl at the anthracene concentration $C_A = 7.5 \times 10^{-3}$ mol/l. The experimental results were analyzed by using the approaches described above. The obtained value of the critical index $\mu \approx 1.45$ was close to the theoretical value. However, a good agreement was also observed when the experimental data were described with the help of formula (37). The coincidence of the theoretical and experimental results in the latter case can be due to the smallness of the range of donor concentration in the system.

4. KINETICS OF ANNIHILATION OF TRIPLET EXCITATIONS IN DISORDERED MEDIA

Apart from the method of excitation capture by traps, the triplet–triplet annihilation (TTA) method is also widely used for studying the electron excitation energy transport over triplet energy levels of complex molecules. This method is most effective for studying the kinetics of energy transport in disordered media, since it has an important advantage over the method of capturing by traps. In the case of triplet–triplet annihilation, continuous time recording can be made for the concentration of triplet excitations through phosphorescence p, as well as the reaction rate through annihilation-induced delayed fluorescence df (proportional to the concentration of singlet excitations), which is proportional to the reaction rate. Consequently, in the study of delayed luminescence, the rate coefficient can be obtained directly for the TTA process, and its time dependence can be analyzed over any interval.

The importance of studying the kinetics of exciton reactions is also due to the fact that the majority of chemical reactions in nature as well as of reactions carried out by man are heterogeneous, i.e., occur in systems with effective dimensionality less than three. The most interesting are reactions occurring on or in fractal structures such as porous glasses, diffusion-controlled aggregates, or percolation clusters. Diffusion in such media differs considerably from the diffusion in a homogeneous Euclidean space, and its analysis has become a new tool for characterizing the fractal properties of inhomogeneous systems. The experiments involving diffusion require microscopic measurements below the optical resolution limit, while anomalous kinetics of reactions can be studied with the help of macroscopic measurements by studying the kinetics of exciton reactions. Consequently, exciton reactions make it possible to study the kinetics of transport in disordered media, polymers, and membranes [124, 125]. These reactions are a brilliant tool for analyzing the topology, morphology, and the structure of molecular aggregates, porous structures, and other media with confined geometry.

4.1. Fractal Properties of Delayed Luminescence in Solid Solutions of Organic Compounds

Annihilation of two triplet excitations leads to the emergence of a highly excited singlet state which rapidly transforms into the first excited singlet state:

$$T_1 + T_1 \longrightarrow S^* \longrightarrow S_1. \tag{39}$$

In view of the short lifetime, the state S_1 decays rapidly by emitting a photon. This gives rise to annihilation-induced delayed fluorescence.

The intensity $I_{df}(t)$ of annihilation-induced delayed fluorescence at any instant t is proportional to the number $N_{\text{ann}}(t)$ of annihilation events:

$$I_{df}(t) \propto N_{\text{ann}}(t). \tag{40}$$

In turn, the number of annihilation events is determined by the following relation:

$$N_{\text{ann}}(t) \propto (dp/dt)_{\text{ann}}, \tag{41}$$

where $p(t)$ is the density of triplet states.

The classical rate coefficient of the reaction of triplet–triplet annihilation does not depend on time. However, inhomogeneous systems display departures from the classical behavior. For these systems, the rate coefficient for the TTA reaction is not constant any longer, which leads to a complex relationship between the decay of phosphorescence and annihilation-induced delayed fluorescence. It was proven in the previous section that the rate coefficient for disordered systems is analyzed in connection with the number $q(t)$ of various sites visited by an excitation during random walks, and its time dependence is described by relationship (31). Consequently, the expression for the triplet–triplet annihilation reaction in inhomogeneous systems has the form

$$-(dp/dt)_{\text{ann}} = t^{-h}p^2, \quad 0 \le h \le 1. \tag{42}$$

Combining formulas (40)–(42), we obtain the following expression describing the annihilation-induced delayed fluorescence with the density of triplet excitations:

$$I_{df}(t) \propto k_{\text{ann}} t^{-h} p^2(t). \tag{43}$$

The time dependences $I_{df}(t)$ and $p(t)$ can be obtained experimentally by detecting the decay of annihilation-induced delayed fluorescence and phosphorescence, respectively. The time dependence $k(t)$ of the rate coefficient for the triplet–triplet annihilation reaction can be derived from the expression

$$I_{df}/I_p^2 \propto k(t). \tag{44}$$

The plot of the $\log(I_{df}/I_p^2)$ vs. $\log t$ is assumed to be linear with a slope $-h$.

The fractal nature of the decay of annihilation-induced delayed fluorescence, which is described by relationship (43), was observed for mixed naphthalene crystals [126] and for naphthalene in PMMA [127]. However, for naphthalene in PMMA, experiments were made only for concentrations higher than the critical value. In the case of mixed molecular crystals, such experiments were made in the range of activator concentrations higher than the critical value as well as lower than this value. In both systems, an increase in the concentration of the activator led to a transition to the classical behavior when the value of h tended to zero. At the same time, the parameter $h = 0.5$ was observed for mixed naphthalene crystals even for concentrations $C \ll C_c$, which contradicts the theory. Indeed, according to formula (4), the average number of molecules in the cluster decreases very rapidly with a decrease in the concentration. Consequently, only miniclusters exist in the range of concentrations considerably lower than the critical value, and the parameter h close to unity should be observed in this case.

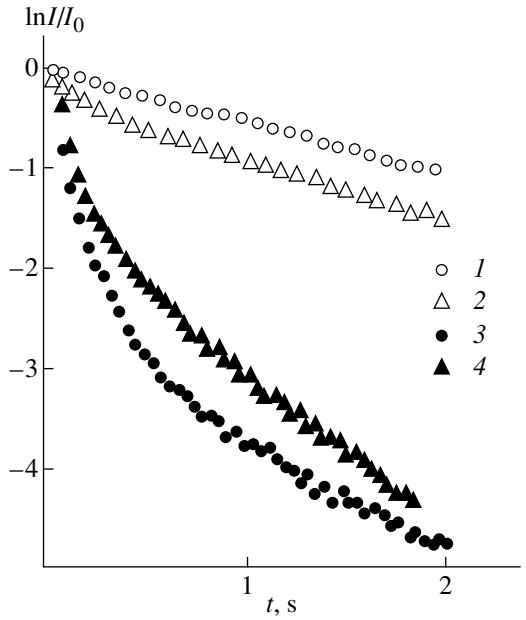

Fig. 21. Kinetics of delayed luminescence of chrysene in polystyrene: (*1*, *2*) phosphorescence, (*3*, *4*) annihilation-induced delayed fluorescence. Chrysene concentration, mol/l: (*1*, *3*) 0.15 and (*2*, *4*) 0.3 [129].

The results of analysis of the kinetics of delayed luminescence of chrysene in a polystyrene matrix at $T = 77$ K are presented in [128]. The delayed luminescence of chrysene in the polystyrene matrix contains two bands: the long-wavelength band is phosphorescence, while the short-wavelength band, which has the same spectrum as for fluorescence, corresponds to annihilation-induced delayed fluorescence. Figure 21 shows the luminescence decay kinetics in various parts of the luminescence spectrum and for various concentrations of the activator. The exponential decay of phosphorescence is observed for the chrysene concentration $C \le 0.15$ mol/l, and the luminescence lifetime is 1.7 s. As the concentration increases further, the decay of phosphorescence at the initial stage does not obey an exponential law any longer. The decay kinetics of annihilation-induced delayed fluorescence also depends on the concentration and remains nonexponential for all investigated concentrations.

Figure 22 shows the time dependence of I_{df}/I_p^2 in double logarithmic scale. It can be seen from the figure that the experimental points fit well on the straight lines whose slope is equal to the parameter h. Table 2 shows the results of processing of experimental data by formula (44). For low concentrations of chrysene, the values of h are close to unity, indicating a strong microscopic inhomogeneity of the medium. In this case, delayed fluorescence appears as a result of annihilation of excitations belonging to miniclusters formed by two

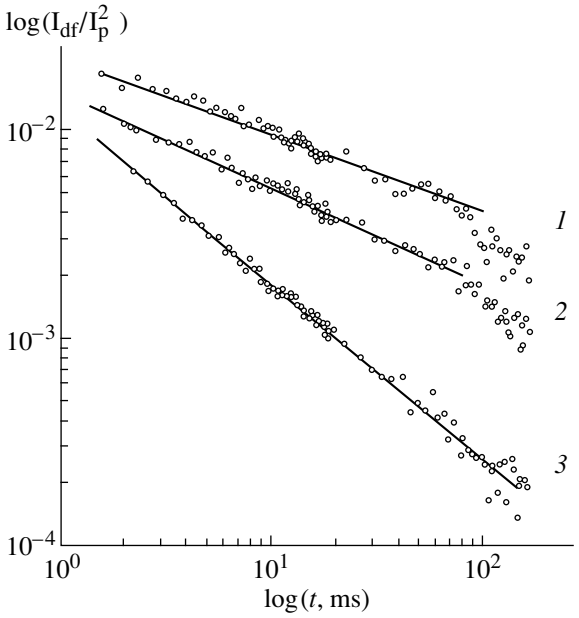

Fig. 22. Dependence of $\log(I_{df}/I_p^2)$ on $\log t$ at different concentrations of chrysene, mol/l: (*1*) 0.3, (*2*) 0.25, and (*3*) 0.15. Straight lines correspond to the parameters h at which the experimental data are described by relationship (31) [129].

molecules. With increasing concentration, the value of h decreases and assumes the value $h \approx 0.4$, which corresponds to $d_s \approx 1.2$ at the maximum concentration $C = 0.3$ mol/l. This value is close to the effective spectral dimensionality of a three-dimensional system at the critical point. Such a behavior for a given concentration is also preserved for time periods longer than the lifetime of the triplet state [129]. This leads to the conclusion that this concentration is close to the critical value, since the fractal properties of the system are preserved for this concentration even in the limit of long time periods [110, 111]. This behavior can be explained by the fact that a percolation cluster is a purely fractal object only at the critical point [130].

The results obtained for samples with a chrysene concentration $C < 0.15$ mol/l agree well with the results

Table 2. Parameters h for different concentrations of chrysene in polystyrene

C, mol/l	h
0.01	0.84
0.1	0.84
0.15	0.88
0.25	0.5
0.3	0.4

of investigation of annihilation-induced delayed fluorescence of solid solutions of aromatic hydrocarbons in low-molecular solvents [131]. Efremov *et al.* [131] explained the nonexponential annihilation-induced decay of delayed fluorescence in solid solutions on the basis of formation of molecular pairs in which annihilation takes place. Its intensity is determined not by the average concentration n_T of triplet-excited molecules, but by a relatively small number of close annihilating pairs:

$$I_{df}(t) \propto n_T^2(t)\int w_{TTA}(r)g(r, t)r^2 dr, \qquad (45)$$

where $w_{TTA}(r)$ is the TTA rate leading to a transition of a pair to the first singlet state and $g(r, t)r^2$ is the distribution function for triplet-excited pairs over their size r. For a strong dependence of the annihilation rate on r, pairs of different sizes must contribute to the annihilation-induced delayed fluorescence over different time intervals. This means that the rate coefficient for the triplet–triplet annihilation varies with time, and the kinetics of annihilation-induced delayed fluorescence (especially at early stages of decay) should be nonexponential even in the case of an exponential decay of phosphorescence. An analysis of experimental results proved that, at early stages of decay ($t < \tau_T$), the kinetics of annihilation-induced delayed fluorescence is successfully described by a power dependence

$$I_{df}(t) \propto t^{-\xi}, \quad \xi = 0.8\text{–}0.9. \qquad (46)$$

An analysis of annihilation-induced delayed fluorescence and phosphorescence under the conditions of bimolecular quenching of excitations [132–134] led to the value $R_0 = 55 \pm 5$ Å for the critical radius of energy transport for the TTA reaction, which is much higher than the value of similar parameter for the triplet–triplet (T–T) energy transport according to the exchange mechanism ($R_0 \approx 10$–20 Å) [3]. This led the authors of [132–134] to the conclusion that the triplet–triplet annihilation is a considerably longer-range process than the T–T energy transport.

Gulis *et al.* [135] proposed that such a large value of the critical transport radius can be due to triplet–triplet annihilation following the resonance-inductive mechanism. Such a process is possible in principle due to a high probability of intercombination conversion $T_n \longrightarrow S_n$ for a number of compounds. In this case, TTA can be regarded as a pair transition in which the acceptor transition is $T_1 \longrightarrow T_n$, and annihilation-induced delayed fluorescence emerges as a result of the $T_n \longrightarrow S_n \longrightarrow S_1$ transition. A theoretical model was developed for describing the kinetic and steady-state characteristics of annihilation-induced delayed fluorescence for the triplet–triplet annihilation according to the resonance-inductive mechanism, and a good agreement between the experimental data obtained for erythrosine solution in ethylene glycol and the results of the theoretical model was observed in [136].

Nevertheless, the pair mechanism of emergence of annihilation-induced delayed fluorescence should obviously play a decisive role at low concentrations of the activator, irrespective of the origin of triplet–triplet annihilation. As the activator concentration in the medium increases, conditions for energy transport are created in the medium, which is disregarded in the pair model. The results obtained in [129] for a sample with the chrysene concentration $C = 0.3$ mol/l make it possible to exactly determine the origin of a migrating excitation. For the given concentration of chrysene, the obtained value of the parameter h corresponds to the formation of an infinitely large cluster of activator molecules in the system. Proceeding from this value and using formula (17), which relates the critical concentration to the connectivity radius for molecules in a cluster, we find that the connectivity radius $R = 15.3$ Å. This value correlates well with the critical radius $R = 16$ Å for the energy transport under similar conditions, which was determined for a molecule of 1,2-benzanthracene with a close size and molecular mass [137].

4.2. Kinetics of Transport of Triplet Excitation in Solid Organic Media

The fractal model described above can be used for describing the decay kinetics of phosphorescence not only for solutions of organic compounds, but also for solid disordered media. According to the cluster model, it is the geometry of clusters formed by activator molecules that determines the kinetics of energy transport. The lack of structural order in disordered solids leads to strong inhomogeneous broadening of energy levels. At low temperatures for which the value of kT is considerably smaller than the spread in the energy levels, the topology of the subsystem of molecules over which the effective migration of excitation takes place after a transition of the system to the state of dynamic equilibrium differs significantly from the topology of the system as a whole. This difference is the stronger, the lower the temperature and the higher the degree of energetic disorder. The topology of this subsystem of molecules considerably affects the kinetics of energy transport. This effect was observed in the modeling of random walks over an energy-disordered lattice [138] and in the study of the decay kinetics of delayed luminescence of disordered naphthalene [139].

Apart from the approach described above, the model of stochastic transport in disordered media, which was developed by Grunewald *et al.* [140] within the effective-medium approximation with due regard for the asymmetry of the hopping rate between molecules, is also used for describing the dynamics of electron excitation in disordered solids. In this approach, it is assumed that the time dependence of rate coefficients is determined exclusively by energy relaxation. As in the previous approach, the time dependence of the rate coefficients is described by a power law in the form (34). This model was used for interpreting the experimental data obtained for a number of organic glasses [141, 142].

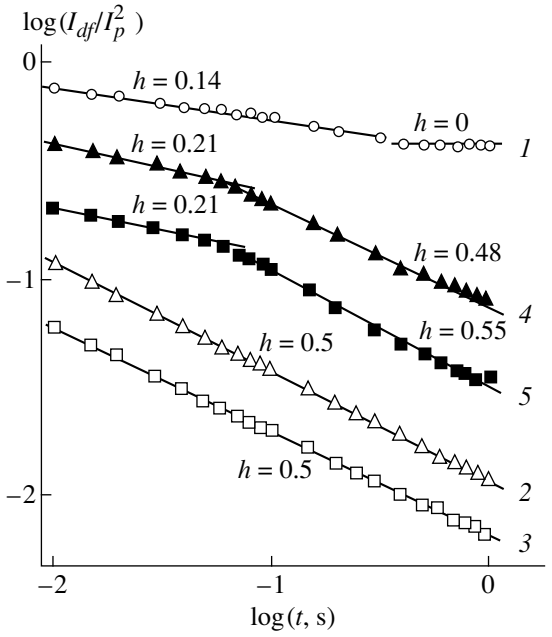

Fig. 23. Dependences of $\log(I_{df}/I_p^2)$ on $\log t$ for different chrysene samples (*1–3*) before and (*4, 5*) after their annealing: (*1*) crystallization from benzene, (*2, 4*) rapidly cooled melt, and (*3, 5*) deposition from vapor [143].

The kinetics of energy transport was studied in [143, 144] by the method of triplet–triplet annihilation on the samples of disordered chrysene obtained by the following three techniques: crystallization from benzene, rapid cooling of its melt, and deposition of its vapor. Figure 23 shows the dependences of $\log(I_{df}/I_p^2)$ on $\log t$. The curve for the sample obtained by crystallization from solution has a linear segment with a slope corresponding to $h = 0.14$. For larger values of time, a transition to the classical behavior ($h = 0$) is observed. Thus, we are dealing with a transition in time from the fractal behavior to the homogeneous case. Such a pattern was observed in the modeling of random walks on a percolation cluster above the percolation threshold [110, 111]. Such a cluster is known to be a homogeneous fractal; i.e., it possesses fractal properties on a small spatial scale and is homogeneous on a large scale. The obtained results lead to the assumption that the topology of the system of chrysene molecules over which triplet excitations migrate until the instant of their annihilation coincides with the topology of a homogeneous fractal.

Let us consider these results in the model of stochastic transport. The parameter $\alpha = 0.86$, which was obtained from the slope of the linear segment, gives, in accordance with formula (34), the value $\sigma = 86$ cm^{-1}, which in turn corresponds to the width $\Delta\omega = 210$ cm^{-1} of a inhomogeneously broadened band in the lumines-

cence spectrum of the activator ($\sigma = (2\sqrt{2\ln 2})^{-1}\Delta\omega$ [114]). This value is very close to the band width in the phosphorescence spectrum of this sample, which corresponds to a transition between zeroth levels of an excited and ground state. However, the behavior over long time periods, namely, an increase in α to unity, can hardly be explained on the basis of this model. Ries and Bassler [115] indeed observed an increase of α with time for amorphous benzophenone. As a matter of fact, $\alpha = 1$ corresponds to $\sigma = 0$. Such a situation is possible in the given model only for energy migration in a system with a crystalline structure. However, the annihilation of excitations, in view of a very high rate of their migration in molecular crystals, should determine the kinetics of delayed fluorescence at an early stage of decay rather than in the limit of long time intervals.

After the experiments, the sample was melted under vacuum and rapidly cooled to room temperature. This procedure leads to a considerable change in the decay kinetics of its delayed luminescence. The phosphorescence decay becomes closer to an exponential law, and the decay rate of annihilation-induced delayed fluorescence increases. The observed decrease in the efficiency of energy transport in this sample is due to the fact that, like other organic substances, a rapid cooling of chrysene melt or its vapor deposition at a low temperature leads to the formation of a nonequilibrium solid with large structural and energetic disorders.

Besides the sample of disordered chrysene formed as a result of rapid cooling of its melt, we also studied a sample obtained by deposition of chrysene vapor on a quartz substrate cooled by liquid nitrogen. The decay kinetics of its phosphorescence virtually coincides with that for the previous sample. The results of analysis of the kinetics of triplet excitation transport on the basis of the time dependence of the rate coefficient for the TTA reaction described by formula (44) for these samples are presented in Fig. 23. It can be seen that the parameters h obtained for the two samples of disordered chrysene prepared by the different methods are very close. An analysis of the dependences obtained for the two samples gives values of h close to 0.5. In the model of stochastic energy transport, an increase in the slope of the linear segment should correspond to an increase in the spread of energy levels. At the same time, a comparison of phosphorescence spectra for these samples, which were recorded under steady-state excitation as well as with a time resolution, demonstrates their closeness. This fact cannot be explained by the above model. At the same time, the observed result can be interpreted taking into account the change in the geometry of the subsystem of chrysene molecules, over which equilibrium migration of excitations takes place.

The change in the method of preparing the disordered sample weakly affects the energetic disorder, since it is determined in any case by the same structural defects. However, the variation of the excited-state energy upon a transition from one molecule to another significantly depends on this procedure. Obviously, we can expect a stronger variation for the second or third sample than for the first sample. The obtained value of the parameter h coincides with the value determined for a solution in polystyrene matrix for a chrysene concentration of 0.2 mol/l. We can rightfully assume that the energy surface of excited states of chrysene molecules may contain fractal-like canyons over which a triplet excitation migrates until its annihilation. The geometry of these canyons is close to the geometry of clusters formed by chrysene molecules in a low-concentration solution. However, the topology of these canyons might correspond to that of one-dimensional channels for which $h = 0.5$.

Sample annealing at $T = 200$°C leads to a considerable change in the decay kinetics of their delayed luminescence. The decay of phosphorescence, as well as of delayed fluorescence, becomes slower. An analysis of the curves presented in Fig. 23 leads to the conclusion concerning the changes in the samples caused by their annealing. It can be seen that the most significant changes in the energy transport kinetics take place at small values of time. For time intervals shorter than 50 ms, the slope of the linear segment decreases by half for all the three dependences. At the same time, it follows from Fig. 23 that the behavior of the dependence $\log(I_{df}/I_p^2)$ vs. $\log t$ for annealed samples in the time range 0.1–1 s is the same as for fresh samples. In the fractal model, the observed behavior can be explained taking into account the change in the energy transport topology in the system after annealing of the sample. Assuming that unannealed samples contain fractal-like or quasi-one-dimensional canyons over which the energy migration takes place, the decrease in the parameter h for short time intervals can be attributed to an increase in the width of these canyons as a result of annealing. Indeed, the decay kinetics of delayed fluorescence at the initial stage is determined by triplet excitations covering distances smaller than or comparable to the canyon width during their lifetime until annihilation. Hence, they exhibit a more consistent behavior. The value of h for such excitations decreases. Excitations whose annihilation occurs at a later time migrate over distances considerably longer than the canyon width. The properties of the medium determining the transport of such excitations do not change as a result of annealing.

4.3. Effective Topology of Electron Excitation Energy Transport in Thin Molecular Wires and Pores

Many chemical and biological processes occur in microscopic channels. Molecular or polymer chains, fibers, strings, and nets exist in most synthetic, natural, and biological organic systems. For this reason, the study of molecular reactions in microchannels is of practical importance. The kinetics of molecular reactions in channels can differ significantly from the kinet-

ics in a homogeneous space, since it is determined by the geometry and size of pores. The effect of the pore size on the decay kinetics of phosphorescence of naphthalene in polymeric membranes was studied in [145–148]. Figure 24 shows the dependences of the parameter h on the pore size at two temperatures. In these publications, the experimental data are interpreted from the viewpoint of possible realization of a low-dimensional (quasi-one-dimensional) energy transport in such systems. It should be noted that the entire body of experimental data on the kinetics of delayed fluorescence of naphthalene in various porous matrices (porous glasses, membranes, and filter paper) [145–148], namely, the dependence of the parameter α on the geometry and size of pores and its decrease upon heating, cannot be explained in the model of stochastic energy transport.

It was mentioned above that the difference between the fractal and quasi-one-dimensional topologies of a porous system is often not quite clear. On the one hand, the porous system is regarded as a random network of the type of a percolation cluster with a fractal dimensionality of the order of two, and on the other hand, it is treated as a quasi-one-dimensional structure. As a result of analysis of the kinetics of delayed luminescence of naphthalene in porous glass, Kopelman *et al.* [148] obtained the effective spectral dimensionality $d_s = 1.05$, which led them to the conclusion about the quasi-one-dimensional nature of its porous system.

The results of investigation of energy transport in porous glasses by the method of capturing in traps (see Section 2.2) demonstrate the invariability in the critical concentration of the donor upon the introduction of the system into the matrix. This can be due to the following two reasons. The topology of the glass used in the experiments is probably fractal rather than one-dimensional. On the other hand, it follows from Fig. 24 that one-dimensional transport in membranes with cylindrical pores is observed only when the displacement of an excitation during its lifetime is much larger than the pore size. In experiments on excitation capture by traps, the magnitude of displacement was only comparable to the pore size in the glass under investigation. In order to clarify this question, we studied [149, 150] the decay kinetics of delayed luminescence of chrysene in porous sodium borosilicate glass and in natural chrysotyl–asbestos minerals. Single-crystal layers of chrysotyl–asbestos are characterized by a natural curvature of 8.8 nm and are coiled inward and outward during their growth, thus forming fibers in the form of hollow cylinders with an outer diameter of 20–30 nm and an inner diameter of 2–10 nm. Bundles of fibers packed parallel to one another into a hexagonal lattice form transparent crystals whose length reaches a few centimeters. An analysis of the delayed luminescence of chrysene in the above matrices led to time dependences of the rate coefficient for the triplet–triplet annihilation reaction. The time dependence of chrysene in porous sodium borosilicate glass is linear with a slope corresponding

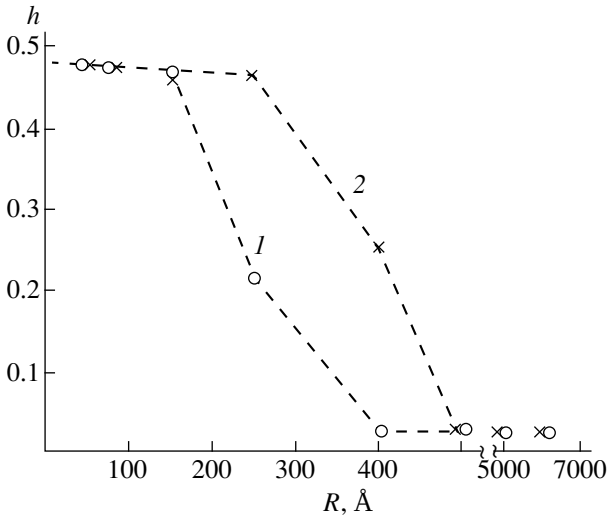

Fig. 24. Dependence of the parameter h for naphthalene in a polymer membrane on the pore radius. Temperature, K: (*1*) 4 and (*2*) 77 [146].

to $h = 0.35$ ($d_s' = 1.3$). According to [102, 103, 145], this value should be observed when the topology of the porous glass system corresponds to a three-dimensional percolation cluster with the fractal dimensionality $d_f \approx 2.5$, which completely coincides with the fractal dimensionality $d_f \approx 2.5$–2.7 of the glass used by us [151]. This conclusion contradicts the results presented in [145, 148]. However, this contradiction can be explained by different methods of sample preparation. In the experiments made in [149, 150], chrysene was introduced into the matrix by immersing the latter in its melt. In this case, the entire volume of pores in the matrix is filled by the substance, and the topology of the substance in the glass coincides with the topology of its pore network. In [145, 148], the substance was introduced into matrix by its sublimation under vacuum. In this case, molecules remain on the surface of pores. Investigations of such objects provide information about the topology of the substance deposited on the pore surface and not of the pore network of the glass. The results of analysis of energy transport between molecules on the surface of pores [151] reveal that this topology can indeed be one-dimensional.

In the case of chrysene in chrysotyl–asbestos, a linear dependence with a slope corresponding to the parameter $h = 0.45$ is observed on the time interval 0.03–1.2 s. This value indicates that, as expected, a one-dimensional energy transport takes place in this matrix.

The dispersive nature of energy transport in disordered media is due to structural disorder, and hence, the energetic disorder typical of such systems. Obviously, an increase in temperature should lead to a transition to the consistent (classical) behavior, for which the rate coefficient becomes independent of time.

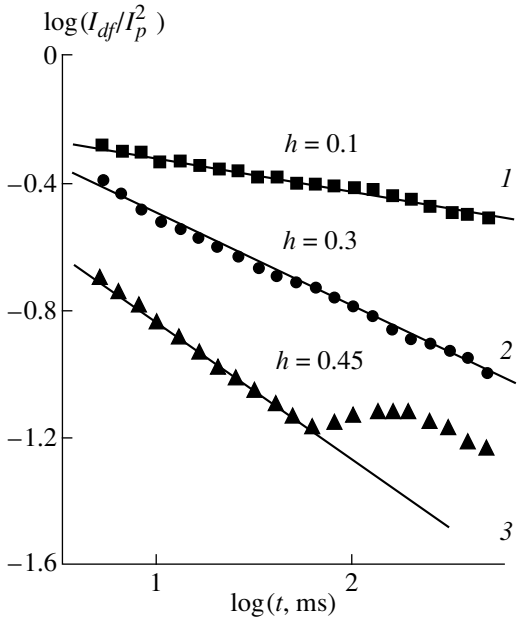

Fig. 25. Dependences of $\log(I_{df}/I_p^2)$ on log$t$ in the time interval 5 ms ≤ t ≤ 500 ms for different chrysene samples: (*1*) rapidly cooled chrysene melt, (*2*) chrysene in porous glass, and (*3*) chrysene in chrysotyl–asbestos. T = 95 K [150].

Such a transition was indeed observed for various disordered systems [152].

An increase in temperature is accompanied by a strong increase in the fraction of annihilation-induced delayed fluorescence in the overall spectrum of delayed luminescence of disordered chrysene; in this case, the phosphorescence decay rate also increases. An analysis of the phosphorescence decay kinetics for the given sample at 95 K (Fig. 25) suggests that the behavior of the system is very close to classical ($h \approx 0.1$) even at this temperature. Thus, the effect of energetic disorder on the kinetics of energy transport at this temperature is insignificant. For chrysene in porous glass at 95 K, a slower decay of phosphorescence and a faster decay of delayed fluorescence than in the previous sample are observed. The dependence of $\log(I_{df}/I_p^2)$ on log$t$ for chrysene in porous glass displays a linear segment with a slope corresponding to the parameter h = 0.3. The following two conclusions can be drawn from this result. First, since the temperature variation virtually does not affect the kinetics of triplet excitation transport of chrysene in porous glass, we can state that its disperse nature is just due to geometrical properties of the given system. Second, the effective topology of the porous system of silicate glass is actually close to the topology of a three-dimensional percolation cluster rather than to the quasi-one-dimensional topology.

A more complex pattern is observed for chrysene in chrysotyl–asbestos. Figure 25 shows that a linear dependence with a slope corresponding to the value of h = 0.45 is observed at t < 70 ms. However, at t > 70 ms, the time dependence of the rate coefficient for the TTA reaction of triplet excitations of chrysene in this sample changes drastically. It was shown [150] that this effect is associated with the impossibility to completely remove chrysene from the surface of fibers and from voids between them, whose size is much larger than the diameter of channels.

CONCLUSION

The above analysis of the results described in this review led to the following conclusions. A comparative analysis of the cluster model of energy transport and the Blumen–Silbey model without regard for the fine structure of the medium revealed that both models predict the critical dependence of the efficiency of energy migration on the concentration of the activator and also the dependences of its critical concentration on the lifetime of the excited state, temperature, and trap concentration. At the same time, these models describe in different ways the influence of these parameters and the dimensionality of energy migration on the dependence of the probability of excitation capture by a trap on the reduced donor concentration in the system. An analysis of the triplet excitation migration in mixed molecular crystals and in solid solutions of carbonyl compounds indicates a critical dependence of the energy transport efficiency on the activator concentration in the system. An increase in temperature and trap concentration does not smear the sharp critical transition, and the absolute value of the critical concentration decreases. The dependences of the probability of excitation capture by a trap on the reduced donor concentration, which are obtained for various temperatures and acceptor concentrations, exhibit a universal behavior; i.e., they coincide with one another and are determined by the critical indices whose values correspond to theoretical values over a wide concentration range. The problem of enveloping spheres in the percolation theory and the Blumen–Silbey model for the exchange-resonant interaction between molecules are used for deriving analytic expressions establishing a relation between the critical concentration of the activator in the system and the lifetime of the excited state, temperature, and trap concentration. An analysis of experimental data obtained on the basis of these models proves the necessity of the inclusion of the molecular clusterization effect for obtaining an adequate description of energy transport in disordered systems in the case of exchange-resonant and superexchange interactions between molecules.

The use of amorphous polymers and porous glasses as matrices shows that microscopic inhomogeneity of amorphous polymers and confined geometry of channels in porous glasses determine the effective topology of the space in which processes of percolation of electron excitation energy evolve. This effect manifests itself in the change in the critical indices, which determine the growth of clusters formed by activator mole-

cules and the concentration dependence of the efficiency of energy transport in the system.

The phosphorescence decay in solid solutions of organic compounds under the conditions of migration of energy and its capture by traps deviates from an exponential law. The deviation increases with the donor and acceptor concentrations. An analysis of experimental results shows that the nonexponential decay of phosphorescence at low temperatures is due not only to spatial inhomogeneity of the medium, but also to a large (compared to kT) inhomogeneous broadening of energy levels, which is typical of solid solutions of organic compounds. At high temperatures, the phosphorescence decay and the dependence of the diffusion coefficient for triplet excitations on the concentration of activator are correctly described by the cluster model of energy transport in inhomogeneous media.

The kinetics of annihilation-induced delayed fluorescence of complex molecules in solid solutions is also nonexponential. The experimental results are successfully described by the model with time-dependent rate coefficient for triplet–triplet annihilation. At low concentrations of the activator, the annihilation-induced delayed fluorescence emerges as a result of annihilation of triplet excitations in molecular pairs formed in the course of sample preparation. However, as the concentration increases, conditions for energy transport are created, and, in this case, the kinetics of annihilation-induced delayed fluorescence is determined by the fractal properties of the system over which excitations migrate until their annihilation. The energy transport in disordered solids is dispersive, i.e., depends on time. The time dependence of the rate coefficients can be described in the fractal model accounting for the geometry of the molecular subsystem over which the equilibrium migration of excitations occurs until their annihilation. The geometry of this subsystem of molecules is determined by the relationship between kT and the inhomogeneous broadening of energy levels, as well as by the method of sample preparation. As the temperature increases, disordered media experience a transition to a homogeneous energy transport. In the presence of a substance in porous matrices, the kinetics of energy transport is determined by the topology of their channels and only slightly depends on temperature.

REFERENCES

1. R. J. Elliott, J. A. Krumhansl, and P. L. Leath, Rev. Mod. Phys. **46**, 465 (1974).
2. I. M. Lifshits, S. A. Gredeskul, and L. A. Pastur, *Introduction to the Theory of Disordered Systems* (Nauka, Moscow, 1982; Wiley, New York, 1988).
3. V. L. Ermolaev, E. N. Bodunov, E. B. Sveshnikova, and T. A. Shakhverdov, *Nonradiative Energy Transfer of Electronic Excitation* (Nauka, Leningrad, 1977).
4. V. M. Agranovich and M. D. Galanin, *Electronic Excitation Energy Transfer in Condensed Matter* (Nauka, Moscow, 1978; North-Holland, Amsterdam, 1982).
5. M. D. Galanin and I. M. Frank, Zh. Éksp. Teor. Fiz. **21**, 114 (1951).
6. M. D. Galanin, Zh. Éksp. Teor. Fiz. **21**, 126 (1951).
7. Th. Forster, Ann. Phys. **2**, 55 (1948).
8. D. L. Dexter, J. Chem. Phys. **21**, 836 (1953).
9. E. N. Bodunov, Opt. Spektrosk. **74**, 518 (1993).
10. E. N. Bodunov, Opt. Spektrosk. **84**, 540 (1998) [Opt. Spectrosc. **84**, 350 (1998)].
11. R. Kopelman, in *Spectroscopy and Excitation Dynamics of Condensed Molecular Systems*, Ed. by V. M. Agranovich and R. M. Hochstrasser (North-Holland, Amsterdam, 1983; Nauka, Moscow, 1987).
12. R. Kopelman, E. M. Monberg, and F. W. Ochs, Chem. Phys. **19**, 413 (1977).
13. E. M. Monberg and R. Kopelman, Mol. Cryst. Liq. Cryst. **57**, 271 (1980).
14. R. Kopelman, E. M. Monberg, F. W. Ochs, and P. N. Prasad, J. Chem. Phys. **62**, 292 (1975).
15. R. Kopelman, J. Phys. Chem. **80**, 2191 (1976).
16. D. C. Ahlgren and R. Kopelman, Chem. Phys. Lett. **77**, 135 (1981).
17. H. K. Hong and R. Kopelman, J. Chem. Phys. **55**, 5380 (1971).
18. V. K. S. Shante and S. Kirkpatrick, Adv. Phys. **20**, 325 (1971).
19. J. W. Essam, Rep. Prog. Phys. **43**, 833 (1980).
20. B. I. Shklovskiĭ and A. L. Éfros, Usp. Fiz. Nauk **117**, 401 (1975) [Sov. Phys. Usp. **18**, 845 (1975)].
21. D. Stauffer, *Introduction to Percolation Theory* (Taylor and Francis, New York, 1985).
22. J. Hoshen and R. Kopelman, J. Chem. Phys. **65**, 2817 (1976).
23. J. Hoshen, R. Kopelman, and E. M. Monberg, J. Stat. Phys. **19**, 219 (1978).
24. F. B. Tudron and S. D. Colson, J. Chem. Phys. **65**, 4184 (1976).
25. S. D. Colson, R. E. Turner, and V. Vaida, J. Chem. Phys. **66**, 2187 (1977).
26. S. D. Colson, S. M. George, T. Keyes, and V. Vaida, J. Chem. Phys. **67**, 4941 (1977).
27. S. D. Colson and M. Okumura, Mol. Cryst. Liq. Cryst. **57**, 255 (1980).
28. C. von Borczyskowski and T. Kirski, Ber. Bunsenges. Phys. Chem. **93**, 1373 (1989).
29. J. Klafter and J. Jortner, Chem. Phys. Lett. **49**, 410 (1977).
30. J. Klafter and J. Jortner, Chem. Phys. Lett. **60**, 5 (1978).
31. J. Klafter and J. Jortner, J. Chem. Phys. **71**, 1961 (1979).
32. R. Kopelman, in *Excitons in Pure and Mixed Molecular Crystals in Excited States II*, Ed. by E. C. Lim (Academic, New York, 1975), p. 33.
33. N. F. Mott and E. A. Davis, *Electronic Processes in Non-Crystalline Materials* (Clarendon, Oxford, 1979; Mir, Moscow, 1982).
34. P. W. Klymko and R. Kopelman, J. Lumin. **24–25**, 475 (1981).
35. D. C. Alhgren and R. Kopelman, J. Chem. Phys. **70**, 3133 (1979).
36. J. Klafter and J. Jortner, J. Chem. Phys. **73**, 1004 (1980).
37. D. C. Ahlgren and R. Kopelman, J. Chem. Phys. **73**, 1005 (1980).

38. H. Scher and M. Lax, Phys. Rev. B **10**, 4491 (1973).
39. H. Scher and M. Lax, Phys. Rev. B **10**, 4502 (1973).
40. A. I. Burshteĭn, Zh. Éksp. Teor. Fiz. **62**, 1695 (1972) [Sov. Phys. JETP **35**, 882 (1972)].
41. V. P. Sakun, Fiz. Tverd. Tela (Leningrad) **14**, 2199 (1972) [Sov. Phys. Solid State **14**, 1906 (1972)].
42. V. V. Bryksin, Fiz. Tverd. Tela (Leningrad) **22**, 2048 (1980) [Sov. Phys. Solid State **22**, 1194 (1980)].
43. V. V. Bryksin, Fiz. Tverd. Tela (Leningrad) **22**, 2441 (1980) [Sov. Phys. Solid State **22**, 1421 (1980)].
44. T. Odagaki and M. Lax, Phys. Rev. B **24**, 5284 (1981).
45. I. Webman, Phys. Rev. Lett. **47**, 1496 (1981).
46. C. R. Gochanour, H. C. Andersen, and M. D. Fayer, J. Chem. Phys. **70**, 4254 (1979).
47. R. F. Loring, H. C. Andersen, and M. D. Fayer, J. Chem. Phys. **76**, 2015 (1982).
48. S. T. Gentry and R. Kopelman, J. Chem. Phys. **81**, 3022 (1984).
49. R. C. Powell, in *Energy Transfer Processes in Condensed Matter, Erice, 1983*, Ed. by B. Di Bartolo and A. Karipidou (Plenum, New York, 1984); NATO Adv. Study Inst. Ser., Ser. B **114**, 655 (1984).
50. A. Blumenb and R. Silbey, J. Chem. Phys. **70**, 3707 (1979).
51. A. I. Burshteĭn, Usp. Fiz. Nauk **143**, 553 (1984) [Sov. Phys. Usp. **27**, 579 (1984)].
52. Yi Lin and D. M. Hanson, J. Phys. Chem. **91**, 2279 (1987).
53. Yi Lin and D. M. Hanson, J. Phys. Chem. **93**, 1851 (1989).
54. S. A. Bagnich and A. V. Dorokhin, Zh. Prikl. Spektrosk. **54**, 919 (1991).
55. S. A. Bagnich, Fiz. Tverd. Tela (S.-Peterburg) **36**, 2185 (1994) [Phys. Solid State **36**, 1191 (1994)].
56. S. A. Bagnich, Chem. Phys. **185**, 229 (1994).
57. R. Kopelman, in *Radiationless Processes in Molecules and Condensed Phases*, Ed. by F. K. Fong (Springer-Verlag, Berlin, 1976), p. 298.
58. D. Stauffer, Phys. Rep. **54**, 1 (1979).
59. I. M. Sokolov, Usp. Fiz. Nauk **150**, 221 (1986) [Sov. Phys. Usp. **29**, 924 (1986)].
60. R. Kopelman, E. M. Monberg, J. S. Newhouse, and F. W. Ochs, J. Lumin. **18/19**, 41 (1979).
61. M. Inokuti and F. Hirayana, J. Chem. Phys. **43**, 1978 (1965).
62. R. F. Loring and M. D. Fayer, Chem. Phys. **70**, 139 (1982).
63. D. D. Smith, D. P. Millar, and A. H. Zewail, J. Chem. Phys. **72**, 1187 (1980).
64. A. S. Davydov, *The Theory of Molecular Crystals* (Nauka, Moscow, 1968).
65. G. D. Talapatra, D. N. Rao, and P. N. Prasad, J. Chem. Phys. **89**, 3217 (1985).
66. J. Lange, B. Ries, and H. Bassler, Chem. Phys. **128**, 47 (1988).
67. S. A. Bagnich, Fiz. Tverd. Tela (S.-Peterburg) **36**, 1229 (1994) [Phys. Solid State **36**, 672 (1994)].
68. S. A. Bagnich, A. V. Dorokhin, and P. P. Pershukevich, Fiz. Tverd. Tela (S.-Peterburg) **34**, 3475 (1992) [Sov. Phys. Solid State **34**, 1859 (1992)].
69. S. A. Bagnich and A. V. Dorokhin, Preprint No. 646, Inst. Fiz. Akad. Nauk Belarusi (Inst. of Physics, Academy of Science of Belarus, Minsk, 1991).
70. G. E. Pike and C. H. Seager, Phys. Rev. B **10**, 1421 (1974).
71. V. V. Korolev, N. P. Gritsan, I. V. Khmelinskiĭ, and N. N. Bazhin, Khim. Fiz. **6**, 892 (1987).
72. N. P. Gritsan, V. V. Korolev, I. V. Khmelinskiĭ, *et al.*, Izv. Akad. Nauk SSSR, Ser. Fiz. **54**, 454 (1990).
73. S. A. Bagnich, A. V. Dorokhin, and P. P. Pershukevich, Fiz. Tverd. Tela (S.-Peterburg) **35**, 2065 (1993) [Phys. Solid State **35**, 1027 (1993)].
74. P. P. Kobeko, *Amorphous Materials* (Khimiya, Moscow, 1952).
75. V. V. Korolev, A. L. Mamaev, and N. N. Bazhin, Opt. Spektrosk. **83**, 611 (1997).
76. S. A. Bagnich and A. V. Dorokhin, Fiz. Tverd. Tela (Leningrad) **33**, 1382 (1991) [Sov. Phys. Solid State **33**, 779 (1991)].
77. I. M. Fraser, J. R. MacCallum, and K. T. Moran, Eur. Polym. J. **20**, 425 (1984).
78. S. A. Bagnich, A. V. Dorokhin, and P. P. Pershukevich, Fiz. Tverd. Tela (S.-Peterburg) **34**, 504 (1992) [Sov. Phys. Solid State **34**, 269 (1992)].
79. R. Brown, J.-P. Lemaistre, J. Megel, *et al.*, J. Chem. Phys. **76**, 5719 (1982).
80. K. Horie, K. Morishita, and I. Mita, Macromolecules **17**, 1746 (1984).
81. S. A. Bagnich and A. V. Dorokhin, Chem. Phys. **172**, 153 (1993).
82. S. A. Bagnich, A. V. Dorokhin, and P. P. Pershukevich, Fiz. Tverd. Tela (S.-Peterburg) **34**, 2867 (1992) [Sov. Phys. Solid State **34**, 1534 (1992)].
83. P. E. Parris, J. Chem. Phys. **90**, 2416 (1989).
84. S. A. Bagnich, A. V. Dorokhin, and P. P. Pershukevich, Fiz. Tverd. Tela (S.-Peterburg) **35**, 2071 (1993) [Phys. Solid State **35**, 1029 (1993)].
85. G. S. Y. Yeh, J. Macromol. Sci., Phys. **6**, 465 (1972).
86. U. Even, K. Rademann, J. Jortner, *et al.*, Phys. Rev. Lett. **58**, 285 (1987).
87. W. D. Schaefer, B. C. Bunker, and J. P. Wilcoxon, Phys. Rev. Lett. **58**, 284 (1987).
88. S. A. Bagnich and P. P. Pershukevich, Fiz. Tverd. Tela (S.-Peterburg) **37**, 3655 (1995) [Phys. Solid State **37**, 2013 (1995)].
89. S. A. Bagnich, V. N. Bogomolov, D. A. Kurdyukov, and P. P. Pershukevich, Fiz. Tverd. Tela (S.-Peterburg) **37**, 2979 (1995) [Phys. Solid State **37**, 1642 (1995)].
90. S. A. Bagnich, I. M. Mel'nichenko, E. N. Poddenezhnyĭ, *et al.*, Opt. Spektrosk. **79**, 936 (1995) [Opt. Spectrosc. **79**, 856 (1995)].
91. S. A. Bagnich, Opt. Spektrosk. **80**, 773 (1996) [Opt. Spectrosc. **80**, 695 (1996)].
92. S. A. Bagnich, in *Proceedings of the 2nd International Conference on Tunable Solid State Lasers, Wroclaw, Poland, 1996*; Proc. SPIE **3176**, 208 (1997).
93. S. A. Bagnich, Chem. Phys. **218**, 277 (1997).
94. S. A. Bagnich, Zh. Fiz. Khim. **73**, 1125 (1999).
95. S. A. Bagnich, Opt. Spektrosk. **80**, 769 (1996) [Opt. Spectrosc. **80**, 691 (1996)].
96. S. A. Bagnich, Fiz. Tverd. Tela (S.-Peterburg) **39**, 1498 (1997) [Phys. Solid State **39**, 1331 (1997)].

97. S. A. Bagnich, Opt. Spektrosk. **82**, 567 (1997) [Opt. Spectrosc. **82**, 524 (1997)].
98. S. A. Bagnich, in *Proceedings of the 2nd International Conference on Tunable Solid State Lasers, Wroclaw, Poland, 1996*; Proc. SPIE **3176**, 212 (1997).
99. R. Zallen and H. Scher, Phys. Rev. B **4**, 4471 (1971).
100. A. Einstein, *Investigation on the Theory of the Brownian Movement* (Dutton, New York, 1926).
101. R. Kopelman and P. Argyrakis, J. Chem. Phys. **72**, 3053 (1980).
102. R. Rammal and G. Toulouse, J. Phys. Lett. **44**, 13 (1983).
103. S. Alexander and R. Orbach, J. Phys. Lett. **43**, 625 (1982).
104. P. W. Klymko and R. Kopelman, J. Phys. Chem. **87**, 4565 (1983).
105. G. Duportail, J. C. Brochon, and P. Lianos, J. Phys. Chem. **96**, 1460 (1992).
106. J. Klafter, A. Blumen, and G. Zumofen, J. Stat. Phys. **36**, 561 (1984).
107. I. Webman, J. Stat. Phys. **36**, 603 (1984).
108. D. C. Ahlgren, E. M. Monberg, and R. Kopelman, Chem. Phys. Lett. **64**, 122 (1979).
109. S. A. Bagnich, Chem. Phys. **214**, 351 (1997).
110. P. Argyrakis and R. Kopelman, Phys. Rev. B **29**, 511 (1984).
111. P. Argyrakis and R. Kopelman, J. Chem. Phys. **81**, 1015 (1984).
112. J. Klafter and A. Blumen, Chem. Phys. Lett. **119**, 377 (1985).
113. H. Scher and E. W. Montroll, Phys. Rev. B **12**, 2455 (1975).
114. G. Schornerr, R. Eiermann, H. Bassler, and M. Silver, Chem. Phys. **52**, 287 (1980).
115. B. Ries and H. Bassler, Phys. Rev. B **35**, 2295 (1987).
116. S. A. Bagnich, Fiz. Tverd. Tela (S.-Peterburg) **37**, 1022 (1995) [Phys. Solid State **37**, 555 (1995)].
117. S. A. Bagnich and A. V. Dorokhin, in *Lasers and Optical Nonlinearity*, Ed. by P. A. Apanasevich and A. S. Rubanov (Minsk, 1989), p. 169.
118. N. A. Borisevich, S. A. Bagnich, and A. V. Dorokhin, Opt. Spektrosk. **69**, 383 (1990) [Opt. Spectrosc. **69**, 231 (1990)].
119. S. A. Bagnich and A. V. Dorokhin, Opt. Spektrosk. **69**, 1404 (1990) [Opt. Spectrosc. **69**, 833 (1990)].
120. S. Havlin, D. Ben-Avraham, and H. Sompolinsky, Phys. Rev. A **27**, 1730 (1983).
121. B. I. Shklovskiĭ and A. L. Éfros, *Electronic Properties of Doped Semiconductors* (Nauka, Moscow, 1979; Springer-Verlag, New York, 1984).
122. P. Argyrakis and R. Kopelman, J. Lumin. **31–32**, 654 (1984).
123. S. A. Bagnich, in *Proceedings of the 5th Conference of Young Scientists of Physical Faculty of Uzhgorod State University, Uzhgorod, 1990*, Part 2, Available from Ukr-NIINTI No. 1744 UK-90 (Oct. 23, 1990), Ref. Zh.: 18L. Fiz., No. 2, 2L528DEP, 68 (1991).
124. R. Kopelman, Science **241**, 1620 (1988).
125. R. Kopelman, J. Stat. Phys. **42**, 185 (1986).
126. L. W. Anacker, P. W. Klymko, and R. Kopelman, J. Lumin. **31–32**, 648 (1984).
127. E. I. Newhouse and R. Kopelman, Chem. Phys. Lett. **143**, 106 (1988).
128. S. A. Bagnich and A. V. Dorokhin, in *Topical Problems of Spectroscopy, Laser Physics, and Plasma Physics*, Ed. by S. P. Apanasevich (Minsk, 1989), p. 1.
129. N. A. Borisevich, S. A. Bagnich, and A. V. Dorokhin, Opt. Spektrosk. **69**, 102 (1990).
130. B. Ben-Avraham and S. Havlin, J. Phys. A **15**, L691 (1982).
131. N. A. Efremov, S. G. Kulikov, P. I. Personov, and Yu. V. Romanovskiĭ, Fiz. Tverd. Tela (Leningrad) **31** (3), 103 (1989) [Sov. Phys. Solid State **31**, 407 (1989)].
132. N. A. Efremov, S. G. Kulikov, P. I. Personov, and Yu. V. Romanovskiĭ, Fiz. Tverd. Tela (S.-Peterburg) **34**, 445 (1992) [Sov. Phys. Solid State **34**, 239 (1992)].
133. Yu. V. Romanovskiĭ, S. G. Kulikov, and P. I. Personov, Fiz. Tverd. Tela (S.-Peterburg) **34**, 1188 (1992) [Sov. Phys. Solid State **34**, 629 (1992)].
134. S. G. Kulikov, N. A. Efremov, P. I. Personov, and Yu. V. Romanovskiĭ, Fiz. Tverd. Tela (S.-Peterburg) **34**, 2415 (1992) [Sov. Phys. Solid State **34**, 1294 (1992)].
135. I. M. Gulis, E. A. Ermilov, and S. A. Sakharuk, Zh. Prikl. Spektrosk. **64**, 342 (1997).
136. E. A. Ermilov, O. A. Markovskiĭ, and I. M. Gulis, Zh. Prikl. Spektrosk. **64**, 629 (1997).
137. R. D. Burkhart, Chem. Phys. **46**, 11 (1980).
138. P. Argyrakis, L. W. Anacker, and R. Kopelman, J. Stat. Phys. **36**, 579 (1984).
139. L. A. Harmon and R. Kopelman, J. Chem. Phys. **94**, 3454 (1990).
140. M. Grunewald, B. Pohlmann, B. Movaghar, and D. Wurtz, Philos. Mag. B **49**, 341 (1984).
141. R. Richert and H. Bassler, J. Chem. Phys. **84**, 3567 (1986).
142. H. Bassler, in *Disorder Effects on Relaxational Processes*, Ed. by R. Richert and A. Blumen (Springer-Verlag, Berlin, 1994).
143. S. A. Bagnich, Chem. Phys. **237**, 359 (1998).
144. S. A. Bagnich, Opt. Spektrosk. **86**, 449 (1999) [Opt. Spectrosc. **86**, 392 (1999)].
145. R. Kopelman, S. Parus, and J. Prasad, Phys. Rev. Lett. **56**, 1742 (1986).
146. J. Prasad and R. Kopelman, Phys. Rev. Lett. **59**, 2103 (1987).
147. R. Kopelman, S. Parus, and J. Prasad, J. Lumin. **38**, 289 (1987).
148. R. Kopelman, S. Parus, and J. Prasad, Chem. Phys. **128**, 209 (1988).
149. S. A. Bagnich, Ceramics **57**, 85 (1998).
150. S. A. Bagnich, Phys. Rev. B **60**, 11374 (1999).
151. V. N. Beger, Yu. L. Kolesnikov, and A. V. Sechkarev, Opt. Spektrosk. **78**, 249 (1995) [Opt. Spectrosc. **78**, 221 (1995)].
152. B. Kozankiewicz, J. Lumin. **71**, 37 (1997).

Translated by N. Wadhwa

Physics of the Solid State, Vol. 42, No. 10, 2000, pp. 1802–1806. Translated from Fizika Tverdogo Tela, Vol. 42, No. 10, 2000, pp. 1757–1761.

METALS AND SUPERCONDUCTORS

Clusterization of Light Interstitial Impurities and the 1/*f* Noise in Metals

A. A. Berzin, A. I. Morozov, and A. S. Sigov

Moscow State Institute of Radio Engineering, Electronics, and Automation (Technical University), pr. Vernadskogo 78, Moscow, 117454 Russia

e-mail: morosov@eot-gw.eot.mirea.ac.ru

Received March 9, 2000

Abstract—The effect of clusterization of light interstitial impurities on the 1/*f* noise spectrum in metals has been studied by numerical simulation. It is shown that an increase in the intensity of the 1/*f* noise may serve as an indication of clusterization, and that the shape of the activation energy spectrum can provide information on the character of impurity ordering in the clusters formed. © *2000 MAIK "Nauka/Interperiodica".*

Light interstitial impurities in a metal matrix, for instance, hydrogen isotopes, retain their mobility at low temperatures due to tunneling. In view of the alternating nature of the long-range interaction potential between impurities, which is the sum of the elastic interaction and the interaction through Friedel electron-density oscillations, a large number of bound states are formed in the metal for an impurity pair [1, 2]. This leads to the clusterization of mobile defects upon a decrease in temperature.

Cooling of crystals with low impurity concentrations x ($x < 10^{-2}$–10^{-1}) results, instead of in a large-scale separation into phases with a high and a low impurity concentration, in the formation of a metastable state characterized by the presence of a large number of clusters consisting of several defects. This metastable state is long lived, because clusterization dramatically reduces the mobility of the impurities. Metastable states differ in the size, shape, and mutual arrangement of clusters.

While the adatom clusterization processes on the crystal surface can be observed by scanning tunneling microscopy or similar methods [3, 4], the formation of small clusters in the bulk of a crystal is difficult to identify directly. Variation of the kinetic characteristics of the metal is an indirect indication of clusterization.

This work describes the computer simulation of the modification of the 1/*f* noise spectrum occurring in the course of clusterization and demonstrates the possibility of its detection, as well as of determining the characteristics of the formed clusters by studying noise spectra.

The first part of the work is a theoretical introduction. The second part describes the model, and the third, the results of the simulation.

1. THEORETICAL INTRODUCTION

According to the commonly accepted model, the low-frequency resistance fluctuations with a frequency close to the 1/*f* dependence observed in metals are due to electron scattering from defects with a varying cross section, also known as fluctuator defects [5–7]. In simple metals, such a scattering center is a pair of closely spaced point defects (in our case, interstitial impurities), which changes its scattering cross section as one of the defects in the pair goes over to a new position.

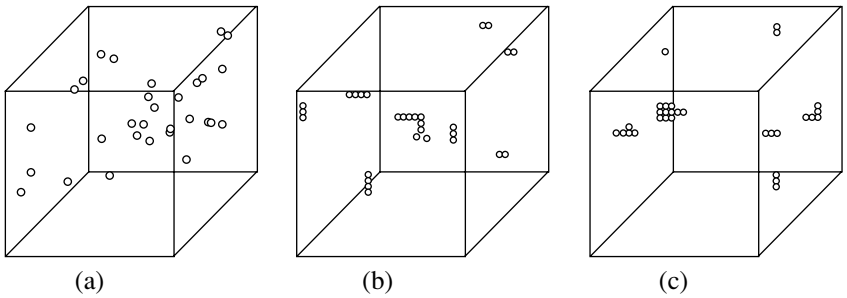

Fig. 1. Distribution of interstitial impurities for (a) $T > T_{cl}$ and (b, c) $T < T_{cl}$ for the parameters $b = 0.8$ and $x = 1.1 \times 10^{-3}$.

1063-7834/00/4210-1802$20.00 © 2000 MAIK "Nauka/Interperiodica"

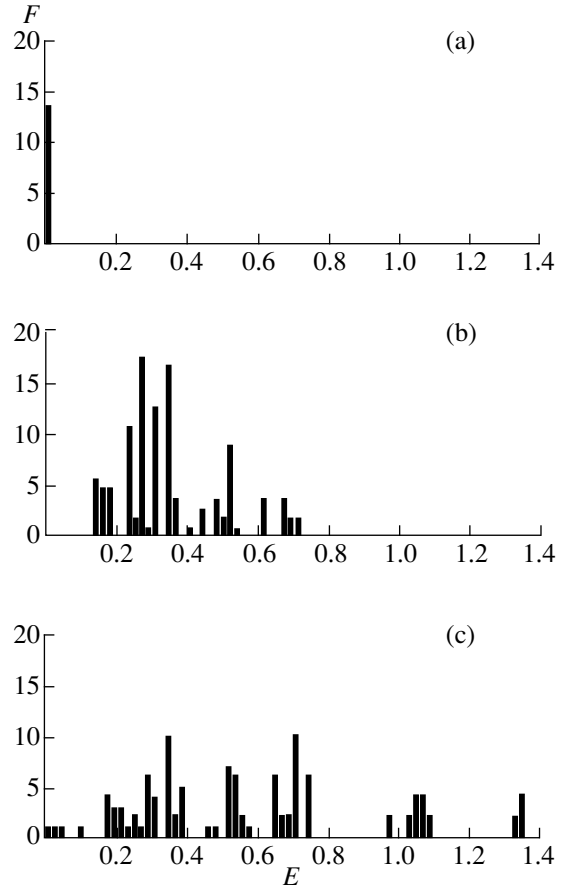

Fig. 2. Typical activation-energy spectra for fluctuator defects at (a) $T > T_{cl}$ and (b, c) $T < T_{cl}$, obtained for the parameters $b = 0.8$ and $x = 1.1 \times 10^{-3}$.

At high temperatures, $T \gg T_{cl}$ (T_{cl} is the clusterization temperature), where the positions of the impurities are not correlated, the concentration of such pairs $n \sim x^2$.

In the case of classical defects, the characteristic frequency of impurity hopping to a neighboring interstice is given by the Arrhenius relation

$$f = f_0 \exp(-E/T), \quad (1)$$

where $f_0 \sim 10^{13}$–10^{14} and E is the barrier energy. By measuring the spectral parameters of the noise, one can obtain the energy distribution function $F(E)$ for the fluctuator defects.

The noise spectral density is given by [5, 6]

$$S_V(f) = 2\int_{-\infty}^{\infty} dt e^{i2\pi ft}\langle V(0)V(t)\rangle = V^2\frac{\alpha(f, T)}{fN_e}, \quad (2)$$

where V is the voltage across the sample, t is the time averaged over the initial instant of time that is denoted by angle brackets, N_e is the carrier concentration, and $\alpha(f, T)$ is the Hooge dimensionless parameter characterizing the noise intensity. The $1/f$ dependence corresponds to the case $\alpha(f) = \text{const}$. For classical fluctuator defects, the $F(E)$ function is defined through the Hooge parameter [5–7]

$$F(E) = \alpha(E)/TN_e, \quad (3)$$

where $\alpha(E)$ is obtained by substituting (1) into the expression for $\alpha(f)$.

In the case of the quantum defects under consideration, the probability of tunneling to a neighboring equivalent interstice at low temperatures is determined by the tunneling matrix element J_0: $f_0 \sim J_0/\hbar$. For hydrogen in a transition metal, f_0 is of the order of 10^{11} Hz (see, for example, review [2]). However, interaction with other defects makes the interstices involved in the tunneling inequivalent. In this case, the energy deficit (excess), which is equal to the energy difference between the impurities occupying the given interstices, should be made up for by the thermostat.

The hopping probability associated with the interaction with electrons can be written as [8]

$$w_{el} \sim \frac{J_0^2}{\hbar\xi_{if}[\exp(\xi_{if}/T) - 1]}, \quad (4)$$

where $\xi_{if} = \varepsilon_f - \varepsilon_i$, ε is the impurity energy at an interstice, and the subscripts f and i refer to the final and initial states, respectively.

The corresponding probability associated with the phonon emission and absorption processes has the

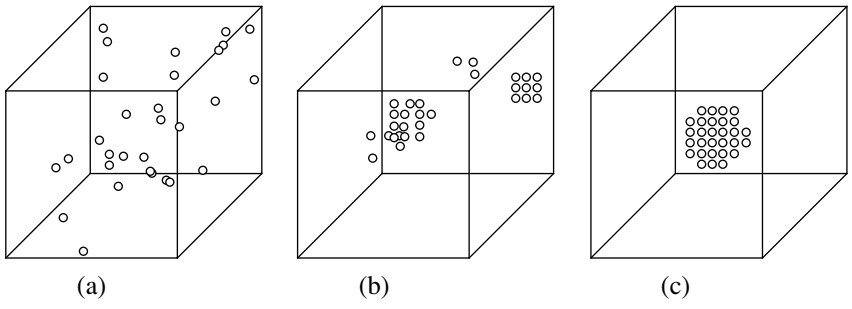

Fig. 3. Distribution of interstitial impurities at (a) $T > T_{cl}$ and (b, c) $T < T_{cl}$ for the parameters $b = 0.5$ and $x = 1.1 \times 10^{-3}$.

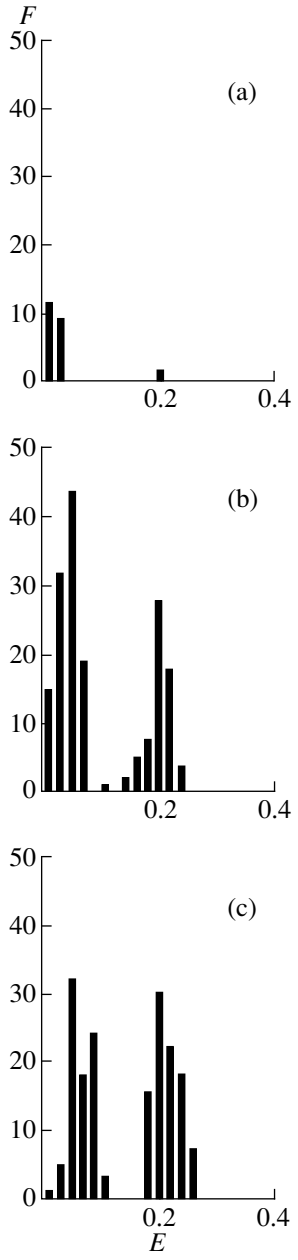

Fig. 4. Typical activation-energy spectra for fluctuator defects at (a) $T > T_{cl}$ and (b, c) $T < T_{cl}$, obtained for the parameters $b = 0.5$ and $x = 1.1 \times 10^{-3}$.

form [9]

$$w_{ph} \sim \frac{J_0^2 \tilde{E} \xi_{if}}{\hbar \theta^3 [\exp(\xi_{if}/T) - 1]}, \quad (5)$$

where $\tilde{E}$ is of the order of atomic energy and θ is the Debye temperature. For the characteristic hopping frequency, we have

$$f = w_{el} + w_{ph}$$
$$= \frac{(\theta^3 + \tilde{E}\xi_{if}^2) J_0^2}{\hbar \theta^3 \xi_{if}} [\exp(\xi_{if}/T) - 1]^{-1}. \quad (6)$$

The noise undergoes a change at frequencies $f < 10^6$ Hz. For the hopping frequency to fall in this interval, the condition $\exp(\xi_{if}/T) \gg 1$ must be met. Thus, we are interested in the values of $\xi_{if} \gg T$ for $T \sim 10$–100 K. Within these ranges of ξ_{if} and T, we can assume that the dependence of f on ξ_{if} is mainly determined by the exponential factor, and that the prefactor in (6) is nearly constant and is equal to 10^{10}–10^{11} Hz, which is three to four orders of magnitude smaller than in the case of over-the-barrier transitions.

Thus, we can find the activation energy spectrum from experimental data by using Eq. (3) with the corresponding value of f_0.

An isolated pair of closely spaced defects has a discrete set of values of ξ_{if}. The interaction with other defects, which are randomly distributed for $T \gg T_{cl}$, results, however, in a blurring of each of these discrete values and the formation of a continuous distribution of ξ_{if}. Since both the elastic interaction among impurities and the interaction through Friedel electron-density oscillations become weaker with increasing distance R between the impurities in proportion to R^{-3}, the influence of other defects gives rise to a Lorentzian distribution of the quantity ξ_{if} with a characteristic width δ [10] given by

$$\delta \sim xW_0, \quad (7)$$

where W_0 is the paired interaction energy of impurities separated by interatomic distances. At the same time, the action of randomly distributed defects which are not coupled in pairs does not affect the magnitude of J_0 [10].

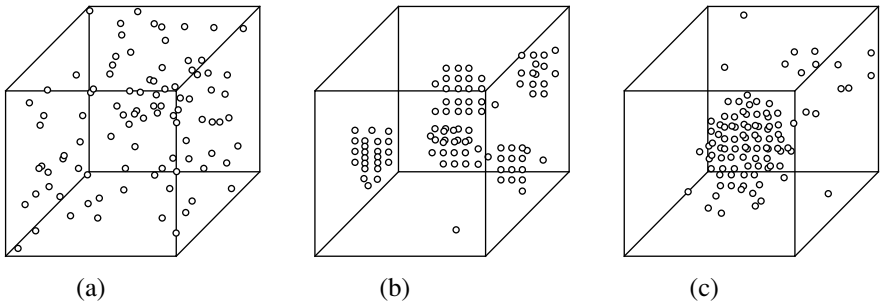

Fig. 5. Distribution of interstitial impurities at (a) $T > T_{cl}$ and (b, c) $T < T_{cl}$, obtained for the parameters $b = 0.5$ and $x = 3.7 \times 10^{-3}$.

Let as now consider the situation in the low-temperature phase. For $T \ll T_{cl}$, most of the defects are bound in clusters. Therefore, the fluctuator defect concentration becomes of the order of x/z, where z is the characteristic number of impurities in a cluster. Thus, for $x \ll 1$, we can expect an increase in the number of fluctuator defects. Moreover, if clusters with $z > 2$ appear, the $F(E)$ dependence may acquire new peaks corresponding to the activation energies of the processes which are capable of changing the impurity distribution in such a cluster.

It is this factor that allows us to use noise spectra for studying the clusterization process and the shape of the clusters formed.

2. DESCRIPTION OF THE MODEL

The distribution of impurities in a crystal is determined by their interaction with one another and with the matrix atoms. We shall treat the latter type of interaction as dominant by assuming that the interstitial impurities occupy the sites of a cubic lattice formed by interstices, which corresponds to tetrahedral pores in an fcc lattice. The position of an impurity in such a lattice is given by three integral coordinates.

The interaction of impurities with one another is described by a paired potential whose short-range component corresponds to repulsion and prevents two impurities from occupying the same site. The long-range component of the paired potential has the form [11]

$$W_{ij} = \frac{b[3/5 - (X/\rho)^4 - (Y/\rho)^4 - (Z/\rho)^4] + (1-b)\cos(\gamma\rho)}{\rho^3}, \quad (8)$$

where the first term corresponds to elastic interaction in a weakly anisotropic cubic crystal [12], and the second, to interaction through Friedel electron-density oscillations. The parameter $b < 1$ determines the relative magnitude of the contributions. The vector $\boldsymbol{\rho}$ with integral coordinates (X, Y, Z) connects two interacting impurities, and the coordinate axes coincide with the crystallographic axes of the crystal. The parameter $\gamma = 2k_F d$, where k_F is the Fermi wave vector of electrons, and d is the interstice lattice constant.

With the potential defined in the form (8), the temperature is found to be dimensionless, i.e., expressed in terms of the paired interaction energy of impurities residing at neighboring interstices.

The quantity ξ_{if} can be written as

$$\xi_{if} = \sum_{m \neq i} (W_{fm} - W_{im}), \quad (9)$$

where the summation is carried out over all impurities, except the chosen one.

The arrangement of the impurities at a given temperature was found by simulation annealing at temperatures $T > T_{cl}$. The simulation was performed by the Metropolis Monte Carlo algorithm on a cube of $30 \times 30 \times 30$ interstices, which was periodically continued in space to avoid boundary effects. The number of impurities was chosen to be equal to 30 and 100, which corresponds to the concentrations 1.1×10^{-3} and 3.7×10^{-3} per interstice (or to doubled concentrations per matrix atom). The variation of temperature from T_i to T_f followed an exponential law:

$$T = T_f + (T_i - T_f)\exp(-ct), \quad (10)$$

and the attainment of steady state was identified from the total energy of the impurity system.

After the attainment of steady state, a histogram of ξ_{if} values was constructed. We are interested in impurity jumps resulting in a change of the fluctuator defect cross section. Therefore, we took into account only the jumps in which either the initial or the final state of the impurity was separated from any other impurity by a distance less than a critical value r_0.

The histogram constructed in this way differs from the one plotted from experimental data, because the $F(E)$ function is obtained by multiplying the number of fluctuator defects with a given value of E by a factor $(\Delta\sigma/\sigma)^2$, where $\Delta\sigma/\sigma$ is the relative change of the electron scattering cross section from fluctuator defects in hopping with a given activation energy. However, these relations are qualitatively similar.

3. RESULTS OF SIMULATION

Figures 1–6 display interstitial impurity distributions and the corresponding activation-energy spectra obtained for $r_0 = 2$ and $\gamma = 0.75$.

In the high-temperature phase [figures denoted by (a)], where the impurities are randomly distributed, the intensity of the $1/f$ noise is low because of the low concentration of fluctuator defects (Figs. 2a, 4a, and 6a). In addition, the activation energies of transitions are also small.

Clusterization results in a sharp increase in the number of fluctuator defects. For $b = 0.8$ (Figs. 1, 2), planar clusters with a close in-plane impurity packing are formed. A comparison of Figs. 1b and 1c with Figs. 2b and 2c suggests that the formation of larger clusters leads to the emergence of fluctuator defects with higher activation energies.

For $b = 0.5$, planar clusters with impurities forming a square lattice with an edge equal to 2 (Figs. 3, 5) are created. Thus, in-plane hopping from one interstice to another within a cluster is possible. It is these hops that

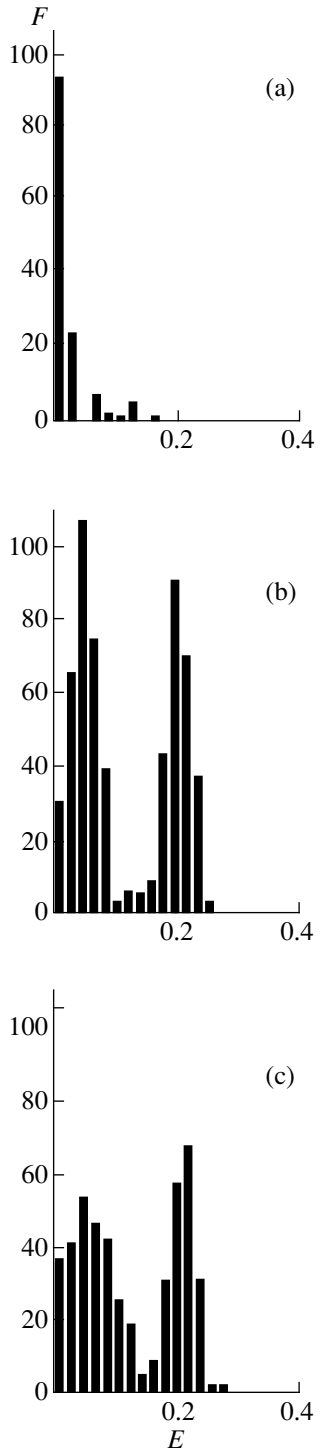

Fig. 6. Typical activation-energy spectra for fluctuator defects at (a) $T > T_{cl}$ and (b, c) $T < T_{cl}$ for the parameters $b = 0.5$ and $x = 3.7 \times 10^{-3}$.

correspond to the activation energy region containing the second peak in Figs. 4b, 4c and 6b, 6c. The energy region containing the first peak is associated with hops in the cluster periphery and those involving the emergence from the cluster plane.

A change in the impurity concentration from 1.1×10^{-3} to 3.7×10^{-3} (Figs. 5, 6) does not affect the shape of the activation energy spectrum.

The above results lead to the following conclusions:

(1) Clusterization of mobile defects results in a sharp increase in the number of fluctuator defects responsible for the $1/f$ noise in metals.

(2) The newly formed fluctuator defects are characterized by high activation energies, which gives rise to an increase in the $1/f$ noise intensity in the low-frequency region accessible for experimental observation. This makes it possible to identify the clusterization process from the intensity of the $1/f$ noise.

(3) The shape of the activation energy spectra provides information on the character of impurity distribution in the formed clusters.

REFERENCES

1. A. I. Morozov and A. S. Sigov, Zh. Éksp. Teor. Fiz. **95** (1), 170 (1989) [Sov. Phys. JETP **68**, 97 (1989)].
2. A. I. Morozov and A. S. Sigov, Usp. Fiz. Nauk **164** (3), 243 (1994) [Phys. Usp. **37**, 229 (1994)].
3. S. C. Wang, U. Kurpick, and G. Ehrlich, Phys. Rev. Lett. **81** (22), 4923 (1998).
4. S. Renisch, R. Schuster, J. Wintterlin, and G. Ertl, Phys. Rev. Lett. **82** (19), 3839 (1999).
5. P. Dutta and P. M. Horn, Rev. Mod. Phys. **53** (3), 497 (1981).
6. Sh. M. Kogan, Usp. Fiz. Nauk **145** (2), 285 (1985) [Sov. Phys. Usp. **28**, 170 (1985)].
7. M. B. Weissman, Rev. Mod. Phys. **60** (2), 537 (1988).
8. Yu. Kagan and N. V. Prokof'ev, Zh. Éksp. Teor. Fiz. **90** (6), 2176 (1986) [Sov. Phys. JETP **63**, 1276 (1986)].
9. J. Jackle, L. Piche, W. Arnold, and S. Hunklinger, J. Non-Cryst. Solids **20** (3), 365 (1976).
10. A. I. Morozov and A. S. Sigov, Fiz. Tverd. Tela (Leningrad) **33** (6), 1772 (1991) [Sov. Phys. Solid State **33**, 996 (1991)].
11. A. A. Berezin, A. I. Morozov, and A. S. Sigov, Fiz. Tverd. Tela (St. Petersburg) **40** (3), 475 (1998) [Phys. Solid State **40**, 435 (1998)].
12. R. A. Masumura and G. Sines, J. Appl. Phys. **41** (10), 3930 (1970).

Translated by G. Skrebtsov

Physics of the Solid State, Vol. 42, No. 10, 2000, pp. 1807–1812. From Fizika Tverdogo Tela, Vol. 42, No. 10, 2000, pp. 1762–1767.

METALS AND SUPERCONDUCTORS

Photomagnetism of Metals. First Observation of Dependence on Polarization of Light[1]

V. L. Gurevich and R. Laiho***

**Wihuri Physical Laboratory, Department of Physics, University of Turku, FIN-20014 Turku, Finland*

***Solid State Physics Division, Ioffe Physicotechnical Institute, Russian Academy of Sciences, Politekhnicheskaya ul. 26, St. Petersburg, 194021 Russia*

Received February 24, 2000; in final form, April 13, 2000

Abstract—We report the first observation of the polarization dependence of the d.c. photocurrent induced by illumination in Cu. The dependence of a d.c. photocurrent on the direction of the plane of light polarization is measured. In agreement with the theoretical considerations, the current parallel to the plane of light incidence is a symmetric function of the angle between this plane and the plane of light polarization. The angular-dependent part of the current perpendicular to the plane of light incidence is an antisymmetric function of the angle. *© 2000 MAIK "Nauka/Interperiodica".*

1. INTRODUCTION

The purpose of the present paper is to investigate the dependence of the photoinduced magnetic flux in normal metals on the polarization of light. For the first time, the photoinduced magnetic flux in a metal has been observed by Lashkul and the present authors in [1]. Further experimental investigations of the effect have been made in [2]. The foundations of the theory of the surface photocurrent in metals are developed in [1, 3]. It is shown that a circular photocurrent excited in a sample of special geometry builds up a magnetic flux. The effect appears to be rather significant and can be easily measured by a SQUID magnetometer [1]. Like the second harmonic generation, a well-known phenomenon investigated in detail in a large number of papers, this is a nonlinear effect proportional to the electromagnetic amplitude squared; i.e., to the intensity of light Q. Its observation, and particularly, the investigation of its dependence on the polarization of light, can yield valuable information about the properties of metals including unique data concerning the behavior and properties of electrons excited by light well above the Fermi surface.

2. PHYSICAL CONSIDERATIONS

There are two contributions to the d.c. surface current responsible for the photomagnetism. These may be referred to as the photogalvanic current and the quasimomentum transfer current (see [3]). Both contributions exist for any electron spectrum and interaction of conduction electrons with light. In our theoretical analysis, we will consider the simplest form of the spectrum and interaction and give only brief comments concerning the general case. The first contribution is due to the anisotropy of electron transition probability relative to the direction of light polarization, in combination with the diffuse reflection of electrons at the metal surface. The second one is due to the fact that the light reflected from a metal surface not only transfers some of its energy to the conduction electrons, but also some of its quasimomentum and thus creates a d.c. photocurrent.

As we have mentioned, the photogalvanic contribution is due to a diffuse scattering of the electrons from the surface (cf. [4, 5], where such effects were considered for semiconductors). In general, the transition probability is an anisotropic function of the electron quasi-momentum. The anisotropy exists even in the case of an isotropic electron spectrum due to the directional asymmetry brought about by the electric a.c. field vector, **E**. Let us assume that **E** lies in the plane xz where z is perpendicular and x is parallel to the metal's

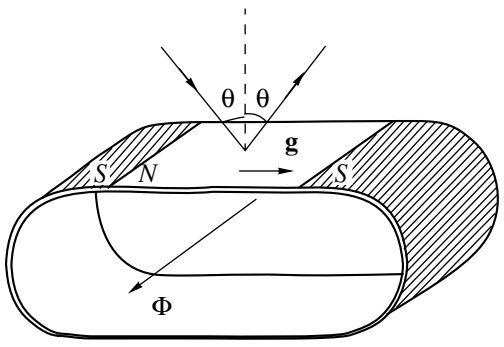

Fig. 1. Arrangement for detection of a current **g** excited by light. The light falls at an angle θ to the perpendicular of a normal metal surface N and is partly reflected. The current is short-circuited with a superconductor S, so that the current encircles the orifice. The magnetic flux Φ created by the current within the loop is detected with a SQUID magnetometer.

[1] This article was submitted by the authors in English.

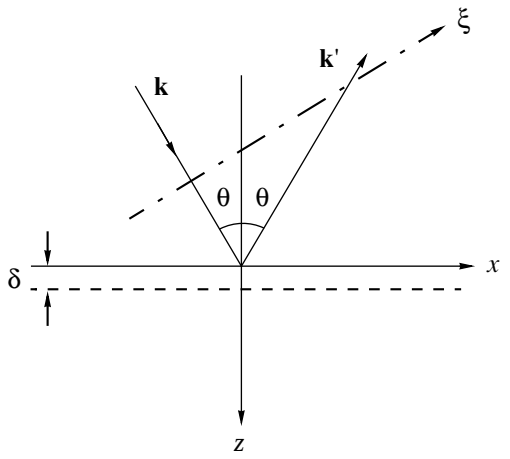

Fig. 2. The plane of light incidence and reflection. The metal surface coincides with the *x* axis; the *z* axis is perpendicular to the surface; **k** is the wave vector of the incident light, while **k**' is the wave vector of the reflected light; ξ axis is perpendicular to the direction of incident light propagation; *y* and η axes coincide and are perpendicular to the plane of the figure; δ is the depth of light penetration.

surface (Fig. 1). In the simplest (isotropic) case, the transition probability can have a component proportional to $(\mathbf{Ep})^2$, **p** being the electron quasimomentum. As a result of the invariance of the transition probability to the change of the sign of quasi-momentum, the number of electrons generated by light and moving along the positive direction of the *x* axis and, at the same time, towards the surface would be equal to the number of electrons moving along $-x$ and away from the surface. The electrons of the first group would be scattered from the surface, and if the scattering is diffuse, they would not contribute appreciably to the current. The electrons of the second group would be scattered only in the bulk of the sample, and therefore their contribution to the current parallel to the surface would be larger.

This effect should disappear for specular reflection of the electrons from the surface [5]. It should not exist for the polarization of a.c. electric field, **E**, in the *y* direction; i.e., perpendicular to the plane of light propagation. The last statement is valid for an isotropic case, which can be seen directly from the form of angular dependence of the surface current (see Section 3). This should also be true if, for instance, the plane of light propagation coincides with a crystal symmetry plane or if the direction of the surface current coincides with an axis of symmetry of the crystal (provided it has a center of symmetry, as is usually the case with most metals).

To clarify the second contribution, let us consider the plane surface of a uniformly illuminated metal. The light falls at an angle θ to the normal (Fig. 2). It penetrates into a thin layer at the metal surface. Due to interaction with the conduction electrons within this layer, a part of the light energy is absorbed by the electrons (usually in the course of their interband transitions, as we assume in the present paper) so that one can write for the Poynting vectors **Q** and **Q**' of the wave incident from vacuum onto the metal surface and the wave reflected from the surface

$$Q_z' = -(1-r)Q_z.$$

Here $r > 0$,

$$\mathbf{Q} = (c/4\pi)[\overline{\mathbf{E}, \mathbf{H}}],$$

where the bar indicates averaging over time. Along with energy, light carries a momentum. The average flux of the *x* component of momentum of light through the metal surface can excite a d.c. surface electron current.

This reasoning should be modified in one aspect. As electrons move in a spatially periodic field, their momentum is not conserved. This means that one should discuss the phenomenon in terms of quasi-momentum (rather than momentum) both for electrons and for light propagating in optically homogeneous media and in vacuum (where the quasi-momentum equals the ordinary momentum). This is why we call this contribution the quasi-momentum transfer (QT) contribution.

The physical picture can be described as follows. There is a continuous influx of quasi-momentum into the system of conduction electrons. Like in vacuum, quasi-momentum becomes ordinary momentum, and the quasi-momentum flux in this case is just the momentum flux. Its average *zx* component is given by $(Q/c)\sin\theta\cos\theta$. If the illuminated part of the sample is larger than the electron mean free path, the balance is established due to the scattering of electrons (for example, by impurities). Therefore, the effect is proportional to the electron mean free time [1, 3]. (It should be very interesting to investigate this effect in metallic nanostructures, where there is no scattering of electrons, and balance is established due to the fact that the path of an electron within the illuminated part of the nanostructure is finite—cf. [6].)

The photoinduced d.c. current depends on the polarization of light. For an appropriate polarization, there is a component of the current not only in the *x* but also in the *y* direction. One of the sources of the polarization dependence can be visualized as follows. As the effect exists already for an isotropic case, let us discuss it for this simplest situation. It was mentioned above that the interband transition probability depends on the direction of electron quasi-momentum. It has a maximum when the quasi-momentum is oriented along the oscillating (a.c.) field and a minimum when the quasi-momentum is perpendicular to the field. This means that the transition probability has the term $\mathrm{Re}(E_x^* E_y p_x p_y)$ [3]. Assume that the electric field lies in the *xy* plane. Let the quasimomentum transfer from the reflected electromagnetic wave to the electrons give rise to a surplus of the electrons with $p_x > 0$. Then, because of the aforementioned term, there should also

be a surplus of the electrons with $p_y > 0$, which would create a net d.c. current in the y direction. These considerations show, in particular, that g_y should vanish for the cases where the a.c. electric field is polarized either in the plane xz (where z is perpendicular to the metal's surface) or along the y axis. The microscopic calculation (see Section 4) shows that g_y is indeed proportional to $\sin 2\phi$ whereas g_x is proportional to $\cos 2\phi$. Here, ϕ is the angle between the electric field vector and the line of intersection of two planes, namely, the plane $\xi\eta$ perpendicular to the wave vector of the falling light and the plane of light incidence. We will choose this line as the ξ axis.

3. PHOTOGALVANIC CONTRIBUTION

We start with the phenomenological equation (see [3]) describing one of the two contributions to the surface current density $\mathbf{g}$

$$\mathbf{g} = \frac{\lambda}{2}\{[\mathbf{E}_0 - \mathbf{n}(\mathbf{n}\cdot\mathbf{E}_0)](\mathbf{n}\cdot\mathbf{E}_0^*) + \text{c.c.}\}, \quad (1)$$

where $\mathbf{E}_0$ is the electric field amplitude, $\mathbf{n}$ is the normal to the metal surface, while λ is a factor depending on the electron spectrum (see below) and the frequency of light.

Let the reference frame x, y, z be directed so that the z axis is parallel to the inward normal to the metal surface, while the x axis is parallel to the plane of light propagation. We will also need another reference frame ξ, η, ζ which will be chosen in such a way that the ζ axis is parallel to the direction of light incidence, while the η axis coincides with the y axis. We can write for the light polarized in the plane making angle ϕ with the ξ axis

$$\begin{aligned} E_{0\xi} &= \mathscr{E}_0\cos\phi, \\ E_{0\eta} &= \mathscr{E}_0\sin\phi, \end{aligned} \quad (2)$$

where $\mathscr{E}_0$ is the electric field amplitude in the light falling on the metal surface.

Now

$$\begin{aligned} E_{0x} &= \mathscr{E}_0\cos\theta\cos\phi, \\ E_{0y} &= \mathscr{E}_0\sin\phi, \\ E_{0z}^{(\text{out})} &= \mathscr{E}_0\sin\theta\cos\phi, \end{aligned} \quad (3)$$

where θ is the angle between the wave vector of light and the z axis. Here $E_z^{(\text{out})}$ is the z component of the electric field just outside the metal surface. The z component of the electric field just inside the metal near the surface is given by

$$E_{0z} = (1/\varepsilon)\mathscr{E}_0\sin\theta\cos\phi, \quad (4)$$

where ε is the (complex) permittivity of the metal.

Finally, one gets

$$g_x = \frac{\lambda}{2}|\mathscr{E}_0|^2\,\mathrm{Re}(\varepsilon^{-1})\sin 2\theta(1+\cos 2\phi) \quad (5)$$

and

$$g_y = \frac{\lambda}{2}|\mathscr{E}_0|^2\,\mathrm{Re}(\varepsilon^{-1})\sin\theta\sin 2\phi. \quad (6)$$

We will give an order-of-magnitude estimate of λ. For the electron spectrum in the lower band 1 and in the upper band 2, we assume

$$\varepsilon^{(1)}(p) = p^2/2m^{(1)}; \quad \varepsilon^{(2)}(p) = \varepsilon_g + p^2/2m^{(2)}, \quad (7)$$

and we use the notation

$$\frac{1}{m} = \frac{1}{m^{(2)}} - \frac{1}{m^{(1)}}$$

and

$$\hbar\omega' = \hbar\omega - \varepsilon_g, \quad p_{\omega'} = \sqrt{2m\hbar\omega'}.$$

In the present paper, we assume for simplicity that the electrons of the upper band 2 yield the main contribution to the current as $m^{(2)} \ll m^{(1)}$, within the accepted accuracy $m_2 \approx m$. According to [3], we have

$$\lambda \approx \frac{e\alpha^2\tau^{(2)}p_{\omega'}^4\delta}{4\pi m\hbar^4}\left(\frac{e}{m_0\omega}\right)^2. \quad (8)$$

Here, m_0 is the free electron mass, ω is the frequency of light, δ is the penetration depth of light into the metal (we assume that it is much smaller than the electron mean free path $\tau^{(2)}p_{\omega'}/m$), and α is a constant (it is a measure of interaction of electrons with light). By order of magnitude, we have

$$\alpha \approx P_{21}(\mathbf{p}', \mathbf{p})/(p + p'),$$

where P_{21} is the matrix element of interband transition induced by light, and p and p' are the initial and final values of the electron quasimomentum, respectively.

The principal result of this analysis can be formulated as follows. The x component of the surface current is proportional to $\cos 2\phi$, while the y component is proportional to $\sin 2\phi$.

4. QUASI-MOMENTUM TRANSFER CURRENT

In the present section, we are interested in the QT surface current $\mathbf{g}$, where for $l \gg \delta$ we have [3]

$$g_\mu = g_\mu^{(1)} + g_\mu^{(2)}. \quad (9)$$

Here [2]

$$g_\mu^{(1)} = \frac{4\pi\zeta_1\omega}{c^2}Q_\mu, \quad (10)$$

$$g_\mu^{(2)} = \frac{i\zeta_2}{2}\left(E_\nu\frac{\partial E_\mu^*}{\partial x_\nu} - E_\nu^*\frac{\partial E_\mu}{\partial x_\nu}\right), \quad (11)$$

[2] There are three terms in Eq. (5) of [3] for the surface QT current. Actually, the two last terms can be merged into one and therefore there are only two terms in Eq. (9).

where

$$\mathbf{Q} = \frac{c}{4\pi}\mathrm{Re}[\overline{\mathbf{E}, \mathbf{H}^*}] \quad (12)$$

is the time-averaged Pointing vector inside the metal. A summation over the recurring indices is implied in (11), μ, ν run through values x and y, and E_μ are the components of the electric field at the surface.

For a simple model of the electron spectrum adopted in [3], we have

$$\mathbf{g}^{(1)} = \frac{e^3\alpha^2 p_{\omega'}^3 \tau^{(2)}\delta}{3\pi\hbar^3 m_0^2\omega^2}|\mathbf{E}|^2\mathbf{k} \quad (13)$$

and

$$g_i^{(2)} = \sum_l A_{il}k_l, \quad (14)$$

$$A_{xx} = -\frac{e^3\alpha^2 p_{\omega'}^3 \tau^{(2)}\delta}{3\pi\hbar^3 m_0^2\omega^2}(3|E_x|^2 + |E_y|^2 + |E_z|^2), \quad (15)$$

$$A_{xy} = A_{yx} = -\frac{2e^3\alpha^2 p_{\omega'}^3 \tau^{(2)}\delta}{3\pi\hbar^3 m_0^2\omega^2}\mathrm{Re}(E_x^* E_y). \quad (16)$$

More detailed equations valid for a two-band model can be found in [3].

We can easily analyze the polarization dependence of the QT current using (3), (4), (14), (15), and (16). We can also assume that, as is true for metals,

$$|\varepsilon| \gg 1. \quad (17)$$

We can neglect the contribution due to the terms proportional to E_{0z} as compared to other contributions. This leads to a ϕ-dependence of the surface currents, which is almost the same as in the previous section; i.e.,

$$g_x \propto (\mathrm{const} + \cos 2\phi), \quad g_y \propto \sin 2\phi, \quad (18)$$

where the constant depends on the spectrum of electrons and on their interaction with light. Of course, the two contributions essentially differ in their θ dependence. However, the most important feature is the vanishing of g_y for the light polarized in the plane xz resulting from the symmetry of the metal surface.

The following circumstance is also worth noting. In general, η_1 and η_2 are tensors. Their symmetry for monocrystals depends on the symmetry of the crystal surface under consideration. In particular, η_2 is a 4th rank tensor. If its symmetry is low enough, a nonvanishing g_x component can exist together with g_y component for the light polarized in the plane xz.

5. EXPERIMENTAL

A square-shaped sample of the size $5 \times 5 \times 1$ mm^3 was cut from a 99.999% pure polycrystalline Cu brick. One of the broad faces of the sample plate was polished to optical grade. The average flux of quasi-momentum of light through the metal surface can excite a d.c. surface electron current. When short-circuited within a loop (Fig. 1), the current creates a magnetic flux. To observe this flux, two opposite ends of the Cu plate were connected to a 0.2 mm thick Pb strip of a semicircular shape to form what we call the sample coil. At the temperature of measurements, $\approx$4.2 K, the Pb strip is in the superconducting state. This assembly was enclosed in a chamber containing elements for controlling the sample temperature and provided with a window for the laser light. The window of the chamber was brought into close contact with the bottom window of a quartz tube (ID = 10 mm, length = 80 cm) fixed from the upper end to the top flange of a He bath cryostate. Outside the sample chamber was fixed a pair of signal coils (8 turns of 5 μm thick NbTi wire, the diameter of the coil was 10 mm), forming part of the flux transformer of a quantum interference device (rf SQUID). The planes of the sample coil and of the signal coils were parallel. The system allowed us to investigate the photoinduced current on the Cu plate by measuring the related magnetic flux within the sample coil. For adjusting the direction of the light polarization plane on the Cu plate, a precisely oriented polarization rotator was fixed to the top flange of the cryostate.

The entire upper surface of the Cu plate was illuminated with linearly polarized light from an Ar ion laser (λ = 514.5 nm). The light falls on the Cu plate at an angle of 30° to a normal to its surface. To minimize heating of the sample by light, the laser beam was chopped at a frequency of 30 Hz, and the applied power density was limited to $\approx$100 mW/cm^2. Before the measurement, it was confirmed that within this power range the SQUID output was directly proportional to the intensity of the laser beam. Chopping of the light also allowed recording of the SQUID output signal by using the lock-in technique.

Figure 3 shows the data on the x component of the surface current I obtained from the output signal of the SQUID electronics as a function of the light polarization direction (ϕ is the angle between the electric field **E** and the ξ axis). As shown by the dots in the upper part of the figure, the polarization-dependent surface current oscillates between the values defined by points A and B when ϕ is changed from 0° to 90°. The midpoint O between A and B, shown by the cross, is observed for ϕ = 45°. The lower part of the figure depicts the sections O–A and O–B, showing, within the accuracy of the measurement, a linear dependence of the x component of the surface current on the value of $|\cos 2\phi|$. The oscillating part of I between points A and B, I_A–I_B, amounts to 45% of the I_B. We will call I_B the background current as it shows no dependence on the light polarization. Both the angular variation of I and the existence of the polarization-independent component agree with the prediction $g_x \propto (\mathrm{const} + \cos 2\phi)$ in (18).

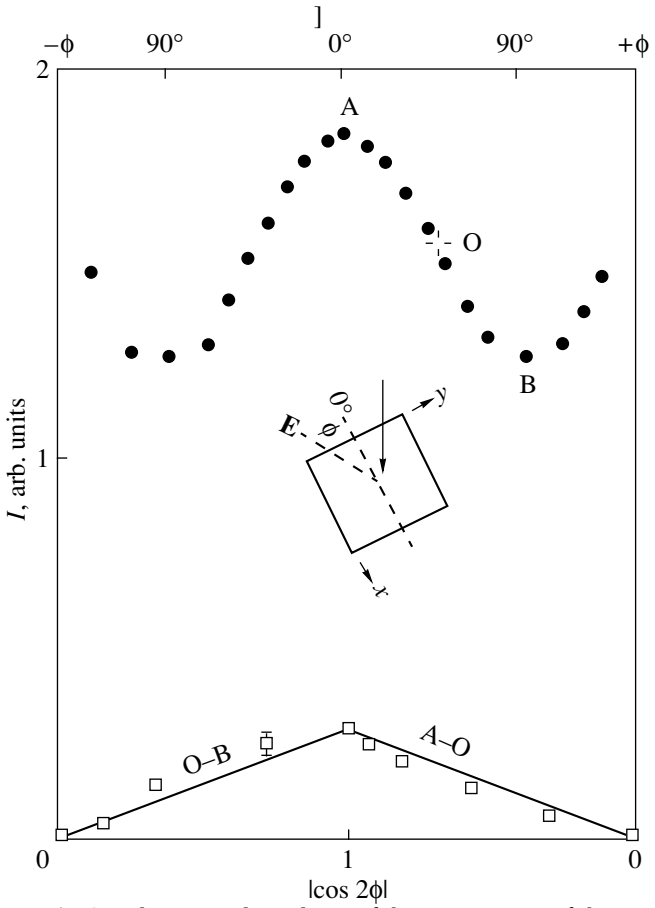

Fig. 3. Polarization dependence of the *x* component of the surface current g_x. The upper part of the figure shows the variation of the total current ($I \propto$ SQUID output signal) when the angle ϕ between the direction of the ξ axis and the electric vector of the incident light *E* is changed (dots). The lower part shows the amplitudes of the ϕ-dependent parts of *I*, O–A and O–B, plotted as a function of cos2ϕ. The solid lines are for guiding the eye.

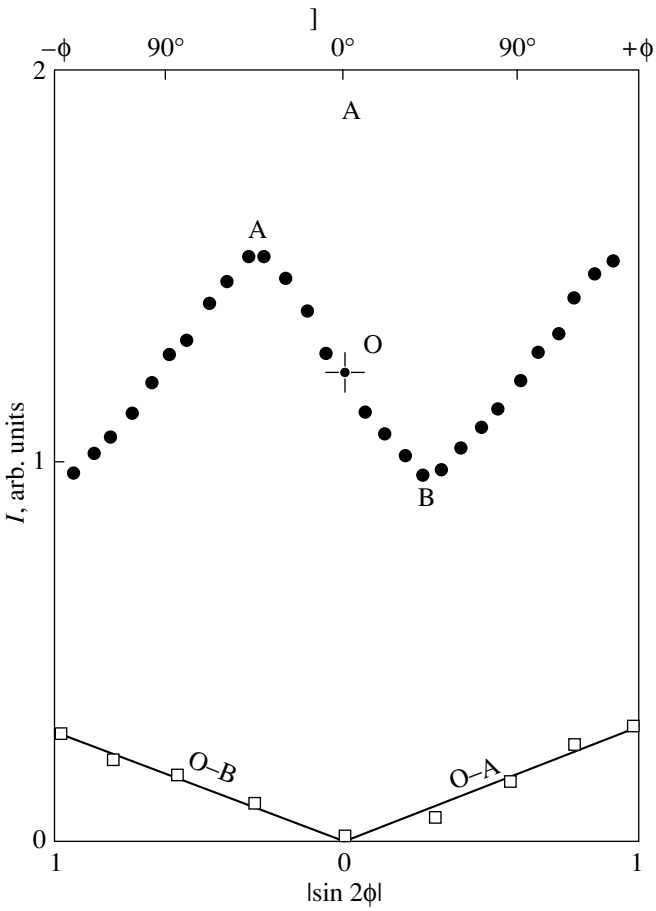

Fig. 4. Polarization dependence of the *x* component of the surface current g_y. The upper part of the figure shows the variation of the ϕ-dependent portion (dots) of the current *I*. In the lower part, this portion is plotted as a function of sin2ϕ for the sections O–A and O–B. The solid lines are for guiding the eye.

Figure 4 depicts the polarization dependence for g_y observed under the same temperature (measured with a thermometer fixed inside a copper pillar holding the specimen) and the same laser light power density as for g_x. A strong modulation of *I* is also observed for g_y, but now the points A and B, related to the extremal values of the current, are shifted to ±45°. The data between the sections O–A and O–B can be well fitted to the linear relation with sin2ϕ. This agrees with the prediction for g_y in (18), disregarding the fact that no polarization-independent current should exist in this case. The value of I_A–I_B in Fig. 4 corresponds to 60% of I_B.

At least a part of the background current can be attributed to changes in the polarization state of the light induced by the strain in the windows of the sample chamber and on the bottom of the quartz tube after cooling them from room temperature to 4.2 K. Under uneven distribution of the strain, this effect may lead to locally varying ellipticity of the light on the surface of the sample and to a nonvanishing background current I_B in the case of g_y (see below).

6. DISCUSSION

We have observed the polarization dependence of the surface photocurrent in the polycrystalline samples of copper. This should be considered as the first effort to observe the effect that proved to be successful. We believe that this is related to the high symmetry of copper, due to which the faces [100] and [111] may form an essential part of the surface.

The *x* component of the surface current has a part proportional to cos2ϕ superimposed on a ϕ-independent background, which is in accordance with the theory (18). The plot of the *y* component has a part proportional to sin2ϕ which is also superimposed on a ϕ-independent background. To explain this behavior, we can offer the following considerations.

As an example, let us consider the photogalvanic contribution (Section 3). According to (5) and (6), g_x and g_y are proportional to $\mathrm{Re}(E_{0x}E_{0z}^*)$ and $\mathrm{Re}(E_{0y}E_{0z}^*)$, respectively. This means, in particular, that much

depends on the phase relations between E_{0x} and E_{0y} on the one hand and E_{0x} and E_{0z} on the other hand. As we have seen, for a linearly polarized light there should be no contribution to g_y for both $\phi = 0$ and $\pi/2$. However, as indicated in [3], for a circular (generally, elliptical) polarization of the light there can be such a contribution. The observed background for g_y, as well as a part of the background for g_x, may be due to the ellipticity of the light polarization; this possibility is indicated in Section 5.

Another contribution to the background may be associated with the following phenomenon. Under illumination, the electrons make transitions from the lower band 1 to the upper band 2 within a thin layer of the width δ near the surface. Under a stationary illumination, the influx of the electrons into band 2 should be counterbalanced by their transitions back to band 1. Estimating the rate of transitions, one should take into consideration that in our experiment the energy of the light quanta $\hbar\omega = 2.41$ eV is so great that the electrons in band 2 are well above the Fermi level.

The rate of the $2 \longrightarrow 1$ transitions may be comparatively low as they mostly take place via phonon emission. The electron energy loss after such a transition cannot exceed the maximal phonon energy $\hbar\omega_D$. (The electron–electron collisions can also play a role in this process.) As a result, the electrons, while still in band 2, can diffuse (together with the holes of band 1—to maintain neutrality) out of the layer of the width δ into the bulk of the copper sample. Due to the nonhomogeneity of the sample, their spatial distribution should also be nonhomogeneous. This effectively means that the temperature distribution over the sample can bring about a thermoelectric current, which is short-circuited by the superconductor. This can also result in a background that is superimposed on the $\sin 2\phi$-dependence of g_y.

7. CONCLUSION

Thus λ, the coefficient in Eq. (1), is actually a rank 2 tensor. Our considerations are valid for the simplest case where the tensor is equivalent to a scalar. This is true, for instance, for the surfaces [100] or [111] of a cubic crystal. One can use the phenomenological considerations to analyze more complicated geometries; i.e., crystalline surfaces of a lower symmetry.

The QT current has, in general, a more complicated structure because ζ_2 is, as we have already indicated, a rank 4 tensor. This means that a careful investigation of the polarization dependence of the photocurrent may allow one to separate the photogalvanic and QT contributions.

Extremely interesting phenomena, as we have already seen, can be predicted and observed for a circularly polarized light. These we hope to discuss in detail in a separate paper.

In general, the observed effect is a powerful way to study the interaction of the electrons with the light in metals. It can also provide a way of studying various aspects of the interaction of conduction electrons with the surface of a metal.

Thus, we have measured the polarization dependence of the surface photocurrent in polycrystalline high-purity samples of copper. In accordance with the results of the theory, the current parallel to the plane of light incidence is a symmetric function of the angle between this plane and the plane of light polarization. The ϕ-dependent part of the current perpendicular to the plane of light incidence (apart from the ϕ-independent background, which most probably originates as a secondary effect) is an antisymmetric function of the angle.

ACKNOWLEDGMENTS

One of the authors (V.L.G.) wishes to thank Turku University for the hospitality extended to him in the course of this research. He is also grateful to the Wihuri Foundation and the Russian Foundation for Basic Research (grant no. 97-02-18286-a) for financial support.

REFERENCES

1. V. L. Gurevich, R. Laiho, and A. V. Lashkul, Phys. Rev. Lett. **69**, 180 (1992).
2. R. Laiho, Phys. Rev. B **52**, 15054 (1995).
3. V. L. Gurevich and R. Laiho, Phys. Rev. B **48**, 8307 (1993).
4. L. I. Magarill and M. V. Entin, Fiz. Tverd. Tela (Leningrad) **21**, 1280 (1979) [Sov. Phys. Solid State **21**, 743 (1979)].
5. V. L. Al'perovich, V. I. Belinicher, V. N. Novikov, and A. S. Terekhov, Zh. Éksp. Teor. Fiz. **80**, 2298 (1981) [Sov. Phys. JETP **53**, 1201 (1981)].
6. V. L. Gurevich and A. Thellung, Phys. Rev. B **56**, R10013 (1997).

Physics of the Solid State, Vol. 42, No. 10, 2000, pp. 1813–1818. Translated from Fizika Tverdogo Tela, Vol. 42, No. 10, 2000, pp. 1768–1773.

METALS AND SUPERCONDUCTORS

Behavior of Higher Harmonics of the Granular HTSC Response to a Low-Frequency Magnetic Field

M. A. Zelikman

St. Petersburg State Technical University, ul. Politekhnicheskaya 29, St. Petersburg, 195251 Russia

Received December 28, 1999

Abstract—A theoretical explanation is proposed for the experimental results on the behavior of higher harmonics of the granular HTSC response to a variable magnetic field of frequencies ~10^2 Hz. The theory explains the periodicity in the dependence of the harmonics amplitudes on a static external magnetic field; the dependence of the period on the harmonics number and on the amplitude of the variable magnetic field; the existence of the threshold in the dependence of the odd-harmonics amplitudes on the amplitude of the variable magnetic field; and the possible formation of pairs for these dependences for the neighboring odd harmonics. It is shown that the experimental dependences can be explained without a detailed analysis of microprocesses in individual Josephson loops only by treating HTSC as a macroscopic medium characterized by the dependence $\Phi(H)$ of the magnetic flux on the external magnetic field, which is typical of type II superconductors. © *2000 MAIK "Nauka/Interperiodica".*

In recent years, the electrodynamic properties of HTSC materials have attracted the attention of theoretical, as well as experimental, physicists. The study of these properties may help clarify the physics of the processes in HTSC materials and the mechanism of the formation of the superconducting state, and help to pave the way for the improvement of HTSC technical parameters, such as the critical field, with a view to extending the field of their practical application.

Usually, the explanation of the experimental facts is based on an analysis of the microscopic processes occurring in a Josephson medium. This has led to a number of very important results: the existence of several phase transitions [1, 2] corresponding to the spin glass states, the existence of vortex lattices, vortex liquid, the possibility of new dissipation mechanisms [3], the quasi-two-dimensional nature of HTSC [4], etc.

However, the processes of the rearrangement of the microscopic pattern upon a variation of the external magnetic field remain unclear. One of the possible approaches to the experimental investigation of these processes involves the analysis of the nonlinear response of the sample to a variable magnetic field. For field frequencies lying in the range of 10^2–10^4 Hz, the behavior of higher harmonics in the output signal has a number of features which appear peculiar at first glance. It was shown in [5, 6] that the harmonics amplitudes are periodic functions of the constant component of the external magnetic field with a period depending on the harmonics number. To explain this fact theoretically, Jeffries *et al.* [6] proposed a model of the effect, in which the superconductor was treated as a system of noninteracting loops containing Josephson junctions, whose area distribution is described by a certain distribution function.

Although this pattern is in qualitative agreement with the experiment, the possibility of considering noninteracting loops and individual SQUIDs is questionable. Besides, it is not clear why only the areas and no other parameters of the loops, such as the values of critical current in Josephson junctions or the number of junctions in the loops, are distributed at random. The identity of the experimental results for the solid specimens and powders in [6] appears to be strange, because the areas of their surfaces must differ significantly.

The theory [6] also fails to explain the strong temperature dependence of the sample characteristics (Fig. 1), observed in [7], because the loop size in the model of spin glass is determined by the size of granules and must not change with temperature.

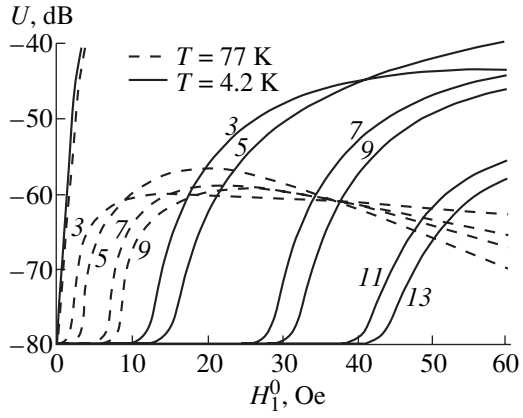

Fig. 1. Experimental dependences of the odd-harmonics amplitudes on the amplitude of the variable magnetic field for a $YBa_2Cu_3O_{7-\delta}$ specimen in zero constant field at the various temperatures.

1063-7834/00/4210-1813$20.00

The above arguments do not make the model proposed in [6], or the resulting conclusions, very convincing: the explanation of peaks on the dependence of the harmonics power on the constant field H_0 by magnetic flux quantization in the loops; the statement that the loops with larger areas determine the behavior of higher harmonics; the attempt to determine the characteristic areas of the loops on the basis of the experimental data; and so on. However, although Jeffries *et al.* [6] reported their results 10 years ago, many authors continue to refer to the model of noninteracting loops even today (e.g., [8–10]), in spite of all the above-mentioned drawbacks.

In our work, we will show that the qualitative agreement between the experimental results and the predictions of the model of noninteracting loops [6] is not due to the adequate microscopic basis of the model itself, which includes the tuning area distribution function for the loops, but is a consequence of the nonlinear response of the sample to the variable external magnetic field for a certain type of nonlinearity. In other words, in order to explain the experimental results, it is sufficient to consider the sample as a macroscopic medium with a certain nonlinear dependence $\Phi(H)$ of the magnetic flux on the external magnetic field. Indeed, the generation of harmonics is a consequence of the nonlinear properties of type II superconductors, including HTSC ceramics. The nonlinearity must manifest itself in the fields higher than the lower critical field H_{c1}^*, which is inherent to HTSC together with the upper critical field H_{c2}^* (the notation used corresponds to H_{c1J} and H_{c2J} in [11]). This nonlinear dependence can be regarded as a macroscopic characteristic of the material, although the reasons behind the emergence of such a dependence can naturally be determined from an analysis of the microprocesses, taking into account the rearrangement of the entire pattern of current distribution over the loops (which by no means can be treated as noninteracting) upon a variation of the external magnetic field.

The theory proposed by us provides a qualitative and quantitative explanation of all the facts described in [6], as well as the existence of a threshold for the dependences of the odd-harmonics amplitudes on the amplitude of the variable field and of possible pairing of such dependences for the neighboring odd harmonics (Fig. 1), as established in [7].

Let us consider a cylindrical HTSC sample placed in two cylindrical coils, one of which generates an external longitudinal variable magnetic field $H(t) = H_0 + H_1^0 \sin\omega t$, while the other serves as a secondary winding for recording the output signal $U(t)$. Let the sample exhibit a certain dependence $\Phi(H)$, where Φ is the magnetic flux through the sample cross section. In fact, the output signal is compensated in the experiment; therefore, in the following, $\Phi(H)$ denotes only the magnetic flux generated by the sample itself, which implies that we subtract from the entire flux the component which is linear in H and does not affect higher harmonics. The output signal $U(t)$ is proportional to the rate of $\Phi(H)$ variation, $U(t) \sim \Phi'(t)$. If we assume that $\Phi(H)$ is an odd function of H, it can be represented as the Fourier integral in sines, and then expanded into a series in Bessel's functions after the substitution of $H(t)$:

$$\Phi(H) = \sqrt{\frac{2}{\pi}}\int_0^\infty F(x)\sin(xH)\,dx$$

$$= \sqrt{\frac{2}{\pi}}\int_0^\infty F(x)\sin(xH_0 + xH_1^0\sin\omega t)\,dx$$

$$= 2\sqrt{\frac{2}{\pi}}\int_0^\infty F(x)\left\{\sum_{l=1}^\infty [J_{2l-1}(xH_1^0)\cos(xH_0)\sin(2l-1)\omega t\right.$$

$$\left. + J_{2l}(xH_1^0)\sin(xH_0)\cos 2l\omega t] + \frac{1}{2}J_0(xH_1^0)\sin(xH_0)\right\}dx$$

$$= \sqrt{\frac{2}{\pi}}\int_0^\infty F(x)J_0(xH_1^0)\sin(xH_0)\,dx$$

$$+ 2\sqrt{\frac{2}{\pi}}\sum_{l=1}^\infty \sin(2l-1)\omega t\int_0^\infty F(x)J_{2l-1}(xH_1^0)\cos(xH_0)\,dx$$

$$+ 2\sqrt{\frac{2}{\pi}}\sum_{l=1}^\infty \cos 2l\omega t\int_0^\infty F(x)J_{2l}(xH_1^0)\sin(xH_0)\,dx.$$

Introducing, as in [6], the dimensionless quantities $\alpha = 2\pi S_0 H_0/\Phi_0$, $\beta = 2\pi S_0 H_1^0/\Phi_0$, where Φ_0 is the magnetic flux quantum and S_0 is a quantity, which has the dimensions of area, we obtain

$$U(t) = \sum_{l=1}^\infty (U_{2l-1}\cos(2l-1)\omega t + U_{2l}\sin\omega t), \quad (1)$$

where

$$U_{2l-1} = k(2l-1)\omega\int_0^\infty J_{2l-1}(z\beta)\cos(z\alpha)F(z)\,dz, \quad (1a)$$

$$U_{2l} = k2l\omega\int_0^\infty J_{2l}(z\beta)\sin(z\alpha)F(z)\,dz, \quad (1b)$$

and k is a constant factor.

Note that the normalization of the magnetic fields to the quantity $\Phi_0/2\pi S_0$ is chosen for the convenience of comparing the results with those obtained in [6]. In fact, it would be more logical to normalize it to a char-

acteristic magnetic field, e.g., H_0 or H_1^0; in this case, the question of areas would not arise.

The obtained relations (1a) and (1b) coincide with formulas (2a) and (2b) from [6]; i.e., we have obtained the same result as in [6], but without using the independent loop approximation, and even without analyzing the microscopic features of the process. Thus, $F(z)$ is not a function of Josephson loop distribution over areas in HTSC, as was assumed in [6]. The function $F(z)$ can be determined not only by the areas of the loops, but also by other parameters, as well as by the interactions of loops with one another, which was disregarded in [6]. A solid argument supporting this point of view is the strong temperature dependence of the characteristics [7] (Fig. 1), which cannot be explained in the theory described in [6], because the size of a loop in the model of spin glass is determined by the size of a granule and should not change with temperature. Consequently, it seems to be more expedient to consider z (whose physical meaning is not yet clear) as a certain characteristic of the Josephson medium.

Let us define the form of dependence $\Phi(H)$ that ensures the agreement of the above approach with the experimental data. In [6], the function $F(A)$ was proposed in the following form (the coefficient A was taken into account in (2a) and (2b)):

$$F(A) = \frac{\sinh A\pi/2}{\cosh A\pi - 1} = \frac{1}{2\sinh A\pi/2}. \qquad (2)$$

For small A, the function is truncated at $a = \delta$ (the behavior of $F(A)$ is undefined for small A), while for large A, $F(A) \approx \exp(-\pi A/2)$. This type of dependence $F(z)$ follows, for example, from the function $\Phi(H) = \frac{2aH}{a^2 + H^2}$, for which the Fourier transform is given by $F(z) = \sqrt{\pi/2}\,2ae^{-\gamma z}$, where $\gamma = 2\pi S_0 a/\Phi_0$. Figure 2 depicts the experimental dependence $\Phi(H)$, which was obtained by using the known experimental procedure [12] which shows that the function $\Phi(H) = 2aH/(a^2 + H^2)$ provides a reasonable approximation of the experimental curve for $a = 5$ Oe. Note that the dependence $\Phi(H)$ is qualitatively similar to the analogous curves for type II superconductors. Thus, the well-known type of nonlinearity of $\Phi(H)$ can and must explain the observed experimental facts, in particular, the existence of quasi-periodic peaks on the dependence of harmonics amplitudes on the constant field H_0.

Substituting $F(z) = e^{-\gamma z}$ into Eqs. (1a) and (1b), we must naturally obtain the same results as in [6]. But the particular form of $F(z)$ makes it possible to obtain an analytical expression for the output signal, which allows us to formulate certain conclusions.

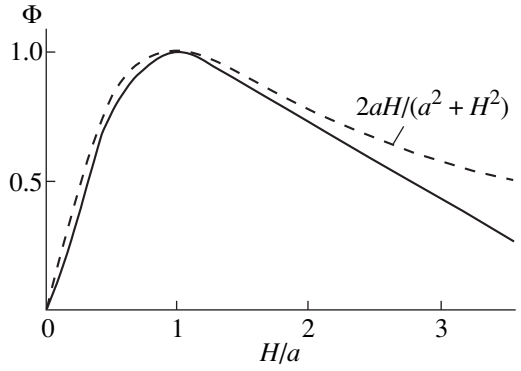

Fig. 2. Experimental dependence of the normalized magnetic flux on the external magnetic field. The dashed line corresponds to the function $\Phi(H) = 2aH/(a^2 + H^2)$ for $a = 5$ Oe.

For calculating the integrals in Eqs. (1a) and (1b), we will use the tabulated result [13]

$$S_\nu(p, \beta) = \int_0^\infty e^{-px} J_\nu(\beta x)dx = \frac{\beta^{-\nu}(\sqrt{p^2 + \beta^2} - p)^\nu}{\sqrt{p^2 + \beta^2}}, \qquad (3)$$
$$(\mathrm{Re}\,\nu > -1, \quad \mathrm{Re}(p + i\beta) > 0).$$

Substituting $p = \gamma - i\alpha$ into Eq. (3), we obtain instead of Eqs. (1a) and (1b)

$$U_{2l-1} \sim \int_0^\infty J_{2l-1}(z\beta)\cos(z\alpha)e^{-\gamma z}dz = \mathrm{Re}\frac{(\sqrt{(\gamma - i\alpha)^2 + \beta^2} - \gamma + i\alpha)^{2l-1}}{\beta^{2l-1}\sqrt{(\gamma - i\alpha)^2 + \beta^2}}, \qquad (4)$$

$$U_{2l} \sim \int_0^\infty J_{2l}(z\beta)\sin(z\alpha)e^{-\gamma z}dz = \mathrm{Im}\frac{(\sqrt{(\gamma - i\alpha)^2 + \beta^2} - \gamma + i\alpha)^{2l}}{\beta^{2l}\sqrt{(\gamma - i\alpha)^2 + \beta^2}}. \qquad (5)$$

Let us consider some special cases.

(1) $\alpha = 0$, i.e., $H_0 = 0$. Even harmonics vanish, while for odd harmonics, we obtain

$$U_{2l-1} \sim \frac{\beta^{2l-1}}{\sqrt{\gamma^2 + \beta^2}(\sqrt{\gamma^2 + \beta^2} + \gamma)^{2l-1}}. \qquad (6)$$

Figure 3 shows the results of calculations based on (6) for the harmonics with different numbers. The quantity $\beta/\gamma = H_1^0/a$ is plotted on the abscissa axis. The curves indicate the existence of a threshold value for β/γ, i.e., for the ratio H_1^0/a (on a logarithmic scale in U), which exactly agrees with the experiment (Fig. 1). Note that

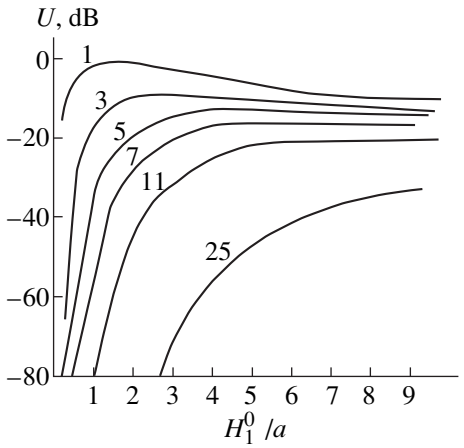

Fig. 3. Dependences of the odd-harmonics amplitudes on the amplitude of the variable magnetic field H_1^0 in zero constant field, calculated on the basis of the chosen function $\Phi(H) = 2aH/(a^2 + H^2)$.

the threshold value of H_1^0/a is determined not by the value of the critical field H_{c1}^*, but by the sensitivity of the experimental setup. If the quantity a is a certain characteristic of the critical field in a multiple Josephson medium, the increase of the "threshold" at $T = 4.2$ K (Fig. 1) can be explained just by an increase in the critical field H_{c2}^* (H_{c2J} in the notation of [11]).

The phenomenon of pairing of the harmonics $U_{2l-1}(H_1^0)$ (3–5, 7–9, 11–13), discovered in [7], which is pronounced most clearly in $YBa_2Cu_3O_7$ samples (Fig. 1), cannot be explained by the form of the proposed function $F(z)$ (and, hence, $\Phi(H)$). However, a modification of these functions may cause the abovementioned pairing. This can be easily understood if we expand the odd function $\Phi(H)$ into a power series:

$$\Phi(H) = \sum_{k=0}^{\infty} a_{2k+1} H^{2k+1} = \sum_{k=0}^{\infty} a_{2k+1} (H_1^0)^{2k+1} (\sin\omega t)^{2k+1}. \quad (7)$$

Each term of this series makes a contribution to all lower order harmonics, and the total amplitudes of the harmonics are determined by the distribution of the expansion coefficients a_{2k+1}. As a rule, the coefficients a_{2k+1} decrease with increasing k, and the amplitude of the ith harmonic is mainly determined by the value of a_i. If, however, there are anomalies in the a_{2k+1} distribution, for example, some coefficients vanish, the amplitude of the corresponding ith harmonics is defined by the next coefficient a_{i+2}; i.e., the ith harmonics becomes closer to the $(i + 2)$th harmonic.

Let us consider the function $\Phi(H) = a^3H/(4a^4 + H^4)$. In its Taylor series expansion, the terms with the numbers 3, 7, 11, etc. are absent, which leads to the pairing of the harmonics 3–5, 7–9, 11–13, and so on. The plot of the function $\Phi(H)$ is qualitatively similar to the curve presented in Fig. 2, and, hence, the assumption about the applicability of a function of such a type is not improper. Note that the function $F(z)$ for such a $\Phi(H)$ is of the form $F(z) \sim e^{-\gamma z}\sin(\gamma z)$, which allows us to derive formulas of the type of Eq. (5). Naturally, we do not affirm that the dependence $\Phi(H)$ should be the same for all specimens. Our intention is just to show that fine features in the form of the function $\Phi(H)$ may lead to significant modifications in the harmonics distribution even when the functions are qualitatively similar. The study of regularities of such a kind will make it possible to analyze the form of the functions $\Phi(H)$ in greater detail. This problem requires a more thorough investigation.

(2) Let us assume that $x \equiv \gamma/\beta \gg 1$, $y \equiv \alpha/\beta \gg 1$. This means that the amplitude of the variable magnetic field H_1^0 is small in comparison with H_0 and with the parameter a of the function $\Phi(H)$. In this case, Eq. (3) can be transformed to

$$S_\nu(x, y) = \frac{1}{\beta 2^\nu (x^2 + y^2)^{(\nu+1)/2}} \times (\cos(\nu + 1)\psi + i\sin(\nu + 1)\psi), \quad (8)$$

where $\tan\psi = y/x = \alpha/\gamma$.

It follows hence that the dependence $|U_\nu(H_0)|$ represents a sequence of peaks (due to the cosine and sine terms in (8)). Let us determine the position of the minima for odd harmonics from the condition

$$\cos(\nu + 1)\psi = 0 \longrightarrow \psi_k = \frac{\pi(2k+1)}{2(\nu+1)} \longrightarrow \alpha_k = \gamma\tan\psi_k = \gamma\tan\frac{\pi(2k+1)}{2(\nu+1)}. \quad (9)$$

It follows from Eq. (9) that the sequence of peaks is not strictly periodic. However, for large ν, when $\psi_k = \frac{\pi(2k+1)}{2(\nu+1)} \ll 1$, we have $\tan\psi_k \approx \psi_k$, i.e.,

$$\alpha_k \approx \frac{\pi(2k+1)}{2(\nu+1)}\gamma. \quad (10)$$

Thus, the first peaks of higher harmonics for small values of H_1^0 are arranged with a period

$$\Delta\alpha = \frac{\pi\gamma}{\nu+1}. \quad (11)$$

(3) Let us carry out the following transformations of (1a) for odd values of ν by expanding J_ν into a Taylor

series, confining ourselves to the first two terms and using the inverse Fourier transform:

$$U_\nu = k\nu\omega\int_0^\infty J_\nu(\beta z)\cos(\alpha z)F(z)dz \approx k\nu\omega$$

$$\times\int_0^\infty F(z)\cos(\alpha z)\left(\frac{\beta z}{2}\right)^\nu\left(\frac{1}{\nu!}-\frac{1}{(\nu+1)!}\left(\frac{\beta z}{2}\right)^2\right)dz$$

$$= \frac{k\omega}{(\nu-1)!}\left(\frac{\beta}{2}\right)^\nu\int_0^\infty F(z)\cos(\alpha z)z^\nu\left(1-\frac{\beta^2 z^2}{4(\nu+1)}\right)dz \quad (12)$$

$$= \frac{k\omega}{(\nu-1)!}\left(\frac{\beta}{2}\right)^\nu \mathrm{Re}\left[\left(-\frac{1}{i}\right)^\nu\int_0^\infty F(z)e^{-i\alpha z}(-iz)^\nu\right.$$

$$\left.\times\left(1-\frac{\beta^2 z^2}{4(\nu+1)}\right)dz\right] = \frac{k\omega}{(\nu-1)!}\left(\frac{\beta}{2}\right)^\nu$$

$$\times\mathrm{Re}\left[i^{\nu+1}\Phi^{(\nu)}(\alpha)-\frac{\beta^2}{i^{\nu+3}4(\nu+1)}\Phi^{(\nu+2)}(\alpha)\right],$$

where $\Phi^{(\nu)}$ is the νth-order derivative of Φ.

After similar transformations of Eq. (1b) for even values of ν, we obtain the general formula

$$U_\nu \sim \Phi^{(\nu)}(\alpha), \quad (13)$$

for which the condition specifying the possibility of disregarding the remaining terms of the expansion has the form

$$\beta^2 \ll \frac{4(\nu+1)\Phi^{(\nu)}(\alpha)}{\Phi^{(\nu+2)}(\alpha)}. \quad (14)$$

Therefore, for small H_1^0, the dependence of the νth harmonic on H_0 is equal to the νth-order derivative of the basic function $\Phi(H)$, which can also be verified in experiments. This fact provides the possibility of a more detailed analysis of the function $\Phi(H)$ based on an analysis of the set of harmonics.

(4) Let us consider the case when $\gamma \ll \beta$, $\beta > \alpha$, i.e., when the amplitude of the variable field H_1^0 is larger than a. Then expression (4) assumes the form

$$U_{2l-1} \sim \frac{\cos[(2l-1)\arcsin\alpha/\beta]}{\sqrt{\beta^2-\alpha^2}}. \quad (15)$$

Strictly speaking, there is no periodicity in the arrangement of peaks in this case either, since Eq. (15) corresponds to the Chebyshev polynomials in α/β. However,

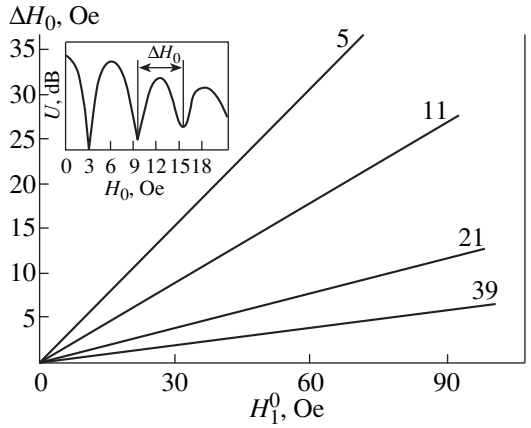

Fig. 4. Dependence of the period ΔH_0 on the amplitude of the variable magnetic field H_1^0 for the various harmonics; the inset shows a typical dependence of the harmonics amplitude on the constant field H_0 and illustrates the calculation of ΔH_0.

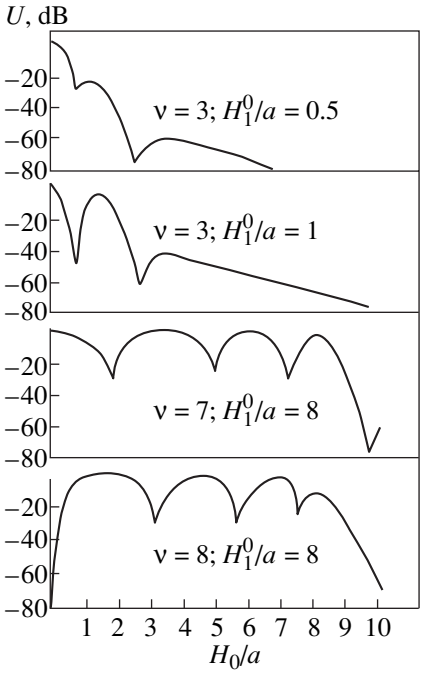

Fig. 5. Calculated dependences of the amplitudes of the various harmonics on the constant magnetic field H_0 for various values of the amplitude of the variable field H_1^0.

for large harmonic numbers ν, the first peaks can be considered as equidistant with a period

$$\Delta\alpha = \frac{\pi\beta}{\nu}. \quad (16)$$

Thus, the period in H_0 is directly proportional to H_1^0 and inversely proportional to the harmonic number ν.

The experimental results presented in Fig. 4 are in qualitative and quantitative agreement with Eq. (16).

(5) In a general case of arbitrary values of the parameters α, β, and γ (i.e., of x and y), computer calculations based on formulas (4) and (5) can be carried out. The curves in Fig. 5 correspond to various values of the parameters.

The main conclusion of this work can be formulated as follows: in order to explain the experimental results on harmonics generation in HTSC, a detailed analysis of microprocesses in individual Josephson loops, which was carried out in [6, 14], is not required. The experimentally obtained dependences can be explained if we regard HTSC as a type II superconductor, which can be characterized by certain values of the critical fields.

This does not mean that the proposed approach can be used to explain all experimental facts concerning a multiple Josephson medium, such as the macroscopic quantum effects, differences in values of the critical fields obtained by different methods, and microwave power absorption in single crystals of $YBa_2Cu_3O_{7-\delta}$. Obviously, in some experiments, the properties of HTSC as a set of Josephson loops (spin glass) are manifested, and an appropriate corresponding model should be used in these cases.

ACKNOWLEDGMENTS

This work was supported by a grant from the Ministry of Science and Technology in the program "Superconductivity."

REFERENCES

1. J. Morgenstern, K. A. Muller, and J. G. Bednorz, Physica B (Amsterdam) **152** (1–2), 85 (1988).
2. N. C. Yeh, Phys. Rev. B **40** (7), 4566 (1989).
3. M. A. Dubson, S. T. Herbert, J. J. Calabrese, *et al.*, Phys. Rev. Lett. **60** (11), 1061 (1988).
4. S. Martin, A. T. Fiory, R. M. Fleming, *et al.*, Phys. Rev. Lett. **62** (6), 677 (1989).
5. C. D. Jeffries, Q. H. Lam, Y. Kim, *et al.*, Phys. Rev. B **37** (14), 9840 (1988).
6. C. D. Jeffries, Q. H. Lam, Y. Kim, *et al.*, Phys. Rev. B **39** (16), 11526 (1989).
7. V. F. Masterov, M. A. Zelikman, Z. T. Maksutova, *et al.*, Sverkhprovodimost': Fiz., Khim., Tekh. **4** (3), 470 (1991).
8. I. Ciccarello, C. Fazio, M. Guccione, *et al.*, Phys. Rev. B **49** (9), 6280 (1994).
9. H. Kawamura and M. S. Li, Phys. Rev. B **54** (1), 619 (1996).
10. S. F. Wahid and N. K. Jaggi, Physica C (Amsterdam) **194** (1–2), 211 (1992).
11. A. A. Abrikosov, *Fundamentals of the Theory of Metals* (Nauka, Moscow, 1987; North-Holland, Amsterdam, 1988).
12. E. M. Gyorgy, R. B. van Dover, S. Jin, *et al.*, Appl. Phys. Lett. **53** (22), 2223 (1988).
13. I. S. Gradshteyn and I. M. Ryzhik, *Table of Integrals, Series, and Products* (Nauka, Moscow, 1971; Academic, New York, 1980).
14. T. K. Xia and D. Stroud, Phys. Rev. B **39** (7), 4792 (1989).

Translated by N. Ostrovskaya

Physics of the Solid State, Vol. 42, No. 10, 2000, pp. 1819–1824. Translated from Fizika Tverdogo Tela, Vol. 42, No. 10, 2000, pp. 1774–1779.

METALS AND SUPERCONDUCTORS

Oxygen Ordering in $YBa_2Cu_3O_{7-y}$ in Terms of the Landau Theory

A. Yu. Gufan, Yu. M. Gufan, Yu. V. Prus, and K. Nakamura

North-Caucasian Higher Education Scientific Center, Rostov-on-Don, 344006 Russia

e-mail: gufan@gufan.rnd.runnet.ru

Received February 16, 2000; in final form, March 27, 2000

Abstract—Oxygen ordering in nonstoichiometric compositions of $YBa_2Cu_3O_{7-y}$ is considered in terms of the Landau theory of second-order phase transitions. It is shown that there can only be ten types of homogeneous long-range order, of which two types correspond to the OI and OII phases. The Landau theory predicts that the filling of vacant positions $2(f)D_{4h}^1$ by oxygen must follow a scenario that is far from forming chains but compatible with known facts. Such a scenario of filling vacancies with oxygen was not considered earlier. It is demonstrated that the predicted structures can be experimentally identified from the spectra of copper ions. In the course of identification of diffraction patterns, the symmetry-allowed displacement of copper ions from centrosymmetric positions in a $Cu(1)(O_x\square_{1-x})_2$ layer should be taken into account. © *2000 MAIK "Nauka/Interperiodica".*

It is generally accepted that oxygen ordering in $YBa_2Cu_3O_{7-y}$ compositions considerably affects their remarkable electrodynamic parameters. At least two different types of ordered distribution of oxygen and vacancies in the $Cu(1)(O_x\square_{1-x})_2$ layer separating BaO layers in these compounds with a layered perovskite structure [1] have been established (here, □ is an oxygen vacancy). The stoichiometric composition for one of the ordered O–□ distributions over a system of regular points $2(f)D_{4h}^1$ is the $YBa_2Cu_3O_7$ composition[1] (the OI phase with an orthorhombic symmetry). It is assumed that, in the completely ordered state of the OI structure, oxygen fills precisely half the system of regular points $2(f)D_{4h}^1$, thus forming the chains …Cu(1)OCu(1)O… parallel to the direction of the larger period in the basal plane of the orthorhombic phase. It is generally agreed [1, 5–7] that the second type of the O–□ ordering has also been established. It corresponds to compositions close to $YBa_2Cu_3O_{6.5}$ (OII phase). In this phase, the unit cell of $YBa_2Cu_3O_7$ is doubled along the *a* axis due to alternation of the chains …OCu(1)OCu(1)… and …Cu(1)□Cu(1)□ … oriented along the *b* axis. A number of experimental results were interpreted as the presence of other types of O–□ ordered structures that correspond to the predicted stoichiometry of the layer composition [1, 5, 6, 8–12]. However, only the conclusions concerning the difference in the oxygen population densities of regular systems of points with the coordinates (1/2 0 0) and (0 1/2 0): φ, which is averaged over the sample volume, can be regarded as reliable [1, 3, 6, 13, 14]. The difference in the occupancies of these positions can be established from the fact that diffraction patterns of $YBa_2Cu_3O_{7-y}$ contain nonoverlapping reflections with a different parity in *h* and *k*, whose difference in intensities is proportional to φ. For this reason, the theoretical works predicting the possible fine structure of equilibrium ordered oxygen–vacancy states at given φ and *y* in $Cu(1)(O_x\square_{1-x})_2$ layers are of fundamental importance.

A large number of theories have been proposed for the O–□ ordering in $Cu(1)(O_x\square_{1-x})_2$ layers [7–12, 15]. Most of them are only based on the inclusion of pair interactions and only in the first three coordination spheres [8, 9, 11, 15]. As shown below, this is insufficient for establishing the stability of the OII phase to heterophase fluctuations [16, 17]. Some authors constructed phenomenological theories of oxygen–vacancy ordering [7, 8, 11]. However, the starting models [7] completely disregard the presence of copper atoms in the structure. As a result, the unit cell in the models describing the structure of the $Cu(1)(O_x\square_{1-x})_2$ layer contains, according to [7], one effective atom ($\square_{1-x}O_x$) instead of two atoms, as in the real $YBa_2Cu_3O_{7-y}$ structure.

In this paper, we further develop the phenomenological Landau theory of oxygen ordering in $Cu(1)(O_x\square_{1-x})_2$ layers, which is based on the generally accepted concepts concerning the structure of OI and OII phases. It is known that, in the Landau theory, the equilibrium energies of the phases induced by the same irreducible representation, i.e., the same order parameter (OP), differ only in the phenomenological coefficients of high (higher than second) powers of the OP [18]. Since the OP components for unlimited orderings are linear functions of the probabilities of filling certain positions in the lattice with oxygen, the components of the Landau

[1] Note that the structure of nondecomposing solid solutions with the composition $YBa_2Cu_3O_{7-y}$, which is denoted as 1212 in catalogs [2], is stable only in the range $0.07 \le y \le 0.955$ [3, 4]. Speaking of the $YBa_2Cu_3O_7$ structure, we mean the structure of compositions $YBa_2Cu_3O_{7-y}$ with $0.07 < y < 0.15$.

potential correspond, to a high degree of accuracy, to effective interactions with three, four, or a larger number of particles [16, 17, 19]. Since many-particle interactions are weaker than pair interactions, we should admit that types of ordering with the closest energies are described by the same irreducible representation or the same OP. However, it should be emphasized that the inclusion of the second OP (if it emerges as an improper order parameter) is essential; otherwise, the relationship between the phenomenology and the microscopic theory [17] is lost.

The following order of presentation of the paper is used by us. At first, we determine all possible OP that can lead to a superstructure typical of the OII phase. Then, we establish a relation between the Landau OP and the probability of populating certain vacancies accessible for oxygen in the large unit cell in the structure of the $Cu(1)(O_x\square_{1-x})_2$ layer. Then, we list all possible oxygen–vacancy orderings that can occur as second-order transitions from the disordered state.[2]

Then, the group-theoretical method of counting stable phases is also used to determine the phases whose equilibrium free energies differ insignificantly from the energies of phases in which a second-order transition is possible. This difference in energies only appears due to many-particle interactions. In conclusion, the possible experimental identification of phases is considered.

1. STRUCTURE OF THE ORDER PARAMETER

The symmetry of $YBa_2Cu_3O_6$ indicates that the oxygen ordering in the $Cu(1)(O_x\square_{1-x})_2$ layer, which corresponds to the orthorhombic OII phase, is determined by the two-pronged star of the vector $\mathbf{k}^{(1)}$ (point X of the Brillouin zone (BZ) of the D^1_{4h} group):

$$\mathbf{k}^{(1)} = \mathbf{i}(\pi/|a|) \quad \mathbf{k}^{(2)} = \mathbf{j}(\pi/|b|). \tag{1}$$

Here a and b are the vectors of translations of a unit cell along x(**i**) and y(**j**). The large unit cell includes eight positions populated with equal probabilities by oxygen atoms in the tetragonal phase. According to [16, 17], expressions (1) imply that the microscopic theory, which completely reflects the symmetry of the problem, should take into account interactions in at least five coordination spheres. We choose a copper atom as the origin of the Cartesian reference frame and enumerate the 2(*f*) positions in the large unit cell of the tetragonal phase:

$$\begin{gathered}1\text{—}(\tau\,0\,0);\quad 2\text{—}(0\,\tau\,0);\quad 3\text{—}(-\tau\,0\,0);\\ 4\text{—}(0\,-\tau\,0);\quad 5\text{—}(\tau\,2\tau\,0);\quad 6\text{—}(2\tau\,\tau\,0);\\ 7\text{—}(-\tau\,2\tau\,0);\quad 8\text{—}(2\tau\,-\tau\,0).\end{gathered} \tag{2}$$

Here and below, we use Kovalev's notation [21]: $|a| = |b| = 2\tau$ in the tetragonal phase. Let P_i be the probability that oxygen occupies the ith position from (2). We can establish the dependence of the Landau potential Φ on P_i using the linear combinations of P_i ($i = 1, \ldots, 8$), which form the basis for irreducible representations of the D^1_{4h} group. The following linear combinations of P_i form the basis for the T_i representations of the D^1_{4h} group, which are characterized by $\mathbf{k}^{(1)}$ and $\mathbf{k}^{(2)}$ (1), $\mathbf{k} = 0$ and $\mathbf{k} = 1/2(\mathbf{b}_1 + \mathbf{b}_2)$ (the X, F, and R points of the BZ [21]):

$$\begin{aligned}\chi_1(T_1) &= (P_2 + P_4 - P_6 - P_8)/2,\\ \chi_2(T_1) &= (P_1 + P_3 - P_5 - P_7)/2,\end{aligned} \tag{3}$$

$$\begin{aligned}\eta_1(T_2) &= (P_1 - P_3 + P_5 - P_7)/2,\\ \eta_2(T_2) &= (P_2 - P_4 + P_6 - P_8)/2,\end{aligned} \tag{4}$$

$$\begin{aligned}\Psi_1(R) &= (P_1 - P_3 - P_5 + P_7)/2,\\ \Psi_2(R) &= (P_2 - P_4 - P_6 + P_8)/2,\end{aligned} \tag{5}$$

$$8^{1/2}c = (P_1 + P_2 + P_3 + P_4 + P_5 + P_6 + P_7 + P_8)/8^{1/2}, \tag{6}$$

$$8^{1/2}\varphi = (P_1 - P_2 + P_3 - P_4 + P_5 - P_6 + P_7 - P_8)/8^{1/2}. \tag{7}$$

Here, $c = 1 - y$ is the oxygen concentration in the $Cu(1)(O_x\square_{1-x})_2$ layer, and φ is the averaged difference in the probabilities of filling the positions (0 1/2 0) and (1/2 0 0). The Landau potential depends on the seven linear combinations of P_i (3)–(5) and (7) through 19 polynomials forming the complete rational basis of vector invariants of the $L(D^1_{4h})$ group:

$$\Psi_1^2 + \Psi_2^2;\quad \Psi_1^2 \times \Psi_2^2;\quad (\Psi_1^2 - \Psi_2^2)\varphi, \tag{8}$$

$$\chi_1^2 + \chi_2^2;\quad \chi_1^2 \times \chi_2^2;\quad (\chi_1^2 - \chi_2^2)\varphi, \tag{9}$$

$$\eta_1^2 + \eta_2^2;\quad \eta_1^2 \times \eta_2^2;\quad (\eta_1^2 - \eta_2^2)\varphi, \tag{10}$$

$$\begin{gathered}\Psi_1\chi_2\eta_1 + \Psi_2\chi_1\eta_2;\quad \Psi_1^3\chi_2\eta_1 + \Psi_2^3\chi_1\eta_2,\\ \Psi_1\chi_2^3\eta_1 + \Psi_1\chi_1^3\eta_2;\quad \Psi_1\chi_2\eta_1^3 + \Psi_2\chi_1\eta_2^3,\\ (\Psi_1\chi_2\eta_1 - \Psi_2\chi_1\eta_2)\varphi;\quad \Psi_1\Psi_2\chi_1\chi_2\eta_1\eta_2;\end{gathered} \tag{11}$$

$$\Psi_1^2\chi_1^2 + \Psi_2^2\chi_2^2, \tag{12}$$

$$\Psi_1^2\eta_1^2 + \Psi_2^2\eta_2^2;\quad \chi_1^2\eta_1^2 + \chi_2^2\eta_2^2;\quad \varphi^2. \tag{13}$$

[2] In the publications whose authors emphasize that experiments were made on homogeneous samples, it is stated that no indications of a first-order transition between the tetragonal and orthorhombic phases of $YBa_2Cu_3O_{7-y}$ are observed, both upon the attainment of the orthorhombic state due to a change in temperature [20], and upon the variation of oxygen concentration [3, 4, 6].

Analyzing the form of invariants (8)–(13), we can draw the following conclusions [17].

(1) The ordering determined by the proper (leading) OP φ cannot give rise to additional improper orderings upon second-order phase transitions, even though it has the strongest effect on the stability of phases to heterophase fluctuations determined by other OPs.

(2) The orderings determined by any of the proper OPs (Ψ_1, Ψ_2), (χ_1, χ_2), or (η_1, η_2) are characterized by identical phase diagrams.

(3) In two out of three phases induced by one of the two-component OP (3)–(5), there appears an additional improper ordering described by φ (see below).

(4) If an ordered phase is only induced by one two-component OP (a second-order transition always gives rise to only one OP), the other two-component OP cannot emerge as an improper order parameter. However, the interaction with the second two-component OP (even if it is equal to zero in equilibrium) determines the stability of the ordered phase to heterophase fluctuations. Among other things, this follows [17] from the appearance of the first three invariants in polynomials (13).

(5) If an ordering is determined by two two-component OPs, the third two-component OP can also be induced in some phases.

2. PHASE DIAGRAM AND ORDERED PHASES

A one-component OP φ can only induce one ordered phase. Two-component OPs determine identical L groups [17]. Consequently, the phase diagrams for all the three two-component OPs are similar and contain four phases each, with different symmetries (including the high-symmetry phase). The symmetries of ordered phases are characterized by the following relations between OP components: (1) $\xi_2 = 0$, $\xi_1 \neq 0$, (2) $\xi_1^2 = \xi_2^2$, and (3) $\xi_1 \neq 0$, $\xi_2 \neq 0$. Hereafter, ξ_i in each of the three types of OP denotes either Ψ_i, χ_i, or η_i. In order to describe all three low-symmetry phases with the help of the Landau potential, it must have, in accordance with (8)–(13), a power not lower than the eighth in the OP components [17]. Hence, it follows that at least some of the "eight-particle" interactions in the microscopic theory determine to a considerable extent the elementary excitation spectrum near the region of the existence of phase *3*. We will henceforth assume that all the phenomenological parameters describing the interaction between OPs are "small." According to (8)–(13), the Landau potential has the form

$$\Phi = a_1 I_1 + a_2 I_1^2 + a_3 I_1^3 + a_4 I_1^4 + 4b_1 I_2 + b_2 I_2^2 + 4c_{12} I_1 I_2 + 4c_{112} I_1^2 I_2 + \alpha(\xi_1^2 - \xi_2^2)\varphi + \beta\varphi^2. \quad (14)$$

Here $I_1 = (\xi_1^2 + \xi_2^2)$, $I_2 = \xi_1^2 \xi_2^2$, and the smallness of the interaction parameters presumes that $4\beta a_2 \gg \alpha^2$.

Assuming [in addition to the required global minimality of potential (14)] that $a_2 > 0$ and $a_2 + 4b_1 > 0$, we obtain the phase diagram (Fig. 1). It will be demonstrated below that, in order to describe the phase diagram for $YBa_2Cu_3O_{7-y}$, it suffices to confine the analysis to the expansion of $a_1(b_1)$, retaining the third degree of the polynomial $a_1(b_1)$. For the boundary between phases *1* and *3*, we obtain

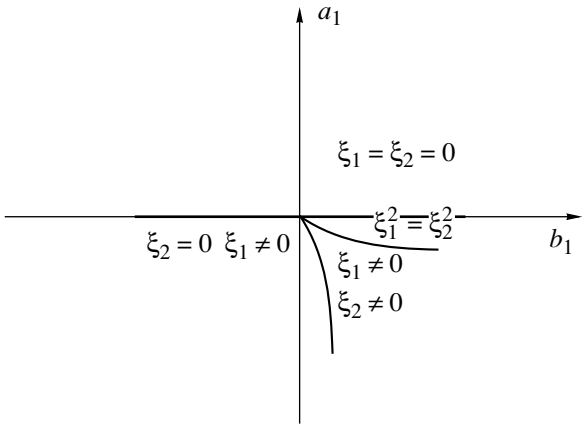

Fig. 1. Phase diagram corresponding to the nonequilibrium potential (14) near the line of transition between the tetragonal and orthorhombic phases (phase notation, see in Section 2).

$$a_1 = 2a_2/c_{12}b_1' + (2a_2c_{112} - 3a_3c_{12})/c_{12}^3 b_1'^2 + [4a_2c_{112}^2/c_{12}^5 - 62a_3c_{112}/c_{12}^4 + 4a_4/c_{12}^3]b_1'^3. \quad (15)$$

Here, $b_1' = b_1 - \alpha^2/4\beta$. The analytical form of the expression for the boundary between phases *2* and *3* will be exactly the same, but c_{112} should be replaced by $(c_{112} + b_2/8)$. Hence, it is obvious that $b_2 \neq 0$ determines the conditions for the existence of phase *3*.

All ten possible structures of the phases, which are induced by the same OP, are presented in Fig. 2. Triangles, squares, circles, and crosses in Figs. 2a–2j symbolize that the positions accessible for oxygen and marked by the same symbol for a given ordering have the same probability to be populated by oxygen at any concentration. The structure with the maximum ordering, which is induced by the proper OP φ (we choose the domain with $\varphi > 0$), is formed at $c = 1/2$. It is this structure which is identified in compositions of $YBa_2Cu_3O_{7-y}$ with $y \approx 0.1$ ($c \approx 0.45$).

The structure of the $Cu(1)(O_x\square_{1-x})_2$ layer for the leading OP $\mathbf{\Psi}$ and the condition $\Psi_1 = \Psi_2$ (Fig. 2c) is also characterized by a filling of chains, but only those aligned along the direction $x = y$. In Figs. 2f and 2i, we can see chains along the directions of elementary translations in the square lattice. They alternate similarly in the type of filling positions by oxygen in the transverse direction with period 4τ. For the maximum ordering attained at $\chi_1 = \chi_2 = 2c$, the chains are characterized by the following periodicity: … empty, half-empty, filled, half-empty, … . Both structures (Figs. 2f, 2i) are char-

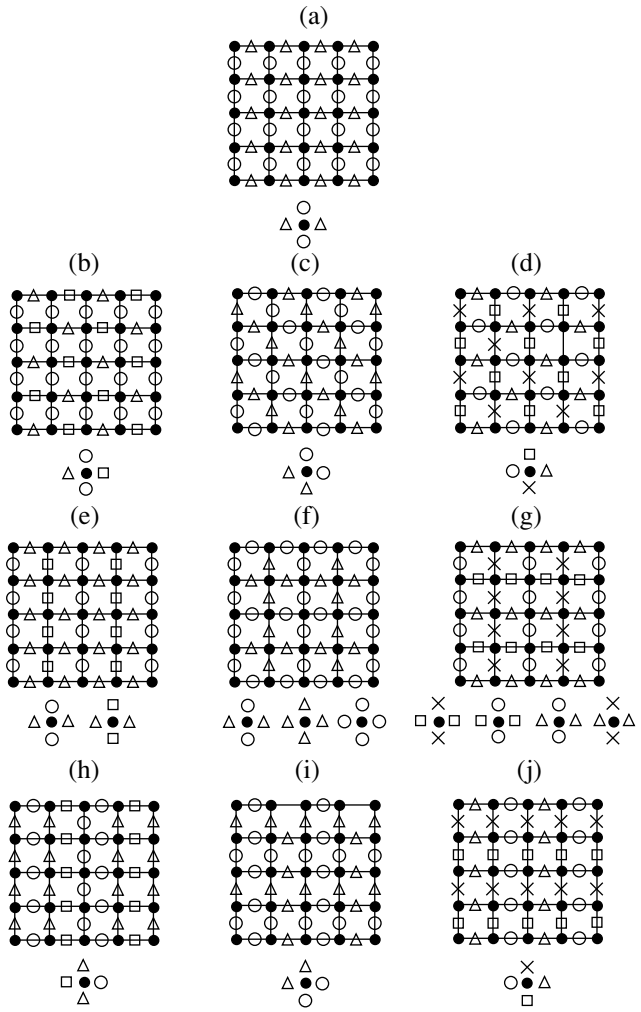

Fig. 2. Structures of ordered oxygen–vacancy states in the $Cu(1)(O_x\square_{1-x})_2$ layer, which are attained as a result of (a, b, c, e, f, h, i) the second-order transitions and (d, g, j) transitions with close energies. Designations: • correspond to copper; and □, ○, △, and × are the $2(f)D_{4h}^1$ positions accessible for oxygen with different probabilities for a given type of ordering. Orderings correspond to the following leading components of OP (3)–(5) and (7): (a) φ; (b) $\Psi_1 \neq 0$; (c) $\Psi_1^2 = \Psi_2^2 \neq 0$; (d) $\Psi_1 \neq 0$, $\Psi_2 \neq 0$; (e) $\chi_1 \neq 0$; (f) $\chi_1^2 = \chi_2^2 \neq 0$; (g) $\chi_1 \neq 0$, $\chi_2^2 \neq 0$; (h) $\eta_1 \neq 0$; (i) $\eta_1^2 = \eta_2^2 \neq 0$, and (j) $\eta_1 \neq 0$, $\eta_2 \neq 0$. The clusters (formed by a copper ion and the nearest oxygen ions) encountered in the structure are given at the bottom of each structure.

acterized by φ = 0. This means that such an ordering of oxygen will not be manifested at all in the experiments upon measuring the averaged difference in the populations of the positions (1/2 0 0) and (0 1/2 0) in $YBa_2Cu_3O_{7-y}$, but it should lead to superstructure reflections.

It should be noted that the theories proposed earlier for oxygen ordering in the $Cu(1)(O_x\square_{1-x})_2$ layer include the purely phenomenological theory [7], which used the same mathematical apparatus (proposed by one of the authors [16–19]) as the one we used here. However, it was assumed in [7] that the presence of copper ions in the $Cu(1)(O_x\square_{1-x})_2$ layer can be disregarded while constructing the theory of oxygen ordering. This assumption has made it possible to choose in [7] a primitive cell of the layer with an area equal to half the value used in the theory proposed here. Formally, this simplified the calculations but led to two basically erroneous conclusions. (1) The pairs of ordered structures shown in Figs. 2e, 2h, 2f, and 2i, as well as in Figs. 2g and 2j, appear in [7] as identical, i.e., having the same structure and mutual arrangement of (purely oxygen) chains. (2) According to [7], the ordering presented in Fig. 2a corresponds to the multiplication of the unit cell area; i.e., it should be manifested in the emergence of superstructure reflections on diffraction patterns. The latter result contradicts not only the inferences of the more comprehensive theory proposed by us here, but also all the available experimental results.

3. LIMITATIONS IMPOSED ON COMPONENTS OF ORDER PARAMETER

The OP components describing phases in Figs. 2a–2j are determined by the equations of state that follow from the nonequilibrium potential (14), and their dependence on external conditions is determined by the dependence of the phenomenological parameters on T and y. However, since $0 \le P_i \le 1$, purely "geometrical" limitations are imposed on the spatial region (φ, ξ_1, ξ_2) in which the solutions of the equations of state that have a physical meaning can exist. Indeed, for the ordering in phases depicted in Figs. 2a, 2c, 2f, and 2i, the nonzero OP components φ, $\Psi_1 = \Psi_2$, $\chi_1 = \chi_2$, and $\eta_1 = \eta_2$ can only be smaller than 0.5. The phases described by two components of different OPs, viz., Ψ_1 and φ, χ_1 and φ, and η_1 and φ (see Figs. 2b, 2e, and 2h) on the (φ, ξ) planes, are characterized by the regions of variations in OP components, whose shape is determined by the oxygen concentration in the $Cu(1)(O_x\square_{1-x})_2$ layer. For example, if $c < 1/4$ ($y > 0.5$), the region physically accessible for φ and Ψ_1 in the plane with the Cartesian coordinates (φ, $\Psi_1/2$) for a domain with $\Psi_1 > 0$ is a triangle with vertices at the points ($-c$, 0), (c, 0), (c, $2c$). Considering that $c < 1/4$, we obtain the limitation $-1/4 < \varphi < 1/4$, $\Psi_1/2 \le 1/2$. For $c > 1/4$, the region of physical values of φ and Ψ_1 in the (φ, $\Psi_1/2$) plane is a pentagon whose vertices lie at the points ($-c$, 0), ($1/2 - c$, $-1/2$), (c, $2c - 1$), (c, $1 - 2c$), ($1/2 - c$, 1/2). Thus, the values of the two OP components φ and $1/2\Psi_1$ do not exceed 1/2, even for the maximum oxygen concentration attainable in the $Cu(1)(O_x\square_{1-x})_2$ layer of $YBa_2Cu_3O_{7-y}$. It is the smallness of the OP components that determines the validity of relation (15).

The sequence of oxygen filling of systems of regular points in an ordered structure with increasing oxygen concentration in the layer, which is predicted by the theory, is also interesting. Let us assume that the lead-

ing OP is Ψ_1 and that $c < 1/4$. We confine our analysis to the limit of rather low temperatures T at which the ordering is close to the maximum possible for a given concentration c and assume that $\alpha < 0$. Under these assumptions, the theory developed above predicts that all oxygen is distributed only among positions *1* and *7* (2), and $P_1 = P_7 = 4c$. The rest of the positions remain empty. For $c > 1/4$, positions *2*, *4*, *6*, and *8* start being occupied, and $P_2 = P_4 = P_6 = P_8 = (2c - 1)/2$. Similarly, when χ_1 is the leading OP and $c < 1/4$, positions *2* and *4* (2) are first to be filled for the maximum possible value of χ and $\alpha > 0$, while positions *1*, *3*, *5*, and *7* are filled when $c > 1/4$. Positions *6* and *8* remain empty up to the limiting filling of vacancies with oxygen in the $Cu(1)(O_x\square_{1-x})_2$ layer of $YBa_2Cu_3O_{7-y}$, which corresponds to $c = 0.465$. If an ordering of the type depicted in Fig. 2h is realized, positions *1* and *5* are the first to be filled, while positions *3* and *7* remain empty in the case of complete ordering for any oxygen concentration retaining the 1212 structure ($1 \geq y \geq 0.07$).

4. EXPERIMENTAL IDENTIFICATION OF PHASES

Only two versions of the structures shown in Fig. 2 on the T–y phase diagram for $YBa_2Cu_3O_{7-y}$ are considered to be identified. The structure depicted in Fig. 2a is referred to as OI and exists near $c \approx 0.5$ [1]. The $\varphi^2(T)$ dependence analyzed in a number of publications [13, 14, 22] indicates that, in all probability, the OI ordering is described by the proper OP φ (Fig. 3). The structure in Fig. 2e for $y > 0.5$ corresponds to the OII phase. However, the changes in this structure (Fig. 2e) upon an increase in oxygen concentration, which were predicted by the theory developed on the basis of potential (14), differ significantly from those considered earlier during the interpretation of experimental data [1, 5–8, 10–12, 15]. The choice could be made on the basis of experiments, because the structure in Fig. 2e presumes the existence of an improper OP φ that can be measured directly in structural studies. However, we are not aware of any measurements of the dependences $\varphi(T)$ for $y \leq 0.5$ ($c \leq 0.25$), and such dependences would not reveal the differences between the structures presented in Figs. 2b, 2e, and 2h. The dependence of the average population of the (τ 0 0) and (0 τ 0) positions on y was determined in [3, 13, 14]. The data obtained in [3] and processed by us (Fig. 4) lead to the conclusion that $\varphi \sim (y_0 - y)^6$ near $y_0 \approx 0.65$. This fact calls for a separate analysis.

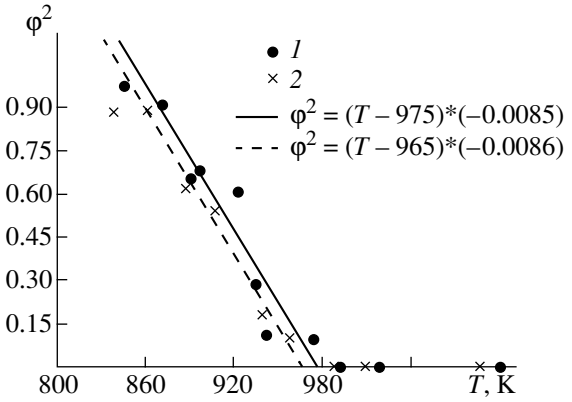

Fig. 3. Temperature dependence of the square of the degree of "average" oxygen ordering over positions $2(f)D^1_{4h}$ according to (*1*) [14] and (*2*) [13].

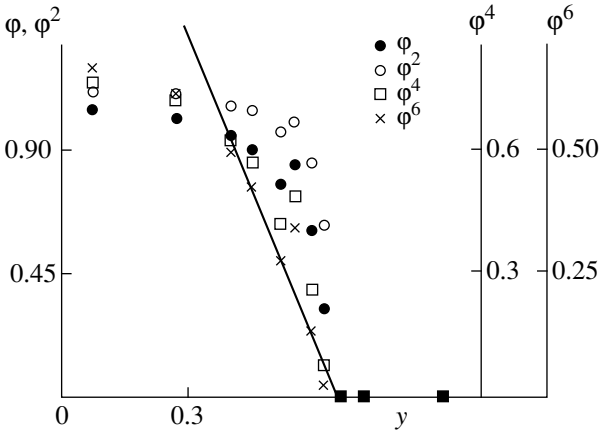

Fig. 4. Dependence of different powers of $\varphi = [n(0\ 1/2\ 0) - n(1/2\ 0\ 0)]/(1 - y)$ on the oxygen nonstoichiometry in $YBa_2Cu_3O_{7-y}$ [3].

APPENDIX

THE LANDAU THEORY ON THE STRUCTURE OF THE $Cu(1)(O_x\square_{1-x})_2$ LAYER

Since the $Cu(1)(O_x\square_{1-x})_2$ layer is encountered in many HTSC materials, we consider another possibility (that has not been analyzed before) of identifying homogeneous ordered states of oxygen-deficient structures of this layer, which are predicted by the Landau theory (see Fig. 2). Versions of clusters, which are formed by a copper ion surrounded by nearest oxygen neighbors typical of the given type of ordering, are depicted at the bottom of Figs. 2a–2j. The mutual orientations of these clusters in the structure can be easily determined from the figure. Since the copper ion is paramagnetic and the Cu nucleus is of the Mössbauer type, all ten structures can be singled out using the corresponding spectra.

For example, in the structures in Figs. 2a and 2e–2g, the decomposition of the crystal field at copper ions in multipoles starts from the quadrupole. The crystal fields of the clusters in Figs. 2b–2d and 2h–2j also contain a dipole component oriented in a certain way relative to the crystal lattice. In structures with a dipole field at Cu, (1) the electron densities of copper ions are not the only ones to be ordered (as, for instance, was observed in a perovskite with a similar structure [23]),

and (2) Cu ions will be displaced from the centrosymmetric position relative to the nearest oxygen surroundings. Since we are not aware of any publication in which models with the asymmetric displacement of copper ions in the $Cu(1)(O_x\square_{1-x})_2$ layer were considered for refining the $YBa_2Cu_3O_{7-y}$ structure by using diffraction patterns, we briefly consider a more rigorous proof for the existence of such an effect. We label four copper ions in a large unit cell as follows:

$$\begin{aligned} &1\text{—}(0\,0\,0); \quad 2\text{—}(2\tau\,0\,0); \\ &3\text{—}(2\tau\,2\tau\,0); \quad 4\text{—}(0\,2\tau\,0). \end{aligned} \tag{A1}$$

Possible ordering of the electron density of charge in positions 1–4 in (A1) is described by the following three functions:

$$R(T_1) = (f_1 - f_2 - f_4 + f_3)/2, \tag{A2}$$

$$\begin{aligned} X_1(T_1) &= (f_1 - f_2 + f_3 - f_4)/2; \\ X_2(T_1) &= (f_1 + f_2 - f_4 - f_3)/2. \end{aligned} \tag{A3}$$

Capital letters in the notation of functions (A2)–(A3) correspond to the D^1_{4h} point of the Brillouin zone; the subscript of T_i corresponds to the number of the irreducible representation according to [21], whose basis is formed by the given function; and f_i are spherically symmetric electron density distributions, which differ from zero near *i* positions from (A1). According to [17, 21], we find that the charge redistribution (i.e., ordering of valence states) should be observed in the structures depicted in Figs. 2e–2g. "Weak" charge ordering at copper sites, which is proportional to interactions with the third coordination sphere, should be observed in Figs. 2b–2d, and 2h–2j.

Displacements of copper atoms in the plane of the $Cu(1)(O_x\square_{1-x})_2$ layer are described by eight functions $V_i(T_j)$ whose symmetry coincides with that of the product of functions (A2)–(A3) into the components of the displacement vector in the plane:

$$\begin{aligned} &(V_1(\Gamma);\, V_2(\Gamma)) - E_u(\Gamma); \\ &(V_1(R);\, V_2(R)) - E(R); \\ &(V_1(X_1);\, V_2(X_2)) - T_2(X); \\ &(V_1(X_2);\, V_2(X_1)) - T_2(X). \end{aligned} \tag{A4}$$

Comparing these expressions with Eqs. (3)–(5) and Eq. (7), we find that certain displacements of copper atoms from symmetry positions should be proportional to the leading OP in the structures depicted in Figs. 2b–2d and 2h–2j.

ACKNOWLEDGMENTS

The authors are grateful to the Russian Foundation for Basic Research and the Japan Science and Technology Corporation (JST) for the financial support of this research.

REFERENCES

1. G. P. Shveĭkin, V. A. Gubanov, A. A. Fotiev, G. V. Bazuev, and A. A. Evdokimov, *Electronic Structure and Physicochemical Properties of High-Temperature Superconductors* (Nauka, Moscow, 1990).
2. H. Shaked, P. M. Keane, J. C. Rodriguez, F. F. Owen, R. L. Hitterman, and J. D. Jorgensen, *Crystal Structures of High-Tc Superconducting Copper Oxides*, *Materials of Scientific Division of Argonne National Laboratory* (Argonne, 1994).
3. J. D. Jorgensen, B. W. Veal, A. P. Paulikas, *et al.*, Phys. Rev. B **41** (4), 1863 (1990).
4. J. Ye and K. Nakamura, Phys. Rev. B **48** (10), 7554 (1993).
5. R. J. Cava, A. W. Hewat, E. A. Hewat, *et al.*, Physica C (Amsterdam) **165**, 419 (1990).
6. P. Burlet, P. Bourges, J. Bossy, *et al.*, J. Supercond. **9** (4), 357 (1996).
7. K. B. Blagoev and L. T. Wille, Phys. Rev. B **48** (9), 6588 (1993).
8. D. de Fontaine, L. T. Wille, and S. C. Moss, Phys. Rev. B **36** (10), 5709 (1987).
9. G. Ceder, M. Asta, and D. de Fontain, Physica C (Amsterdam) **177** (1–3), 106 (1991).
10. A. A. Aligia and J. Garces, Phys. Rev. B **49** (1), 524 (1994).
11. S. Semenovskaya and A. G. Khachaturyan, Phys. Rev. B **46** (10), 6511 (1992).
12. A. G. Panfilov, A. I. Rykov, S. Tajima, and A. Yamanaka, Phys. Rev. B **58** (18), 12459 (1998).
13. K. Nakamura and K. Ogawa, Jpn. J. Appl. Phys. **27** (4), 577 (1987).
14. J. Jorgensen, M. A. Beno, D. G. Hinks, *et al.*, Phys. Rev. B **36** (7), 3608 (1987).
15. V. E. Zubkus, E. E. Tornau, S. Lapinskas, and P. J. Kundrotas, Phys. Rev. B **43** (16), 13112 (1991).
16. Yu. M. Gufan and V. P. Dmitriev, Fiz. Met. Metalloved. **53** (3), 447 (1982); **53** (5), 852 (1982).
17. Yu. F. Gufan, *Structural Phase Transitions* (Nauka, Moscow, 1982).
18. Yu. M. Gufan and V. P. Sakhnenko, Zh. Éksp. Teor. Fiz. **63** (5), 1909 (1972) [Sov. Phys. JETP **36**, 1009 (1972)]; **69** (4), 1428 (1975) [Sov. Phys. JETP **42**, 728 (1975)].
19. Yu. M. Gufan and V. P. Dmitriev, Kristallografiya **25** (1), 14 (1980) [Sov. Phys. Crystallogr. **25**, 6 (1980)].
20. P. P. Freitas and T. S. Plaskett, Phys. Rev. B **36** (10), 5723 (1987).
21. O. V. Kovalev, *Irreducible and Induced Representations and Corepresentations of Fedorov Groups* (Nauka, Moscow, 1986).
22. J. D. Jorgensen, B. W. Veal, W. K. Kwonk, *et al.*, Phys. Rev. B **36** (10), 5731 (1987).
23. Y. Murakami, J. P. Hill, D. Gibbs, *et al.*, Phys. Rev. Lett. **81** (3), 582 (1998).

Translated by N. Wadhwa

Physics of the Solid State, Vol. 42, No. 10, 2000, pp. 1825–1831. Translated from Fizika Tverdogo Tela, Vol. 42, No. 10, 2000, pp. 1780–1785.

METALS AND SUPERCONDUCTORS

Critical Current, Trapped Magnetic Fields, and Ruptured Vortices in HTSC Ceramic Samples

A. A. Kozlovskiĭ and V. F. Khirnyĭ

Institute of Single Crystals, National Academy of Sciences of Ukraine, pr. Lenina 60, Kharkov, 310141 Ukraine

e-mail: root@isc.kharkov.ua

Received in final form March 31, 2000

Abstract—Dependences of critical currents on the trapped H_{TRAP} and remanent H_{REM} magnetic fields in granular ceramic HTSC samples of $YBa_2Cu_3O_x$ and $Bi_{1.6}Pb_{0.4}Sr_2Ca_2Cu_3O_x$ are obtained. The contribution of dissipation fields of ruptured quantized magnetic vortices to these fields is taken into account for the first time. © *2000 MAIK "Nauka/Interperiodica".*

A study of critical current I_c invariably requires an analysis of the magnetic flux trapping in type II superconductors. In most cases, the effect of magnetic fields remaining in samples after switching off an external magnetic field on the value of I_c was studied (see, for example, [1]). However, the origin of the trapped magnetic field is still not quite clear. In fact, the influence of trapped magnetic fields induced by the self-magnetic field H_i of the transport current I_t after its switching off on I_c was not analyzed. It is known [2] that as the measuring current I reaches the critical value I_c, the field H_i penetrates into ceramic high-temperature superconductor (HTSC) samples in the form of rings formed by quantized magnetic vortices. After switching off the current, vortex rings remain in the sample. This work is devoted to the analysis of the effect of not only the magnetic fields of the vortices on I_c, but also the external fields H parallel to the sample and the current.

1. TRANSVERSE CIRCULAR FIELDS

The $I_c(I_t)$ dependence was studied on seven HTSC ceramic samples: samples nos. 1–3 had the composition 1–2–3 (in sample no. 2, yttrium was replaced by erbium), and samples nos. 4–7 had the composition $Bi_{1.6}Pb_{0.4}Sr_2Ca_2Cu_3O_x$ (these samples were investigated in [2]). The characteristic parameters of the samples are given in the table, where D is the diameter and L is the length. A circular magnetic field at room temperature was created by passing current I_t through the samples. In this circular magnetic field, the samples were cooled to T = 77 K (the FC mode), after which the current I_t was switched off. The circular magnetic field was trapped in superconducting samples in the form of vortex rings. The critical current I_c were measured by using the four-point probe method. The samples were kept in liquid nitrogen. The value of I_c to be measured corresponded to the minimum voltage $\cong 1.5 \times 10^{-6}$ V across the sample. The measurements were made in the magnetic field of the Earth. The critical value I_c of the measuring current was denoted by $I_{c\uparrow\uparrow}$ for the coinciding directions of the transport (I_t) and measuring (I) currents, and by $I_{c\uparrow\downarrow}$ for their opposite directions.

Curves *1* and *2* in Fig. 1a show the dependences $I_{c\uparrow\uparrow}(I_t)$ and $I_{c\uparrow\downarrow}(I_t)$ for sample no. 1, which are typical of all the samples of the 123 composition. Curves *1* and *2*

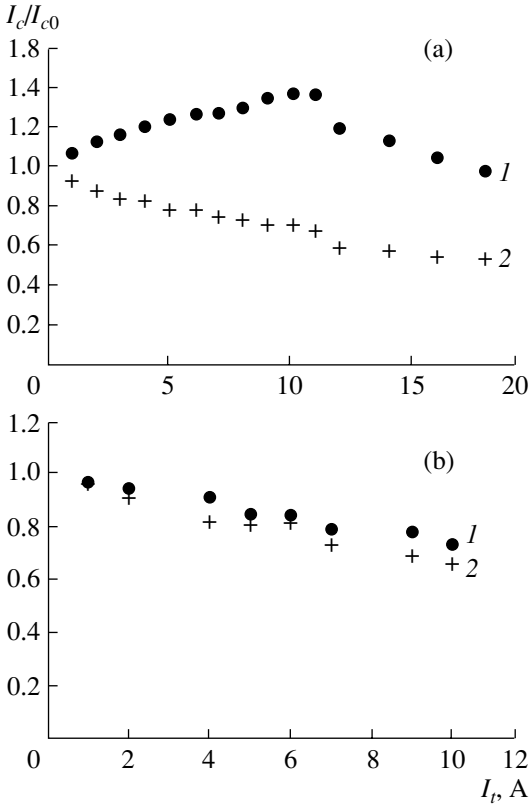

Fig. 1. Reduced critical currents I_c/I_{c0} as a function of the transport current I_t in (a) $YBa_2Cu_3O_x$ and (b) $Bi_{1.6}Pb_{0.4}Sr_2Ca_2Cu_3O_x$ samples: (*1*) parallel currents I_t and I, and (*2*) antiparallel currents.

1063-7834/00/4210-1825$20.00 © 2000 MAIK "Nauka/Interperiodica"

Properties of studied samples with L = 1.5 cm

Sample no.	1	2	3	4	5	6	7
Composition	YBCO	ErBCO	YBCO	BPSCCO	BPSCCO	BPSCCO	BPSCCO
I_{c0}, A	3.83	6.75	13.6	1.2	2.88	2.92	8.15
D, mm	2.3	2.5	6.2	2.0	3.1	3.1	1.6

display singularities, viz. a peak and a change in the slope, respectively, for the same current I_t; I_{c0} is the critical current (see table) obtained at T = 77 K and H = 0 after cooling in zero magnetic field (the ZFC mode). The current I_{c0} produces a field $H_0 \cong 6.6$ Oe at the sample surface. Figure 1b shows the results obtained for the $Bi_{1.6}Pb_{0.4}Sr_2Ca_2Cu_3O_x$ sample (no. 4).

The results presented in Fig. 1a can be explained qualitatively by the presence of circular rings formed by Josephson and Abrikosov vortices trapped in the sample. The number of Josephson vortices in dense YBCO samples at T = 77 K is considerably smaller than the number of Abrikosov vortices. At this temperature, the latter vortices are pinned inside the grains, in which they were formed even at $T \cong T_c$ when the first critical magnetic field H_{c1g} of the grains differed from zero only slightly. Consequently, the rings pierced grains, intergranular links, and inhomogeneities. The rings are ruptured due to the presence of voids and nonsuperconducting inclusions whose size is larger than the London penetration depth λ_L for the magnetic field, and the magnetic coupling between the ring parts is broken. The ruptured (magnetically disconnected) vortices have been known to exist long ago [3]. The possibility of their presence in HTSC ceramics follows from an analysis of the operation of dc low-temperature superconducting thin-film transformers [3].

Unlike a continuous superconducting medium in which the magnetic field H_v is inside vortices, the magnetic field in granular HTSC materials also exists outside the fragments of vortices forming ruptured rings. The magnetic flux lines of this dissipation field H_d (except those lying near the vortex axis) are closed outside the ruptured vortex rings and grains, since $H_d < H_{c1g}$. The distribution of the field H_d outside sample no. 1 was measured with the help of a Hall probe at 77 K. The circular field H_d was of the order of 0.5 Oe and resembled the field of a magnet for which $\oint H_d\, dl = 0$ along the closed path L passing outside the sample. We will discuss this at a later stage.

The averaged field $H_{\mathrm{REM}} = \sum_n (H_v - H_d)$, created inside the sample by ruptured vortex rings, is of the same polarity as the field created by unruptured vortices. Here, n is the number of ruptured vortex rings in the sample. We assume that, at $I = I_c$, the field H_{REM} affects the penetration of vortex rings into the sample as follows. When the rings having the same sign as ruptured pinned rings penetrate the sample, the energy barrier $E_{\uparrow\uparrow}$ to this process is higher than the barrier E_0 in the measurement of the critical current I_{c0}. This is due to repulsive forces exerted by the magnetic fields of ruptured vortex rings on a ring entering the sample. Consequently, the magnetic field H_i required for attaining the critical value of the measuring current I should be stronger than H_0. This leads to the fulfillment of the inequality $I_{c\uparrow\uparrow} > I_{c0}$ for coinciding directions of the currents I and I_t. When the currents I and I_t are antiparallel, the polarity of the circulation of the vortex rings penetrating the sample is opposite to that of ruptured rings pinned in the sample. The latter rings attract the rings entering the sample and create the condition under which the inequality $I_{c\uparrow\downarrow} < I_{c0}$ holds. The changes in the shape of the $I_c(I_t)$ curves in Fig. 1a for $I_t \geq 10$ A are apparently due to a decrease in the energy barrier height upon an increase in the current I_t.

The above analysis is also applicable to macroscopic inclusions of a frozen flux, i.e., bundles of Abrikosov vortices.

The values of $I_{c\uparrow\uparrow}$ and $I_{c\uparrow\downarrow}$ for the $Bi_{1.6}Pb_{0.4}Sr_2Ca_2Cu_3O_x$ sample (no. 4) with weak pinning forces (i.e., with a small value of I_{c0}) decrease with an increase in the magnetic field, but to a different extent (Fig. 1b). This is apparently due to the presence of circular Josephson vortices in porous $Bi_{1.6}Pb_{0.4}Sr_2Ca_2Cu_3O_x$ ceramic samples [2]. The interactions between penetrating and pinned rings are of the fluxquantum–fluxquantum type for coinciding directions of the currents I_t and I, and of the fluxquantum–antifluxquantum soliton type [4] for the opposite directions of these currents. In both cases, heat is liberated. The critical current decreases due to energy dissipation. Samples nos. 5 and 6 exhibited a similar behavior.

In the $Bi_{1.6}Pb_{0.4}Sr_2Ca_2Cu_3O_x$ sample (no. 7), the magnetic flux was not trapped, and, hence, $I_{c\uparrow\uparrow}$ and $I_{c\uparrow\downarrow}$ were equal to I_{c0}.

Flux trapping was not observed either in the case when an ac current of frequency 50 Hz was passed through samples nos. 1, 4, and 7.

2. LONGITUDINAL LINEAR FIELDS

The dissipation fields should also exist for linear quantized magnetic vortices in HTSC ceramics. These fields contribute to the remanent field H_{REM} and influence the critical current I_c. In order to verify this assumption, we studied the $I_c(H)$ dependence at T = 77 K with the field H parallel to the current. The measurements

were made in the ZFC and FC modes. In the former case, the measured critical current was denoted by $I_{1c}(H)$ in an increasing external field and by $I_{2c}(H)$ in a decreasing field. The critical current $I_{3c}(H)$ was measured in a magnetic field, which remained in the sample after the application and removal of the external magnetic field upon the sample cooling to 77 K. In the FC mode of measurements, the sample was cooled in a magnetic field to 77 K, and the critical current, which was denoted by $I_{4c}(H)$, was measured without switching off the field. The critical current $I_{5c}(H)$ was measured in the magnetic field remaining in the sample after cooling to 77 K followed by switching off the magnetic field. Finally, the critical current $I_{6c}(H)$ was measured after cooling the sample in the field followed by the magnetic field switching off and on.

Figure 2 presents the results obtained for the yttrium-based sample no. 1. In the ZFC mode, the hysteresis appeared on the $I_{1c}(H)$ and $I_{2c}(H)$ curves as a result of magnetic flux trapping in grains after the magnetic field H attained the value $H_{c1g} \cong 300$ Oe. The invariability of the dependences $I_{3c}(H) \cong I_{c0}(H)$ indicates that, as the external magnetic field decreases to zero, either the magnetic flux leaves the sample, or the trapped field is smaller than the lower critical field H_{c1j} of intergranular links.

It can be seen from Fig. 2 that the inequality $I_{1c} < I_{4c}$ is observed for all fields. This is due to a partial compensation of the external field by the trapped magnetic field H_{TRAP}, created by the dissipation field of ruptured linear magnetic vortices which were pinned in grains at $T = T_c$.

In the case of FC-mode measurements, $I_{6c} \cong I_{4c}$ and $H_{\mathrm{REM}} = H_{\mathrm{TRAP}}$ at $H \leq 75$ Oe, where H_{REM} is the field remaining in the sample after switching off the external field. However, starting from $H \geq 75$ Oe, the inequality $I_{6c} < I_{4c}$ was observed. In other words, during measurements of I_{6c}, the external field was compensated to a lesser extent than during the I_{4c} measurements. Consequently, $H_{\mathrm{REM}} < H_{\mathrm{TRAP}}$. The observed feature can be explained by the influence of the Bean–Livingston surface barrier of grains on the properties of vortices [5]. In the I_{4c} measurements, the surface barrier of grains is lowered by the applied magnetic field. The vortices separated by a distance $x \cong \lambda_L$ from the surface of grains are attracted to this surface with a force $F(x)$. If $F(x) < F_p$ (where F_p is the pinning force), all the pinned vortices remain in the sample. In the case of I_{5c} measurements, i.e., after the removal of the field, the barrier is elevated. The value of $F(x)$ increases and may become greater than F_p. In this case, the vortices separated from the surface by a distance x leave the sample. When the field is applied again (I_{6c} measurements), the number of vortices in the sample remains unchanged since $H < H_{c1g}$. Consequently, the value of H_{REM} remains unchanged.

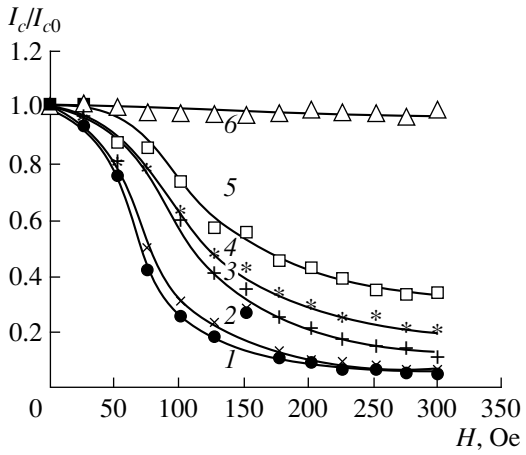

Fig. 2. Dependences of the reduced critical currents on the external magnetic field H: (*1*) $I_{1c}(H)$, (*2*) $I_{2c}(H)$, (*3*) $I_{6c}(H)$, (*4*) $I_{4c}(H)$, (*5*) $I_{5c}(H)$, and (*6*) $I_{3c}(H)$.

2.1. Determination of Trapped H^j_{TRAP} and Remanent H^j_{REM} Magnetic Fields in the Intergranular Region

For determining the remanent magnetization, we used the equality of the currents I_{1c} and I_{5c} measured under different conditions (see Fig. 2). For the I_{1c} measurements in the ZFC mode, the effective field in the intergranular region can be represented in the form

$$H_{\mathrm{eff1}} = H_1 + H_i + H_1^g - 4\pi M_1^j, \tag{1a}$$

where H_1 is the field in which the sample was placed during the I_{1c} measurements; H_i is the field generated by the measuring current I; and H_1^g is the field in the intergranular region, which is created by the shielding currents in grains. This field is basically directed along the external field. In the above formula, M_1^j is the magnetization of the intergranular region, which is associated with shielding currents in this region (this component of the magnetic moment is directed against the applied field) as well as with Josephson vortices penetrating the intergranular region (this moment component is directed along the field). Since $H_1 < H_{c1g} \cong 300$ Oe, the contribution to H_{eff1} from the vortices inside the grains is equal to zero. The expression for the effective field in the I_{5c} measurements has the form

$$H_{\mathrm{eff5}} = H^j_{\mathrm{REM}} + H_i, \tag{1b}$$

where H^j_{REM} is the dissipation field of the remanent magnetic flux in the intergranular region, which is produced by fragments of ruptured Abrikosov vortices. The equality of currents and effective fields gives

$$H^j_{\mathrm{REM}} = H_1 + H_1^g - 4\pi M_1^j. \tag{2}$$

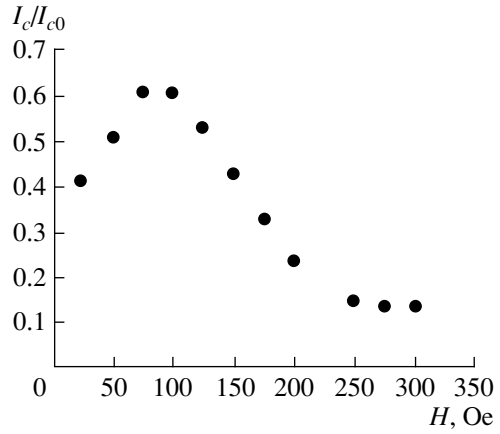

Fig. 3. Dependence of the reduced critical current on the external magnetic field applied after the sample cooling in the field H_m = 250 Oe.

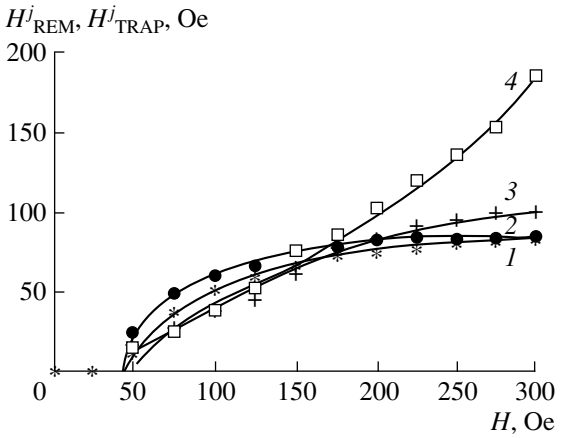

Fig. 4. Dependences of (*1–3*) H^j_{REM} and (*4*) H^j_{TRAP} on the field H, obtained in different ways: (*1*) calculation by formula (3), (*2*) graphical method, (*3*) calculation by formula (4), and (*4*) calculation by formula (5).

We cannot estimate the value of M^j_1 or H^g_1; however, since they are antiparallel, we assume that the second and third terms in Eq. (2) are mutually compensated, i.e.,

$$H^j_{REM} \cong H_1. \quad (3)$$

Similarly, by comparing I_{1c} and I_{6c}, we can easily obtain

$$H^j_{REM} \cong H_6 - H_1, \quad (4)$$

where H_6 is the field in which the sample was placed during the I_{6c} measurements.

The value of $H^j_{REM}(H)$ was also determined graphically using the $I_c(H)$ curves obtained after the sample was cooled in field H_m parallel to the current. The field H_m was then removed, and the critical current was measured in fields H varying from 0 to 300 Oe. These curves had peaks observed for the maximum possible compensation for the applied field by the remanent field. Figure 3 depicts such a dependence for H_m = 250 Oe. It can be seen that the peak corresponds to a field of 87.5 Oe; i.e., the magnetic field remaining in the intergranular region after sample cooling to 77 K in a field of 250 Oe, and the subsequent removal of the field, is H^j_{REM} = 87.5 Oe. Measuring $I_c(H)$ at different values of the field H_m, we obtained the dependence $H^j_{REM}(H)$. Figure 4 shows the $H^j_{REM}(H)$ curves plotted by using formulas (3) and (4) as well as the graphical method. A comparison of these curves shows that calculations based on formula (3) give an error of up to 10% (which is within the error of measurements), while only a qualitative correspondence is attained by using formula (4).

The trapped field H^j_{TRAP} cannot be determined experimentally. For this reason, the field H^j_{TRAP} was calculated using a formula similar to expression (4) with the help of the equalities $I_{4c} = I_{1c}$ and $H_{eff4} = H_{eff1}$. This gives

$$H^j_{TRAP} \cong H_4 - H_1, \quad (5)$$

where H_4 is the field in which the sample was placed during the measurements of I_{4c}. The variation of H^j_{TRAP} upon an increase in H, which was calculated from expression (5), is illustrated in Fig. 4.

2.2. Estimation of Trapped H^j_{TRAP} and Remanent H^g_{REM} Magnetic Fields in Grains

The magnitude of the field is inversely proportional to the areas of the surfaces through which the magnetic flux penetrates. Assuming that the number N of grains in the cross-sections of the sample is nearly the same over the entire sample length and writing the cross-sectional area of the sample in the form $S = N(S_g + S_j)$, we obtain

$$H^j_{TRAP}/H^g_{TRAP} = H^j_{REM}/H^g_{REM} = 2.7V_g/V_j, \quad (6)$$

where S_g is the cross-sectional area of a grain, S_j is the cross-sectional area of the surrounding intergranular space per grain, V_g is the volume fraction of grains in the sample, and $V_j = 1 - V_g$ is the volume fraction of intergranular links. The calculations were made under the assumption that grains have a spherical shape and the average distance between them is the same; hence, $S_g/S_j = 2.7V_g/V_j$. The ratio V_g/V_j was obtained from the measurements of the real component of the magnetic

susceptibility $\chi' = V_g\chi'_g + V_j\chi'_j$ [2], where $V_g\chi'_g$ is the magnitude of the signal from the grains, and $V_j\chi'_j$ is the signal from the intergranular links. For the yttrium-based sample no. 1, the ratio $S_g/S_j \cong 0.7$; hence, $H^g_{\mathrm{TRAP}} = 1.43H^j_{\mathrm{TRAP}}$ and $H^g_{\mathrm{REM}} = 1.43H^j_{\mathrm{REM}}$.

In order to determine the extent of magnetic flux trapping in grains for the FC mode, we introduced the flux trapping coefficient $k_{\mathrm{TRAP}} = H^g_{\mathrm{TRAP}}/H$, which is similar to that analyzed in [6]. Its magnitude shows the fraction of the applied field remaining in the grains. The fraction of the magnetic flux remaining in grains after the removal of the external field is determined by introducing the remanent magnetization coefficient $K_{\mathrm{REM}} = H^g_{\mathrm{REM}}/H^g_{\mathrm{TRAP}}$. Figure 5 shows the dependences $K_{\mathrm{TRAP}}(H)$ and $k_{\mathrm{REM}}(H)$ for sample no. 1. It can be seen that $K_{\mathrm{TRAP}}(H)$ increases with the field, while $K_{\mathrm{REM}}(H)$ decreases upon an increase in the field. This is due to the fact that the force $F(x)$ acting on vortices changes with H. The coefficients $K_{\mathrm{TRAP}}(H)$ and $K_{\mathrm{REM}}(H)$ presented in Fig. 5 were obtained from the $F(x/\lambda_L, H)$ dependences for $\lambda_L = 2.3 \times 10^{-7}$ m and $F_p = 1.5 \times 10^{-4}$ H/m. The coefficients $K_{\mathrm{TRAP}}(H)$ and $K_{\mathrm{REM}}(H)$ calculated for these values of λ_L and F_p were in best agreement with the experimental values. The force $F(x)$ was determined by the formula $F(x) = -dE(x, H)/dx$, where E is the linear energy of a vortex per unit length [5]. We assumed that the grains have the shape of a sphere of radius $R \sim 10^{-7}$ m, and all the vortices trapped at $T \le T_c$ during sample cooling in the FC mode remain in the grains. The expression for the force F acting on the first row of vortices obtained by using Gibbs' thermodynamic potential is given in [7].

It should be noted that the HTSC ceramic sample $Bi_{1.6}Pb_{0.4}Sr_2Ca_2Cu_3O_x$ (no. 4) had similar properties.

3. SPIRAL MAGNETIC FIELDS

An external magnetic field H applied parallel to the cylinder axis does not affect the conditions of penetration of a vortex ring, created by the self-magnetic field of the transport current, into the sample. Similarly, the transport current does not suppress the critical field of penetration of a linear vortex parallel to the cylinder axis [8]. In this case, zero-force configurations are observed, and linear and circular vortices exist in the sample independently. However, other configurations, viz., helicoidal vortices [9], can also exist, for which the field H influences the critical current. The conditions under which a transition is made from one case to the other are considered in this section.

We measured the critical current $I_c(H)$ as a function of the applied magnetic field H. Before the measurements, the current I_{tr} was passed through the sample (no. 1), and the external magnetic field H_0 was applied to it parallel to the current. The sample was cooled from

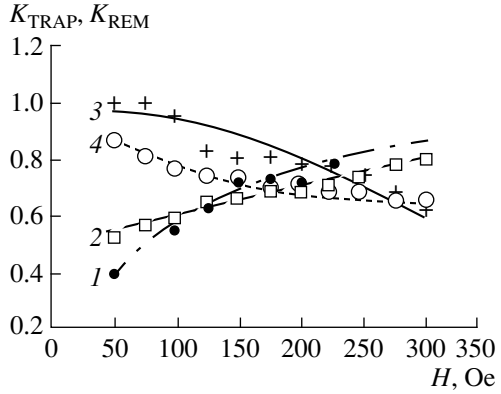

Fig. 5. (*1*, *3*) Experimental and (*2*, *4*) theoretical dependences of (*1*, *2*) the flux trapping coefficients K_{TRAP} and (*3*, *4*) the coefficient of the remanent magnetization K_{REM} on the external magnetic field H.

$T > T_c$ to 77 K. This created a premise for trapping helicoidal vortices, since the sample was under the action of the total helicoidal magnetic field $H_f = (H^2_{tr} + H^2_0)^{0.5}$. Here, H_{tr} is the circular field created by the transport current. Helicoidal vortices encountering inhomogeneities with a size greater than λ_L were ruptured. Their dissipation fields were concentrated in the intergranular space and produced the trapped helicoidal field affecting the value of I_c.

After the sample was cooled to 77 K, the current I_{tr} was switched off. When the field H_0 was not removed after the attainment of a temperature of 77 K and the measurements were made in this field, the current I_c was denoted by $I_{4c\uparrow\uparrow}$ and $I_{4c\uparrow\downarrow}$. If H_0 is switched off and $H = 0$, I_c can be represented in the form $I_{5c\uparrow\uparrow}$ and $I_{5c\uparrow\downarrow}$. When the current I_c was measured after switching off H_0 and the external longitudinal magnetic field $H = H_0$ was switched on again, I_c was denoted as $I_{6c\uparrow\uparrow}$, $I_{6c\uparrow\downarrow}$, $I_{7c\uparrow\uparrow}$, and $I_{7c\uparrow\downarrow}$. The measurements of $I_{6c\uparrow\uparrow}$ and $I_{6c\uparrow\downarrow}$ were made for the same direction of H_0 and H, whereas $I_{7c\uparrow\uparrow}$ and $I_{7c\uparrow\downarrow}$ were measured for opposite directions of these fields. After each measurement, the sample was heated to $T > T_c$. As before, the symbols $\uparrow\uparrow$ and $\uparrow\downarrow$ indicate that the currents I_{tr} and I were parallel and antiparallel, respectively.

The behavior of the $I_c(H)$ dependences was analyzed for four values of I_{tr} (A): 2, 4, 6, and 8. The curves in Fig. 6 were obtained for $I_{tr} = 8$ A. It can be seen from the figure that the curves $I_{4c\uparrow\uparrow}(H)$ and $I_{6c\uparrow\uparrow}(H)$, as well as $I_{4c\uparrow\downarrow}(H)$ and $I_{6c\uparrow\downarrow}(H)$, coincide up to $H \cong 75$ Oe. A similar behavior was observed when the sample was under the action of longitudinal linear fields. Consequently, we assume that the difference between the trapped (H_{TRAP}) and remanent (H_{REM}) fields is manifested due to the effect of the Bean–Livingston barrier [5]. We will only consider the effect of H_{REM} on I_c. For

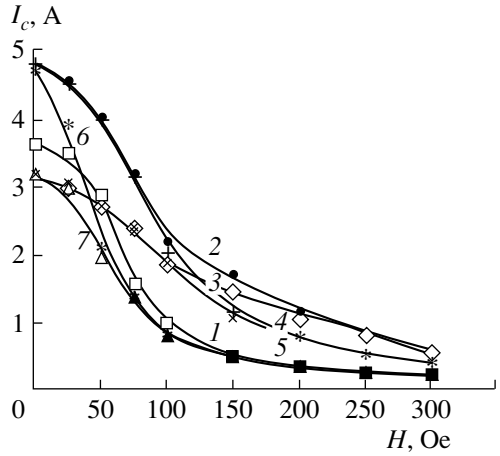

Fig. 6. Experimental dependences $I_c(H)$ obtained under different conditions of measurements: (*1*) I_{1c}, (*2*) $I_{4c\uparrow\uparrow}$, (*3*) $I_{4c\uparrow\downarrow}$, (*4*) $I_{6c\uparrow\uparrow}$, (*5*) $I_{6c\uparrow\downarrow}$, (*6*) $I_{7c\uparrow\uparrow}$, and (*7*) $I_{7c\uparrow\downarrow}$; I_{tr} = 8 A.

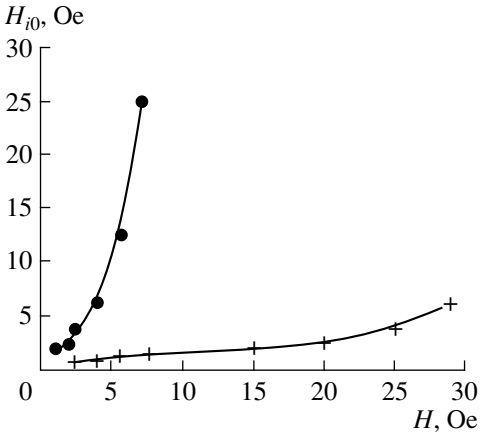

Fig. 7. State diagram for the existence of helicoids and a superposition of circular and longitudinal linear vortices in the sample.

comparison, Fig. 6 shows the dependence $I_{1c}(H)$. It can be seen that the condition $I_{4c\uparrow\uparrow}(H)$ and $I_{6c\uparrow\uparrow}(H) > I_{1c}$ holds for all values of H. At the same time, $I_{4c\uparrow\downarrow}(H)$, $I_{6c\uparrow\downarrow}(H) > I_{1c}$ for $H > H^*$, while $I_{4c\uparrow\downarrow}$, $I_{6c\uparrow\downarrow} < I_{1c}$ for $H < H^*$. With increasing I_{tr}, i.e., with the increasing contribution of the transverse component H_i of the field to H_f, the value of H^* increased. At $H \geq 150$ Oe, the dependences $I_{7c\uparrow\uparrow}(H)$ and $I_{7c\uparrow\downarrow}(H)$ coincide with $I_{1c}(H)$. In weaker fields, the $I_{7c\uparrow\downarrow}$ curve lies below $I_{1c}(H)$. The curves $I_{7c\uparrow\uparrow}(H)$ and $I_{1c}(H)$ intersect for $H = H^{**}$. At $H > H^{**}$, the inequality $I_{7c\uparrow\uparrow} < I_{1c}$ holds. The fields H^{**} and H^* increased with I_{tr}.

In order to explain the behavior of the obtained curves, we made a special experiment to find the conditions under which circular and linear vortices and helicoids exist in the sample. An analysis of the conditions for the transition from the penetration of helicoids into the superconductor to the penetration of circular and linear vortices was carried out for the HTSC ceramic $Bi_{1.6}Pb_{0.4}Sr_2Ca_2Cu_3O_x$ sample (no. 5). A longitudinal hole was drilled in the sample, and a copper wire was drawn through it. The electric current I_0 passing through the wire created transverse circular fields H_{i0}. Simultaneously, the sample was subjected to an external magnetic field H parallel to the current and the sample axis. In order to determine the types of vortices existing in the sample, we obtained, as in [9], the dependence of the critical temperature T_c^j of intergranular links on the longitudinal and circular magnetic field, as well as on their superpositions. The temperature T_c^j corresponded to the temperature at which the signal of the real component $\chi'(T)$ of the complex magnetic susceptibility changed by 50% in the region of the superconducting transition of weak links [2]. Under the effect of H and H_{i0}, the $\chi'(T)$ dependences were shifted by ΔT toward lower temperatures. According to Genenko [8], the field H does not affect the conditions of penetration of vortex rings, and the field H_{i0} does not suppress the critical field for the penetration of a linear vortex. Consequently, the form of the variation of ΔT as a function of H and H_{i0} can be used to determine the boundary between the values (H_{i0}, H) for which the resistive states characterized by the penetration of circular and longitudinal vortices and helicoids are formed in the sample. Figure 7 shows a diagram of these states. The curves mark the lower and upper boundaries of the region of existence of helicoids. Outside the region bounded by these curves, the sample contains a superposition of circular and longitudinal linear vortices in the fields H and H_{i0} differing from each other by approximately an order of magnitude. In other words, we can state that helicoids exist at commensurate values of the magnetic fields H_i and H; otherwise, linear and circular vortices are present in the sample.

Returning to Fig. 6, we see that the curves $I_{4c\uparrow\uparrow}(H)$, $I_{4c\uparrow\downarrow}(H)$, $I_{6c\uparrow\downarrow}(H)$, and $I_{6c\uparrow\uparrow}(H)$ do not reach saturation at large H, and the $I_{7c\uparrow\uparrow}(H)$ and $I_{7c\uparrow\downarrow}(H)$ curves coincide with the $I_{1c}(H)$ curve and have a singularity. They decrease monotonically up to $H \cong 150$ Oe and then attain saturation. We assume that helicoids penetrate the sample up to this value of the magnetic field, and for $H \geq 150$ Oe, circular vortex rings and linear vortices enter the sample independently. This apparently also explains the absence of a difference in the values of I_{1c}, $I_{7c\uparrow\uparrow}$, and $I_{7c\uparrow\downarrow}(H)$ in spite of the fact that the longitudinal component of the field during the $I_{7c\uparrow\uparrow}$ and $I_{7c\uparrow\downarrow}(H)$ measurements is larger than that for the I_{1c} measurements. Similar arguments lead to the conclusion that the monotonic decrease of $I_{4c\uparrow\uparrow}(H)$, $I_{4c\uparrow\downarrow}(H)$, $I_{6c\uparrow\downarrow}(H)$, and $I_{6c\uparrow\uparrow}(H)$, as well as the lack of saturation in the field region under investigation, is due to the penetration of helicoids when the longitudinal component has become smaller than in the case of $I_{1c}(H)$ measurements.

REFERENCES

1. J. E. Evetts and B. A. Glowacki, Cryogenics **28**, 641 (1988).
2. V. F. Khirnyĭ, V. P. Seminozhenko, A. A. Kozlovskiĭ, and Yu. A. Grinchenko, Fiz. Nizk. Temp. **20** (8), 774 (1994) [Low Temp. Phys. **20**, 607 (1994)].
3. J. R. Clem, Phys. Rev. B **12** (6), 1742 (1975).
4. A. Barone and G. Paterno, *Physics and Applications of the Josephson Effect* (Wiley, New York, 1982; Mir, Moscow, 1984).
5. C. P. Bean and J. D. Livingston, Phys. Rev. Lett. **12** (1), 14 (1964).
6. A. I. D'yachenko and V. V. Chabanenko, Sverkhprovodimost': Fiz., Khim., Tekh. **6** (2), 252 (1993).
7. K. I. Kugel', L. G. Mamsurova, K. S. Pigal'skiĭ, and A. L. Rakhmanov, Fiz. Nizk. Temp. **24** (8), 823 (1998) [Low Temp. Phys. **24**, 617 (1998)].
8. Yu. A. Genenko, Pis'ma Zh. Éksp. Teor. Fiz. **59** (5), 807 (1994) [JETP Lett. **59**, 841 (1994)].
9. V. F. Khirnyĭ, V. P. Seminozhenko, and A. A. Kozlovskiĭ, Fiz. Tverd. Tela (S.-Peterburg) **38** (10), 2951 (1996) [Phys. Solid State **38**, 1614 (1996)].

Translated by N. Wadhwa

Physics of the Solid State, Vol. 42, No. 10, 2000, pp. 1832–1834. Translated from Fizika Tverdogo Tela, Vol. 42, No. 10, 2000, pp. 1786–1788.

SEMICONDUCTORS AND DIELECTRICS

Optical Properties of a Polymer Host Matrix Containing Mercuric Iodide Microcrystals

V. F. Agekyan, A. Yu. Serov, and Yu. A. Stepanov

Research Institute of Physics (Petrodvorets Branch), St. Petersburg State University, Ul'yanovskaya ul. 1, Petrodvorets, 198904 Russia

Received March 6, 2000

Abstract—Microcrystals of mercuric iodide have been grown in a polymer matrix with pores 200 nm in diameter. The absorption and luminescence spectra indicate the formation of microcrystals of two (red and orange) modifications in the host matrix. The temperature dependence of the emission spectra and the evolution of absorption and emission spectra in the course of sample ageing have been studied. The evolution of the spectra is governed by the transition from the orange to red modification and the increase in size of microcrystals. © *2000 MAIK "Nauka/Interperiodica".*

1. INTRODUCTION

Mercuric iodide HgI_2, whose optical spectra have been studied for many years, exhibits a clearly pronounced excitonic spectrum [1–3]. The HgI_2 compound is one of the best materials for manufacturing x-ray and gamma-ray detectors [4, 5]. Recently, Sochinskii *et al.* [6] demonstrated the possibility of using heterostructures of HgI_2-based solid solutions for these purposes. This stimulated interest in systems containing spatially confined crystals of mercuric iodide. Investigations of the iodides of mercury and other metals in matrices have recently been performed [7–9]. These studies have two aspects, namely, the observation of quantum confinement effects in microcrystals and the investigation of the effect of a host matrix on the lattice symmetry. It was found that, in some cases, spatial confinement favors the formation of metastable modifications, which can only be realized in bulk samples if rigorously set growth parameters are maintained. In place of the usual tetragonal structure, CuI microcrystals embedded in poly(methyl methacrylate) reside predominantly in the hexagonal modification, whereas mercuric iodide confined in glasses with pore radii up to 50 nm has both the conventional tetragonal red modification and the tetragonal orange modification [10]. In the present work, we studied the absorption and luminescence spectra of HgI_2 embedded in a polymer matrix with pores of large diameter, about 200 nm.

2. EXPERIMENTAL TECHNIQUES

The samples were prepared by filling the matrix pores with a saturated solution of HgI_2 in acetone at room temperature with subsequent evaporation of acetone and the formation of mercuric iodide microcrystals in the pores. To obtain samples with a high microcrystal concentration, the procedure was repeated several times. Our main measurements were performed on a sample subjected to six such cycles. The luminescence was excited by a molecular nitrogen laser producing pulses 5 ns long. The spectra were obtained both in CW operation and in the time-resolved, nanosecond-scale mode. The average laser power did not exceed a few mW, so that the photoinduced processes apparently played an insignificant part in phase transformations and defect formation. The changes in absorption and emission spectra were recorded in the course of sample ageing over several months, starting from the instant of their preparation.

3. RESULTS AND DISCUSSION

The absorption spectrum of HgI_2 microcrystals exhibits two absorption edges near 2.33 and 2.47 eV (Fig. 1). The first feature corresponds to the $M_7^- - M_6^-$ interband transition in the HgI_2 red modification. The second feature can be due to either the second interband transition $M_6^- - M_6^-$ in the red modification [11] or the ground interband transition in the HgI_2 orange modification. Since the matrices containing mercuric iodide are characterized by two luminescence regions related to two absorption edges, the 2.47-eV edge should be assigned to the HgI_2 orange modification. As is seen from Fig. 2, the luminescence bands of red and orange modifications in as-grown samples are similar in intensity, but as the samples age, the metastable orange modification, as in samples based on porous glasses [9], transforms to the red modification, so that the corresponding emission band weakens several times in three months.

Besides the HgI_2 luminescence, the samples exhibit a broad emission band of the capron matrix with a maximum at 2.9 eV. This band increases in intensity and decays more slowly than the luminescence of micro-

1063-7834/00/4210-1832$20.00

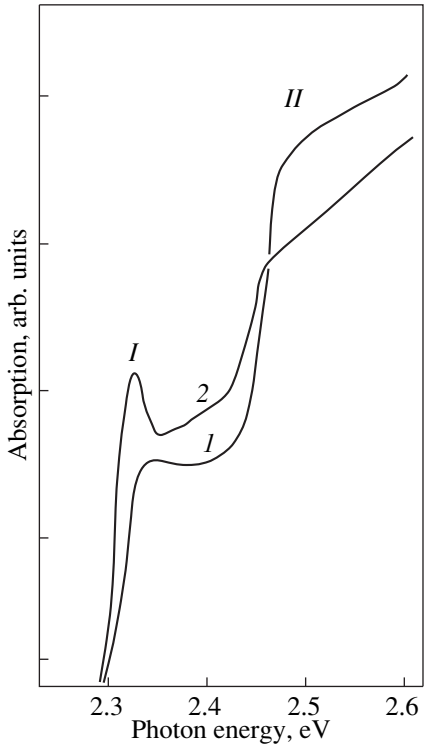

Fig. 1. Absorption spectrum of a polymer matrix containing (*I*) red and (*II*) orange modifications of mercuric iodide: (*1*) as-grown sample and (*2*) the same sample after storage in air for 2.5 months. $T = 80$ K.

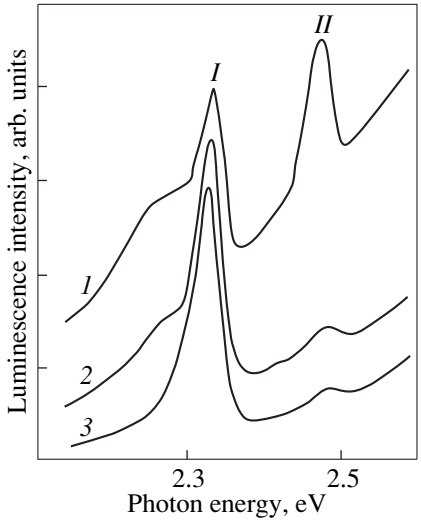

Fig. 2. Evolution of the luminescence spectrum of the polymer matrix containing mercuric iodide microcrystals in the course of ageing: (*1*) as-grown sample and the same sample after storage in air for (*2*) 1 month and (*3*) 2.5 months. *I* and *II* correspond to the free-exciton emission in the red and orange modifications of HgI_2. $T = 80$ K.

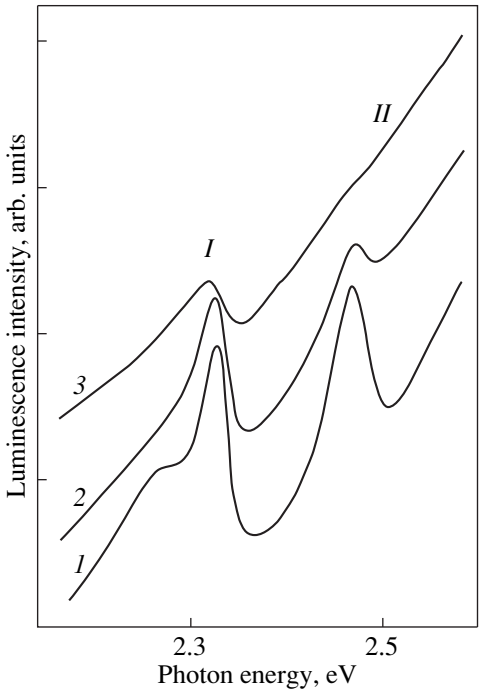

Fig. 3. Temperature dependence of the luminescence of a polymer matrix containing mercuric iodide microcrystals (as-grown sample). *I* and *II* correspond to the exciton luminescence of the red and orange modifications, respectively. *T* (K): (*1*) 80, (*2*) 100, and (*3*) 120.

crystals; therefore, the most distinct spectra of HgI_2 can be obtained by measuring the luminescence during the rise of the pump laser pulse. The spectra obtained in this mode indicate that when a sample is heated, the emission of the nonequilibrium orange modification decays more rapidly than that of the red modification (Fig. 3). At 80 K, the luminescence intensity of both modifications in as-grown samples is approximately the same, whereas at 120 K, only the emission of the red modification is observed. When cooled again to 80 K, the spectrum recovers its initial shape. The reason for the fast thermal quenching of the exciton emission from the HgI_2 orange modification consists in the stronger electron–phonon coupling in the nonequilibrium orange modification of HgI_2 OM.

The coincidence of the absorption and luminescence maxima implies that the free exciton emission dominates in the spectra of both HgI_2 modifications at $T = 80$ K and that exciton–impurity complexes with a comparatively low binding energy become also manifest in the red modification. The absence of bands associated with the impurity–band and donor–acceptor transitions, which are characteristic of HgI_2, can be accounted for in the case of the CW mode by the high excitation level in a pulse when saturation of luminescence of the impurity nature becomes an essential factor. When studied in the time-resolved mode, the interimpurity transitions should be suppressed still more strongly because of their slow kinetics. However, note that free excitons and shallow exciton–impurity complexes also dominate under weak CW excitation, which implies a fairly high quality of microcrystals of both

modifications produced by crystallization from solution. As is seen from Fig. 1, as the sample ages, the exciton absorption peak of the red modification becomes stronger and narrower, whereas the absorption edge of the orange modification weakens. The changes in the spectrum reflect the transformation of the orange modification of mercuric iodide to the red modification, as well as the improving quality of microcrystals of the red modification, probably in the course of their growing. In the course of ageing, the free-exciton luminescence line of the red modification becomes narrower, which is accompanied by a weakening of the emission of exciton–impurity complexes (Fig. 2).

The pores in the polymer matrices used by us are so large that the microcrystal size noticeably exceeds the exciton radius in HgI_2. As a result, our samples do not reveal the energy shifts associated with size quantization.

We note, in conclusion, that the results of our work, in accordance with those reported in [9], indicate that, during crystal growth, spatial constraints favor the formation of nonequilibrium phases, which are not produced in similar conditions in the absence of these constraints.

REFERENCES

1. T. Goto and Y. Nishina, Solid State Commun. **25**, 173 (1978).
2. X. J. Bao, T. E. Schlesinger, R. B. James, *et al.*, J. Appl. Phys. **68**, 2951 (1990).
3. I. Kh. Akopyan, B. V. Bondarenko, O. N. Volkova, *et al.*, Fiz. Tverd. Tela (S.-Peterburg) **39**, 67 (1997) [Phys. Solid State **39**, 58 (1997)].
4. M. Piehotka, Mater. Sci. Eng., R. **18**, 1 (1997).
5. R. Farrell, F. Olschner, K. Shah, and M. R. Squillante, Nucl. Instrum. Methods Phys. Res., Sect. A **387**, 194 (1997).
6. N. V. Sochinskii, V. Munos, J. M. Perez, *et al.*, Appl. Phys. Lett. **72**, 2023 (1998).
7. Z. K. Tang, Y. Nozue, and T. Goto, J. Phys. Soc. Jpn. **61**, 2943 (1992).
8. V. F. Agekyan, Fiz. Tverd. Tela (S.-Peterburg) **40**, 1724 (1998) [Phys. Solid State **40**, 1568 (1998)].
9. I. Kh. Akopyan, O. N. Volkova, B. V. Novikov, and B. I. Venzel', Fiz. Tverd. Tela (S.-Peterburg) **39**, 468 (1997) [Phys. Solid State **39**, 407 (1997)].
10. K. Kanzaki and I. Imai, J. Phys. Soc. Jpn. **32**, 1003 (1972).

Translated by G. Skrebtsov

Physics of the Solid State, Vol. 42, No. 10, 2000, pp. 1835–1839. Translated from Fizika Tverdogo Tela, Vol. 42, No. 10, 2000, pp. 1789–1793.

SEMICONDUCTORS AND DIELECTRICS

Study of the Spectral Characteristics of the Photoacoustic Effect in HgI_2 Crystals at Different Levels of Vibrational Strain Amplitude

B. K. Kardashev

Ioffe Physicotechnical Institute, Russian Academy of Sciences, Politekhnicheskaya ul. 26, St. Petersburg, 194021 Russia
e-mail: B.Kardashev@pop.ioffe.rssi.ru

Received March 20, 2000

Abstract—An experimental study is reported of the effect of light on the acoustic characteristics of a HgI_2 crystal at two levels of the vibrational strain amplitude, one of which lies in the amplitude-independent (AI), and the other in the amplitude-dependent (AD) ultrasound absorption (UA). These studies led to the spectral parameters of the photoacoustic effect (PAE) both for the decrement and for Young's modulus of the HgI_2 crystal. It was shown that the PAE spectra of a sample exposed to high-amplitude ultrasound undergo, in some cases, substantial changes compared to those for low amplitudes (the AIUA region). These changes may be related both to the diffusion of photosensitive dislocation-pinning centers (photocarrier trapping centers) and to their creation–annihilation induced by light and high amplitudes in the ADUA region. It is shown that the excitation of electron–hole pairs captured by vacancies or iodine or mercury interstices can also noticeably affect the dislocation mobility in HgI_2. *© 2000 MAIK "Nauka/Interperiodica".*

Investigation of dislocation-related photocarrier trapping centers in a wide-band semiconductor crystal of HgI_2 is of interest from two viewpoints, viz., practical application and basic research. The first is connected with the use of this crystal as a sensitive element for detectors of ionizing (x-ray and gamma) radiation, which can operate at room temperature. The effect of performance improvement in a detector under the action of high-intensity ultrasound (in the ADUA region) discovered several years ago [1] is directly associated with the destruction by strong ultrasonic vibrational stresses of dislocation-related trapping centers. From the standpoint of solid-state physics, HgI_2 is of interest as the only available crystal in which the photoacoustic effect associated with dislocations is manifested in the purest form [2–4]. In this respect it differs considerably from the A_2B_6 and A_3B_5 piezoelectric crystals, for which a light-induced change of ultrasound attenuation may appear both due to dislocations and to photocarriers drifting in the electric field created in a piezoelectric by an ultrasound wave.

The most interesting characteristic of the PAE, which reveals possible mechanisms suitable for describing the observed relationships, is its spectral response. The spectral response of the PAE for the HgI_2 crystal, without using high amplitudes in a photoacoustic experiment, was obtained without any difficulties [2]. It was shown that, at low amplitudes (the AIUA region), the PAE spectrum practically coincides with the spectral response of photoconductivity. It was concluded [2] that the charge carriers (photoelectrons and/or holes) participate in the observed phenomenon. However, the very first studies [2, 3] showed that the behavior of nonlinear acoustic parameters, such as the amplitude-dependent decrement and Young's modulus defect, is not so simple; indeed, these parameters could increase or decrease under illumination by light of the same wavelength. It was also noticed that the strain-amplitude and illumination past history of a sample considerably affects these parameters.

The present work reports on the measurement of the PAE spectral characteristics for the nonlinear acoustic parameters obtained in the ADUA region. It is shown that sample past history and high amplitudes affect the PAE spectra in the low-amplitude region, where ultrasound attenuation still remains amplitude-independent.

1. EXPERIMENTAL TECHNIQUES

As in [2–4], in this work we studied HgI_2 crystals grown by static sublimation from the vapor phase. The sample size was $9 \times 3 \times 0.5$ mm. The broad face of the plate coincided with the (001) crystallographic plane.

Longitudinal ultrasonic vibrations were excited along the long edge of the plate. Acoustic measurements were made by the resonance method using a composite piezoelectric vibrator. A quartz transducer was employed to excite and receive the ultrasonic vibrations. The technique used to study the PAE is described in detail in [2–4]. We only note here that the acoustic parameters being measured were the vibration decrement δ and the resonance frequency f of the sample. In our experiments, we used two levels of the vibrational strain amplitude ε, one of which was in the low-

1063-7834/00/4210-1835$20.00

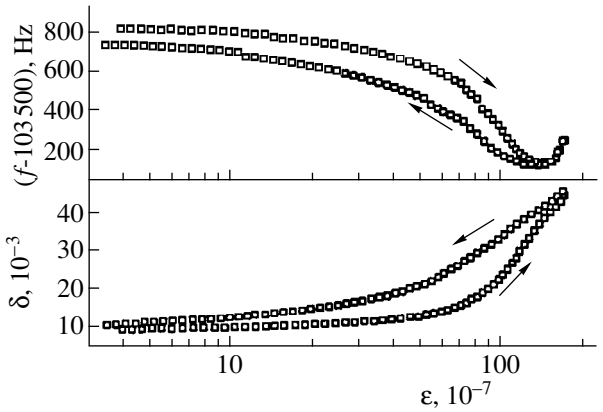

Fig. 1. Strain-amplitude dependences of the decrement δ and resonance frequency f of a HgI_2 sample. The measurements were made in the dark; the arrows indicate the direction of amplitude variation.

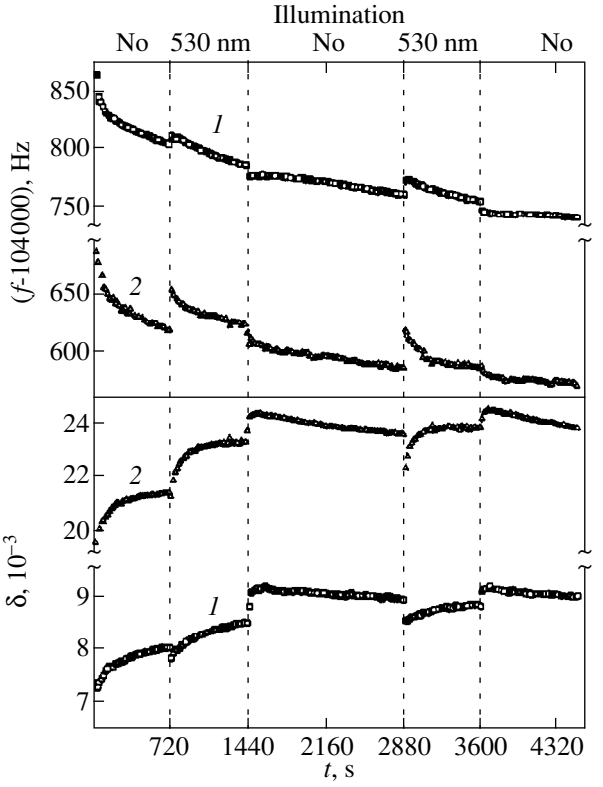

Fig. 2. Effect of illumination (λ = 530 nm) on the evolution of the decrement δ and the resonance frequency f of a HgI_2 sample at two vibrational strain amplitudes (*1*) $\varepsilon = 1.0 \times 10^{-6}$, and (*2*) $\varepsilon = 1.0 \times 10^{-5}$ in the AIUA and ADUA regions, respectively.

amplitude region with AIUA, and the other had amplitudes an order of magnitude higher, belonging to the ADUA region. During the experiment, which lasted for an hour and a half, a high amplitude was maintained in the sample. A low level of ε was set only for a short time of about 1 s. This time was long enough to stabilize the chosen amplitude and to make measurements. Immediately after the measurement at a low ε, the amplitude was again raised to a high level. The strain stabilization error was less than 2%. The time interval between two measurements at both levels of the ε was about 15 s.

Light with a wavelength λ was switched on or off at predetermined instants of time. The wavelength range was 360 to 660 nm. The light source was a mercury lamp. The results of measurements were used to obtain PAE spectral characteristics for various vibrational-strain amplitude levels.

The measurements were carried out in air at atmospheric pressure and room temperature.

2. EXPERIMENTAL RESULTS

Figure 1 shows the amplitude dependences of the vibrational decrement δ and of the resonance frequency f obtained in the dark upon an increase and subsequent decrease in the amplitude of ε. It can be readily seen that there is an amplitude region where the crystal behaves elastically (small ε), and where the decrement and the resonance frequency become nonlinear and amplitude-dependent. The main feature of these dependences is that the curves obtained for increasing and decreasing amplitude do not coincide. This phenomenon is usually caused by the time dependence of the acoustic parameters f and δ when the sample is acted upon by high-amplitude strain in the ADUA region. Figure 2 presents the time dependences obtained on the same sample as the amplitude dependences shown in Fig. 1. Measurements were made in the dark in the interval 0–720 s. The time $t = 0$ on the plot corresponds to the instant of stabilization of a high amplitude in the sample.

Figure 2 is another illustration (for the case of λ = 530 nm) of the effect of illumination on the evolution of the acoustic parameters f and δ, where the sample is acted upon by high-amplitude ultrasound. One readily sees that light exerts a considerable effect on the parameters measured at both a high and a low amplitude.

Having obtained the values of f and δ for two amplitude levels, we can obtain information on the behavior of Young's modulus ($E \sim f^2$) and of the decrement both in the linear, amplitude-independent region, and in the nonlinear, ADUA region. The known values of f and δ were used to calculate the amplitude-dependent Young's modulus defect $(\Delta E/E)_h = 2(f_2 - f_1)/f_1$ and the decrement $\delta_h = (\delta_2 - \delta_1)$. Here, the subscripts 2 and 1 refer to the curves of Fig. 2, measured at high and low amplitudes, respectively. As for the amplitude-independent Young's modulus defect $(\Delta E/E)_i$, which appears and varies in time under the action of high-amplitude ultrasound and illumination, it is proportional to the change of f_1 and can be obtained from a similar relation, with the reference point f_0 measured at the instant $t = 0$, when a high value of ε sets in for the first time in the sample in the experiment: $(\Delta E/E)_i = 2(f_1 - f_0)/f_0$; the amplitude-independent decrement $\delta_i = \delta_1$.

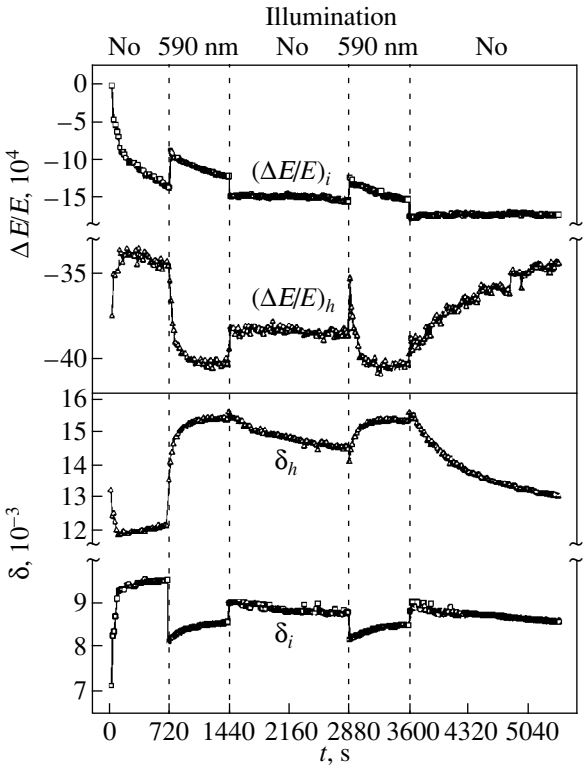

Fig. 3. Effect of illumination (λ = 590 nm) on the evolution of the amplitude-independent decrement δ_i and Young's modulus defect $(\Delta E/E)_i$, and the amplitude-dependent δ_h and $(\Delta E/E)_h$.

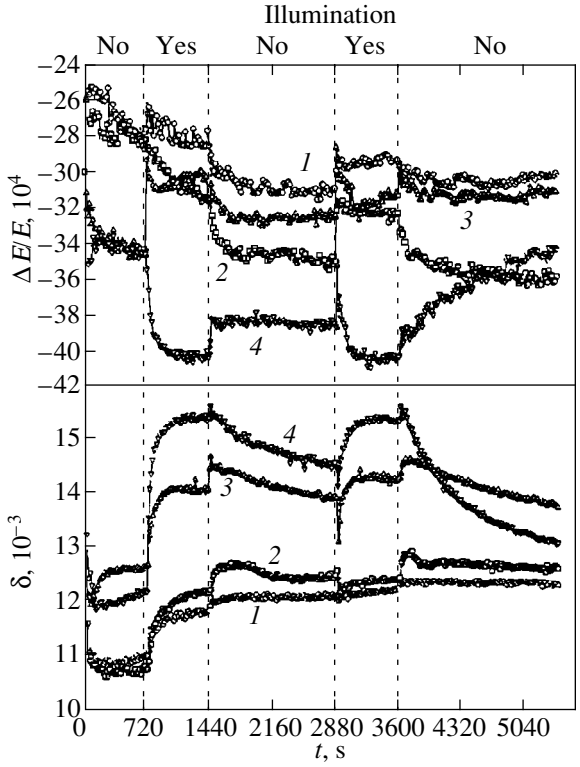

Fig. 4. Effect of illumination on the evolution of the amplitude-dependent decrement δ_h and Young's modulus defect $(\Delta E/E)_h$ for different wavelengths of incident light (nm): (*1*) 360, (*2*) 480, (*3*) 530, and (*4*) 590.

Figure 3 illustrates the behavior of these parameters under illumination (λ = 590 nm) and high-amplitude strain acting on the sample. Similar results were also obtained on the same sample with other wavelengths. Figure 4 presents the behavior of the amplitude-dependent Young's modulus defect $(\Delta E/E)_h$ and decrement δ_h measured at wavelengths of 360, 480, 530, and 590 nm. For other wavelengths λ (410 and 660 nm) used in the experiment, the sensitivity to illumination was not high enough and practically did not differ from the data obtained for λ = 360 nm.

As already mentioned, the main purpose of this work was to obtain the PAE spectral responses, i.e., the dependences of the changes $\Delta(\Delta E/E)_i$, $\Delta(\Delta E/E)_h$, $\Delta\delta_i$, and $\Delta\delta_h$ on wavelength λ with the light switched on and off. Figure 5 presents the results in the most comprehensive form. In carrying out the experiments, we tried, first, to avoid the effect of past history of the sample and, second, to demonstrate the possible kinds of PAE spectral characteristics. In order to minimize the effect of past history, we made measurements similar to those depicted in Figs. 2–4 a day or two after the preceding experiment. During this time, the sample recovered in the dark. In addition, the first 720 s (see Figs. 2–4) were used for high-amplitude treatment of the sample in the dark, after which the light of the chosen wavelength was switched on and off at 720 and 1440 s, respectively.

Figure 5 displays four kinds of the spectral responses obtained (a) in the dark in the 1440–2880 s interval, (b) at the instant of switching on the light at 2880 s, (c) with the sample illuminated in the time interval from 2880 to 3600 s, and (d) in the dark in the interval 3600–5400 s. The negative sign of the changes of Young's modulus and decrement indicates their decrease, and the positive sign, an increase, under a change of the external conditions.

It can be seen from the figure that there are many different kinds of responses, and one could plot a lot more of them. The diversity of the spectral characteristics originates from operation in the region of ultrasound absorption which is nonlinear in amplitude. We can readily notice that most of the responses have the highest or lowest sensitivity (when the change of the parameter is approximately zero) at the incident light wavelength λ = 590 nm. There are also a number of exceptions, which will be considered below.

3. DISCUSSION

As mentioned in the introduction, the investigation of PAE spectral characteristics carried out [2] in experiments without using high amplitudes in the ADUA region led to the conclusion that the carriers (photoelectrons and/or holes) participate in the creation of additional, photosensitive pinning centers, besides those already available for mobile dislocations. The model

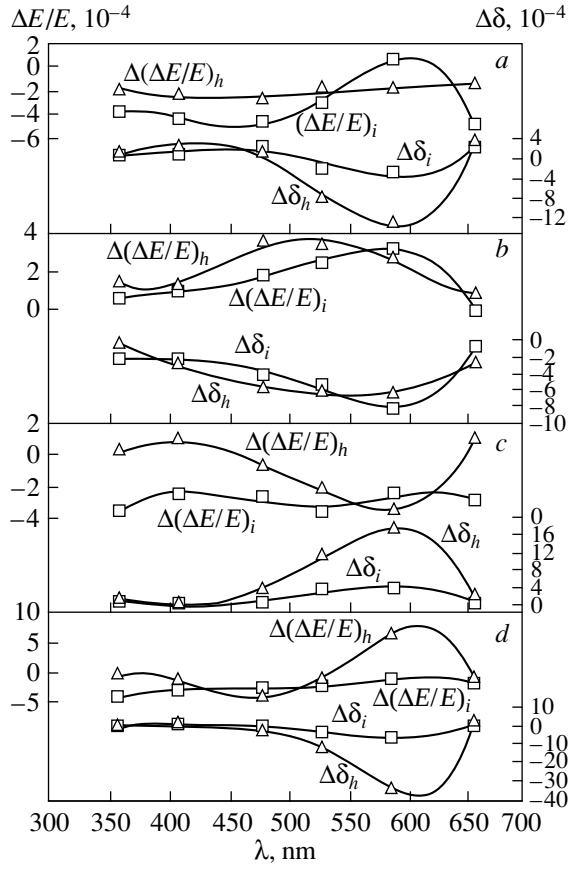

Fig. 5. Spectral characteristics of the photoacoustic effect in the HgI_2 crystal for Young's modulus E and decrement δ measured in the AIUA (i) and ADUA (h) ranges. The curves are plotted using the data of Fig. 3 and similar results obtained at various wavelengths; (a) response of the acoustic parameters corresponding to the variation of E and δ within the interval 1440–2880 s; (b) same for the switching-on of light at 2880 s, (c) same for the sample illuminated within the time interval 2880–3600 s; (d) same for the interval 3600–5400 s.

chosen to interpret the PAE makes it possible, subsequently, it possible to predict and, later, to experimentally observe a number of hitherto unknown phenomena, such as (1) the acousto-electric effect, in which carriers are released from the dislocation-related trapping centers under the action of a high-amplitude strain in the ADUA region to be later removed from the crystal by an external electric field, thus considerably improving the spectral characteristics of γ-radiation detectors [1]; (2) the acousto-optic and photo-optic effects, in which one of the HgI_2 photoluminescence bands originating from intrinsic lattice point defects (iodine or mercury vacancies or interstices) was found to be sensitive to treatment by high-amplitude ultrasound, as well as to preliminary illumination of the sample by light with a wavelength $\lambda = 590$ nm [4]. This explains why these defects, which are capable of trapping a photoelectron and/or hole, were called photosensitive pinning centers (photostoppers) for mobile dislocations. Moreover, the acousto- and photo-optic effects were found in a similar way in the excitation spectrum of one of the HgI_2 photoluminescence lines [5], which makes it possible to determine the characteristic range of binding energies of the dislocation-related photocarrier trapping centers by the optical method. Thus, the dislocation-related photocarrier-trapping center in HgI_2 can be regarded as an iodine or mercury vacancy or interstice which has trapped a photoelectron and/or a hole, is located close to a dislocation, and interacts with this dislocation with a binding energy of 0.03–0.1 eV [5].

The spectral characteristics obtained in this work (see Fig. 5), as well as the time dependences, some of which are depicted in Figs. 3 and 4, make it possible to describe, in greater detail, the defect dynamics in a HgI_2 crystal exposed to light of a given wavelength or to high-amplitude ultrasound.

The fact that most of the spectral responses presented in Fig. 5 pass through an extremum at $\lambda = 590$ nm indicates that both the amplitude-dependent decrement δ_h and Young's modulus defect $(\Delta E/E)_h$, as well as the amplitude-independent δ_i and $(\Delta E/E)_i$, are governed under the given experimental conditions by the creation in the crystal of free photocarriers and by their trapping by iodine or mercury vacancies or interstices. This process leads to the formation of additional obstacles (photosensitive pinning centers), which give rise to an additional dissipation of the ultrasound energy by vibrating dislocations at high amplitudes.

However, Fig. 5 illustrates a number of exceptions. First, such parameters as $(\Delta E/E)_h$ (Fig. 5a), $(\Delta E/E)_i$ (Fig. 5c), and $(\Delta E/E)_i$ (Fig. 5d) turned out to be practically insensitive to the variation of the incident light wavelength. Second, and this is the most remarkable observation, the maximum of the spectral response for $(\Delta E/E)_h$ (Fig. 5b) was displaced to the 470 to 530-nm wavelength interval. Note also the nonmonotonic, slow variation of the decrement δ_h (curve *2* in Fig. 4) observed in the dark in time intervals 1440–2880 and 3600–5400 s in experiments with light having a wavelength exactly in this range ($\lambda = 480$ nm).

Such a complex behavior of $(\Delta E/E)_h$ and δ_h, as well as of $(\Delta E/E)_i$ under the action of light and high-amplitude ultrasound, can be due to a number of factors. For instance, in a sample, high-amplitude ultrasound may produce changes associated with diffusion of point defects (both photosensitive and others) along dislocation lines or with the motion of pinning centers toward the dislocations or away from them. Such processes may take place because the HgI_2 sample under study has a clearly manifested tendency towards microcreep, which is seen from the mismatching of the amplitude dependences obtained under the increase and subsequent decrease of the amplitude (Fig. 1) and from the time dependences presented in Figs. 2–4. In these conditions, one may expect a practically complete compensation of the changes associated with the location of obstacles and with variation of the concentration of

photosensitive pinning centers for some parameters under the action of light or high-amplitude ultrasound, both during illumination with light of a given wavelength and in the dark. Obviously enough, diffusion processes may affect the spectra only in the case where spectral response measurements cover a long enough interval of time (see Figs. 5a, 5c, and 5d).

This explanation is not suitable, however, for the case illustrated by Fig. 5b, where the spectral sensitivity peak for $(\Delta E/E)_h$ is shifted toward shorter wavelengths as compared to the curves obtained for other parameters, because the data presented in this figure were recorded practically instantaneously on turning on the light. It is worth noting that the wavelength interval from 450 to 520 nm is typical of the HgI_2 crystal. Experiments [5] show that light in this wavelength interval is capable of exciting luminescence, which is due to recombination of photocarriers localized at intrinsic point defects of the HgI_2 lattice (iodine or mercury vacancies or interstices). Electron transfer to an energy band ensuring a nonradiative transition to the luminescence level, as well as the subsequent emission (recombination) process, apparently may substantially affect the dislocation mobility, which was clearly pronounced in the shift of the spectral response peak for $(\Delta E/E)_h$, shown in Fig. 5b.

This mechanism can certainly affect other acoustic parameters as well, in particular, the amplitude-dependent decrement δ_h. The δ_h spectrum in Fig. 5b is broader than the other spectra presented in Fig. 5. The effect of excitation of the electronic subsystem by light with a wavelength near 480 nm and the significant role played by subsequent relaxation of this excitation in the dark, along with the above-mentioned diffusion processes, may contribute to the nonmonotonic time dependence of δ_h (*2* in Fig. 4) and to the behavior of the spectral responses for $(\Delta E/E)_h$ (Fig. 5a), $(\Delta E/E)_i$ (Fig. 5c), and $(\Delta E/E)_i$ (Fig. 5d). It was mentioned above that the latter are practically insensitive to the variation of the incident light wavelength. The specific action of illumination by light with $\lambda = 480$ nm compared to light with $\lambda = 590$ nm is clearly manifest in Fig. 4 as well, where the variation of $(\Delta E/E)_h$ within the 3600–5400 s interval occurs even with opposite signs. All this indicates is that the excitation of the electron–hole pairs trapped by intrinsic point defects of the HgI_2 lattice and its subsequent relaxation may noticeably affect the dislocation mobility.

Unfortunately, it is not possible to describe, at present, the whole range of obstacles that dislocations in crystals (including HgI_2) have to surmount in their motion under various external conditions, although this is a major problem in the physics of defects. A comparison of PAE spectral responses obtained in the nonlinear ADUA region with the luminescence excitation spectra presented in [5], which was carried out in this work, has revealed a hitherto unknown mechanism of the effect of excitation by light of the electronic subsystem on the dislocation dynamics in the HgI_2 wide-band semiconducting crystal. This phenomenon may exist in other wide-band semiconductors as well.

ACKNOWLEDGMENTS

The author is indebted to V. M. Zaletin for providing the crystals used in this work.

REFERENCES

1. B. K. Kardashev, V. M. Zaletin, and V. I. Fomin, RF Patent No. 2065180 (1996).
2. B. K. Kardashev, S. N. Golyandin, S. B. Kustov, and V. M. Zaletin, Fiz. Tverd. Tela (St. Petersburg) **34** (7), 2148 (1992) [Sov. Phys. Solid State **34**, 1149 (1992)].
3. B. K. Kardashev, J. Alloys Compd. **211/212**, 160 (1994).
4. B. K. Kardashev, A. V. Rezvushkin, P. A. Stepanov, *et al.*, Fiz. Tverd. Tela (St. Petersburg) **38** (5), 1511 (1996) [Phys. Solid State **38**, 832 (1996)].
5. B. K. Kardashev, V. A. Stepanov, P. A. Stepanov, and V. M. Chernov, Fiz. Tverd. Tela (St. Petersburg) **41** (11), 1965 (1999) [Phys. Solid State **41**, 1801 (1999)].

Translated by G. Skrebtsov

Physics of the Solid State, Vol. 42, No. 10, 2000, pp. 1840–1845. Translated from Fizika Tverdogo Tela, Vol. 42, No. 10, 2000, pp. 1794–1799.

SEMICONDUCTORS AND DIELECTRICS

Relaxation Processes in Colored Crystals of LiF after the Coaction of UV Radiation and a Shock Wave

M. G. Abramishvili, Z. G. Akhvlediani*, T. L. Kalabegishvili*, V. G. Kvachadze**, and Z. K. Saralidze***

**Institute of Physics, Academy of Sciences of Georgia, ul. Guramishvili 6, Tbilisi, 380077 Georgia*
e-mail: zurab@iph.hepi.edu.ge
***Skhivi Research Institute of Automatic Systems, Tbilisi, 380082 Georgia*
Received February 16, 2000

Abstract—The relaxation of F_2^+ centers in radiation-colored crystals of lithium fluoride starting from the moment of the coaction of pulsed UV irradiation and a shock wave is investigated. It is shown that the annealing curve of these centers displays a nonmonotonic character at room temperature and is a consequence of three processes. The first two are the processes of disintegration of unstable (short-lived) and stable F_2^+ centers, and the third process involves the formation of stable centers upon a random encounter of appropriate constituents in the course of their diffusive wandering over the lattice. © *2000 MAIK "Nauka/Interperiodica".*

The anion vacancies in crystals of lithium fluoride, as well as the color centers and their complexes, possess high mobilities at room temperature. Therefore, color centers of different types undergo interconversion in radiation-colored crystals when they are kept in darkness for a long time (several months or years) at room temperature. This is also true of charged F_2^+ centers [1, 2]. These centers can move over the crystal as a result of successive 60° reorientations [3]. Consequently, they can effectively interact with other color centers and various structural defects, and, eventually, are either annihilated (destroyed) or become incorporated into more complicated complexes. Such processes, involving defects which are mobile at room temperature (V_a^+, $V_a^+ : O^{2-}$, F, F_2^+), were observed in our experiments, also with some peculiarities that have never been detected before. This convinced us that the investigation of relaxation processes over a long period of time is of considerable interest. Such investigations can be used to verify the correctness of existing concepts concerning the processes of defect and color center formation, in particular, to clarify the mechanisms of stabilization of laser centers (F_2^+) under the coaction of various fields, which were proposed by us earlier [4, 5].

After six months following the investigations of the destruction of stable F_2^+ centers formed in radiation-colored crystals subjected to the coaction of UV irradiation and a shock wave [5], we again recorded the optical absorption spectrum of the investigated crystal (more than seventeen months after the exposure). An appreciable increase in the number of F_2^+ centers was observed compared with the previous measurement (more than eleven months after the exposure). This result astonished us initially because the holding conditions were the same as in the previous period (the only exception was the hot summer, which raised room temperature by 10–15°C). However, a comparison of this result with the behavior of the other related color centers showed that it is a consequence of the general process of the center interconversion occurring in the stored crystal.

The aim of the present work is the observation of this process in the investigated colored crystal starting the moment of the coaction.

1. EXPERIMENT

The investigated crystals of lithium fluoride were pricked from a monocrystal line block which was preliminarily subjected to isothermal annealing at a temperature no less than 700°C for three hours; this was followed by a slow cooling to room temperature. The prepared samples (with sizes $10 \times 10 \times 0.5$ mm) were repeatedly annealed at the same conditions as mentioned above and then exposed to radiation in the free state in the channel of the IRT-M reactor at the Institute of Physics, Academy of Sciences of Georgia. The differential flux of thermal neutrons incident on the crystal was $(2.5 \pm 0.3) \times 10^{12}$ n/cm^2 s, the integral dose being 2.4×10^{14} n/cm^2. The optical absorption spectra contained, along with the F band (250 nm), an intensive F_2 band (450 nm). Centers of the F_2^+ type were absent.

The creation of F_2^+ centers (640–650 nm) was observed as a result of the exposure of these crystals to hard pulsed UV radiation accompanied by a shock wave.[1]

The centers revealed quite high thermal stability. In spite of the fact that half of such centers are destroyed

during the first ten days, the concentration of the remaining centers changes slowly for more than two years (see also [5]).

2. RESULTS AND DISCUSSION.

The time dependences of the absorption coefficients of the crystal at the maxima of the F and F_2 bands are presented in Fig. 1 (curves *2* and *3*). It can be seen from the figure that, as a result of the coaction of UV radiation and a shock wave on the radiation-colored crystal, along with the formation of the stable complexes $F_2^+ : O^{2-}$ [5], the intensity of the F_2 band (curve *3*) appreciably decreases (as shown by the broken lines) because of a decrease in the concentration of F_2 centers, which are the main constituents for the creation of stable complexes with F_2^+ centers ($F_2^+ : O^{2-}$), and the intensity of the F band also noticeably drops (curve *2*). It can also be seen from this figure that a decrease in the absorption coefficients of the crystal at the maxima of the F and the F_2 bands lasts for a long time after the cessation of the action. It is worth noting that, although the number of F centers disappearing per unit time exceeds the number of F_2 centers by almost an order of magnitude, their relative rates of vanishing are almost identical and approximately mount to 1.2–1.4% per month.

For the formation of the complexes $F_2^+ : O^{2-}$, in which F_2^+ centers are stabilized by O^{2-} ions, in addition to the reactions

$$\left.\begin{aligned} F_2 &\longrightarrow F_2^+ + e \\ F_2^+ + O^{2-} &\longrightarrow F_2^+ : O^{2-} \end{aligned}\right\}, \qquad (1)$$

the following reactions involving both F centers and O^{2-} ions are possible:

$$F + V_a^+ \longrightarrow F_2^+, \qquad (2)$$

$$F_2^+ + O^{2-} \longrightarrow F_2^+ : O^{2-}, \qquad (2')$$

as well as reactions with F centers and $V_a^+ : O^{2-}$ complexes

$$V_a^+ : O^{2-} + F \longrightarrow F_2^+ : O^{2-}. \qquad (3)$$

For the last reaction to occur, the presence of the dipole-type $V_a^+ : O^{2-}$ centers is required in the crystal. These centers can be created in the reactions involving vacancies,

$$\left.\begin{aligned} O^- + e &\longrightarrow O^{2-} \\ O^{2-} + V_a^+ &\longrightarrow V_a^+ : O^{2-} \end{aligned}\right\}, \qquad (4)$$

[1] This action was exerted in a device using a sliding discharge on an insulator surface (a modification of a "plasma plateau") [6] as a source of UV radiation and shock waves.

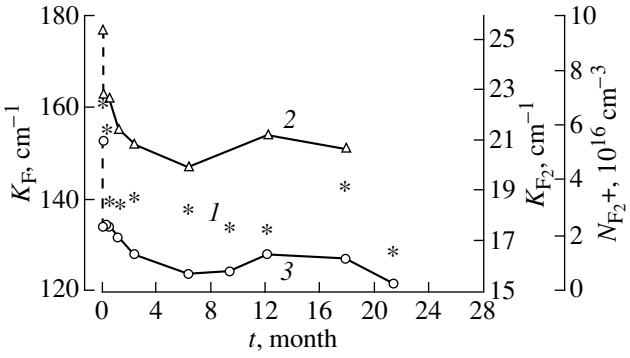

Fig. 1. Dependences of the concentration of F_2^+ centers (*1*) and of the absorption coefficients at the maxima of the F and F_2 bands (curves *2* and *3*, respectively) on the time of crystal holding in the dark at room temperature.

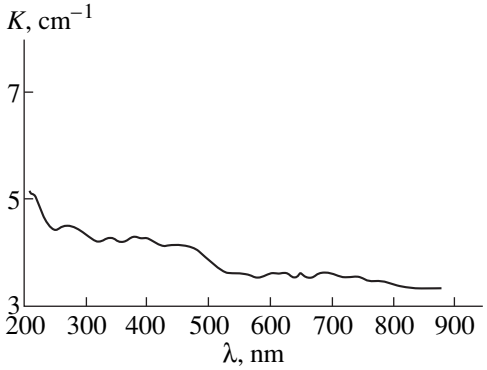

Fig. 2. Optical absorption spectrum of the initial (noncolored) crystal of LiF.

or F centers

$$O^- + F \longrightarrow V_a^+ : O^{2-}. \qquad (5)$$

Continuous absorption was observed in the UV region of the optical absorption spectrum (200–500 nm) of the initial crystals of LiF (before they were preliminarily exposed to radiation). This is evidence of the presence of a small number of $V_a^+ : O^{2-}$ dipoles (Fig. 2): the absorption considerably increases below 250 nm, and the band whose maximum must appear below 200 nm appears (it is known that the maxima of the absorption bands typical of these dipole centers must be located near 113 and 190 nm [1]). The main part of these oxygen-vacancy dipole centers and their aggregates are created, obviously, in the process of crystal growth in air, although the process might continue at room temperature under normal conditions also, but it occurs too slowly.

During the exposure to radiation, as well as during the coaction of UV radiation and a shock wave, the number of dipoles increases significantly. However, an estimation of the number of such dipole centers by

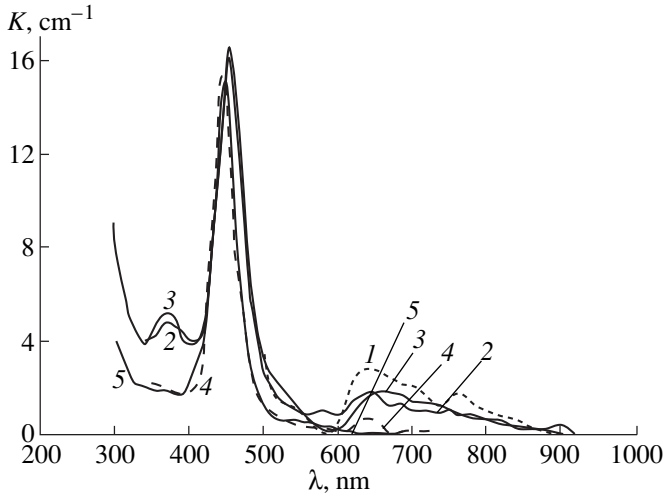

Fig. 3. Optical absorption spectrum of the investigated colored LiF crystal after the action of UV radiation and a shock wave (*1*) and holding in the dark at room temperature during 12 (*2*), 18 (*3*), 21 (*4*), and 27 (*5*) months.

measuring absorption or emission is, unfortunately, complicated. The reason is that the intense *F* band dominates in the UV region of the spectrum after radiation coloring. As regards the mobility of these complexes, they are as mobile at room temperature as the anion vacancies. The migration activation energies of the dipoles $V_a^+ : O^{2-}$ and the anion vacancies are equal to 1.3 ± 0.2 and 1.0 ± 0.2 eV, respectively, according to Courrol *et al.* [1].

Earlier [5], we proposed from the results of the relaxation processes obtained during the first year that the destruction of F_2^+ centers in the crystal held in darkness at room temperature is a two-stage process due to the presence of F_2^+ centers of two types. The first type is low-stability (isolated) F_2^+ centers, which are destroyed mostly during the 10–15 days following the coaction of UV radiation and a shock wave on the crystal. The second type includes stabilized configurations of complexes with F_2^+ centers (in all probability, these are the complexes of $F_2^+ : O^{2-}$ [5]), which remain in the crystal for more than one year. These F_2^+-type centers, which are stabilized in the specified complexes, are destroyed in two stages. The first stage is the slow destruction of the long-lived complexes of $F_2^+ : O^{2-}$ in accordance with the reaction

$$F_2^+ : O^{2-} \longrightarrow F_2^+ + O^{2-}. \qquad (6)$$

The second stage is fast destruction of the formed short-lived solitary F_2^+ centers. The centers of the F_2^+ type can be destroyed due to deionization ($F_2^+ + e \longrightarrow F_2$) or as a result of the reaction $F_2^+ \longrightarrow F + V_a^+$. These reactions are the sources of *F* and F_2 centers. Nevertheless, the number of these centers decreases during the first eight months (curves *2* and *3* in Fig. 1), during the process of crystal holding. This can be explained by the fact that these centers are consumed by the creation of more complicated color centers (for example, $F_2^+ + F \longrightarrow F_3^+$, etc.). Such a tendency is indeed traced (for example, an increase of absorption around 500–550 nm on curve *2* in Fig. 3) and is a definite result of F_4 color centers.

In accordance with the concepts described above, the destruction curve for F_2^+ centers must be the sum of the two exponentials with the corresponding characteristic times. However, the destruction curve descends more slowly at the second stage than it could be accounted for by an exponential. In addition, as has already been mentioned at the beginning of this article, the measurements of the optical absorption spectrum of the investigated crystal six months after the end of the experiments [5] indicate an appreciable increase in the number of F_2^+ centers as compared to the last measurements (curves *3* and *2*, respectively, in Fig. 3). These facts indicate that intensive diffusion processes occurring in the stored crystal along with the other effects, such as an increase in the number of F_3^- (682, 790 nm) and F_3 (375 nm) centers and a decrease in the absorption at 500–550 nm, result in a recreation of the complexes $F_2^+ : O^{2-}$ stabilizing F_2^+ centers.

It follows from what has been said above that the annealing curve for F_2^+ centers at room temperature must be a result of three processes: the destruction of the unstable (short-lived) and the stable (stabilized in the $F_2^+ : O^{2-}$ complexes) F_2^+ centers, and the creation of stable centers upon a random encounter of the appropriate constituents during diffusive wandering, for example, according to reaction (3). However, several assumptions should be made to explain the nonmonotonic nature of the time dependence of the number of

F_2^+ centers (an increase in the number of the centers in a certain time interval against the background of an overall decrease).

(1) The formation of anisotropic complexes (F_2^+, $F_2^+ : O^{2-}$, $V_a^+ : O^{2-}$) involving oxygen ions (reactions of types (1) or (4)) or isotropic defects (reactions of type (2)) is strongly complicated under normal conditions of crystal holding. Their formation energy is too large, and these reactions can occur intensely in the presence of oriented fields only [5]. In our case, such anisotropic complexes could be created exclusively during the action of an electrical field or a shock wave, simultaneously with UV radiation, on the crystal. They could be accumulated in a sufficient amount by the moment of cessation of the action.

(2) The formation of anisotropic complexes according to reactions involving anisotropic defects (for example, reactions of type (3)), can occur with a high probability.

(3) The centers (complexes) participating in combination reactions display quite a high mobility.

(4) The decay of anisotropic complexes into the constituent parts is possible, with the half-life depending on the type of the complex.

Under the above assumptions, it could be considered that the following reactions take place in crystals exposed simultaneously to UV radiation and a shock wave, or an electric field, after cessation of the action:

$$\left.\begin{aligned} &F_2^+ : O^{2-} \xrightarrow{\alpha_1} F_2^+ + O^{2-} \\ &F_2^+ : O^{2-} \underset{\gamma_2}{\overset{\alpha_2}{\rightleftarrows}} V_a^+ : O^{2-} + F \\ &V_a^+ : O^{2-} \xrightarrow{\alpha_3} V_a^+ + O^{2-} \\ &F_2^+ \xrightarrow{\alpha_4} V_a^+ + F \end{aligned}\right\}, \qquad (7)$$

where α and γ are the rates of the direct (decay) and reverse (combination) reactions. In accordance with the first assumption, $\gamma = \gamma_3 = \gamma_4 \equiv 0$. Denoting the concentrations of $F_2^+ : O^{2-}$ complexes (stabilized by an F_2^+ center) by N, of $V_a^+ : O^{2-}$ complexes by n, of unstable F_2^+ centers by N', and of F centers by n_F, we can write the following complete system of equations for describing the processes specified by reactions (7):

$$\left.\begin{aligned} \dot{N} &= -(\alpha_1 + \alpha_2)N + \gamma_2 n n_F \\ \dot{n} &= -\alpha_3 n + \alpha_2 N - \gamma_2 n n_F \\ \dot{N}' &= \alpha_1 N - \alpha_4 N' \\ \dot{n}_F &= \alpha_2 N + \alpha_4 N' - \gamma_2 n n_F \end{aligned}\right\}. \qquad (8)$$

Here, the initial values of the concentrations $N(0) = N_0$, $n(0) = n_0$, $N'(0) = N_0'$, and $n_F(0) = n_F^0$ are defined by the combined action and are assumed to be known quantities.

Assuming that unstable F_2^+ centers (F_2^+ centers that are not incorporated in complexes) are "short-lived" as compared to stabilized complexes $F_2^+ : O^{2-}$ and $V_a^+ : O^{2-}$, we can state that the quasi-stationary state is stabilized quickly ($\alpha_4 \gg \alpha_{1,2,3}, \gamma_2 n_F^0$), and the quasi-stationary concentration N' can be determined from the condition $\dot{N}' = 0$; i.e., $\alpha_4 N' \equiv \alpha_1 N$. We can verify that $\dot{N} = -\dot{n}_F$ by using this condition. Such a qualitative correlation between the time dependences of the concentrations of $F_2^+ : O^{2-}$ complexes and F centers is indeed observed in Fig. 1. The last condition allows us to express n_F in terms of N, $n_F(t) = N_0 + n_F^0 - N(t)$, and to obtain for the concentrations $N(t)$ and $n(t)$ the following system of equations:

$$\left.\begin{aligned} \dot{N} &= -(\alpha_1 + \alpha_2)N + \gamma_2 n(N_0 + n_F^0 - N) \\ \dot{n} &= -\alpha_3 n + \alpha_2 N - \gamma_2 n(N_0 + n_F^0 - N) \end{aligned}\right\}. \qquad (9)$$

Unfortunately, it is impossible to solve this system of equations analytically because of nonlinearity. It is not difficult to solve this system numerically using mathematical computer programs. However, such a solution is not of practical interest, because the exact values of the equation parameters (coefficients α and γ) and the initial concentrations of the centers are unknown. Therefore, we confine ourselves to a qualitative analysis only.

It is not difficult to verify that system (9) has a solution which tends to zero asymptotically. At the same time, the initial value of $\dot{N}$ ($t = 0$), depending on the values of the parameters appearing in the equation, can be negative as well as positive ($\gamma_2 n_0 n_F^0 \gtrless (\alpha_1 + \alpha_2)N_0$). Consequently, for the concentration of stabilized F_2^+ centers, i.e., the complexes $F_2^+ : O^{2-}$, we can obtain a nonmonotonic dependence $N(t)$, displaying initial growth, attaining its maximum value, and asymptotically decreasing to zero. In this case, the characteristic time of these processes is incomparably longer than the lifetime of unstable F_2^+ centers.

It follows from what has been said above that the time dependence of the total concentration of F_2^+ centers (both stabilized and unstable) can have a quickly decreasing segment which mainly describes the disappearance of the unstable centers. The next segment is characterized by a weak dependence in the form of a plateau, with a gradual increase at large values of time. On the last segment, the concentration decreases again, gradually approaching zero. This dependence is in qualitative agreement with the one observed by us and fully depicted in Fig. 1 (the curve presented in Fig. 6 in [5] and describing the results of observations of the first twelve months is a part of this net curve).

The nonmonotonic character of the relaxation is obviously not an exclusive feature of stabilized F_2^+

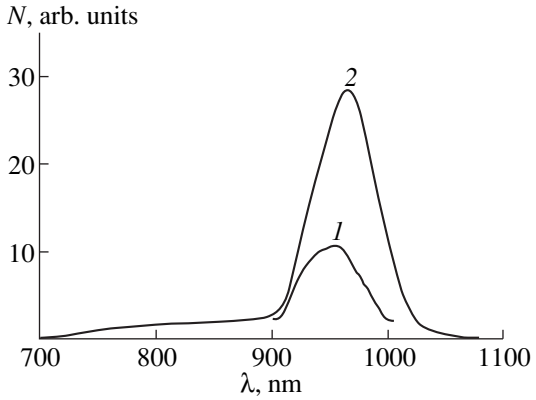

Fig. 4. Luminescence spectra of stable (*1*) and unstable (*2*) F_2^+ centers. The latter was measured one hour after the action of UV radiation on the colored crystal.

color centers in the crystals exposed to the coaction of hard UV radiation and a shock wave. The nonmonotonicity must obviously be manifested in relaxation processes also, at least in those involving color centers which participated in the formation of the above-mentioned charged centers or are the products of their decay. Indeed, the absorption coefficients at the maxima of the F and F_2 bands also exhibit a complex nonmonotonic dependence on the time of crystal holding at room temperature. Slow and gradual destruction of F_2^+ color centers (curve *1* in Fig. 1) resulted in the accumulation (partial recovery) of both F and F_2 color centers by the beginning of the second year of holding (curves *2* and *3*, respectively). In this case, the number of F_3 and F_3^- centers decreases by this moment along with the number of F_2^+ centers. Curves *2* and *3* pass through the maxima and begin to decrease just in the time interval where the increase of the number of F_2^+ centers is observed. The correlation between curve *1* and curves *2* and *3* is convincing evidence of the reactions occurring in the investigated crystals, which formed the basis of the theoretical analysis.

The processes of accumulation of $F_2^+ : O^{2-}$ complexes during prolonged holding of LiF colored crystals at room temperature were also observed in [1, 2]. According to [1], the number of such complexes increased by a factor of 1.5 during eight months. The process of formation of $F_2^+ : O^{2-}$ complexes in [2] was completed in a few hours either, and a slow increase in the intensity of their absorption band is observed during several months. For example, the absorption of $F_2^+ : O^{2-}$ complexes almost doubled during eight months of holding of a colored crystal at room temperature. However, it should be emphasized that the concentrations of the oxygen-containing impurities, and, hence, of O^{2-} ions, were more than an order of magnitude higher in these crystals than in those investigated by us and exposed to the coaction of UV radiation and a shock wave after coloring. Therefore, the reverse reactions with formation of the oxygen-containing complexes in cases [1, 2] probably occur at an appreciable rate due to large values of the concentrations of O^{2-} ions. In our case, according to [4, 5], these reactions can effectively occur in a uniaxial external field even for low concentrations of O^{2-} ions (the energy barrier is lowered in definite directions, resulting in an effective increase of the coefficients γ_1 and γ_3). In [1, 2], simultaneous relaxation of the other color centers is also observed: the absorption of F and F_2 centers decreases, the absorption at λ_m = 390 nm increases, etc. The absorption bands of $F_2^+ : O^{2-}$ centers in [2] are shifted towards short waves, relative to thermally unstable F_2^+ centers (640 nm), and have a peak at λ_m = 620 nm. In contrast, a slight but clearly pronounced shift (~ 15 nm) of the $F_2^+ : O^{2-}$ band towards long waves is observed (cf. curves *2* and *3* in Fig. 3) in the optical absorption spectrum of the crystals investigated by us.

The present article completes a stage of our investigations of the stabilization mechanisms of F_2^+ laser centers in lithium fluoride crystals subjected to the coaction of various fields. The next stage will be the investigation of their generation properties; a preliminary result of this investigation is presented in Fig. 4. This is the luminescence spectrum of the colored LiF crystal, measured in the twenty-first month after the coaction of UV radiation and a shock wave with the aim of determining the main characteristics of the active center, namely, the location of the emission band, its half-width, and so on. The emission band of stable F_2^+ centers with a maximum at 950 nm and a spectral width of 65 nm can be seen in the figure. The luminescence spectrum of unstabilized F_2^+ centers (with a maximum at 965 nm and with an identical half-width, curve *2*) is presented in the same figure for comparison. This spectrum is observed on the test sample one hour after the action of only UV radiation (DRSh-250) for 15 minutes. After the luminescence measurements, an appreciable decrease in the intensity of the F_2^+ band, the disappearance of peaks of F_3^- centers, and the narrowing of the F_2 band, as well as the shift of the F_2 band maximum to the short-wave region of the spectrum, are observed (curve *4* in Fig. 3). The last effect seems to be a result of the destruction of F_3^+ centers, where the band strongly overlaps with the F_2 band. The destruction of the uncharged F_3 centers (370 nm) is also established. The considerable decrease in the F_2^+ band and the disappearance of the peaks of F_3^- color centers were discovered in the optical absorption spectrum of the investigated crystal after measurements of the luminescence spectra were made. This could be due to [7] energy transfer from an excited F_2^+ center to an F_3^- center in the course of excitation. The excited F_3^- centers

may be ionized, and the free electrons produced as a result can neutralize F_2^+ centers.

ACKNOWLEDGMENTS

The authors are grateful to S. V. Sobolevskaya for her assistance in preparation of the manuscript.

This research was supported by grant no. 2.15 of the Academy of Sciences of Georgia, and additionally financed by the Department of Science and Technology of Georgia.

REFERENCES

1. L. C. Courrol, L. Gomes, and I. M. Ranieri, Phys. Rev. B **42** (7), 4741 (1990).
2. B. D. Lobanov, N. T. Maksimova, E. D. Isyanova, *et al.*, Opt. Spektrosk. **63** (1), 816 (1987) [Opt. Spectrosc. **63**, 485 (1987)].
3. V. I. Baryshnikov, V. A. Grigorov, B. D. Lobanov, *et al.*, Izv. Akad. Nauk SSSR, Ser. Fiz. **54** (8), 1467 (1990).
4. M. G. Abramishvili, V. G. Kvachadze, and Z. K. Saralidze, Fiz. Tverd. Tela (Leningrad) **29** (1), 39 (1987) [Sov. Phys. Solid State **29**, 22 (1987)].
5. M. G. Abramishvili, Z. G. Akhvlediani, T. L. Kalabegishvili, *et al.*, Fiz. Tverd. Tela (St. Petersburg) **40** (11), 2044 (1998) [Phys. Solid State **40**, 1850 (1998)].
6. M. G. Abramishvili, Z. G. Akhvlediani, É. M. Barkhudarov, *et al.*, Fiz. Tverd. Tela (St. Petersburg) **37** (8), 2526 (1995) [Phys. Solid State **37**, 1385 (1995)].
7. Yu. L. Gusev, S. P. Marennikov, and V. P. Chebotarev, Izv. Akad. Nauk SSSR, Ser. Fiz. **44** (10), 2018 (1980).

Translated by N. Kovaleva

Physics of the Solid State, Vol. 42, No. 10, 2000, pp. 1846–1853. Translated from Fizika Tverdogo Tela, Vol. 42, No. 10, 2000, pp. 1800–1807.

SEMICONDUCTORS AND DIELECTRICS

Electronic Excitations and Luminescence in $CsLiB_6O_{10}$ Crystals

I. N. Ogorodnikov*, V. A. Pustovarov*, A. V. Kruzhalov*, L. I. Isaenko, M. Kirm***, and G. Zimmerer*****

** Ural State Technical University, ul. Mira 19, Yekaterinburg, 620002 Russia*

e-mail: ogo@dpt.ustu.ru

*** Institute of Single Crystals, Siberian Division, Russian Academy of Sciences, Novosibirsk, 630058 Russia*

**** II. Institut für Experimentalphysik der Universität Hamburg, Luruper Chaussee 149, Hamburg, D-22761 Germany*

Received March 3, 2000

Abstract—The paper presents the results of a complex investigation into the dynamics of electronic excitations in the $CsLiB_6O_{10}$ crystal (CLBO) by low-temperature luminescence VUV spectroscopy with subnanosecond time resolution under photoexcitation by synchrotron radiation. Strong broad-band low-temperature photoluminescence (PL) of the CLBO crystal has been revealed. Data on the PL decay kinetics, time-resolved PL and PL excitation spectra, and reflectance spectra at 9.3 and 295 K are obtained. It is shown that the intrinsic PL of $CsLiB_6O_{10}$ in the 3.5-eV range is caused by radiative annihilation of self-trapped excitons. The channels of creation and decay of relaxed and unrelaxed excitons in cesium lithium borate are discussed. The band gap of CLBO is estimated as $E_g \approx 8.5$ eV. A monotonic increase in the excitation efficiency of intrinsic CLBO luminescence at exciting photon energies above 19 eV is identified as the photon multiplication process. © *2000 MAIK "Nauka/Interperiodica".*

1. INTRODUCTION

Alkali and alkaline-earth metal borate crystals are of considerable interest for generation and conversion of coherent UV radiation in solid-state short-wavelength laser technology and integrated optics. These materials exhibit a unique combination of high radiation resistance and optical stability with good nonlinear characteristics. Among the most well-known crystals in this group are the β modification of barium borate β-BaB_2O_4 (BBO) [1, 2] and lithium triborate LiB_3O_5 (LBO) [3], which are widely used in the second and third harmonic generation with YAG : Nd or Al_2O_3 : Ti lasers and in designing parametric oscillators and integrated optical waveguides. However, despite the broad transparency region extending to 6–7 eV, these crystals are virtually inapplicable for the generation of higher harmonics because of fundamental crystallophysical limitations [4–7]. To eliminate this shortcoming, an analog of LBO, namely, the cesium lithium borate $CsLiB_6O_{10}$ (CLBO), was developed and synthesized, whose crystal lattice was purposefully distorted by replacing half of the lithium atoms in the unit cell (UC) by cesium atoms having a larger ionic radius [8–10]. The CLBO crystal was found to be efficient for the generation of the fourth (266 nm) and fifth (213 nm) harmonics for high-power picosecond lasers. The rapid incorporation of this crystal in present-day laser technologies is explained by the high conversion efficiency, the broad operating spectral range, and the possibility of working with high-power laser radiation (up to 26 GW cm^{-2} [9]).

The possibility of growing large crystals of a high optical quality by a simple technology is definitely not an insignificant asset. For instance, a CLBO crystal $13 \times 12 \times 10$ cm in size was grown by the Kyropoulos method in air at a temperature of about 848°C for 12 days [8, 11–14]. However, in order to reach long-term stability of the properties, a special post-growth treatment is needed [15, 16].

The CLBO crystals are colorless with a transparent region of 180–2750 nm. They belong to the tetragonal space symmetry group ($I\bar{4}2d$) with the unit cell parameters $a = 10.494(1)$ Å and $c = 8.939(2)$ Å, and with four formula units (72 atoms) in the unit cell [17, 18] (Table 1). The main boron–oxygen framework of CLBO, LBO, and CsB_3O_5 (CBO) is formed by $[B_3O_7]^{5-}$ anionic groups made up of similar structural units based on threefold- and fourfold-coordinated boron atoms. CLBO represents a six-element boron–oxygen ring with two threefold- and one fourfold-coordinated boron atoms. This structural unit is surrounded by eightfold-coordinated Cs atoms and fourfold-coordinated Li atoms occupying alternate positions in the channels along the *C* axis [19].

There are many publications dealing with the growth technology and the nonlinear and fundamental physicochemical properties of CLBO (see, e.g., [4–19]). However, the properties of the CLBO crystal which are not directly connected to nonlinear frequency conversion remain poorly known. For instance, there are no data on the electronic structure, luminescence, and point defects of CLBO. At the same time,

1063-7834/00/4210-1846$20.00

Table 1. Crystallographic and luminescence (T = 9.3 K) properties of some borates of alkali and alkaline-earth metals

Parameter	LBO	LTB	CLBO	BBO
Number of formula units per UC, Z	4	8	4	6
Number of atoms in UC	36	104	72	42
UC volume, Å^3	320.3	923.8	984.4	391.3
Symmetry group	$Pna2_1$	$I4_1cd$	$I\bar{4}2d$	$R3c$
Anionic group	$[B_3O_7]$	$[B_4O_9]$	$[B_3O_7]$	$[B_3O_6]$
Luminescence maximum E_m, eV	3.6	3.7	3.45	3.5
FA edge E_a, eV	7.8	7.3	6.9	6.6
Luminescence excitation maximum E_{ex}, eV	8.0	8.0	8.7	6.4
$\mu = (E_{ex} - E_m)/E_{ex}$	0.550	0.538	0.604	0.470
ΔE_m, meV	+60	–300	<10	–
$\gamma = I(E_{ex}/I(15\ \text{eV}))$	>40	4–5	1.2–1.5	3.5

Note: The crystallographic data are taken from [19–21], luminescence data on LBO and $Li_2B_4O_7$ (LTB) from [22], and the data on BBO from [23]; E_a is the energy at the fundamental absorption (FA) edge at $k \approx 50$ cm^{-1}; and ΔE_m is the difference between the locations of the maxima of the self-trapped exciton σ and π luminescence bands.

some information on the dynamics of electronic excitations (EE) is already available for other related crystals. Studies of the EE dynamics in LBO and $Li_2B_4O_7$ (LTB) by time-resolved low-temperature VUV luminescence optical spectroscopy are reported [22]. It was established that, for the LBO and LTB crystals, the excitation by photons above the fundamental absorption (FA) edge leads to the formation of a molecular exciton (ME) which represents chemical-bond excitation in the corresponding anionic group of these crystals. Self-trapping of the ME and subsequent radiative annihilation of the self-trapped exciton (STE) give rise to broad-band luminescence of the LBO and LTB crystals in the 3.6-eV range. A study of BBO luminescence by low-temperature VUV spectroscopy without time resolution was made in [23]. According to [22, 23], the low-symmetry borate crystals exhibit both common features and substantial differences in the EE dynamics. From this standpoint, the CLBO crystal is of particular interest, because it occupies an intermediate position. Indeed, on the one hand, CLBO has the same boron–oxygen framework as LBO and CBO, and on the other, it contains a comparatively heavy cation, as CBO and BBO have.

The purpose of this work was to investigate the dynamics of electronic excitations in the CLBO crystal by time-resolved low-temperature optical-luminescence VUV spectroscopy under selective photoexcitation by synchrotron radiation. This work is a continuation of the studies started in [22].

2. EXPERIMENTAL TECHNIQUE

The samples used in the work were nominally pure CLBO single crystals grown by the Czochralski method from the stoichiometric melt at high temperature gradients of up to 30 K cm^{-1}. By properly optimizing the growth regimes, we succeeded in producing crystals without cracks and inclusions visible under 10× magnification. The samples 8 × 8 × 1 mm in size had polished plane-parallel laser-quality surfaces perpendicular to the crystallographic axis C.

The measurements were performed at the SUPERLUMI setup of the HASYLAB laboratory (DESY) [24]. A detailed description of the available instrumentation, techniques, and experimental conditions was given in our earlier work [22]. We note here only some of the experimental parameters differing from those described in [22]. In the present work, the repetition period of the exciting pulses of the DORIS storage-ring synchrotron radiation was 192 ns. The time-resolved photoexcitation and luminescence spectra were measured simultaneously in two independent time windows of width Δt_1 = 8.5 ns (the fast component) and Δt_2 = 158 ns (the slow component), which were delayed with respect to the excitation pulse by δt_1 = 1.9 ns and δt_2 = 19.5 ns, respectively. The spectral resolution of the primary monochromator with a platinum-coated diffraction grating was 0.25 nm. The luminescence in the visible and UV ranges was recorded with a 0.5 m monochromator (a Czerny–Turner arrangement) equipped with an XP2020Q photomultiplier tube. The luminescence excitation spectra presented in this work are normalized to equal numbers of incident photons with the use of sodium salicylate. The luminescence decay kinetics were analyzed using the convolution integral with due regard for an instrumental profile of the excitation pulse (FWHM ≈ 350 ps). The channel width used in studying the luminescence decay kinetics for times up to 200 ns long was 214 ps.

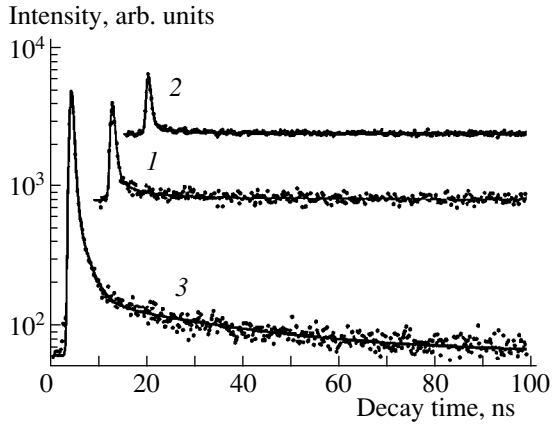

Fig. 1. Photoluminescence decay kinetics of the CLBO crystal at the luminescence-band maximum under excitation by photons of energies (*1*) 7.65 and (*2*, *3*) 24.7 eV at temperatures of (*1*, *2*) 9.3 and (*3*) 295 K. For clarity, curves *1* and *2* are shifted horizontally by 10 and 15 ns, respectively.

3. RESULTS

No luminescence was observed in CLBO under optical excitation within the transparency region of the crystal. By contrast, photoexcitation at photon energies above the CLBO FA edge, E_a = 6.9 eV (Table 1), produces broad-band short-wavelength photoluminescence (PL) with a maximum at 3.3–3.5 eV.

Selective photoexcitation by photons of different energies revealed three exponential components with different initial intensities in the CLBO luminescence (Table 2). At 9.3 K, the fastest and strongest component has a time constant $\tau_1 < 500$ ps, which is comparable to the length of the excitation-pulse instrumental profile. The time constants of the other two components are $\tau_2 = 3.5$ ns and $\tau_3 = 25$ ns. Most of the light sum is contained in the components whose time constants are longer than the excitation pulse repetition period (192 ns) and which are presented in our measurements as a steady component, namely, the pedestal. The contribution of the pedestal to the total light sum, as estimated by the technique described in [25], is as high as 98% at 9.3 K.

Table 2. Spectral parameters of the CLBO photoluminescence kinetics

Parameter	E_{ex}, eV		
	7.65	24.7	24.7
Temperature, K	9.3	9.3	295
I_1, arb. units	3627	5265	5726
I_2, % of I_1	4.4	3.5	8
I_3, % of I_1	1.2	1	0.8
I_p, % of I_1	21.8	45.5	1.03
Light sum Σ, arb. units	342	1000	46
Pedestal contribution to Σ, %	95.2	98.3	53.4
$E_m(\Delta t_1)$, eV	3.46	3.36	3.29
$E_m(\Delta t_2)$, eV	3.44	3.37	3.28
$FWHM(\Delta t_1)$, eV	0.95	0.88	1.07
$FWHM(\Delta t_2)$, eV	0.90	0.91	1.00

Note: E_{ex} is the exciting-photon energy; I_i is the initial intensity of the ith component (i = 1, 2, 3); I_p is the pedestal height; Σ is the light sum under the decay curve; E_m is the location of the maximum, and *FWHM* is the full width at half-maximum of the luminescence band measured in the time window (Δt_j), j = 1, 2.

An analysis of Table 2 shows that excitation of the CLBO luminescence at the FA edge is less efficient than that in the interband transition region. Indeed, the initial intensities I_i of the exponential components excited by 24.7-eV photons increase by 45% (I_1), 15% (I_2), and 20% (I_3), and the pedestal height and, accordingly, the light sum, nearly threefold. This is caused by the increasing contribution of slow components in the micro- and millisecond ranges, which increase the pedestal contribution to the light sum from 95.2 to 98.3%.

An increase in the temperature to 295 K does not noticeably affect the decay times of the three components. The initial intensity of the first component increases by 9%, and the intensity ratio only slightly changes in favor of the second component I_2 (Table 2). At the same time, the pedestal height decreases by nearly a factor of 40, thus reducing the contribution of the slow components down to 53.4%, and the light sum, by almost a factor of 22.

The PL spectrum of the CLBO crystal at 9.3 K is confined within a broad band (FWHM is about 1 eV) with a maximum at 3.3–3.5 eV. No other luminescence bands were observed in the range from 2 eV to the FA edge (6.9 eV). Figure 2 shows the time-resolved PL spectra of CLBO. The spectrum of steady-state PL of CLBO coincides with that of the slow component. An analysis of the luminescence band parameters measured under various experimental conditions (Table 2) allows certain conclusions. For instance, the difference in locations of the band maxima between the fast and slow components in each pair does not exceed 10–20 meV and does not exhibit a systematic pattern under variation of experimental conditions. This gives grounds to believe that the locations of these maxima virtually coincide. The difference between the FWHMs of all the spectra measured at 9.3 K does not exceed 30–50 meV. This suggests that the spectral shapes of the CLBO luminescence bands at 9.3 K are identical for the different excitation conditions. Note that, as the exciting photon energy is changed from 7.65 to 24.7 eV, the luminescence band shifts to longer wavelengths by approximately 70–100 meV. As the temperature increases up to 295 K, the luminescence band somewhat broadens, the intensity decreases, and the maximum shifts by 70–100 meV toward the long-wavelength range (Table 2).

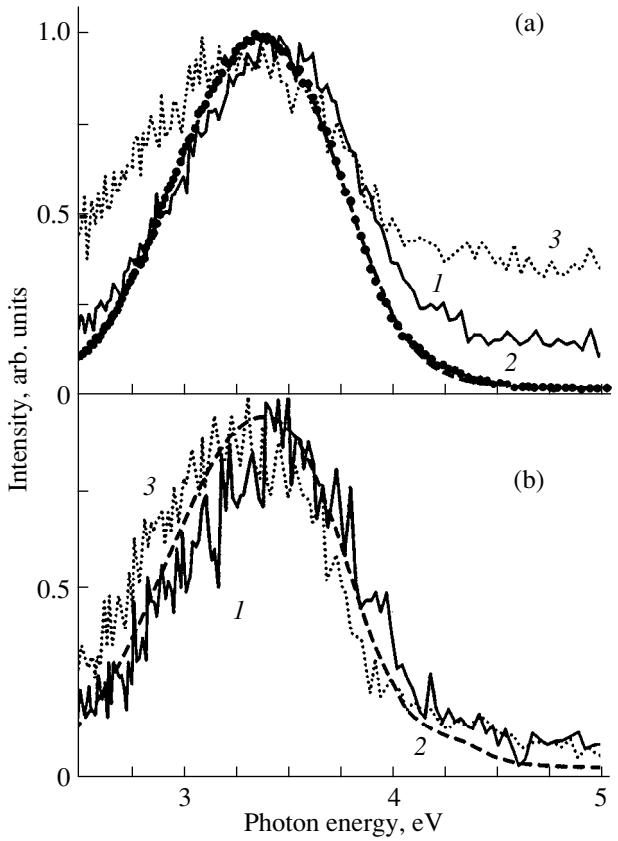

Fig. 2. Time-resolved photoluminescence spectra measured in the time windows (a) Δt_2 and (b) Δt_1 for CLBO crystals at (*1, 2*) 9.3 and (*3*) 295 K and exciting-photon energies of (*1*) 7.65 and (*2, 3*) 24.7 eV.

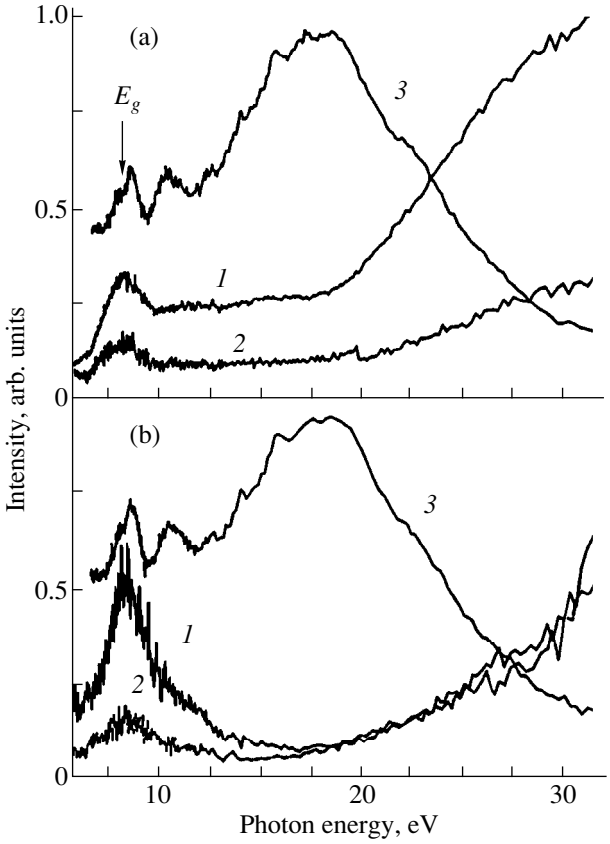

Fig. 3. Excitation spectra of (*1*) the slow and (*2*) fast photoluminescence components in the 3.35-eV band and (*3*) reflectance spectra of the CLBO crystal measured at (a) 9.3 and (b) 295 K.

Figure 3a displays the time-resolved luminescence excitation (LE) spectra obtained on CLBO crystals at 9.3 K. The photoexcitation efficiency in the slow-component spectrum smoothly increases to 6.9 eV and reaches a maximum at 8.7 eV (FWHM ≈ 2 eV). After this, the LE spectra fall off smoothly to 72% of the maximum at 10 eV. This level remains virtually unchanged up to 18 eV. The excitation spectra of steady-state PL coincide with the LE spectra of the slow component. The LE profile of the fast component exhibits slight differences, namely, the excitation efficiency above 10 eV is about 60% of that at the maximum, and a small hump appears near 7.5 eV. As the temperature increases to 295 K, the PL intensity of CLBO decreases several tens of times. A broad maximum of all components in the LE spectra is also observed at 8.7 eV (Fig. 3b). However, the intensity in the short-wavelength wing of the LE peak continues to drop to reach 12–15% at 15 eV. Note that, in the energy range corresponding to the short-wavelength wing of the CLBO LE band at 8.7 eV, the reflectance spectrum exhibits a broad, clearly pronounced peak (Fig. 3). This close match of the LE peak to the feature in the reflectance spectrum was observed by us earlier in LBO and LTB crystals [22], where the main low-energy LE peak was assigned to excitation of the molecular-type exciton. However, the assignment of the fine structure of the reflectance spectrum in this range requires additional high-precision measurements on natural growth faces of the crystal or cleavage surfaces.

4. DISCUSSION

The experimental data obtained for the first time in this work indicate that the CLBO crystals are characterized by broad-band short-wavelength luminescence with a large Stokes shift (about 5 eV) and a high quantum yield ($\eta > 1\%$ at 9.3 K). This luminescence is not excited in the transparency region of the crystal, does not exhibit any distinct connection with a specific intrinsic or impurity defect, is efficiently excited both at the FA edge (where the penetration depth of the exciting radiation is fairly large and reaches a few tenths of a millimeter) and throughout the fundamental absorption region studied for the crystal, undergoes a flare-up when cooled from room temperature to 9.3 K, and reveals a fast exponential exponent in the decay kinetics.

It is known that, in alkali halide (AH) crystals, similar properties are identified with STE luminescence

[26]. Recent studies made on alkali and alkaline-earth metal borates (for instance, BBO [23], LBO and LTB [22]) also revealed an intrinsic luminescence with similar properties, which was assigned to STE radiative annihilation, or annihilation of electronic excitations localized at small lattice distortions. A qualitative comparison of the main luminescence properties among the borate crystals (Table 1) gives sufficient grounds to maintain that the final stage in the luminescence of the four given borates (including CLBO) is of the same nature. This permits one to assign the intrinsic luminescence of the CLBO crystal at 3.4–3.6 eV to radiative annihilation of STEs, as is the case in LBO and LTB.

At the same time, a quantitative comparison of the luminescence properties (Table 1) reveals certain differences in the dynamics of electronic excitations of the borates under consideration. For instance, the relative Stokes shift $\mu = (E_{ex} - E_m)/E_{ex}$ of the luminescence increases in the order BBO–LTB–LBO–CLBO from $\mu = 0.470$ (BBO) to $\mu = 0.604$ (CLBO). Compare these values with the data available for other crystals. According to [27], the STE luminescence in AH crystals is characterized by the relative stokes shifts $\mu_1 = 0.08–0.15$ (single-halide STEs) and $\mu_2 = 0.50–0.71$ (two-halide STEs). For the AH crystals, one has typically $\mu_1 \ll \mu_2$, which is due to a fairly large relaxation of the AH crystal lattice upon formation of the X_2^- quasi-molecule in the case of a two-halide STE. However, the values of μ_1 for single-site STEs in wide-band-gap oxides are somewhat larger, namely, 0.15 and 0.26 for Al_2O_3 and $Y_3Al_5O_{12}$ [28], 0.36 for BeO [29], and 0.42 for Y_2O_3 [30]. The relative Stokes shift of the luminescence for all the borates considered, specifically for CLBO, exceeds the values of μ_1 for the known oxides. This fact alone gives no grounds for suggesting a possibility of two-site exciton self-trapping, because in borates the quantitative criteria can be different. Nevertheless, it is evidence of a substantial relaxation of the borate crystal lattice due to the STE formation. For comparison, we note that, in Y_2O_3 ($\mu_1 = 0.42$), a large displacement of the O^- ion from the regular site upon the STE relaxation was experimentally observed by optically detected EPR [30]. This large lattice relaxation in the CLBO crystal apparently accounts for the absence of observable differences in spectral position between the maxima of the CLBO luminescence σ and π bands (Fig. 2).

Another important difference follows from a comparison of the locations of the LE maximum E_{ex} and the FA edge E_a for the borates (Table 1). For LBO and LTB crystals, the long-wavelength wing of the LE band is a steeply rising curve coinciding in profile with the exponential increase in the optical density at the FA edge ($E_{ex} - E_a = 0.2$ and 0.5 eV, respectively). The LE band maxima of LBO and LTB lies in the optical-absorption coefficient region $k \approx 50$ cm^{-1}, which corresponds to an exciting photon penetration depth of about 200 μm. In BBO, the LE maximum is observed at a lower energy, ($E_{ex} - E_a = -0.2$) in the region where $k \approx 20$ cm^{-1}. The CLBO crystal occupies an intermediate position between LTB and BBO in the location of the FA edge, but the LE maximum of CLBO is located at shorter wavelengths, which results in $E_{ex} - E_a = 1.8$ eV.

The reasons for this lie in the specific features of electronic structure of the valence band (VB) top and the conduction band (CB) bottom, which determine the nature of the lowest-energy electronic transitions. These features are associated with both the differences in crystalline structures of the borates and the specific contribution of heavy cations (Ba and Cs) to the CB electronic structure. Consider this in greater detail. The electronic band structure and linear optical properties of LBO, CBO, and BBO crystals were calculated by the linearized augmented plane wave method [31]. It was established that the LBO and CBO crystals have a qualitatively similar VB structure formed from the same anionic groups. At the same time, the CBO and BBO crystals are similar in CB structure, which is a consequence of equal contributions of the Cs and Ba cations to the CB electronic structure. The ground state of the low-energy electronic transition (the VB top) in LBO is derived from anionic states, while the excited state (the CB bottom) represents hybridized boron–oxygen orbitals of the BO_3 trigonal anionic groups. The lithium states neither contribute to the partial composition of the CB bottom nor play a noticeable part in the low-energy electronic transitions. Because an electronic transition in LBO essentially represents an intraatomic (intraoxyanionic) transition characterized by a fairly high oscillator strength, this is made responsible for the steep increase in the calculated optical-absorption coefficient at the FA edge. The results of direct experimental measurements of optical absorption near the FA edge [32, 33] are in complete agreement with this reasoning.

A different pattern was predicted for the CBO and BBO crystals in [31]. Although states of the heavy cations Cs and Ba dominate in the partial composition of the CB bottom, they exert a substantially weaker effect, compared to the anionic-group states, on optical transitions because of the weak oscillator strength. Therefore, the FA edge in CBO and BBO contains two energy regions [31]: close to the FA edge, within an interval about 1 eV wide, optical absorption increases very slowly. This corresponds to transitions from the VB top to states of the CB bottom deriving from the heavy-cation orbitals. Because these transitions are interatomic (involving charge transfer), the absorption coefficient is comparatively small. After the energy of the photons has increased above the FA edge by about 1 eV, they initiate transitions to the excited CB states formed by the boron–oxygen orbitals (intra-atomic transitions) [31], as is the case in LBO. As a result, the optical absorption coefficient increases rapidly. Therefore, the lowest-energy optical transitions between states of the anionic group will be observed above the FA edge by about 1 eV, which should affect both the PL excitation and reflectance spectra of these crystals.

Indeed, a narrow band was observed at 7.6 eV near the FA edge in BBO reflectance spectra [23]. This band was assigned to the formation of exciton-like electronic excitations which correspond in energy to the interband transitions in the anionic group. Note that the BBO FA edge lies at 6.6 eV, i.e., lower by 1 eV (Table 1). Indications of the existence of MEs were observed in the LBO and LTB crystals. They represent chemical-bond excitations in the anionic group and appear directly at the FA edge [22]. It is the excitation of these MEs at the FA edge that can be responsible for the origin of the main LE band in the spectra of LBO and LTB [22]. The BBO crystals exhibit a different pattern: the LE maximum lies at 6.4 eV, which is below the onset of optical transitions in the anionic group by about 1 eV. In this connection, the LE band in the spectra of BBO was assigned to excitation of the O–Ba oscillator [22].

We are not aware of any band calculations of the electronic structure in the CLBO crystal. However, recently, the approximate calculation of this structure has been performed by the cluster method with partial neglect of differential overlap [34]. Therefore, we will make a qualitative analysis of the CLBO electronic structure by using the experimental PL excitation and reflectance spectra of CLBO (obtained in this work) and invoking the calculations [34] and data available in the literature for other borates. The structure of the LBO, CBO, and CLBO crystals is based on the same anionic group $[B_3O_7]^{5-}$; it forms a three-dimensional boron–oxygen framework—the so-called triborate structure made up of planar triangular BO_3 units and BO_4 tetrahedra, which assumes a considerable similarity among the LBO, CBO, and CLBO crystals from the standpoint of the VB structure. The band-structure calculations of LBO, CBO [31], CLBO [34], and LTB [35–37] are in reasonable agreement with the above assumption and predict that the electronic transitions within the anionic groups of these crystals should lie in the range 8–15 eV. Because the reflectance spectra of LBO, LTB, and CLBO in this range are closely similar, this part of the CLBO reflectance spectrum (Fig. 3) can be explained by optical transitions within the $[B_3O_7]^{5-}$ anionic group. Earlier [22], based on electronic structure calculations, the maxima observed in the BBO reflectance spectrum in the range 8–15 eV were also assigned to transitions in the corresponding anionic group.

The CB structure calculations performed for LBO, CBO [31], and CLBO [34] permit the conclusion that, in CLBO, as in CBO, the Cs states make a substantial contribution to the formation of the CB bottom, which should lead to a shift of the FA edge toward lower energies. The experimental data (Table 1) indicate that, as one passes from LBO to CLBO, the FA edge is actually shifted by ~1 eV toward the low-energy range. In this connection, the lowest-energy optical transitions in CLBO should be assigned to charge-transfer electronic transitions between the anionic group and the Cs cation. At the same time, unlike BBO, the LE band maximum in CLBO falls in the region of the anionic-group electronic transitions rather than in the region of charge-transfer transitions (Table 1). On the one hand, this indicates that, in CLBO, absorption of a photon with an energy above the onset of optical transitions in the anionic group initiates formation of a molecular-type exciton, as this was established earlier for the LBO and LTB crystals [22]. It is the evolution of this ME that eventually leads to the formation of STEs, whose radiative annihilation gives rise to the wide-band intrinsic luminescence in CLBO at 3.4 eV. On the other hand, the energy location of the LE maximum in the spectra of CLBO within the region of intra-anion transitions unambiguously indicates a substantially smaller role of the Cs heavy cation in the EE dynamics of CLBO as compared to that for Ba in BBO. An appreciable role of Ba in the EE dynamics of BBO is primarily due to the specific features of the BBO crystal structure: the main structural motif of BBO, namely, the anionic group $[B_3O_6]^{-3}$, is made up of solely the BO_3 planar units and forms only a two-dimensional boron–oxygen layer. The Ba^{2+} ions not only provide charge neutrality of the crystal as a whole but join the neighboring layers to form a three-dimensional structure and play a noticeable part in the EE energy transport between the layers. In LBO, CBO, LTB, and CLBO crystals, the interaction of atoms within the anionic group is substantially stronger than that with the Li or Cs cations lying in the voids of the three-dimensional boron–oxygen framework. Obviously, the EE energy transport in this case is mainly contributed by the anionic-group states, whereas the role of the cations appears to be less significant. In our opinion, this is responsible for the difference in locations of the LE maxima in the spectra of the BBO, LBO, and CLBO crystals.

Experimental data needed to determine the magnitude of E_g for the alkali metal borates are lacking. Indeed, there are no spectra of photoconductivity, thermally stimulated luminescence excitation, and optical constants. At the same time, the band gap E_g = 7.5 eV for the BBO crystal was reliably established for the direct Γ–Γ transition from the data obtained by low-temperature optical-luminescence VUV spectroscopy [23]. A comparison of this value of E_g with the results of band-structure calculations made for BBO (5.61 [38] and 4.88 eV [31]) permits the conclusion that calculations underestimate the energy gap, which appears to be comparable to the short-wavelength edge of the transparency region of the crystal (see Table 1). Such a situation is typical of other crystals: theoretical estimations of the band gap for LBO yield 6.95 [31], 7.26 [34] and 7.37 eV [38], and for CLBO, 6.31 eV [34], which is comparable to the energy E_a (Table 1). Assuming that the theoretical data correctly reflect the trend of band gap variation in the series LBO–CLBO–BBO, and taking into account the experimental value of E_g = 7.5 eV for BBO, we obtain an average value E_g = 9.5 eV for LBO and E_g = 8.5 eV for CLBO. Despite the approximate character of the estimation, the obtained values of

E_g are needed for analysis of the LE and reflectance spectra of the LBO and CLBO crystals over a wide spectral range.

A detailed analysis of LE spectra over a wide range of energies requires considering the spectra of optical constants, primarily of the absorption coefficient $k(E)$. In particular, the reflectance spectrum (Fig. 3) indicates substantial changes in the absorption coefficient in the studied range, which can affect the observed LE spectral profile. These points will be analyzed in a separate publication. However, certain conclusions can be drawn already even from the available data.

In the energy range 10–20 eV, the luminescence excitation efficiency at 9.3 K remains constant at a level of 72% of the maximum value reached at 8.7 eV (Fig. 3). As follows from general considerations and an analysis of the reflectance spectrum, the absorption coefficient at these energies should increase by several orders of magnitude and cause the corresponding be less pronounced in the exciting photon penetration depth and an increase in the surface energy losses (SEL) in the presence of high-mobility EEs. The SEL effect should obviously be less pronounced with a decrease in the mobility and, thus, reduce the dependence of the luminescence yield on the exciting photon energy. Consider this dependence by the specific example of the LBO and CLBO crystals. Incorporation of cesium atoms increases the degree of lattice "looseness," which can be roughly evaluated as the average volume per atom. As follows from Table 1, this parameter varies from 8.90 (LBO) to 13.67 Å^3 (CLBO). This naturally results in a weakening of the interaction between atoms of the anionic group, a decrease in the mobility of the corresponding EEs and, hence, a decrease in the SELs and of the energy dependence of the LE spectra. Table 1 presents the parameter γ, which is the ratio of the luminescence intensity upon excitation by photons of energy E_{ex} to that upon excitation in the interband transition region at 15 eV. Note that E = 15 eV lies below the assumed threshold of photon multiplication for the borates under consideration. A decrease in the γ parameter, with all other factors being the same, can indicate a decrease in the EE mobility. As is seen from Table 1, the γ parameter actually varies from $\gamma > 40$ (LBO) to $\gamma \sim 1.5$ (CLBO). The LTB and BBO crystals are intermediate in this parameter (Table 1). Bearing in mind the common nature of the luminescence and common structural features of the three-dimensional boron–oxygen framework, we can suggest a decrease in the EE (molecular exciton) mobility in the series LBO–LTB–CLBO order at low temperatures. As the CLBO crystal is heated up to 295 K, the γ parameter increases to ≈ 8. In a general case, the temperature dependence observed can be caused by a number of reasons. Among the reasons which are the most probable and which deserve a further detailed study are the EE (molecular exciton) motion by the hopping diffusion mechanism and the recombination mechanism of luminescence excitation. In the former case, an increase in temperature leads to an increase in the ME mobility, and in the latter case, to an increase of the contribution of thermally stimulated recombination processes. Taking into account the considerable (by a few tens of times) drop in the quantum yield of CLBO luminescence upon heating from 9 K to room temperature, the first mechanism appears to be quite probable. Indeed, the LBO crystal (in which the recombination excitation channel was revealed) at similar temperature conditions exhibits an increase in the luminescence intensity by a factor of 20–25, rather than its decrease [33].

A monotonic increase in the excitation efficiency of low-temperature luminescence at energies above 19 eV (Fig. 3a) can be assigned to the photon multiplication process, as this was observed earlier in other wide-band-gap oxides, for instance, BBO [23] or Al_2O_3 [39]. However, this aspect requires a separate detailed consideration.

Thus, we have performed first measurements of the PL decay kinetics with subnanosecond time resolution over wide spectral and temperature ranges, PL spectra with time resolution, and the time-resolved PL excitation spectra and reflectance spectra of the $CsLiB_6O_{10}$ crystal under selective photoexcitation by synchrotron radiation. The experimental data obtained for the CLBO crystal revealed excitation of the unrelaxed molecular-type exciton whose main decay channels are migration with subsequent nonradiative decay and self-trapping. It was also shown that the broad-band short-wavelength CLBO luminescence with a maximum at 3.3–3.5 eV has an intrinsic nature due to radiative annihilation of the self-trapped exciton. Moreover, a decrease in the mobility of electronic excitations (the molecular exciton) was observed in the series LBO–LTB–CLBO at low temperatures. The band gap in CLBO was estimated as $E_g \approx 8.5$ eV. The monotonic increase in the excitation efficiency of the CLBO intrinsic luminescence at exciting photon energies above 19 eV was assigned to the photon multiplication process.

ACKNOWLEDGMENTS

This work was supported by the European Commission (grant no. IC15CT960721) and, in part, by the DFG (grant no. ZI-159/4-1).

REFERENCES

1. R. French, J. Ling, F. Ohuchi, and C. Chen, Phys. Rev. B **44** (16), 8496 (1991).
2. F. Huang and L. Huang, Appl. Phys. Lett. **61** (15), 1769 (1992).
3. C. T. Chen, Y. C. Wu, A. D. Jiang, *et al.*, J. Opt. Soc. Am. B **6** (4), 616 (1989).
4. Y. Mori, S. Nakajima, A. Miyamoto, *et al.*, Proc. SPIE **2633**, 299 (1995).
5. Y. Mori, S. Nakajima, A. Taguchi, *et al.*, AIP Conf. Proc. **369** (1), 998 (1996).

6. L. B. Sharma, H. Daido, Y. Kato, *et al.*, Appl. Phys. Lett. **69** (25), 3812 (1996).
7. T. Sasaki and Y. Mori, Proc. SPIE **3244**, 88 (1998).
8. T. Sasaki, I. Kuroda, S. Nakajima, *et al.*, OSA Proc. Adv. Solid-State Lasers **24**, 91 (1995).
9. Y. Mori, I. Kuroda, S. Nakajima, *et al.*, J. Cryst. Growth **156** (3), 307 (1995).
10. Y. Mori and T. Sasaki, Proc. SPIE **2700**, 20 (1996).
11. G. Ryu, C. Yoon, T. Han, and H. Gallagher, J. Cryst. Growth **191** (3), 492 (1998).
12. K. Bai and S. Jung, J. Cryst. Growth **186** (4), 612 (1998).
13. Y. Yap, T. Inoue, H. Sakai, *et al.*, Opt. Lett. **23** (1), 34 (1998).
14. Y. Yap, K. Deki, N. Kitatochi, *et al.*, Opt. Lett. **23** (13), 1016 (1998).
15. Y. Yap, M. Inagaki, S. Nakajima, *et al.*, Opt. Lett. **21** (17), 1348 (1996).
16. Y. Yap, S. Haramura, A. Taguchi, *et al.*, Opt. Commun. **145** (1–6), 101 (1998).
17. Y. Mori, I. Kuroda, S. Nakajima, *et al.*, Appl. Phys. Lett. **67** (13), 1818 (1995).
18. Y. Mori, I. Kuroda, S. Nakajima, *et al.*, Jpn. J. Appl. Phys., Part 2 **34** (3A), L296 (1995).
19. T. Sasaki, Y. Mori, I. Kuroda, *et al.*, Acta Crystallogr., Sect. C: Cryst. Struct. Commun. **51**, 2222 (1995).
20. S. Radaev, L. Muradyan, L. Malakhova, *et al.*, Kristallografiya **34** (6), 1400 (1989) [Sov. Phys. Crystallogr. **34**, 842 (1989)].
21. S. Radaev, E. Genkina, V. Lomonov, *et al.*, Kristallografiya **36** (6), 1419 (1991) [Sov. Phys. Crystallogr. **36**, 803 (1991)].
22. I. N. Ogorodnikov, V. A. Pustovarov, A. V. Kruzhalov, *et al.*, Fiz. Tverd. Tela (S.-Peterburg) **42** (3), 454 (2000) [Phys. Solid State **42**, 464 (2000)].
23. V. Kisand, R. Kink, M. Kink, *et al.*, Phys. Scr. **54**, 542 (1996).
24. G. Zimmerer, Nucl. Instrum. Methods Phys. Res., Sect. A **308**, 178 (1991).
25. T. Matsumoto, T. Kawata, A. Miyamoto, and K. Kan'no, J. Phys. Soc. Jpn. **61** (11), 4229 (1992).
26. Ch. Lushchik, in *Excitons*, Ed. by E. I. Rasba and M. D. Sturge (North-Holland, Amsterdam, 1982), Vol. 2, p. 505.
27. Ch. Lushchik, A. Lushchik, E. Vasil'chenko, and F. Savikhin, Fiz. Tverd. Tela (S.-Peterburg) **37** (2), 525 (1995) [Phys. Solid State **37**, 284 (1995)].
28. M. Kirm, A. Lushchik, C. Lushchik, and G. Zimmerer, in *Physics and Chemistry of Luminescent Materials*, Ed. by C. Ronda (Pennington, 2000); The Electrochemical Society Proceedings Series **PV 99-40**, 113 (2000).
29. I. Ogorodnikov, V. Ivanov, and A. Kruzhalov, Fiz. Tverd. Tela (S.-Petersburg) **36** (11), 3287 (1994) [Phys. Solid State **36**, 1748 (1994)].
30. W. Hayes, M. Kane, O. Salminen, and A. Kuznetsov, J. Phys. C **17** (14), L383 (1984).
31. J. Li, C.-G. Duan, Z.-Q. Gu, and D.-S. Wang, Phys. Rev. B **57** (12), 6925 (1998).
32. I. Ogorodnikov, E. Radzhabov, L. Isaenko, and A. Kruzhalov, in *Excitonic Processes in Condensed Matter*, Ed. by R. Williams and W. Yen (Pennington, 1998); The Electrochemical Society Proceedings Series **PV 98-25**, 426 (1998).
33. I. Ogorodnikov, E. Radzhabov, L. Isaenko, and A. Kruzhalov, Fiz. Tverd. Tela (S.-Peterburg) **41** (2), 223 (1999) [Phys. Solid State **41**, 197 (1999)].
34. W.-D. Cheng, J.-T. Chen, Q.-S. Lin, *et al.*, Phys. Rev. B **60** (16), 11747 (1999).
35. Ya. Burak, Ya. Dovgiĭ, and I. Kityk, Fiz. Tverd. Tela (Leningrad) **31** (9), 275 (1989) [Sov. Phys. Solid State **31**, 1634 (1989)].
36. W. Cheng, J. Chen, J. Huang, and Q. Zhang, J. Chem. Soc., Faraday Trans. **92** (24), 5073 (1996).
37. A. Kuznetsov, L. Isaenko, A. Kruzhalov, *et al.*, Fiz. Tverd. Tela (S.-Petersburg) **41** (1), 57 (1999) [Phys. Solid State **41**, 48 (1999)].
38. Y.-N. Xu, W. Ching, and R. French, Phys. Rev. B **48** (24), 17695 (1993).
39. M. Kirm, G. Zimmerer, E. Feldbach, *et al.*, Phys. Rev. B **60** (1), 502 (1999).

Translated by G. Skrebtsov

Physics of the Solid State, Vol. 42, No. 10, 2000, pp. 1854–1860. Translated from Fizika Tverdogo Tela, Vol. 42, No. 10, 2000, pp. 1808–1813.

SEMICONDUCTORS AND DIELECTRICS

Spatial Rectification of Fields of Photorefractive Waves

V. V. Bryksin and M. P. Petrov

Ioffe Physicotechnical Institute, Russian Academy of Sciences, Politekhnicheskaya ul. 26, St. Petersburg, 194021 Russia

Received March 21, 2000

Abstract—A theory of rectifying electric fields associated with photorefractive waves is presented. The rectification effect is caused by scattering of photorefractive waves from the static grating of a space charge, which is formed as a result of excitation of photorefractive waves due to an interference pattern oscillating about its equilibrium position. The theory predicts high values of rectified fields (of the order of 100 V cm^{-1}) and agrees well with the available experimental data. *© 2000 MAIK "Nauka/Interperiodica".*

Space charge waves, which are normal vibrational modes of an electron subsystem with deep traps in a crystal, can exist in photorefractive crystals (e.g., $Bi_{12}TiO_{20}$, $Bi_{12}SiO_{20}$, $Bi_{12}GeO_{20}$, and GaAs) and semi-insulating semiconductors (e.g., Ge doped with gold). In the first publication [1], where the concept of these waves was proposed, they were referred to as trap recharging waves. The term "photorefractive wave" that will be used by us here is usually employed for photorefractive crystals. These waves are specific quasi-particles with a peculiar dispersion law, which have become an object of intense study in recent years [2, 3].

The variety of effects associated with photorefractive waves is largely determined by the methods of their excitation. We will not dwell here on enumerating many known methods and will discuss only the technique of exciting photorefractive waves by illuminating the sample with an interference pattern oscillating about an equilibrium position [3]. This technique is widely used in practical applications and makes it possible to observe the effect of spatial rectification of electric fields induced by photorefractive waves.

If a crystal is exposed to two coherent light beams, one of which is subjected to phase modulation with amplitude Θ and frequency Ω (Fig. 1), the interference pattern can be described by the expression

$$I(x, t) = I_0\{1 + m\cos(kx + \Theta\cos\Omega t)\},$$

where I_0 is the mean intensity of incident light, $k = 2\pi/\Lambda$ is the wave vector, Λ is the period, and m is the contrast of the interference pattern. Setting $\Theta \ll 1$ and confining ourselves to only the first-order terms in Θ, we can rewrite the expression for $I(x, t)$ in the form

$$I(x, t) = I_0\left\{1 + m\cos kx + \frac{1}{2}m\Theta[\sin(kx + \Omega t) + \sin(kx - \Omega t)]\right\}.$$

Here, the first term describes the uniform (background) illumination, the second term describes the static interference pattern, and the last two terms represent two running interference waves propagating in the opposite direction. In conformity with the mechanism of formation of a space charge in the crystals under investigation, the above illumination of the crystal leads to the writing of a static charge grating with the wave vector k and two running space charge waves propagating in opposite directions with the wave vectors k and $-k$ and frequency Ω. If the values of k and Ω for one of these waves coincide with the wave vector and frequency of a photorefractive wave, the resonance excitation of natural vibrations of the system (photorefractive waves) takes place. The following conditions must be met for the weak attenuation of photorefractive waves. First,

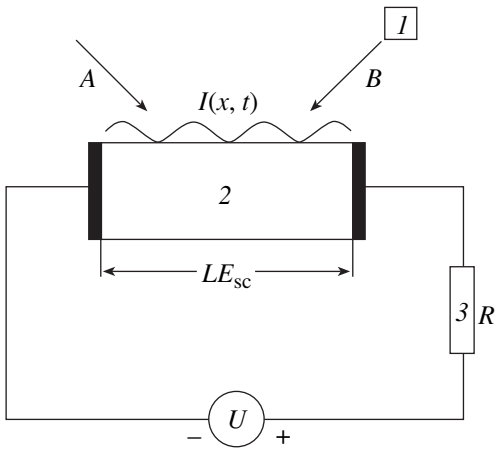

Fig. 1. *A* and *B* are the light beams forming the interference pattern $I(x, t)$, *1* is the phase modulator ensuring the phase modulation of beam *B* according to the law $\exp(i\Theta\cos\Omega t)$, *2* is the crystal with electrodes, and *3* is the resistance R equal to the sum of the actual load resistance, internal resistance of the source, and the resistance of the contact regions of the crystal. The voltage drop $u(t) = LE_{sc}(t)$ across the sample describes the effect of field rectification under investigation.

1063-7834/00/4210-1854$20.00

the applied electric field E_0 should be strong enough so that $kL_0 > 1$, where $L_0 = \mu E_0 \tau$ is the drift length, μ is the charge carrier mobility, and τ is the lifetime of photoelectrons in the conduction band. Second, the drift length should be greater than the diffusion length.

If photorefractive waves are excited with a small contrast ($m \ll 1$), nonlinear effects (i.e., the effects proportional to m^2) can be neglected, and spatial rectification of the field of a photorefractive wave is not observed. If, however, the value of m is not too small, we consider nonlinear effects proportional to m^2, e.g., the interaction between the propagating and static charge gratings. In this case, while analyzing the field created by the space charge, we should take into account products of the type $m^2\Theta\cos(kx)\sin(kx - \Omega t)$, which contain, in particular, terms of the type $m^2\Theta\sin\Omega t$. These term describe the space-charge field, which is uniform in space but oscillates in time. The emergence of such contributions in the expression for the space-charge field actually reflects spatial rectification of the field induced by the photorefractive wave. Thus, the spatial rectification of the field of photorefractive waves can be interpreted as the result of scattering of a running photorefractive wave with the wave vector k and frequency Ω from the field of the static charge grating with a wave vector $-k$ (and frequency $\Omega = 0$).

The uniform oscillating field naturally induces an alternating current in the external circuit, which can be treated as the rectification of the space-charge current. It should be noted that the effects of rectification of current and voltage due to interaction of induced oscillations (and not normal modes) with the static charge grating were encountered and studied in detail earlier (see, for example, [4–7]). These effects are known as the transient photoemf effect, which plays a decisive role in the absence of an external field. Spatial rectification of a current due to the excitation of photorefractive waves was detected by Mansurova *et al.* [8] and interpreted as a giant spike of photoemf. A direct experimental proof of the field rectification was obtained by us in [9], where the piezoelectric effect was used to observe crystal deformation by a rectified field. Later, we detected a rectified field with the help of the electrooptical effect.

The present work presents a theoretical analysis of rectification of the electric field (and current) produced by photorefractive waves. We assume that a crystal is illuminated by the aforementioned oscillating interference pattern under a constant external electric field. The illumination leads to the generation of photoelectrons at the rate

$$g(x, t) = g_0\{1 + m\cos(kx + \Theta\cos\Omega t)\}, \qquad (1)$$

where $g_0 = WI_0$ (W is the coefficient determined by the photon energy, quantum yield, and the absorption coefficient of the crystal). As a result of motion of photoelectrons in the external electric field followed by their pinning in traps, the charges are separated, and an internal electric field is induced. A detailed calculation of such an internal field is given in [10]. However, in that work (and in other publications where the space-charge field was considered in the presence of an external electric field), it was assumed that the crystal is connected to a voltage generator. In this model, the voltage across the sample is determined by external conditions, and the constant component of the internal field sought does not appear. In the present work, we reject this assumption and consider an equivalent series circuit containing a generator of the emf U with an internal resistance R and a sample with a voltage drop $u(t)$. The circuit carries an alternating current $I(t)$. The voltage drop across the sample and the current in the external circuit are functions of time in view of the time variations of the space charge distribution and the electric field in the crystal. Ohm's law for this circuit has the form (Fig. 1)

$$u(t) = U - I(t)R.$$

The resistance R can in principle include not only the internal resistance of the source, but also a resistive load. It is more convenient to write this relation in a different form, going over from voltages, current, and resistances to specific characteristics, such as the electric field strength, current density, and the resistivity of the load (normalized to the geometrical dimensions of the sample):

$$E(t) = \tilde{E} - J(t)\rho. \qquad (2)$$

Here, $\tilde{E} = U/L$, $E(t) = u(t)/L$, $J(t) = I(t)/S$, and $\rho = RS/L$, where L and S are the length and the cross-sectional area of the sample, respectively. The quantity $E(t)$ is the sought component of the internal field $E(x, t)$, which is uniform in space:

$$E(t) = \frac{1}{L}\int_0^L dx E(x, t). \qquad (3)$$

In the present work, relations (2) and (3) play the role of boundary conditions. The problem considered in [10] corresponds to the case of a voltage generator with $\rho = 0$.

Henceforth, the induced internal field will be calculated with the following standard system of equations [11] (see also [10]):

$$\frac{n(x, t)}{\tau} - \frac{1}{e}\frac{\partial j(x, t)}{\partial x} = g(x, t), \qquad (4)$$

$$j(x, t) = e\mu n(x, t)E(x, t), \qquad (5)$$

$$\frac{\varepsilon}{4\pi}\frac{\partial E(x, t)}{\partial t} + j(x, t) = J(t). \qquad (6)$$

Here, $j(x, t)$ is the nonuniform current density, $n(x, t)$ is the concentration of photoelectrons, τ is the lifetime of photoelectrons in the conduction band, μ is the mobil-

ity of photoelectrons, and ε is the dielectric constant. The current density $J(t)$ in the external circuit has to be determined from the boundary conditions (2) and (3). As in [10], we disregard the diffusive contribution to the current $j(x, t)$ and use the simplest model of photoelectron recombination, which is applicable for not very strong electric fields. In addition, we use the quasistatic approximation and omit the time derivative $\partial n(x, t)/\partial t$ in Eq. (4). It should be noted that the right-hand side of Eq. (5) contains the product of the charge carrier density into the internal field, which is a source of nonlinear effects, including the rectification of the field of photorefractive waves.

Let us now linearize Eqs. (4)–(6) in the parameter Θ by assuming that the phase modulation amplitude is small

$$\begin{aligned} g(x, t) &= g^{(0)}(x) + \delta g(x, t), \\ g^{(0)}(x) &= g_0(1 + m\cos kx), \\ \delta g(x, t) &= -g_0 m\Theta \sin kx \cos\Omega t. \end{aligned} \tag{7}$$

Accordingly, we can write

$$\begin{aligned} E(x, t) &= E^{(0)}(x) + \mathrm{Re}[\delta E(x)\exp(i\Omega t)], \\ n(x, t) &= n^{(0)}(x) + \mathrm{Re}[\delta n(x)\exp(i\Omega t)], \\ J(t) &= J^{(0)} + \mathrm{Re}[\delta J\exp(i\Omega t)]. \end{aligned} \tag{8}$$

Here, $E^{(0)}(x)$, $n^{(0)}(x)$, and $J^{(0)}$ are the steady-state values of the internal field, concentration of photoelectrons, and total current (for $\Theta = 0$), respectively; δE, δn, and δJ are corrections linear in Θ.

Since the steady-state current does not depend on the coordinate, Eq. (4) gives $n^{(0)}(x) = \tau g^{(0)}(x)$, which leads to

$$E^{(0)}(x) = \frac{J^{(0)}}{e\mu g^{(0)}(x)\tau}. \tag{9}$$

Using the boundary conditions (2) and (3), we can now determine the steady-state current $J^{(0)}$. For this purpose, we first determine the mean value of the steady-state field in the sample from Eq. (9), that is,

$$E_0 = \frac{1}{L}\int_0^L dx \frac{J^{(0)}}{e\mu g^{(0)}(x)\tau} = \frac{J^{(0)}}{\sigma}\frac{1}{\sqrt{1-m^2}},$$

where $\sigma = e\mu g_0\tau$ is the electrical conductivity of the photoconductor under uniform illumination. Here, we assume that the length L of the sample contains an integral number of periods of the interference pattern. Obviously, this assumption is immaterial for a large number of grating periods along the sample length ($L \gg \Lambda$). Then, the steady-state photocurrent is given by

$$J^{(0)} = \tilde{E}\frac{\sigma\sqrt{1-m^2}}{1 + \rho\sigma\sqrt{1-m^2}} \tag{10}$$

and, accordingly,

$$E_0 = \frac{\tilde{E}}{1 + \rho\sigma\sqrt{1-m^2}}. \tag{11}$$

We can now find the corrections to the internal electric field, which are linear in Θ and oscillate with time. Linearizing the system of equations (4)–(6) (i.e., retaining the contributions only from the zeroth and first orders in the phase modulation amplitude Θ), we obtain the following linear equations for $\delta n(x)$ and $\delta E(x)$:

$$\frac{\delta n(x)}{\tau} + i\Omega\frac{\varepsilon}{4\pi e}\frac{d\delta E(x)}{dx} = -g_0 m\Theta\sin kx,$$

$$\delta J - i\Omega\frac{\varepsilon}{4\pi}\delta E(x) = e\mu n^{(0)}(x)\delta E(x) + e\mu\delta n(x)E^{(0)}(x).$$

Eliminating δn from this system of equations, we obtain the linear differential equation for the sought quantity δE

$$\begin{aligned} (1 + m\cos z + i\omega)\delta E(z) - i\omega k L_0\frac{E^{(0)}(z)}{E_0}\frac{d\delta E(z)}{dz} \\ = \frac{4\pi}{\varepsilon}\tau_M\delta J + m\Theta E^{(0)}(z)\sin z. \end{aligned} \tag{12}$$

Here, we have introduced the dimensionless coordinate $z = kx$, the dimensionless modulation frequency $\omega = \Omega\tau_M$, the Maxwell relaxation time $\tau_M = e/4\pi e\mu g_0\tau$, and the drift length $L_0 = \mu E_0\tau$, while the static internal field E_0 is defined by Eq. (11). Note that, in the presence of a load resistance presumed here, $E_0 \neq \tilde{E}$. The general solution of Eq. (12) was obtained in [10]. For this purpose, the dependence $\delta E(z)$ should be expanded into a Fourier series

$$\delta E(z) = \sum_{p=-\infty}^{\infty}\sigma E_p\exp(ipz). \tag{13}$$

Equation (12) can be used to determine the Fourier components of the internal field

$$\delta E_p = \frac{1}{2i}\sum_{p'=-\infty}^{\infty}\frac{r_{p+p'}\left\{m\sqrt{1-m^2}\Theta E_0(r_{p'+1} - r_{p'-1}) + \frac{4\pi i}{\varepsilon}\tau_M\delta J(2r_{p'} + mr_{p'+1} + mr_{p'-1})\right\}}{1 + i\omega - p'\omega d + m^2/2}, \tag{14}$$

where $d = kL_0\sqrt{1-m^2}$ and

$$r_p = \frac{1}{2\pi} \times \int_0^{2\pi} dz \exp\left\{-ipz + \frac{m}{i\omega d}\sin z(2 + i\omega + m\cos z)\right\}. \quad (15)$$

We are interested in the zeroth Fourier component of the field, which can be represented, in accordance with expression (14), in the form

$$\delta E_0 = P + \delta\rho J Q, \quad (16)$$

$$P = \frac{m\sqrt{1-m^2}}{2i}\Theta E_0 \sum_{p=-\infty}^{\infty} \frac{r_p(r_{p+1} - r_{p-1})}{1 + i\omega - p\omega d + m^2/2}, \quad (17)$$

$$Q = \frac{2\pi\tau_M}{\varepsilon\rho} \sum_{p=-\infty}^{\infty} \frac{r_p(2r_p + mr_{p+1} + mr_{p-1})}{1 + i\omega - p\omega d + m^2/2}. \quad (18)$$

In order to find an explicit form of the steady component of the induced field

$$E_{sc}(t) = \mathrm{Re}[[\delta E_0 \exp(i\Omega t)]] = E_{sc}\cos(\Omega t + \varphi), \quad (19)$$

$$\delta E_0 = \delta E_0' + i\delta E_0'', \quad E_{sc} = \sqrt{\delta E_0'^2 + \delta E_0''^2}, \quad \tan\varphi = \frac{\delta E_0''^2}{\delta E_0'^2} \quad (20)$$

we use the boundary conditions to determine the relation between δE_0 and δJ:

$$\delta J = -\frac{1}{\rho}\delta E_0, \quad (21)$$

$$\delta E_0 = \frac{P}{1+Q}. \quad (22)$$

Using simple calculations, we obtain

$$E_{sc} = \sqrt{\frac{P'^2 + P''^2}{(1+Q')^2 + Q''^2}}, \quad (23)$$

$$\tan\varphi = \left(\frac{P''}{P'} - \frac{Q''}{1+Q''}\right)\left(1 + \frac{P''}{P'}\frac{Q''}{1+Q'}\right)^{-1}. \quad (24)$$

The quantities P (17) and Q (18) are represented in the form of series. In the case of a weak contrast ($m \ll 1$), for which $r_p \propto m^p$ in accordance with Eq. (15), the series decrease in powers of m and can be truncated. In the lowest order in m, we have

$$r_p \cong \delta_{p,0} - m\frac{2 + i\omega}{2\omega d}(\delta_{p,1} - \delta_{p,-1}).$$

Thus, in the weak contrast approximation, we obtain the following expressions for P and Q accurate to within contributions of the order of m^2:

$$P - \frac{1}{2}m^2 i\omega d\Theta E_0 \frac{2 + i\omega}{(1 + i\omega)}\frac{1}{\omega^2 d^2 - (1 + i\omega)^2},$$

$$(1+Q)^{-1} = \frac{1 + i\omega}{\rho^{-1}\sigma^{-1} + 1 + i\omega}.$$

Hence, the amplitude of the rectified field is given by

$$E_{sc} = m^2\omega d\Theta E_0 \frac{\sqrt{1 + (\omega/2)^2}}{\sqrt{\omega^2 + (\rho^{-1}\sigma^{-1} + 1)^2}} + \frac{1}{\sqrt{1 + 2\omega^2(1-d^2) + \omega^4(1+d^2)^2}}. \quad (25)$$

The phase can be determined using Eq. (24) and taking into account the fact that, at $m \ll 1$,

$$\frac{P''}{P'} = \frac{1}{\omega}\frac{2 - \omega^2(3 + 2d^2) - \omega^4(1 + d^2)}{5 + \omega^2(1 - d^2)}, \quad \frac{Q''}{1+Q'} = -\frac{\omega}{1 + \sigma\rho(1 + \omega^2)}. \quad (26)$$

It is convenient to represent the phase as $\varphi = \varphi_1 + \varphi_2$ and

$$\tan\varphi_1 = \frac{1 + \rho^{-1}\sigma^{-1}}{\omega}, \quad \tan\varphi_2 = \frac{\omega}{2}\frac{3 + \omega^2(1 + d^2)}{\omega^2 d^2 - 1}. \quad (27)$$

Let us now consider the role of the dimensionless parameter $\sigma\rho = GR$, where G is the total conductivity of the sample, and R is the resistance of the external circuit. Under real experimental conditions, the situation is close to that of a voltage generator; i.e., $\sigma\rho \ll 1$. It is important to take into account the following circumstance. If the resistance of the contacts is significant, their contribution should be added to the resistance R of the external circuit. This can be done by assuming that the internal field in the sample can be separated into a component varying rapidly with the coordinate in the vicinity of the contacts and the component slowly varying in the bulk of the sample, which we are actually interested in. The parameter $\sigma\rho$ can be treated as a fitting quantity for comparing the theoretical results with

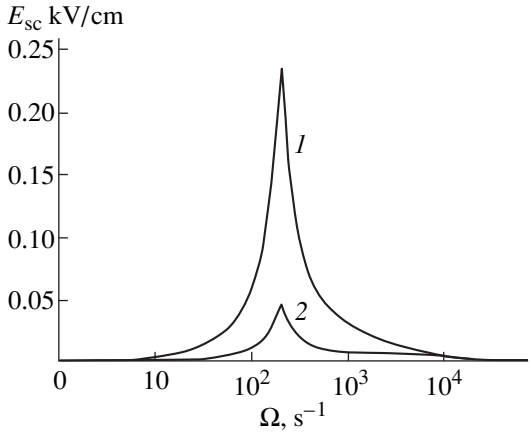

Fig. 2. Calculated dependences of the amplitude E_{sc} of the oscillating field on the phase modulation frequency according to formula (25) at the following parameters: $m = 0.3$, $\Theta = 0.2$, $d = 5$, $E_0 = 10$ kV/cm, $\tau_M = 10^{-3}$ s; curve *1* corresponds to $\sigma^{-1}\rho^{-1} = 0$, and curve *2*, to $\sigma^{-1}\rho^{-1} = 5$.

the experimental values. In the most interesting case when $\sigma\rho \ll \omega$, $\sigma\rho \ll 1$, we have

$$E_{sc} = m^2\omega d\Theta E_0\sigma\rho \times \frac{\sqrt{1+(\omega/2)^2}}{\sqrt{1+2\omega^2(1-d^2)+\omega^4(1+d^2)^2}}, \quad (28)$$

$$\tan\varphi = \frac{2}{\omega}\frac{(1-\omega^2d^2)}{3+\omega^2(1+d^2)}. \quad (29)$$

It can be seen from formula (25) that $E_{sc} = 0$ for an ideal source of voltage ($\rho = 0$). For this reason, it was always assumed earlier (except in [9]) that the uniform component of the space-charge field is identically equal to zero. This relation played the role of the central boundary conditions in earlier publications.

For $d \gg 1$, the frequency dependence $E_{sc}(\omega)$ (25) has a maximum at the point $\omega d = 1$. This condition corresponds to $\Omega = \frac{4\pi e g_0}{k\varepsilon E_0}$, i.e., to the resonance between the phase modulation frequency and the frequency of photorefractive waves [1, 3, 10]. Note a considerable difference in the frequency dependences $E_{sc}(\omega)$ for generators of current and voltage. In the case of a current generator ($\sigma\rho \gg 1$), we have

$$E_{sc} = m^2\omega d\Theta E_0\frac{\sqrt{1+(\omega/2)^2}}{\sqrt{1+\omega^2}} \times \frac{1}{\sqrt{1+2\omega^2(1-d^2)+\omega^4(1+d^2)^2}} \quad (30)$$

and the field $E_{sc} \longrightarrow 0$ according to the law $1/\omega$ at $\omega \longrightarrow \infty$, whereas, in the limit of a voltage generator, the field E_{sc} has a flat segment at high frequencies in accordance with Eq. (25). Relation (30) for the frequency dependence of the field is given in [9]. Figure 2 shows the frequency dependences of the rectified field calculated by using formula (25) for the two limiting cases, viz., current generator and $\sigma\rho \ll 1$.

Now, we estimate the absolute value of the field E_{sc}. For $m \approx 0.3$, $\Theta \approx 0.2$, $d \approx 5$, and $E_0 \approx 10$ kV/cm, we have $E_{sc} \approx 250$ V/cm at a maximum for a current generator ($\sigma\rho \gg 1$) and $E_{sc} \approx \sigma\rho 250$ V/cm for a nonideal source of voltage. For a reasonable value of $\sigma\rho \approx 0.1$, we have $E_{sc} \approx 25$ V/cm. Consequently, the theoretical values of E_{sc} can be easily achieved in experiments.

Let us consider again expression (17) for *P*. It is a series, each of whose terms has a pole structure at the points $p\omega d = 1$ (at small *m*), where *p* is an integer, and the corresponding singularities are clearly pronounced in the case when $\omega \ll 1$; i.e., in strong fields for $d \gg 1$. The physical reason behind the emergence of these poles is as follows. In the approximation nonlinear in *m*, the static charge gratings with wave vectors *pk* (and the amplitude proportional to $\propto m^p$) are formed in the crystal. Then, the scattering of photorefractive waves with wave vectors *pk* exhibits characteristic peaks at frequencies Ω/p, because, in accordance with the dispersion law for photorefractive waves, their frequency is inversely proportional to the wave vector [1, 10]. Expression (25) was derived above for the induced field with allowance made only for the first pole with $p = 1$. The contributions from next poles with $p > 1$ are proportional to m^{2p}, i.e., are small for a weak image contrast, but they may become significant against the background of the first peak at frequencies close to the resonance condition $\omega = 1/pd$.

Let us now analyze the corresponding peak near the second resonance $p = 2$ under the conditions of a weak contrast $m \ll 1$ and at $d \gg 1$ (accordingly, $\omega \ll 1$). For this purpose, in formula (17), we take into account the contribution from the term with $p = 2$ to the series. It follows from Eq. (15) that for $m \ll 1$, we have

$$r_2 = \frac{m^2}{4\omega d}\left\{\frac{(2+i\omega)^2}{2\omega d} - 1\right\} \cong \frac{3}{2}m^2.$$

Here, we consider a neighborhood of $\omega \ll 1$ and $\omega d \cong 1/2$. In the vicinity of this point, we have

$$P \cong \frac{2m^2}{3i}\Theta E_0\left\{1 + \frac{9m^2}{4}\frac{1}{1+i\omega-2\omega d}\right\}. \quad (31)$$

The first term in the braces is the contribution from the terms with $p = 0, \pm 1$, and the second term is due to the term with $p = 2$, which has a singularity in the investigated neighborhood of $2\omega d = 1$. From expression (31), in particular, it follows that the contribution from the second pole singularity is small against the background of the main resonance under the condition of a very weak contrast if $m^2 \ll \omega$.

Using relationship (23) and (31), we can now easily find the contribution from the second pole to the induced field near the resonance $\omega d = 1/2$ at $m^2/\omega \ll 1$ [i.e., under the conditions when this contribution is smaller than that from the first pole (25)]:

$$\delta E_{sc} = \frac{3m^4\Theta E_0}{2\sqrt{1+\sigma^{-1}\rho^{-1}}}\frac{1-2\omega d}{(1-2\omega d)^2+\omega^2}. \quad (32)$$

It should be noted that the electric field δE_{sc}, provided that it is small against the background of the main contribution (25) (i.e., at $m^2 \ll \omega$), appears not as an additional peak, but as an alternating singularity with a center at the point $\omega d = 1/2$ and with a width of the order of ω on the frequency scale ωd. As the parameter m^2/ω increases, this singularity is naturally transformed into a peak having a width of the order of ω, so that, for a sufficiently strong contrast (when $m^2 \geq \omega$), the frequency dependence $E_{sc}(\omega)$ for $d \gg 1$ has the form of a series of peaks with maxima at frequencies $\omega d = 1/p$, whose amplitude decreases with increasing p in proportion to m^{2p}.

The total field, with due regard for the first and second resonant peaks, has the form

$$E_{sc} = m^2\omega d\Theta E_0\frac{\sqrt{1+(\omega/2)^2}}{\sqrt{\omega^2+(\rho^{-1}\sigma^{-1}+1)^2}} \times\frac{1}{\sqrt{1+2\omega^2(1-d^2)+\omega^4(1+d^2)^2}} + \frac{3m^4\Theta E_0}{2(1+\rho^{-1}\sigma^{-1})}\frac{1-2\omega d}{(1-2\omega d)^2+\omega^2}. \quad (33)$$

We have derived above the relations for the electric field (uniform in space and oscillating in time), which is induced in the sample as a result of the interaction of oscillating and static gratings of electric fields and charge carriers. The amplitude E_{sc} of such a rectified field is obviously connected with the expression for an alternating current $I(t)$ in the external circuit through the relationship

$$I(t) = \frac{L}{R}E_{sc}\cos(\Omega t+\varphi) = \frac{S}{\rho}E_{sc}\cos(\Omega t+\varphi). \quad (34)$$

For $\sigma\rho \ll 1$ (voltage generator), the quantity E_{sc}/R and, hence, $I(t)$ are independent of the load resistance if $R \longrightarrow 0$, whereas for $\sigma\rho \gg 1$ (current generator), $I(t) \propto 1/R$ in the limit $R \longrightarrow \infty$.

It is interesting to note that the effect of rectification of current considered here can be described with the help of a simple equivalent series circuit consisting of the load resistance R, a capacitor $C = \tau_M/(R + G^{-1})$ (G^{-1} is the total ohmic resistance of the sample), and an effective voltage generator

$$U_{ef} = \frac{1}{2}m^2 d\Theta E_0 L\frac{2+i\omega}{\omega^2 d^2-(1+i\omega)^2}. \quad (35)$$

This effective generator describes the physical process of rectification of the electric field in the sample due to the interaction of the oscillating and static gratings. The complex nature of formula (35) takes into account the phase shift of the effective generator relative to the phase of vibrations of the interference pattern. The experimentally measured quantity $E_{sc}(t)$ is the result of voltage drop across the load ohmic resistance R, and the capacitor describes the Maxwell relaxation of the charge induced in the sample through the load resistance $R + G^{-1}$. The current $I(t)$ in Eq. (34) is the total current of the equivalent circuit. The quantities φ_1 and φ_2 introduced in Eq. (27) are the phase shifts due to the RC circuit and the effective generator, respectively. At the point corresponding to a maximum of the frequency dependence of E_{sc} for $\omega = 1/d$, the phase of the effective generator is $\varphi_2 = \pi/2$. This allows us to directly measure the phase φ_1 of the RC circuit directly with the help of Eq. (27) and to use it to determine the effective load resistance R, including the contribution from the contact resistance.

In experiments, we usually measure either the voltage across the load resistance or the value of E_{sc} directly by using piezo- or electrooptical effects. The meager available experimental data [8, 9, 12] agree reasonably with the inferences of our theory. For instance, a clearly pronounced resonance is observed in the dependence of the rectified field amplitude E_{sc} on the phase modulation frequency (of vibrations of the interference pattern) Ω, indicating the excitation of photorefractive waves. All principal functional dependences, such as the field E_{sc} and the position of the resonance as a function of the wave vector k and the applied electric field E_0, also agree with the experimental data. However, a detailed comparison of the absolute values of E_{sc} calls for more meticulous experimental investigations.

ACKNOWLEDGMENTS

This work was supported by the Russian Foundation for Basic Research, project no. 98-02-18254.

REFERENCES

1. R. F. Kazarinov, R. A. Suris, and B. I. Fuks, Fiz. Tekh. Poluprovodn. (Leningrad) **6** (3), 572 (1972) [Sov. Phys. Semicond. **6**, 500 (1972)].
2. H. C. Pedersen, D. J. Webb, and P. M. Johansen, J. Opt. Soc. Am. B **15**, 2573 (1998).
3. M. P. Petrov, V. V. Bryksin, V. M. Petrov, *et al.*, Phys. Rev. A **60** (3), 2413 (1999).
4. M. P. Petrov, I. A. Sokolov, S. I. Stepanov, and G. S. Trofimov, J. Appl. Phys. **68** (5), 2216 (1990).

5. I. Sokolov and S. Stepanov, J. Opt. Soc. Am. B **10**, 1483 (1993).
6. S. L. Sochava, V. V. Kulikov, I. A. Sokolov, and M. P. Petrov, Opt. Commun. **125**, 262 (1996).
7. C. C. Wang, F. Davidson, and S. Trivedi, J. Opt. Soc. Am. B **14**, 21 (1997).
8. S. Mansurova, S. Stepanov, N. Korneev, and C. Dibon, Opt. Commun. **152**, 207 (1998).
9. M. P. Petrov, A. P. Paugurt, and V. V. Bryksin, Pis'ma Zh. Éksp. Teor. Fiz. **70** (4), 253 (1999) [JETP Lett. **70**, 260 (1999)]; M. P. Petrov, A. P. Paugurt, V. V. Bryksin, *et al.*, Appl. Phys. B **69**, 341 (1999).
10. V. V. Bryksin and M. P. Petrov, Fiz. Tverd. Tela (S-Peterburg) **40** (8), 1450 (1998) [Phys. Solid State **40**, 1317 (1998)].
11. N. V. Kukhtarev, V. B. Markov, S. G. Odulov, *et al.*, Ferroelectrics **22**, 949 (1979).
12. M. P. Petrov, A. P. Paugurt, V. V. Bryksin, *et al.*, Phys. Rev. Lett. **84** (22), 5114 (2000).

Translated by N. Wadhwa

Physics of the Solid State, Vol. 42, No. 10, 2000, pp. 1861–1864. Translated from Fizika Tverdogo Tela, Vol. 42, No. 10, 2000, pp. 1814–1817.

DEFECTS, DISLOCATIONS, AND PHYSICS OF STRENGTH

Influence of Magnetic Field on Acoustic Emission in Dislocation-Containing Silicon under Current Loading

A. A. Skvortsov, A. M. Orlov, V. A. Frolov, L. I. Gonchar, and O. V. Litvinenko

Ul'yanovsk State University, Ul'yanovsk, 432700 Russia

e-mail: scvor@sv.uven.ru

Received November 23, 1999; in final form, March 10, 2000

Abstract—The influence of weak (< 1 T) magnetic fields on acoustic emission (AE) of dislocation-containing *n*-Si(111) under current loading $j = (1–5) \times 10^5$ A/m^2 is investigated. It is found that the combined effect of the magnetic and electric fields leads to an increase in the acoustic emission response by a factor of 1.5 and is responsible for the emergence of an additional peak in the AE spectra at a frequency of 1.7–1.8 Hz. The result is explained by the influence of magnetic fields, which changes the energy state of paramagnetic stoppers. This facilitates the separation and motion of dislocations. Withdrawal of the magnetic field leads to the relaxation of acoustic emission processes, which is determined by the dynamics of excited point centers interacting with a dislocation. © *2000 MAIK "Nauka/Interperiodica".*

For a number of crystals (NaCl, LiF, Al, Zn), the application of a magnetic field can lead to an increase in dislocation mobility even in the absence of additional external loads (of mechanical, electrical, or thermal origin) [1–5]. Such changes in the samples must affect the acoustic emission (AE), which carries information on the parameters and character of the dislocation structure transformation. It was convincingly demonstrated [1–5] that linear defects are sensitive to a static magnetic field. However, the evolution of the dislocation structure and the acoustic emission of semiconductors under the action of a magnetic perturbation have not been studied comprehensively. This severely complicates the description of the mechanism of the magnetoplastic effect in semiconductors. This paper is devoted to an investigation of the influence of a static magnetic field ($B \le 1$ T) on acoustic emission in the dislocation-containing silicon samples in direct current and under the action of thermal agencies.

The *p*-doped dislocation-free Si(111) wafers ($40 \times 0.35 \times 10$ mm) with a resistivity of 0.01 Ω cm were used as starting material. Dislocations were introduced by 10–30 min annealing of the wafers under a load applied along the [111] direction at 1000°C. The average dislocation density N_d attained a value of 10^5 cm^{-2}. The experimental technique and the results of data processing are described in [6].

Acoustic emission in a silicon wafer was excited by the simultaneous effect of a direct current $j = (1–5) \times 10^5$ A/m^2 along the [110] direction and an external magnetic field $B = 0.05–0.7$ T lasting for 1.5–2 h. The magnetic induction vector lay in the (111) plane and was normal to the electric field lines. The energy W of acoustic emission signals was estimated from the spectra obtained by passing a current through the sample and was found to be proportional to the square of the harmonic amplitude U_n of the experimental spectrum:

$$W \sim \sum_n U_n^2. \quad (1)$$

It is noteworthy that a direct current passing through a dislocation-containing wafer in zero magnetic field gen-

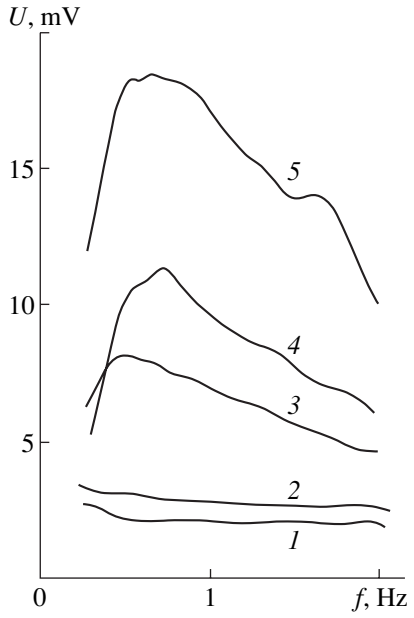

Fig. 1. Acoustic emission spectra for (*1*, *2*) dislocation-free and (*3–5*) dislocation-containing silicon wafers, $N_d = 10^5$ cm^{-2}, $T = 400$ K: (*1*, *2*, *4*) $j = 3 \times 10^5$ A/m^2, $B = 0$ T, (*3*) $j = 2 \times 10^5$ A/m^2, $B = 0$ T, and (*5*) $j = 3 \times 10^5$ A/m^2, $B = 0.3$ T.

1063-7834/00/4210-1861$20.00

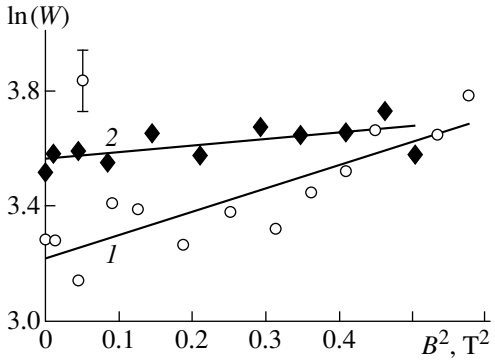

Fig. 2. Magnetic field dependence of the acoustic emission energy W for (*1*) increasing and (*2*) decreasing the magnetic field strength.

erates an acoustic response. Unlike dislocation-free samples (curve *1* in Fig. 1), this response exhibits a clearly pronounced peak at frequencies $f \approx 0.5$–1 Hz (curves *3*, *4* in Fig. 1). The distinctions, which are clearly fixed in this case, confirm the specific role of dislocations in acoustic emission processes. We attribute these distinctions to the separation of the pinned dislocations and their motion through the Peierls potential relief in a constant electric field [6], which was independently observed for semiconductors [7], metals [8], and ionic crystals [9]. We found that, under the above-mentioned current loading, dislocations in silicon move toward the positive electrode. Since edge dislocations in *n*-silicon exhibit clearly pronounced acceptor properties [10], the most probable mechanism of motion in our case is an additional electric transport of single dislocations.

The additional application of a magnetic field, which is combined with the current loading, facilitates an increase in the emission response of the material. Indeed, the acoustic emission of samples subjected both to current loading and to simultaneous magnetic treatment increased by a factor of 1.5 (Fig. 1, curves *4*, *5*).

The observed effect points to an increase in dislocation mobility in a static magnetic field. As in the case of ionic crystals [5], this effect is associated with the presence of magnetosensitive defects in the vicinity of dislocations. For doped semiconductors, these defects are impurity ions located on dislocations, which form the so-called Cottrell cloud and possess paramagnetic properties [11]. The cloud has the form of a cylindrical region enriched by the dopant and extended along the dislocation axis with a radius $R \approx 10$ nm [12].

The average concentration N of impurity atoms in the cloud is defined as

$$N = N_0 \exp\left\{-\frac{W_m}{kT}\right\}, \tag{2}$$

where N_0 is the concentration of impurity atoms in a semiconductor at a large distance from the dislocation, $W_m \geq 0.2$ eV is the binding energy, and T is the temperature. It is clear that, after high-temperature annealing most of the atoms in the cloud are arranged at a minimum distance (of the order of the Burgers vector) from the dislocation. The impurity atoms play the role of stoppers. A moving dislocation is detached from a stopper and is displaced to the periphery of the Cottrell cloud, which is followed by diffusion of the impurity atmosphere to a new position of the dislocation core.

For a shift of the dislocation through a distance x without a change in the cloud position, its binding energy per unit length $U(x)$ is defined as [12]

$$U(x) = \int_0^\infty \int_{-\pi}^{\pi} \frac{N(r, \theta) - N_0}{b^3} W_m(\rho, \varphi) dr d\theta, \tag{3}$$

where r, θ, and z are the cylindrical coordinates, $r = r^2 + x^2 - 2rx\cos\theta$ and $\sin\varphi = (r/\rho)\sin\theta$.

The strain exerted on a dislocation by the cloud has the form

$$\sigma = -\frac{1}{b}\frac{dU}{dx}. \tag{4}$$

The application of a magnetic perturbation removes the prohibition imposed on the reaction between point defects and paramagnetic centers at the dislocation core, thus facilitating the separation of the dislocation from the stoppers [5]. The key role of edge dislocations in the magnetically stimulated variation of the acoustic emission response is emphasized by the exponential dependence

$$W \sim \exp(\alpha B^2), \tag{5}$$

where B is the magnetic induction and α is the dimensional constant. This is illustrated by curves *2* and *5* in Fig. 1 and by curve *1* in Fig. 2.

The facilitated detachment of dislocations from the stoppers should manifest itself in a qualitative variation of the AE spectra, which is due to the dynamics of dislocation transitions. Regarding the magnetic field influence, the rate ν of the dislocation transition from one metastable state to another can be written as

$$\nu = (1 - f_1 - f_2)(\nu_1 + \nu_2)\exp\left(-\frac{E_1 + E_2}{kT}\right). \tag{6}$$

Here, f is the fraction of the dislocations being detached, E is the activation energy, ν is the effective transition frequency, and T is the temperature. Subscripts "1" and "2" refer to the current and magnetic effects, respectively. For this reason, an additional peak, which is associated with the magnetically induced transitions of linear defects, should appear in the AE spectra.

Indeed, the "fine" structure is observed in the AE spectra of dislocation-containing *n*-silicon (Figs. 3a, 3b). This suggests an increase in the number and rate of dislocation transitions due to the destruction of certain

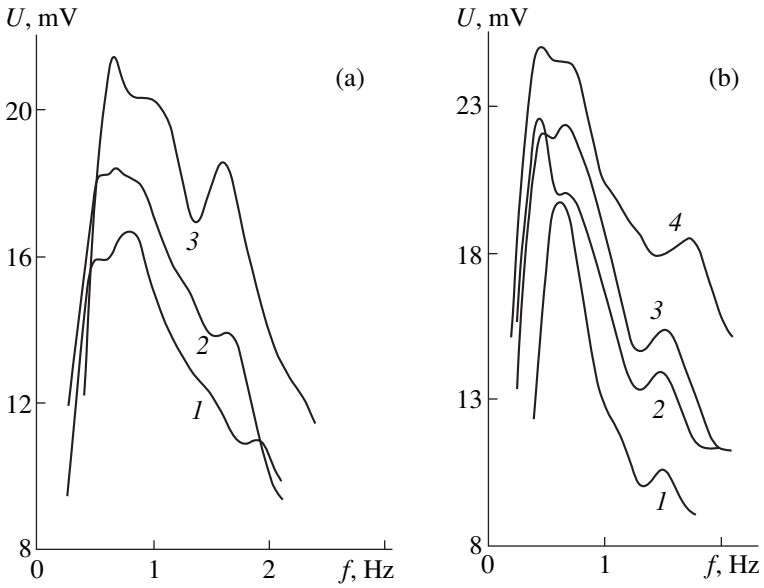

Fig. 3. Acoustic emission spectra for (a) increasing and (b) decreasing the magnetic field strength: (a) B = (*1*) 0.1, (*2*) 0.2, and (*3*) 0.5 T; (b) B = (*1*) 0.1, (*2*) 0.5, and (*3*) 0.7 T, and (*4*) 35 min after removal of the magnetic field, respectively.

potential barriers for spin-dependent reactions of point defects occurring in the dislocation core [5].

A decrease in B should lead to gradual relaxation of the dislocation structure. Experimental results indicate a decrease in the AE response upon a smooth decrease in B and gradual relaxation of the system to the initial state (Fig. 3b). However, an analysis of Fig. 2 and the spectra in Fig. 3 clearly demonstrates the difference in dynamics of acoustic emission upon an increase (curve *1* in Fig. 2) and a decrease (curve *2* in Fig. 2) in the magnetic induction. As a result, both numerical values of W for the ascending and descending curves and the emission spectra themselves are substantially different for $B = 0$ (curve *1* in Fig. 3a and curve *2* in Fig. 3b). This is apparently due to the fact that the structure elements remember the process of magnetic treatment. This phenomenon is the so-called "magnetic memory" effect, which was detected earlier in ionic crystals [13].

In order to investigate W relaxation in greater detail, the kinetics of variation of the acoustic emission energy was registered after withdrawal of the magnetic field. The magnetoplastic effect in ionic crystals was investigated in [5, 11]. It was found that the bonds formed between a dislocation and point defects are weakened by a magnetically induced interaction, and the mobility of linear defects increases. However, the withdrawal of the magnetic field leads to a hyperbolic time dependence of the acoustic emission kinetics, which is determined by the concentration $C(t)$ of the excited defects. The latter, in turn, follows the hyperbolic time dependence [5]

$$C(t) \sim \frac{C_0}{(1 + \beta t^n)}, \qquad (7)$$

where C_0 is the concentration of centers at $t = 0$, $n > 0$, t is the time, and β is the coefficient characterizing the activation energy of the process.

Indeed, an analysis of the acoustic emission spectra for doped silicon samples in a magnetic field demonstrated that, after the withdrawal of the field ($B = 0$), the energy of acoustic emission signals decreases (curves *1*, *2* in Fig. 3b) and attains the quasi-stationary value in 35 min, which exceeds by 15% the value of W observed prior to the magnetic field application (Fig. 4). This indicates the relaxation processes in the investigated samples. The experimental data processing proved that the decay obeys the power law (7) with an exponent $n = 0.4$ at room temperature, suggesting several time decay mechanisms for the acoustic emission energy.

Thus, weak magnetic fields ($B < 0.75$ T) combined with current loading ($j = 1–5 \times 10^5$ A/m^2) strongly

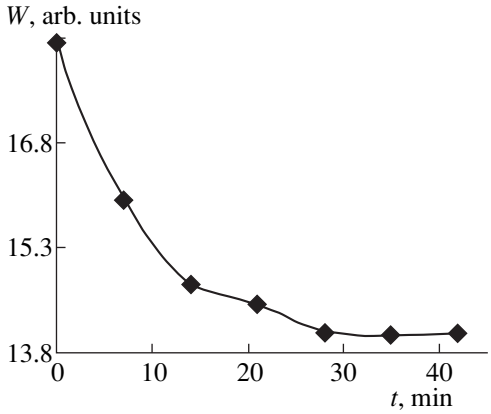

Fig. 4. Kinetics of the variation in the acoustic emission energy W after removal of the magnetic field.

affect the mobility of linear defects and acoustic emission for *n*-type silicon. This is due to the magnetic field effect on the energy state of the paramagnetic impurity in the semiconductor. After the withdrawal of the magnetic field, the relaxation of acoustic emission processes takes place, which is controlled by the dynamics of excited point defects interacting with a dislocation.

ACKNOWLEDGMENTS

The authors are grateful to Yu.I. Golovin for his interest in this research and for valuable discussions on the obtained results.

This work was supported by the Ministry of Higher Education, the Program "Radio Engineering", and by the Russian Foundation for Basic Research, project no. 98-02-03335.

REFERENCES

1. V. I. Al'shits, E. V. Darinskaya, and E. A. Petrzhik, Fiz. Tverd. Tela (St. Petersburg) **34** (1), 155 (1992) [Sov. Phys. Solid State **34**, 81 (1992)].
2. V. I. Al'shits, E. V. Darinskaya, T. M. Perekalina, and A. A. Urusovskaya, Fiz. Tverd. Tela (Leningrad) **29** (2), 467 (1987) [Sov. Phys. Solid State **29**, 265 (1987)].
3. V. I. Davydov, E. A. Loskutova, and E. P. Naĭden, Fiz. Tekh. Poluprovodn. (Leningrad) **23** (9), 1596 (1989) [Sov. Phys. Semicond. **23**, 989 (1989)].
4. Yu. I. Golovin, R. B. Morgunov, and V. E. Ivanov, Fiz. Tverd. Tela (St. Petersburg) **39** (11), 2016 (1997) [Phys. Solid State **39**, 1803 (1997)].
5. Yu. I. Golovin and R. B. Morgunov, Zh. Éksp. Teor. Fiz. **115** (2), 605 (1999) [JETP **88**, 332 (1999)].
6. A. M. Orlov, A. A. Skvortsov, and V. A. Frolov, Pis'ma Zh. Tekh. Fiz. **25** (3), 28 (1999) [Tech. Phys. Lett. **25**, 95 (1999)].
7. V. A. Kalitenko, I. Ya. Kucherov, and V. M. Perga, Fiz. Tekh. Poluprovodn. (Leningrad) **22** (4), 578 (1988) [Sov. Phys. Semicond. **22**, 361 (1988)].
8. E. E. Vdovin and A. Yu. Kasumov, Fiz. Tverd. Tela (Leningrad) **30** (1), 311 (1988) [Sov. Phys. Solid State **30**, 180 (1988)].
9. V. I. Al'shits, E. V. Darinskaya, E. Yu. Mikhina, and E. A. Petrzhik, Fiz. Tverd. Tela (St. Petersburg) **38** (8), 2426 (1996) [Phys. Solid State **38**, 1333 (1996)].
10. V. B. Shikin and Yu. V. Shikina, Usp. Fiz. Nauk **165** (8), 887 (1995) [Phys. Usp. **38**, 845 (1995)].
11. S. V. Vonsovskiĭ, *Magnetism* (Nauka, Moscow, 1971; Wiley, New York, 1974).
12. J. Friedel, *Dislocations* (Pergamon, Oxford, 1964; Mir, Moscow, 1967).
13. Yu. I. Golovin and R. B. Morgunov, Fiz. Tverd. Tela (St. Petersburg) **35** (9), 2582 (1993) [Phys. Solid State **35**, 1280 (1993)].

Translated by N. Korovin

Physics of the Solid State, Vol. 42, No. 10, 2000, pp. 1865–1867. Translated from Fizika Tverdogo Tela, Vol. 42, No. 10, 2000, pp. 1818–1820.

DEFECTS, DISLOCATIONS, AND PHYSICS OF STRENGTH

Nondislocation Plasticity and Its Role in the Mass Transfer and Formation of the Indentation under Dynamic Conditions

Yu. I. Golovin and A. I. Tyurin

Tambov State University, Tambov, 392622 Russia

e-mail: golovin@tsu.tmb.ru; golovin@inbox.ru

Received March 20, 2000

Abstract—The share of nondislocation plasticity in the process of mass transfer from under the indenter is determined by a novel method of dynamical indentation for a number of ionic, semiconducting, and metallic materials. © *2000 MAIK "Nauka/Interperiodica".*

The possible nondislocation mechanisms of macroplasticity and their probable role under various regimes of deformation have been discussed for several decades. As is shown in [1–3], the strains caused by the motion of point defects can be the most competitive (with respect to dislocation strains) under high pressures and large local stresses. The manifestations of interstitial plasticity during the formation of an indentation under the indenter even in highly plastic crystals of the NaCl type are presented in [4–11]. These results were obtained by several independent methods, e.g., an analysis of the shape of microreliefs (specific hillocks) on the lateral and rear surfaces of the sample after pricking, and cathodoluminescence data for the material near the indentation. However, the quantitative role of point defects and interstitial (crowdion) mechanisms of mass transfer under the indentation, depending on the type of material and conditions of local loading, has practically not been studied.

It is shown in [12–16] that information on the activation volume γ and its change as a result of the indenter intrusion can be obtained by receiving the time dependence of the kinetics of indenter intrusion into the material with a high time resolution (about 100 μs) at different temperatures and under various conditions of intrusion.

The mechanisms of thermally activated mass transfer are characterized by an activation volume $\gamma \leq V_a$ (where V_a is volume per atom or ion in the lattice) if they are associated with the noncorrelated motion of individual point defects, and by $\gamma \leq 10V_a$ [17] if they are associated with the correlated motion of clusters formed by a small number of atoms (crowdions). The dislocation mechanisms are characterized by the volume $\gamma \gg V_a$ [18]. The values of γ differ strongly for various mechanisms of plastic flow, which makes it possible to distinguish the mechanisms of mass transfer involving a small number of atoms from the dislocation mechanisms, displaying a much larger degree of collectivization of the atomic displacements even for a relatively low accuracy of its determination. This situation is typical of the dynamical methods (especially under the conditions of a strongly inhomogeneous stressed state, which appears under the indentation).

This paper aims at an *in situ* estimation of the share of nondislocation plasticity in the process of indentation formation in materials with different types of binding during the measurements of microhardness.

Contribution of point defects to the process of the indentation formation under dynamic conditions

Type of material	Force of intrusion F, N	Duration of the indenter holding in material under loading, τ	Fraction of point defects	
			$\Delta h_i/h_0$	$\Delta V_i/V_0$
KCl	0.11	10 s	0.7	0.34
		<10 ms	1.00	1.00
NaCl	0.11	10 s	0.69	0.33
		<9 ms	1.00	1.00
LiF	0.11	10 s	0.64	0.26
		<8 ms	1.00	1.00
MgO	6.0	10 s	0.68	0.31
		<12 ms	1.00	1.00
Pb	0.25	10 s	0.46	0.10
		<13 ms	1.00	1.00
Al	0.25	10 s	0.58	0.20
		<10 ms	1.00	1.00
$Co_{50}Fe_{35}B_{15}$	0.25	6 ms	1.00	1.00
Ge	2.3	10 s	0.67	0.30
		<7 ms	1.00	1.00
GaAs	3.8	10 s	0.49	0.12
		<8 ms	1.00	1.00

1063-7834/00/4210-1865$20.00

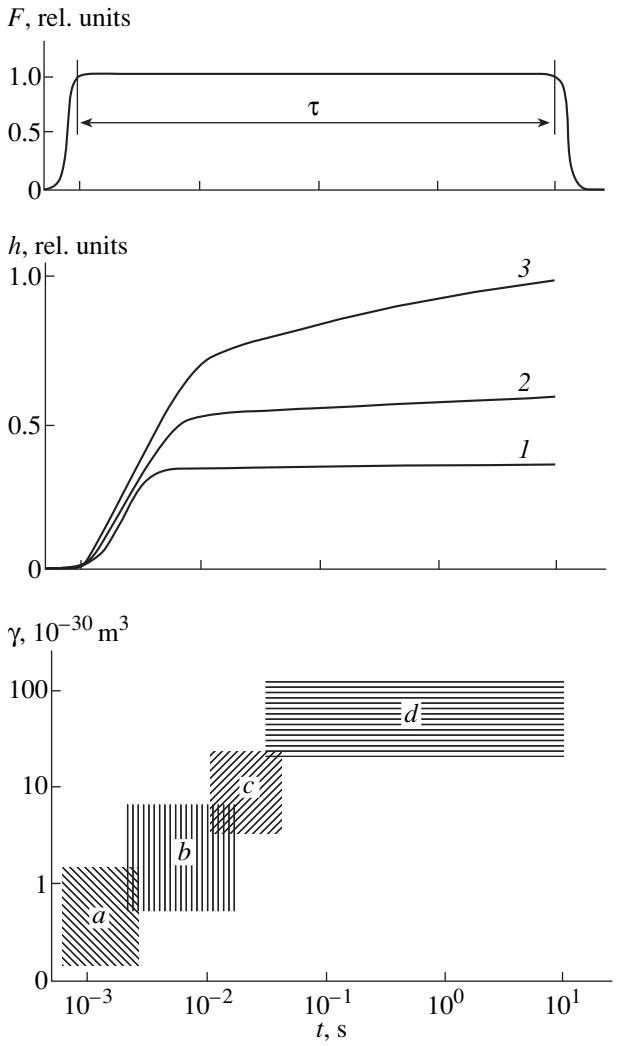

Schematic diagram illustrating the dynamics and atomic mechanisms of deformation in the microcontact region, revealed by the methods of dynamic nanoindentation: F is of the force of contact interaction between the indenter and the material, τ is the loading duration, h is the indentation depth; γ is the activation volume. (*1*) Amorphous metallic alloy ($Co_{50}Fe_{35}B_{15}$), (*2*) Si, and (*3*) NaCl; (a) elastic deformation, (b) interstitial atoms, (c) crowdions, and (d) dislocations.

We experimentally studied the kinetics of intrusion of an indenter in the form of diamond Vickers or Berkovich pyramids mounted at the end of a horizontally suspended rod to which a force pulse $F(t)$ of rectangular shape (see figure), having a controlled amplitude and duration (from 1 ms up to 10 s), was applied with the help of an electrodynamic drive. A capacitance displacement transducer allowed us to register instantaneous values of the depth $h(t)$ of indenter intrusion with a resolution of 10 nm, while a piezoelectric transducer measured the force of resistance to the intrusion. The signals from the sensors of displacement, force, and instantaneous value of the current in the drive were fed to a computer via a commutator and an analog-to-digital converter. The program for the processing of the recorded information allowed us to determine instantaneous values of the depth $h(t)$, intrusion velocity $v(t) = dh/dt$, dynamic hardness $H_d(t)$, the volume of the indentation $V(t)$, and the activation volume $\gamma(t)$.

Such a technique allows us to continuously analyze *in situ* the strain rate as a function of the instantaneous value of contact stresses, to separate various phases of a process from the features of the kinetic curve, to carry out their thermal-activation analysis, and to determine, on the basis of its results, the micromechanisms of mass transfer in the contact region [12–16].

The activation volume γ was determined using the relation $\gamma = (d[\ln(v)]/d\sigma)kT$, proceeding from the slopes of curves $\ln(v) = f(\sigma)$, where σ is the instantaneous value of the mean contact stress under the indenter, k is the Boltzmann constant, and T is a temperature. Comparing the data obtained on the magnitude of γ with the values characteristic of various structural defects (point defects, crowdions, and dislocations), we can identify the mechanisms of plastic strain determining the process of the indentation formation. In combination with the data on the increase of the indentation depth Δh_i at each ith stage, this allows us to find the contribution of various micromechanisms of mass transfer at each of the revealed stages and to estimate the share of the size $\Delta h_i/h_0$ and the volume $\Delta V_i/V_0$ expelled during the formation of the indentation through certain micromechanisms of plastic deformation. Here, h_0 and V_0 are the steady-state values of the depth and volume of the indentation.

For a quantitative evaluation of the share of plastic deformation associated with the motion of individual point defects and their clusters (crowdions) or dislocations, we will arbitrarily take the intervals of characteristic values of γ for them as $\gamma_p < 10 \times 10^{-30}$ m^3 and $\gamma_d < 10 \times 50^{-30}$ m^3, respectively. It follows from the experiment that the transition from small values of γ (of the order of atomic or ionic volumes) to large values (of the order of tens of b^3, where **b** is the Burgers vector for glide dislocations) occurs quite abruptly (if it occurs at all in the structure under study), so that the variation of γ_p and γ_d within reasonable limits only slightly affects the estimates of relative contributions of the processes under consideration to the final result, i.e., the formation of an indentation of known size.

It follows from the table that, even for a long-term holding of the indenter, a significant fraction of plastic strain in all the materials studied is due to the monoatomic micromechanisms of mass transfer or those involving a small number of atoms. In some structures (e.g., iron-based amorphous alloys), their share reaches 100%, but even in soft crystals (NaCl, KCl, Al, and Pb) it amounts to ten percent.

It is worthwhile to note that since $H \sim 1/h^2$, and $V \sim h^3$, the relative contribution of point defects to the formation of the microhardness H is even larger (and the

dislocation plasticity is lower) than to the magnitude of the expelled volume *V*. It follows that the change in the conditions of motion and drag of dislocations in a crystal, as well as in their mobility and density, cannot result in proportional changes of *H*, which is actually observed in experiments [19]. Moreover, a change of the temperature and preliminary treatment is often followed by an increase in the hardness along with an apparently paradoxical increase in the dislocation mobility [19, 20], which can be explained in the light of the data obtained on the role of dislocation plasticity under microindentation. The data presented above also indicate the increasing contribution of point defects and the decreasing role of dislocations upon a decrease in the duration of the contact interaction and the size of the indentation. Therefore, an analysis of the microcontact plasticity appearing important in many situations for practical applications (collisions of small particles, abrasive wear, grinding, vibration treatment, and mechanochemical reactions involving atomization, fine grinding, etc.) should be mainly based on the concepts of plasticity modes involving point defects rather than dislocations.

Thus, in this paper, we have estimated quantitatively the role of various macromechanisms of plastic deformation in the process of indentation formation under dynamic microindentation. It is shown that even in soft crystals, the share of point defects in the formation of microhardness is always significant, as we go over to rigid materials (e.g., amorphous alloys) and small contact durations, the formation of an indentation can be completely determined by nondislocation plasticity.

ACKNOWLEDGMENTS

This work was supported by the Russian Foundation for Basic Research, project no. 98-02-16549.

REFERENCES

1. V. L. Indenbom, Pis'ma Zh. Éksp. Teor. Fiz. **12**, 526 (1970) [JETP Lett. **12**, 369 (1970)].
2. V. L. Indenbom and A. N. Orlov, Fiz. Met. Metalloved. **43** (3), 469 (1977).
3. V. L. Indenbom and A. N. Orlov, Usp. Fiz. Nauk **76**, 557 (1962) [Sov. Phys. Usp. **5**, 272 (1962)].
4. V. N. Rozhanskiĭ and M. A. Velednitskaya, Phys. Status Solidi A **8**, 551 (1971).
5. M. A. Velednitskaya, V. N. Rozhanskii, L. F. Comolova, *et al.*, Phys. Status Solidi A **32**, 123 (1975).
6. V. N. Rozhanskiĭ, N. L. Sizova, and A. A. Urusovskaya, Fiz. Tverd. Tela (Leningrad) **13**, 411 (1971) [Sov. Phys. Solid State **13**, 335 (1971)].
7. M. N. Chaudhri, J. T. Hagan, and J. K. Wells, J. Mater. Sci. **15** (5), 1189 (1980).
8. J. Llopis, C. Ballasteros, J. Pigueras, *et al.*, Phys. Status Solidi A **78**, 679 (1983).
9. M. Sh. Akchurin, V. G. Galstyan, and V. R. Regel, Scanning **14**, 194 (1992).
10. M. Sh. Akchurin and V. R. Regel, Chem. Rev. **23**, 59 (1998).
11. M. Sh. Akchurin, V. G. Galstyan, V. R. Regel, and V. N. Rozhanskiĭ, Poverkhnost' **3**, 119 (1983).
12. Yu. I. Golovin and A. I. Tyurin, Pis'ma Zh. Éksp. Teor. Fiz. **60** (10), 722 (1994) [JETP Lett. **60**, 742 (1994)].
13. Yu. I. Golovin and A. I. Tyurin, Izv. Ross. Akad. Nauk, Ser. Fiz. **59**, 49 (1995).
14. Yu. I. Golovin and A. I. Tyurin, Kristallografiya **40** (5), 884 (1995).
15. Yu. I. Golovin and A. I. Tyurin, Fiz. Tverd. Tela (St. Petersburg) **38**, 1812 (1996) [Phys. Solid State **38**, 1000 (1996)].
16. Yu. I. Golovin, A. I. Tyurin, V. Z. Bengus, *et al.*, Fiz. Met. Metalloved. **88** (6), 103 (1999).
17. M. Koyanagi, T. Tsutsumi, K. Ohsawa, and E. Kuramoto, Comput. Mater. Sci. **14**, 103 (1999).
18. A. Ivens and R. Roulings, in *Thermally Activated Processes in Crystals* (Mir, Moscow, 1973).
19. Yu. S. Boyarskaya, D. Z. Grabko, and M. S. Kats, *Physics of Microindentation Processes* (Kishinev, Shtiintsa, 1986).
20. Yu. S. Boyarskaya, D. Z. Grabko, and R. P. Zhitaru, Preprint (Moldavian Academy of Science, Kishinev, 1986).

Translated by T. Galkina

Physics of the Solid State, Vol. 42, No. 10, 2000, pp. 1868–1872. Translated from Fizika Tverdogo Tela, Vol. 42, No. 10, 2000, pp. 1821–1825.

MAGNETISM AND FERROELECTRICITY

Resonant Two-Photon Absorption in the Cr_2O_3 Antiferromagnet

S. I. Shablaev, I. P. Areshev, and R. V. Pisarev

Ioffe Physicotechnical Institute, Russian Academy of Sciences, Politekhnicheskaya ul. 26, St. Petersburg, 194021 Russia

Received February 28, 2000

Abstract—Two-photon absorption (TPA) spectra of the Cr_2O_3 model antiferromagnet have been studied for two polarization configurations at energies ranging from 2.5 to 3.55 eV. Several strong TPA peaks with the maximum coefficient $\beta \sim 0.08$ cm/MW are observed in the 2.7–3.1-eV range characterized by the ${}^4A_2(F) \longrightarrow {}^4T_1(F)$ *d–d* one-photon transition of the Cr^{3+} ion. An analysis of the results obtained suggests that the general form of the TPA spectrum in this range is primarily determined by the resonance at the ${}^2E(G)$ and ${}^2T_1(G)$ intermediate levels. At energies above 3.44 eV, the TPA coefficient sharply increases up to $\beta \sim 0.1$ cm/MW due to transitions between the valence and conduction bands. © *2000 MAIK "Nauka/Interperiodica".*

1. INTRODUCTION

Two-photon nonlinear optical spectroscopy is widely used in investigating semiconductors (see, e.g., [1–3]), ferroelectric dielectrics [4, 5], and magnetically ordered dielectrics [6, 7]. This method provides a means for studying the spectral response of the additional absorption of probing light with the intensity I_1, which appears when a high-power laser pulse with the intensity I_2 passes through a crystal. Taken separately, both pulses are barely absorbed at all in the crystal, because the probing light energy $\hbar\omega_1$ is less than E_g, and the pump energy $\hbar\omega_2$ is less than $1/2(E_g)$. These conditions offer a possibility of studying two-photon absorption at energies of the order of $\hbar\omega_2$. The more complex selection rules for two-photon absorption [8, 9] often make it possible to obtain new information on the electronic states in a crystal as compared to that derivable from the linear-absorption spectra. This allows one to precisely determine the band gap E_g, the character of optical transitions, and the structure of the edge (valence and conduction) bands.

Chromium oxide Cr_2O_3 crystallizes in a corundum-type centrosymmetric trigonal structure described by the space group $D_{3d}^6(R\bar{3}c)$. The unit cell contains four chromium ions Cr^{3+} with an unfilled electronic shell $3d^3$. Below the Néel temperature, the chromium ion spins are ordered antiferromagnetically (+–+–) along the trigonal axis *c*. For many years, Cr_2O_3 served as a model object in the physics of antiferromagnetism. One-photon optical absorption spectra of Cr_2O_3 were studied in [10]. In the last few years, Cr_2O_3 has become a subject of renewed interest. The first observations of the second optical-harmonic [11] and magnetoelectric [12] spectra in this material have been reported recently. These studies provided proof of the existence of new kinds of optical susceptibilities associated with spin ordering.

This paper reports the results of our investigation of two-photon transitions in the Cr_2O_3 antiferromagnet at different orientations of the linear-polarization unit vectors of light beams of the laser ($\mathbf{e}_2$) and the flash lamp ($\mathbf{e}_1$) with respect to the *c* trigonal axis of the crystal. The TPA spectra we obtained in the *d–d* transition range differ strongly from the one-photon spectrum [10] and exhibit a clearly pronounced resonant nature. A theoretical model accounting for the main features of two-photon spectra is proposed.

2. EXPERIMENTAL TECHNIQUE

TPA spectra were studied on a 38-μm-thick polished plane-parallel Cr_2O_3 plate with the *c* axis in the sample plane.

A pulse I_2 of an LTIPCh-6 Nd : YAG laser (pulse length, 12 ns; pulse energy $\hbar\omega_2 = 1.17$ eV) and a probing light pulse I_1 of an ISSh-100-3M xenon flash lamp (pulse length, 1.5 μs; pulse energy $1.34 < \hbar\omega_1 < 2.38$ eV) simultaneously traversed the sample in opposite directions [4]. At the instant of passage of the laser beam through the crystal, a dip-shaped modulation signal formed on the probing pulse. The probing light I_1 was supplied to a FÉU-79 photomultiplier tube through an SPM-2 monochromator. The laser pulse I_2 was monitored by a FÉK-09 photodetector. On passing through delay lines, the signals from the photomultiplier tube and the photodetector were fed into a three-channel gated detector and, after expanding to 7 ms, were fed into the computer unit. During each cycle (cycle frequency, 12.5 Hz), the detector measured the pulse amplitudes of the laser I_2 and the lamp I_1 (gate width, 4.5 ns). The amplitude of the probing pulse I_1 was gated twice. Directly before the dip, we determined the amplitude I_1, and at the dip, the difference $I_1 - \Delta I$. The computer unit isolated the ΔI signal and computed the β coefficient from the expression $\beta = \Delta I/(I_1 I_2 d)$, where *d* is the length of the beam interaction region in the crystal. The β values thus obtained were averaged over approximately 10^4 pulses.

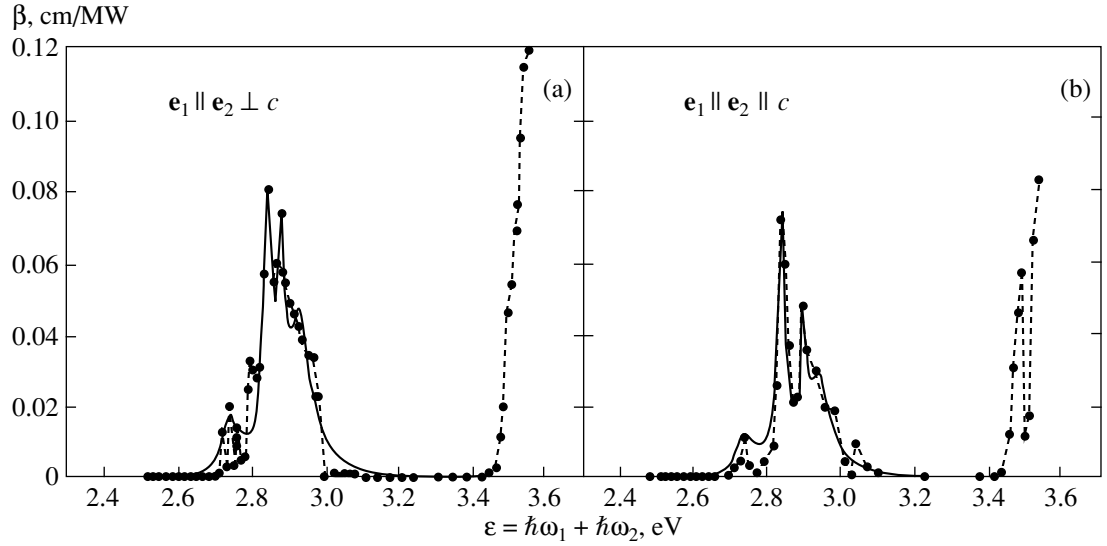

Fig. 1. Two-photon absorption spectrum of a Cr_2O_3 single crystal: (a) perpendicular and (b) parallel polarization configurations.

3. EXPERIMENTAL RESULTS

Figures 1a and 1b show the TPA spectra of a Cr_2O_3 single crystal (dashed lines). The spectrum obtained in the polarization configuration $\mathbf{e}_1 \parallel \mathbf{e}_2 \perp c$ (where $\mathbf{e}_1$ and $\mathbf{e}_2$ are unit vectors of the linear polarization of the lamp and the laser, respectively) exhibits a number of narrow peaks of different intensities in the energy range 2.71–2.99 eV and in the range of a sharp increase in absorption at about 3.466 eV (Fig. 1a). There are three small narrow peaks at 2.72, 2.74, and 2.75 eV, and a small feature at 2.79 eV. Two strong narrow peaks are observed at 2.845 and 2.88 eV. In addition, there is also a smooth shoulder at energies of 2.9–2.99 eV and a weak feature near 3.05 eV. When the crystal is rotated through 90° about the beam propagation direction, the polarization unit vectors $\mathbf{e}_1$ and $\mathbf{e}_2$ become oriented parallel to the c crystal axis ($\mathbf{e}_1 \parallel \mathbf{e}_2 \parallel c$). In this case, one observes the spectrum displayed in Fig. 1b, which is similar in common features to the spectrum shown in Fig 1a, but differs from it in some details. In place of the three small peaks in the low-energy range of the TPA spectrum, there is one medium-amplitude peak at 2.745 eV, no peak is observed at 2.795 eV, and the peak at 3.05 eV has a higher intensity. In the energy range from 3.1 to 3.41 eV, two-photon absorption is practically zero. The high-energy TPA threshold for the parallel orientation is observed at a lower energy (3.445 eV) than that for the perpendicular one (3.466 eV). We believe that the narrow dip at this threshold at an energy of 3.51 eV is associated with the second optical harmonic generation in the crystal; i.e., it corresponds to the process in which the light pulse at a doubled laser frequency adds to the pulse of the probing light of the same energy $\hbar\omega_1 = 2.34$ eV. This results in an increase in amplitude of the probing light that has passed through the monochromator rather than in its decrease, as is the case with TPA. In the TPA spectra, this process can be identified with the dip at the energy $\varepsilon = \hbar\omega_1 + \hbar\omega_2 = 2.34$ eV + 1.17 eV = 3.51 eV. The spectral intensity in the parallel orientation is substantially less than that in the perpendicular one.

4. THEORETICAL MODEL AND DISCUSSION OF THE RESULTS

Theoretical analysis of two-photon absorption spectra [1–3] is usually based on the following expression for the β coefficient, which is obtained in the second order of perturbation theory in the electric dipole approximation

$$\beta = A\sum_{f,i}\left|\sum_m\left[\frac{\langle f|\mathbf{e}_2\mathbf{p}|m\rangle\langle m|\mathbf{e}_1\mathbf{p}|i\rangle}{E_m - E_i - \hbar\omega_1} + \frac{\langle f|\mathbf{e}_1\mathbf{p}|m\rangle\langle m|\mathbf{e}_2\mathbf{p}|i\rangle}{E_m - E_i - \hbar\omega_2}\right]\right|^2, \quad (1)$$

where $\sum_{f,i}$ is the sum over all initial (i) and final (f) states, and $\sum_m$ is the sum over all intermediate states, both initial and final. The TPA probability $W^{(2)}$, which is defined as the number of two-photon transitions occurring in 1 cm^3 of the crystal for 1 s, is related to the β coefficient for a photon of energy $\hbar\omega_1$ when acted upon by a photon of energy $\hbar\omega_2$ through the expression $W^{(2)} = \beta_{12} I_1 I_2/\hbar\omega_1$, where β has the dimension [cm/MW]. The light beam intensities are measured in units of [MW/cm^2], and the photon energy $\hbar\omega_1$, in [MJ]. The dependences of the β coefficient on beam polarization are given in a general form for all 32 point groups in [8, 9]. The terms in square brackets correspond to different

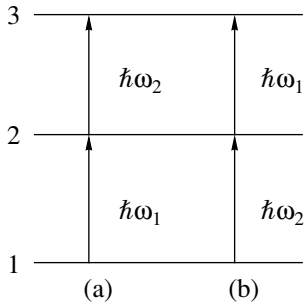

Fig. 2. Optical transition diagram for a three-level system.

orders of photon absorption from the probing ($\hbar\omega_1$) and laser ($\hbar\omega_2$) beams, as shown in Fig. 2 for the simplest three-level scheme.

Far from the resonances, all intermediate levels are virtual, and their population has no significance at all. An analysis of the spectrum of probing beam modulation in a crystal upon exposure to a laser beam becomes substantially complicated if intermediate resonances appear, because, under these conditions, the two-stage absorption and resonant two-photon absorption processes can occur independently and simultaneously. The probabilities of two-photon transitions in an ideal three-level system (Fig. 2) were calculated by the density matrix method within the approximation of the transverse (τ) and longitudinal (T) relaxation times [13]. Deriving the kinetic equations was constrained by the condition $\tau \ll T$, under which the relaxation of the off-diagonal density-matrix elements proceeds until the population of the energy levels reaches equilibrium. It is in this case that the two-stage and resonant two-photon processes are physically different.

The power $Q(\omega_1)$, which is absorbed by a three-level system at frequency ω_1 near the resonance $\hbar\omega_1 = E_2 - E_1$ under exposure to light at frequency ω_2, can be written as follows [13]:

$$Q(\omega_1) = \hbar\omega_1[W_{12}^{(1)}(\sigma_{11} - \sigma_{22}) + W_{13}^{(2)}(\sigma_{11} - \sigma_{33})]/N, \quad (2)$$

where σ_{ii} is the population of the ith level, $W_{12}^{(1)}$ is the probability of one-photon absorption of the $\hbar\omega_1$ photons upon transitions between levels 1 and 2, and $W_{13}^{(2)}$ is the probability of two-photon absorption upon transitions between levels 1 and 3. The β quantity measured in the experiment can be found as

$$\beta = \frac{1}{d}\frac{\Delta j_1}{j_1 j_2} = \frac{1}{d j_1 j_2 SN}[Q(\omega_1) - Q_0(\omega_1)] = \frac{\hbar\omega_1}{d j_1 j_2 SN}[W_{12}^{(1)}(\Delta\sigma_{11} - \Delta\sigma_{22}) + W_{13}^{(2)}(\sigma_{11} - \sigma_{33})], \quad (3)$$

where $\Delta\sigma_{11} = \sigma_{11} - \sigma_{11}^{(0)}$ and $\Delta\sigma_{22} = \sigma_{22} - \sigma_{22}^{(0)}$ are the changes in the population of the initial and intermediate levels when acted upon by pumping laser photons with energy $\hbar\omega_2$, S is the cross-sectional area of the probing beam, and N is the concentration of the three-level systems.

Since the pumping photon energy $\hbar\omega_2$ is fixed, the coincidence with the energy difference $(E_2 - E_1)$ can be only accidental. In our case, this does not occur, and resonant absorption in the $E_1 \longrightarrow E_2$ transition can only take place for a probing beam photon with energy $\hbar\omega_1$ [version (a) in Fig. 2]. The density I_1 of the probing beam flux incident on the crystal is small, and, therefore, $\sigma_{11} \approx \sigma_{11}^{(0)} = 1$ and $\sigma_{22} \approx \sigma_{22}^{(0)} = 0$ by virtue of the condition $kT \ll E_2 - E_1$. Thus, the two-stage transitions described by the first term in the parentheses can be neglected. Setting $\sigma_{11} = 1$ and $\sigma_{33} = 0$, we obtain the expression for β in the form

$$\beta = \frac{\hbar\omega_1}{d j_1 j_2 SN} W_{13}^{(2)}, \quad (4)$$

where $W_{13}^{(2)}$ is the probability of resonant two-photon absorption.

Attempts made by different authors to generalize expression (1) to the case of resonance were discussed in [13]. We used the density matrix method to derive a general expression for β in the case of resonant two-photon absorption for multilevel systems in the following form:

$$\beta = iB\sum_{f,n}\left\{\frac{1}{E_f - E_n - \hbar(\omega_1 + \omega_2) + i\gamma_{f,n}} \times \sum_l\left[\frac{\langle l|\mathbf{e}_2\mathbf{p}|f\rangle\langle n|\mathbf{e}_1\mathbf{p}|l\rangle}{E_1 - E_n - \hbar\omega_1 + i\gamma_{l,n}} + \frac{\langle l|\mathbf{e}_1\mathbf{p}|f\rangle\langle n|\mathbf{e}_2\mathbf{p}|l\rangle}{E_1 - E_n - \hbar\omega_2 + i\gamma_{l,n}}\right] \times \sum_q\left[\frac{\langle f|\mathbf{e}_2\mathbf{p}|q\rangle\langle q|\mathbf{e}_1\mathbf{p}|n\rangle}{E_q - E_n - \hbar\omega_1 + i\gamma_{q,n}} + \frac{\langle f|\mathbf{e}_1\mathbf{p}|q\rangle\langle q|\mathbf{e}_2\mathbf{p}|n\rangle}{E_q - E_n - \hbar\omega_2 + i\gamma_{q,n}}\right] - \text{c.c.}\right\}, \quad (5)$$

where B is a real constant, the quantity $\gamma_{l,n} = \hbar/\tau_{l,n}$ defines the Lorentz halfwidth of the corresponding transition, $\tau_{l,n}$ are the transverse relaxation times, and c.c. are the complex conjugate terms. As is seen from Eq. (5), the narrowest intermediate levels have a dominant role in the resonant TPA.

Recall that resonant absorption involving intermediate levels can only take place for the probing beam photon $\hbar\omega_1$. We restrict ourselves to two final (*3*, *3*') and three intermediate (*2*', *2*, *2*") states, as shown in Fig. 3. Neglecting the interference terms in Eq. (5), since, in

the resonance region, they are substantially smaller than the Lorentzian terms, we obtain for β

$$\beta = B\left\{\frac{\gamma_3}{(E_3 - E_1 - \varepsilon)^2 + \gamma_3^2} + \frac{\gamma_{3'}}{(E_{3'} - E_1 - \varepsilon)^2 + \gamma_{3'}^2}\right\}$$
$$\times\left\{\frac{G_{32}^2(2)G_{21}^{(2)}(1)}{(E_2 - E_1 + \hbar\omega_2 - \varepsilon)^2 + \gamma_2^2}\right.$$
$$+\frac{G_{32'}^2(2)G_{2'1}^{(2)}(1)}{(E_{2'} - E_1 + \hbar\omega_2 - \varepsilon)^2 + \gamma_{2'}^2} \quad (6)$$
$$\left.+\frac{G_{32''}^2(2)G_{2''1}^{(2)}(1)}{(E_{2''} - E_1 + \hbar\omega_2 - \varepsilon)^2 + \gamma_{2''}^2}\right\},$$

where $G_{32}(2) = \langle 3|\mathbf{e}_2\mathbf{p}|2\rangle$ and $\varepsilon = \hbar(\omega_1 + \omega_2)$. To reduce the number of the fitting parameters in Eq. (6), we assumed that $G_{32} = G_{3'2}$, $G_{32'} = G_{3'2'}$, and $G_{32''} = G_{3'2''}$.

Selecting intermediate and final states for calculating the TPA spectrum for Cr_2O_3 according to Eq. (6) allowed us to obtain a good fit of the theoretical to experimental TPA spectra (the solid and dashed lines in Fig. 1) by numerically varying the parameters. The TPA spectra differ strongly from the one-photon absorption spectra for Cr_2O_3, which were discussed in considerable detail in [10]. The one-photon absorption spectrum of Cr_2O_3 crystals derives from optical transitions between the electronic states of the unfilled Cr^{3+} $3d^3$ shell split by the crystal field [14, 15]. Figure 3 shows the splitting of the lowest ion terms with the d^3 configuration in the strong cubic-symmetry crystal-field approximation [15]. The broad one-photon absorption bands correspond to the transitions ${}^4A_2(F) \longrightarrow {}^4T_2(F)$ (near 2.1 eV) and ${}^4A_2(F) \longrightarrow {}^4T_1(F)$ (near 2.6 eV). Besides the broad bands, the one-photon absorption spectrum obtained at low temperatures exhibits narrow peaks [10], which correspond to the spin-forbidden transitions ${}^4A_2(F) \longrightarrow {}^2E(G)$ and ${}^4A_2(F) \longrightarrow {}^2T_1(G)$ (near 1.67–1.76 eV). In Fig. 3, the initial (*1*), intermediate (*2*, *2*', *2*''), and final (*3*, *3*') energy levels accepted in the calculation scheme are identified with the real levels in the Cr_2O_3 crystal in the cubic-symmetry approximation. The ${}^4T_2(F)$ and ${}^2T_2(G)$ levels are disregarded in the calculations, because they do not contribute noticeably to resonant two-photon absorption. Figure 3 also shows the approximate width of the energy levels, which was obtained upon fitting the parameters.

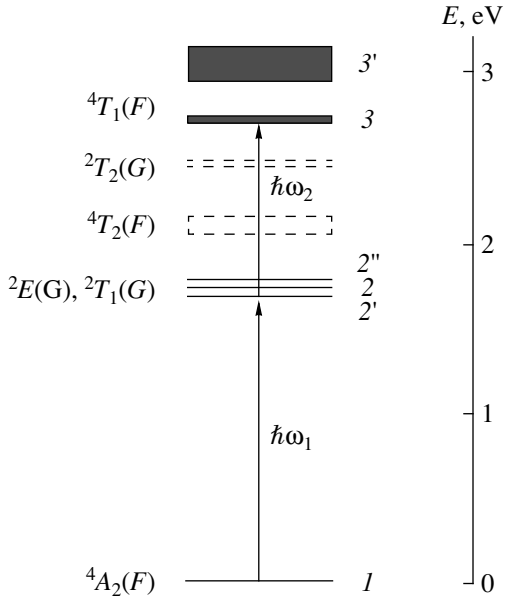

Fig. 3. Diagram of resonant two-photon absorption in a Cr_2O_3 crystal.

The expression for β can be written in a more convenient form for choosing the fitting parameters:

$$\beta = a\left\{\frac{1}{(E_3 - E_1 - \varepsilon)^2 + \gamma_3^2} + \frac{b}{(E_{3'} - E_1 - \varepsilon)^2 + b^2\gamma_3^2}\right\}$$
$$\times\left\{\frac{1}{(E_2 - E_1 + \hbar\omega_2 - \varepsilon)^2 + \gamma_2^2}\right.$$
$$+\frac{c}{(E_{2'} - E_1 + \hbar\omega_2 - \varepsilon)^2 + \gamma_{2'}^2} \quad (7)$$
$$\left.+\frac{d}{(E_{2''} - E_1 + \hbar\omega_2 - \varepsilon)^2 + \gamma_{2''}^2}\right\},$$

where $a = B\gamma_3 G_{32}^2(2)G_{21}^2(1)$, $b = \gamma_{3'}/\gamma_3$, $c = \dfrac{G_{32'}^2(2)G_{2'1}^2(1)}{G_{32}^2(2)G_{21}^2(1)}$, and $d = \dfrac{G_{32''}^2(2)G_{2''1}^2(1)}{G_{32}^2(2)G_{21}^2(1)}$.

In the calculation of the two-photon spectrum, the initial positions of the intermediate levels and the final level 3, as well as their widths, were taken from the one-photon absorption spectrum [10]. The results of the calculation are shown in Fig. 1 (solid lines) for two light-beam polarization orientations relative to the *c* axis: $\mathbf{e}_1 \parallel \mathbf{e}_2 \parallel c$ and $\mathbf{e}_1 \parallel \mathbf{e}_2 \perp c$. The values of the parameters are given in Table 1. It is readily seen that, except for a few details, the calculated and experimental two-photon absorption spectra are in good agreement. Note a number of essential differences between the two- and

The values of parameters

Orientation	a	$E_3 - E_1$, eV	γ_3^2	b	$E_{3'} - E_1$, eV	$E_2 - E_1$, eV	γ_2^2
$\perp$	5.79×10^{-8}	2.73	0.001	6.47	3.04	1.71	1.6×10^{-4}
$\parallel$	4×10^{-8}	2.74	0.001	4.55	3.04	1.735	1.6×10^{-4}

Orientation	c	$E_{2'} - E_1$, eV	$\gamma_{2'}^2$	d	$E_{2''} - E_1$, eV	$\gamma_{2''}^2$
$\perp$	1.3	1.675	1.6×10^{-4}	6.68	1.76	1.3×10^{-3}
$\parallel$	1.8	1.69	1.6×10^{-4}	4	1.79	1.2×10^{-3}

one-photon absorption spectra of Cr_2O_3 (the lines of two-photon absorption are substantially narrower than the one-photon ones, they are split and shifted toward higher energies). The main difference consists in that the general pattern of the two-photon absorption spectrum of Cr_2O_3 in the range 2.7–3.1 eV is determined primarily by the resonances at the narrow intermediate levels $^2E(G)$ and $^2T_1(G)$.

As follows from the calculations performed by our model, the best fit to experimental two-photon absorption spectra is reached for the split final level $^4T_1(F)$ (2.74 and 3.04 eV), even though the $^4T_1(F)$ broad band in the one-photon absorption spectrum has a maximum at about 2.63 eV. The splitting of the $^4T_1(F)$ level into two sublevels, namely, E^T and A_2^T, is accounted for by the combined effect of the trigonal field and spin-orbit coupling [14, 15]. According to our calculation, this splitting is equal to 0.3 eV, which agrees in order of magnitude with the experimental data quoted by other authors [16]. However, the positions of the resonance levels involved in two-photon absorption correspond in energy to the $^2E(G)$ and $^2T_1(G)$ narrow lines in the one-photon absorption spectrum. The lower spectral intensity observed for the polarization configuration $\mathbf{e}_1 \parallel \mathbf{e}_2 \parallel c$ can be explained by the selection rules for two-photon transitions [8, 9], because, in this polarization configuration, the $A_2^T \longrightarrow E^T$ two-photon transitions in the field of trigonal symmetry C_{3v} are forbidden. We assign the first peak at 2.74 eV to transitions to the narrow final split state 3, and the three peaks at 2.845, 2.88, and 2.93 eV, to resonances observed at the 1.675-, 1.71-, and 1.76-eV intermediate levels upon transitions to the second, broader final level *3'*.

Thus, the results of the calculations demonstrated that the narrow energy levels near 1.7 eV strongly affect the two-photon absorption in Cr_2O_3 at room temperature, even though in one-photon absorption spectra, these levels manifest themselves only at low temperatures.

ACKNOWLEDGMENTS

This work was supported by the Russian Foundation for Basic Research (project no. 00-02-16946) and the "Laser Optics" Program.

REFERENCES

1. V. I. Bredikhin, N. D. Galanin, and V. N. Genkin, Usp. Fiz. Nauk **110** (1), 3 (1973) [Sov. Phys. Usp. **16**, 299 (1973)].
2. J. M. Worlock, in *Laser Handbook*, Ed. by F. T. Arecchi and E. O. Sehulz-Dubois (North-Holland, Amsterdam, 1972), Vol. 2, p. 1324.
3. H. Mahr, in *Quantum Electronics*, Ed. by H. Rabin and C. L. Tang (Academic, New York, 1975), Vol. 1, p. 285.
4. S. I. Shablaev, A. M. Danishevskiĭ, V. K. Subashiev, and A. A. Babashkin, Fiz. Tverd. Tela (Leningrad) **21** (4), 1140 (1979) [Sov. Phys. Solid State **21**, 662 (1979)].
5. S. I. Shablaev, A. M. Danishevskiĭ, and V. K. Subashiev, Fiz. Tverd. Tela (Leningrad) **26** (1), 179 (1984) [Sov. Phys. Solid State **26**, 105 (1984)]; Zh. Éksp. Teor. Fiz. **86** (6), 2158 (1984) [Sov. Phys. JETP **59**, 1256 (1984)].
6. S. I. Shablaev and R. V. Pisarev, Pis'ma Zh. Éksp. Teor. Fiz. **45** (10), 490 (1987) [JETP Lett. **45**, 626 (1987)].
7. S. I. Shablaev, Zh. Éksp. Teor. Fiz. **96** (6), 1959 (1990) [Sov. Phys. JETP **70**, 1105 (1990)]; Pis'ma Zh. Tekh. Fiz. **19** (9), 79 (1993) [Tech. Phys. Lett. **19**, 289 (1993)].
8. T. R. Bader and A. Gold, Phys. Rev. **171**, 997 (1968).
9. M. N. Denisov and V. P. Makarov, J. Phys. C **5**, 2651 (1972).
10. D. S. McClure, J. Chem. Phys. **38** (9), 2289 (1963).
11. M. Fiebig, D. Fröhlich, B. B. Krichevtsov, and R. V. Pisarev, Phys. Rev. Lett. **73**, 2127 (1994).
12. B. B. Krichevtsov, V. V. Pavlov, R. V. Pisarev, and V. N. Gridnev, Phys. Rev. Lett. **76**, 4628 (1996).
13. Z. A. Demidenko, Kvantovaya Élektron. (Moscow) **6** (7), 1416 (1979).
14. S. Sugano, Y. Tanabe, and H. Kamimura, *Multiplets of Transition Metal Ions in Crystals* (Academic, New York, 1970).
15. D. T. Sviridov and Yu. F. Smirnov, *The Theory of Optical Spectra of Transition Metal Ions* (Nauka, Moscow, 1977).
16. D. S. McClure, J. Chem. Phys. **36**, 2757 (1962).

Translated by G. Skrebtsov

Physics of the Solid State, Vol. 42, No. 10, 2000, pp. 1873–1880. Translated from Fizika Tverdogo Tela, Vol. 42, No. 10, 2000, pp. 1826–1832.

MAGNETISM AND FERROELECTRICITY

New Nonlinear Intensity Kerr Effect in the Polar Geometry

V. I. Belotelov*, **, A. P. Pyatakov*, **, S. A. Eremin*, G. G. Musaev***, and A. K. Zvezdin*, ****

** Institute of General Physics, Russian Academy of Sciences, ul. Vavilova 38, Moscow, 117942 Russia*

*** Moscow State University, Vorob'evy gory, Moscow, 119899 Russia*

**** Dagestan State University, Makhachkala, 367025 Russia*

Received February 4, 2000; in final form, March 9, 2000

Abstract—The problem of the electromagnetic wave reflection on the second optical harmonic from a semi-infinite optically isotropic magnetic medium is considered for the uniform magnetization direction corresponding to the polar Kerr effect. In the first approximation in magnetization, the method of Green's tensor functions is used to derive expressions for the complex amplitudes of the wave fields for the incidence of *s*- and *p*-polarized waves (as well as of their superposition) on the medium. It is shown that, in the latter case, the nonlinear polar Kerr effect is of the intensity type. The dependences of the intensity effect on the angle of incidence of the inducing wave and on the angle of its polarization, which were obtained in numerical experiments, are presented. A comparative analysis of the linear and nonlinear intensity Kerr effects is carried out. © *2000 MAIK "Nauka/Interperiodica".*

The new magnetooptical (MO) effects associated with the surface of magnetic media, namely, the nonlinear Kerr effects on the second harmonic, were predicted recently and later detected in experiments [1–5]. It is known that the generation of a second harmonic is forbidden in materials with a center of inversion, such as the majority of widespread materials (Fe, Co, Ni, FeNi, etc.). However, symmetry with respect to spatial inversion is broken on a surface or interface. It is the symmetry breaking that results in the emergence of magnetooptical effects on the second harmonic, which were found to be much stronger than the analogous linear effects [4, 5]. Nonlinear MO effects are a new promising instrument for examining magnetic surfaces and interfaces in magnetic films and multilayer structures with a high space and time resolution. A large value of the rotation angle in the wave polarization plane on the second harmonic (relatively to polarization of the inducing wave) ensures a high contrast between regions with opposite magnetizations [6–10]. For example, the contrast may exceed 50% for the multilayer structure of Co/Cu(100).

Together with the rotation of the polarization plane, the intensity of the reflected wave can vary with the magnetization of the specimen in some geometries. Such effects were called intensity effects. Both the linear and nonlinear equatorial Kerr effects are intensity effects. In [11], the existence of the linear intensity polar effect is discussed in the case of the incidence of a wave on a medium whose polarization plane makes a certain angle other than 0° or 90° with the incidence plane.

We can propose that, together with this linear effect, there must exist an analogous nonlinear effect, which is comparable with, or even greater than, the linear effect. The main purpose of our work is to explore theoretically the possibility of the existence of such a nonlinear intensity effect.

The configuration corresponding to the polar Kerr effect was studied in [10], where the incidence of an *s*- or *p*-polarized wave on a semi-infinite magnetic medium was considered. From the Maxwell equations, the normal field modes of the frequency 2ω were found in a magnetic and transparent medium, and the second-harmonic field of the reflected wave was calculated with the help of the boundary conditions.

In this work, we also examine the geometry of the polar effect. However, we consider not only the *s*- and *p*-polarizations of the inducing wave, but also the more general case of incidence of a plane-polarized wave representing the superposition of *s*- and *p*-polarized waves on a magnetic medium.

In all three cases, we seek the field of the reflected wave by Green's tensor electrodynamic functions method [12–14], which will be described below. This approach is very convenient and promising for solving problems associated with the reflection of a wave from magnetic media with different magnetization distributions. One of the advantages of the method is that the Maxwell boundary conditions are already taken into account in Green's functions.

In this work, it is shown that, in the case when the angle between the plane of polarization of an incident wave and the plane of incidence differs from 0° and 90°, the nonlinear polar Kerr effect is of the intensity type; i.e., a contrast emerges between regions having opposite magnetizations. For the *s*- and *p*-polarized waves, the intensity effect vanishes. The angles of polarization rotation and of the ellipticity of reflected waves coincide with those presented in [10]. We

1063-7834/00/4210-1873$20.00

present below the analytical formulas describing the effect, and the results of the numerical experiments characterizing the intensity effect as compared to the correspondent linear effect.

1. EQUATIONS FOR THE FIELD OF FREQUENCY 2ω

Let an optical wave $\mathbf{E}^{(i)}(\mathbf{r}, t) = \mathbf{E}^{(i)}\exp(-i(\mathbf{kr} - \omega t))$ with wave vector $\mathbf{k} = (k_x, 0, k_z)$ be incident at a certain angle φ on the surface of a ferromagnetic medium which fills the entire half-space $z < 0$ (Fig. 1). Under the action of the wave field, the medium acquires a polarization **P**, which can be represented as a sum of the polarization linear in the electric field and the surface polarization quadratic in the field. The surface polarization varies in time with a frequency 2ω and generates plane waves of frequency 2ω, attenuating in the semi-infinite magnetic medium. Hence, the polarization of the medium acquires one more component which is a linear function of the field of frequency 2ω.

Therefore, we have

$$\mathbf{P} = \mathbf{P}_\omega(\mathbf{r})\exp(i\omega t) + \mathbf{P}_{2\omega}(\mathbf{r})\exp(i2\omega t) + \tilde{\mathbf{P}}^{\text{surf}}(\mathbf{r})\exp(i2\omega t)\delta(z), \tag{1a}$$

$$\mathbf{P} = \varepsilon_0\chi_\omega\mathbf{E}(\mathbf{r})\exp(i\omega t) + \varepsilon_0\chi_{2\omega}\mathbf{E}(\mathbf{r})\exp(i2\omega t) + \tilde{\mathbf{P}}^{\text{surf}}(\mathbf{r})\exp(i2\omega t)\delta(z). \tag{1b}$$

The constitutive relation $\mathbf{D} = \varepsilon_0\mathbf{E}_{\text{tot}} + \mathbf{P}$ assumes the form

$$\mathbf{D} = \varepsilon_0\bar{\varepsilon}(\mathbf{r})\mathbf{E}(\mathbf{r})\exp(i\omega t) + \varepsilon_0\tilde{\varepsilon}(\mathbf{r})\tilde{\mathbf{E}}(\mathbf{r})\exp(i2\omega t) + \tilde{\mathbf{P}}^{\text{surf}}(\mathbf{r})\exp(i2\omega t)\delta(z), \tag{2}$$

where $\bar{\varepsilon}$ and $\tilde{\varepsilon}$ are the permittivity tensors of the magnetic medium at frequencies ω and 2ω, respectively [10, 15]:

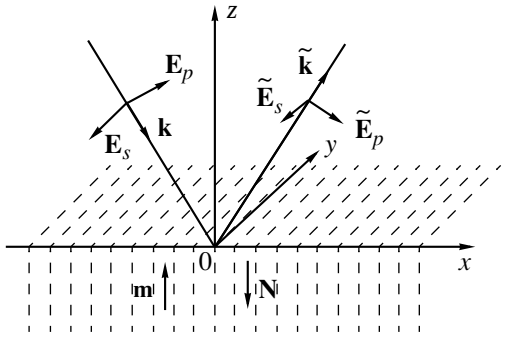

Fig. 1. Geometry of the problem. The incidence of an optical wave on a semi-infinite ferromagnetic medium.

$$\bar{\varepsilon} = n^2\begin{pmatrix} 1 & -im_3Q & im_2Q \\ im_3Q & 1 & -im_1Q \\ -im_2Q & im_1Q & 1 \end{pmatrix} \quad \text{for } z < 0;$$
$$\bar{\varepsilon} = \begin{pmatrix} 1 & 0 & 0 \\ 0 & 1 & 0 \\ 0 & 0 & 1 \end{pmatrix}, \quad z > 0, \tag{3}$$

$$\tilde{\varepsilon} = \tilde{n}^2\begin{pmatrix} 1 & -im_3\tilde{Q} & im_2\tilde{Q} \\ im_3\tilde{Q} & 1 & -im_1\tilde{Q} \\ -im_2\tilde{Q} & im_1\tilde{Q} & 1 \end{pmatrix} \quad \text{for } z < 0;$$
$$\tilde{\varepsilon} = \begin{pmatrix} 1 & 0 & 0 \\ 0 & 1 & 0 \\ 0 & 0 & 1 \end{pmatrix}, \quad z > 0, \tag{4}$$

where n and $\tilde{n}$ are complex refractive indices ($\text{Im}\,n > 0$) for the frequencies ω and 2ω, respectively; Q, $\tilde{Q}$ are the magnetooptic parameters which are linear functions of the magnetization **M** at frequencies ω and 2ω, respectively; and m_1, m_2, and m_3 are the coordinates of the vector $\mathbf{m} = \mathbf{M}/M$ characterizing the direction of the magnetization.

If (2) is taken into account, the Maxwell equation ($\mu = 1$)

$$\text{curl}\,\text{curl}\,\mathbf{E}_{\text{tot}} = -\frac{1}{c^2}\frac{\partial^2\mathbf{D}}{\partial t^2} \tag{5}$$

splits into two parts, the first of which is a function of time with frequency ω, and the second one, with frequency 2ω:

$$\text{curl}\,\text{curl}\,\mathbf{E}(\mathbf{r}) - \varepsilon_0\frac{\omega^2}{c^2}\bar{\varepsilon}\mathbf{E}(\mathbf{r}) = 0, \tag{6a}$$

$$\text{curl}\,\text{curl}\,\tilde{\mathbf{E}}(\mathbf{r}) - \varepsilon_0\frac{4\omega^2}{c^2}\tilde{\varepsilon}\tilde{\mathbf{E}}(\mathbf{r}) = \frac{4\omega^2}{c^2}\tilde{\mathbf{P}}^{\text{surf}}(\mathbf{r})\delta(z). \tag{6b}$$

It will be shown below that the field of the second harmonic of the reflected wave can be found from Eq. (6b).

2. NONLINEAR POLARIZATION AND MAGNETIZATION OF THE MEDIUM

The surface nonlinear second-order optical polarization can be presented in the form [1, 16]

$$\tilde{P}_i^{\text{surf}} = \chi^{(2)}_{i,j,k}(\mathbf{M})E_jE_k, \tag{7}$$

where the surface nonlinear susceptibility tensor $\chi^{(2)}$ is linear in magnetization **M**, and E_j is the electric-field component of the optical wave in the medium. It follows from symmetry considerations that the polarization $\tilde{\mathbf{P}}^{\text{surf}}$ can be presented in the form [10, 15, 17]

$$\tilde{\mathbf{P}}^{\text{surf}} = \tilde{\mathbf{P}}_0 + \tilde{\mathbf{P}}_m, \tag{8}$$

where

$$\tilde{\mathbf{P}}_0 = \chi_1\mathbf{E}(\mathbf{EN}) + \chi_2\mathbf{E}^2\mathbf{N}, \tag{8a}$$

and the contribution linear in magnetization is

$$\begin{aligned}\tilde{\mathbf{P}}_m &= \chi_3\mathbf{E}(\mathbf{E}(\mathbf{mN})) + \chi_4\mathbf{E}^2[\mathbf{mN}]\\ &+ \chi_5[\mathbf{Em}](\mathbf{EN}) + \chi_6[\mathbf{EN}][\mathbf{Em}].\end{aligned} \tag{8b}$$

Here, χ_1 and χ_2 are the nonlinear optical parameters; χ_3, χ_4, χ_5, and χ_6 are the nonlinear magnetooptic parameters; $\mathbf{m} = \mathbf{M}/M$ is the vector characterizing the direction of magnetization; and **N** is the normal to the surface.

3. COMPLEX AMPLITUDES OF THE WAVE FIELD OF FREQUENCY ω

The right-hand side of Eq. (6b) contains a nonlinear surface polarization, which depends on the electric field **E** of frequency ω in the magnetic material. Hence, to solve Eq. (6b), it is necessary to determine the field $\mathbf{E}(\mathbf{r})$ for $z < 0$ from Eq. (6a).

This equation was solved in [15], and we will present here only the results for the polar configuration that interest us, with $\mathbf{m} = (0, 0, \pm 1)$, when the magnetization is orthogonal to the medium surface and lies in the plane of light incidence.

The complex amplitude of the electric field in the magnetic medium may be presented as a sum of two terms: $\mathbf{E} = \mathbf{E}^0 + \mathbf{E}^a$, where $\mathbf{E}^0$ is the part of the field, which is independent of the magnetic anisotropic properties of the medium at the frequency ω, and $\mathbf{E}^a$ is the part taking anisotropy into account.

The components of the electric field in the material are given by

$$\begin{aligned}\mathbf{E}_1 &= \mathbf{E}_1^0 + \mathbf{E}_1^a,\\ \mathbf{E}_1^0 &= \frac{2\beta\cos\varphi}{Y}\mathbf{E}_p^{(i)}, \quad \mathbf{E}_1^a = \pm\frac{iQn^2\cos^2\varphi}{XY}\mathbf{E}_s^{(i)},\\ \mathbf{E}_2 &= \mathbf{E}_2^0 + \mathbf{E}_2^a,\\ \mathbf{E}_2^0 &= \frac{2\cos\varphi}{X}\mathbf{E}_s^{(i)}, \quad \mathbf{E}_2^a = \mp\frac{iQn^2\cos\varphi}{XY}\mathbf{E}_p^{(i)},\\ \mathbf{E}_3 &= \mathbf{E}_3^0 + \mathbf{E}_3^a,\\ \mathbf{E}_3^0 &= \frac{2\alpha\cos\varphi}{Y}\mathbf{E}_p^{(i)}, \quad \mathbf{E}_3^a = \mp\frac{iQ\alpha\cos\varphi}{XY}\mathbf{E}_s^{(i)},\end{aligned} \tag{9}$$

where $\alpha = \sin\varphi$, $X = \beta + \cos\varphi$, $Y = \beta + n^2\cos\varphi$, $\beta = \sqrt{n^2 - \alpha^2}$; n is the refractive index of the medium at the frequency ω; and $\mathbf{E}_s^{(i)}$ and $\mathbf{E}_p^{(i)}$ are the complex amplitudes of the *s*- and *p*-components of the polarization of the incident wave.

4. SOLUTION OF THE EQUATION FOR THE FIELD OF FREQUENCY 2ω

Let us rewrite Eq. (6b) in terms of the components

$$\begin{aligned}&\left(\frac{\partial^2}{\partial x_\mu\partial x_\nu} - \delta_{\mu\nu}\frac{\partial^2}{\partial x_\nu^2} - \varepsilon_0\tilde{\varepsilon}_{\mu\nu}(\mathbf{r})\frac{4\omega^2}{c^2}\right)\tilde{E}_\nu(\mathbf{r})\\ &= \frac{4\omega^2}{c^2}\tilde{P}_\mu^{\text{surf}}(\mathbf{r})\delta(z).\end{aligned} \tag{10}$$

For $z < 0$, the permittivity tensor can be presented in the form

$$\begin{aligned}\tilde{\varepsilon}_{\mu\nu}(\mathbf{r}) &= \tilde{\varepsilon}\delta_{\mu\nu} + \Delta\tilde{\varepsilon}_{\mu\nu},\\ \Delta\tilde{\varepsilon}_{\mu\nu} &= -i\tilde{n}^2\tilde{Q}e_{\mu\nu\kappa}m_k,\end{aligned} \tag{11}$$

where $e_{\mu\nu\kappa}$ is the antisymmetric Levi–Civita tensor ($\tilde{\varepsilon}_{\mu\nu}(\mathbf{r}) = \delta_{\mu\nu}$ for $z > 0$).

Let us introduce the operators

$$L_{\mu\nu}^0 = \frac{\partial^2}{\partial x_\mu\partial x_\nu} - \delta_{\mu\nu}\frac{\partial^2}{\partial x_\nu^2} - \varepsilon_0\tilde{\varepsilon}\frac{4\omega^2}{c^2}\delta_{\mu\nu}, \tag{12a}$$

$$L_{\mu\nu}^1 = \varepsilon_0\frac{4\omega^2}{c^2}\Delta\tilde{\varepsilon}_{\mu\nu}. \tag{12b}$$

Then, Eq. (10) can be presented in the following form:

$$(L_{\mu\nu}^0 - L_{\mu\nu}^1)\tilde{E}_\nu(\mathbf{r}) = \frac{4\omega^2}{c^2}\tilde{P}_\mu^{\text{surf}}(\mathbf{r})\delta(z). \tag{13}$$

Confining ourselves to the approximation linear in magnetization, we present the vector $\tilde{\mathbf{P}}_0$ as the sum of two components: $\tilde{\mathbf{P}}_0(\mathbf{r}) = \tilde{\mathbf{P}}^{00}(\mathbf{r}) + \tilde{\mathbf{P}}^a(\mathbf{r})$ (see (8a)), where

$$\tilde{\mathbf{P}}^{00}(\mathbf{r}) = \chi_1\mathbf{E}^0(\mathbf{r})(\mathbf{E}^0(\mathbf{r})\mathbf{N}) + \chi_2(\mathbf{E}^0(\mathbf{r})\mathbf{E}^0(\mathbf{r}))\mathbf{N} \tag{14a}$$

is the component of the polarization $\tilde{\mathbf{P}}_0(\mathbf{r})$, which does not depend on the magnetooptic (anisotropic) properties of the medium at the frequency ω;

$$\begin{aligned}\tilde{\mathbf{P}}^a(\mathbf{r}) &= \chi_1\mathbf{E}^0(\mathbf{r})(\mathbf{E}^a(\mathbf{r})\mathbf{N}) + \chi_1\mathbf{E}^a(\mathbf{r})(\mathbf{E}^0(\mathbf{r})\mathbf{N})\\ &+ 2\chi_2(\mathbf{E}^0(\mathbf{r})\mathbf{E}^a(\mathbf{r}))\mathbf{N}\end{aligned} \tag{14b}$$

is the component of the polarization $\tilde{\mathbf{P}}_0(\mathbf{r})$, which depends on these properties, $\mathbf{E}^0(\mathbf{r})$ and $\mathbf{E}^a(\mathbf{r})$ are the

components of the electric field in the medium at frequency ω, whose complex amplitudes were introduced by formula (9).

In this approximation, the expression for the polarization $\tilde{\mathbf{P}}_m$ (see (8b)) contains only the field $\mathbf{E}^0$.

The field satisfying Eq. (13) can be presented as a sum of three terms:

$$\tilde{\mathbf{E}}(\mathbf{r}) = \tilde{\mathbf{E}}^{00}(\mathbf{r}) + \tilde{\mathbf{E}}^{0}(\mathbf{r}) + \tilde{\mathbf{E}}^{1}(\mathbf{r}), \quad (15)$$

where the field $\tilde{\mathbf{E}}^{00}(\mathbf{r})$ satisfies the equation

$$L^0_{\mu\nu}\tilde{E}^{00}_\nu(\mathbf{r}) = \frac{4\omega^2}{c^2}\tilde{P}^{00}_\mu(\mathbf{r})\delta(z), \quad (16)$$

while the field $\tilde{\mathbf{E}}^{0}(\mathbf{r})$ satisfies the equation

$$L^0_{\mu\nu}\tilde{E}^{0}_\nu(\mathbf{r}) = \frac{4\omega^2}{c^2}\tilde{P}^{a}_\mu(\mathbf{r})\delta(z), \quad (17)$$

and $\tilde{\mathbf{E}}^{1}(\mathbf{r})$ is the correction to the field, which takes into account the anisotropic magnetic properties of the material at frequency 2ω.

In the first approximation, which takes into account only the terms linear in magnetization, Eq. (13) can be written in the form

$$L^0_{\mu\nu}\tilde{E}^{1}_\nu(\mathbf{r}) = \frac{4\omega^2}{c^2}\tilde{P}^{m}_\mu(\mathbf{r})\delta(z) + L^1_{\mu\nu}\tilde{E}^{00}_\nu(\mathbf{r}). \quad (18)$$

The calculation of the second harmonic of the reflected wave is reduced to the solution of the partial differential Eqs. (16)–(18).

These equations can be solved using Green's tensor electrodynamic functions $D_{\mu,\nu}(\mathbf{r}, \mathbf{r}', 2\omega)$ [12–14].

Let us introduce Green's functions through the equation

$$\left(\frac{\partial^2}{\partial x_\lambda \partial x_\mu} - \delta_{\lambda\mu}\frac{\partial^2}{\partial x_\mu^2} - \varepsilon_0\tilde{\varepsilon}(\mathbf{r})\frac{4\omega^2}{c^2}\delta_{\lambda\mu}\right)D_{\mu\nu}(\mathbf{r}, \mathbf{r}', 2\omega) = -\delta_{\lambda\nu}\delta(\mathbf{r}-\mathbf{r}'). \quad (19)$$

The boundary conditions that are used in solving these equations follow from the requirement of continuity of the tangential components of **E** and **H** and the normal component of **D** and **H** upon a transition through the plane $z = 0$. Consequently, the fields obtained in terms of Green's functions will certainly satisfy Maxwell's boundary conditions.

In terms of Green's functions $D_{\mu,\nu}(\mathbf{r}, \mathbf{r}', 2\omega)$, the solution of Eqs. (16)–(18) can be presented in the form

$$\tilde{E}^{00}_\mu(\mathbf{r}) = -\frac{4\omega^2}{c^2}\int d\mathbf{r}' D_{\mu\nu}(\mathbf{r}, \mathbf{r}', 2\omega)\tilde{P}^{00}_\nu(\mathbf{r}')\delta(z'), \quad (20a)$$

$$\tilde{E}^{0}_\mu(\mathbf{r}) = -\frac{4\omega^2}{c^2}\int d\mathbf{r}' D_{\mu\nu}(\mathbf{r}, \mathbf{r}', 2\omega)\tilde{P}^{a}_\nu(\mathbf{r}')\delta(z'), \quad (20b)$$

$$\tilde{E}^{1}_\mu(\mathbf{r}) = -\frac{4\omega^2}{c^2}\left(\int d\mathbf{r}' D_{\mu\nu}(\mathbf{r}, \mathbf{r}', 2\omega)\tilde{P}^{m}_\nu(\mathbf{r}')\delta(z') + \int\limits_{z<0} d\mathbf{r}' D_{\mu\nu}(\mathbf{r}, \mathbf{r}', 2\omega)\varepsilon_0\Delta\tilde{\varepsilon}_{\nu\kappa}\tilde{E}^{00}_k(\mathbf{r}')\right). \quad (20c)$$

To calculate the integrals in Eqs. (20), we go over to the Fourier transforms of Green's functions:

$$D_{\mu\nu}(\mathbf{r}, \mathbf{r}', 2\omega) = \int\frac{4d^2\mathbf{k}_\parallel}{(2\pi)^2}\exp(2i\mathbf{k}_\parallel(\mathbf{r}_\parallel - \mathbf{r}'_\parallel))d_{\mu\nu}(2\mathbf{k}_\parallel, 2\omega, z, z'), \quad (21)$$

$$d_{\mu\nu}(2\mathbf{k}_\parallel, 2\omega, z, z') = \int d(\mathbf{r}-\mathbf{r}'_\parallel)\exp(-2i\mathbf{k}_\parallel(\mathbf{r}_\parallel - \mathbf{r}'_\parallel))D_{\mu\nu}(\mathbf{r}, \mathbf{r}', 2\omega), \quad (22)$$

where $\mathbf{k}_\parallel = (k_x, 0, 0) = \mathbf{k}(\alpha, 0, 0)$, $\alpha = \sin\varphi$, and $\mathbf{r}_\parallel = (x, y, 0)$.

Let us present the fields appearing in the expression for $\tilde{\mathbf{P}}^{\text{surf}}(\mathbf{r})$ in the form

$$E^0_\nu(\mathbf{r}) = \exp(i\mathbf{k}_\parallel\mathbf{r}_\parallel)E^0_\nu(z), \quad E^a_\nu(\mathbf{r}) = \exp(i\mathbf{k}_\parallel\mathbf{r}_\parallel)E^a_\nu(z). \quad (23)$$

Substituting (23) into Eqs. (16)–(18) and taking (22) into account, we obtain

$$\tilde{E}^{00}_\mu(\mathbf{r}) = -\frac{4\omega^2}{c^2} \times \exp(2i\mathbf{k}_\parallel\mathbf{r}_\parallel)d_{\mu\nu}(2\mathbf{k}_\parallel, 2\omega, z, 0-)\tilde{P}^{00}_\nu(0-), \quad (24a)$$

$$\tilde{E}^{0}_\mu(\mathbf{r}) = -\frac{4\omega^2}{c^2} \times \exp(2i\mathbf{k}_\parallel\mathbf{r}_\parallel)d_{\mu\nu}(2\mathbf{k}_\parallel, 2\omega, z, 0-)\tilde{P}^{a}_\nu(0-), \quad (24b)$$

$$\tilde{E}^{1}_\mu(\mathbf{r}) = -\frac{4\omega^2}{c^2} \times \exp(2i\mathbf{k}_\parallel\mathbf{r}_\parallel)\left(d_{\mu\nu}(2\mathbf{k}_\parallel, 2\omega, z, 0-)\tilde{P}^{m}_\nu(0-) + \varepsilon_0\int\limits_{-\infty}^{0} dz' d_{\mu\nu}(2\mathbf{k}_\parallel, 2\omega, z, z')\Delta\tilde{\varepsilon}_{\nu\kappa}\tilde{E}^{00}_k(z')\right), \quad (24c)$$

where $d_{\mu\nu}(2\mathbf{k}_\parallel, 2\omega, z, 0-) = \lim_{z' \to 0-} d_{\mu\nu}(2\mathbf{k}_\parallel, 2\omega, z, z')$, $\tilde{\mathbf{P}}(0-) = \lim_{z' \to 0} \tilde{P}(z')$, and $\tilde{\mathbf{P}}(z)\exp(2i\mathbf{k}_\parallel\mathbf{r}_\parallel) = \tilde{\mathbf{P}}(\mathbf{r})$. Integration with respect to z' in (20a), (20b), and in the first term in (20c) is carried out, taking into consideration the fact that the term $\tilde{\mathbf{P}}^{\text{surf}}$ represents the surface polarization of the medium and differs from zero only in a thin surface layer.

Thus, using the expressions for the Fourier transform of Green's functions and carrying out the integration in (24c), which is reduced to determining the antiderivative function of the exponential integrand, we can obtain an expression for the reflected-wave field in explicit form.

5. FOURIER TRANSFORMS OF GREEN'S FUNCTIONS

The Fourier transforms of Green's functions, which are required for calculating the field of the reflected wave, will be presented below [12] (note that not all of them are continuous functions of z; some of them have discontinuities at $z = 0$).

(1) The Fourier transforms of Green's functions for $z > 0$, $z' < 0$ are

$$d_{11} = -\eta\frac{\cos\varphi\tilde{\beta}}{\tilde{Y}}\exp(2ik_z z)\exp(-2ik\tilde{\beta}z'),$$

$$d_{12} = 0,$$

$$d_{13} = \eta\alpha\frac{\cos\varphi}{\tilde{Y}}\exp(2ik_z z)\exp(-2ik\tilde{\beta}z'),$$

$$d_{21} = 0,$$

$$d_{22} = -\frac{\eta}{\tilde{X}}\exp(2ik_z z)\exp(-2ik\tilde{\beta}z'), \qquad (25)$$

$$d_{23} = 0,$$

$$d_{31} = \eta\frac{\tilde{\beta}\alpha}{\tilde{Y}}\exp(2ik_z z)\exp(-2ik\tilde{\beta}z'),$$

$$d_{32} = 0,$$

$$d_{33} = \frac{-\eta\alpha^2}{\tilde{Y}}\exp(2ik_z z)\exp(-2ik\tilde{\beta}z').$$

(2) The Fourier transforms of Green's functions for $z < 0$, $z' = (0-)$ (for calculating the field $\mathbf{E}^{00}$ in the medium) are

$$d_{11} = -\eta\frac{\cos\varphi\tilde{\beta}}{\tilde{Y}}\exp(-2ik\tilde{\beta}z),$$

$$d_{12} = 0,$$

$$d_{13} = -\eta\alpha\frac{\tilde{\beta}}{\tilde{Y}\tilde{n}^2}\exp(-2ik\tilde{\beta}z),$$

$$d_{21} = 0,$$

$$d_{22} = -\frac{\eta}{\tilde{X}}\exp(-2ik\tilde{\beta}z), \qquad (26)$$

$$d_{23} = 0,$$

$$d_{31} = \frac{-\eta\alpha\cos\varphi}{\tilde{Y}}\exp(-2ik\tilde{\beta}z),$$

$$d_{32} = 0,$$

$$d_{33} = \frac{-\eta\alpha^2}{\tilde{Y}\tilde{n}^2}\exp(-2ik\tilde{\beta}z) + \frac{\eta}{2ik\tilde{n}^2}\delta(z).$$

In formulas (25) and (26), $\alpha = \sin\varphi$, $k = \frac{\omega}{c}$, $\tilde{\beta} = \sqrt{\tilde{n}^2 - \alpha^2}$, $\tilde{X} = \tilde{\beta} + \cos\varphi$, $\tilde{Y} = \tilde{\beta} + \tilde{n}^2\cos\varphi$, $\eta = \frac{i}{2k\varepsilon_0}$, $k_z = k\cos\varphi$, and $\tilde{n}$ is the refractive index of the medium at frequency 2ω.

6. COMPLEX AMPLITUDES OF THE REFLECTED WAVE FIELD AT FREQUENCY 2ω

In the case of $\mathbf{m} = (0, 0, +1)$, which corresponds to the configuration of the polar Kerr effect, the components of $\tilde{P}^{\text{surf}}$ are equal, according to (8), (14), to

$$\begin{aligned}
\tilde{P}_1 &= -\chi_1(E_1E_3^0 + E_1^0E_3^a) \mp (\chi_5 + \chi_6)E_2^0E_3^0,\\
\tilde{P}_2 &= -\chi_1(E_2E_3^0 + E_2^0E_3^a) \pm (\chi_5 + \chi_6)E_1^0E_3^0,\\
\tilde{P}_3 &= -\chi_2((E_1^0)^2 + 2E_1^0E_1^a) - \chi_2((E_2^0)^2 + 2E_2^0E_2^a)\\
&\quad -(\chi_1 + \chi_2)((E_3^0)^2 + 2E_3^0E_3^a),
\end{aligned} \qquad (27)$$

where the complex amplitudes E_1, E_2, and E_3 are known from (9).

Thus, with the help of (9), (24)–(27), the components of the reflected-wave field at frequency 2ω can be defined through s- and p-components of the incident-wave field (E_p^i and E_s^i) and magnetooptic parameters of the magnetic medium.

For the sake of convenience of the subsequent analysis of the obtained results and reflected-wave fields, we will distinguish between terms that are independent of the medium magnetization, $C = \tilde{E}^{00}$, and the terms that are linear functions of it, $D = \tilde{E}^0 + \tilde{E}^1$.

The complex amplitude of the reflected-wave field at frequency 2ω is the sum of the components $\tilde{E}_s$ and

$\tilde{E}_p$ corresponding to the *s*- and *p*-polarization, respectively.

If the incident wave is *s*-polarized, we have

$$\begin{aligned}
\tilde{E}_s^{\pm} &= C_s^{\pm} + D_s^{\pm},\\
C_s^{\pm} &= 0,\\
D_s^{\pm} &= \mp\frac{\alpha k}{\varepsilon_0\tilde{\tilde{X}}}\left(\frac{2\cos\varphi}{X}E_s^{(i)}\right)^2\left(\chi_1\frac{Q}{Y}+\chi_2\frac{\tilde{Q}}{\tilde{\tilde{Y}}}\right),\\
\tilde{E}_p^{\pm} &= C_p^{\pm} + D_p^{\pm},\\
C_p^{\pm} &= \frac{2i\alpha k}{\varepsilon_0\tilde{\tilde{Y}}}\left(\frac{2\cos\varphi}{X}E_s^{(i)}\right)^2\chi_2,\\
D_p^{\pm} &= 0.
\end{aligned} \tag{28}$$

If the wave is *p*-polarized, we have

$$\begin{aligned}
C_s^{\pm} &= 0,\\
D_s^{\pm} &= \mp\frac{\alpha k}{\varepsilon_0\tilde{\tilde{X}}}\left(\frac{2\cos\varphi}{Y}E_p^{(i)}\right)^2\\
&\times\left[\chi_1\left(\frac{n^2Q}{X}+\frac{\tilde{Q}}{\tilde{\tilde{Y}}}(\beta\tilde{n}^2\cos\varphi+\alpha^2)\right)\right.\\
&\left.+\chi_2\frac{n^2\tilde{Q}}{\tilde{\tilde{Y}}}-2i(\chi_5+\chi_6)\beta\right],\\
C_p^{\pm} &= -\frac{2i\alpha k}{\varepsilon_0\tilde{\tilde{Y}}}\left(\frac{2\cos\varphi}{Y}E_p^{(i)}\right)^2[\chi_1(\beta\tilde{\beta}-\alpha^2)-\chi_2 n^2],\\
D_p^{\pm} &= 0.
\end{aligned} \tag{29}$$

Let a wave whose polarization plane forms an angle ψ with the plane of incidence be incident on a magnetic medium. In this case, $E_p^{(i)} = E^i\cos\psi$ and $E_s^{(i)} = E^i\sin\psi$.

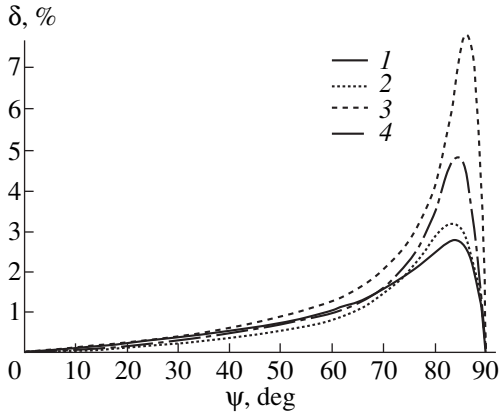

Fig. 2. Diagrams of the relative variation of the intensity δ as a function of the polarization angle ψ for different angles of incidence φ: (*1*) 0°, (*2*) 60°, (*3*) 80°, and (*4*) 90°.

In this configuration, we obtain the following expressions for the complex amplitudes of the components of the reflected-wave field:

$$\begin{aligned}
C_p^{\pm} &= -\frac{2ki\alpha(2\cos\varphi)^2}{\varepsilon_0\tilde{\tilde{Y}}}\\
&\times\left[\frac{\chi_1}{Y^2}(E_p^{(i)})^2\{\beta\tilde{\beta}-\alpha^2\}-\chi_2\left\{\frac{n^2}{Y^2}(E_p^{(i)})^2+\frac{(E_s^{(i)})^2}{X^2}\right\}\right],\\
D_p^{\pm} &= \mp\frac{2k\alpha(2\cos\varphi)^2}{\varepsilon_0\tilde{\tilde{Y}}}\left[\frac{\chi_1 Q}{2Y^2X}(\beta\tilde{\beta}-n^2\tilde{\beta}\cos\varphi-2\alpha^2)\right.\\
&-\chi_1\frac{\tilde{Q}\tilde{n}^2}{2X\tilde{\tilde{X}}Y}+\chi_2 Q\left\{\frac{n^2\beta\cos\varphi}{Y^2X}-\frac{\alpha^2}{Y^2X}-\frac{n^2}{X^2Y}\right\}\\
&\left.+i(\chi_5+\chi_6)\frac{\tilde{\beta}}{XY}\right]E_p^{(i)}E_s^{(i)},\\
C_s^{\pm} &= -\frac{2ki\alpha\chi_1(2\cos\varphi)^2}{\varepsilon_0\tilde{\tilde{X}}XY}E_p^{(i)}E_s^{(i)},\\
D_s^{\pm} &= \mp\frac{2k\alpha(2\cos\varphi)^2}{\varepsilon_0\tilde{\tilde{X}}}\left[\frac{\chi_1 Q}{2}\left\{\frac{(E_s^{(i)})^2}{X^2Y}+\frac{n^2(E_p^{(i)})^2}{X^2Y}\right\}\right.\\
&+\frac{\tilde{Q}}{2\tilde{\tilde{Y}}}\left[\chi_1\left\{\frac{\tilde{n}^2\beta}{Y^2}\cos\varphi+\frac{\alpha^2}{Y^2}\right\}(E_p^{(i)})^2\right.\\
&\left.\left.+\chi_2\left\{\frac{n^2}{Y^2}(E_p^{(i)})^2+\frac{(E_s^{(i)})^2}{X^2}\right\}\right]-\frac{i(\chi_5+\chi_6)\beta E_p^{(i)}}{Y^2}\right].
\end{aligned} \tag{30}$$

7. NONLINEAR INTENSITY KERR EFFECT

Let us define the nonlinear intensity Kerr effect as a relative variation $\delta = (I_+ - I_-)/(I_+ + I_-)$ of the reflected-wave intensity upon a transition of the medium from a state with uniform magnetization $\mathbf{m} = (0, 0, +1) - I_+$ to a state with uniform magnetization $\mathbf{m} = (0, 0, -1) - I_-$.

Let us express the quantities I_+ and I_- through the components $C^{\pm}$ and $D^{\pm}$ of the reflected wave:

$$\begin{aligned}
I_{\pm} &= (\mathbf{E}_s^{\pm}+\mathbf{E}_p^{\pm})(\mathbf{E}_s^{\pm}+\mathbf{E}_p^{\pm})^*\\
&= (C_s^{\pm}+D_s^{\pm})(C_s^{\pm}+D_s^{\pm})^* + (C_p^{\pm}+D_p^{\pm})(C_p^{\pm}+D_p^{\pm})^*.
\end{aligned}$$

Noting that $C_{s,p}^{+} = C_{s,p}^{-}$ and $D_{s,p}^{+} = D_{s,p}^{-}$, we obtain

$$\begin{aligned}
I_+ - I_- &= 2(C_s^+(D_s^+)^* + (C_s^+)^*D_s^+ + C_p^+(D_p^+)^* + (C_p^+)^*D_p^+),\\
I_+ + I_- &= 2(|C_s^+|^2 + |D_s^+|^2 + |C_p^+|^2 + |D_p^+|^2).
\end{aligned}$$

Consequently,

$$\delta = \frac{C_s^+(D_s^+)^* + (C_s^+)^* D_s^+ + C_p^+(D_p^+)^* + (C_p^+)^* D_p^+}{\left|C_s^+\right|^2 + \left|D_s^+\right|^2 + \left|C_p^+\right|^2 + \left|D_p^+\right|^2}, \quad (31)$$

where C_s, C_p, D_s, and D_p are defined by formulas (30).

If an *s*- or *p*-polarized wave is incident on the medium, then $C_s = D_p = 0$; hence, $\delta = 0$, and the intensity effect vanishes.

If a polarized wave with the rotation angle ψ of the polarization plane is incident on a magnetic medium $\left(\psi \neq 0,\ \psi \neq \frac{\pi}{2}\right)$, then all the components of C and D are nonzero, and, in a general case, δ also differs from zero. In such a geometry, the nonlinear polar Kerr effect is of the intensity type.

By way of an example, we consider the typical dependences of δ on the angle of incidence φ and on the angle ψ of incident-light polarization for the nonlinear polar Kerr effect for $\tilde{n} = n = 2.36 + 3.48i$, $Q = \tilde{Q} = -0.034 + 0.003i$ (Q and n correspond to iron [10]), $\chi_2/\chi_1 = 0.1$, $\chi_5/\chi_1 = \chi_6/\chi_1 = 0.01i$, and $\mathrm{Im}\chi_1 = 0$ (the values of these ratios are close to those given in [18, 19]).

The diagrams of δ versus the polarization angle ψ of the incident light are presented in Fig. 2 for various angles of incidence φ. The value of the intensity effect at the peak ($\psi \approx 85°$) increases monotonically with the angle φ, and attains its maximal value at the glancing angle ($\varphi \approx 90°$).

The dependence of δ on the angle φ is shown in Fig. 3 for the optimal polarization angle $\psi \approx 85°$.

For the sake of comparison, Fig. 4 shows the dependence of the linear and nonlinear effects on the polarization angle ψ for an angle of incidence $\varphi \approx 60°$.

It should be emphasized that the nonlinear intensity Kerr effect is *T*-odd, i.e., changes sign upon time reversal (and, therefore, upon the reversal of magnetization and the magnetic field). This important property allows us to use this effect to investigate the domain structures, magnetic solitons and vortices, domain walls, Bloch lines, etc.

The main results of this work are predicting the nonlinear intensity polar Kerr effect and deriving the formulas for *s*- and *p*-components of the reflected wave on the second harmonic in terms of optical and magnetooptic parameters of the medium for the incidence of *s*- or *p*-polarized waves, or a plane-polarized superposition of *s*- and *p*-polarized waves incident on a semiinfinite magnetic medium in the geometry of the polar effect. All of the results are obtained in the linear approximation in parameters dependent on the magnetization.

For known values of the parameters, the dependences of the intensity effect on the incidence angle and on the angle of polarization of the incident wave are presented. A comparative analysis of the linear and nonlinear intensity effects is carried out.

It is shown that Green's tensor electrodynamic functions method is very promising for solving the problems of wave reflection from the magnetic media with different distributions of magnetization.

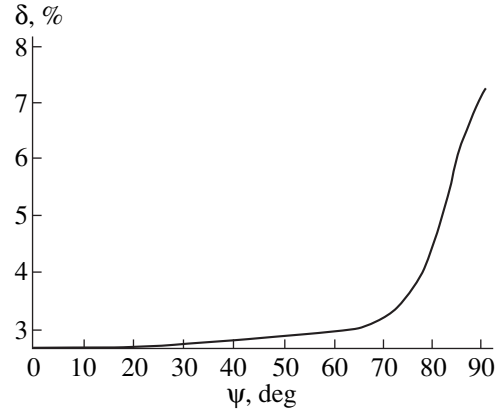

Fig. 3. Diagram of the relative variation of the intensity δ as a function of the angle of incidence φ for the polarization angle $\psi \approx 85°$.

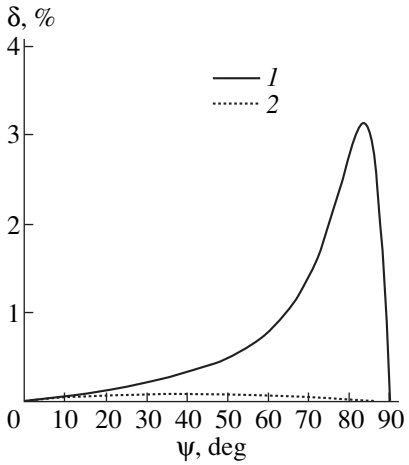

Fig. 4. Dependences of the relative variation of the intensity δ on the polarization angle ψ for the angle of incidence $\varphi \approx 60°$: (*1*) nonlinear effect, (*2*) linear effect.

ACKNOWLEDGMENTS

The work was supported by RFBR, project no. 99-02-17830, by the Ministry of Science, project no. 97-1071, and by INTAS, project no. 97-705.

REFERENCES

1. R. P. Pan, H. D. Wei, and Y. R. Shen, Phys. Rev. B **39**, 1229 (1989).

2. J. Reif, J. C. Zink, C. M. Schneider, and J. Kirschner, Phys. Rev. Lett. **67**, 2878 (1991).
3. G. Spierings, V. Koutsos, H. A. Wierenga, *et al.*, Surf. Sci. **287**, 747 (1993).
4. U. Pustogowa, W. Hübner, and K. H. Bennemann, Phys. Rev. B **49**, 10031 (1994).
5. B. Koopmans, M. Groot Koerkamp, Th. Rasing, and H. van den Berg, Phys. Rev. Lett. **74**, 3692 (1995).
6. G. Spierings, V. Koutsos, H. A. Wierenga, *et al.*, J. Magn. Magn. Mater. **121**, 109 (1993).
7. H. A. Wierenga, M. V. Prins, and Th. Rasing, Physica B (Amsterdam) **204**, 281 (1995).
8. T. M. Crawford, C. T. Rogers, T. J. Silva, and Y. K. Kim, J. Appl. Phys. **81**, 4354 (1997).
9. T. M. Crawford, C. T. Rogers, T. J. Silva, and Y. K. Kim, IEEE Trans. Magn. **38**, 3598 (1997).
10. A. K. Zvezdin and N. F. Kubrakov, Zh. Éksp. Teor. Fiz. **116** (1), 141 (1999) [JETP **89**, 77 (1999)].
11. G. S. Krinchik, *Physics of Magnetic Phenomena* (Mosk. Gos. Univ., Moscow, 1985).
12. A. A. Maradudin and D. L. Mills, Phys. Rev. B **11** (4), 1392 (1975).
13. V. A. Kosobukin, Fiz. Tverd. Tela (S.-Peterburg) **35** (4), 884 (1993) [Phys. Solid State **35**, 457 (1993)].
14. V. A. Kosobukin, J. Magn. Magn. Mater. **153**, 397 (1996).
15. A. K. Zvezdin and V. A. Kotov, *Modern Magnetooptics and Magnetooptical Materials* (Inst. of Phys. Publ., Bristol, 1997).
16. Y. R. Shen, *The Principles of Nonlinear Opticals* (Willey, New York, 1984; Nauka, Moscow, 1989).
17. A. K. Zvezdin, Physica A (Amsterdam) **241**, 444 (1997).
18. U. Pustogowa, W. Hübner, and K. H. Bennemann, Phys. Rev. B **48**, 8607 (1993).
19. U. Pustogowa, W. Hübner, and K. H. Bennemann, Surf. Sci. **307**–**309**, 1129 (1994).

Translated by N. Ostrovskaya

Physics of the Solid State, Vol. 42, No. 10, 2000, pp. 1881–1886. Translated from Fizika Tverdogo Tela, Vol. 42, No. 10, 2000, pp. 1833–1838.

MAGNETISM AND FERROELECTRICITY

Spin-Reorientational Phase Transition in the Basal Plane in an α-Fe_2O_3 : (Ga, Dy) Crystal

G. S. Patrin*, **, E. V. Eremin, and A. V. Shabalin***

**Krasnoyarsk State University, Krasnoyarsk, 660041 Russia*

***Kirenskiĭ Institute of Physics, Siberian Division, Russian Academy of Sciences, Akademgorodok, Krasnoyarsk, 660036 Russia*

e-mail: pat@iph.krasnoyarsk.su

Received March 14, 2000

Abstract—A spin-reorientational phase transition in the basal plane, which was experimentally observed earlier, is explained in terms of a model in which the crystalline Fe-ion matrix is considered as a continuum, while dopant Dy ions are treated as quasi-Ising ions. The transition is established to be due to the Fe-subsystem anisotropy competing with that of the rare-earth subsystem. © *2000 MAIK "Nauka/Interperiodica"*.

INTRODUCTION

Magnetic compounds containing rare-earth (RE) elements differ widely in their observed properties [1]. Due to special features of the electronic structure of RE ions, the characteristic properties of these ions are most pronounced at low temperatures, where fluctuation interactions are frozen out, as a rule, and the effects of interest can be observed without hindrance. In individual cases, even a low RE-ion concentration produces marked changes in the magnetic properties.

Hematite crystals are convenient for studying induced anisotropic interactions, because almost all features of the temperature dependence of the latter are determined by the balance between magnetic anisotropies that differ in nature but make nearly equal contributions. It is well known [2] that adding several percent of 3*d* or diamagnetic ions causes the Morin transition temperature to shift to the low-temperature region $T <$ 4.2 K. The authors have found that dopant RE ions impart new, hitherto unobserved properties to hematite crystals. For instance, the addition of several percent of Tb ions to a hematite crystal containing 4 at. % Ga restores the uniaxial antiferromagnetic state [3], while introducing the same amount of Dy ions induces a spin-reorientational transition in the basal plane [4].

In this paper, earlier reported experimental dependences of the magnetic-resonance parameters in the vicinity of the phase transition in α-Fe_2O_3 : (Ga, Dy) are explained theoretically.

1. MODEL

First of all, we will discuss the facts that form the basis for an impurity-center model and its interaction with the host crystal. Experimentally, it was found [4] that adding several atomic percent of Dy ions does not distort the crystal lattice markedly, which is indicated by a virtually hexagonal magnetic anisotropy at temperatures $T > 6$ K. Above the spin-reorientational phase transition temperature T_{ph}, the easy magnetization axis has the same direction in both dysprosium-doped and undoped crystals. Also, earlier EPR studies revealed [5] that, in an isomorphic α-Al_2O_3 crystal, dopant RE ions occupy Al sites with no change in their local symmetry. In addition, it is known [6] that, at temperatures $T < 300$ K, the magnetization of hematite is virtually independent of temperature and all changes in the shape of a microwave signal are mainly due to the change in the magnetic-resonance linewidth. In our case, the intensity of an antiferromagnetic resonance (AFMR) signal, which is defined as the area under the curve of microwave absorption, is the same everywhere over the temperature range investigated (except for the phase transition region). This means that the magnetic-moment component of the Fe-ion system lies in the basal plane of the crystal (because it is this component that determines the intensity of the AFMR signal [7]) and is temperature independent, and, therefore, the magnetic moment of Dy ions also lies in the basal plane all the time.

The trivalent Dy ion has a $4f^9$ electron configuration and its ground state is a $^6H_{15/2}$ multiplet [8]. The crystal field of low symmetry splits this multiplet into a number of Kramers doublets, which are further split by the exchange field. Because the crystal-field splitting of electron *f* states corresponds to the case of a weak crystal field, the amounts of splitting will differ only slightly in different oxide compounds if the local symmetry is the same in them [1]. As a basis for our model, we use the calculations performed in [9, 10]. With the parameters $A_2^0\langle r^2\rangle = -22$, $A_2^2\langle r^2\rangle = 141$, $A_4^2\langle r^4\rangle = 181$, $A_6^2\langle r^6\rangle = -108$, and $A_6^6\langle r^6\rangle = -57$ cm^{-1} (under the condition that $B_4/B_6 = (1/4)F(6)/F(4)$ in the notation of [9]),

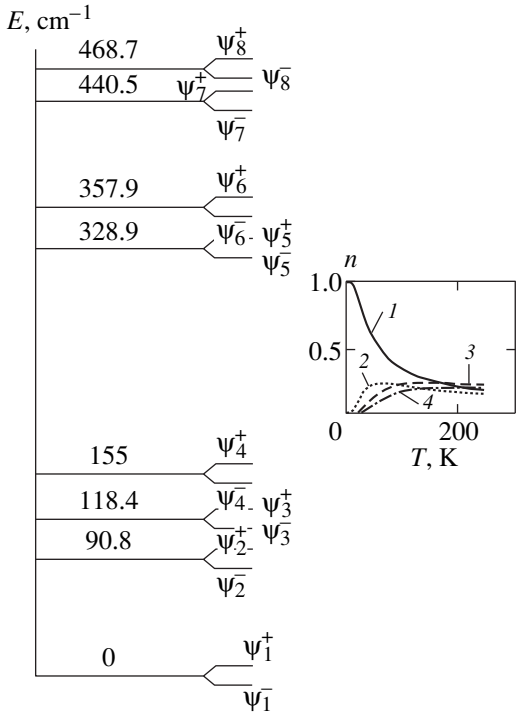

Fig. 1. Energy levels of a Dy ion in a crystal (schematic). The numbers indicate the energy in cm^{-1}. The inset shows the temperature dependence of the occupancies of the four lower energy levels.

which are typical of Dy ions in an yttrium gallium garnet host crystal, we obtain the energy levels depicted in Fig. 1 and the set of wave functions Ψ_L presented in Appendix I. Because the exchange interaction of RE ions with a host crystal is, as a rule, an order of magnitude weaker than the crystal-field splitting in magnetically ordered crystals [1], we calculate the exchange-interaction contribution to the first order in the perturbation theory. For this set of wave functions, we find the magnetic moment μ^L of an ion in each state (Appendix I). In all calculations, the exchange interaction of a Dy ion with its neighboring Fe ions is assumed to be of a quasi-Ising character [1].

We suppose that impurity ions occupy Fe^{3+} sites and are randomly distributed over 24 nonequivalent positions in the crystal. These positions are specified by a set of indices $\{k = 1, 2; s = 1, 2; t = 1, 2, \ldots, 6\} = \{p\}$. The first index specifies one of the two sublattices to which the sites belong; the second indicates the angle $(\pm\alpha)$ through which the axes ξ and η of the local coordinate frame are turned in the basal plane relative to the crystallographic C_2 axes (the X or Y axis of the crystal); and the third index specifies the nonequivalent angles in a given sublattice. The impurity ions occupying one of these nonequivalent positions are labeled by index q. The quantization axis Z' for Dy^{3+} ions in a local coordinate frame is taken to be aligned with the ξ axis.

In this case, the energy of an impurity ion occupying the pq position and being in the lth state has the form

$$E^l_{pq} = E^{lo}_{pq} + (-g\mathbf{H}_0 + \lambda\mathbf{M})\boldsymbol{\mu}^l_{Z'_{pq}}, \quad (1)$$

where $E^{l_0}_{pq}$ is the crystal-field splitting, $\mathbf{H}_0$ is the external magnetic field, $\lambda\mathbf{M}$ is the molecular field exerted on the pq ion by the other sublattice (the intrasublattice exchange interaction can be ignored in rhombohedral antiferromagnets, because it is much weaker than the intersublattice exchange interaction), and $\boldsymbol{\mu}^l_{Z'_{pq}}$ is the magnetic moment of an ion in the lth state. We also have $N_k = N_0/2$, $N_{ks} = N_0/4$, $N_{kst} = N_0/24$, and $\sum_{\{kstq\}} N_{kstq} = N_0$, where N_0 is the total number of impurity centers.

The total energy of the impurity subsystem is

$$F = \sum_{\{pql\}} n^l_{pq}E^l_{pq} - ST, \quad (2)$$

where n^l_{pq} are the equilibrium occupation numbers of the energy levels and S is the entropy of the system.

2. MAGNETIC-RESONANCE CALCULATIONS

The magnetic energy of the crystal, including the energy of the impurity subsystem, can be written as [7]

$$W = W_Z + W_E + W_D + W_{AU} + W_{AB} + W_\Delta + F. \quad (3)$$

In what follows, we consider only the case where the external magnetic field and the magnetic moments of the sublattices lie in the basal plane and, therefore, the uniaxial anisotropy energy W_{AU} makes no contribution to the low-frequency branch of the magnetic resonance. W_Δ is a contribution containing an adjustable parameter Δ and responsible for an isotropic gap in the spectrum, the term F is given by Eq. (2), while the other terms in Eq. (3) can be written in a spherical coordinate system in the form

$$W_Z = -H_0M_0[\cos(\varphi_H - \varphi_1) + \cos(\varphi_H - \varphi_2)],$$

$$W_E = A_EM_0^2\cos(\varphi_1 - \varphi_2),$$

$$W_D = -A_DM_0^2\sin(\varphi_1 - \varphi_2),$$

$$W_{AB} = A_BM_0^2(\cos6\varphi_1 + \cos6\varphi_2),$$

and they are the Zeeman interaction, intersublattice interaction, Dzyaloshinskiĭ interaction, and anisotropy energy in the basal plane, respectively. Here, M_0 is the saturation magnetization of a sublattice; φ_1 and φ_2 are the azimuthal angles of the sublattice magnetizations; φ_H is the angle between the magnetic field and the C_2 axis; A_E and A_D are the interaction constants; and A_B is the anisotropy constant.

The equilibrium values of the azimuthal angles of the sublattice magnetizations are determined from the minimum-energy condition

$$\partial W/\partial \varphi_k = 0, \quad (k = 1, 2) \tag{4}$$

with $\varphi_1 - \varphi_2 = \pi - \delta_1 - \delta_2$, where δ_k are the canting angles of the sublattices. If the sublattices are identical and impurity ions are randomly distributed over the sublattice sites, we have $\delta_1 = \delta_2 = \delta$.

From Eq. (4), the canting angle is found to be (for $\delta \ll 1$)

$$\delta \approx (H_0 + H_D - 6H_{AB}\sin 6\varphi_H - \partial F/\partial \varphi_1)/(2H_E + 36H_{AB}\cos 6\varphi_H), \tag{5}$$

where we have put $\varphi_1 = \varphi_H + \pi/2 - \delta$ at equilibrium, and H_0, H_E, H_D, and H_{AB} are the effective fields corresponding to the energy contributions in Eq. (3).

By solving the Landau–Lifshitz equations in a linear approximation, the following expression is obtained for the uniform-mode resonance field H_r of low-frequency oscillations:

$$H_r = -(H_D/2) + \{(H_D/2)^2 + (\omega/\gamma)^2 + \Delta^2 - 2H_E(36H_{AB}\cos 6\varphi_H + E_{\varphi\varphi})\}^{1/2}. \tag{6}$$

Here, ω is the microwave frequency, γ is the gyromagnetic ratio, Δ is the isotropic band gap, and $F_{\varphi\varphi}$ is the second derivative of the impurity-subsystem energy with respect to either of the φ_1 and φ_2 angles.

As is seen from Appendix I, the structure of the wave functions is such that the magnetic moment has a maximum value in the ground doublet state, whereas it is much smaller in the next and higher doublet states. Taking into account the Boltzmann factor characterizing the occupancies of excited energy levels (see the inset in Fig. 1), the calculation of $F_{\varphi\varphi}$ can be simplified by retaining only the four lower levels in the model. In this case, the magnetic contributions from the upper three doublets (next in energy after the ground doublet) can be ignored, and the levels themselves can be replaced by an effective twofold degenerate level E^* (with $\mu_{pq}^{\pm(2)} = 0$) positioned at the centroid of this group of levels. The results are not altered radically in the case of a higher degeneracy of the effective excited level. The expression for $F_{\varphi\varphi}$ thus calculated is presented in Appendix II.

Calculations are performed for the parameters $H_E = 9.7 \times 10^6$, $H_D = 21.7 \times 10^3$ Oe, $\alpha = 23.1°$, $\lambda M = 3.5 \times 10^5$ Oe, $E^* = 121$ cm^{-1}, $\mu_{pq}^{1,2} = \mp 2.83\mu_B$, and $N_0 = 8.2 \times 10^{17}$ cm^{-3}. The temperature dependences of the anisotropy field in the basal plane and of the isotropic band gap are approximated by polynomials by using the experimental curves obtained for hematite crystals without Dy ions, $H_{AB}(T) = (4.4 - 0.011T + 3.12T^2 \times 10^{-4} - 3.63T^3 \times 10^{-6} + 1.31T^4 \times 10^{-8} - 1.5T^5 \times 10^{-11}) \times 10^6$ Oe and $\Delta^2(T) = (28.4 - 0.016T) \times 10^6$ Oe^2.

3. RESULTS AND DISCUSSION

The first feature to note is that the exchange interaction of the Fe-ion subsystem with a Dy ion has to be taken as ferromagnetic in the case under consideration, despite the exchange interaction with RE ions being antiferromagnetic in all known oxide compounds [1].

Figure 2 shows the theoretically calculated temperature dependences of the resonance field H_r for angles of $\varphi_H = 0°$ and 30° (curves *1* and *2*, respectively) and the experimental dependences taken from [4] (curves *3*, *4*). On the whole, the results are seen to agree satisfactorily with the experiment, except for the clearly defined high-temperature peak on the experimental curve *4* (which is associated with high energy levels), although the theoretical curve also shows a peak (curve *1*). The reason for this discordance is that the magnetic moments in the high excited states have been taken to be zero. Nevertheless, this fact has no effect on the character of the spin-reorientational phase transition and its temperature for the given position of the energy levels. The occupancies of higher energy levels become noticeable at temperatures $T \geq 100$ K and, as the number of occupied excited levels increases, their relative contribution decreases.

Figure 3 shows the angular dependence of the resonance field calculated for different temperatures. It is seen that, for the parameters chosen, the angular dependence is changed in character near $T_{ph} \cong 12$ K; namely, the maxima and minima interchanged places, which can be interpreted as the change in sign of the magnetocrystalline anisotropy constant in the basal plane. There is some discordance between the calculated and experimental dependences, which may be due to the fact that the calculations include the experimental

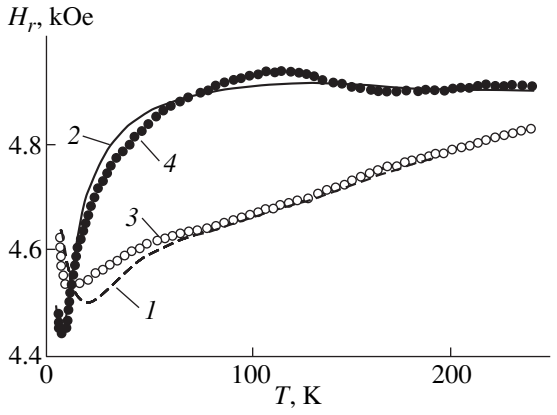

Fig. 2. Temperature dependences of the calculated (*1*, *2*) and experimentally measured [4] (*3*, *4*) resonance field for $\varphi = 0°$ (*1*, *3*) and $\varphi = 30°$ (*2*, *4*).

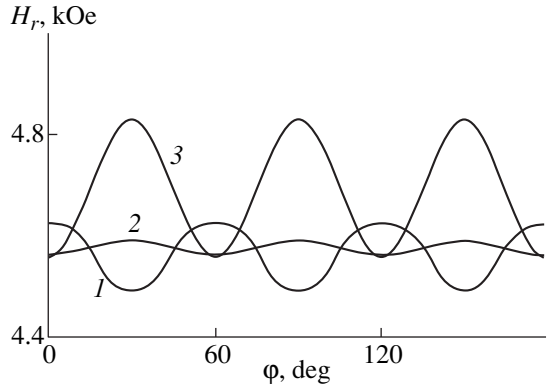

Fig. 3. Angular dependence of the resonance field for different temperatures *T*: 7 (*1*), 12 (*2*), and 36 K (*3*).

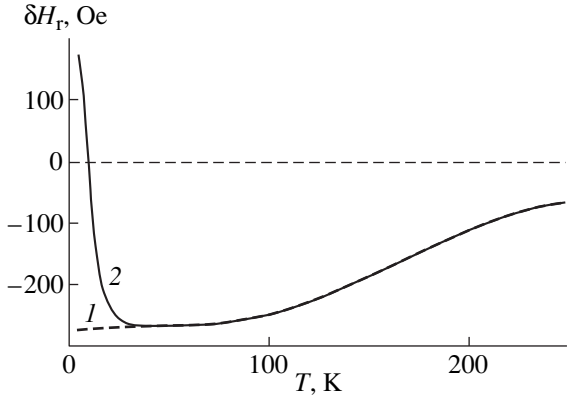

Fig. 4. Temperature dependence of the magnetic anisotropy field times $2H_E$ for a hematite crystal without an RE impurity (*1*) and doped with Dy^{3+} ions (*2*).

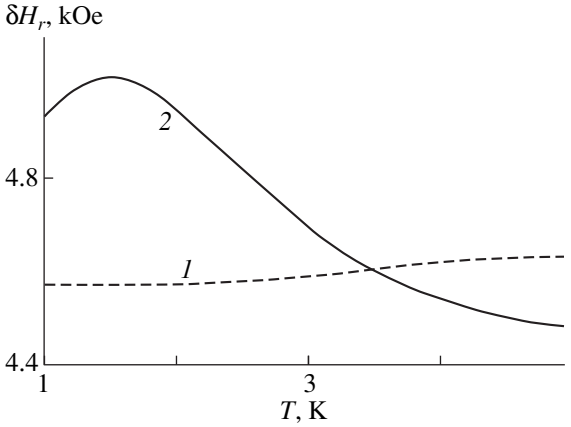

Fig. 5. Temperature dependences of the resonance field in the vicinity of a low-temperature anomaly for φ = 0 (*1*) and φ = 30° (*2*).

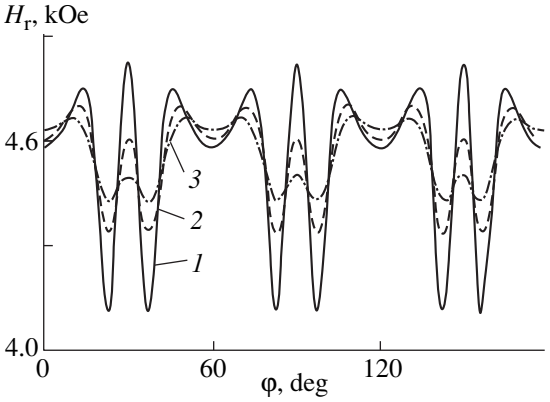

Fig. 6. Angular dependences of the resonance field for different temperatures *T*: 2.5 (*1*), 3.5 (*2*), and 4.5 K (*3*).

$H_{AB}(T)$ dependence for α-Fe_2O_3 : Ga (4 at. %) crystals, but the possible effect of Dy ions is not taken into account. Nonetheless, on the whole, the results also agree satisfactorily with the experiment in this case. The $\Delta(T)$ dependence is taken such that H_r at φ = 15° is equal to the experimental values at T = 7 and 300 K. The dependence

$$\delta H_r(T) = H_r(T, \varphi = 0) - H_r(T, \varphi = 30°), \qquad (7)$$

which is frequently used in processing experimental data, may tell something about the temperature dependence of the magnetic anisotropy field (Fig. 4). It is seen from Fig. 4 that the contribution from the RE-ion subsystem becomes noticeable only at T < 48 K (curve *2*), whereas the contribution from the crystal host dominates at higher temperatures (curve *1*; cf. Fig. 1 in [4]). When expression (7) is used to process the data, it may appear that another spin-reorientational phase transition occurs at $T^* \cong 3.5$ K in this case (see Fig. 5), and the easy magnetization axis has the same direction at $T < T^*$ and $T > T_{ph}$. However, analysis of the $H_r(T, \varphi)$ angular dependence at different temperatures in the range T < 5 K (Fig. 6) reveals that this dependence is complicated and determined by the balance between the contributions from Dy ions at different inequivalent crystallographic positions. Therefore, in this case, there occurs a change in the character of the temperature dependence, rather than a change in the hard and easy magnetization directions.

4. CONCLUSION

This study established the cause and the features of the spin-reorientational phase transition that occurs in an α-Fe_2O_3 : Ga crystal with its doping with dysprosium. According to the model calculations, the low energy levels of impurity ions make the dominant contribution. Taking higher levels into account does not

alter the results radically, although the agreement with the experiment becomes better. The surprising thing is that, for the theoretical results to agree with the experimental data, the exchange interaction between RE ions and the Fe-ion subsystem must be taken to be of the ferromagnetic type, which is not typical of oxide compounds containing RE ions. This fact calls for further investigation.

APPENDIX I

$$\Psi_1 = 0.633\left|\pm\frac{13}{2}\right\rangle - 0.582\left|\pm\frac{5}{2}\right\rangle - 0.451\left|\mp\frac{3}{2}\right\rangle - 0.239\left|\mp\frac{11}{2}\right\rangle$$

$$\mu_1 = \pm 2.83\mu_B$$

$$\Psi_2 = -0.397\left|\pm\frac{15}{2}\right\rangle - 0.398\left|\pm\frac{11}{2}\right\rangle - 0.352\left|\pm\frac{7}{2}\right\rangle - 0.447\left|\pm\frac{3}{2}\right\rangle + 0.458\left|\mp\frac{1}{2}\right\rangle - 0.125\left|\mp\frac{5}{2}\right\rangle + 0.095\left|\mp\frac{9}{2}\right\rangle - 0.354\left|\mp\frac{13}{2}\right\rangle$$

$$\mu_2 = \pm 1.79\mu_B$$

$$\Psi_3 = -0.396\left|\pm\frac{15}{2}\right\rangle + 0.399\left|\pm\frac{11}{2}\right\rangle - 0.352\left|\pm\frac{7}{2}\right\rangle + 0.448\left|\pm\frac{3}{2}\right\rangle + 0.458\left|\mp\frac{1}{2}\right\rangle + 0.125\left|\mp\frac{5}{2}\right\rangle + 0.095\left|\mp\frac{9}{2}\right\rangle + 0.354\left|\mp\frac{13}{2}\right\rangle$$

$$\mu_3 = \pm 1.79\mu_B$$

$$\Psi_4 = 0.582\left|\pm\frac{15}{2}\right\rangle + 0.331\left|\pm\frac{7}{2}\right\rangle + 0.718\left|\mp\frac{1}{2}\right\rangle + 0.191\left|\mp\frac{9}{2}\right\rangle$$

$$\mu_4 = \pm 2.5\mu_B$$

$$\Psi_5 = -0.047\left|\pm\frac{15}{2}\right\rangle - 0.502\left|\pm\frac{11}{2}\right\rangle + 0.03\left|\pm\frac{7}{2}\right\rangle + 0.314\left|\pm\frac{3}{2}\right\rangle - 0.164\left|\mp\frac{1}{2}\right\rangle + -0.24\left|\mp\frac{5}{2}\right\rangle + 0.705\left|\mp\frac{9}{2}\right\rangle + 0.254\left|\mp\frac{13}{2}\right\rangle$$

$$\mu_5 = \mp 1.26\mu_B$$

$$\Psi_6 = -0.044\left|\pm\frac{15}{2}\right\rangle + 0.53\left|\pm\frac{11}{2}\right\rangle + 0.029\left|\pm\frac{7}{2}\right\rangle - 0.331\left|\pm\frac{3}{2}\right\rangle - 0.155\left|\mp\frac{1}{2}\right\rangle + 0.253\left|\mp\frac{5}{2}\right\rangle + 0.668\left|\mp\frac{9}{2}\right\rangle - 0.286\left|\mp\frac{13}{2}\right\rangle$$

$$\mu_6 = \mp 0.92\mu_B$$

$$\Psi_7 = -0.376\left|\pm\frac{15}{2}\right\rangle + 0.232\left|\pm\frac{11}{2}\right\rangle + 0.514\left|\pm\frac{7}{2}\right\rangle - 0.333\left|\pm\frac{3}{2}\right\rangle + 0.076\left|\mp\frac{1}{2}\right\rangle - 0.547\left|\mp\frac{5}{2}\right\rangle - 0.029\left|\mp\frac{9}{2}\right\rangle + 0.353\left|\mp\frac{13}{2}\right\rangle$$

$$\mu_7 = \pm 0.88\mu_B$$

$$\Psi_8 = -0.449\left|\pm\frac{15}{2}\right\rangle - 0.194\left|\pm\frac{11}{2}\right\rangle + 0.614\left|\pm\frac{7}{2}\right\rangle + 0.279\left|\pm\frac{3}{2}\right\rangle + 0.09\left|\mp\frac{1}{2}\right\rangle + 0.458\left|\mp\frac{5}{2}\right\rangle - 0.035\left|\mp\frac{9}{2}\right\rangle - 0.295\left|\mp\frac{13}{2}\right\rangle$$

$$\mu_8 = \pm 2.06\mu_B$$

APPENDIX II

$$Z_{pq} = \cosh\left(\frac{E_{pq}^{(1)}}{T}\right) + 4\exp\left(\frac{-E_{pq}^{(2)}}{T}\right),$$

$$F_{\varphi_1\varphi_2} = \sum_{\{pq\}}\left\{\frac{\partial^2 E_{pq}^{(1)}}{\partial\varphi^2}\frac{\sinh(E_{pq}^{(1)}/T)}{Z} + \frac{8}{T}\left[\left(\frac{\partial E_{pq}^{(1)}}{\partial\varphi}\right)^2 + \frac{1}{2}E_{pq}^{(1)}\frac{\partial^2 E_{pq}^{(1)}}{\partial\varphi^2}\right]\frac{1+\cosh(E_{pq}^{(1)}/T)\exp(-E^{(2)}/T)}{Z^2} - \frac{4}{T^2}E_{pq}^{(1)}\left(\frac{\partial E_{pq}^{(1)}}{\partial\varphi}\right)^2\frac{\sinh(E_{pq}^{(1)}/T)\exp(-E^{(2)}/T)}{Z^2} - \frac{8}{T^2}E_{pq}^{(1)}\left(\frac{\partial E_{pq}^{(1)}}{\partial\varphi}\right)^2 \times\frac{[1+\cosh(E_{pq}^{(1)}/T)\exp(-E^{(2)}/T)]\sinh(E_{pq}^{(1)}/T)}{Z^3} + \frac{2}{T}E^{(2)}\frac{\partial^2 E_{pq}^{(2)}}{\partial\varphi^2}\frac{\sinh(E^{(2)}/T)\exp(-E^{(2)}/T)}{Z^2} - \frac{2}{T^2}E^{(2)}\left(\frac{\partial E_{pq}^{(1)}}{\partial\varphi}\right)^2\frac{\exp(-E^{(1)}/T)}{Z^2} \times\left[\cosh(E_{pq}^{(1)}/T) - \frac{2\sinh^2(E_{pq}^{(1)}/T)}{Z}\right]\right\}$$

REFERENCES

1. A. K. Zvezdin, V. M. Matveev, A. A. Mukhin, and A. I. Popov, *Rare-Earth Ions in Magnetically Ordered Crystals* (Nauka, Moscow, 1985).
2. V. N. Vasil'ev and E. N. Matveĭko, in *Physical Properties of Ferrites* (Inst. Fiz. Sib. Otd. Akad. Nauk SSSR, Krasnoyarsk, 1987), p. 46.
3. G. S. Patrin, N. V. Volkov, and V. N. Vasiliev, Phys. Lett. A **230**, 96 (1997).
4. G. S. Patrin, N. V. Volkov, and E. V. Eremin, Pis'ma Zh. Éksp. Teor. Fiz. **63** (12), 941 (1996) [JETP Lett. **63**, 725 (1996)].
5. S. Geschwind and J. P. Remeika, Phys. Rev. **122** (3), 757 (1961).
6. E. J. Samuelsen and G. Shirane, Phys. Status Solidi **42**, 241 (1970).
7. A. G. Gurevich, *Magnetic Resonance in Ferrites and Antiferromagnets* (Nauka, Moscow, 1973).
8. E. F. Kustov, G. A. Bondurkin, É. N. Murav'ev, and V. P. Orlovskiĭ, *Electronic Spectra of Rare-Earth Compounds* (Nauka, Moscow, 1981).
9. K. R. Lee, M. J. Leask, and W. P. Wolf, J. Phys. Chem. Solids **23** (10), 1381 (1962).
10. P. Grunberg, S. Hufner, E. Orlich, and J. Schmitt, J. Appl. Phys. **40** (3), 1501 (1969).

Translated by Yu. Epifanov

Physics of the Solid State, Vol. 42, No. 10, 2000, pp. 1887–1890. Translated from Fizika Tverdogo Tela, Vol. 42, No. 10, 2000, pp. 1839–1841.

MAGNETISM AND FERROELECTRICITY

Study of the Thermal Properties of $Ba_{1-x}Sr_xTiO_3$ Thin Films by the AC Hot-Probe Method

S. T. Davitadze*, S. N. Kravchun*, B. A. Strukov*, S. A. Taraskin*, B. M. Gol'tsman, V. V. Lemanov**, and S. G. Shul'man****

** Moscow State University, Vorob'evy gory, Moscow, 119899 Russia*

*** Ioffe Physicotechnical Institute, Russian Academy of Sciences, Politekhnicheskaya ul. 26, St. Petersburg, 194021 Russia*

Received March 28, 2000

Abstract—The heat capacity and heat conductivity of $Ba_{1-x}Sr_xTiO_3$ (x = 0.2, 0.5, 0.8) polycrystalline films 1.5–2.0 μm thick on a massive substrate have been studied by the ac hot-probe method for three-layer systems (conducting probe–dielectric film–substrate) at temperatures ranging from 100 to 400 K. It is found that the thermal properties exhibit anomalies in the phase transition range. *© 2000 MAIK "Nauka/Interperiodica".*

1. INTRODUCTION

Investigations of the heat capacity and heat conductivity of thin ferroelectric films are of considerable scientific and practical interest. However, the thermal properties of these materials remain very poorly understood. The reason for this is that traditional ac calorimetry is only applicable to measuring the heat capacity of samples with thicknesses of 100 μm and more [1]. When applied to thinner ferroelectric films, this method determines the total heat capacity of the film–substrate system, which complicates analysis of the properties of the thin film itself [2]. In some experiments, the substrate thickness was reduced to the micron scale [3], and, in these conditions, ac calorimetry became applicable to investigating the heat capacity of thin superconductor films.

As was shown earlier [4–6], the most promising approach for measuring the heat capacity and heat conductivity of thin dielectric films uses the ac hot-probe method. In the present work, this method was employed to study the heat capacity and heat conductivity of the $Ba_{1-x}Sr_xTiO_3$ (BST) thin ferroelectric films with x = 0.2, 0.5, and 0.8, which undergo phase transitions within the temperature range from 100 to 400 K.

2. EXPERIMENTAL TECHNIQUE

Essentially, the ac hot-probe method is as follows. Two metal strips (probes) of negligible thickness are deposited onto the film to be studied and directly onto the substrate on which the film was deposited, and an ac electric current is passed through these strips (Fig. 1). Heating the probes by the current results in a periodic variation of their temperature, which manifests itself in probe resistance oscillations. By measuring the amplitude and phase of these oscillations, one can determine those of the probe temperature oscillations. In turn, the amplitude and phase of the probe temperature oscillations depend on the thermal characteristics (heat capacity and heat conductivity) of the material in thermal contact with the probes. As follows from the theoretical treatment of this heat problem [5], the ratio of the complex amplitudes $\tilde{\Theta}_1/\tilde{\Theta}_2$ of the temperature oscillations of these two probes depends in a complex way on the heat conductivity and heat capacity of the film under study (Eq. (7) in [5]). (Hereafter, subscript 1 refers to the film, and subscript 2, to the substrate.) As was shown, the highest accuracy of measuring the film thermal properties is attained when the penetration depth of the heat wave, which is equal to $(a_1/\omega)^{1/2}$, is comparable to or less than the film thickness h_1, i.e., when $z_1 = h_1(\omega/a_1)^{1/2} \geq 1$ (here, ω is the circular frequency of the ac electric current of the probe, $a = \lambda/(C_p\rho)$ is the thermal diffusivity, λ is the heat conductivity, C_p is the heat capacity, and ρ is the density).

For BST films about 1 μm thick at room temperature, this condition is met for frequencies of about 100 kHz. However, in our experimental setup, the maximum current frequency was 10 kHz, which corre-

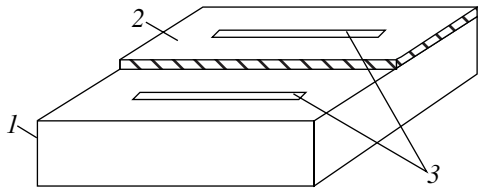

Fig. 1. Film arrangement on the substrate: (*1*) substrate, (*2*) BST film, and (*3*) palladium probes.

1063-7834/00/4210-1887$20.00 © 2000 MAIK "Nauka/Interperiodica"

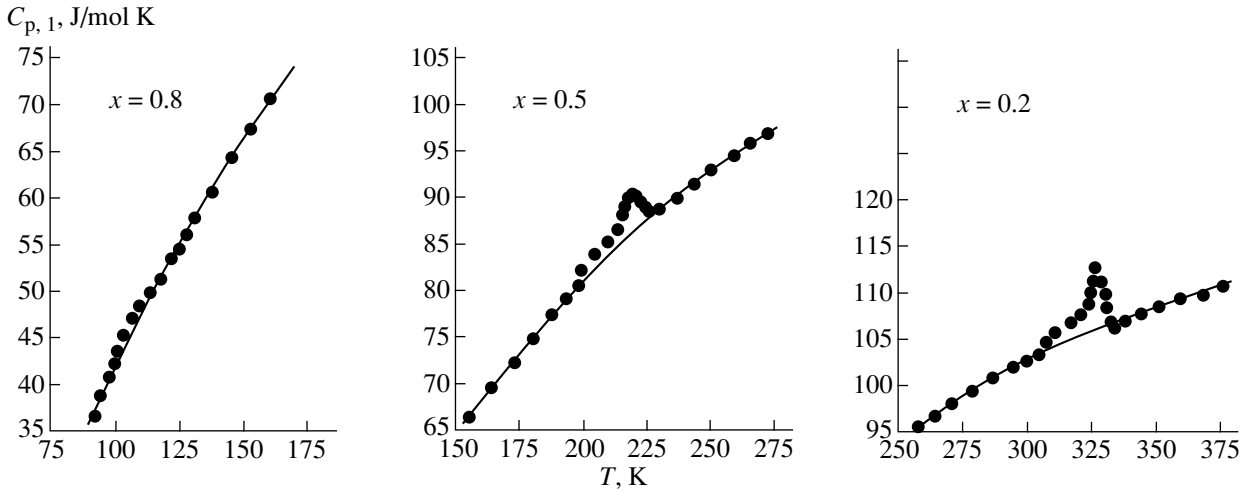

Fig. 2. Temperature dependence of the heat capacity of $Ba_{1-x}Sr_xTiO_3$ film samples in the region of the ferroelectric phase transition.

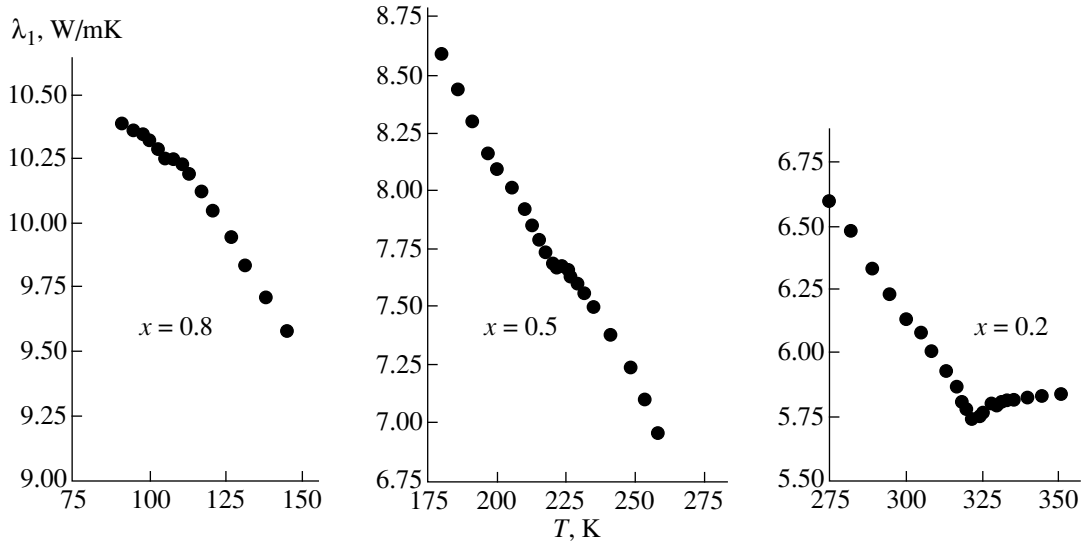

Fig. 3. Temperature dependence of the heat conductivity coefficient of $Ba_{1-x}Sr_xTiO_3$ film samples in the region of the ferroelectric phase transition.

sponds to $z_1 < 1$. This allows one to apply asymptotic approximation methods to the experimental data.

If the penetration depth of a temperature wave into the film is noticeably larger than its thickness ($z_1 \leq 0.1$–0.3) but considerably less than the substrate thickness ($z_2 \longrightarrow \infty$), a condition that holds in our experiment, the $\tilde{\Theta}_1/\tilde{\Theta}_2$ ratio can be recast in a simpler form

$$\tilde{\Theta}_1/\tilde{\Theta}_2 \approx 1 + (1 + i)(X - 1/X)z_1. \quad (1)$$

Here, $X = b_2/b_1$ is the thermal contrast factor, and $b = (\lambda C_p \rho)^{1/2}$ is the thermal activity.

If $X^2 \ll 1$, from relationship (1), we can derive the expression containing only one thermal parameter of a film, namely, the heat capacity

$$\tilde{\Theta}_1/\tilde{\Theta}_2 \approx 1 - (1 + i)C_p\rho_1 h_1 \omega^{1/2}/b_2. \quad (2)$$

It is readily seen that, in the asymptotic limit, the film heat capacity can be determined by means of Eq. (2) from measurements of the amplitude and phase of the probe temperature oscillations. For the reverse condition $X^2 \gg 1$, Eq. (1) yields the expression that contains not the heat capacity of a film, as in Eq. (2), but the heat conductivity

$$\tilde{\Theta}_1/\tilde{\Theta}_2 \approx 1 + (1 + i)h_1 \omega^{1/2} b_2/\lambda_1. \quad (3)$$

Thermal properties of $Ba_{1-x}Sr_xTiO_3$ films in the region of the phase transitions

x	T_c, K	ΔQ, J/mol	ΔS, J/mol K	λ_1, W/m K
0.2	325	93	0.33	5.7
0.5	224	78	0.38	7.7
0.8	106	44	0.45	10.3

Note: T_c is the phase transition temperature, ΔQ is the excess transition energy, ΔS is the excess entropy, and λ_1 is the heat conductivity coefficient at T_c.

Thus, Eq. (3) permits the determination of the heat conductivity of a film.

With this in mind, we chose as substrates for measurements of the heat capacity and heat conductivity of $Ba_{1-x}Sr_xTiO_3$ films [thermal activity b_1 = 5000 W $c^{1/2}$/(m^2 K) at $T \approx 300$ K] materials with substantially different thermal activities, namely, fused silica SiO_2 [$b_2 \approx 1500$ W $s^{1/2}$/(m^2 K) at $T \approx 300$ K], which satisfies the condition $X^2 \ll 1$, and leucosapphire Al_2O_3 [$b_2 \approx 12\,500$ W $s^{1/2}$/(m^2 K) at $T \approx 300$ K], which meets the condition $X^2 \gg 1$. It is seen that, for measurements of the heat capacity, $X^2 \approx 0.1$, and, for those of the heat conductivity, $X^2 \approx 6.3$.

The samples studied were polished plates of fused silica or leucosapphire (4 × 4 mm in size), half their surface was coated with the $Ba_{1-x}Sr_xTiO_3$ films 1.5–2 μm thick. Two thermal probes in the form of narrow palladium strips were deposited on each sample. One probe was on the ferroelectric film, and the other, directly on the substrate (Fig. 1). The probe area was equal to 4.0 × 0.5 mm, the thickness was 0.1 μm, and the resistance ranged from 25 to 150 Ω. The probe parameters were chosen based on the following considerations: in accordance with the theoretical model considered, the probe geometry should provide a plane heat-flow front, the resistance should be not too large to maintain a high enough heat flow power, and the thickness should be absolutely minimal so that the probe does not noticeably contribute to the measured signal due to its own heat conductivity and capacity. The substrate thickness was 0.3–0.5 mm for fused silica and 0.7–1 mm for leucosapphire, which satisfied the condition $z_2 \longrightarrow \infty$ (in our case, $z_2 > 10$) for the heating frequency range chosen by us (1000–1500 Hz).

The $Ba_{1-x}Sr_xTiO_3$ ferroelectric films were prepared by RF magnetron sputtering with the substrate in the off-axis position [7]. Ceramic targets of the appropriate composition were sputtered in a mixture of argon with oxygen at a substrate temperature of 700°C. The film growth rate was 5–8 nm/min.

3. RESULTS

The results of the heat-capacity and heat-conductivity measurements of BST film samples are presented in Figs. 2 and 3. It is seen that all samples exhibit clearly pronounced anomalies in the phase transition range, and their positions correspond to the known phase diagram of the BST system [8, 9]. This means that the ac hot-probe method is an efficient way of detecting phase transitions in thin dielectric films.

The table lists the thermal parameters characterizing the phase transitions in the $Ba_{1-x}Sr_xTiO_3$ films, which were calculated from experimental data. The excess transition energy ΔQ for films with $x = 0.2$ agrees well with the value derived for bulk ceramic samples of the same composition, $\Delta Q = 91.5$ J/mol [10].

Note that the phase transition temperatures presented in the table and determined from the anomalies in the thermal properties of the films (Figs. 2, 3) are slightly lower than those derived from the maximum of the temperature dependence of the permittivity for the bulk ceramics [8, 9]. For bulk ceramics, the phase transition temperatures are 345 K ($x = 0.2$), 240 K ($x = 0.5$), and 120 K ($x = 0.8$); i.e., the transition temperature in films is lower by 15–20 K. This effect was observed in earlier studies [11] of the permittivity of films and ceramic targets which were ablated in the preparation of these films, and it can be due to a deviation from stoichiometry, a change in the solid-solution composition, and mechanical stresses in the films.

It is seen from Fig. 2 and the table that, as x, i.e., the $SrTiO_3$ concentration, increases, a decrease in the transition temperature is accompanied by a decrease in the height of the heat-capacity peak at $T = T_c$ and a substantial smearing of the phase transition. This can apparently be accounted for by the fact that, at $x \geq 0.8$, BST solid solutions possess properties approaching those of relaxors.

ACKNOWLEDGMENTS

This work was supported by the Universities of Russia Program and by the Russian Foundation for Basic Research, project no. 00-02-16916.

REFERENCES

1. P. F. Sullivan and G. Seidel, Phys. Rev. **173** (3), 679 (1968).
2. A. Onodera, K. Yoshio, C. C. Myint, *et al.*, in *Abstracts of 9th European Meeting on Ferroelectricity, Prague, 1999*, p. 262.

3. F. Fominaya, T. Fournier, P. Gandit, and J. Chaussy, Rev. Sci. Instrum. **68**, 4191 (1997).
4. H. P. Filippov, S. N. Kravchun, and A. S. Tleubaev, in *Compendium of Thermophysical Property Measurement Method 2* (Plenum, New York, 1992), Chap. 13, p. 375.
5. S. N. Kravchun, S. T. Davitadze, N. S. Mizina, and B. A. Strukov, Fiz. Tverd. Tela (S.-Peterburg) **39**, 762 (1997) [Phys. Solid State **39**, 675 (1997)].
6. S. T. Davitadze, S. N. Kravchun, B. A. Strukov, *et al.*, Fiz. Tverd. Tela (S.-Peterburg) **39**, 1299 (1997) [Phys. Solid State **39**, 1154 (1997)].
7. B. M. Gol'tsman, N. V. Zaĭtseva, Yu. L. Kretser, *et al.*, Fiz. Tverd. Tela (S.-Peterburg) **37**, 3723 (1995) [Phys. Solid State **37**, 2052 (1995)].
8. V. V. Lemanov, Fiz. Tverd. Tela (S.-Peterburg) **39**, 1645 (1997) [Phys. Solid State **39**, 1468 (1997)].
9. V. V. Lemanov, E. P. Smirnova, P. P. Syrnikov, and E. A. Tarakanov, Phys. Rev. B **54**, 3151 (1996).
10. K. Ya. Borman, B. A. Strukov, S. A. Taraskin, and V. Ya. Fritsberg, Izv. Akad. Nauk SSSR, Ser. Fiz. **33**, 1162 (1969).
11. B. M. Gol'tsman, A. I. Dedyk, V. V. Lemanov, *et al.*, Fiz. Tverd. Tela (S.-Peterburg) **38**, 2493 (1996) [Phys. Solid State **38**, 1368 (1996)].

Translated by G. Skrebtsov

Physics of the Solid State, Vol. 42, No. 10, 2000, pp. 1891–1897. Translated from Fizika Tverdogo Tela, Vol. 42, No. 10, 2000, pp. 1842–1847.

LATTICE DYNAMICS AND PHASE TRANSITIONS

Nonsphericity of Atomic Wave Functions in the Theory of Peierls-Type Structural Phase Transition

A. L. Semenov

Ul'yanovsk State University, Ul'yanovsk, 432700 Russia

e-mail: semenov@quant.ulsu.ru

Received February 15, 2000

Abstract—A theory of Peierls-type metal–semiconductor phase transition has been developed. The proposed model accounts for the cubic anharmonicity of interatomic interaction and the nonsphericity of atomic wave functions of electronic quantum states. The wave function overlapping results in the formation of a quasi-one-dimensional Peierls band in the electronic spectrum of the system. It is shown that structural transformations of the crystal lattice upon the phase transition represent a pairwise approach of atoms along the crystal axis *C* and a uniform strain of atomic chains taking on a zigzag shape. The theoretical results obtained are applied to the interpretation of experimental data on the metal–semiconductor phase transition in vanadium dioxide.

1. INTRODUCTION

It is known that, at temperature T below the critical temperature T_0, a chain of equidistantly arranged interacting atoms that have one outer-shell electron each is unstable toward the pairwise approach of atoms and the formation of the energy gap in the electronic spectrum at the Fermi level [1–7]. This phase transition is usually referred to as the Peierls transition, and the system in which this transition occurs, as the Peierls system [1–7].

The Peierls-type phase transition was experimentally observed in a number of quasi-one-dimensional materials with different occupancies of the quasi-one-dimensional conduction band: complexes of platinum with a mixed valence [1], TCNQ salts [1], blue bronze $K_{0.3}MoO_3$ [2, 8], vanadium dioxide [3], TaS_3, $TaSe_3$, NbS_3, $NbSe_3$, $(NbSe_4)_{10/3}I$, $(NbSe_4)_2I$, etc. [2]. The distinctive feature indicating the Peierls nature of the phase transition in the above materials is that the wave number q of the static phonon mode, which is formed upon transition to the low-temperature semiconducting phase, is equal to double the quasi-wave number k_f of an electron at the Fermi level ($q = 2k_f$) for all these compounds.

The transition to the low-temperature semiconducting phase can be accompanied by a uniform strain of the Peierls-type atomic chain due to a strong phonon–phonon interaction. In turn, this gives rise to a uniform strain of the quasi-one-dimensional material as a whole. In the case of tensile strain, the Peierls chain can take on a zigzag shape, as is shown in the figure for vanadium atoms in vanadium dioxide [3]. The theory of this effect for spherically symmetric electronic wave functions of atoms within the four-level model approximation for the density of states in the Peierls system was elaborated in [7].

It is seen from the figure that the overlap integral of electronic wave functions of the neighboring atoms upon transition to the low-temperature semiconducting phase changes owing to the chain dimerization (the pairwise approach of atoms along the chain) and the nonsphericity of electronic wave functions of atoms upon their displacement from the chain axis. However, to our knowledge, the nonsphericity of wave functions of electronic quantum states in an atom has never been considered in the theory of Peierls-type metal–semiconductor phase transition.

In the present work, we proposed the theory of a structural phase transition of the Peierls type. This theory describes the transition in a chain of equidistantly arranged atoms to the state in which the distances between the nearest neighboring atoms alternate and the chain itself has a zigzag shape (figure). The interaction between atoms involves two components. The first component has a covalent nature and describes the interatomic attraction. This component is determined by the overlapping of electronic wave functions of the

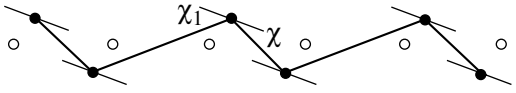

Schematic arrangement of vanadium atoms in metallic (open circles spaced at equal intervals $r_0 = 2.85$ Å) and semiconducting (closed circles spaced at alternating intervals $r_1 = 2.65$ Å and $r_2 = 3.12$ Å) phases of vanadium oxide. The angles between the axis of the dumbbell-like 3*d* wave function and the directions to the nearest neighboring atoms in the low-temperature semiconducting phase of VO_2 are denoted as χ and χ_1.

1063-7834/00/4210-1891$20.00 © 2000 MAIK "Nauka/Interperiodica"

neighboring atoms and can be calculated in the framework of the microscopic theory with allowance made for the nonsphericity of atomic wave functions. The second component represents the interatomic repulsion and is phenomenologically treated by way of expanding into a Taylor series in terms of atomic displacements from the equidistant equilibrium position up to the third-order terms (inclusion of the cubic anharmonicity of interatomic interaction).

2. ELECTRONIC SPECTRUM OF SYSTEM

Let us consider a chain of atoms, each with one outer shell electron. Within the tight binding approximation, the Hamiltonian of the electronic subsystem can be written in the following form [1]:

$$H = \sum_n B_{n,n+1}(a_n^+ a_{n+1} + a_{n+1}^+ a_n), \quad (1)$$

where n is the number of an atom in the chain, a_n^+ and a_n are the creation and annihilation operators for an electron of the nth atom,

$$B_{n,n+1} = B + (-1)^n G \quad (2)$$

is the overlap integral of electronic wave functions for the nth and $(n+1)$th neighboring atoms,

$$B = \frac{B_{n,n+1} + B_{n-1,n}}{2} \quad (3)$$

is the mean value of the $B_{n,n+1}$ overlap integral, and

$$G = (-1)^n \frac{B_{n,n+1} + B_{n-1,n}}{2} \quad (4)$$

is the deviation of the $B_{n,n+1}$ overlap integral from the mean value B.

Hamiltonian (1) can be diagonalized using the Bogoliubov canonical transformation [9]. Now, we introduce the Fermi collective second quantization operators c_k and c_k^+ according to the formula

$$a_n = \frac{1}{\sqrt{N}} \sum_k c_k e^{ikn}, \quad (5)$$

where N is the number of atoms in the chain, $k = -\pi + 2\pi l/N$ ($l = 1, \ldots, N$), and $c_{k+2\pi} = c_k$. In the new operator representation, Hamiltonian (1) takes the form

$$H = \sum_k 2(B\cos k c_k^+ c_k + iG\sin k c_k^+ c_{k-\pi}). \quad (6)$$

In Hamiltonian (6), we perform one more canonical transformation to the Fermi operators α_k and α_k^+ according to the formula

$$c_k = \frac{\alpha_k + i\varphi_k \alpha_{k-\pi}}{\sqrt{1+\varphi_k^2}}. \quad (7)$$

The function φ_k in formula (7) is chosen so that the Hamiltonian in the new variables α_k and α_k^+ has the diagonal form

$$H = \sum_k \varepsilon_k \alpha_k^+ \alpha_k. \quad (8)$$

Substituting Eq. (7) into Hamiltonian (6) and setting off-diagonal elements equal to zero, we obtain φ_k and the dispersion ε_k, that is,

$$\varphi_k = \frac{B\cos k - \mathrm{sgn}(\cos k)\sqrt{(B\cos k)^2 + (G\sin k)^2}}{G\sin k}, \quad (9)$$

$$\varepsilon_k = 2\,\mathrm{sgn}(\cos k)\sqrt{(B\cos k)^2 + (G\sin k)^2}. \quad (10)$$

From relationship (10), it follows that the electronic spectrum ε_k for the atomic chain with alternating overlap integrals (2)–(4) of electronic wave functions for the neighboring atoms (at $G \neq 0$) is characterized by two bands: the lower band in the ground state is completely filled, and the upper is empty (the semiconducting phase). For the chain with the equidistantly arranged atoms (at $G = 0$), spectrum (10) represents one half-filled band (the metallic phase).

The B and G quantities entering into Eq. (10) can be calculated with due regard for the fact that the $3d$ wave function $\psi(r)$ in the spherical coordinates r, θ, and φ is defined by the relationship

$$\psi(\mathbf{r}) = \frac{1}{81\sqrt{6\pi}} \exp\left(-\frac{\rho}{3}\right)\rho^2(1 - 3\cos^2\theta), \quad (11)$$

where

$$\rho = \frac{zr}{a_B}, \quad a_B = \frac{\hbar^2}{me^2}. \quad (12)$$

Here, a_B is the Bohr radius, z is the charge of the atomic core (in terms of elementary charge), m is the electron mass, and e is the electron charge.

In the case when the distance $r_{n,n+1}$between the neighboring atoms is several times larger than the effective radius R of the atomic wave function and the angle $\chi_{n,n+1}$ between the axis of the dumbbell-like $3d$ wave function of the nth [$(n+1)$th] atom and the straight line connecting the centers of the nth and $(n+1)$th atoms is considerably less than unity ($\chi_{n,n+1} \ll 1$), the overlap integral $B_{n,n+1}$ in view of Eq. (11) is defined by the following approximate relationship:

$$B_{n,n+1} \propto \exp\left\{-\frac{r_{n,n+1}}{R}\right\}(1 - 3\cos^2(\chi_{n,n+1}))^2. \quad (13)$$

In the particular case of spherically symmetric wave functions or at $\chi_{n,n+1} = 0$, relationship (13) transforms into the well-known result [7, 10].

With allowance made for the possible pairwise approach of the neighboring atoms and a uniform strain of the chain, the distance $r_{n,n+1}$ between the neighboring atoms can be written as

$$r_{n,n+1} = r_0 + R\zeta + (-1)^{n+1}R\xi, \quad (14)$$

where r_0 is the interatomic distance in the metallic phase, ζ is the parameter accounting for the change in the chain length (the uniform strain parameter), and ξ is the parameter characterizing the pairwise approach of atoms in the chain (the reduced amplitude of the static phonon at the Brillouin zone edge). Taking into account expression (14) and the condition $\chi_{n,n+1} \ll 1$, the overlap integral $B_{n,n+1}$ (13) takes the form

$$B_{n,n+1} = b\exp(-\zeta + (-1)^n\xi)(1 - 3\chi^2_{n,n+1}), \quad (15)$$

where b is the overlap integral of 3d wave functions for the nearest neighboring atoms in the metallic phase at $\xi = \zeta = 0$. The phases of atomic wave functions in Hamiltonian (1) are chosen so that the b integral in expression (15) is the real positive quantity.

Substituting Eq. (15) into Eqs. (3) and (4) with due regard for the relationship (see figure)

$$\chi_{n,n+1}\begin{cases}\chi, & n = 2l\\ \chi_1, & n = 2l+1\end{cases} \quad (16)$$

(where l is an integer) gives the relationships for the B and G quantities

$$B = b\exp\{-\zeta\} \times\left[\cosh(\xi) - \frac{3}{2}(\exp\{\xi\}\chi^2 + \exp\{-\xi\}\chi_1^2)\right], \quad (17)$$

$$G = b\exp\{-\zeta\} \times\left[\sinh(\xi) - \frac{3}{2}(\exp\{\xi\}\chi^2 - \exp\{-\xi\}\chi_1^2)\right]. \quad (18)$$

As follows from the figure and Eq. (14), the χ and χ_1 angles are related by the expression

$$\cos(\chi + \chi_1) = \frac{(R\zeta)^2 + 2r_0R\zeta - (R\xi)^2 - r_0^2}{(r_0 + R\zeta)^2 - (R\xi)^2}. \quad (19)$$

Therefore, the electronic spectrum of the system is described by formula (10) with the B and G quantities defined by Eqs. (17) and (18) and the χ and $\chi_1$angles related by Eq. (19). The reduced amplitude χ of the static phonon mode at the Brillouin zone edge, the dimensionless parameter ξ of the uniform elongation of the atomic chain ζ, and the angle χ between the axis of the 3d wave function of the atom and the direction to the nearest neighboring atom are the independent order parameters of the metal–semiconductor phase transition.

3. THERMODYNAMIC EQUILIBRIUM EQUATIONS FOR THE χ, ξ, AND ζ ORDER PARAMETERS OF METAL–SEMICONDUCTOR PHASE TRANSITION IN THE PEIERLS SYSTEM

The potential energy U of the interatomic interaction in the atomic chain is given by

$$U = F_e + \sum_{n=1}^{N-1} W(r_{n,n+1}) + \sum_{n=1}^{N}\gamma\delta_n^2, \quad (20)$$

where

$$F_e = \mu N - k_BT\sum_k \ln\left(1 + \exp\left(\frac{\mu - \varepsilon_k}{k_BT}\right)\right) \quad (21)$$

is the covalent component of the potential energy due to the overlapping of the electronic wave functions of the neighboring atoms, μ is the chemical potential of electrons, and ε_k is the electronic spectrum defined by Eqs. (10), (17), and (18). The summation over k in expression (21) is performed over all the possible one-electron states with allowance made for the spin degeneracy. Equation (21) represents the free energy F_e of the electronic subsystem, which depends on the mutual arrangement of atoms in the chain.

The second term in the right-hand side of Eq. (20) describes the total potential energy of the interatomic interaction within the atomic chain minus the covalent component (21). This term can be phenomenologically represented as the expansion in a Taylor series in terms of atomic displacements from the equidistant position in the chain

$$W(r) = W_1(r - r_0) + \frac{W_2}{2}(r - r_0)^2 + \frac{W_3}{6}(r - r_0)^3, \quad (22)$$

where W_i is the expansion coefficient of the ith order term in the Taylor series.

The third term in the right-hand side of Eq. (20) within the harmonic approximation describes the potential energy of the interaction between the chain atoms and atoms outside the chain. In this term, γ is the effective coefficient of the interaction between the chain atoms and the surrounding atoms, and δ_n is the displacement of the nth atom from the equidistant equilibrium position in the metallic phase.

As is seen from the figure, the atomic displacements δ_n are identical for all the atoms and, at $\zeta \geq 0$, are defined by the expression

$$\delta_n = \delta = \frac{1}{4}\sqrt{2r_1^2 + 2r_2^2 - 4r_0^2}, \quad (23)$$

where $r_{1,2} = r_0 + R\zeta \mp R\xi$ determines the minimum and maximum interatomic distances in the semiconducting phase, respectively.

The thermodynamically equilibrium order parameters ξ, ζ, and χ of the metal–semiconductor phase transition in the mean field approximation are determined

from the condition for the minimum of the potential energy U defined by Eq. (20), that is,

$$\frac{\partial U}{\partial \xi} = 0, \quad \frac{\partial U}{\partial \zeta} = 0, \quad \frac{\partial U}{\partial \chi} = 0. \tag{24}$$

In the last equation of system (24), it is assumed that the function $\chi_1(\chi)$ is described by Eq. (19).

Substituting Eqs. (20)–(23) into relationships (24), we obtain the thermodynamic equilibrium equations for the Peierls system

$$b(\alpha_2\xi + \alpha_3\xi\zeta) + \frac{1}{N}\sum_k f_k\frac{\partial \varepsilon_k}{\partial \xi} = 0, \tag{25}$$

$$b\left(\alpha_1 + \alpha_2\zeta + \frac{\alpha_3}{2}(\xi^2 + \zeta^2)\right) + \frac{1}{N}\sum_k f_k\frac{\partial \varepsilon_k}{\partial \zeta} = 0, \tag{26}$$

$$\sum_k f_k\frac{\partial \varepsilon_k}{\partial \chi} = 0. \tag{27}$$

Here,

$$f_k = [1 + \exp((\varepsilon_k - \mu)/k_BT)]^{-1} \tag{28}$$

is the Fermi–Dirac distribution. In Eqs. (25)–(27), we introduced the following designations:

$$\alpha_1 b = (W_1 + \gamma r_0/2)R, \quad \alpha_2 b = (W_2 + \gamma/2)R^2, \quad \alpha_3 b = W_3 R^3. \tag{29}$$

At small atomic displacements from the equidistant positions when the following relationships are met

$$\xi \ll r_0/R, \quad \zeta \ll r_0/R,$$

expression (19) can be approximately rearranged to give

$$\chi + \chi_1 = \sqrt{\frac{8R\zeta}{r_0}}. \tag{30}$$

In this case, the overlap integral (15) takes the approximate form

$$B_{n,n+1} = b\exp\{-\zeta_1 + (-1)^n\xi_1\}, \tag{31}$$

where

$$\xi_1 = \xi + \frac{3}{2}\left(\left(\sqrt{\frac{8R\zeta}{r_0}} - \chi\right)^2 - \chi^2\right), \tag{32}$$

$$\zeta_1 = \zeta + \frac{3}{2}\left(\left(\sqrt{\frac{8R\zeta}{r_0}} - \chi\right)^2 + \chi^2\right). \tag{33}$$

According to Eqs. (2)–(4) and (31), the expressions for the functions B [Eq. (17)] and G [Eq. (18)], which enter into the electronic spectrum (10), can be written as follows:

$$G = b\exp\{-\zeta_1\}\sinh(\xi_1), \tag{34}$$

$$B = b\exp\{-\zeta_1\}\cosh(\xi_1). \tag{35}$$

Now, we substitute Eqs. (28) and (10) into Eqs. (25)–(27) and pass on from $\sum_k$ to $\int \nu(E)dE$. Here,

$$\nu(E) = \frac{2N|E|}{\pi\sqrt{(4b^2\exp\{-2\zeta_1\}\cosh^2(\xi_1) - E^2)(E^2 - 4b^2\exp\{-2\zeta_1\}\sinh(\xi_1))}} \tag{36}$$

is the density of states, which corresponds to the electronic spectrum defined by Eq. (10). Then, we obtain

$$\alpha_2\xi + \alpha_3\xi\zeta + I_1 = 0, \tag{37}$$

$$\alpha_1 + \alpha_2\zeta + \frac{\alpha_3}{2}(\xi^2 + \zeta^2) + I_2 + (I_1 + I_2)\left(12\frac{R}{r_0} - \chi\sqrt{\frac{18R}{r_0\zeta}}\right) = 0, \tag{38}$$

$$I_2\chi - (I_1 + I_2)\sqrt{\frac{2R\zeta}{r_0}} = 0, \tag{39}$$

where

$$I_1 = -\frac{2GB}{\pi b}\int_G^B \frac{\tanh(E/(2k_BT))dE}{\sqrt{(B^2 - E^2)(E^2 - G^2)}}, \tag{40}$$

$$I_2 = \frac{2}{\pi b}\int_G^B \frac{E^2\tanh(E/(2k_BT))dE}{\sqrt{(B^2 - E^2)(E^2 - G^2)}}. \tag{41}$$

The constants α_1 and α_2, which enter into the thermodynamic equilibrium equations (37)–(39) for the Peierls system, can be determined from the following conditions. From expression (38) with allowance made for the condition

$$\xi(T_0) = \zeta(T_0) = \chi(T_0) = 0, \tag{42}$$

we have the relationship for the α_1 constant

$$\alpha_1 = -\frac{2}{\pi b}\int_0^{2b} \frac{E\tanh(E/(2k_BT_0))}{\sqrt{4b^2 - E^2}}dE. \tag{43}$$

Calculation of the integral in formula (43) gives the approximate expression

$$\alpha_1 = -\frac{4}{\pi}\left(1 - \frac{1}{6}\left(\frac{k_B T_0}{b}\right)^2\right). \quad (44)$$

The critical temperature T_0 of the Peierls-type structural phase transition within the mean field approximation is determined from the equation

$$\left.\frac{\partial^2 U}{\partial \xi^2}\right|_{\xi = \zeta = \chi = 0,\ T = T_0} = 0. \quad (45)$$

Hence, taking into account Eqs. (20)–(22), we obtain the relationship for the α_2 constant

$$\alpha_2 = \frac{8b}{\pi}\int_0^{2b} \frac{\tanh(E/(2k_B T_0))}{E\sqrt{4b^2 - E^2}}dE. \quad (46)$$

Calculation of the integral in formula (46) gives the approximate expression

$$\alpha_2 = \frac{4}{\pi}\ln\left(\frac{2be}{k_B T_0}\right). \quad (47)$$

Thus, we derived the thermodynamic equilibrium equations (37)–(39), which represent the closed system for determining the temperature dependences of the order parameters $\xi(T)$, $\zeta(T)$, and $\chi(T)$ for the Peierls system with allowance for the cubic anharmonicity of interatomic interaction and the nonsphericity of the 3*d* electron wave functions. The α_1 and α_2 constants, which enter into the thermodynamic equilibrium equations (37)–(39) for the Peierls system, are determined from formulas (44) and (47).

4. EQUATIONS FOR THE ξ, ζ, AND χ ORDER PARAMETERS OF METAL–SEMICONDUCTOR PHASE TRANSITION IN THE PEIERLS SYSTEM AT LOW TEMPERATURES

Let us now analyze the thermodynamic equilibrium equations (37)–(39) for the ξ, ζ, and χ order parameters of the metal–semiconductor phase transition at low temperatures when the following condition is met:

$$k_B T \ll b\exp\{-\zeta_1\}\sinh(\xi_1). \quad (48)$$

Then, in formulas (40) and (41), it is possible to put

$$\tanh\left(\frac{E}{2k_B T}\right) \cong 1. \quad (49)$$

By calculating the integrals in Eqs. (40) and (41), we approximately obtain

$$I_1 = -\frac{4\exp\{-\zeta_1\}\sinh(\xi_1)}{\pi}K\left(\frac{1}{\cosh(\xi_1)}\right), \quad (50)$$

$$I_2 = -\frac{4\exp\{-\zeta_1\}\cosh(\xi_1)}{\pi}E\left(\frac{1}{\cosh(\xi_1)}\right), \quad (51)$$

where $K(x)$ and $E(x)$ are the Legendre complete normal elliptic integrals of the first and second kinds, respectively. By expanding the elliptic integrals $K(x)$ and $E(x)$ into a series in the vicinity of the point $x = 0$ [11], and the functions $\sinh(\xi_1)$ and $\cosh(\xi_1)$ into a Taylor series at the point $\xi_1 = 0$, from Eqs. (37)–(39), (50), and (51) at $\xi_1 < 1$, we obtain

$$\alpha_2\xi + \alpha_3\xi\zeta - \frac{5\exp\{-\zeta_1\}\xi_1}{2}\left(2 - \frac{\xi_1^2}{30}\right) = 0, \quad (52)$$

$$\alpha_1 + \alpha_2\zeta + \frac{\alpha_3}{2}(\xi^2 + \zeta^2) + \frac{3\exp\{-\zeta_1\}}{2} \times\left[1 + \frac{5}{6}\xi_1^2 + \frac{12R}{r_0}\left(1 - \chi\sqrt{\frac{r_0}{8R\zeta}}\right)\left(1 - \frac{5}{3}\xi_1 + \frac{5}{6}\xi_1^2\right)\right] = 0, \quad (53)$$

$$\left(1 + \frac{5}{6}\xi_1^2\right)\chi - \left(1 - \frac{5}{3}\xi_1 + \frac{5}{6}\xi_1^2\right)\sqrt{\frac{2R\zeta}{r_0}} = 0. \quad (54)$$

Relationships (52)–(54) with the parameters defined by Eqs. (32) and (33) represent the equilibrium equations for the ξ, ζ, and χ order parameters of the Peierls system at low temperatures T [condition (48)].

5. NUMERICAL ESTIMATES AND DISCUSSION

Numerical estimates were obtained for vanadium dioxide, which is characterized by the one-dimensional conduction band. This band is formed by the overlapping of the 3*d* wave functions of the vanadium atoms arranged in chains aligned parallel to the crystal axis *C* [3]. In the high-temperature metallic phase, the width E_0 of the one-dimensional conduction band is equal to $4b \cong 1.1$ eV, and the distance between the nearest neighboring vanadium atoms along the chain is $r_0 \cong 0.285$ nm. The metal–semiconductor phase transition in VO_2 is observed at the critical temperature $T_0 = 340$ K. In the low-temperature phase, the band gap E_g in the electronic spectrum is equal to approximately 0.6 eV, and the distances between the nearest neighboring vanadium atoms along the chain alternate: $r_1 = 0.265$ nm and $r_2 = 0.312$ nm. Since $r_1 + r_2 > 2r_0$, the vanadium atoms are displaced with respect to the chain axis, and the chain has a zigzag shape (figure).

Setting the numerical parameters characteristic of VO_2 in Eqs. (44) and (47), we determine the dimensionless coefficients α_1 and α_2 [Eq. (29)] in expansion (22) for the repulsive part of the potential energy of the interatomic interaction into a Taylor series in terms of atomic displacements from the equidistant position in the chain

$$\alpha_1 \cong -1.27, \quad \alpha_2 \cong 5.02. \quad (55)$$

From expression (10) for the electronic spectrum and Eqs. (32)–(35), we have

$$2\frac{E_g}{E_0} = \exp\{\xi - \zeta - 3\chi^2\} - \exp\left\{-\xi - \zeta - 3\left(\sqrt{\frac{8R\zeta}{r_0}} - \chi\right)^2\right\}, \quad (56)$$

where ξ and ζ, according to Eq. (14), are defined by the relationships

$$\xi = \frac{r_2 - r_1}{2R}, \quad (57)$$

$$\zeta = \frac{r_2 + r_1 - 2r_0}{2R}. \quad (58)$$

Upon substitution of relationships (57) and (58) into Eqs. (54) and (56), the last two expressions can be treated as the set of equations for determining the effective radius R of the atomic wave function and the χ angle. Substitution of the numerical parameters that correspond to vanadium dioxide into Eqs. (54) and (56) and the calculations with the use of Eqs. (30), (57), (58), (32), and (33) give

$$R \cong 0.46\ \text{Å}, \quad \chi \cong 0.032, \quad \chi_1 \cong 0.281, \quad \xi \cong 0.51, \quad \zeta \cong 0.076, \quad \zeta_1 \cong 0.196. \quad (59)$$

With these data, condition (48) for the applicability of Eqs. (52)–(54) takes the form

$$T \ll 10^3\ \text{K}. \quad (60)$$

Note that the effective radius R of the 3*d* wave function [see relationships (59)] is consistent with the general concepts of small localization radius of the *d* and *f* wave functions for transition metal compounds [3].

Relationships (52) and (53), with the parameters defined by Eqs. (32) and (33) and the numerical parameters (55) and (59) known from experiments, can be treated as the set of equations for determining the theoretical constant α_3 of the cubic anharmonicity of interatomic interaction and the dimensionless parameter ζ, which accounts for the elongation of atomic chain. However, the solution of the set of equations (52) and (53) for the unknown α_3 and ζ parameters presents considerable difficulties. It is more convenient to take the parameter ζ as being known from the experiment [see relationships (59)] and to solve the set of equations (52) and (53) for the unknown α_3 and α_2 parameters. Upon substitution of the numerical parameters (59) into Eqs. (52) and (53), we approximately obtain

$$\alpha_3 \cong -16.9, \quad \alpha_2 \cong 3.79. \quad (61)$$

As can be seen, this value of α_2 [in relationships (61)], which was obtained from the thermodynamic equilibrium equations (52)–(54) for the Peierls system at low temperatures $T \ll 10^3$K, is close to the value of α_2 [see relationships (55)] calculated from formula (47), which follows from condition (45) for the loss of stability of the metallic phase at the critical temperature T_0.

Note that the α_2 and α_3 coefficients (29) in expansion (22) can be independently estimated from the formula

$$\alpha_2 \cong \frac{ER^2 r_0}{b} \quad (62)$$

(where E is the Young modulus of the material along the crystal axis C) and the relationship [12]

$$\alpha_3 \approx -\frac{2\alpha_T r_0 \alpha_2^2 b}{k_B R}, \quad (63)$$

where α_T is the linear thermal expansion coefficient of the material along the crystal axis C.

Setting the characteristic numerical values $E \cong 3 \times 10^{12}$ dyn/cm^2 and $\alpha_T \approx 10^{-5}$ in expressions (62) and (63), we obtain the numerical coefficients $\alpha_2 \cong 5$ and $\alpha_3 \cong -10$. These values are close to the corresponding coefficients [relationships (55) and (61)], which were calculated in terms of the theory considered in the present work.

Thus, the quasi-one-dimensional model of Peierls-type metal–semiconductor phase transition was proposed in this work. The model accounts for the cubic anharmonicity of interatomic interaction and the nonsphericity of wave functions of electronic quantum states in the atom. It was shown that the phase transition to the semiconducting state is accompanied by the pairwise approach of atoms in the chain (dimerization) and a uniform strain of atomic chains, which leads to the formation of a zigzag structure.

The results obtained were applied to the interpretation of the experimental data on the metal–semiconductor phase transition in vanadium dioxide [3]. The effective radius R of the 3*d* wave function, the dimensionless elastic coefficient α_2, and the dimensionless coefficient of cubic anharmonicity α_3 were calculated in the framework of the proposed theory. The numerical values of these parameters are in good agreement with the independent estimates.

In closing, it should be noted that the experimental band gaps E_g ($T \ll T_0$) in the electronic spectrum for the majority of the known quasi-one-dimensional materials (TCNQ salts, TaS_3, $TaSe_3$, NbS_3, $NbSe_3$, $K_{0.3}MoO_3$, $(NbSe_4)_{10/3}I$, $(NbSe_4)_2I$, etc. [2]) are several times larger than those calculated within the harmonic and mean-field approximations [2]

$$E_g(T \ll T_0) \cong 3.5 k_B T_0. \quad (64)$$

The inclusion of the fluctuation effects (which is beyond the scope of the mean field approximation) in the treatment leads to a better agreement between theoretical and experimental results [13], but, most likely,

does not solve the problem, because even a small deviation of the system from the one-dimensionality results in strong suppression of fluctuations [1]. In the present work, we demonstrated that the inclusion of another important factor—the cubic anharmonicity of interatomic interaction (which is beyond the scope of the harmonic approximation)—can increase the band gap E_g several times as compared to the E_g value specified by Eq. (64).

REFERENCES

1. L. N. Bulaevskiĭ, Usp. Fiz. Nauk **115** (2), 263 (1975) [Sov. Phys. Usp. **18**, 131 (1975)].
2. G. Gruner, Rev. Mod. Phys. **60** (4), 1129 (1988).
3. A. A. Bugaev, B. P. Zakharchenya, and F. A. Chudnovskiĭ, in *Metal–Semiconductor Phase Transition and Its Applications* (Nauka, Leningrad, 1979), p. 28.
4. A. L. Semenov, Zh. Éksp. Teor. Fiz. **111** (4), 1398 (1997) [JETP **84**, 774 (1997)].
5. A. L. Semenov, Zh. Éksp. Teor. Fiz. **114** (4), 1407 (1998) [JETP **87**, 764 (1998)].
6. A. L. Semenov, Zh. Éksp. Teor. Fiz. **115** (4), 1297 (1999) [JETP **88**, 716 (1999)].
7. A. L. Semenov, Fiz. Tverd. Tela (S.-Peterburg) **39** (5), 925 (1997) [Phys. Solid State **39**, 826 (1997)].
8. S. N. Artemenko, A. F. Volkov, and S. V. Zaĭtsev-Zotov, Usp. Fiz. Nauk **166** (4), 434 (1996) [Phys. Usp. **39**, 403 (1996)].
9. N. N. Bogolyubov and N. N. Bogolyubov, Jr., *Introduction to Quantum Statistical Mechanics* (Nauka, Moscow, 1984; World Scientific, Singapore, 1982).
10. O. Madelung, *Introduction to Solid State Theory* (Springer-Verlag, Berlin, 1978; Nauka, Moscow, 1985).
11. H. B. Dwight, *Tables of Integrals and Other Mathematical Data* (Macmillan, London, 1961; Nauka, Moscow, 1983).
12. A. I. Ansel'm, *Introduction to the Theory of Semiconductors* (Nauka, Moscow, 1978).
13. M. V. Sadovskiĭ, Fiz. Tverd. Tela (Leningrad) **16**, 2504 (1974) [Sov. Phys. Solid State **16**, 1632 (1974)].

Translated by O. Borovik-Romanova

Physics of the Solid State, Vol. 42, No. 10, 2000, pp. 1898–1907. Translated from Fizika Tverdogo Tela, Vol. 42, No. 10, 2000, pp. 1848–1856.

LOW-DIMENSIONAL SYSTEMS AND SURFACE PHYSICS

Electronic Structure and Polarizability of Quantum Metallic Wires

A. N. Smogunov, L. I. Kurkina, and O. V. Farberovich

Voronezh State University, Universitetskaya pl. 1, Voronezh, 394893 Russia

e-mail: san@jok.vsu.ru

Received January 12, 2000

Abstract—The electronic structure and the linear response to an external electric field of simple metal wires with a quantum-size cross-section have been studied within the density-functional theory and the "jellium" model. It is found that an increase in the wire radius leads to a nonmonotonic change in the work function and static polarizability of the wire. The photoabsorption spectra of Na wires with different cross-sections are obtained. The effect of a dielectric environment on the properties of metallic wires is investigated. An increase in the permittivity of a medium brings about a decrease in the static polarizability of metallic wires. It is demonstrated that the surface plasma resonance in the photoabsorption cross-section for Na wires placed in a dielectric matrix is shifted from the continuous spectrum toward the range somewhat below the ionization threshold.

1. INTRODUCTION

In recent years, great interest has been expressed in the properties of low-dimensional quantum systems such as quasi-two-dimensional thin films, quasi-one-dimensional wires and tubes, and zero-dimensional quantum dots. These systems having a cross-section of an order of several nanometers exhibit pronounced quantum-well effects, and the size dependence of their characteristics is nonmonotonic. Moreover, the properties of size-quantized systems considerably depend on their effective dimension, which substantially affects the energy spectrum of quasi-particles. Specifically, a decrease in the dimension of an electronic system leads to a decrease in the number of final states upon electron scattering and, hence, to an increase in the electron mobility [1], which renders these systems promising for applications in high-speed elements of micro- and nanoelectronics. A reduction of the dimension in semiconductors brings about a substantial increase in the binding energy of impurity atoms due to an increase in the strength of the effective Coulomb field in the intrinsic region [2]. Furthermore, the effective dimension of the system affects the ratio between the number of atoms at the surface and the number of atoms in the bulk and, thus, changes the surface effects.

Unfortunately, the application of first-principles techniques known from the band theory to calculations of the electronic structure of low-dimensional systems involves considerable difficulties because of the lack of translational symmetry in at least one direction. For this reason, the study of similar objects requires the development of special models and methods. The properties of simple metals can be adequately described within the "jellium" model, according to which discrete charges of ionic skeletons of the lattice are uniformly "distributed" over the entire volume of the system. This model permits one to take into account the electron–electron interaction without substantial complications and to elucidate how the effective dimension of the system affects the properties of the electronic subsystem. The jellium model was successfully used to investigate the electronic properties of infinite and semi-infinite crystals [3–5], thin films [6], and clusters of simple metals [7–12]. In particular, the jellium model, as applied to clusters of simple metals, made it possible to interpret virtually all the main experimental results: the shell nature of the electronic structure and magic numbers [7, 8], an increase in the static polarizability [8–12] and a decrease in the frequency of surface plasmon [10–12] as compared to classical values, etc.

In the present work, we have studied the electronic structure of size-quantized wires of simple metals and their interaction with an electromagnetic field in the framework of the density-functional theory. The real metallic wires were simulated by infinite cylindrical jellium wires with the background density defined on the cylindrical coordinates as

$$n_+(\mathbf{r}) = n_0\Theta(R-r), \qquad (1)$$

where R is the wire radius, $n_0(r_s) = 3/(4\pi r_s^3)$ is the mean density of valence electrons in the bulk metal, and r_s is the Wigner–Seitz electron radius. The wire axis was chosen to be coincident with the Z axis.

1063-7834/00/4210-1898$20.00

2. THEORY

Within the density-functional theory, the ground-state electron density $n(\mathbf{r})$ of a metallic wire can be determined by solving the Kohn–Sham self-consistent single-particle equations [13–15] (hereafter, we will use the atomic units $e^2 = \hbar = m = 1$)

$$\left[-\frac{\nabla^2}{2} + V_{\text{eff}}(\mathbf{r})\right]\psi_j(\mathbf{r}) = \epsilon_j\psi_j(\mathbf{r}), \tag{2}$$

$$V_{\text{eff}}(\mathbf{r}) = V_C(\mathbf{r}) + V_{xc}(\mathbf{r}), \tag{3}$$

$$V_C(\mathbf{r}) = \int\frac{n(\mathbf{r}') - n_+(\mathbf{r}')}{|\mathbf{r} - \mathbf{r}'|}d\mathbf{r}', \tag{4}$$

$$n(r) = \sum_j f_j|\psi_j(\mathbf{r})|^2, \tag{5}$$

where the occupation numbers of electronic states f_j are equal to 0 and 2 for the spin-confined case under consideration. The effective potential energy V_{eff} of an electron involves the Coulomb V_C and exchange–correlation V_{xc} components. The positive charge density $n_+(\mathbf{r})$ in the jellium model is described by formula (1). For the V_{xc} component, we used the local approximation proposed by Vosko *et al.* [16].

The axial symmetry of the problem enables us to choose the wave functions ψ_j in the form of eigenfunctions of rotation and translation operators along the Z axis

$$\psi_j(\mathbf{r}) = \frac{e^{i(m\varphi + kz)}}{\sqrt{2\pi L}}R_{nm}(r).$$

The ψ_j functions are normalized to the bulk of height L, and the wave vector along the wire axis is $k = 2\pi p/L$. The integers m and p characterize the irreducible representations of the rotation and translation operators along the Z axis. Certainly, all the physical results are independent of the L parameter.

The radial wave functions R_{nm} are conveniently represented in the form $R_{nm}(r) = P_{nm}(r)/\sqrt{r}$, where the functions P_{nm} satisfy the one-dimensional Schrödinger equation

$$\left[\frac{1}{2}\left(\frac{d^2}{dr^2} - \frac{m^2 - 1/4}{r^2}\right) - V_{\text{eff}}(r) + \varepsilon_{nm}\right]P_{nm}(r) = 0.$$

Thus, the energy states are characterized by the quantum numbers n, m, and k

$$\varepsilon_j = \varepsilon_{nm} + \frac{k^2}{2},$$

i.e., each level ϵ_{nm} forms the one-dimensional parabolic quantum-well subband, which is characterized by the quantum numbers n and m (Fig. 1).

Let us introduce the quantity $N(\epsilon)$ equal to the number of states with energies less than ϵ

$$N(\epsilon) = (2L/\pi)\sum_{\epsilon_{nm} < \epsilon}\sqrt{\epsilon - \epsilon_{nm}}.$$

The Fermi energy E_F is determined from the transcendental equation

$$N = N(E_F) = (2L/\pi)\sum_{\epsilon_{nm} < E_F}\sqrt{E_F - \epsilon_{nm}}, \tag{6}$$

where the number of valence electrons in the bulk is given by

$$N = \frac{3R^2L}{4r_s^3}. \tag{7}$$

Apart from the free wires, it is of interest to investigate wires placed in a dielectric matrix. In this work, the influence of a dielectric environment on the properties of metallic wires was examined using the model proposed by Lushnikov and Simonov [17]. This model was successfully applied to clusters [12, 18–21]. In this approach, the dielectric matrix is modeled by the parameter $\varepsilon(\mathbf{r})$. The electric field strength in the presence of a dielectric medium $\mathbf{E}^\varepsilon(\mathbf{r}) = \nabla V_C^\varepsilon(\mathbf{r})$ follows the Maxwell equation

$$\text{div}\mathbf{D}(\mathbf{r}) = 4\pi[n_+(\mathbf{r}) - n(\mathbf{r})],$$

where $\mathbf{D}(\mathbf{r}) = \varepsilon(\mathbf{r})\mathbf{E}^\varepsilon(\mathbf{r})$ is the electric displacement vector. In the case when the metallic wire of radius R is placed in a homogeneous dielectric matrix, the macroscopic permittivity ε of the medium, to a first approximation, can be taken as the $\varepsilon(\mathbf{r})$ parameter. Then, taking into account the continuity of V_C^ε and vector $\mathbf{D}$ (which,

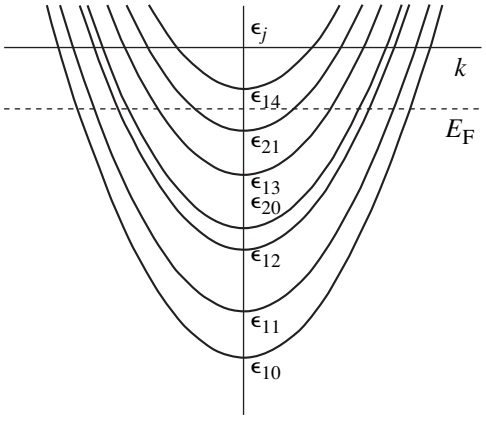

Fig. 1. Schematic representation of the energy band structure for systems with axial symmetry. $\epsilon_j = \epsilon_{nm} + k^2/2$, where $k = 2\pi p/L$, and p is an integral number.

by symmetry, has only the radial component), we obtain

$$V_C^\varepsilon(\mathbf{r}) = \begin{cases} V_C(r) - V_C(R)(\varepsilon - 1)/\varepsilon, & r \le R \\ V_C(r)/\varepsilon, & r > R. \end{cases}$$

Therefore, the ground-state electron density of the wires placed in a dielectric matrix is determined by solving the self-consistent equations (2)–(5), where $V_C(r)$ in Eq. (3) is replaced by $V_C^\varepsilon(r)$. Note that, in our approach, the exchange–correlation potential for the wires in a dielectric is described by the same functional as for the free wires.

If the system occurs in a weak time-dependent electric field $\delta V_{ext}(\mathbf{r}, t)$, the electron density varies with time: $n(\mathbf{r}, t) = n(\mathbf{r}) + \delta n(\mathbf{r}, t)$. In the framework of the density-functional theory [22, 23], the induced electron density $\delta n(\mathbf{r}, t)$ can be obtained by considering the response of a system of noninteracting electrons to the perturbation $\delta V_{eff}(\mathbf{r}, t)$ of the effective field. In this case, up to the terms linear in the external field, the Fourier component $\delta n(\mathbf{r}, \omega)$ and the corresponding component $\delta V_{eff}(\mathbf{r}, \omega)$ of the effective field are related by the expression [24]

$$\delta n(\mathbf{r}, \omega) = \int \chi^0(\mathbf{r}, \mathbf{r}', \omega)\delta V_{eff}(\mathbf{r}', \omega)d\mathbf{r}', \quad (8)$$

$$\delta V_{eff}(\mathbf{r}, \omega) = \delta V_C(\mathbf{r}, \omega) + \left.\frac{\partial V_{xc}[n]}{\partial n}\right|_{n = n(r)} \delta n(\mathbf{r}, \omega), \quad (9)$$

$$\delta V_C(\mathbf{r}, \omega) = \delta V_{ext}(\mathbf{r}, \omega) + \int \frac{\delta n(\mathbf{r}'', \omega)}{|\mathbf{r} - \mathbf{r}'|} d\mathbf{r}', \quad (10)$$

where the perturbation of the effective field δV_{eff} consists of the induced Coulomb and exchange–correlation components. For the latter component, we used the adiabatic approximation proposed by Gross and Kohn [23].

The response function χ^0 for the system of noninteracting electrons is expressed in terms of the eigenfunctions ψ_j and the eigenvalues ϵ_j of the Kohn–Sham equations (2) in the following way:

$$\chi^0(\mathbf{r}, \mathbf{r}', \omega) = \lim_{\Delta \to +0} \sum_{i,j} (f_i - f_j) \frac{\psi_i^*(\mathbf{r})\psi_j(\mathbf{r})\psi_j^*(\mathbf{r}')\psi_i(\mathbf{r}')}{\omega - (\epsilon_j - \epsilon_i) + i\Delta}. \quad (11)$$

By using the retarded Green functions

$$G(\mathbf{r}, \mathbf{r}', \epsilon) = \lim_{\Delta \to +0} \sum_j \frac{\psi_j(\mathbf{r})\psi_j^*(\mathbf{r}')}{\epsilon - \epsilon_j + i\Delta},$$

it is possible to obtain the response functions in a more convenient form for the calculation

$$\chi^0(\mathbf{r}, \mathbf{r}', \omega) = \sum_i f_i [\psi_i^*(\mathbf{r})\psi_i(\mathbf{r}')G(\mathbf{r}, \mathbf{r}', \epsilon_i + \omega) + \psi_i(\mathbf{r})\psi_i^*(\mathbf{r}')G^*(\mathbf{r}, \mathbf{r}', \epsilon_i - \omega)].$$

In this work, we used the dipole approximation, because, for the studied wires ($R \le 10$ au) in the optical range of electromagnetic radiation, the wavelength $\lambda \gg R$. Furthermore, by symmetry, the electromagnetic wave component polarized along the wire axis (the Z axis) does not induce the electron density and, hence, is not absorbed. Consequently, the electric field can be treated as being aligned along the X axis; in this case, the potential energy of an electron has the form

$$\delta V_{ext}(\mathbf{r}, t) = E_\perp r \cos\varphi e^{-i\omega t}, \quad (12)$$

where $E_\perp$ is the amplitude of the electric field strength.

The induced electron density δn and δV_C exhibit angular dependences identical to that for the external perturbation

$$\delta n(\mathbf{r}, \omega) = \delta n(r, \omega)\cos\varphi,$$
$$\delta V_C(\mathbf{r}, \omega) = \delta V_C(r, \omega)\cos\varphi$$

and are related by the expression

$$\delta V_C(r, \omega) = E_\perp r + 2\pi \int_0^\infty \frac{r_<}{r_>} \delta n(r', \omega) r' dr', \quad (13)$$

where $r_<(r_>)$ is the smaller (larger) quantity among r and r'.

The radial parts of $\delta n(r, \omega)$ and $\delta V_{eff}(r, \omega)$ are related through the radial response function

$$\delta n(r, \omega) = \int_0^\infty \chi^0(r, r', \omega)\delta V_{eff}(r', \omega) r' dr',$$

$$\chi^0(r, r', \omega) = \frac{\sqrt{8}}{\pi^2} \sum_{\epsilon_{nm} < E_F} \sqrt{E_F - \epsilon_{nm}} R_{nm}(r) R_{nm}(r')$$
$$\times [G_{m+1}(r, r', \epsilon_{nm} + \omega) + G_{m-1}(r, r', \epsilon_{nm} + \omega)$$
$$+ G_{m+1}^*(r, r', \epsilon_{nm} - \omega) + G_{m-1}^*(r, r', \epsilon_{nm} - \omega)].$$

The radial Green function G_m is constructed from regular and singular solutions of the radial Schrödinger equation with the effective field V_{eff} [25].

The effect of the dielectric environment on the linear response of metallic wires can be investigated within the above approach. In this case, the dielectric medium is described by the frequency-dependent parameter $\varepsilon(\mathbf{r}, \omega)$. The strength of the induced electric

field in the presence of a dielectric $\delta\mathbf{E}^{\varepsilon}(\mathbf{r}, \omega) = \nabla\delta V_C^{\varepsilon}(\mathbf{r}, \omega)$ obeys the Maxwell equation

$$\mathrm{div}\,\delta\mathbf{D}(\mathbf{r}, \omega) = -4\pi\delta n(\mathbf{r}, \omega),$$

where $\delta\mathbf{D}(\mathbf{r}, \omega) = \varepsilon(\mathbf{r}, \omega)\delta\mathbf{E}^{\varepsilon}(\mathbf{r}, \omega)$ is the change in the electric displacement vector. As in calculations of the electronic structure, when the metallic wire is placed in a homogeneous dielectric medium, the $\varepsilon(\mathbf{r}, \omega)$ parameter, to a first approximation, is replaced by the frequency-dependent macroscopic permittivity $\varepsilon(\omega)$ of the medium. Moreover, the band gap of many dielectric media appears to be larger than the energies of electronic transitions in many metallic systems. For these dielectrics, the frequency-dependent permittivity can be replaced by the static permittivity ε in the appropriate frequency range.

The radial part of $\delta V_C^{\varepsilon}(r, \omega)$ for the external field symmetry defined by expression (12) can be determined from the Poisson equation

$$\left[\frac{1}{r}\frac{d}{dr}\left(r\frac{d}{dr}\right) - \frac{1}{r^2}\right]\delta V_C^{\varepsilon}(r, \omega) = -\frac{4\pi}{\varepsilon}\delta n(r, \omega).$$

For a wire of radius R in the matrix with permittivity ε, the boundary conditions at $r = R$ lead to the following relationship for δV_C^{ε}:

$$\delta V_C^{\varepsilon}(r, \omega) = \begin{cases} \delta V_C(r, \omega) - \left(\dfrac{\varepsilon - 1}{\varepsilon + 1}\right)\dfrac{r}{R}\delta V_C(R, \omega), & r \le R \\ \left[\delta V_C(r, \omega) + \left(\dfrac{\varepsilon - 1}{\varepsilon + 1}\right)\dfrac{R}{r}\delta V_C(R, \omega)\right]\varepsilon^{-1}, & r > R, \end{cases}$$

where $\delta V_C(r, \omega)$ is expressed in terms of the induced density in the same manner as for the free wires [see Eq. (13)].

Thus, the linear response of wires in a dielectric matrix is described by a set of self-consistent equations (8)–(10), where $\delta V_C(\mathbf{r}, \omega)$ in Eq. (9) must be replaced by $\delta V_C^{\varepsilon}(r, \omega)\cos\varphi$. It should be noted that the inclusion of the dielectric in the description of the electronic structure also implicitly affects the linear response of wires through the change in the ground-state electron density $n(r)$ and the function χ^0. The latter function is constructed from the modified ψ_j, ϵ_j, and G quantities [see Eq. (11)]. The induced exchange–correlation potential in the proposed approach, as in the description of the electronic structure, has a form identical to that for the free wires and depends on ε only through $n(r)$ and $\delta n(\mathbf{r})$.

3. ELECTRONIC STRUCTURE

Figure 2 displays the electron densities and the potential energies of electrons for jellium wires with

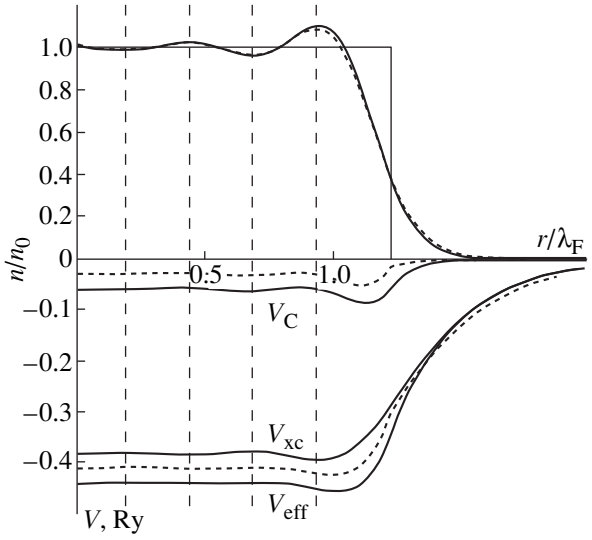

Fig. 2. Electron densities and potential energies of an electron for the Na wire of radius $R = 16$ au in vacuum (solid lines) and dielectric medium with $\varepsilon = 5$ (dotted lines). Vertical dashed lines are drawn at $\lambda_F/4$ intervals, where $\lambda_F = 2\pi/k_F = 3.274r_s$ au is the electron wavelength at the Fermi energy.

$r_s = 4.00$ au (which corresponds to the density of valence electrons in Na) and radius $R = 16$ au in vacuum and a dielectric matrix with $\varepsilon = 5$. Noteworthy are two characteristic features inherent in all the surface problems (semi-infinite crystals, films, wires, and clusters). First, the electron density distribution does not exhibit a sharp edge. This means that electrons penetrate outside the boundaries of the positive background ($r > R$). Hence, the effective wire radius turns out to be larger than the radius of the positive background: $R_{\mathrm{eff}} = R + \delta(R)$. This difference is characterized by the parameter $\delta(R)$, which is associated with the electron charge "spilled-out" outside the background surface [8] and weakly depends on the wire radius R. Second, the electron density and the potential energy of an electron in the intrinsic region oscillate with period $\lambda_F/2$ (Friedel oscillations). A comparison of our results with similar data for clusters [7, 8, 12], thin films [6], and semi-infinite metals [3, 4] demonstrates that the role of surface effects (the spilled-out electron charge and the amplitude of Friedel oscillations) increases with a decrease in the dimension of the system (from semi-infinite crystals to two-dimensional films, one-dimensional wires, and zero-dimensional clusters), which is a consequence of an increase in the number of atoms on the surface as compared to their number in the bulk.

The oscillating (with period $\lambda_F/2$) behavior of the electron density in the intrinsic region permits us to make certain assumptions regarding the occupation of energy bands with an increase in the wire radius. At small r, the wave function $R_{nm}(r) \sim r^m$. Hence, it follows

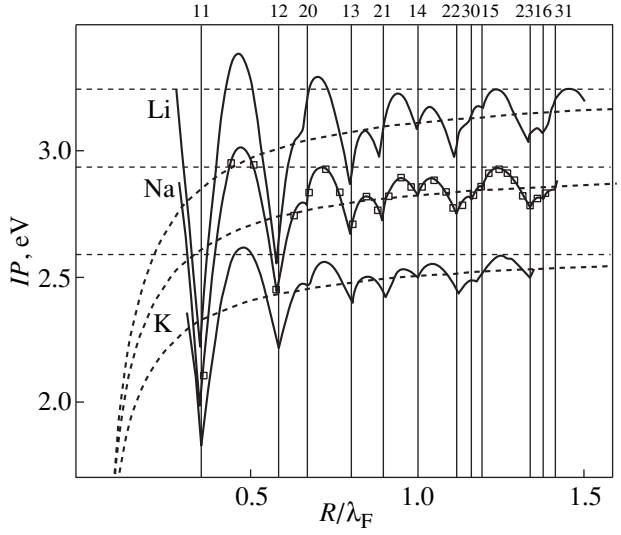

Fig. 3. Dependences of the work function on R/λ_F for the Li, Na, and K wires. Vertical lines with indices *nm* indicate the wire radii that correspond to the onset of filling the next energy band with the quantum numbers *n* and *m*.

that only bands with $m = 0$ make a nonzero contribution to the electron density at the wire axis (at $r = 0$). Therefore, the occupation of the next band with $m = 0$ leads to a new period in the electron density distribution. Consequently, it can be assumed that the occupation of energy bands with $m = 0$ is periodic (with period $\lambda_F/2$).

The effect of the dielectric environment on $n(r)$ reduces to the spill-out of the electron density outside the boundary of the positive background ($r > R$) and to an insignificant decrease in the amplitude of the Friedel oscillations. Moreover, in the intrinsic region, the effective potential energy of an electron V_{eff}, as a whole, shifts upward virtually without change in its form. A decrease in the depth of the potential well and an increase in its width lead to about the same increase in the energy levels ϵ_{nm}. These effects were also observed for spherical clusters [19, 20].

As is known [15, 26], the work function (IP) for extended systems (films, wires, etc.) is related to the Fermi energy by the expression

$$IP = -E_F.$$

The dependences of the work function on the radius for Li (r_s = 3.25 au), Na (r_s = 4.00 au), and K (r_s = 4.86 au) wires are depicted in Fig. 3. In order to obtain smooth curves, the calculations were carried out with a rather small step in wire radius *R*. However, the real metallic wires are characterized by a discrete set of radii, which can be evaluated from the following reasoning. We assume that the bulk of height *L* (it is convenient to use the lattice parameter of a bulk crystal as *L*) can be occupied by the integer number *N* of atoms. As follows from formula (7), the radius of a Na wire (L = 8 au) in this case can take the values $R_N \approx 3.3\sqrt{N}$ (these values are designated by squares in Fig. 3).

As the wire radius increases, the work function oscillates according to the occupation of the energy bands and approaches from below the work function *W* of the corresponding bulk crystal (horizontal dashed lines). The averaged size dependence of the work function (dotted lines) can be represented by the formula

$$\tilde{IP} = W - C/R,$$

where C = 1.5 eV. Similar investigations of other low-dimensional systems (clusters and films) revealed that the work function of clusters tends from above to *W* [7], whereas the averaged work function of films does not depend on the film thickness [6]. This result agrees with the data obtained by Makov and Nitzan [27] on the effect of the surface curvature in a system on its different characteristics (including the work function).

Note that the work functions for wires of different metals are represented in Fig. 3 on the R/λ_F scale, on which their size dependences exhibit a similar behavior. This can be explained as follows. At the same values of R/λ_F, the number of electrons in the bulk of Li, Na, and K wires is determined by formula (7) and varies proportionally with $1/\lambda_F$ (because $r_s \sim \lambda_F$).

After replacing the coordinates $r' = r/\lambda_F$, the effective potential energy $V_{\text{eff}}(r')$ takes an identical form (oscillates in the intrinsic region with a period of 1/2) for wires of different metals. Therefore, at the same value of R/λ_F, the energy levels ϵ_{nm} and, as can be seen from Eq. (6), the Fermi energies E_F for wires of different metals are proportional to $1/\lambda_F^2$, and the number of the filled energy bands appears to be identical.

4. STATIC POLARIZABILITY

The dipole polarizability of a wire per unit length is expressed through the induced electron density by the relationship

$$\alpha(\omega) = -\frac{\pi}{E_\perp}\int_0^\infty \delta n(r, \omega) r^2 dr. \qquad (14)$$

At $\omega = 0$, this expression determines the static polarizability α. The classical theory that adequately describes the properties of bulk metals turns out to be inapplicable to systems with quantum-size cross-sections. The size dependences of the static polarizability for the Li, Na, and K wires are shown in Fig. 4. The found polarizability α is larger than the classical value ($\alpha_{cl} = R^2/2$) and can be represented as

$$\alpha = \frac{(R + \delta(R))^2}{2}. \qquad (15)$$

Therefore, the metallic wire in an external field is polarized as a classical conducting cylinder with the effective radius $R_{\text{eff}} = R + \delta(R)$. An increase in the effective wire radius [characterized by the parameter $\delta(R)$] can be explained by the penetration of electrons outside the boundary of the ground-state positive background (this effect was discussed above). A similar result was obtained for spherical clusters [8–12], whose polarizability is larger than the classical value ($\alpha_{cl} = R^3$) and has the form

$$\alpha = (R + \delta(R))^3. \quad (16)$$

Lushnikov and Simonov [28] proved that the inclusion of electron–electron interaction leads to a decrease in the polarizability of metallic clusters. Consequently, the found increase in the static polarizability of size-quantized systems as compared to the predictions of the classical theory can be also treated as a consequence of a weakening in the effective electron–electron interaction due to the penetration of electrons outside the positive background boundary. It follows from Eqs. (15) and (16) that the difference in polarizabilities of the size-quantized and classical metallic systems depends on the system dimension: at the same radius, this difference for wires is less than that for clusters. As for spherical clusters [9], it can be demonstrated that, as the wire radius increases, $\delta(R) \longrightarrow \delta_p$, where δ_p is the position of the center of gravity of the induced electron density for the appropriate semi-infinite metal. Consequently, at large radii, the wire polarizability can be written as

$$\alpha \approx \frac{(R + \delta_p)^2}{2}.$$

According to our calculations, the δ_p values for Li, Na, and K are equal to 1.25, 1.20, and 1.15 au, respectively.

As follows from the classical electrostatics, a conducting cylinder (similar to other metallic systems), when placed in a dielectric matrix, does not change its own induced density and, hence, polarizability. The quantum-mechanical calculations lead to a different result: the polarizability of wires decreases with an increase in ε. The larger the radius r_s (Fig. 5a) and the smaller the wire radius R (Fig. 5b), the faster the decrease in the polarizability. This effect is also observed in clusters [18] and stems from the competition of two processes. On the one hand, the dielectric shielding of the electron–electron interaction brings about an increase in $\delta n(r)$ outside the boundary of the positive background [a similar result for the ground-state electron density $n(r)$ was considered above] and an increase in the oscillation amplitude of $\delta n(r)$ in the intrinsic region. On the other hand, the dielectric shielding of the external field considerably decreases $\delta n(r)$ over the entire range of radii. The effect of the latter process (resulting in a decrease in α) is enhanced with an increase in r_s and a decrease in R. Note that, unlike clusters, the effect of the external field shielding for wires is predominant. For example, as the value of ε increases, the polarizability of a Na cluster with R = 10 au increases [18], whereas the polarizability of a Na wire with R = 10 au decreases (Fig. 5b).

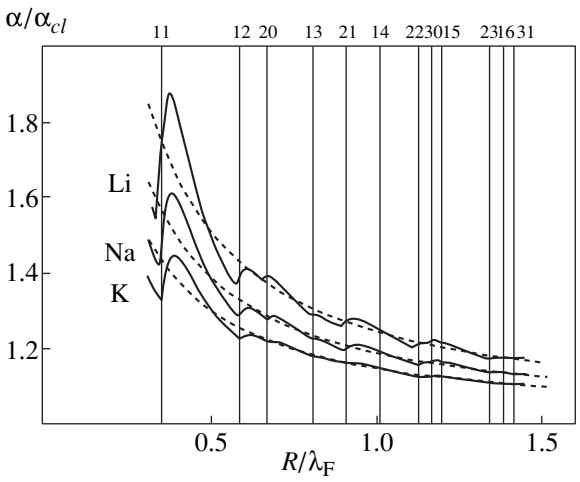

Fig. 4. Static polarizability (in terms of the classical quantity $\alpha_{cl} = R^2/2$) as a function of R/λ_F for the Li, Na, and K wires. Averaged size dependences are represented by dashed lines.

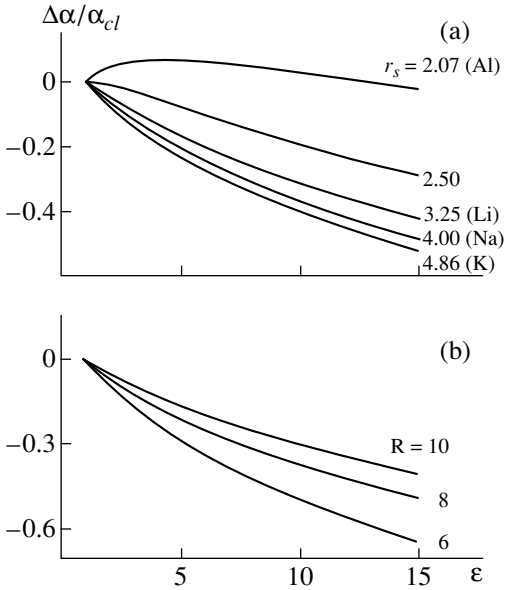

Fig. 5. Changes of the static polarizability compared to the polarizability in vacuum with an increase in permittivity of the medium for (a) wires with radius R = 8 au at different densities of valence electrons and (b) Na wires with R = 6, 8, and 10 au.

5. DYNAMIC POLARIZABILITY

When studying the dynamic response of wires, the small imaginary quantity Δ = 0.001 Ry was added to the frequency of the electromagnetic field with the aim

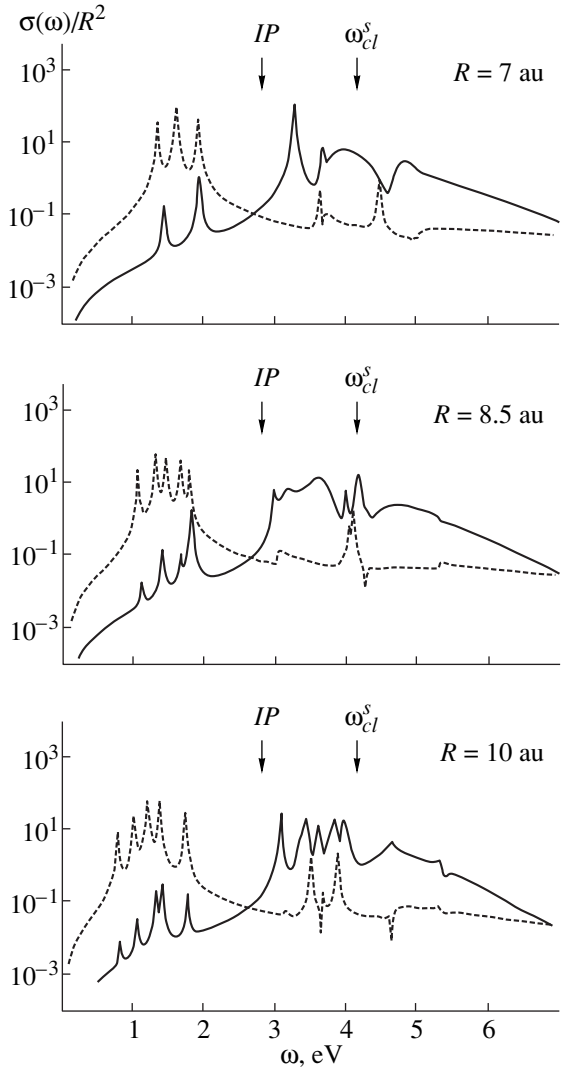

Fig. 6. Photoabsorption cross-sections of the Na wires of radii R = 7, 8.5, and 10 au with (solid lines) and without (dashed lines) inclusion of electron–electron interaction. Arrows indicate the locations of the ionization thresholds (*IP*) and the classical frequencies ω_{cl}^s of surface plasma resonance.

of modeling the finite lifetime of excited states. Furthermore, this quantity makes it possible to eliminate the singularities in the response function χ^0 defined by formula (11) and to improve the convergence of an iterative process for solving self-consistent Eqs. (8)–(10).

The photoabsorption cross-section is determined by the imaginary part of the dynamic polarizability (14), that is,

$$\sigma(\omega) = \frac{4\pi\omega}{c}\mathrm{Im}\alpha(\omega).$$

By using Eqs. (8)–(10) and (14), it is possible derive the equivalent expression for $\sigma(\omega)$ [29]

$$\sigma(\omega) = -\frac{4\pi\omega}{E_\perp^2} \times \int \delta V_{\mathrm{eff}}^*(\mathbf{r}, \omega)\mathrm{Im}\chi^0(\mathbf{r}, \mathbf{r}', \omega)\delta V_{\mathrm{eff}}(\mathbf{r}', \omega)d\mathbf{r}d\mathbf{r}'. \quad (17)$$

Figure 6 demonstrates the photoabsorption spectra of the Na wires of radii R = 7, 8.5, and 10 au (which correspond to the occupation of two, three, and four bands) with and without inclusion of the electron–electron interaction [in the latter case, δV_{eff} in Eq. (17) is replaced by the external field δV_{ext}]. For noninteracting electrons, at $\Delta \longrightarrow 0$, we obtain the known relationship

$$\sigma(\omega) = \frac{4\pi^2\omega}{E_\perp^2} \times \sum_{i,j} f_i(2 - f_j)|\langle\psi_i|\delta V_{\mathrm{ext}}|\psi_j\rangle|^2\delta(\omega - \epsilon_j + \epsilon_i).$$

Here, as before, the occupation numbers f_j of electronic states are equal to 0 and 2 for the spin-confined case. It can be seen that, in the framework of the dipole approximation (12), the direct (Δk = 0) interband transitions become possible at $\Delta m = \pm 1$. Within the approximation of noninteracting electrons, the locations of the photoabsorption peaks associated with the band-to-band transitions completely coincide with the differences in the corresponding energy levels ϵ_{nm}. For interacting electrons, formula (17) in the limit $\Delta \longrightarrow 0$ transforms into the relationship

$$\sigma(\omega) = \frac{4\pi^2\omega}{E_\perp^2} \times \sum_{i,j} f_i(2 - f_j)|\langle\psi_i|\delta V_{\mathrm{eff}}|\psi_j\rangle|^2\delta(\omega - \epsilon_j + \epsilon_i),$$

which, as could be expected, gives the photoabsorption spectrum of the noninteracting electron in the perturbed effective field δV_{eff}.

The main difference between the photoabsorption spectra of interacting and noninteracting electrons consists in increasing the photoabsorption in the range of $\omega \approx 3.8$ eV, which can be explained by the excitation of collective vibrations (the surface plasma resonance). In the classical electrodynamics, the frequency of a surface plasmon for a conducting cylinder [$\omega_{cl}^s = \omega_p/\sqrt{2}$, where $\omega_p = (4\pi e^2 n_0/m)^{1/2} = (3/r_s^3)^{1/2}$ au is the frequency of the bulk plasmon] is higher than that for a conducting sphere ($\omega_{cl}^s = \omega_p/\sqrt{3}$). Therefore, unlike the Na clusters [21], the frequency of the surface plasmon for Na wires falls in the range of continuous spectrum [above the ionization threshold (*IP*)], which leads to a

superposition of the plasmon and single-particle excitations and complicates the identification of the photoabsorption peaks.

Moreover, as is seen from Fig. 6, the frequency of the surface plasmon for Na wires is less than the classical value ω_{cl}^{s}. This discrepancy with the prediction of the classical theory (which was also found for Na clusters [10–12]), as for the static polarizability, can be caused by a decrease in the effective electron–electron interaction due to the penetration of electrons outside the boundary of the positive background. As for metallic clusters [30], the shift in the frequency of the surface plasmon for a wire with respect to ω_{cl}^{s} can be estimated within the classical approach under the assumption that the same number N of electrons occupy the volume of a cylinder with radius $R_{\text{eff}} = R + \delta(R)$ and height L. This leads to an increase in the Wigner–Seitz electron radius $r_s' = r_s(1 + \delta(R)/R)^{2/3}$ and, hence, a decrease in the frequency of the surface resonance

$$\frac{\omega^{s'}}{\omega_{cl}^{s}} = \left[\frac{R}{R + \delta(R)}\right]. \tag{18}$$

For metallic clusters, similar reasoning gives the following expression for the modified frequency of the surface plasmon:

$$\frac{\omega^{s'}}{\omega_{cl}^{s}} = \left[\frac{R}{R + \delta(R)}\right]^{3/2}. \tag{19}$$

A comparison of Eqs. (15)–(19) allows us to reveal the general relationship between the "red" shift in frequency of the surface plasmon and an increase in the static polarizability with respect to α_{cl} for clusters and wires

$$\left[\frac{\omega^{s'}}{\omega_{cl}^{s}}\right]^{2} = \frac{\alpha_{cl}}{\alpha}. \tag{20}$$

As follows from Eqs. (18)–(20), the lower the dimension of the system, the larger the difference between the surface plasma resonance frequency (as well as the static polarizability) and its classical value. This inference, as applied to the static polarizability, was discussed above.

According to the classical electrodynamics, the frequency of the surface plasma mode for a conducting cylinder decreases when it is placed in a dielectric matrix with permittivity ε, that is,

$$\omega_{cl}^{s} = \frac{\omega_p}{\sqrt{1 + \varepsilon}}. \tag{21}$$

This effect is caused by the shielding of the electron–electron interaction with a dielectric matrix. The quantum-mechanical calculations predicted a similar pattern. As an example, Fig. 7 displays the photoabsorption spectra of the Na wire with radius $R = 10$ au in vacuum and in a dielectric medium with $\varepsilon = 5$. In the case when the Na wire is placed in a dielectric matrix, the frequency of the surface plasmon decreases, and, hence, the photoabsorption increases in the range of $\omega \approx 2$ eV and decreases at $\omega > 3$ eV. Moreover, it was found that, as ε increases, the single-particle resonances for Na wires more slowly shift toward the red range as compared to the surface plasma mode. As a result, the surface plasmon shifts from the continuous spectrum to the range somewhat below the ionization threshold and can be well identified ($\omega^s = 2.17$ eV). Note that the reverse situation is observed for Na clusters [21]: the surface plasmon shifts from the range below the ionization threshold (free clusters) toward the range of continuous spectrum (clusters in a dielectric matrix).

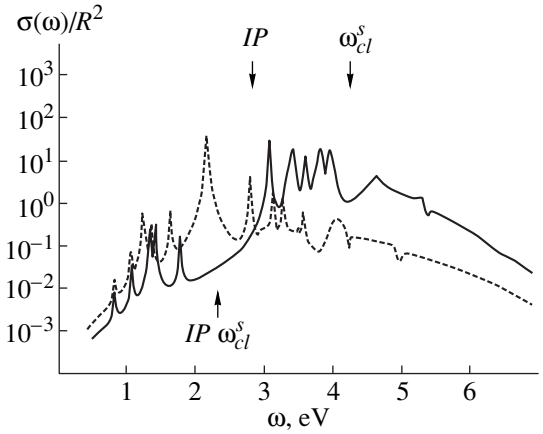

Fig. 7 Photoabsorption cross-sections of the Na wire with radius $R = 10$ au in vacuum (solid line) and in a dielectric medium with $\varepsilon = 5$ (dashed line). Locations of the ionization thresholds (IP) and the classical frequencies ω_{cl}^{s} of surface plasma resonance for the wire in vacuum and dielectric matrix are indicated by downward and upward arrows, respectively (the coincidence of the ionization threshold and ω_{cl}^{s} for this wire in dielectric matrix with $\varepsilon = 5$ is accidental).

As for free wires, the frequency of the surface plasmon for Na wires in a dielectric with $\varepsilon = 5$ ($\omega^s = 2.17$ eV) is less than the classical value [$\omega_{cl}^{s} = 2.4$ eV Eq. (21)] by the quantity $\Delta\omega^s = 0.23$ eV. Similar calculations for clusters led to $\Delta\omega^s \approx 0.5$ eV. As could be expected, the discrepancy with the predictions of the classical theory for clusters is larger than that for wires. It should be noted that the surface plasmon frequency $\omega^{s'} = 2.16$ eV, which was calculated from Eqs. (18) and (21) for the Na wire in a dielectric matrix with $\varepsilon = 5$ [under the assumption that $\delta(R) \approx 1.20$ au, as was found from analysis of the static response], is in good agreement with the frequency $\omega^s = 2.17$ eV.

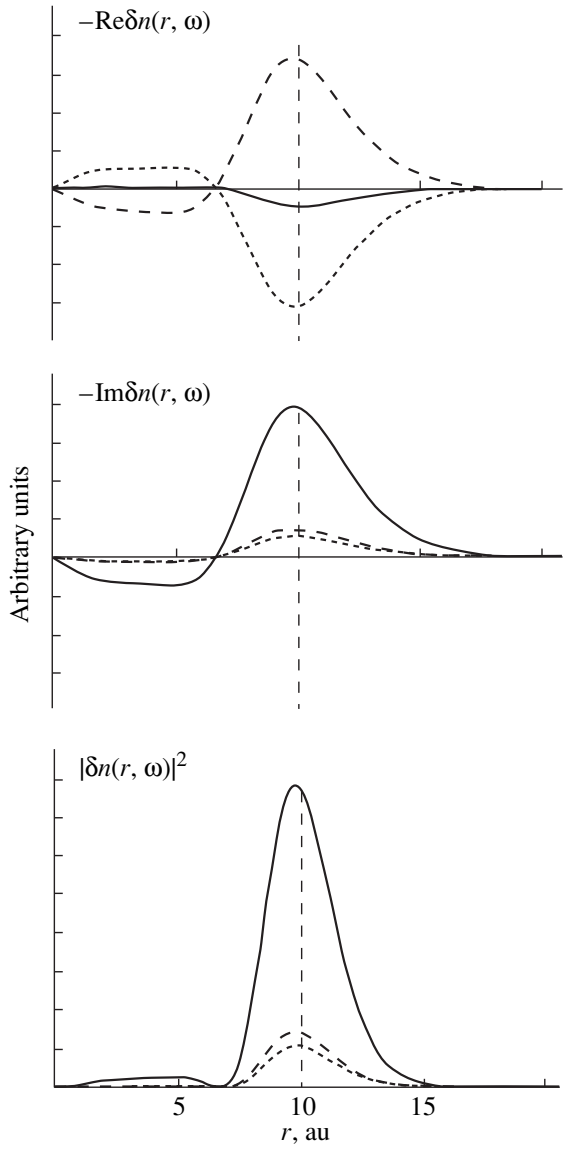

Fig. 8. Changes in the complex induced electron density $\delta n(r, \omega)$ and its magnitude $|\delta n(r, \omega)|^2$ for the Na wire (R = 10 au, $\varepsilon = 5$) upon transition through surface plasma resonance at frequencies $\omega = 2.15$ (dashed lines), 2.17 (solid lines), and 2.20 (dotted lines) eV.

In order to demonstrate that the photoabsorption peak at $\omega^s = 2.17$ eV corresponds to the excitation of the surface plasmon, we studied the changes in different dynamic characteristics upon transition through this resonance. In particular, let us consider a continuity equation that, for the given symmetry, takes the form

$$-i\omega\delta n(x, y, \omega) = \frac{\partial}{\partial x} j_x(x, y, \omega) + \frac{\partial}{\partial y} j_y(x, y, \omega).$$

Integration of this equation over the coordinate x from 0 to ∞ and over coordinate y from $-\infty$ to ∞ gives the relationship for current $I(\omega) = \int j_x(0, y, \omega)dy$, which flows across the plane $X = 0$

$$I(\omega) = 2i\omega \int_0^\infty \delta n(r, \omega) r dr. \quad (22)$$

It is seen from Fig. 8 that, upon transition through a photoabsorption peak at frequency $\omega^s = 2.17$ eV, the real part of the induced density [and, hence, the imaginary part of the current $I(\omega)$ (22)] changes sign over the entire range of radii. This implies that electrons in an electromagnetic field with frequency ω^s move in phase with the external field. Furthermore, the electron density oscillates with a maximum amplitude (determined by $|\delta n(r, \omega)|$) only at the wire surface. These results are characteristic of the surface plasma resonance and, thus, indicate that the photoabsorption peak at frequency ω^s is actually associated with the excitation of the surface collective mode.

ACKNOWLEDGMENTS

This work was supported by the Russian Foundation for Basic Research, project no. 99-15-96028.

REFERENCES

1. B. Tanatar and A. Gold, Phys. Rev. B **52** (3), 1996 (1995).
2. G. W. Bryant, Phys. Rev. B **29** (12), 6632 (1984).
3. N. D. Lang, Solid State Commun. **7**, 1047 (1969).
4. N. D. Lang and W. Kohn, Phys. Rev. B **1** (12), 4555 (1970).
5. N. D. Lang and W. Kohn, Phys. Rev. B **7** (8), 3541 (1973).
6. F. K. Schulte, Surf. Sci. **55**, 427 (1976).
7. W. Ekardt, Phys. Rev. B **29** (4), 1558 (1984).
8. D. E. Beck, Phys. Rev. B **30** (12), 6935 (1984).
9. D. R. Snider and R. S. Sorbello, Phys. Rev. B **28** (10), 5702 (1983).
10. V. Kresin, Phys. Rev. B **39** (5), 3042 (1989).
11. W. Ekardt, Phys. Rev. B **31** (10), 6360 (1985).
12. M. J. Puska, R. M. Nieminen, and M. Manninen, Phys. Rev. B **31** (6), 3486 (1985).
13. P. Hohenberg and W. Kohn, Phys. Rev. B **136** (3), 864 (1964).
14. W. Kohn and L. J. Sham, Phys. Rev. A **140** (4), 1133 (1965).
15. *Theory of the Inhomogeneous Electron Gas*, Ed. by S. Lundqvist and N. H. March (Plenum, New York, 1983; Mir, Moscow, 1987).
16. S. H. Vosko, L. Wilk, and M. Nusair, Can. J. Phys. **58** (8), 1200 (1980).
17. A. A. Lushnikov and A. J. Simonov, Z. Phys. **270** (1), 17 (1974).
18. L. I. Kurkina and O. V. Farberovich, Z. Phys. D **37** (4), 359 (1996).
19. L. I. Serra and A. Rubio, Z. Phys. D **26**, S122 (1993).

20. M. M. German, V. Ya. Kupershmidt, and O. V. Farberovich, Poverkhnost' **7**, 45 (1989).
21. L. I. Kurkina and O. V. Farberovich, Phys. Rev. B **54** (20), 14791 (1996).
22. E. Runge and E. K. U. Gross, Phys. Rev. Lett. **52** (12), 997 (1984).
23. E. K. U. Gross and W. Kohn, Phys. Rev. Lett. **55** (26), 2850 (1985).
24. A. I. Akhiezer and S. V. Peletminskiĭ, *Methods of Statistical Physics* (Nauka, Moscow, 1977; Pergamon, Oxford, 1981).
25. A. I. Baz', Ya. B. Zel'dovich, and A. M. Perelomov, *Scattering, Reactions, and Decays in Nonrelativistic Quantum Mechanics* (Nauka, Moscow, 1971, 2nd ed.; Israel Program for Scientific Translations, Jerusalem, 1966).
26. J. P. Perdew, R. G. Parr, M. Levy, and J. L. Balduz, Phys. Rev. Lett. **49** (23), 1691 (1982).
27. G. Makov and A. Nitzan, Phys. Rev. B **47** (4), 2301 (1993).
28. A. A. Lushnikov and A. J. Simonov, Phys. Rev. Lett. A **44** (1), 45 (1973).
29. A. Zangwill and P. Soven, Phys. Rev. A **21** (5), 1561 (1980).
30. A. Dellafiore and F. Matera, Phys. Rev. B **41** (6), 3488 (1990).

Translated by O. Borovik-Romanova

Physics of the Solid State, Vol. 42, No. 10, 2000, pp. 1908–1910. Translated from Fizika Tverdogo Tela, Vol. 42, No. 10, 2000, pp. 1857–1859.

LOW-DIMENSIONAL SYSTEMS AND SURFACE PHYSICS

Neutron Transport in Ultradisperse Copper Layers under Strong Scattering Conditions

B. R. Meshcherov* and P. Geltenbort**

** Russian Research Center Kurchatov Institute, pl. Kurchatova 1, Moscow, 123182 Russia*
e-mail: meshcherov@dap.kiae.ru, meshch@tapdki.ips.ras.ru
*** Institut Laue–Langevin, 38042 Grenoble Cedex 9, France*
Received January 24, 2000

Abstract—The character of neutron transport in ultradisperse copper near the total reflection boundary is studied. The dependence of the ultracold neutron transmission on the thickness of a nonuniform layer under the strong scattering condition $kl \le 10$ (k is the wave vector and l is the mean free path) is obtained for the first time. *© 2000 MAIK "Nauka/Interperiodica".*

The transmission of waves and particles of any kind through random media under the conditions of strong scattering is of particular interest in connection with possible localization effects. The most impressive result have been obtained for electromagnetic radiation [1], which is characterized by the critical regime $T(L) \propto L^{-2}$ (L is the thickness of the disordered layer and T is transmission) at $kl \approx 1.6$, where k is the wave vector and l is the mean free path, i.e., near the mobility edge $kl \sim 1$. However, despite a large number of theoretical and experimental works dealing with the propagation of elastic and electromagnetic waves, as well as of electrons in disordered structures, the phenomenon of strong (Anderson) localization [2, 3] has not been observed to date. As regards electrons, specifically the electron transport in condensed media, the efforts spent over many years have led to the conclusion that observation of the Anderson transition in its pure form is in principle, impossible, because it is always accompanied by the Mott transition [4].

Recently, a proposal was put forward to use ultracold neutrons (UCN) as an object for such studies [5]. A subsequent experiment [6] confirmed the realizability of the condition of strong ultracold neutron scattering near the total reflection boundary. The best values $l \sim 150$–200 nm and $kl \sim 10$ (in the sense of the effects under discussion) turned out to be two or three orders of magnitude less than those observed in the earlier neutron measurements, but nearly one order of magnitude larger than was required to reach the mobility edge. The character of the $l(E)$ dependence (the mean free path l decreases rapidly with a decrease in the neutron energy E) [6] suggests that further attempts at minimizing the kl parameter apparently should be directed to increasing the barrier height E_c of the material of the scatterers formed the disordered structure. This increase could make possible a more comprehensive investigation of the range $E < E_c$, including the low-energy bound corresponding to the total reflection cutoff of the effective medium (whose density is equal to the average density of the disordered layer). In contrast to the earlier work [6], which dealt with ultracold neutron propagation through quartz microstructures ($E_c \approx 90$ neV), the present paper reports on the measurement of neutron transmission through layers of ultradisperse copper ($E_c \approx 170$ neV).

From the viewpoint of detecting the localized state, the most informative way apparently consists of measuring the $T(L)$ dependence with decreasing parameter kl [3], namely, the change from $T(L) \sim l/L$ ($kl \gg 1$, classical diffusion) to $T(L) \sim (l/L)^2$ (critical regime, $kl \ge 1$) and, finally, to $T(L) \propto \exp[-L(l_c - l)/l^2]$ at $kl < 1$, i.e., below the mobility edge $kl_c \approx 1$. Near the total reflection boundary, the parameters characterizing neutron interaction with matter can vary considerably with variations in the energy; hence, in order to obtain as full a picture as possible, it is desirable to study the $T(L, E)$ dependence throughout the range corresponding to the strong ultracold neutron scattering. Therefore, in this experiment, both scale and spectral dependences of the transmission were measured. The energy range from 70 to 300 neV was scanned with a resolution of about 15 neV by means of a gravitational spectrometer, whose arrangement and detailed description can be found in [6]. The source of ultracold neutrons was a PF2 output channel of the reactor at the Institut Laue–Langevin (Grenoble, France).

The samples were produced in two stages: the preparation of an ultradisperse powder consisting of copper microparticles of a given size and its deposition on substrates representing the standard single-crystal silicon wafers, 0.5 mm thick and 100 mm in diameter, polished on both sides. At the first stage, a certain necessary amount of finely divided copper was obtained using a VChG4-10/0.44 RF installation modified to provide

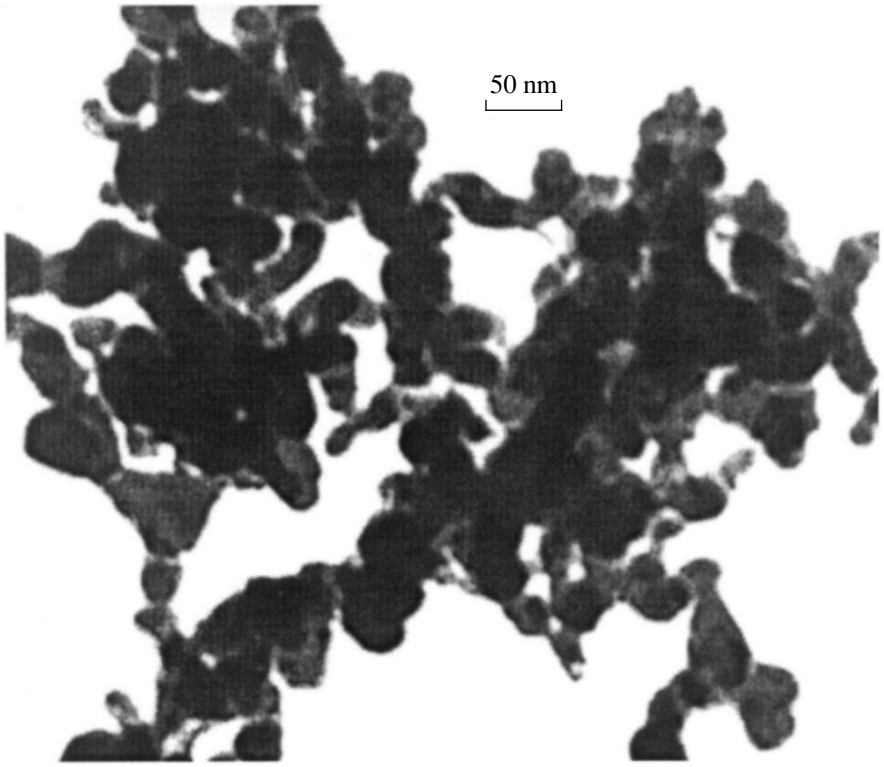

Fig. 1. Electron microscope image of copper microparticles.

evaporation with subsequent condensation: in this process, a drop of the melt was blown over in an argon flow, and the particles formed in the gas jet were separated by a filter. The powder thus produced was passed through a sieve to remove the coarse fractions. This technique permits one to control over a wide range the average particle size d, which is determined by the velocity of the inert gas blowing over the melt. The structures with $d \approx 30$ nm were studied in our experiment. A typical image of the microparticles used in the sample preparation is displayed in Fig. 1.

Prior to deposition on the substrates, the powder was dispersed by ultrasonic agitation in a 35% alcohol solution in acetone. The mixture thus prepared was sprayed by an A-2 spray gun reciprocating relative to a fixed silicon wafer. In the course of layer formation, the substrates were heated up to 45–50°C. This temperature corresponded to the optimum liquid evaporation rate at which drops did not form, so that no surface tension effects could be present. The thickness was checked by weighing the deposited powder. The values of L were varied from one sample to another at a constant step within the range 0.7–2 μm. Despite all the measures taken, the degree of agglomeration remained fairly high, so that the filling fraction f did not exceed 0.3.

Figure 2 shows the spectral dependence $T(E)$ for several samples. The transmission decreases monotonically with a decrease in the energy of ultracold neutrons, which would seem to indicate a decrease in the mean free path, the key parameter in diffusive trans-

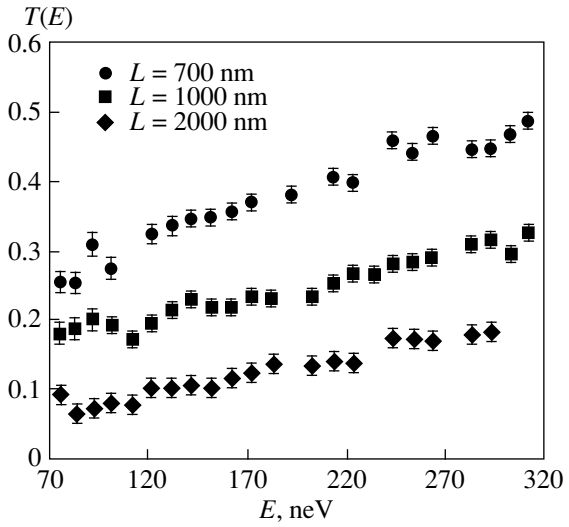

Fig. 2. Spectral response of the ultracold neutron transmission.

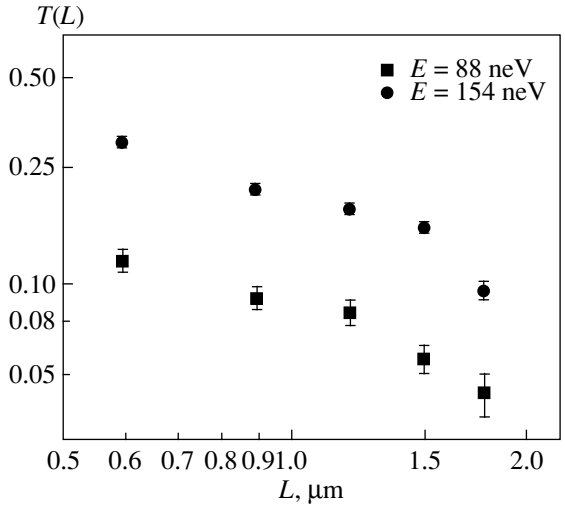

Fig. 3. Neutron transmission versus layer thickness.

port. However, it appears that the behavior of neutron transport in our experiment differs somewhat from that in classical diffusion. This is convincingly illustrated by the main result of the measurements, namely, by the scale dependences of the transmission displayed in Fig. 3. The power-function fitting with $T \propto L^{-n}$ yields $n < 1$, which means that the dependence is even weaker than $1/L$.

This behavior of the transmission is apparently caused by the high degree of intrinsic agglomeration of ultradisperse copper powders. In such a medium, a sizable part of the neutrons will execute a random walk between agglomerates. This means that the diffusion associated with scattering from single particles can also be accompanied by the percolation along a system of interaggregate pores with well reflecting walls. Unfortunately, the character of transport in these media greatly depends on their actual structure. Note that the problems of two-dimensional transport in two-phase media formed by randomly distributed regions with two different diffusion coefficients allow exact solutions for some specific cases; however, there are no solutions in three dimensions [7]. In other words, the existence of interaggregate gaps with sizes exceeding the neutron wavelength does not make the behavior of the system near the total reflection cutoff any more universal. A similar situation was apparently met by the authors of [1], who succeeded in realizing a microwave radiation transport regime close to the mobility edge. In their study of the scale dependence of transmission through a mixture of aluminum and teflon spheres, they had to perform averaging at each point over an extremely large number of measurements, $N = 6 \times 10^4$, which differed in the scattering layer configuration. Since even after the averaging, the deviation of the obtained values from the fitting curve was as high as 10% (see [1]), it can be assumed that the results of individual measurements differed by a factor of 25 due to the percolation. Therefore, the experimental data obtained in a single scanning in thickness could hardly be fitted by any one functional dependence.

If we disregard percolation, it turns out that the scattering in the samples studied in this work is very strong. Measurements of the transmission T_c for a collimated beam (with collimation not only of the input flux, but of the transmitted ultracold-neutron beam as well) on the thinnest layers provided an upper estimate for the neutron mean free path with respect to the elastic scattering from copper particles. The value obtained at the lower boundary of the spectral range (70 neV) is $l \leq 200$ nm. As one would expect, ultradisperse copper scatters ultracold neutrons under the same conditions that are no weaker than the SiO_2 particles [6].

It should be pointed out, in conclusion, that we have obtained for the first time the thickness dependences of neutron transmission under strong scattering conditions, $kl \leq 10$. To progress further toward smaller values of the kl parameter, one should use structures approaching close packing with the filling fraction $f \approx 0.5$ to exclude the presence of agglomerates.

REFERENCES

1. N. Garcia and A. Z. Genack, Phys. Rev. Lett. **66**, 1850 (1991).
2. P. W. Anderson, Phys. Rev. **109**, 1492 (1958).
3. P. W. Anderson, Philos. Mag. B **52**, 505 (1985).
4. D. Belitz and T. R. Kirkpatrick, Rev. Mod. Phys. **66**, 261 (1994).
5. B. R. Meshcherov, Fiz. Tverd. Tela (S.-Peterburg) **38**, 1081 (1996) [Phys. Solid State **38**, 598 (1996)].
6. B. R. Meshcherov, A. I. Fomin, S. M. Chernyavskiĭ, *et al.*, Pis'ma Zh. Éksp. Teor. Fiz. **67**, 291 (1998) [JETP Lett. **67**, 307 (1998)].
7. M. B. Isichenko, Rev. Mod. Phys. **64**, 961 (1992).

Translated by G. Skrebtsov

Physics of the Solid State, Vol. 42, No. 10, 2000, pp. 1911–1913. Translated from Fizika Tverdogo Tela, Vol. 42, No. 10, 2000, pp. 1860–1862.

LOW-DIMENSIONAL SYSTEMS AND SURFACE PHYSICS

Specific Features of Magnetooptical Spectra of Co/SiO_2 Hybrid Multilayers

E. A. Gan'shina*, A. B. Granovskiĭ*, B. Dieny, R. Yu. Kumaritova*, and A. N. Yurasov***

**Moscow State University, Vorob'evy gory, Moscow, 119899 Russia*

e-mail: granov@magn.phys.msu.su

*** CEA, Département de Recherche Fondamentale sur la Matiére Condensée, SP2M/NM, Grenoble Cédex 9, 38054 France*

Received February 24, 2000

Abstract–Magnetooptical spectra of $Co(x)/SiO_2(y)$ bilayers and $[Co(x)/SiO_2(y)]_n$ hybrid multilayers (x and y are the layer thicknesses) are studied in the range 1.5–4.0 eV. In these layers, the ultrathin ferromagnetic layers are not continuous but consist of ellipsoidal Co nanoparticles with a concentration near the percolation threshold. It is found that (a) the sign, magnitude, and spectral shape of the magnetooptical signal depend strongly on the Co particle size; (b) the signal for the $[Co(1.6\ nm)/SiO_2(3.0\ nm)]_6$ multilayers at 3.0 eV has a record-high magnitude for Co-based structures, 3×10^{-2}, which exceeds that for bulk Co about fivefold and about 50-fold that for a uniform Co film of an equivalent thickness; (c) the magnetooptical signal of multilayers depends nonlinearly on the number of periods and the thickness of the dielectric layer y; and (d) the dependence of the signal of bilayers and multilayers with x = 1.3 and 1.6 nm on the wavelength is nonmonotonic and exhibits clearly pronounced extrema. The data obtained for bilayers are attributed to the strong influence of percolation on the optical and magnetooptical parameters of the structure and interpreted in the framework of the effective medium approximation and macroscopic Fresnel magnetooptics. © *2000 MAIK "Nauka/Interperiodica".*

This paper presents the results of an experimental study of magnetooptical spectra of Co/SiO_2 hybrid multilayers, whose cross-section is shown schematically in Fig. 1. The ferromagnetic layers in the metal–dielectric hybrid multilayers are not continuous and represent ultrathin films of nanocomposites, with a high concentration of ferromagnetic particles near the percolation threshold. Hybrid multilayers combine the merits of traditional multilayers with those of granular systems, namely, a large magnetoresistance (in the case under consideration, the tunneling magnetoresistance can be as high as 10% [1]), the absence of hysteresis, comparatively low saturation fields, and simple technology, while the existence of accidental contacts between grains in adjacent layers is not critical for the tunneling magnetoresistance of the structure as a whole.

Because the magnetic layers of the metal are made up of grains separated by a dielectric, the optical and magnetooptical properties of these systems should be expected to exhibit features associated with percolation, size effects, surface plasmons, local electric-field enhancement, etc. These systems differ from bulk nanocomposites primarily in the quasi-two-dimensional nature of the magnetic layers and their periodic arrangement.

The magnetooptical spectra were recorded in the geometry of the transverse Kerr effect using p-polarized light at an incidence angle $\varphi = 70°$. The technique of preparing the samples and their structural properties were described in considerable detail in [1]. The substrates were made of crystalline silicon coated with a 20-nm-thick SiO_2 buffer layer (Fig. 1). We studied the $Co(x)/SiO_2(y)$ bilayers with y = 2 nm and x = 1.3, 1.6, and 1.8 nm (here, x and y refer to the thicknesses of the corresponding layers) and $[Co(x)/SiO_2(y)]_n$ multilayers with the number of bilayers n = 6, 8, and 20. According to electron microscopy [1], the Co grains are oblate ellipsoids with an average size larger than the nominal thickness x. Metallic conductivity in the layer plane was observed at $x \approx 2.0$ nm.

The magnetooptical spectra measured on the bilayers and multilayers are displayed in Figs. 2 and 3, respectively. For comparison, Fig. 3b shows a magnetooptical spectrum measured in the same geometry for a Co film whose thickness exceeds the depth of formation of the magnetooptical signal ($D \approx 50$ nm). As is seen from these figures, the spectra obtained on both bi- and multilayers have an anomalous character, which was not observed earlier either for Co-based metallic granular alloys [2], or for $Co_x(Al_2O_3)_{1-x}$ nanocomposites with tunneling magnetoresistance [3], or again for multilayers. These anomalies are as follows:

(1) The sign, magnitude, and spectral shape of the magnetooptical signal depend heavily on the size of the Co particles. In particular, as the thickness x of the Co disperse layer rises from 1.6 to 1.8 nm, the signal changes by an order of magnitude and becomes negative (Fig. 2).

1063-7834/00/4210-1911$20.00 © 2000 MAIK "Nauka/Interperiodica"

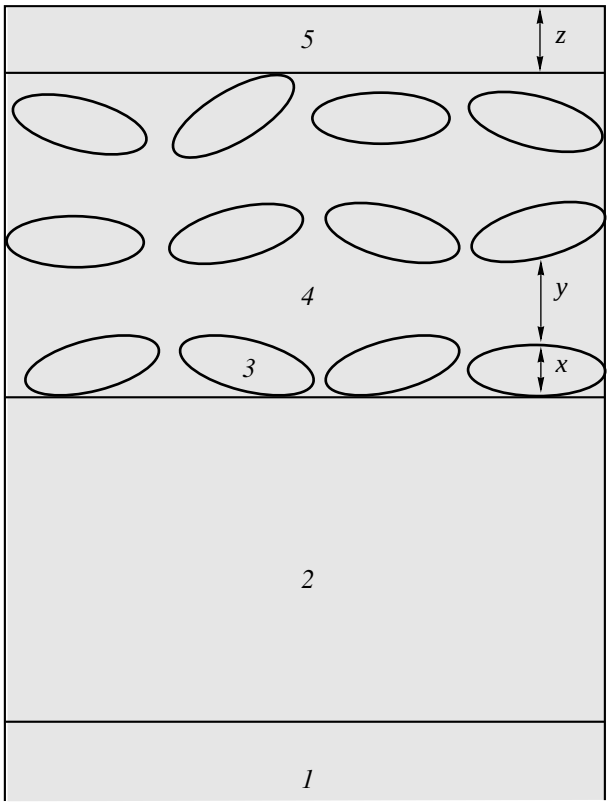

Fig. 1. Schematic representation of the cross-section of $[Co(x)/SiO_2(y)]_n$ hybrid multilayers: (*1*) crystalline Si substrate, (*2*) SiO_2 buffer layer, (*3*) layers of ellipsoidal Co particles of thickness x (nm), (*4*) SiO_2 dielectric layers, and (*5*) SiO_2 layer of thickness $z = 2.0$ nm.

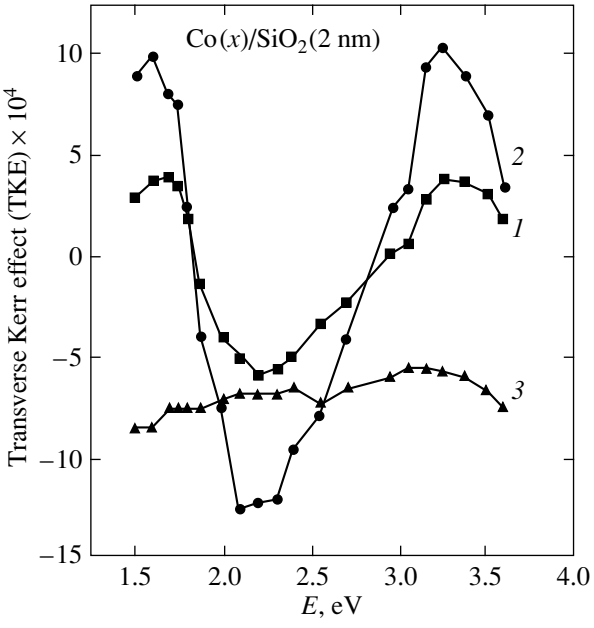

Fig. 2. Magnetooptical spectra of $Co(x)/SiO_2(y)$ bilayers with $y = 2.0$ nm; x (nm): (*1*) 1.3, (*2*) 1.6, and (*3*) 1.8.

(2) The amplitude of the signal for $[Co(1.6)/SiO_2(3.0)]_6$ multilayers at 3.0 eV is 3×10^{-2}, a record-high value for Co-based structures, which exceeds that for bulk Co (Fig. 3b) about fivefold and 50-fold the corresponding value for a uniform Co film of an equivalent thickness (the volume fraction of Co in a monolayer is about 0.5; therefore, for six such layers with $x = 1.6$ nm, the equivalent thickness $d \approx 5$ nm is only one tenth of the depth of formation D of the magnetooptical signal). The amplitude of the signal for bilayer systems (Fig. 2) at the maxima also exceeds that for Co continuous films of an equivalent thickness by several factors.

(3) The magnetooptical signal of multilayers depends nonlinearly on the number of periods (Figs. 3a, 3b), as well as on the thickness of the dielectric layer y.

(4) The dependence of the signal from the bi- and multilayers with $x = 1.3$ and 1.6 nm on the wavelength is nonmonotonic and exhibits distinct extrema.

In order to interpret the experimental data, we calculated the magnetooptical spectra of the bilayer structures in terms of macroscopic Fresnel magnetooptics in a modified effective-medium approximation [3]. First, the technique described in [3] was used to calculate the diagonal and off-diagonal components of the permittivity tensor for a layer of ferromagnetic particles, which was treated as a nanocomposite; in this case, the filling factor and particle form factor were varied. After this, the magnetooptical response of the SiO_2/Co–SiO_2 nanocomposite/SiO_2 buffer layer/Si system (Fig. 1) was calculated using the results [4] and taking into account reflections from the interfaces and absorption in the substrate. The application of the effective medium approach to a quasi two-dimensional layer and macroscopic Fresnel magnetooptics to ultrathin layers was done strictly qualitatively. Nevertheless, the calculations performed allow us reproduce the main features in the pattern of the magnetooptical spectra and give grounds for suggesting that the observed anomalies are connected primarily with the composition of the ferromagnetic layers, which is close to the percolation threshold. The optical parameters of the system, which determine the magnetooptical response, vary strongly near the percolation threshold. It should be emphasized that we have not succeeded in obtaining the correct ratio between the amplitudes of the maxima and the correct depth of the minimum in the spectrum; moreover, the percolation threshold ($x = 1.8$ nm) turns out to be somewhat lower than the experimental value ($x = 2.0$ nm). This is apparently due to the above-mentioned shortcomings of the calculation approach.

The situation becomes substantially more complex in the case of multilayers. Although percolation and the optical parameters also affect the shape of the spectrum and the signal amplitude, there is no correlation between the positions of the extrema for the multilayers and the bilayers, as well as for multilayers with differ-

ent numbers of periods. It can be assumed that the periodic arrangement of the percolation layers exerts a strong influence on the magnetooptical spectra, which requires further experimental and theoretical investigations.

A comparison of the spectra obtained on bi- and multilayers reveals two significant points. First, we did not observe any manifestation of quantum size effects in the magnetooptical properties of the samples studied. By analogy with ultrathin layers [5, 6], quantization of the electronic spectrum in nanoparticles should give rise to oscillations of the magnetooptical response under variation of both particle size and light frequency. Such oscillations of the magnetooptical signal with variations in the film thickness were recently observed in Fe and Co films [6]. It would seem that the two maxima observed in the magnetooptical spectra of the bilayers at 1.5 and 3.0 eV and the strong dependence of their amplitudes on the particle size are also due to quantum size effects. However, the dependences of the Kerr signal on the particle size and light frequency for the bilayers (Fig. 2) and calculations show that these features are not related in any way to the quantization of the electronic spectrum. The most convincing argument for this is the absence of similar maxima at the same frequencies in the magnetooptical spectra of multilayers (Fig. 3). It can be assumed that the grain dispersion in size, unavoidable in granular systems, suppresses the quantum size effect at least at room temperature. Because the magnetooptical properties are frequency counterparts of the anomalous Hall effect, we can thus conclude that the quantum size effect is not the main reason for the giant anomalous Hall effect observed in nanocomposites [7].

Second, one should pay attention to the deep minimum in the bilayer spectra at 2.0 eV, which is caused by plasma oscillations. Indeed, the frequency of plasma oscillations for small spherical particles in a medium with permittivity ε is smaller by a factor of $(2\varepsilon + 1)^{1/2}$ than that of bulk plasma oscillations (for Co, $\omega_p \approx 3.91$ eV) [8], so that the frequency of plasma oscillations for the granular $Co–SiO_2$ system falls in the visible spectral range. This is supported by direct measurements of the optical properties of bilayers. The absence of an analogous minimum at the same or similar frequency in the case of multilayers indicates a strong interaction between the layers of ferromagnetic particles and a possible effect of interlayer tunneling on plasma oscillations. This interaction depends heavily both on the particle size x and the layer thickness y and affects the formation of the optical and, consequently, the magnetooptical properties of hybrid multilayers.

In conclusion, we should note that the observed noticeable enhancement of magnetooptical effects in hybrid multilayers opens new avenues in the search for materials capable of producing a high magnetooptical response.

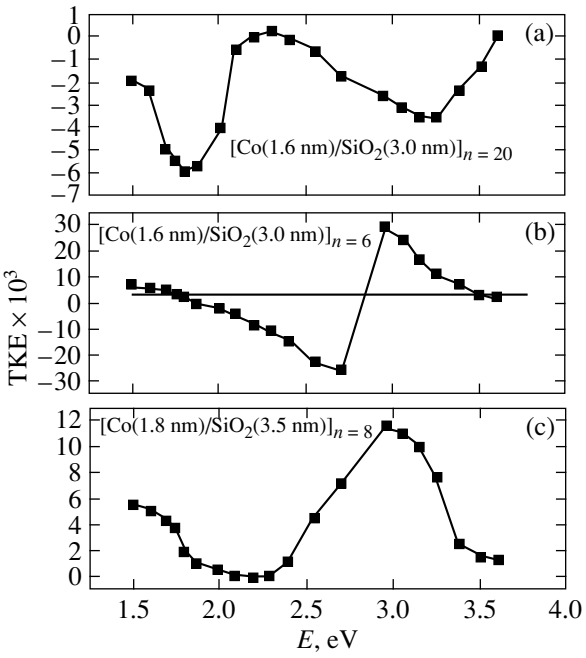

Fig. 3. Magnetooptical spectra of $[Co(x)/SiO_2(y)]_n$ multilayers: (a) $x = 1.6$ nm, $y = 3.0$ nm, and $n = 20$; (b) $x = 1.6$ nm, $y = 3.0$ nm, and $n = 6$ (the horizontal line is a magnetooptical spectrum of thick Co films); and (c) $x = 1.8$ nm, $y = 3.5$ nm, and $n = 8$.

ACKNOWLEDGMENTS

This work was supported by the Russian Foundation for Basic Research (project no. 00-02-17797) and NATO (grant no. 973279).

REFERENCES

1. B. Dieny, S. Sankar, M. R. McCartney, *et al.*, J. Magn. Magn. Mater. **185** (3), 283 (1998).
2. E. Ganshina, A. Granovsky, V. Gushin, *et al.*, Physica A (Amsterdam) **241**, 45 (1997).
3. A. Granovsky, M. Kuzmichov, and J. P. Clerc, J. Magn. Soc. Jpn. **23**, 382 (1999).
4. V. M. Maevskiĭ, Fiz. Met. Metalloved. **59**, 213 (1985).
5. A. Vedayev, N. Ryzhanova, S. Young, and B. Dieny, Phys. Lett. A **215**, 317 (1996).
6. E. E. Shalyguina, I. A. Pogrebnaya, O. A. Shalyguina, and K.H.Shin, in *Proceedings of MISM'99, Moscow, 1999,* Part 1, p. 337.
7. A. B. Pakhomov, X. Yan, N. Wang, *et al.*, Physica A (Amsterdam) **241**, 344 (1997).
8. Yu. Petrov, *Physics of Small Particles* (Nauka, Moscow, 1982).

Translated by G. Skrebtsov

Physics of the Solid State, Vol. 42, No. 10, 2000, pp. 1914–1920. Translated from Fizika Tverdogo Tela, Vol. 42, No. 10, 2000, pp. 1863–1868.

LOW-DIMENSIONAL SYSTEMS AND SURFACE PHYSICS

Elastic Scattering of Light from Quantum-Well Exciton-Polarization Fluctuations in a Microcavity

V. A. Kosobukin and A. V. Sel'kin

Ioffe Physicotechnical Institute, Russian Academy of Sciences, Politekhnicheskaya ul. 26, St. Petersburg, 194021 Russia

Received March 14, 2000

Abstract—A model of exciton polarization fluctuations in a quantum well of a randomly variable lateral width is proposed. The stochastic part of the nonlocal susceptibility of quasi-two-dimensional excitons is expressed through random functions of the shape of quantum well boundaries. A theory of elastic light scattering from a quantum well placed in a Fabry-Perot cavity or a semiconductor microcavity is constructed in the lowest (Born) approximation in interface roughness height. The scattering cross section is calculated for an arbitrary statistics of interface roughness. The spectral and angular dependences of the intensity of light scattered by a quantum well have been studied using Gaussian correlation functions of the interface shape. It follows from numerical estimates that elastic resonant scattering in quantum wells should be observed at an rms roughness height of the order of the atomic monolayer thickness. © *2000 MAIK "Nauka/Interperiodica".*

Many optical phenomena in quantum wells [1, 2] and semiconductor microcavities [3] are studied usually under the assumption that interfaces are perfectly flat. In this case, the in-plane component of the wave vector of light in a quantum well is conserved, and light can be emitted only in specular directions relative to the incident wave. Real quantum wells possess irremovable structural imperfections, the most significant of them being the random shape of the heteroboundaries [4]. The wall roughness of the quantum well makes its width variable in lateral directions, and spatial polarization-field fluctuations generated in this case may cause light scattering.

The role played by statistically rough heteroboundaries in exciton optics was considered in a few theoretical works (see references in [5]). In particular, a model was proposed [5] for exciton-polarization current fluctuations, which, by analogy with the model developed for the surface of dielectrics [6], expresses these fluctuations directly in terms of shape functions of a rough interface. This model was developed in [7, 8] to describe elastic scattering of light from a rough semiconductor surface and provided an explanation for the light scattering observed [7] in the exciton-resonance region. Estimates [5] show that the steady-state elastic scattering of light in quantum wells must be observed at an rms interface roughness height of the order of the monatomic-layer thickness. This model [5] raised a number of interesting theoretical problems in the optics of size-quantized structures taking into account the surface and numerous interfaces in the sample. The crystal surface plays an important part in the photon–exciton coupling, because under real conditions light is incident from the vacuum, and the secondary radiation being registered also emerges in vacuum. The effects associated with many heteroboundaries are of particular interest for semiconductor microcavities in which exciton polaritons [3], which may act as intermediate states in resonant elastic light scattering, are formed.

This work is aimed at a theoretical investigation of resonant elastic light scattering from the fluctuations of exciton polarization in a quantum well with statistically rough boundaries, which is placed in a multilayer medium. The problem is being solved as applied to microcavities, which are formed by distributed Bragg reflectors (DBR) and possess high-Q electromagnetic eigenmodes. The effect of interface roughness on the exciton transition frequency is considered as a perturbation. As a first step, we consider only the roughness of the quantum well walls which have a small height and a large correlation length in the plane of the well. The paper is organized as follows. In Section 1, a statistical model of a quantum well placed in a Fabry–Perot resonator is introduced, and in Section 2, the characteristics of quasi-two-dimensional excitons in an "averaged" quantum well are calculated. Analytical expressions for the observed reflectance spectra are derived in Section 3, and those for light scattering spectra from a quantum well inside a microcavity are described in Section 4. The results of numerical calculations of the spectra are discussed in Section 5.

1. THE MODEL AND BASIC RELATIONS

The main element of the model under consideration is a semiconducting layer ($0 < z < d$ in Fig. 1) which serves as a Fabry–Perot resonator (FPR) with a background permittivity ε_2. The light reflection coefficients from the plane boundaries at $z = 0$ and $z = d$ into the FPR are r_1 and r_2. The resonator contains a quantum

1063-7834/00/4210-1914$20.00

well centered at $z = z_0$ with randomly rough boundaries. The shape of the latter can be described by the equations $z = z_0 - \bar{L}/2 + \xi_1(x)$ and $z = z_0 + \bar{L}/2 + \xi_2(x)$, where $\bar{L}$ is the average well width. The average value of the random shape functions $\xi_n(x)$ of the nth interface (n = 1, 2) is $\langle \xi_n(x) \rangle = 0$, where the angle brackets denote averaging over the ensemble of the random functions $\{\xi_n(x)\}$. For the random quantum-well width, we have

$$L(x) = \bar{L} + \delta L(x) = \bar{L} + \xi_2(x) - \xi_1(x), \qquad (1)$$

where $\delta L(x)$ describes the quantum-well fluctuations.

We assume that a quantum well of variable width (1) in the lateral direction x can be considered as a set of one-dimensional islands, the well width in each of them being nearly constant. The cross section of a light beam in an optical experiment encompasses a large number of islands making up a statistical ensemble. On the other hand, if the lateral dimensions of the island determined by the transverse correlation length of the interface roughness exceed the exciton Bohr radius a_B, the quasi-two-dimensional exciton locally retains its identity relative to an unbounded quantum well of the corresponding width (1). We present the exciton polarization **P** and the electric field of a given frequency ω in the form

$$\mathbf{P}(\mathbf{r};\, \omega) = \mathbf{e}_y [P^0(x;\, Q, \omega) + \delta P(z;\, Q, \omega)] \exp(iQx). \qquad (2)$$

Here, Q is the tangential wave-vector component, which is conserved as the wave traverses the plane boundaries and is a parameter of the problem. Expression (2) corresponds to s-polarized light along the y axis with a unit vector $\mathbf{e}_y$; scattering does not affect the polarization because the disorder is one-dimensional. The Fourier component of the polarization amplitude (2) in a quantum well assumes the form [5]

$$4\pi P(z;\, Q, \omega) = \int dz' \int \frac{dQ'}{2\pi} \chi(z, z';\, Q - Q', \omega) E(z';\, Q', \omega). \qquad (3)$$

We introduce a slow dependence of the random frequency of a quasi-two-dimensional exciton $\omega_0[L(x)]$ on coordinate x through the quantum well thickness $L(x)$. In the case of small roughness, $\sqrt{\langle \delta L \rangle^2} \ll \bar{L}$, the quantity χ in (3) can be conveniently expanded in δL up to the first order. Ignoring the variation of the envelope of the exciton wave function $\psi(z) = \psi(-z)$ and the quantum-well bending [5], we obtain for the nonlocal susceptibility in (3)

$$\chi(z, z', Q' - Q, \omega) = \chi^0(\omega) \times \left[2\pi\delta(Q' - Q) + \frac{\Omega \delta L(\theta' - \theta)}{\Delta_0(\omega)\bar{L}} \right] \psi(z - z_0)\psi(z' - z_0). \qquad (4)$$

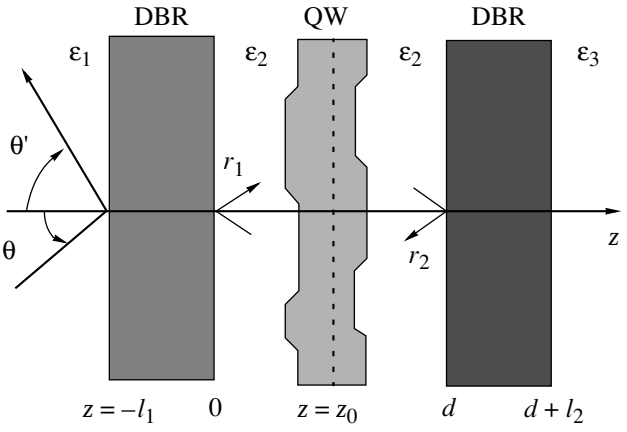

Fig. 1. Geometry of the problem. The figure shows distributed Bragg reflectors (DBR) and a quantum well (QW). The arrows specify the positive directions of reckoning of the angles of light incidence, θ, and scattering, θ'.

This relation holds under the condition $\sqrt{\langle \delta\omega_0^2 \rangle} < \gamma$. Here

$$\chi^0(\omega) = \frac{G_0}{\bar{\omega}_0 - \omega - i\gamma} = \frac{G_0}{\Delta_0(\omega)} \qquad (5)$$

describes the resonant response of an "average" quantum well with plane boundaries $z = \pm\bar{L}/2$ in accordance with [9]. For this quantum well, $\bar{\omega}_0$ is the exciton transition frequency, G_0 is the exciton–photon coupling parameter whose dependence on the average thickness $\bar{L}$ is ignored [10], and γ is the nonradiative exciton-decay rate.

The exciton transition energy, which is dependent on the local quantum well width $L(x)$ from (1), can be written as $\hbar\omega_0(L) = E_{\text{gap}} + E_{\text{conf}}(L) - E_{\text{bind}}(L)$, where E_{gap} is the gap width of the bulk semiconductor, E_{conf} is the total quantum-confinement energy of an unbounded electron and a hole in the quantum well, and E_{bind} is their binding energy in the exciton. As follows from [11], the main contribution to the frequency shift $\omega_0(L)$ relative to the average value $\bar{\omega}_0$ is associated with the $E_{\text{conf}}(L)$ dependence. The random correction $\delta\omega_0(x) = \omega_0(x) - \bar{\omega}_0 \approx \delta L(x)\{\partial\omega_0/\partial L\}_{L=\bar{L}}$, which is proportional to the variation of the quantum-well width (1), can be written, provided that $\sqrt{\langle \delta\omega_0^2 \rangle} \ll \bar{\omega}_0$, in the form

$$\delta\omega_0(x) = -\Omega\frac{\delta L(x)}{\bar{L}} = -2\pi^2\beta\left(\frac{R_x}{\hbar}\right)\left(\frac{a_B}{\bar{L}}\right)^2\frac{\delta L(x)}{\bar{L}}, \qquad (6)$$

where R_x is the Rydberg exciton energy, and $\beta \sim 1$ [5]. Thus, the exciton susceptibility (4) and the exciton frequency shift (6) are expressed directly through the random interface shape functions appearing in (1). The regular (nonstatistical) contribution to susceptibility (4) is taken into account in a self-consistent way, and the random contribution is considered in the lowest order of perturbation theory in the fluctuation of the quantum well thickness (1).

Let us now consider a quantum well in an optical arrangement corresponding to a semiconductor microcavity (MC) (see Fig. 1). We assume that the permittivity is ε_1 for $z < -l_1$ and ε_3 for $z > d + l_2$, where l_1 and l_2 are the thicknesses of the left- and right-hand DBRs representing the MC walls. In the media specified above by the permittivities ε_m, the electric field of the *s* polarized wave (2) can be written as

$$\mathbf{E}(\mathbf{r}; \omega) = \mathbf{e}_y[A_m \exp(ik_m z) + B_m \exp(-ik_m z)]\exp(iQx), \quad (7)$$

where $k_m = k_m(Q) = \sqrt{\varepsilon_m k_0^2 - Q^2}$ in the *m*th medium, $k_0 = \omega/c$, and c is the velocity of light in vacuum. The coefficients A_m and B_m in different media are related to one another through 2×2 transfer matrices through the left and right MC walls.

2. QUASI-TWO-DIMENSIONAL EXCITONS OF AN "AVERAGE" QUANTUM WELL IN A FABRY–PEROT RESONATOR

Following [5, 6], we will solve the zeroth-approximation problem [$\delta L(x) = 0$], which takes into account only the regular part of polarization (2) and of the response function (4), self-consistently by Green's function method. If we take into account the internal reflection coefficients of light $r_1(Q)$ and $r_2(Q)$ from the FPR walls, this approach leads to the following expression for the complex frequency of exciton transition in an "average" quantum well:

$$\omega_0(Q) = \bar{\omega}_0 + \Gamma(Q)\mathrm{Im}F(z_0, Q) - i\{\gamma + \Gamma(Q)[1 + \mathrm{Re}F(z_0, Q)]\}. \quad (8)$$

Here

$$\Gamma(Q) = \Gamma_0\sqrt{\varepsilon_2}k_0/k_2(Q), \quad (9)$$

$$F(z_0, Q) = \frac{1}{D(Q)}\{r_1\exp(2ik_2z_0) + r_2\exp[2ik_2(d - z_0)] + 2r_1r_2\exp(2ik_2d)\}, \quad (10)$$

$$D(Q) = 1 - r_1(Q)r_2(Q)\exp(2ik_2d), \quad (11)$$

and Γ_0 is the exciton radiative decay rate. The difference $\omega_0(Q) - (\bar{\omega}_0 - i\gamma)$ calculated from (8) describes the radiation parameters of the exciton frequency shift $\Gamma\mathrm{Im}F(z_0)$ and of the exciton decay $\Gamma[1 + \mathrm{Re}F(z_0)]$. The latter vanish or are transformed into (9), respectively, for a single quantum well in an unbounded medium with permittivity ε_2, where $r_1 = r_2 = 0$ and $F = 0$. If at least one of the coefficients r_1 and r_2 is not zero, it follows from (8)–(11) that the radiation contributions to the exciton frequency and decay oscillate as functions of z_0 or d as a result of optical interference, the amplitude of these oscillations being equal to (9).

3. LIGHT REFLECTION FROM A MICROCAVITY WITH AN "AVERAGE" QUANTUM WELL

A quantum well placed in a microcavity is acted upon by the electromagnetic eigenmodes of the latter, which can interact with the exciton resonance of the well. In the case of an "average" quantum well, the field in the region $0 < z < z_0 - \bar{L}/2$ inside the MC, which is excited by a wave incident on the MC from the region $z < -l_1$ with an amplitude A_1, can be written as

$$E(z; Q) = A_1\left\{\left[1 + r_1\frac{i\Gamma\Phi^2(z_0)}{D\Delta}\right]\exp(ik_2z) + \left[r_2\exp(2ik_2d) + \frac{i\Gamma\Phi^2(z_0)}{D\Delta}\right]\exp(-ik_2z)\right\}. \quad (12)$$

Here

$$\Phi(z; Q) = \exp(ik_2z) + r_2\exp(2ik_2d)\exp(-ik_2z), \quad (13)$$

$$\Delta(\omega, Q) = \omega_0(Q) - \omega, \quad (14)$$

the last expression containing frequency (8). Using the DBR transfer matrices, we find the following relation for the reflection coefficient of the incident wave specified above:

$$r(Q) = \rho_1 + \tau_1t_1[i\Gamma\Phi^2(z_0)\Delta^{-1}D^{-1} + r_2\exp(2ik_2d)]D^{-1}. \quad (15)$$

Here, ρ_1 is the reflection coefficient of the wave incident along the *z* axis from the isolated left-hand DBR bounded by the media with ε_1 and ε_2, and τ_1 and t_1 are the transmission coefficients for the same element when the light propagates along the *z* axis and in the opposite direction, respectively. Note that the spectrum of the MC electromagnetic eigenmodes is determined by the formal condition $|r(Q)| \longrightarrow \infty$ for $\Gamma = 0$ (i.e., in the absence of a quantum well) in (15). In the presence of a quantum well, this condition results in a dispersion equation describing the bound states formed by an MC eigenmode and a quantum-well exciton. These states manifest themselves directly in the light scattering considered below.

4. LIGHT SCATTERING BY A RANDOM-WIDTH QUANTUM WELL IN A MICROCAVITY

Elastic scattering of light is determined by the random contribution δP to polarization (2), which we shall consider in the first order of perturbation theory in ξ_n (the Born approximation). We assume that a photon hits the microcavity at an angle θ and is scattered back at an angle θ' (Fig. 1 illustrates the measurement of the angles θ and θ' from the z axis with due account of their sign; in the following analysis, we put $\theta > 0$). By analogy with [5], we obtain for the dimensionless scattering cross section

$$\frac{d\sigma}{d\theta'} = W(Q-Q')\frac{\cos^2\theta'}{\cos\theta} \times |SS'\Phi(z_0)\Phi'(z_0)|^2|D'|^{-2}|M_I M'_{II}|^2. \quad (16)$$

Here, the unprimed (primed) quantity was calculated for the tangential component Q (Q') of the wave vector of the incident (scattered) plane wave, with $(Q, Q') = \sqrt{\varepsilon_1}\,k_0(\sin\theta, \sin\theta')$. In relation (16), the quantity $W(Q-Q')$ is proportional to the Fourier transform of the correlation function $\langle\delta L(x-x')\delta L(0)\rangle$, which in a general case is a sum of the correlators

$$\langle\xi_n(Q)\xi^*_{n'}(Q')\rangle = 2\pi h_n h_{n'} g_{nn'}(|Q|)\delta(Q-Q'), \quad (17)$$

where $g_{nn'}(x) = \langle\xi_n(x)\xi_{n'}(0)\rangle/h_n h_{n'}$, and $h_n^2 = \langle\xi_n^2(x)\rangle$ is the dispersion in the roughness height of the quantum well wall. In expressions (17), we assume that the roughness is one-dimensional and, on average, uniform in the quantum-well plane. The exciton resonance features in the scattering spectrum are described by the spectral functions

$$S(\omega, Q) = \frac{\sqrt{\Omega}\Gamma(Q)}{\Delta(\omega, Q)} \quad (18)$$

with resonant denominators (14). The coefficients M_I and M'_{II} in (16) describe light transformation in the forward and backward propagation through the left-hand DBR of the MC wall.

It is essential that expression (16) containing Fourier components (17) of the correlation functions is formally the same for roughness of any statistical distribution, the latter affecting the specific form of the functions $g_{nn'}(|Q|)$ only. Actually, the statistics of the heteroboundary shape is unknown, and therefore, for the estimation of the Gaussian correlation functions, we shall use

$$\langle\xi_n(x)\xi_{n'}(x')\rangle = \delta_{nn'}h_n^2\exp(-|x-x'|^2/\Lambda_n^2) \quad (19)$$

with transverse roughness autocorrelation lengths Λ_n. The Kronecker delta $\delta_{nn'}$ in (19) indicates that the interfaces are not mutually correlated, and

$$W(Q-Q') = W_1(Q-Q') + W_2(Q-Q'), \quad (20)$$

where

$$W_n(Q-Q') = \frac{1}{2\sqrt{\pi}}\frac{\sqrt{\varepsilon_1}k_0\Lambda_n h_n^2}{\bar{L}^2}\exp\left(-\frac{|Q-Q'|^2\Lambda_n^2}{4}\right). \quad (21)$$

Mutual correlation of the interface random shape can be taken into account in analogy with [5, 7]; however, in our problem, this would result in only a very small additional scattering associated with the quantum well bending [5].

5. RESULTS OF CALCULATIONS AND DISCUSSION

Calculated spectra of optical reflectance $|r(\omega, Q)|^2$ from a microcavity with an "average" GaAs/AsGaAs quantum well of thickness $\bar{L}$ are presented in Fig. 2a for a light hole (with an exciton), $1e-1lh$. The variation of the resonant features with the angle of light incidence indicates a strong coupling between the quantum-well exciton and the microcavity electromagnetic eigenmode. The excitation spectrum in the absence of exciton-photon coupling is shown in Fig. 2b by dashed curves; it includes a close-to-parabolic dispersion branch of the microcavity electromagnetic eigenmode with the frequency ω_c at the minimum and the quantum-well exciton branch with frequency $\bar{\omega}_0$ and with a negligible dispersion. The spectrum of resonantly interacting eigenmodes (near the intersection of the branches corresponding to $\theta = \pm 18°$ in Fig. 2b) splits into two exciton–polariton branches $\omega_\pm(\theta)$. The dispersion relation $\omega_\pm(\theta)$ constructed using the positions of the narrow reflectance minima is plotted in Fig. 2b as a function of a dimensionless parameter $\sin\theta = Q/(\sqrt{\varepsilon_1}\,k_0)$. The exciton–polariton splitting results in a redistribution of spectral intensity between the components $\omega_-(\theta)$ and $\omega_+(\theta)$ as the angle θ is varied (this is seen from Fig. 2a), the of the intensities two modes becoming equal near the resonance angle.

Figure 2c presents the results of a numerical calculation of the light elastic-scattering cross sections (16). In expression (20), use is made of Gaussian autocorrelation functions with statistical parameters $\Lambda_1 = \Lambda_2 = \Lambda$ and $h^2 = h_1^2 = h_2^2$. The reflectance spectrum in Fig. 2a displays maxima at the frequencies of the excitonic transitions, each of them corresponding in (16) to its spectral factor (18). The formation of the scattering spectrum (Fig. 2c) is also determined by polariton dispersion curves (Fig. 2b). In a general case of $\theta' \neq \theta$, the resonant light-scattering spectrum contains basically two pairs of frequencies, one of them being determined by the points $\omega_\pm(\theta)$ for the incident light, and the other, by the points $\omega_\pm(\theta')$for the secondary radiation, where θ (>0) and θ' are the angles of incidence and scattering of light outside the microcavity (see Fig. 1). In a general case, the spectral components $\omega_\sigma(\theta)$ and $\omega_\sigma(\theta')$

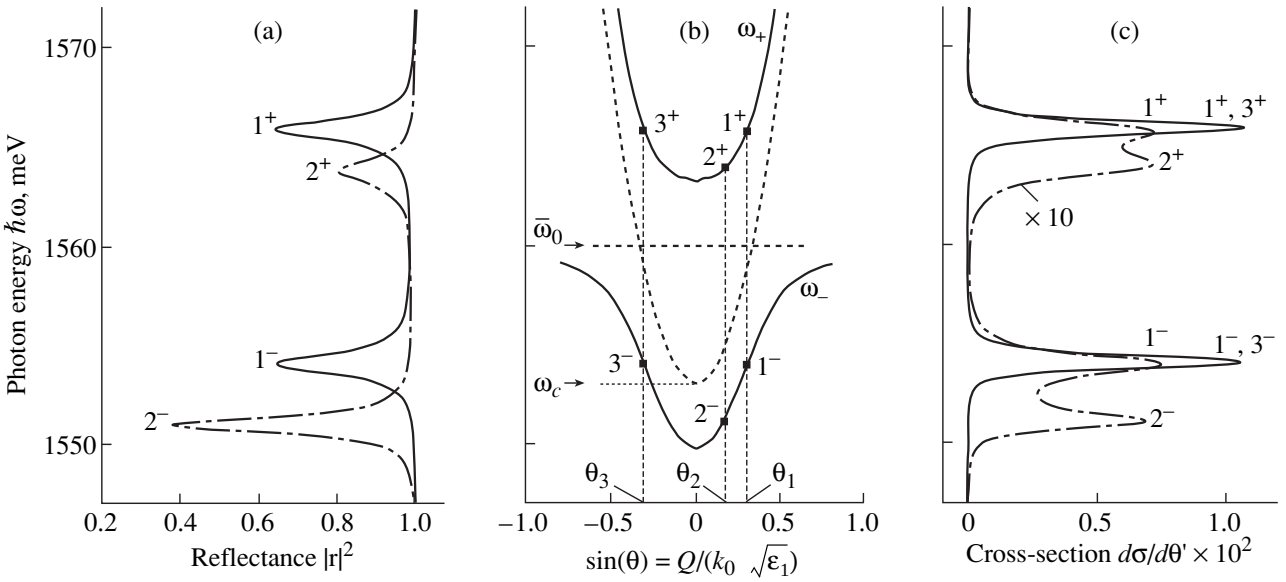

Fig. 2. (a) Reflection coefficient $|r|^2$, (b) exciton polariton dispersion branches $\omega_{\pm}(\theta)$, and (c) dimensionless elastic-scattering cross section of light, $d\sigma/d\theta'$, for a quantum well with stochastically rough walls placed in a microcavity. The parameters of the light-hole exciton 1*e*–1*lh* in a GaAs-based heterostructure used are as follows: $\hbar\bar{\omega}_0$ = 1560 meV, $\hbar\omega_c$ = 1553 meV (microcavity resonance energy), $\hbar\gamma$ = 1.0 meV, $\hbar\Gamma_0$ = 0.25 meV, $\bar{L}$ = 14 nm, $\hbar\Omega$ = 50 meV, $\varepsilon_1 = 1$, $\varepsilon_2 = \varepsilon_3 = 12.5$, the dielectric constant of the quarterwave DBR plates is 8.76 (AlAs) and 12.53 (GaAs), and the numbers of periods of left- and right-hand DBR are 15 and 19, respectively. The calculations are based on Gaussian correlation functions (19)–(21) with the parameters h = 0.2 nm and $\Lambda_1 = \Lambda_2$ = 150 nm. The spectral features in (a) and (c) correspond to the following angles of incidence or scattering: $\theta_1 = 18°$, $\theta_2 = 9°$, $\theta_3 = -18°$ (Fig. 2b).

relating to the same (σth) dispersion branch manifest themselves in the exciton–polariton splitting region as a doublet (shown by the dot-and-dash curves in Fig. 2c). For $|\theta'| \longrightarrow \theta$, the spectral maxima for the incident and scattered light coincide, and therefore the components in each of the doublets merge. The remaining two spectral maxima corresponding to the frequencies $\omega_{\pm}(\theta)$ become enhanced; this effect is illustrated by the solid curve in Fig. 2c for the case of backward scattering in the antispecular direction ($\theta = 18° = -\theta'$).

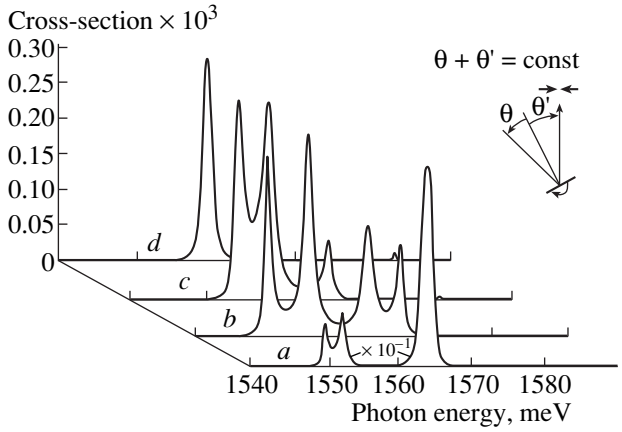

Fig. 3. Dimensionless cross sections $d\sigma/d\theta'$ of elastic light scattering from interface roughness of a quantum well in a microcavity, as functions of the photon energy $\hbar\omega$. The spectra were calculated for the condition $\theta + \theta' = 18°$ (see the inset) for the following angles of light incidence θ: (*a*) 4°, (*b*) 22°, (*c*) 36°, and (*d*) 56°. The other parameters are the same as in Fig. 2.

The rearrangement of the resonant structure of the scattering cross section is displayed in greater detail in Fig. 3 for different angles of light incidence (scattering). These results correspond to the condition $\theta + \theta' = 18°$ (the relation $\theta + \theta' = \text{const}$ usually holds in the experiments [7] where, as shown in the inset to Fig. 3, the angle $\theta + \theta'$ between the radiation source and the detector is fixed, and the angles θ and θ' vary in a correlated way as the crystal is rotated). It can be seen from Fig. 3 that the maxima in the scattering spectrum are displaced in accordance with the dispersion relation $\omega_{\pm}(\theta)$, and their absolute and relative intensities vary. Small angles of incidence and scattering correspond to a clearly pronounced doublet structure of the spectra and equalization in intensity of the doublets relating to the branches $\omega_-(\theta)$ and $\omega_+(\theta)$ near the resonance angles. At large enough angles θ and |θ'|, the spectra undergo a substantial rearrangement. For instance, the components of the doublet associated with the lower dispersion branch $\omega_-(\theta)$ merge because of the small dispersion of this branch in the region of large angles (Fig. 2b). By contrast, the components of the upper-

branch doublet noticeably move apart as a result of the superlinear dispersion $\omega_+(\theta)$ and decrease in intensity. We note in this connection that for $\theta + \theta' = \text{const}$, the scattering intensity (16) may become suppressed substantially at large angles θ and θ' if the transverse correlation length Λ of the roughness is large enough; this is due to a sharp decrease of the correlation function (21), which depends on θ and θ' through $|Q - Q'| = \sqrt{\varepsilon_1}\, k_0 |\sin\theta - \sin\theta'|$. Here, the condition $\Lambda \ll 1/k_0$ corresponds to scattering quasi-isotropic in θ', and therefore, most of the light singly-scattered by the quantum well cannot leave the microcavity because of a large dielectric contrast at the semiconductor–vacuum interface. By contrast, for $\Lambda \gg 1/k_0$, the scattered radiation becomes concentrated within a comparatively small angular interval near the direction of specular reflection, and therefore, most of it can escape from the semiconductor.

The fundamental result of our theory is the estimation of the probability of photon scattering from the heterostructure interface roughness, $w_{QW} \sim (\Lambda h^2)/(\lambda \bar{L}^2)$, where $\lambda \sim 1/k_0$ (two-dimensional disorder in the plane of the quantum-well boundaries will give rise here to an additional factor Λ/λ [5]). According to Figs. 2 and 3, in the exciton-resonance region, $w_{QW} \sim 10^{-3}$–10^{-2} for GaAs-based quantum wells, whose rms roughness height fluctuation $h \sim 10^{-1}$ nm. We note for comparison that for a rough semiconductor surface, this estimate changes to $w_S \sim (\Lambda_s h_s)^2/\lambda^4$, where h_s and λ_s are the parameters of function (21) for a rough surface, [7]. Accepting the usual condition $\bar{L}/\lambda \ll 1$, we find that $w_{QW}/w_S \sim (\lambda/\bar{L})^2 \gg 1$ for $h = h_s$ and $\Lambda = \Lambda_s \sim 1/k_0$. This means that the probability of resonant exciton light scattering from a single quantum well with atomically rough interfaces may exceed in order of magnitude the probability measured in [7] for scattering of the same type from a statistically rough semiconductor surface.

Thus, we have constructed a correlation theory of elastic light scattering through excitonic states of a quantum well with a laterally fluctuating width in a layered medium possessing electromagnetic eigenmodes. The light scattering was studied, with due account of the complex electrodynamic environment and interference, in the lowest approximation in random roughness fluctuations of quantum-well walls, against the background of the reflection (transmission) effects in a quantum well of an "average" width. It has been shown that the intensity of elastic light scattering from fluctuations of exciton polarization in a single quantum well with atomic-scale roughness may substantially exceed the experimental detection threshold [7]. The fact that the resonant elastic light-scattering cross section is expressed directly through statistical parameters of the rough heterostructure boundaries makes the results of the theory convenient for determining these parameters from experimental data.

It should be stressed that additional scattering of light, which was disregarded in our theory, may arise if the interfaces in Bragg reflectors have statistical roughness. The corresponding contribution to the radiation, which is not associated with the quantum well, could be analyzed by our method, but this would involve the solution of the fairly complex problem of finding response functions (electrodynamic Green's functions) of a microcavity. It is expected that light scattering from interface roughness in Bragg's reflectors may bring about a relative redistribution of spectral intensity in favor of those of the resonance peaks discussed above that correspond to scattering through photon-like states of the system.

ACKNOWLEDGMENTS

This work was supported by the Russian Foundation for Basic Research (project no. 00-02-16924) and carried out by one of the authors (A. V. S.) in cooperation with Universidad Autonoma de Puebla, Centro de Investigaciones en Dispositivos Semiconductoros 4 Sur 104, Centro C. P. 72000 Puebla, Mexico.

REFERENCES

1. S. Schmitt-Rink, D. S. Chemla, and D. A. B. Miller, Adv. Phys. **38** (2), 89 (1989).
2. E. L. Ivchenko and G. E. Pikus, in *Superlattices and Other Heterostructures: Symmetry and Optical Phenomena*, Springer Series in Solid State Sciences (Springer, Berlin, 1995), Vol. 110.
3. R. Houdre, C. Weisbuch, R. P. Stanley, *et al.*, Phys. Rev. Lett. **73** (15), 2043 (1994); R. Houdre, R. P. Stanley, U. Oesterle, *et al.*, Phys. Rev. B **49** (23), 16761 (1994).
4. J. Singh, K. K. Bajaj, and S. Chaudhuri, Appl. Phys. Lett. **44** (4), 805 (1984); T. Bechstedt and R. Enderlein, *Semiconductor Surfaces and Interfaces, Their Atomic and Electronic Structures* (Academie, Berlin, 1988; Mir, Moscow, 1990).
5. V. A. Kosobukin, Solid State Commun. **108** (1), 83 (1998); Fiz. Tverd. Tela (St. Petersburg) **41** (2), 330 (1999) [Phys. Solid State **41**, 296 (1999)].
6. A. A. Maradudin and D. L. Mills, Phys. Rev. B **11** (4), 1392 (1975); D. L. Mills and A. A. Maradudin, Phys. Rev. B **12** (8), 2943 (1975).
7. V. A. Kosobukin and A. V. Sel'kin, Pis'ma Zh. Éksp. Teor. Fiz. **44** (8), 377 (1986) [JETP Lett. **44**, 483 (1986)]; Solid State Commun. **66** (3), 313 (1988); V. A. Kosobukin, M. I. Sazhin, and A. V. Sel'kin, Fiz. Tverd. Tela (Leningrad) **32** (4), 1023 (1990) [Sov. Phys. Solid State **32**, 602 (1990)]; Solid State Commun. **94** (11), 947 (1995).

8. G. H. Cocoletzi and S. Wang, Phys. Rev. B **48**, 17413 (1993); J. Madrigal-Melchor, F. Perez-Rodrigues, A. Silva-Castillo, and H. Azucena-Coyotecatl, Fiz. Tverd. Tela (St. Petersburg) **40** (5), 865 (1998) [Phys. Solid State **40**, 796 (1998)]; J. Madrigal-Melchor, H. Azucena-Coyotecatl, A. Silva-Castillo, and F. Perez-Rodriguez, Phys. Rev. B **61** (23), 15993 (2000).
9. L. C. Andreani and F. Bassani, Phys. Rev. B **41** (11), 7536 (1990); E. L. Ivchenko, Fiz. Tverd. Tela (Leningrad) **33** (8), 2388 (1991) [Sov. Phys. Solid State **33**, 1344 (1991)].
10. E. L. Ivchenko, V. P. Kochereshko, P. S. Kop'ev, *et al.*, Solid State Commun. **70** (5), 529 (1989).
11. G. Bastard, E. E. Mendez, L. L. Chang, and L. Esaki, Phys. Rev. B **26** (2), 1974 (1982); R. L. Greene, K. K. Bajaj, and D. E. Phelps, Phys. Rev. B **29** (4), 1807 (1984); M. Matsuura and Y. Shinozuka, J. Phys. Soc. Jpn. **53** (9), 3138 (1984).

Translated by G. Skrebtsov

Physics of the Solid State, Vol. 42, No. 10, 2000, pp. 1921–1926. Translated from Fizika Tverdogo Tela, Vol. 42, No. 10, 2000, pp. 1869–1873.

LOW-DIMENSIONAL SYSTEMS AND SURFACE PHYSICS

Fluctuations of Steps at the Faces of Potassium Dihydrophosphate Crystals in a Solution

L. N. Rashkovich, O. A. Shustin, and T. G. Chernevich

Moscow State University, Vorob'evy gory, Moscow, 119899 Russia

e-mail: rashk@polc49.phys.msu.su

Received January 24, 2000; in final form, March 13, 2000

Abstract—The time dependence of the step-displacement fluctuations at the faces of a prism and a bipyramid of potassium dihydrophosphate (KDP) crystals is determined by *in situ* atomic-force microscopy in the line-by-line scanning mode. It is shown that the build-up of fluctuations follows a $t^{1/4}$ law and not a $t^{1/2}$ dependence as for a single diffusing particle. Measurements are made during growth and dissolution in the vicinity of the equilibrium position. It is found that the fluctuations at the prism face during dissolution are stronger than those during growth. Voronkov's theory is used to compute the basic parameters of crystallization and to interpret the obtained results. © *2000 MAIK "Nauka/Interperiodica".*

Elementary acts of crystallization, viz., the attachment of atoms or molecules of the medium to the crystal, have been studied *in situ* using scanning tunnel and reflection electron microscopy for observing the surface of metals and the growth of epitaxial layers at high temperatures under vacuum [1–4]. Under these conditions, the crystallization is governed by the diffusion of adsorbed atoms to growth sites, i.e., fractures at the steps confining the growth layers [5]. The stochastic nature of the process, which leads to time and space fluctuations of the step movement, was studied theoretically by a number of authors who considered all possible displacements of the adsorbed structural units [6, 7]. The molecular-scale resolution at the surface of the crystals growing in a solution was repeatedly achieved with an atomic-force microscope only in proteins [8–10], but the step fluctuations have only been reported so far in one publication [11]. The results were interpreted with due regard for the limiting role of the surface diffusion, although the observed images of the surface did not clearly reveal whether the molecules were attached from the bulk or due to 2*D* diffusion.

Generally speaking, surface diffusion in solutions (melts) needs not play a significant role, as a sufficient "feeding" itself can ensure a direct incorporation of particles into the fractures. Thus, it has been proved that the surface diffusion does not affect growth kinetics during the crystallization of KDP from an aqueous solution [12]. To our knowledge, only Voronkov [13] has calculated the fluctuations for a direct incorporation of particles from the medium into a step. He has shown that the mean amplitude of fluctuations of a step region is only proportional to the square root of time (as in the case of Brownian movement) for a short period. Subsequently, as the fluctuations engulf the adjoining regions of the step, their amplitude becomes proportional to the fourth root of time.

Molecular resolution at the KDP crystal faces was obtained by us earlier [14]. However, a direct observation of the incorporation of particles in the crystal was not possible on account of their small size. In this case, studies of fluctuations allow us to determine the density of fractures at a step and the frequency of attachment and detachment of structural units. It is also possible to calculate the free linear energy and the kinetic coefficient of the steps. The knowledge of the amplitude of fluctuations is also important for judging the formation of macrosteps and trapping of impurities.

In this work, we used an atomic-force microscope for *in situ* studies of step fluctuations on the faces of a prism and a bipyramid of the KDP crystals in solutions close to saturation.

1. MEASURING TECHNIQUE

Measurements were made on a Nanoscope 3 supplied by Digital Instruments and in a standard liquid cell. Silicon nitride tips with an angle of 36° at the end were used. Contact scanning was carried out. The measuring tip did not affect the fluctuation amplitude (unlike the data obtained by Mugele *et al.* [15] for silver by tunnel microscopy), which was independent of the scanning frequency (5–30 Hz, 512 scans) or the force of interaction between the measuring tip and the sample (which was varied by a factor of ten). The instrumental drift was about 10 nm/min and was determined mainly by the elastic properties of a rubber ring used for a hermetic sealing of the measuring cell, as well as by the quality of sealing by the ring.

Samples of size $\sim 3 \times 3 \times 1$ mm were placed in the measuring cell, which was filled with a weakly super-

1063-7834/00/4210-1921$20.00

saturated solution. The content of Al, Fe, and Cr impurities in the salt used to prepare the solution was 0.6, 0.3, and 0.01×10^{-4} wt %, respectively (the results of an analysis of this salt for 37 elements are given in [16]). The solution was prepared in water with a resistivity of 16 MΩcm. The required precision of temperature stabilization for carrying out measurements under equilibrium conditions could not be ensured; hence, the growth layers moved during observation, but their displacement rate was less than 1 nm/s. In order to keep the step being measured in the field of vision, we had to slightly change the temperature, hence, the crystal alternately grew and dissolved in the course of the experiment. Note that no significant delay was observed between the growth and dissolution for both faces, which indicates the absence of a truly dead supersaturation region for the prism face. Measurements were made at temperatures ranging between 25 and 27°C on different days.

2. EXPERIMENT

Figure 1 shows the image of a step on a prism face. It can be seen under a very large magnification that the step is quite rugged; i.e., it contains a large number of fractures. The plane regions separating the fractures are not resolved. Observations revealed that the form of the steps fluctuates significantly. In order to analyze the fluctuations, the slow motion of the scanner was stopped, and the change in the position of a single point (region) on the step with time was determined. Some images are shown in Fig. 2. The coordinate of the chosen point also varies as a result of fluctuations due to the movement of the step and instrumental drift. It can be seen that the step does not remain immobile, and moves to the left or right; i.e., it grows or dissolves with time. As mentioned above, the growth or dissolution occurred in such a way that the step does not leave the field of vision. Figure 3 shows the time dependence of the coordinate of the point under observation. Measurements were performed with the help of the Femtoscan program [17], which allowed us to pass a section of the relief profile for each scan. Measurements were carried out during alternate scans, and 207 measurements were made for each frame as shown in Fig. 2. Thus, the coordinate was measured at the intervals $\Delta t_{min} = 0.196$ s.

Using these data, we plotted the dependences of $\langle [x(t + \Delta t) - x(t)]^2 \rangle$ on Δt (separately for the growth and dissolution) in order to describe the increase in fluctuations with time. Averaging was carried out for all values of t for Δt = const. It can be seen from Fig. 3 that the step moves as a whole at a rate of about 0.5 nm/s. This dependence for the dissolution is shown in Fig. 4a. It can be seen that, beginning from 5 s, the sublinear dependence is replaced by a nearly linear dependence. This is apparently due to the movement of the step, since the velocity calculated from the last four points coincides with the rate of displacement of the step. We did not make any attempt to eliminate this movement and confined ourselves to an analysis of the curve for the first few seconds only.

It can be seen from Fig. 4b containing the data on growth and dissolution that the mean square of fluctuations is proportional to $\Delta t^{1/2}$. A similar result was obtained for step fluctuations at the face of a bipyramid, but, in this case, no difference was observed between fluctuations for growth and dissolution. This dependence is also shown in Fig. 4b. It can be seen that step fluctuations at the face of the prism during growth are smaller than those during dissolution, and are also smaller at the face of the bipyramid than at the face of the prism. Unfortunately, no information is available

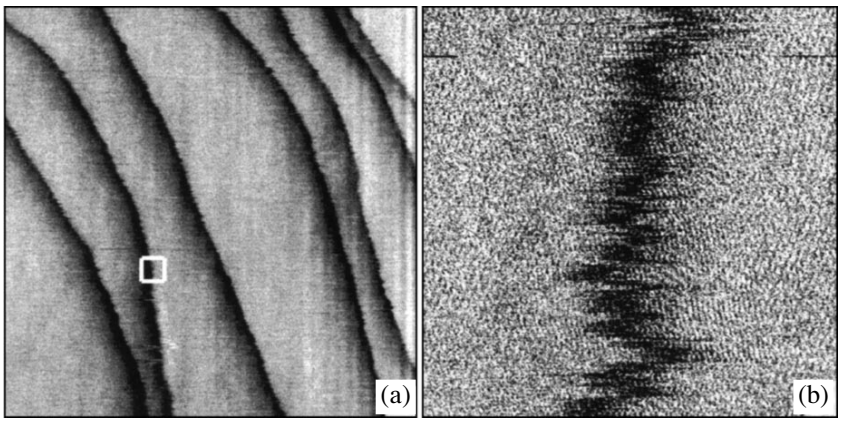

Fig. 1. Steps at a prism face (the step height is equal to 0.37 nm, or half the parameter a of the unit cell). Image size, nm^2: (a) 800×800 and (b) 40×40. The region marked by a square in Fig. 1a is scanned in Fig. 1b at a higher magnification: the molecular structure of the surface is seen.

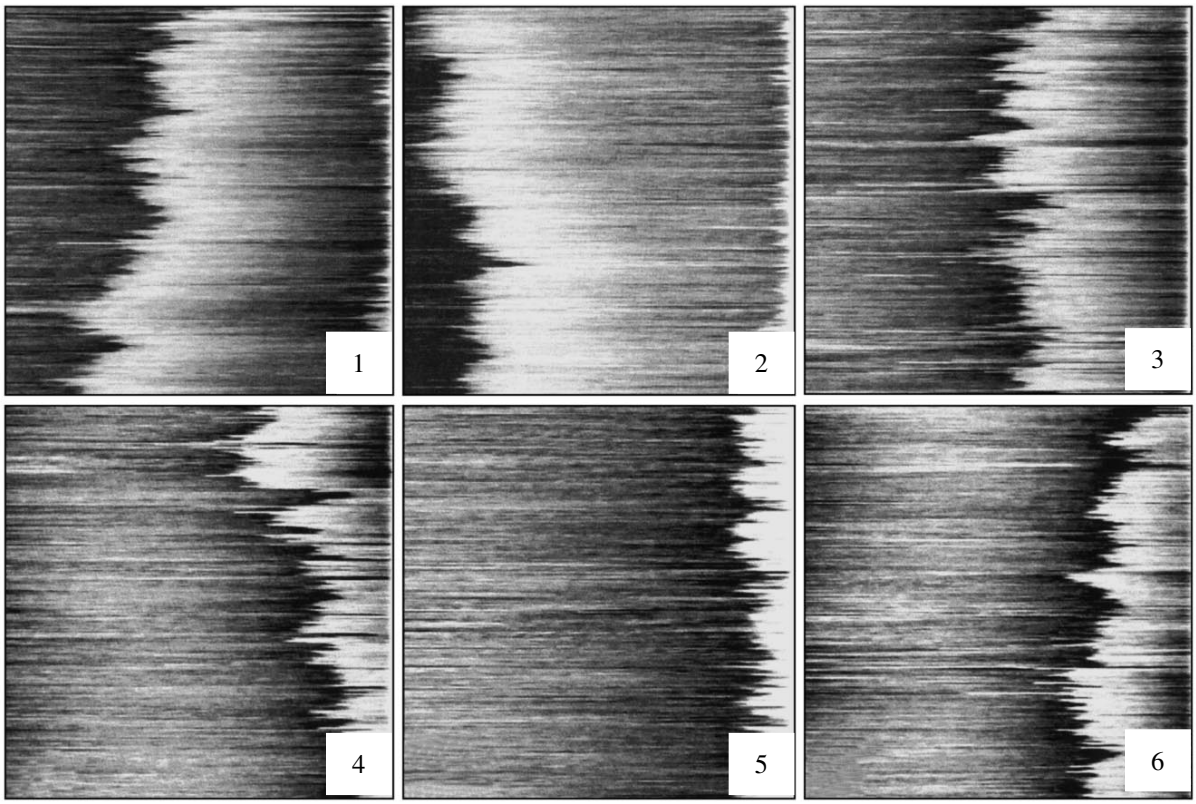

Fig. 2. Time variation of a step segment (150 nm × 50.2 s). The light regions correspond to the upper terrace, and the dark ones to the lower terrace; hence, the motion of the step to the left corresponds to growth (frames 1, 2, and 6), and the motion to the right corresponds to dissolution (frames 3, 4, and 5). The images were obtained at the following instants of time, s: (1) 0, (2) 50, (3) 253, (4) 304, (5) 354, and (6) 456.

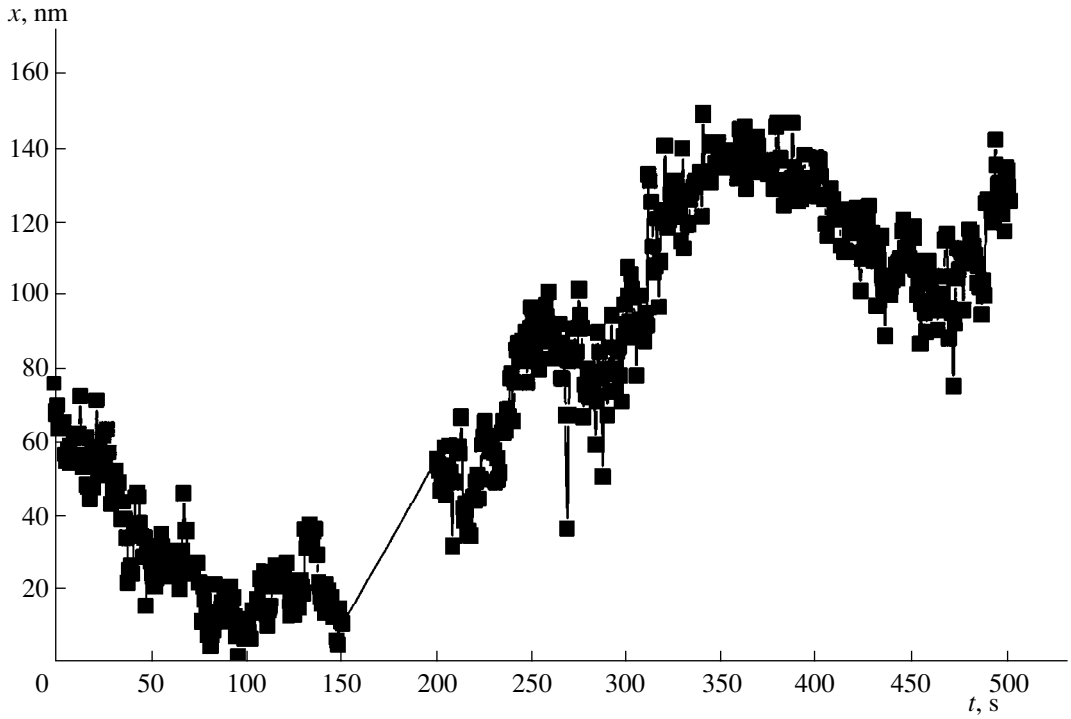

Fig. 3. Time dependence of coordinate x of a chosen step segment (the left edge of the frames shown in Fig. 2 is taken as the origin of coordinates). Fluctuations are seen against the background of the variations associated with the drift, growth, and dissolution of the step.

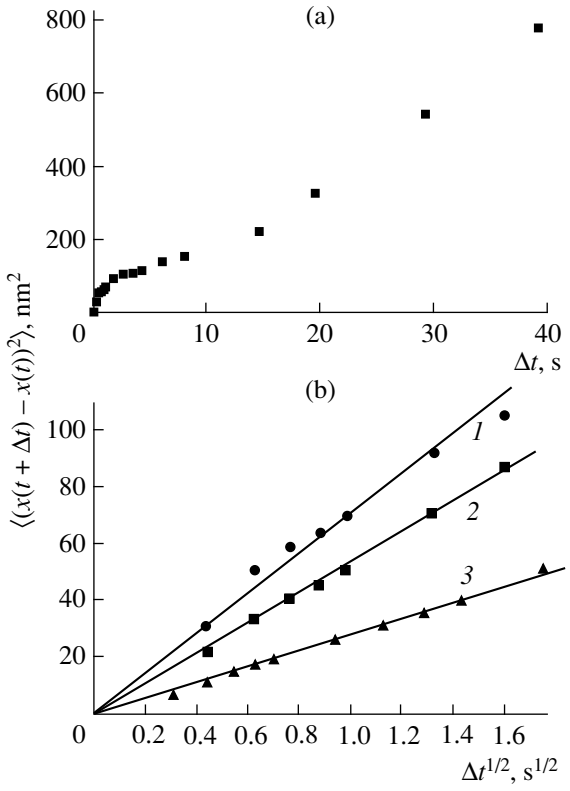

Fig. 4. (a) Correlation function for the process of step dissolution at the face of a prism (from the data of Fig. 3) and (b) the same as a function of $\Delta t^{1/2}$: (*1*) dissolution, (*2*) growth, and (*3*) data for steps at the face of a bipyramid (in this case, no difference is observed between growth and dissolution).

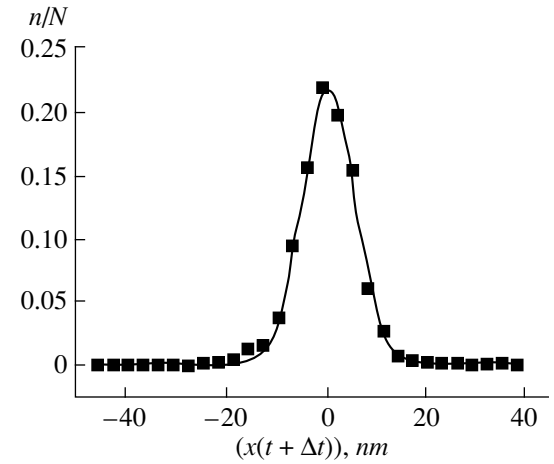

Fig. 5. Distribution function for fluctuations in the case of growth of a prism face for $\Delta t = 0.59$ s.

for the dependences at small and large time periods (<0.2 and >5 s).

For all values of Δt, the fluctuation distribution function for both faces is nearly Gaussian in shape. One such dependence is shown in Fig. 5 by way of an example.

3. DISCUSSION OF RESULTS

The fact that the fluctuations during growth are smaller than during dissolution at the prism face can be attributed to the presence of adsorbed impurity stoppers at the surface, which decelerate the steps [18]. It is obvious that, if the ends of the step are fastened, its midpoint will fluctuate more strongly for longer steps. It is well known that the step at the prism face during growth bulges between the impurity stoppers and, hence, moves at a slower rate [16]. However, these stoppers do not decelerate the steps during dissolution [19]. In all probability, the smaller fluctuations at the bipyramid face are associated with a lower density of fractures in comparison with the prism face: it is well known that the steps at this face are rounded to a considerably smaller extent [12].

The theory of step fluctuations during growth from the melt and solution was developed by Voronkov about 25 years ago [13]. There are three independent phenomenological parameters in the theory, viz., the kinetic coefficient of a step β, the free linear step energy α, and the stability factor $\alpha_e = \alpha + d^2\alpha/d\varphi^2$ characterizing the free energy growth for a small departure of the step from a rectangular shape (here, φ is the angle between the step and a row of closely spaced structural units, and the derivative is taken for $\varphi = 0$). At the microscopic level, these parameters can be represented in terms of the basic characteristics of the crystallization process, viz., the density ρ of fractures at the step and the frequency ω^- of detachment of structural units from the fracture:

$$\beta = h^2\omega^-\rho, \tag{1}$$

$$\alpha_e = k_B T/h^2\rho, \tag{2}$$

where h is the separation between the rows of structural units constituting the step. These parameters, which are of fundamental importance for the theory, can be determined from an analysis of the fluctuations.

Note that the frequency (ω^+) of attachment of the structural units to fractures at equilibrium is equal to the frequency of detachment. In this case, the supersaturation $s = \omega^+/\omega^- - 1$, and the step velocity is given by the expression

$$v = \beta\Omega C_e s, \tag{3}$$

where Ω is the volume of a molecule in the crystal, and C_e is the equilibrium volume concentration of molecules in the solution. For KDP, $\Omega C_e \approx 0.1$ at 27°C.

According to Voronkov, the time dependence of the mean square fluctuations is described by the law

$$\langle(\delta x)^2\rangle = (\chi t)^{1/2}, \tag{4}$$

$$\chi = 2\beta k_B T/\pi q\alpha_e, \tag{5}$$

where q is the surface density of the structural units in the monolayer deposited during the step movement, k_B

is the Boltzmann constant, and T is the temperature. Taking into consideration Eqs. (1) and (2), we can represent Eq. (5) in a different form:

$$\chi = 2h^4\omega^-\rho^2/\pi q. \quad (6)$$

For the tetragonal KDP crystals, the crystal lattice parameters are $a = 7.45 \times 10^{-8}$ cm and $c = 6.97 \times 10^{-8}$ cm. Consequently, $q = (ac)^{-1} = 19.3 \times 10^{14}$ cm^{-2} for the prism face, and $h = c$ for the steps moving in the direction of the c axis. Using the data presented in Fig. 4, we found that $\chi \approx 5 \times 10^{-25}$ cm^4/s for these steps, whence we obtain from Eqs. (5) and (6) that

$$\beta/\alpha_e = 3.7 \times 10^4 \text{ cm}^2/\text{s erg}; \quad \omega^-(a\rho)^2 \approx 3.6 \times 10^5 \text{ s}^{-1} \quad (7)$$

at $T \approx 300$ K ($k_BT \approx 410 \times 10^{-16}$ erg). According to Figs. 1 and 2, we can assume that the coverage of the steps by fractures is $a\rho \approx 0.3$. In this case, $\beta = 0.078$ cm/s, $\alpha_e = 2.1 \times 10^{-6}$ erg/cm, and $\omega^- = 4 \times 10^6$ s^{-1}. The free surface energy of the endface of a step can be roughly estimated as $\alpha_e/a \approx 28$ erg/cm^2. Assuming that the velocity of a step is equal to 0.5 nm/s (see above), we find that the supersaturation (and undersaturation) did not exceed $s = v/\beta\Omega C_e \approx 6 \times 10^{-6}$.

All the data presented above are quite plausible. For example, the value 33 erg/cm^2 is quoted in the literature [20] for the free surface energy of a prism face, and the kinetic coefficient at 31°C is $(7.8 \pm 1.7) \times 10^{-2}$ cm/s [12].

At the same time, the above formulas can only be used to determine a combination of two unknown quantities. Each one of them can be determined from the theory [13] if the space variation of fluctuations is known instead of their time dependence. In this case, the following relation should be satisfied:

$$\langle (x_i - x_k)^2 \rangle = |y_k - y_i| k_BT/\alpha_e = |y_k - y_i| h^2\rho. \quad (8)$$

Here, the mean square difference in the displacements of the ends of the step segment with coordinates y_i and y_k, which is measured at the same instant of time, is proportional to the length of this segment. Such measurements cannot be made at present, since the coordinates of two points on a step are determined at different instants of time with the help of a nanoscope. Hence, it is necessary to further develop theory in order to obtain a type (8) equation, when the coordinates of the points i and k are determined at different instants of time. It is also worth mentioning that there is yet to appear a theory that takes into account the presence of impurity stoppers at the surface.

The obtained values of χ can be used to estimate the separation between steps, which is comparable with the displacement δx of steps as a result of fluctuations. The step segment remains stationary for a period of time approximately equal to the value t_f determined from the condition $(\delta x) \approx vt_f$. From Eq. (4), we obtain $t_f \approx (\chi/v^4)^{1/3}$. Substituting the value of v from Eq. (3), we arrive at the final expression

$$t_f \approx 5.1 \times 10^{-6}/s^{4/3}. \quad (9)$$

During this time, the fluctuations build up to the value $\delta x = 4 \times 10^{-8}/s^{1/3}$ cm. For typical values of supersaturation, this is a small quantity in comparison with the separation between the steps in their equidistant echelon, and a coagulation of adjacent steps as a result of fluctuations is possible only in the case when adjoining steps randomly approach one another to such a distance.

Formula (9) can be used to judge the probability of transporting an impurity from the surface layer into the bulk of the crystal. If the lifetime of the impurity in the surface layer is less than t_f, it leaves the layer before being engulfed by a step. For small values of s, this time is quite long; for example, $t_f = 0.05$ s for a supersaturation of 10^{-3}.

Thus, investigations of the fluctuation-induced displacements of steps during the growth of KDP crystals in a solution can lead to important results from the viewpoint of theory and practice, which cannot be obtained by other means. In this work, we have estimated the basic crystallization parameters, viz., the frequencies of attachment and detachment of structural units, fracture density, and the free linear energy of steps.

ACKNOWLEDGMENTS

The authors are grateful to A. A. Chernov and V. V. Voronkov for their interest in this work and for fruitful discussions.

This work was partially supported by NATO (grant no. PST.CLG.975240) and the Russian Foundation for Basic Research (project no. 00-02-16701).

REFERENCES

1. M. Giesen-Seibert, R. Jentjenns, M. Poensgen, and H. Ibach, Phys. Rev. Lett. **71** (21), 3521 (1993).
2. L. Kuipers, M. S. Hoogeman, and J. W. M. Frenken, Phys. Rev. Lett. **71** (21), 3517 (1993).
3. L. Kuipers, M. S. Hoogeman, J. W. M. Frenken, and H. van Beijeren, Phys. Rev. B **52** (15), 11387 (1995).
4. K. Sudoh, T. Yoshinobu, H. Iwasaki, and E. D. Williams, Phys. Rev. Lett. **80** (23), 5152 (1998).
5. W. K. Burton, N. Cabrera, and F. C. Frank, Philos. Trans. R. Soc. London, Ser. A **243**, 299 (1951).
6. A. Pimpinelli, J. Villain, D. E. Wolf, *et al.*, Surf. Sci. **295**, 143 (1993).
7. T. Ihle, C. Misbah, and O. Pierre-Louis, Phys. Rev. B **58** (4), 2289 (1998).
8. A. I. Malkin, Y. G. Kuznetsov, T. A. Land, *et al.*, Biophys. J. **72** (5), 2357 (1997).
9. Yu. G. Kuznetsov, A. I. Malkin, and A. McPherson, J. Cryst. Growth **196**, 489 (1999).

10. L. N. Rashkovich, N. V. Gvozdev, and I. V. Yaminskiĭ, Kristallografiya **43** (4), 745 (1998) [Crystallogr. Rep. **43**, 696 (1998)].
11. S.-T. Yau, B. R. Thomas, and P. G. Vekilov, Phys. Rev. Lett. **85** (2), 353 (2000).
12. L. N. Rashkovich, *KDP-Family Single Crystals* (Adam Hilger, Bristol, 1991).
13. V. V. Voronkov, in *Crystal Growth, Properties, and Applications*, Vol. 11: *Modern Theory of Crystal Growth I*, Ed. by A. A. Chernov and H. Muller-Krumbhaar (Yerevan. Univ., Yerevan, 1975; Springer-Verlag, Berlin, 1983), p.7.
14. L. N. Rashkovich, O. A. Shustin, and T. G. Chernevich, J. Cryst. Growth **206** (3), 252 (1999).
15. F. Mugele, A. Rettenberger, J. Boneberg, and P. Leiderer, Surf. Sci. **400** (1–3), 80 (1998).
16. L. N. Rashkovich and N. V. Kronsky, J. Cryst. Growth **182**, 434 (1997).
17. A. S. Filonov and I. V. Yaminsky, in *Program for Data Processing and Constructions for Probe Microscopy* (Advanced Technologies Center, Moscow, 1999), p. 42; http:\\spm.genebee.msu.su.
18. N. Cabrera and D. A. Vermilyea, in *Growth and Perfection of Crystals* (Wiley, New York, 1958), p. 393.
19. A. A. Chernov, Prog. Cryst. Growth Charact. **26**, 121 (1993).
20. T. A. Land, J. J. De Yoreo, T. L. Martin, and G. T. Palmore, Kristallografiya **44** (4), 704 (1999) [Crystallogr. Rep. **44**, 655 (1999)].

Translated by N. Wadhwa

Physics of the Solid State, Vol. 42, No. 10, 2000, pp. 1927–1934. Translated from Fizika Tverdogo Tela, Vol. 42, No. 10, 2000, pp. 1874–1881.

LOW-DIMENSIONAL SYSTEMS AND SURFACE PHYSICS

Morphology of (001) and (110) Surfaces of Crystal Layers in Solid Solutions of II–VI Compounds with a High ZnSe Content under Atmospheric Conditions

A. V. Ankudinov*, M. S. Dunaevskiĭ*, V. A. Marushchak*, A. N. Titkov*, S. V. Ivanov*, S. V. Sorokin*, T. V. Shubina*, P. S. Kop'ev*, A. Waag, and G. Landwehr****

** Ioffe Physicotechnical Institute, Russian Academy of Sciences, Politekhnicheskaya ul. 26, St. Petersburg, 194021 Russia*

*** Physikalisches Institut der Universität Würzburg, D-97074 Würzburg, Germany*

Received March 10, 2000; in final form, March 31, 2000

Abstract—The atomic-force microscopy is used for studying the effect of atmospheric conditions on the morphology of (001) growth surfaces and (110) cleavage planes of layers in II–VI compounds with a high ZnSe content. It is proved directly for the first time that the formation of nanoclusters on these surfaces is accompanied by corrosion of the entire surface due to the accumulation of corrosion products. The corrosion of the surface attains saturation even at a depth of a few (2–3) monolayers, which constrains the total volume of nanoclusters on the surface. A further increase in the size of nanoclusters with time occurs due to a decrease in their number. The corrosion depth can locally increase significantly in the surface regions with considerable internal stresses; in particular, corrosion can evolve deep inside the stressed interfaces in instrumental structures. © *2000 MAIK "Nauka/Interperiodica".*

In recent years, semiconducting heterostructures based on solid solutions of Group II–VI compounds with a high ZnSe content have become the subject of intensive studies. This interest is aroused by the prospects of using these structures in developing light-emitting diodes and lasers operating in the blue–green spectral range. An interesting trend in this direction is the study of the formation of quantum dots (QDs) and nanoscale islands based on CdSe in the active ZnSe layer of emitting structures [1]. By analogy with instruments based on III–V compounds (e.g., semiconductor lasers with InAs QDs in the active region of GaAs [2, 3]), it can be expected that the QD formation in the active region in structures based on II–VI compounds should also improve the parameters of the devices. Island structures involving a ZnCdSe ternary solution have been obtained by many authors using the method of molecular-beam epitaxy (MBE) by inserting several CdSe monolayers into a ZnSe matrix [4–6]. The formation of CdZnSe nanoislands was confirmed in experiments on transmission electron microscopy (TEM) [7] and by the analysis of local cathode-luminescence [8], microluminescence [9] spectra, and photoluminescence spectra of submicrometer mesas [10] formed by the structures under investigation. X-ray diffraction studies [11] revealed that the characteristic spreading of nanoislands in the direction of their growth (their height) amounts to 1.5 nm, while the size in the growth plane, which is detected by TEM, varies from one to tens of nanometers.

In experiments aimed at obtaining QDs in Group III–V compounds, an analysis of morphology of unhealed QDs by using atomic-force microscopy (AFM) under atmospheric conditions was very helpful in determining the QD size, shape, and density, as well as the dependence of these parameters on the technological conditions of the growth [12]. Similar AFM studies were also performed for unhealed CdZnSe QDs on the ZnSe surface [13, 16]. It was found that the morphology of the surface with unhealed Cd(Zn)Se nanoislands differs significantly from the results expected from the TEM data [7]. Certain formations (nanoclusters) are indeed observed on such surfaces under atmospheric conditions, but they are very coarse and have heights and diameters larger than tens of nanometers. Moreover, the number of nanoclusters decreases significantly over a characteristic time of several weeks or even days, and the remaining nanoclusters become even coarser. In addition, the formation of nanoclusters with a similar transformation in time was observed on the ZnSe surface even without deposition of CdSe monolayers [17, 18]. An analysis of the nanocluster composition by x-ray photoelectron spectroscopy indicates an increased concentration of selenium [18] and, probably, oxygen [17]. All these observations suggest that nanoclusters detected on the unhealed surfaces are not CdZnSe nanoislands, but rather indicate a runaway corrosion of the ZnSe surfaces under atmospheric conditions. In the case of laser structures based on the layers of II–VI solid solutions with a high ZnSe content, the effect of surface corrosion can be of special significance, since laser mirrors are cleavage surfaces exposed to the atmosphere.

1063-7834/00/4210-1927$20.00

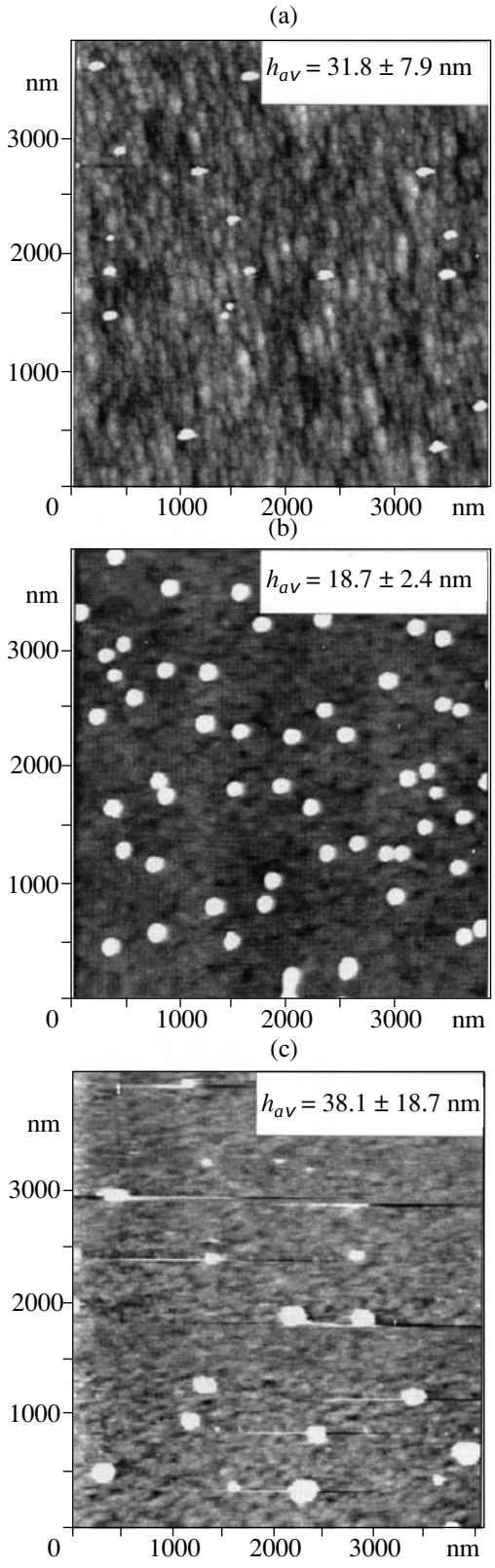

Fig. 1. AFM studies of the morphology of (001) growth surfaces under atmospheric conditions. Surface topographs: (a) ZnSe layer, (b) ZnSe layer with two CdSe grown monolayers, and (c) ZnSe layer with two CdSe monolayers covered with a 10-nm layer of ZnSe. The average heights h_{av} of nanoclusters are shown in the upper right corner of each image.

Despite the fact that such nanoclusters were observed by many authors, corrosion of the entire ZnSe surface was not reported by any of them. Accordingly, the information concerning the correlation between surface corrosion and the evolution of ensembles of time-varying nanoclusters on it is not available either. In order to clarify this situation, we carried out detailed AFM studies of the morphology of ZnSe growth surfaces with and without CdSe deposition, as well as of the cleavage surfaces of laser structures based on II–VI solid solution layers with a high ZnSe content under atmospheric conditions.

The structures investigated by us were grown on GaAs substrates by the MBE method. The growth conditions and the main parameters of the structures were reported earlier in [19]. The AFM studies of the surface morphology of the structures were carried out under atmospheric conditions on an indigenous device R4 fabricated by the NT-MDT company using as probes the Si_3N_4 microcantilevers with a rigidity of 0.16 and 0.68 N/m; the radius of curvature of the probe tip was smaller than 40 nm. The piezoscanner calibration and the test of the device tip were made by using a set of TGS01 and TGT01 calibration gratings supplied by NT-MDT. The number of nanoclusters and their size distribution were determined using the SPM Image Magic program [20].

Figure 1 shows AFM topographs of growth surfaces of a ZnSe layer (a), a ZnSe layer with two CdSe grown monolayers (b), and a ZnSe layer with two CdSe monolayers covered with a ZnSe layer 10 nm thick (c). White spots on the topographs correspond to nanoclusters, and the scale of grey color is chosen so that even the structure of relatively smooth regions of the surface between nanoclusters is resolved. It is worth noting that the observed morphology of the surfaces has a similar character. In all cases, there is a considerable number of nanoclusters with slightly different sizes and densities. The average heights of nanoclusters, which are shown in the insets to figures, fall in the range of values observed earlier [13–18]. The main factor determining the spread in nanocluster size is the difference in the time for which the sample is exposed to the atmosphere. The effect of exposure time is illustrated better in Fig. 2, which shows the change in the surface morphology of a ZnSe layer with two CdSe monolayers upon exposure to the atmosphere for four months. In order to obtain better statistics, the AFM images of a considerably larger area are presented and processed here. For each image, we obtained the average height (h_{av}), base diameter (D_{av}), number density (n), and total volume of nanoclusters (d_{ef}). After four months, the number of clusters on the surface decreased by an order of magnitude. Their average height increased by a factor of 3.7, and the radius, by a factor of 1.7. The results characterizing the volume of nanoclusters are new and especially interesting. First, their formation requires a relatively small amount of the material, approximately

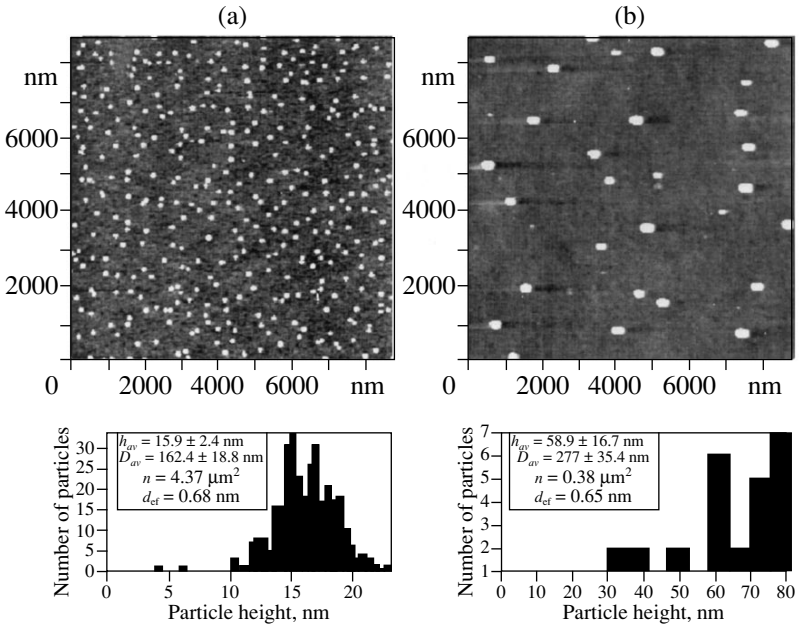

Fig. 2. Coalescence of nanoclusters on the surface of a ZnSe layer with two CdSe grown monolayers as a function of exposure time under atmospheric conditions. Surface morphology: (a) as-grown sample and (b) the same sample after four months. The statistical height distributions of nanoclusters, their average heights h_{av}, base diameters D_{av}, number densities n, and the total volumes d_{ef} (in units of thickness equal to the volume of the surface layer under the assumption that the nanocluster material is distributed uniformly over the surface) are shown below the figures.

0.68–0.65 nm of a layer uniformly covering the surface (i.e., a thickness of approximately two monolayers). Second, this value virtually does not change with the time of exposure to the atmosphere. The volume of nanoclusters is determined directly by numerical integration from the data describing the image relief [20]. The constancy of the nanocluster volume in time indicates an important feature of their formation. They are formed in the initial period of surface exposure under atmospheric conditions, after which the material is only redistributed between the existing nanoclusters. Proceeding from a definite volume of nanoclusters, we can assume that only the uppermost surface layers at a level of a few monolayers participate in the formation of nanoclusters (the thickness of a monolayer on the ZnSe(001) surface is 0.28 nm).

The redistribution of the material among clusters on the surface with their volume remaining unchanged (coalescence) was analyzed theoretically by Lifshitz and Slyozov [21], who showed that the size distribution shifts with time toward larger sizes and becomes diffuse due to the "devouring" of small clusters by large ones. Such a behavior is indeed observed in our case. It can be seen from the results of quantitative analysis presented in Fig. 2 that the surface is initially characterized by a narrow distribution of clusters over the height (with a 15% dispersion). After four months, the distribution is shifted to the right (the heights increase) and becomes diffuse (approximately 30% dispersion). A similar behavior is also traced for lateral dimensions of nanoclusters.

We also obtained interesting results indicating a decrease in the mechanical strength of the observed nanoclusters. Figure 3 shows several AFM images obtained as a result of successive scanning of the same surface regions containing nanoclusters. The topograph in Fig. 3a was measured under a load of 7 nN exerted by the AFM tip on the surface. The nanocluster whose shape was examined on subsequent images is marked by an arrow. It was found that, in a series of topographs obtained under a load increased to 60 nN, the size of this nanocluster decreased successively. The changes in the nanocluster size can be seen especially clearly if we compare Figs. 3b and 3c. Ultimately, the nanocluster disappears from the image altogether (in Fig. 3d, the initial position of the nanocluster is marked by an arrow). The results presented in topographs indicate that the material of a nanocluster is gradually cut by the AFM tip and is removed beyond the area of the frame, remaining on the surface. The image in Fig. 3d shows the remnants of the nanocluster material (marked by an arrow), which are displaced by approximately 1.5 micrometers upward from the initial position. Their volume is approximately equal to the initial volume of the nanocluster.

We can estimate the stresses experienced by the nanocluster material during fracture:

$$\sigma_d = F/S, \tag{1}$$

where F is the force exerted by the tip on the surface and S is the contact area between the tip and the surface.

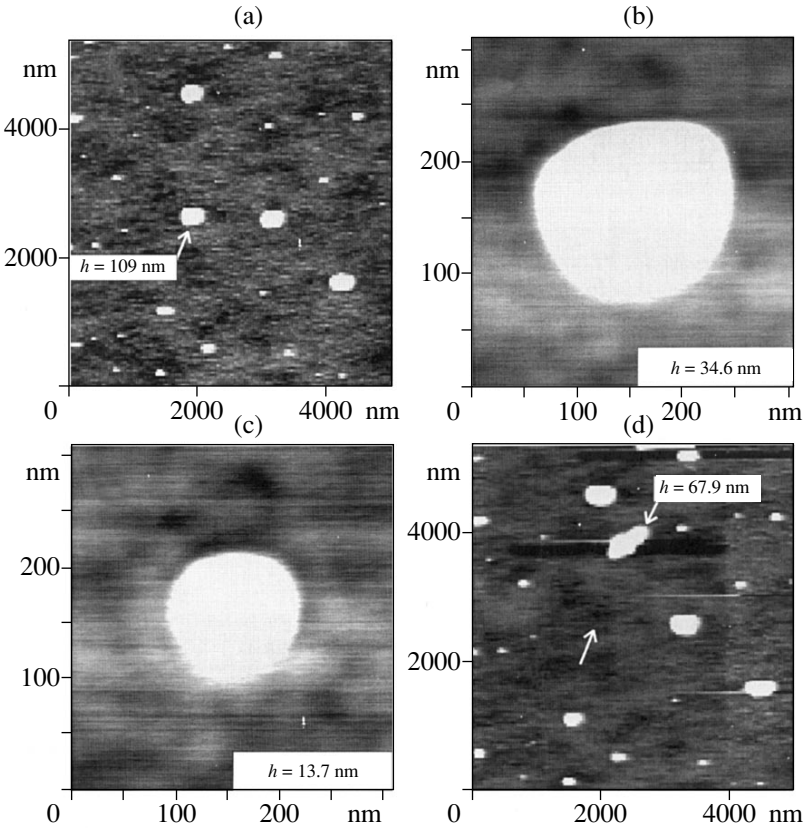

Fig. 3. AFM studies of the mechanical properties of nanoclusters: (a)–(d) images obtained during successive scanning of a surface region with different average forces of (a, d) 7 and (b, c) 60 nN exerted by the AFM tip on the surface. The figures show the maximum height of the nanocluster at the instant of image recording. Arrows indicate (a) the initial nanocluster and (d) its remnants. The initial position of the nanocluster is separately indicated by an arrow in (d).

The value of S can be determined from the Hertz formula [22] for two contacting spheres:

$$S = (FR^*/E^*)^{2/3}, \quad (2)$$

$R^* = R_tR_s/(R_t + R_s)$ and $E^* = E_tE_s/(E_t + E_s)$ are the reduced radius of curvature and Young's modulus at the point of the contact in terms of the corresponding parameters of the tip and the sample marked by the subscripts t and s, respectively. Expression (1) can also be written in the form

$$\sigma_d \approx E_s, \quad (3)$$

since the material fracture occurs at stresses close in magnitude to its Young's modulus. The shape of the tip practically did not change during operation, which was verified from the test on the TGT01 grating. Consequently, the material of the tip is much harder than the nanocluster material, and we can put $E^* \approx E_s$ in formula (2). Combining relationships (1), (2), and (3), we obtain

$$\sigma_d \approx F/R^{*2}.$$

The reduced radius of curvature is defined by the formula $R^* = R_t - R_t^2/R_i$, where R_t and R_i are the radii of curvature of the tip and the nanocluster image at the point of contact, respectively; these are measurable quantities (if we disregard the lateral size of the tip–cluster contact, the condition $R_i = R_s + R_t$ [23] makes it possible to eliminate the contribution R_s from the expression for the reduced radius). Using a force of 60 nN and estimating $R^* = 30$ nm from the topographs, we see that the order of magnitude of the fracture stress is 10^7 N/m^2. Considering that Young's modulus of crystals of II–VI compounds is larger than 10^{10} N/m^2 [24], we can conclude that the nanoclusters under investigation cannot be single crystals and must be made of a more weakly bound ductile material.

Similar results concerning the size, total volume, and a noticeable ductility of nanoclusters were also obtained from the morphological study of growth surfaces for structures with a ZnSe upper layer (Figs. 1a–1c). Consequently, our observations are in accord with the results obtained in [17, 18] and also indicate that the formation of the observed nanoclusters is not associated with the deposition of CdSe monolayers. This also follows from the absence of a correlation between the photoluminescence intensity and the density of similar formations observed earlier [8]. The origin of nanoclus-

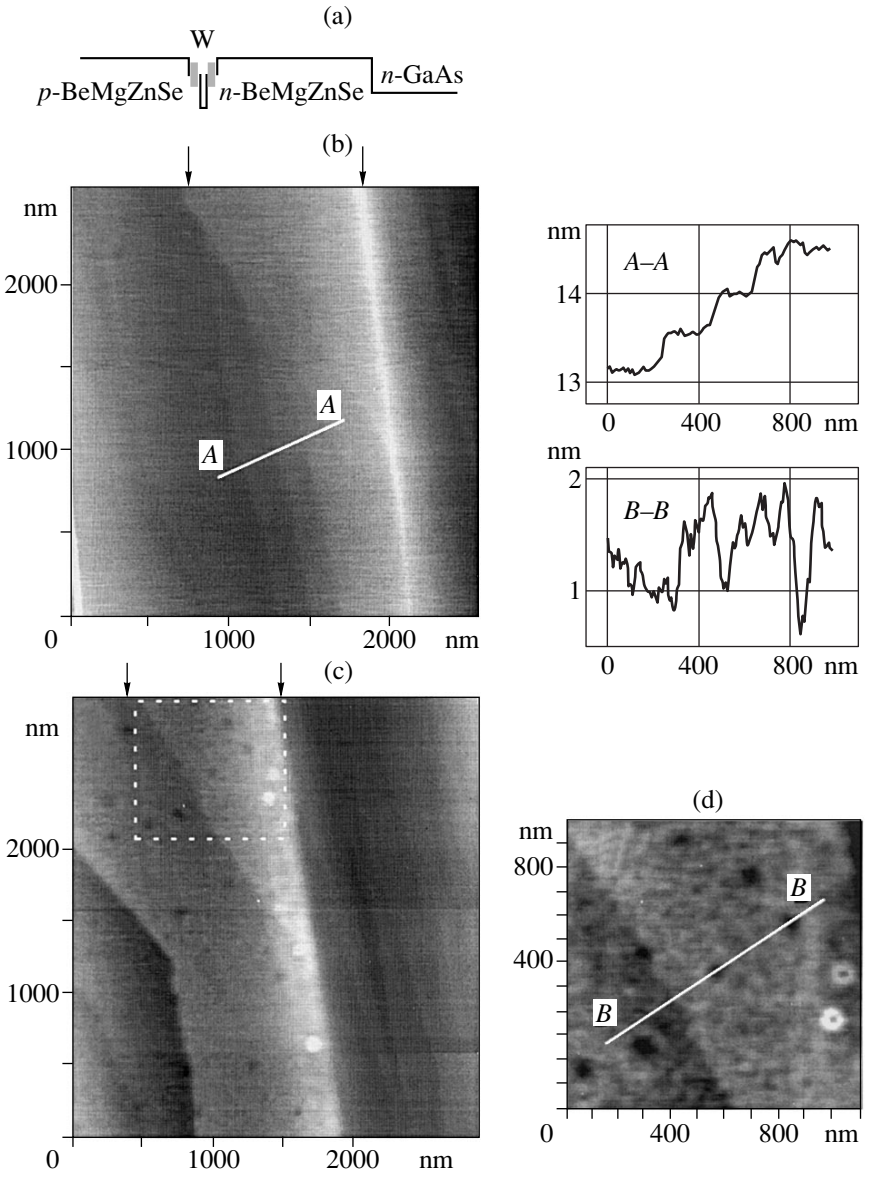

Fig. 4. AFM studies of the morphology of the (110) surface in II–VI layers emerging at the cleavage plane of the laser structure with a superlattice waveguide redistributing mechanical stresses of the active region over the entire waveguide: (a) energy diagram of the laser structure, (b) topography of a freshly cleaved laser surface, (c) topography of the same cleavage plane in the sample after five months, and (d) image with a higher resolution of the surface region confined within dashed lines in (c). Arrows above the images (b) and (c) indicate the positions of the first laser interface and the active region.

ters is associated in all probability with the overall corrosion of the surface and also with an aggregation of the corrosion products into clusters on the surface. This is confirmed by the increased content of Se and O in nanoclusters observed earlier [17, 18] and also by the decrease in their mechanical strength, which was found for the first time in [8] and analyzed in greater detail in this work. It should be noted that we observed preferential localization of nanoclusters on surface defects. Most likely, the ZnCdSe nanoislands observed on the surface, which were detected earlier on overgrown surfaces [4–11], are also nucleation centers in the formation of large corrosion nanoclusters on surfaces exposed to air. The strong transformation of the surface relief due to corrosion and possible decoration of ZnCdSe nanoislands by clusters virtually rule out the AFM observation of ZnCdSe nanoislands on open surfaces.

Direct observation of the modification of surface relief between nanoclusters due to corrosion is of fundamental importance for understanding the morphological changes of the surfaces under investigation. Unfortunately, the pronounced roughness of growth surfaces, which can be clearly seen in Figs. 1 and 2, makes it impossible to detect corrosion-induced

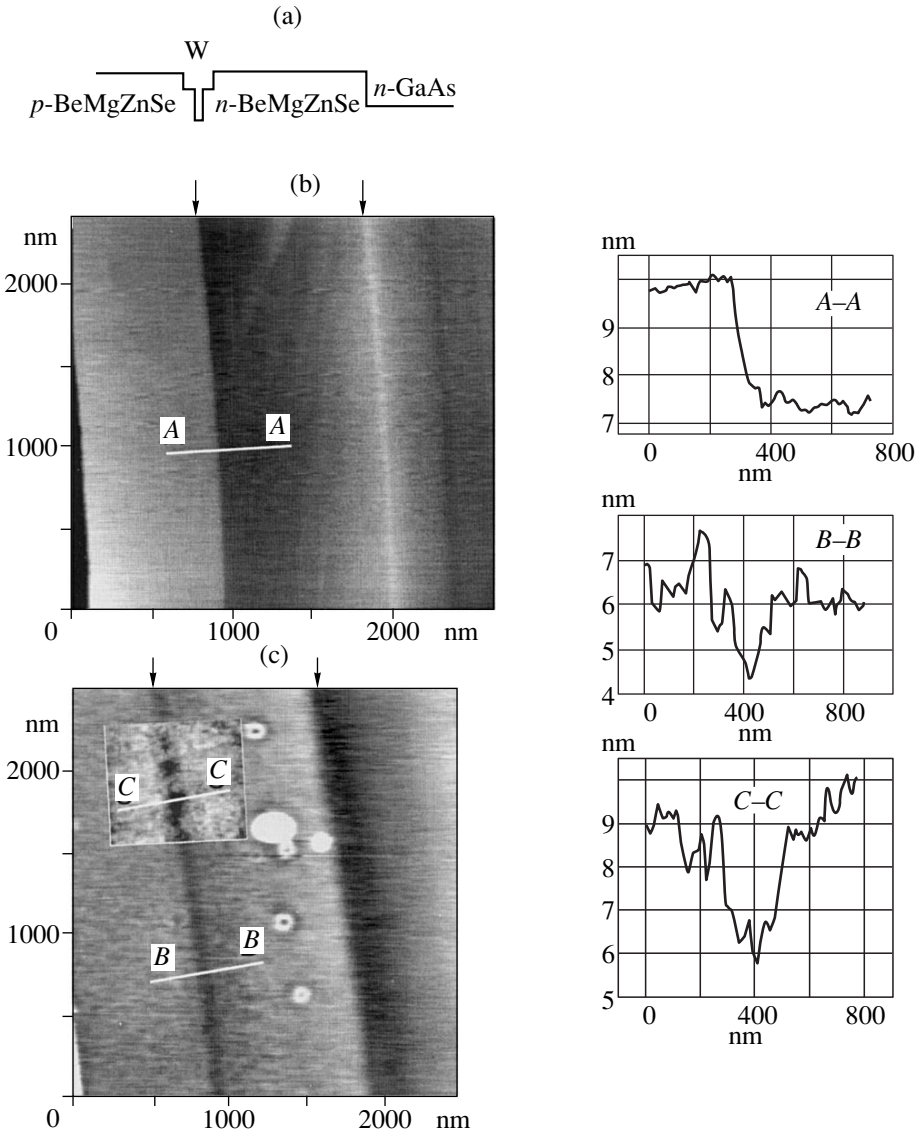

Fig. 5. AFM studies of the morphology of the (110) surface in II–VI layers emerging at the cleavage plane of the laser structure with a bulk waveguide and the stressed active region: (a) energy diagram of the laser structure, (b) topography of a freshly cleaved laser surface, and (c) topography of the same cleavage plane in the sample after five months. The region confined in (c) illustrates the data on the surface morphology obtained in the vicinity of the stressed active region 18 months after the cleavage. Sections *A–A* (fresh cleavage), *B–B* (after five months), and *C–C* (after 18 months) also illustrate the evolution of the relief in the vicinity of the active region. Arrows above the images (b) and (c) indicate the positions of the first laser interface and the active region.

changes of the surface over a few monolayers. In order to observe the overall corrosion, we studied the morphology of cleavage planes of layered laser structures by the AFM method, because the cleaved surfaces are initially atomically smooth.

We investigated the cleavage planes of II–VI laser structures on a GaAs substrate (see energy-level diagrams in Figs. 4a and 5a), in which the *n* and *p* regions surrounding the waveguide (W) were presented by $Be_{0.03}Mg_{0.03}ZnSe$ layers. Figure 4b shows an AFM topographic image of a freshly cleaved surface of one of these structures. The light ridge on the topograph corresponds to the boundary between the *n*-BeMgZnSe layer and the GaAs substrate. In the region of II–VI layers and the GaAs substrate, a certain number of cleavage steps running at an angle to the boundary with the substrate is observed. The terraces between the steps are atomically smooth; this can be seen, for example, from the *A–A* profile shown in the inset. The height of the steps amounts to 0.4 nm, which corresponds to the thickness of two monolayers on the (110) cleavage surface. Figure 4c shows the topograph of the same cleavage plane of the sample, but after the exposure of the cleavage surface to the atmosphere for five months. The clearly seen evolution of the surface corrosion of II–VI layers does not affect the GaAs substrate (see profile *B–*

B in Fig. 4). We can single out the following three features of corrosion: (1) the evolution of general roughness of the surface of II–VI layers having a depth of 2–3 monolayers, (2) the formation of a certain number of nanoclusters (white spots and rings), and (3) the emergence of a number of relatively deep individual pits. Figure 5 illustrates the evolution of the surface corrosion for another similar laser structure. It can be seen that the two main features of surface corrosion are preserved, viz., the evolution of roughness over the entire surface at the level of a few monolayers and the emergence of nanoclusters. Repeated studies of the morphology of cleavage planes after storage for one more year in atmospheric conditions did not reveal any further enhancement of surface corrosion, which points to the stabilization process at the level of modification of just two or three upper monolayers.

This result for cleavage planes agrees well with our observations for growth surfaces, which revealed that the total volume of nanoclusters is stabilized at a level corresponding to approximately two monolayers on the surface layer and does not increase any further.

It is interesting to note that, in the case of the laser structure presented in Fig. 5, solitary corrosion pits do not develop at the surface. It can also be seen that the initial quality of the cleavage plane of the second structure, whose surface is almost free of cleavage steps, is higher. Consequently, it can be assumed that solitary corrosion pits appear in all probability due to surface defects emerging during the formation of rough cleavages with steps.

An important confirmation of the influence of a local imperfection of II–VI surfaces on the corrosion intensity and depth was obtained by comparing the corrosion effects in the waveguide (W) region for structures presented in Figs. 4 and 5. The laser structure in Fig. 4 is distinguished by the presence of the superlattices of alternating positively and negatively stressed $Be_{0.05}Zn_{0.95}Se$ and ZnSe layers on both sides of the active region of the waveguide. The presence of these superlattices makes it possible to redistribute elastic stresses existing in the active region to a much wider layer of the waveguide, thus reducing their magnitude. The structure in Fig. 5 was grown without superlattices in the waveguide region, and high elastic stresses were localized in it in a narrow active region. Different types of stress distributions in these structures were demonstrated by us in the previous publication [25] devoted to AFM studies of the topographs of freshly cleaved surfaces. Stress concentration in the active region leads to a jump of the cleavage plane in this region, which is manifested in the AFM image in the form of a step propagating along the active region (see Fig. 5b and profile *A*–*A*). In the laser with superlattices, no steps are formed along the active region of the waveguide (Fig. 4b). A comparison of topographs of corroded surfaces for the structures presented in Figs. 4c and 5c indicates a severe corrosion in the active region of the structure with a stressed active region. In the laser with distributed stresses, corrosion does not reveal an active region against the background of the cleavage of the entire structure. The increase in the corrosion rate in regions with larger stresses is obviously due to an easier rupture of chemical bonds in the lattice as a result of liberation of the mechanical energy.

Thus, we have used the AFM method to study under atmospheric conditions the morphological variations of the (001) growth surfaces and (110) cleavage planes in the crystal layers of II–VI compounds with a high ZnSe content. The investigations of the initially atomically smooth cleavage planes have revealed that the formation of nanoclusters on the surface under atmospheric conditions is accompanied by corrosion of the entire surface, which, however, attains saturation as the surface roughness attains a level of 2–3 monolayers. At the same time, it was shown that, for growth surfaces, the total volume of emerging islands is also saturated at a level equivalent to the volume of about two monolayers of the material. The entire body of the obtained results can be used to propose the following model for the growth of nanoclusters under atmospheric conditions on the surface layers of II–VI compounds with a high ZnSe content. Nanoclusters are formed from the products of corrosion at a depth of 2–3 monolayers, after which the surface corrosion is saturated, and the total volume of the nanoislands does not increase any further. A subsequent increase in the average size of nanoclusters occurs due to assimilation of smaller clusters by larger ones under the condition of conservation of their total volume. It has been observed that these clusters are localized preferentially in the vicinity of structural inhomogeneities. Our investigations of the mechanical strength of nanoclusters have shown that its value is several orders of magnitude less than that in ZnSe crystal layers. A high ductility of the cluster material has been demonstrated directly. These results agree well with the data presented in other publications indicating the enrichment of nanoclusters in selenium. The analysis of laser structures with a high ZnSe content revealed a considerable enhancement of corrosion at stressed interfaces. For instance, corrosion can be an important reason behind the degradation of active regions of laser structures (near mirrors), which are mismatched in the lattice parameter.

ACKNOWLEDGMENTS

The authors are grateful to A. K. Kryzhanovskiĭ for providing the SPM Image Magic program [20] for statistical processing of the images.

This work was supported by the Volkswagen Foundation and the Russian Foundation for Basic Research, project no. 00-02-16948.

REFERENCES

1. S. V. Ivanov, A. A. Toropov, S. V. Sorokin, *et al.*, Appl. Phys. Lett. **74**, 498 (1999).
2. Q. Xie, A. Kalburge, P. Chen, and A. Madhukar, Photonics Technol. Lett. **8**, 965 (1996).
3. N. Kirstaedter, O. G. Shmidt, N. N. Ledentsov, *et al.*, Appl. Phys. Lett. **69**, 1226 (1996).
4. S. V. Ivanov, A. A. Toropov, T. V. Shubina, *et al.*, J. Appl. Phys. **83**, 3168 (1998).
5. D. Hommel, K. Leonardi, H. Heinke, *et al.*, Phys. Status Solidi B **202**, 835 (1997).
6. H. Kirmse, R. Schneider, M. Rabe, *et al.*, Appl. Phys. Lett. **72**, 1329 (1998).
7. A. Sitnikova, S. Sorokin, T. Shubina, *et al.*, Thin Solid Films **336**, 76 (1998).
8. T. Shubina, S. Sorokin, A. Toropov, *et al.*, in *Proceedings of the 24th International Conference on the Physics Semiconductors, Jerusalem, Israel, 1998*, Mo-P33.
9. J. C. Kim, H. Rho, L. M. Smith, *et al.*, Appl. Phys. Lett. **73**, 3399 (1998).
10. T. Kümmell, R. Weigand, G. Bacher, *et al.*, Appl. Phys. Lett. **73**, 3105 (1998).
11. R. N. Kyutt, A. A. Toropov, S. V. Sorokin, *et al.*, Appl. Phys. Lett. **75**, 373 (1999).
12. R. Notzel, Semicond. Sci. Technol. **11**, 1365 (1996).
13. S. H. Xin, P. D. Wang, A. Yin, *et al.*, Appl. Phys. Lett. **69**, 3884 (1996).
14. M. Arita, A. Avramescu, K. Uesugi, *et al.*, Jpn. J. Appl. Phys., Part 1 **36**, 4097 (1997).
15. H.-C. Ko, D.-C. Park, Y. Kawakami, *et al.*, Appl. Phys. Lett. **70**, 3278 (1997).
16. S. Lee, I. Daruka, C. S. Kim, *et al.*, Phys. Rev. Lett. **81**, 3479 (1998).
17. J. B. Smathers, E. Kneedler, B. R. Bennet, and B. T. Jonker, Appl. Phys. Lett. **72**, 1238 (1998).
18. X. B. Zhang and S. K. Hark, Appl. Phys. Lett. **74**, 3857 (1999).
19. S. V. Ivanov, A. A. Toropov, T. V. Shubina, *et al.*, J. Appl. Phys. **83**, 3168 (1998).
20. http://members.xoom.com/Alex/Kryzh.
21. I. M. Lifshitz and V. V. Slezov, Zh. Éksp. Teor. Fiz. **35**, 479 (1958) [Sov. Phys. JETP **8**, 331 (1958)].
22. L. D. Landau and E. M. Lifshitz, *Course of Theoretical Physics*, Vol. 7: *Theory of Elasticity* (Nauka, Moscow, 1987; Pergamon, New York, 1986).
23. R. Chicon, M. Ortuno, and J. Abellan, Surf. Sci. **181**, 107 (1987).
24. C. Verie, J. Electron. Mater. **27**, 782 (1998).
25. A. V. Ankudinov, A. N. Titkov, T. V. Shubina, *et al.*, Appl. Phys. Lett. **75**, 2626 (1999).

Translated by N. Wadhwa

Physics of the Solid State, Vol. 42, No. 10, 2000, pp. 1935–1941. Translated from Fizika Tverdogo Tela, Vol. 42, No. 10, 2000, pp. 1882–1888.

POLYMERS AND LIQUID CRYSTALS

Charge Transfer in a Metal–Polymer–Nanocrystalline Metal System

A. N. Lachinov*, T. G. Zagurenko*, V. M. Kornilov*, A. I. Fokin*, I. V. Aleksandrov, and R. Z. Valiev****

** Institute of Molecular and Crystal Physics, Ufa Scientific Center, Russian Academy of Sciences, Ufa, 450025 Bashkortostan, Russia*

*** Institute of Physics of Promising Materials, Ufa, 450000 Bashkortostan, Russia*

e-mail: LPP_IPMC@anrb.ru

Received December 15, 1999

Abstract—The electrical conductivity in a metal–polymer–nanocrystalline metal system has been investigated as a function of temperature. It is found that this system undergoes a transition to the high-conductivity state at temperatures of structural transformations in nanocrystalline electrodes. The results are interpreted within the model of charge instability that arises in thin polymer films under changes of the boundary conditions. © *2000 MAIK "Nauka/Interperiodica".*

1. INTRODUCTION

In this work, we studied the electrical conductivity in a metal–polymer–nanocrystalline metal system. In our earlier work [1], it was demonstrated that the change in the effective work function upon structural transformation (melting) of an electrode can be responsible for a considerable increase in the current passing through a "sandwich" structure of the metal–polymer–metal type. This conclusion was based on the following facts. For an ohmic contact, the distribution of potential ψ over the polymer bulk can be described by the relationship [2]

$$d\psi/dx = (2q^2 n_s kT/\varepsilon)^{1/2} \times \{\exp[-(\psi - \varphi_m + \chi)/kT] - \exp[-(\varphi - \varphi_m)/kT]\}^{1/2}, \quad (1)$$

where q is the electronic charge, n_s is the surface charge concentration, k is the Boltzmann constant, T is the temperature, ε is the permittivity, φ_m is the work function of metal, φ is the work function of polymer, and χ is the electron affinity. It is well known [3] that distribution (1) is a result of the redistribution of charges in the surface region of a dielectric due to the leveling of the Fermi levels of the metal and the polymer.

A change in the ψ potential leads to the change in the injection current whose density in the polymer without regard for the diffusion component can be represented as [4]

$$J = -n(x)\mu d\psi/dx, \quad (2)$$

where μ is the mobility of current carriers. A comparison of formulas (1) and (2) shows that a change in the work function of a metal for some reason can bring about the change in the current passing through the polymer.

However, the question as to the magnitude of the work function and its variation in the temperature range of structural transitions in metals is still an open question [5]. There are different viewpoints regarding the ratio between the contributions from volume and surface components of this parameter [6–8]. Moreover, there exist mutually exclusive opinions about the presence or absence of a jump in the work function upon structural transformations in metals. In particular, Bol'shov and Dobretsov [9] conclusively showed that, after deep purification of a metal from different impurities, the work function remains constant upon transition through the melting point, which is accompanied only by the change in the slope of the temperature coefficient of the work function. However, these authors observed a jump in the emission upon melting in the presence of impurities at the metal surface. If the emission current is treated in terms of the known equation

$$J = A_0(1 - R)T^2 \exp[-\varepsilon\varphi(T)/kT], \quad (3)$$

where $A_0 = 120$ A/cm^2 K^2, R is the mean coefficient of electron reflection from the potential barrier at the emitter–vacuum interface, and $\varphi(T)$ is the effective work function, the change in the emission can be caused by a change either in R (which cast serious doubts in [9]) or in $\varphi(T_{melt})$.

It is evident that the layer contacting with the metal surface affects both the emission properties of materials [10, 11] and the temperature behavior of the emission near the temperature of their structural transformations [9, 12, 13], which is reflected in the change in the effective work function.

Under certain conditions, the impurity layer on the metal surface can stimulate the emission from the metal at temperatures in the range of structural transitions. It

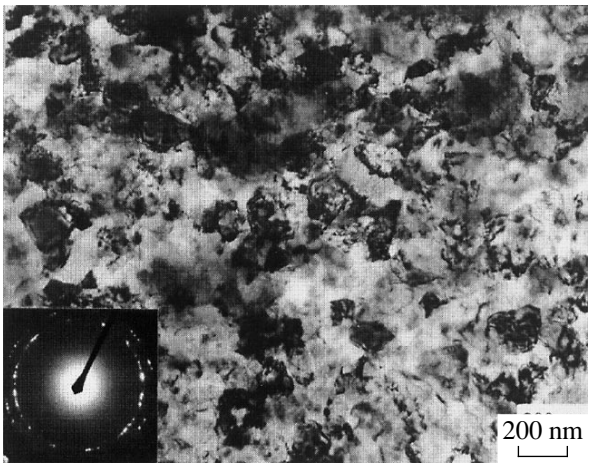

Fig. 1. Electron microscopic (bright-field and diffraction) image of structures in the Cu sample subjected to severe torsional plastic deformation.

can be expected that a similar effect will be observed when a macroscopic dielectric film will be used instead of this layer, which will result in a change in the injection properties of a metallic electrode at temperatures of its structural transitions. In the present work, we measured the injection current (the current from a metal to a solid dielectric) in the metal–dielectric–metal system under the conditions of a nonstationary change in the temperature. The complexity resided in a relatively small expected variation in the injection current. In order to increase such a variation, we used the known polymer dielectric with nonlinear electrical properties. The nonlinearity of properties consists in the fact that a relatively small change in the density of space charge in the polymer at the expense of its injection from the metallic electrode can lead to the electronic transition from the dielectric state to the high-conductivity state in the polymer film. Several ways of realizing this transition are known at present [14–16].

In [1, 17], the effective work function was changed by melting one of the electrodes (In or Wood alloy). At the same time, according to our hypothesis, the method of changing the effective work function should be of no considerable importance. The choice of such a mechanism of the change in the effective work function of a metal, at which its state of aggregation remains unaltered, is fundamental for the understanding of the reasons for an increase in the conductivity of the metal–polymer–metal system. The nanocrystalline state in metallic samples is nonequilibrium, and, hence, the initial coarse-grained structure of the metal is recovered upon annealing at relatively low temperatures below $T \sim 0.4T_{melt}$ owing to the structural transformation [18]. As would be expected, a severe torsional plastic deformation of a metal can lead to a substantial increase in the effective work function, which was estimated to be more than 0.1 eV [19, 20]. In the course of the low-temperature annealing, the effective work function should regain its initial value, which should be reflected in the parameters of the potential barrier at the metal–polymer interface and, correspondingly, in the injection current passing in the metal–polymer–nanocrystalline metal system.

In this respect, the aim of this work was to investigate the features of the charge transfer in the above system in the temperature range of structural transformations in a nanocrystalline metal.

2. SAMPLE PREPARATION AND EXPERIMENTAL TECHNIQUE

Cu and Ni metals with a nanocrystalline structure were used as electrodes (nanocrystalline metal). The nanocrystalline structure of metallic samples was produced by the severe torsional plastic deformation method. As a rule, the samples were strained at a pressure of 6 GPa and the torsional strain $\alpha = 5$. In recent years, the severe plastic deformation method has been successfully applied to the formation of nanostructures in different metals and alloys [21, 22].

The nanocrystalline structure was identified by electron microscopy, x-ray structure analysis, and scanning tunneling microscopy (STM). It was shown earlier [23] that the severe torsional plastic deformation of Cu and Ni results in the formation of an ultrafine-grained structure, which is characterized by a crystallite grain size of 50–100 nm, high microdistortions of the crystal lattice, nonequilibrium boundaries of grains (with a high density of extrinsic grain boundary dislocation), and increased static and dynamic atomic displacements (Fig. 1).

Figure 2 displays the STM images and surface profiles of nanocrystalline copper. Note that the STM technique provides a way of examining the sample surface at all experimental stages. For comparison, the sample surface images prior to and after the low-temperature annealing are depicted in this figure, which clearly demonstrates the difference in the mean grain sizes. The grain size increases with annealing, which manifests itself in the change of the surface profile (Fig. 2). It can be concluded that the results of the morphological examination of the nanocrystalline sample surface by using two different methods—transmission electron microscopy on foils and scanning tunneling microscopy on massive samples—are in good agreement.

A poly(phthalidylidenebiphenylylene) film was used as a polymer interlayer in the metal–polymer–nanocrystalline metal system. The choice of this polymer is explained by the following reasons. First, poly(phthalidylidenebiphenylylene) belongs to the polymers in which transitions to the high-conductivity state were observed earlier and whose electrical properties are best known. Second, it possesses good film-forming properties. As was shown in [24–26], the poly(phthalidylidenebiphenylylene) films prepared under certain conditions were homogeneous and quali-

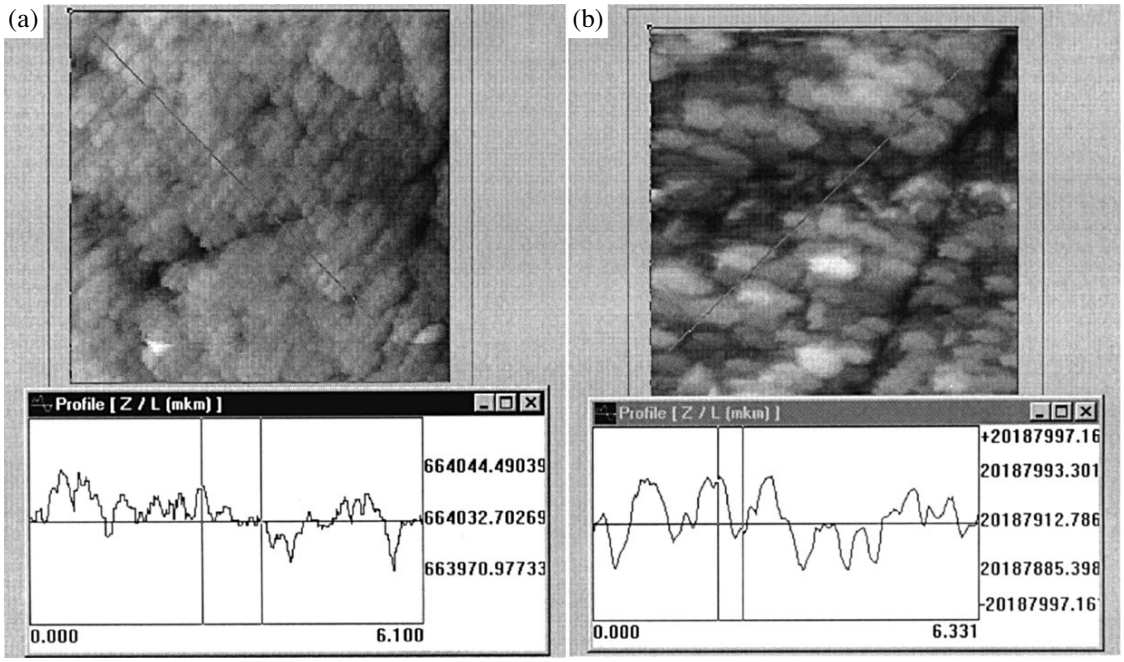

Fig. 2. STM images and surface profiles of nanocrystalline copper. (a) Grain structure on the surface of the copper sample subjected to severe torsional plastic deformation prior to thermal annealing. The scanned area is 5.8×5.8 μm. The surface profile is shown at the bottom (the difference between the heights at points of intersection with 24-nm measuring lines). (b) Grain structure of the same sample after cyclic annealing in the temperature range 20–270°C. The scanned area is 5.8×5.8 μm. The surface profile is shown at the bottom (the difference between the heights at points of intersection with 56-nm measuring lines).

tative in the thickness range used in this work. These results are confirmed by recent STM investigations into the homogeneity of poly(phthalidylidenebiphenylylene) films [27]. Third, this polymer is a thermally stable compound [28], whose temperature dependence of the conductivity does not exhibit features up to the softening temperature (360°C in air). This allows us to use this compound in the temperature range of strong structural transformations (100–250°C) in the copper and nickel nanocrystalline samples.

The polymer film was obtained from a poly(phthalidylidenebiphenylylene) solution in cyclohexanone by spin coating on a polished vanadium electrode. The STM image of the surface and the surface profile of the vanadium electrode are demonstrated in Fig. 3. As can be seen, the irregularity sizes are considerably less than the film thickness. The thickness of the polymer films used in experiments varied in the range 0.5–1 μm. The quality and homogeneity of polymer films were checked by optical and transmission electron microscopy according to the procedure described in [29]. In the latter case, the replica technique was used because of the large film thickness. Furthermore, the check experiments were carried out with the polymer film prepared by casting over a liquid surface. This film after drying at a temperature of 150°C, which was required for removing residual liquid from the surface and solvent from the bulk, was placed between the electrodes.

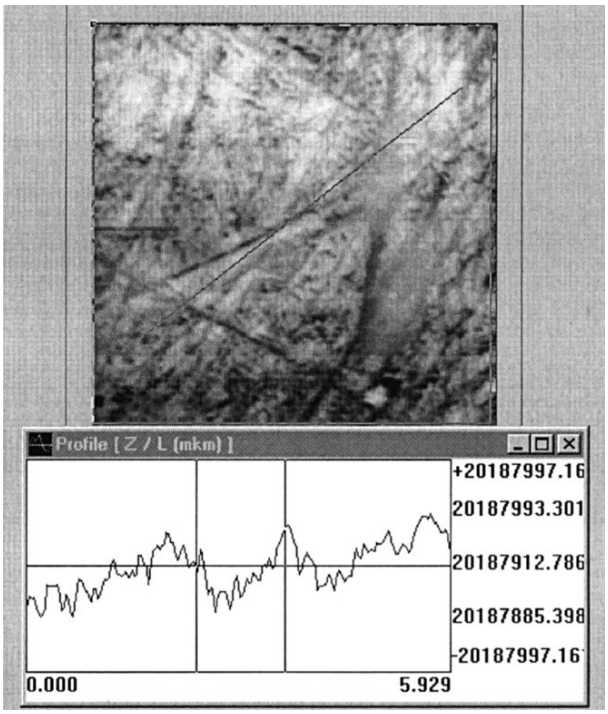

Fig. 3. STM image and surface profile (the difference between the heights at points of intersection with 52-nm measuring lines) of the vanadium substrate. The scanned area is 5.8×5.8 μm.

It was found that the experimental results do not substantially depend on the procedure of the film preparation, even though the conditions of contact between the metal surface and free polymer film in the latter case are evidently worse than those for the case of the film produced by the spin coating when the polymer was directly poured onto the electrode.

A measuring cell represented a planar multilayer sandwich-type structure: metal (vanadium)–polymer [poly(phthalidylidenebiphenylylene)]–nanocrystalline metal (copper or nickel). The polished side of the nanocrystalline metal sample was pressed to the surface of the polymer film prepared on the surface of a polished vanadium plate. The cell was placed in a heating device, which made possible heating and cooling the sample at a specified linear rate.

The current passing through the experimental cell was measured using a circuit typical of electric circuits with a nonlinear load, which is characterized by an *S*-shaped portion of the negative differential resistance. The measuring cell was placed in a heating device, which furnishes a means of heating the cell with a constant rate up to ~350°C.

3. RESULTS

The temperature dependences of the current passing in the metal–polymer–nanocrystalline metal system are shown in Fig. 4. When the copper sample is used as the nanocrystalline metal, an increase in the temperature up to 146°C does not lead to a change in the current. In the temperature range from 146 to 173°C, a peak-shaped change is observed in the dependence $I(T)$. When the nickel sample serves as the nanocrystalline metal, the current remains constant with an increase in the temperature up to 206°C. In the temperature range from 206 to 227°C, exhibits a trapezoidal change in the current the dependence $I(T)$ exhibits a trapezoidal change in the current.

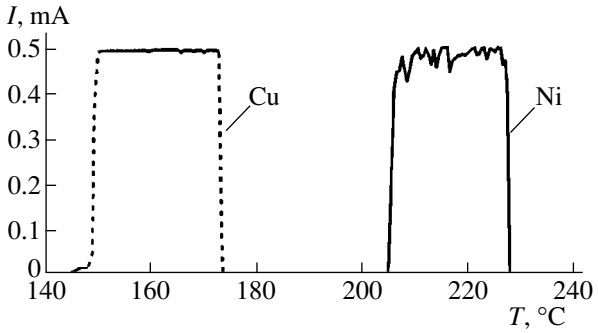

Fig. 4. Temperature dependences of the current passing through the metal–polymer–nanocrystalline metal system. The dashed line corresponds to the heterostructure with nanostructured copper, and the solid line, to the heterostructure with nanostructured nickel. Conditions: polymer film thickness, 1 μm; vanadium substrate; applied voltage, 5 V; heating rate, 8 K/min.

We also performed the check experiments in which the samples with a nanocrystalline structure were replaced by Cu and Ni metallic samples with an equilibrium grain structure. The following samples were used in these experiments:

(1) the initial coarse-grained metallic samples, which were subsequently used for the preparation of nanocrystalline samples, and

(2) the nanocrystalline samples after annealing at 500°C for 30 min, which, as is known [21], leads to a complete destruction of the nanocrystalline structure.

No temperature features in the conductivity of the system were found for these samples in the temperature range under consideration.

The evolution in the microstructure of nanostructured Cu and Ni upon heating was studied in detail in [21, 22] by using the above methods and also by differential scanning calorimetry. The data obtained indicate that severe relaxation processes caused by the rearrangement of the defect structure occur in the course of low-temperature annealing. These processes are observed in the temperature ranges 100–200°C for copper and 180–220°C for nickel. Note that these temperature ranges are close to those in which the changes in the electrical conductivity are found in the present work. This fact enables us to make the conclusion that the mechanisms responsible for these changes are similar and associated with the temperature transformation of the metallic sample microstructure.

The following regularity was revealed in the study of sequentially repeated heating–cooling cycles in the aforementioned temperature ranges. An increase in the number of measuring cycles is accompanied by a gradual decrease in the intensity of the injection current peaks and an increase in the peak width in such a way that the area under the current curve exponentially decreases with the number of cycles. This result is illustrated in Fig. 5.

Let us dwell on the following features in the dependences depicted in Fig. 5.

(i) The sample does not transform into the equilibrium state during one heating cycle. The transition is completed for several cycles.

(ii) The maximum temperature, at which the features in the current are recorded, is usually observed in the first cycles of measurements.

(iii) As the number of cycles increases, there is a tendency to a decrease in the temperature at which these features are observed, and the temperature range of the effect becomes larger.

Figure 6 depicts the dependence of $\int I(T)dT$ on the number of the thermal annealing cycle, which actually reflects the character of the grain structure relaxation to the equilibrium state.

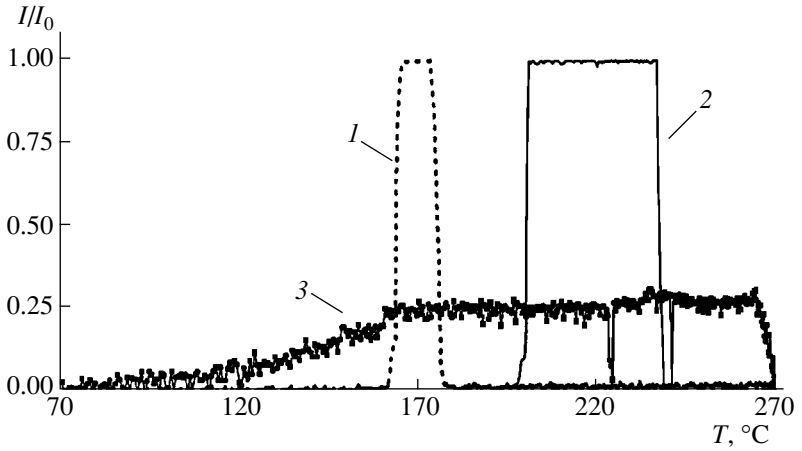

Fig. 5. Temperature dependences of the current passing through the metal–polymer–nanocrystalline metal system upon heating in the temperature range 20–270°C for the (*1*) second, (*2*) fourth, and (*3*) seventh cycles of measurements. Conditions: polymer film thickness, 1 μm; vanadium substrate; applied voltage, 5 V; heating rate, 8 K/min. The upper electrode is nanostructured copper. I_0 is the current passing in a measuring circuit when the sample resistance is equal to zero.

The temperature dependence of the current measured upon cooling the sample demonstrates that the current peak is also observed in the range of temperatures close to the temperature of current excitation upon heating (Fig. 7). Note that the location and shape of this peak, as a rule, are similar to those of the peak arising upon heating the system in the given cycle. This temperature feature is also characterized by the dependence of $\int I(T)dT$ on the cycle number, which is similar to that displayed in Fig. 6. According to our analysis, the data on the possible temperature irreversibility of the growth of nanostructured metal grains are not available in the literature. Most likely, the physical process initiating this growth has a phase transition character. The interpretation of its mechanism is beyond the scope of the present work.

4. DISCUSSION

A comparison of the results obtained in this work and the data reported in [1] revealed an essential difference. Upon melting of the electrode, the high-conductivity state arising at $T > T_{melt}$ is retained over the entire temperature range. In the case of nanocrystalline material, the high-conductivity state is observed in the narrow temperature range corresponding to the structural transformations in the metal. The explanation lies in the fact that the better contact conditions arising after the electrode melting favors the stabilization of the high-conductivity state, whereas the contact conditions in our case do not become better.

The measurements of the current passing through the metal–polymer–nanocrystalline metal system in several sequential heating–cooling cycles (Fig. 6) showed that, as the number of cycles increases, the quantity of the charge passed through the sample decreases down to a certain minimum value that corresponds to the current passing through the sample at room temperature. This is likely explained by the fact that, as the sample structure approaches the equilibrium state, the relative change in the work function [formulas (1) and (2)] in different cycles under identical measuring conditions decreases until the work function becomes equal to its equilibrium value.

According to relationships (1) and (2), the electric field should affect both the work function and the injection current. The temperature dependences of the current passing through the metal–polymer–nanocrystalline metal system at different applied voltages are demonstrated in Fig. 8. The influence of the field was evaluated from the integral of $I_U(T)dT$ taken with respect to T over the interval (T_1, T_2) as a function of applied voltage. This integral is proportional to the total charge passed through the sandwich in the specified temperature range. Here, T_1 and T_2 are the boundary

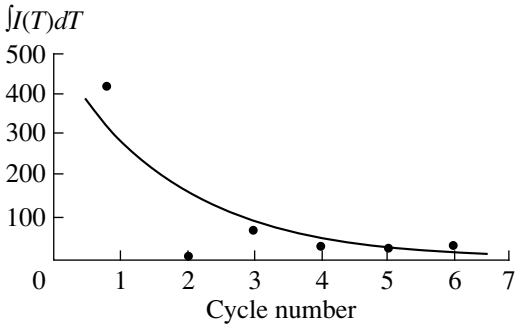

Fig. 6. Dependence of $\int I(T)dT$ on the number of the annealing cycle. Conditions: polymer film thickness, 1 μm; vanadium substrate; applied voltage, 5 V; heating rate, 8 K/min. The upper electrode is nanostructured copper.

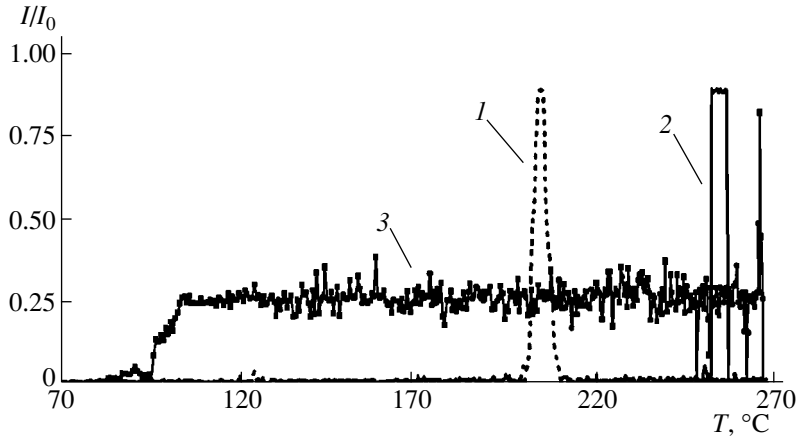

Fig. 7. Temperature dependences of the current passing through the metal–polymer–nanocrystalline metal system upon cooling in the temperature range 270–20°C for the (*1*) second, (*2*) fourth, and (*3*) seventh cycles of measurements. Conditions: polymer film thickness, 1 μm; vanadium substrate; applied voltage, 5 V; cooling rate, 8 K/min. The upper electrode is nanostructured copper. I_0 is the current passing in a measuring circuit when the sample resistance is equal to zero.

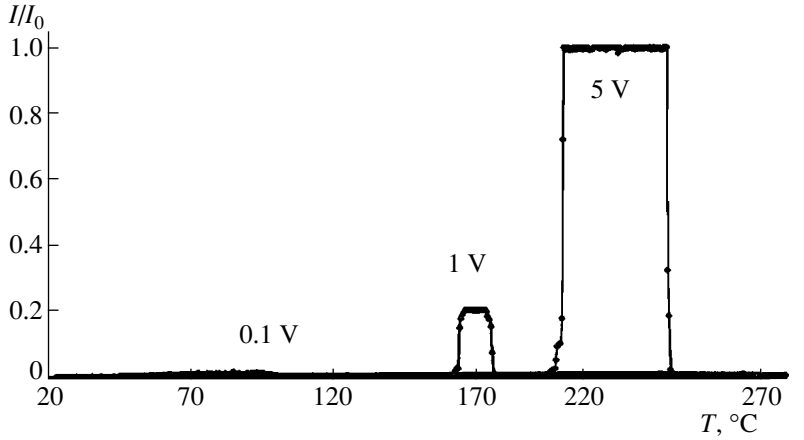

Fig. 8. Temperature dependences of the current passing through the metal–polymer–nanocrystalline metal system at different applied voltages. Conditions: polymer film thickness, 1 μm; vanadium substrate; heating rate, 8 K/min. The upper electrode is nanostructured copper. I_0 is the current passing in a measuring circuit when the sample resistance is equal to zero.

temperatures of the experimental range, and $I_U(T)$ is the temperature dependence of the current at the voltage U across the electrodes.

As follows from analysis of the experimental data, at $U < 0.1$ V, the charge passing through the sample virtually does not depend on the temperature and is minimum (and constant). An increase in the voltage in the range from 0.1 to 5 V leads to a sharp nonlinear increase in the total charge passed through the polymer. Above 5 V, the dependence describing the change in the charge is close to linear. This behavior is observed for virtually all the samples.

The presence of the voltage threshold indicates a considerable contribution of the injection mechanism, in particular, the double injection. In polymers, the holes, as a rule, are the intrinsic charge carriers, and, hence, the features observed in the passage of current through the sample are caused by the electron injection. This conclusion agrees with the experimental data on the direct injection of electrons from a beam into a polymeric matrix [30] and is the first experimental corroboration of the scheme proposed in [1] for the transition to the high-conductivity state in the polymer film. As was shown in [31, 32], the charge injected into the polymer with a certain probability can interact with the poly(phthalidylidenebiphenylylene) macromolecule and transform it to a new state. The polarizability of the molecular fragment with a changed electronic state increases, which results in an increase in the permittivity of the polymer. This state is unstable and, after a time, relaxes, which is attended by the transition of an electron to deeper traps. Owing to the competition between the electron capture and relaxation, the permittivity ε is a function of the electron injection rate.

According to relationship (1), an increase in the permittivity leads to an increase in the equilibrium total charge injected into the bulk and, hence, to the change in the injection level far from the equilibrium. Therefore, the charge transfer in polymers becomes nonlinear. It can easily be shown that there exists a certain critical injection level above which the process will be accelerated until the density of states required for the transition to the high-conductivity state is reached. However, a detailed consideration of this problem is beyond the scope of the present work.

Thus, it was demonstrated that the transition to the high-conductivity state in the metal–polymer–nanocrystalline metal system can occur with a change in the boundary conditions not only due to the melting of the electrode, but also owing to other structural transitions in metallic electrodes at which their state of aggregation remains unchanged. Moreover, the performed studies indicate that the use of thin polymer films of the poly(phthalidylidenebiphenylylene) type in metal–polymer–metal heterostructures makes it possible to investigate the surface transformations of metallic electrodes in the temperature range of their structural transitions. This method is very sensitive, can be easily realized, and, hence, can be very efficient.

ACKNOWLEDGMENTS

We are grateful to V. T. Khismatullin for his assistance in the STM experiments.

This work was supported in part by the Russian Foundation for Basic Research, project nos. 96-02-19208 and 98-03-33322.

REFERENCES

1. V. M. Kornilov and A. N. Lachinov, Zh. Éksp. Teor. Fiz. **111**, 1513 (1997) [JETP **84**, 833 (1997)].
2. K. C. Kao and W. Hwang, in *Electrical Transport in Solids* (Pergamon, Oxford, 1981; Mir, Moscow, 1984), Vol. 1.
3. W. Schottky, J. Phys. B **113**, 367 (1939).
4. P. R. Emtage and J. J. O'Dwyer, Phys. Rev. Lett. **16**, 356 (1966).
5. R. E. Vas'kov, A. F. Vladimirov, E. N. Moos, and N. I. Tabunov, Izv. Akad. Nauk SSSR, Ser. Fiz. **62**, 2044 (1998).
6. A. I. Reznik and N. V. Rudenko, Izv. Akad. Nauk SSSR, Ser. Fiz. **43**, 1823 (1979).
7. V. Heine and C. Hodges, J. Phys. C **5**, 225 (1972).
8. N. Ya. Rukhlyada, A. G. Trefilov, and B. B. Shishkin, Izv. Akad. Nauk SSSR, Ser. Fiz. **43**, 1837 (1979).
9. V. G. Bol'shov and L. N. Dobretsov, Dokl. Akad. Nauk SSSR **98**, 193 (1954).
10. V. S. Fomenko, *Emission Properties of Materials* (Naukova Dumka, Kiev, 1981).
11. J. Vancea, G. Reiss, D. Butz, and H. Hoffmann, Europhys. Lett. **9**, 379 (1989).
12. J. Ameiser, Z. Phys. **69**, 111 (1931).
13. I. V. Krylova and A. G. Petrukhin, Fiz. Tekh. Poluprovodn. (S.-Peterburg) **30**, 415 (1996) [Semiconductors **30**, 231 (1996)].
14. A. Lachinov, A. Zherebov, V. Kornilov, and M. Zolotukhin, Synth. Met. **84**, 735 (1997).
15. V. Kornilov and A. Lachinov, Synth. Met. **84**, 893 (1997).
16. A. Zherebov, A. Lachinov, and V. Kornilov, Synth. Met. **84**, 917 (1997).
17. V. M. Kornilov and A. N. Lachinov, Pis'ma Zh. Éksp. Teor. Fiz. **61**, 902 (1995) [JETP Lett. **61**, 921 (1995)].
18. V. Yu. Gertsman, R. Birringer, R. Z. Valiev, and H. Gleiter, Scr. Metall. Mater. **30**, 229 (1994).
19. S. V. Loskutov, V. V. Levitin, V. V. Pogosov, and M. I. Pravda, Fiz. Met. Metallogr. **79**, 5 (1995).
20. M. B. Partenskiĭ, Fiz. Met. Metalloved. **32**, 510 (1971).
21. R. Z. Valiev, I. V. Alexandrov, and R. K. Islamgaliev, in *Processing and Properties of Nanostructured Materials Prepared by Severe Plastic Deformation. Nanostructured Materials*, Ed. by G. M. Chow and N. I. Noskova (Kluwer Academic, Dordrecht, 1998), p. 121.
22. R. Z. Valiev, A. V. Korznikov, and R. R. Mulyukov, Fiz. Met. Metallogr. **6**, 70 (1992).
23. R. K. Islamgaliev, F. Chmelik, and R. Kuzel, Mater. Sci. Eng. A **234–236**, 335 (1997).
24. J. R. Rasmusson, Th. Kugler, R. Erlandsson, *et al.*, Synth. Met. **76**, 195 (1996).
25. V. S. Korsakov, S. I. Maksimov, L. A. Plavich, *et al.*, Élektron. Prom-st. **7–8**, 118 (1994).
26. O. A. Skaldin, A. Yu. Zherebov, V. V. Delev, *et al.*, Pis'ma Zh. Éksp. Teor. Fiz. **51**, 141 (1990) [JETP Lett. **51**, 159 (1990)].
27. V. M. Kornilov, V. T. Khismatllin, and A. N. Lachinov, in *Abstracts of 10th International Conference on Scanning Tunneling Microscopy, Seoul, Korea, 1999*, p. 138.
28. S. N. Salazkin, M. G. Zolotukhin, V. A. Kovardakov, *et al.*, Vysokomol. Soedin., Ser. A **29**, 1431 (1987).
29. V. M. Kornilov and A. N. Lachinov, Synth. Met. **53**, 71 (1992).
30. V. M. Kornilov and A. N. Lachinov, Pis'ma Zh. Éksp. Teor. Fiz. **61**, 504 (1995) [JETP Lett. **61**, 520 (1995)].
31. N. Johansson, A. N. Lachinov, S. Stafstrom, and W. R. Salaneck, Synth. Met. **67**, 319 (1994).
32. B. G. Zykov, Yu. V. Vasil'ev, V. S. Fal'ko, *et al.*, Pis'ma Zh. Éksp. Teor. Fiz. **64**, 402 (1996) [JETP Lett. **64**, 439 (1996)].

Translated by O. Borovik-Romanova

Physics of the Solid State, Vol. 42, No. 10, 2000, pp. 1942–1945. Translated from Fizika Tverdogo Tela, Vol. 42, No. 10, 2000, pp. 1889–1892.

FULLERENES AND ATOMIC CLUSTERS

Local Geometry and Electronic Structure of Free NaCl Clusters

G. É. Yalovega*, A. V. Soldatov*, K. Novak, M. Riedler**, O. Löfken**, A. Kolmakov**, and T. Möller****

** Rostov State University, ul. Zorge 5, Rostov-on-Don, 344090 Russia*

*** Hamburg, D-22603 Germany*

e-mail: vega@phys.rnd.runnet.ru

e-mail: soldatov@phys.rsu.ru

Received January 13, 2000

Abstract—Experimental x-ray spectra of the Cl $L_{2,3}$ absorption edge for free NaCl clusters of various sizes are presented. X-ray absorption spectra of the Na_4Cl_4 cluster have been theoretically calculated by the total multiple scattering method. A distorted cube is determined as the most probable geometric structure of the Na_4Cl_4 cluster. Curves of the partial densities of states are obtained for the cluster. © *2000 MAIK "Nauka/Interperiodica".*

1. INTRODUCTION

Free clusters are intermediate objects between isolated atoms or molecules and a solid. Of particular interest is an analysis of the changes in the electronic structure with a change in the geometry of these clusters. This paper reports the first studies of the x-ray absorption spectra of free clusters ranging from the molecule to the NaCl crystal. The geometry of small NaCl clusters was investigated earlier by the molecular dynamics method [1, 2]. These calculations showed that a small NaCl cluster has a nearly cubic structure, but the ring structure exhibits practically the same total energy. Note that all the structures proposed (cubic and ring-type) are distorted. There are practically no experimental studies of the geometry of NaCl clusters, except for mass spectroscopy, which only provides information on the cluster stability and size. In this work, we determined the geometry of small NaCl clusters and elucidated their electronic and energy structures on the basis of the theoretical treatment of experimental x-ray absorption spectra.

2. EXPERIMENT

The inner-shell absorption spectra were measured in the range 190–230 eV on the BW3 ondulator line of DESY (Germany) equipped with an SX700 plane-grating monochromator [3]. The cluster beam intercepted the monochromatic x-ray radiation. A toroidal mirror was used to focus the synchrotron radiation into a chamber in which free clusters were produced. The size of the clusters was varied by changing the conditions of their formation (temperature and pressure) and monitored by a mass spectrometer. A charged particle counter served as a detector. Excitation of the core levels of atoms in a cluster results with a high probability in its ionization, and, therefore, the ion yield curves obtained as functions of the photon energy reflect the x-ray absorption spectra of the clusters. The temporal structure of the synchrotron radiation beam was used to produce higher-contrast spectra. The equipment employed to create free clusters was described in more detail in [4].

3. METHOD OF CALCULATION

The algorithm of the total multiple scattering method used in this work is similar to that described earlier in [5]. The phase shifts were calculated using the crystal muffin-tin potential with contacting muffin-tin spheres according to the Mattheis scheme based on the Slater exchange. The calculation included phase shifts with orbital angular momenta of up to 2 for atoms of all types. To compare the theoretical spectrum (derived from the partial density of states) and the dipole matrix element of the transition with the experimental spectrum, the Fermi distribution function was taken into account.

4. RESULTS AND DISCUSSION

Figure 1 shows the partial ion-yield spectra for different NaCl clusters as functions of the x-ray photon energy. All the spectra are normalized to the photon flux intensity and corrected for the background. The absorption spectra scanned in the range 185–240 eV have a fine structure and change noticeably as they change from a molecule to a cluster and, finally, to a NaCl crystal. We start with discussing the bottom spectrum of the [NaCl] molecule. It exhibits only two small

1063-7834/00/4210-1942$20.00

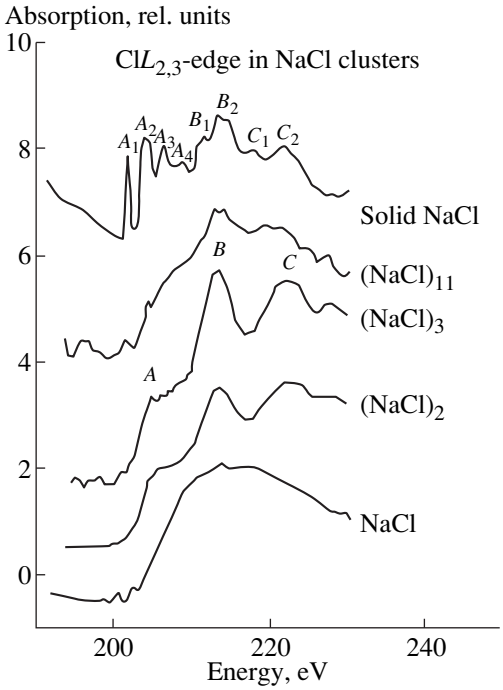

Fig. 1. Experimental x-ray spectra of free NaCl clusters of different sizes.

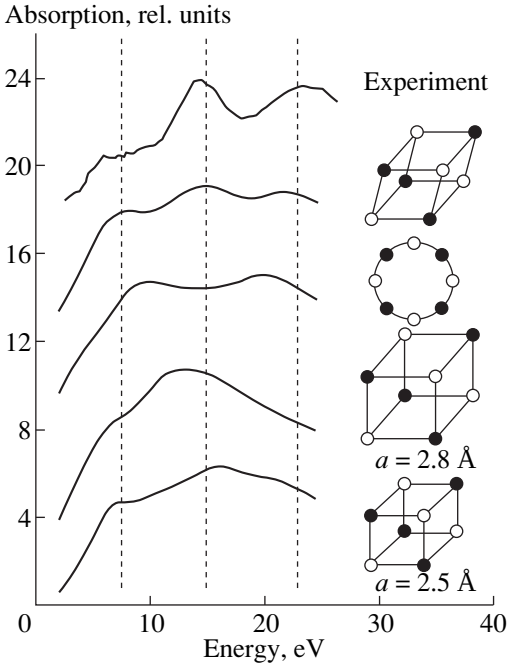

Fig. 2. Comparison of the experimental spectrum of the Na_3Cl_3 cluster (top curve) with theoretical spectra calculated for different cluster models.

peaks at energies of 200.7 and 202.6 eV. These peaks are due to the excitation of the $2p_{3/2}$ and $2p_{1/2}$ electrons into the 4*s* orbitals. Above the 2*p* threshold, the intensity of the spectrum strongly increases, and only a broad structureless band is observed. This band originates primarily from ionization into the 2*p* continuum.

Consider now the spectra of small clusters. In the energy range of the continuum, one can observe a structure, more specifically, three fairly broad features labeled by *A*, *B*, and *C*, whereas the peaks associated with excitation of the 2*p* electron into unfilled orbitals below the continuum threshold practically disappear. As the clusters grow in size even more, the peaks become sharper, and additional features appear. The absorption spectra of even larger clusters become increasingly similar to those of crystalline NaCl. The spectrum already has the *A*, *B*, and *C* maxima, and our results coincide with those obtained in [6]. This spectrum can be conveniently interpreted by dividing it in two regions. The region extending to 13 eV above the edge contains the A_1, A_2, A_3, and A_4 peaks, and the region up to 45 eV above the edge exhibits the B_1, B_2, C_1, and C_2 peaks. The former peaks are apparently due to electronic transitions to exciton states and into the density-of-states maxima in the conduction band. The latter peaks (from B_1 to C_2) are caused by single and multiple scattering of incident photoelectrons by atoms nearest to the absorbing atom and stem from the primary wave interference with the scattered photoelectron wave.

In order to determine the possible structure of small NaCl clusters, the experimental x-ray absorption near the edge structure (XANES) spectra were compared with the results of the theoretical calculations. Consider the structure of small NaCl clusters. The crystal of sodium chloride has a cubic lattice with an edge of 2.85 Å. It is this cluster that was used as one of the possible models to calculate the x-ray absorption spectrum. However, small clusters exhibit a trend toward a decrease in the interatomic spacing due to the absence of outer atoms which compensate for the attractive forces [7]. For this reason, a cluster with an interatomic distance of 2.5 Å was chosen for the second possible model. Two more proposed models were based on the results of molecular dynamics calculations [2]. One of them represents a distorted cube extended along one of the diagonals, and the other model is a ring. According to the general criterion for energy minimization, these models had the same probability of realization, because the total energy was almost the same in both cases. Hence, both these candidates were considered as possible models of the local structure of small clusters. Thus, the cluster models were as follows: (a) a cube with a bond length of 2.8 Å, (b) a cube with a bond length of 2.5 Å, (c) a cube with a bond length of 2.5 Å, but slightly distorted, and (d) a ring. Figure 2 shows how a change in the symmetry of the atomic arrangement in free NaCl clusters consisting of eight atoms affects the fine structure of the x-ray absorption spectrum. The figure depicts the curves calculated for the different cluster models shown on the right and the experimental

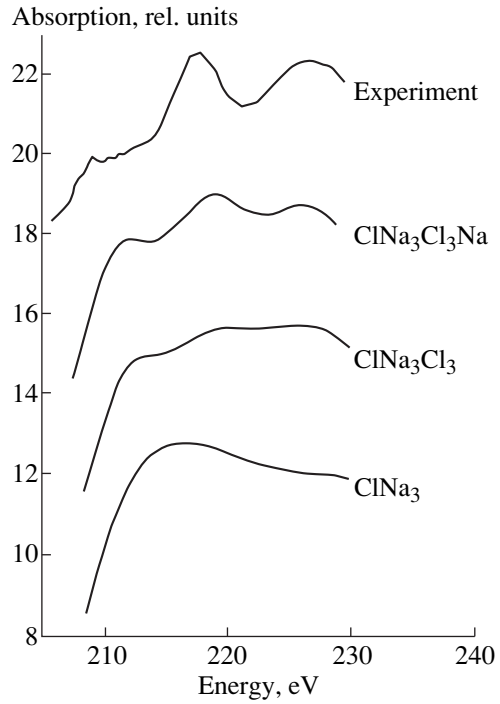

Fig. 3. Comparison of the experimental spectrum of Na_4Cl_4 with theoretical $ClL_{2,3}$ absorption edge spectrum calculated within the distorted-cube model for different numbers of atoms.

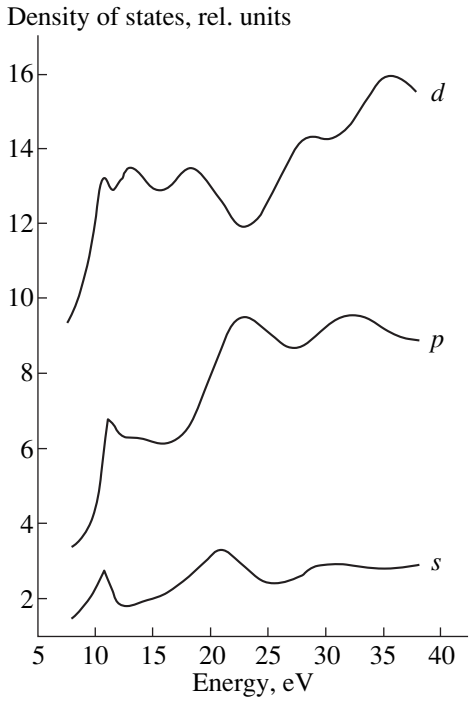

Fig. 4. Unfilled chlorine *s*, *p*, and *d* densities of states in a free Na_4Cl_4 cluster.

curve for the $(NaCl)_3$ cluster. The absorption spectra calculated for cubic structures with the same bond length as in a solid disagree with the experimental spectrum; indeed, none of the structures observed in the experiment fits the calculation. A decrease in the bond length (provided that the cubic structure is retained) somewhat improves the agreement with the experiment; the two first structures, *A* and *B*, agree with the experimental data. The next step for improving the fit consists in distorting the cubic lattice. In this case, the theoretical spectra contain all three structures (*A*, *B*, and *C*), which agrees with the experiment, both in the energy location and relative intensity of the peak. By contrast, the absorption calculated for the ring structure wholly conflicts with the experiment. Thus, the best agreement with the experimental spectrum (the main parameters are the number and energy location of the spectral maxima) is reached for a distorted cube.

A slight difference between the experimental and theoretical spectra in the distorted-cube model is probably caused by the fact that, in the experiment, the cluster size cannot be controlled to better than 10–15%, so that a certain part of the signal detected in the experiment is due to the presence of clusters of different sizes. Moreover, the calculations were performed for a cluster of eight atoms, whereas the experiment was run for clusters with an average size of six atoms.

We also studied the changes observed in the theoretical spectrum upon inclusion of individual atoms of the cluster in the calculation. As is seen from Fig. 3, adding three chlorine atoms to $ClNa_3$ gave rise to three weakly pronounced features in the spectrum. A further increase in the cluster size (adding a corner Na atom) results in a distinct increase in the intensity of the spectral features, which improves the agreement between the theoretical and experimental spectra.

A good agreement between the theoretical and experimental spectra gives grounds to believe that the crystal potential model used is appropriate. The same method of calculating the crystal potential was used to analyze the electronic structure of the cluster under study. Figure 4 displays the partial densities of the *s*, *p*, and *d* states of chlorine in a free Na_4Cl_4 cluster.

Thus, we obtained the first x-ray absorption spectra of free NaCl clusters ranging in size from a molecule to a macroscopic crystal. It was shown that by analyzing x-ray absorption spectra in terms of the multiple scattering method, one can determine the geometry of small clusters, including the bond length and angle. The preliminary results suggest that small NaCl clusters have a distorted cubic structure with a bond length intermediate between the bond length in a molecule and that between atoms in the NaCl crystal.

ACKNOWLEDGMENTS

This work was supported by the Russian Foundation for Basic Research Deutsche Forschungsgemeinschaft, project no. 98-02-04097.

REFERENCES

1. M.-J. Malliavin and C. Coudray, J. Chem. Phys. **106**, 2323 (1997).
2. A. Aguado, A. Ayuela, J. M. Lopez, and J. A. Alonso, Phys. Rev. B **56**, 15353 (1997).
3. C. U. S. Larson, A. Beutler, O. Bjorneholm, *et al.*, Nucl. Instrum. Methods Phys. Res., Sect. A **337**, 603 (1993).
4. O. Bjorneholm, F. Federmann, C. U. S. Larson, *et al.*, Rev. Sci. Instrum. **66**, 1732 (1995).
5. G. É. Yalovega and A. V. Soldatov, Fiz. Tverd. Tela (S.-Peterburg) **41** (8), 1385 (1999) [Phys. Solid State **41**, 1268 (1999)].
6. M. Kasrai, M. E. Fleet, G. M. Bancroft, *et al.*, Phys. Rev. B **43**, 1763 (1991).
7. E. de la Puente, A. Aguado, A. Ayuela, and J. M. Lopez, Phys. Rev. B **56**, 7607 (1997).

Translated by G. Skrebtsov

Physics of the Solid State, Vol. 42, No. 10, 2000, pp. 1946–1951. Translated from Fizika Tverdogo Tela, Vol. 42, No. 10, 2000, pp. 1893–1898.

FULLERENES AND ATOMIC CLUSTERS

On the Cluster Mechanism of Diamond Synthesis from Different Solid Carbon Forms

É. É. Lin

All-Russia Research Institute of Experimental Physics (VNIIEF), Sarov, Nizhegorodskaya oblast, 607190 Russia
e-mail: root@gdd.vniief.ru

Received December 16, 1999; in final form, March 21, 2000

Abstract—The cluster mechanism of diamond synthesis has been proposed. The mechanism is based on the concept of vibrational interactions between objects with the anomalously high Debye temperature. The estimates obtained for the crystal sizes are in good agreement with the experimental data on the dynamic and static syntheses of diamonds from different solid carbon forms such as organic materials, nanodiamonds, fullerite, graphite, and nanotubes.

1. INTRODUCTION

A large number of works are dedicated to the dynamic and static syntheses of diamonds at high pressures P and high temperatures T. In these works, the phase transition from graphite to diamond is treated as the main mechanism of diamond formation (see, for example, [1–3]). This transition becomes thermodynamically possible under the conditions that correspond to the stability region of diamond in the P–T phase diagram of carbon. Many works [4–6] deal with the synthesis of diamonds from fullerene and nanotubes. Another direction of investigations concerns the preparation of ultradisperse diamonds by the dynamic loading of organic compounds [7–14]. The production of polycrystalline diamonds by impact compaction of diamond powders with nanometric sizes of particles is considered in [15–17]. In this case, the reached pressures correspond to the lower boundary of the diamond stability region.

Within a unified approach, we will attempt to consider the dynamic and static syntheses of diamonds from different solid carbon forms subjected to mechanical loads that correspond to the above stability region and prevent the formation of a liquid phase. For this purpose, the formation of diamond crystals will be qualitatively treated as follows. Assume that the structure of initial carbon material under external action breaks into single fragments composed of carbon atoms such as planar graphite hexagons, molecules of the benzene carbon skeleton type, cyclane, etc. The collisions of these fragments can bring about the formation of molecules with a cyclohexane carbon skeleton, which, owing to the mutual orientation of carbon atoms, in essence, are nuclei of the diamond crystal structure (see, for example, [18]). It should be noted that, in the scheme under consideration, we deal not with molecules of different hydrocarbons, but with their carbon skeletons, i.e., the structures with dangling external bonds formed, for example, upon breaking of the C–H and C–O bonds. The collisions between the molecules with the cyclohexane carbon skeleton lead to the mutual compensation for the dangling bonds and appearance of small-sized clusters [14] whose growth results in the formation of carbon mesostructures with the short-range crystal order that matches the diamond lattice. The interaction of these mesostructures with each other and nuclei gives rise to a quasi-long-range order, which corresponds to the formation of nanodiamonds. The coalescence of nanodiamonds is responsible for the growth of the diamond crystals, which, in principle, can occur under metastable conditions [1]: at "zero" pressure and increased residual temperatures.

Therefore, in the proposed model, the synthesis of diamonds from different solid carbon forms is associated with the formation and growth of small-sized crystalline diamond-like structures. It is believed that the phonon excitations of carbon objects are crucial in the considered processes due to the anomalously high Debye temperature of the diamond, which is equal to 2250 K (see, for example, [19]) and is comparable to the temperatures ($T \sim 10^3$ K) reached in the diamond synthesis. It is reasonable to expect that, when the duration of the external action on the objects is considerably longer than the characteristic travel time of vibrational excitation in them, the probability that the excited lattices of touching clusters are joined owing to the mutual compensation for the dangling external bonds of the "boundary" (i.e., surface) atoms is high. In this case, the objects are linked together with the formation of covalent bonds, and the particles increase in size.

The validity of the approach proposed is supported by a number of factors given below.

(1) The nonequilibrium radiation with the wavelength $\lambda = 445$ nm that corresponds to the luminescence of impurity nitrogen centers in the diamond crystal lattice was found in products of the explosion of the solid

1063-7834/00/4210-1946$20.00

explosive [20], which indicates the presence of phonon excitations in nanodiamonds in the course of explosive processes.

(2) The elastic precursor that arises upon impact loading of porous nanodiamond material [21] suggests the phonon excitations in the studied system of crystal clusters.

(3) The crystal lattice parameters of detonation nanodiamonds (the interplanar spacings are $d_{111} \approx 0.206$ nm, $d_{220} \approx 0.126$ nm, and $d_{311} \approx 0.107$ nm) and their pycnometric density $\rho_0 = 3$ g/cm^3 agree with the well-known data for natural polycrystals of cubic diamond (see, for example, [9–11]).

(4) The specific heat capacity of nanodiamonds at the temperature $T = 300$ K is in reasonable agreement with the data for natural diamond [22].

(5) The Debye temperature θ_D of small-sized (2–20 nm) diamond particles with allowance made for the surface density of states [23] is evaluated to be equal to $\theta_D \approx (0.92–0.99)\theta_0$, where $\theta_0 = 2250$ K [19].

According to (3)–(5), the crystal lattice dynamics of nanodiamonds at high temperatures is identical to that of "infinitely" large crystals. In particular, this allows us to use the Debye approximation in the quantitative description of the diamond synthesis from small-sized crystalline structures. In the present work, the formation and growth of these structures was treated within the concept of the probability density in the clusters sizes space with pronounced collective quantum properties [12].

2. APPROXIMATE DESCRIPTION OF THE PROBABILITY DENSITY WAVE IN THE CLUSTER SIZE SPACE

Let us consider the formation of compact clusters in conservative stochastic systems, which are defined as ensembles of quantum objects that interact with each other in a random way. Note that the total mass of the ensemble is limited. The process of the irreversible aggregation of objects will be described in terms of the probability density wave $\varphi(a, t)$ in the space of cluster sizes a. The wave propagates with time t toward an increase in the cluster size. According to the universally accepted notions of the broadening of a wave packet with time (see, for example, [24]), the coordinate and momentum in the cluster size space are related by the following approximate expression:

$$\Delta a \Delta p \sim \frac{\hbar}{2}. \tag{1}$$

Here, $\Delta p \sim p = m\Delta a/\Delta t$ is the "momentum uncertainty," m is the cluster mass, and $\hbar$ is the reduced Planck constant. The momentum uncertainty is equal in the order of magnitude to the momentum itself; i.e., the interaction of objects either occurs or does not occur. The physical meaning of relationship (1) resides in the fact that the precise cluster size cannot be determined on the time interval Δt of an elementary (single) act of the interaction between the objects until the interaction is completed. This is due to the fact that it is impossible to establish a one-to-one correspondence between a given object and its interacting surface atom prior to the completion of an elementary act.

From relationship (1), it follows that $\Delta a \propto \sqrt{\Delta t}$; i.e., the index of the fractional derivative of the cluster size with respect to time is equal to 1/2. Then, the evolution of the probability density function $\varphi(a, t)$ can be described within the diffusion approximation by using the Fokker–Planck equation [25] rewritten for the cluster size space

$$\frac{\partial \varphi(a, t)}{\partial t} + \frac{\partial}{\partial a}[\nu \varphi(a, t)] - \frac{1}{2}\frac{\partial^2}{\partial a^2}[\eta \varphi(a, t)] = 0.$$

Here, $\nu = \langle da \rangle/dt$ is the mean velocity of kinematic transfer of φ, and $\eta = \langle (da)^2 \rangle/dt$ is the diffusion coefficient in the cluster size space. The function $\varphi(a, t)$ satisfies the condition of total mass conservation

$$M_{\text{nucl}}(t) + M_{\text{cl}}(t) = M_{\text{nucl}}(t) + \int_0^{a_{\max}} \varphi(a, t) m(a, t) da = \text{const}, \tag{2}$$

where $M_{\text{nucl}}(t)$ and $M_{\text{cl}}(t)$ are the current total masses of nuclei and clusters, respectively. The cluster mass can be defined as $m \approx m_0(a/a_0)^3$, where a_0 and m_0 are the size and the mass of the nucleus.

Now, we introduce the dimensionless variables $\xi = a/a_0$ and $\tau = t/t_i$, where t_i is the characteristic time scale of the interaction between the objects. For the clusters with sizes much greater than the nucleus sizes ($\xi \gg 1$), the diffusion term in the Fokker–Planck equation can be ignored. In this case, the evolution of φ can be described with the use of the traveling wave equation

$$\frac{\partial \varphi(\xi, \tau)}{\partial \tau} + \Psi(\tau)\frac{\partial \varphi(\xi, \tau)}{\partial \xi} = 0. \tag{3}$$

Here, $\Psi(\tau) = d\langle \xi \rangle/d\tau$ is the growth rate of a medium-sized cluster. Equation (3) is derived from the Fokker–Planck equation under the assumption that $\langle d\xi \rangle/d\tau \sim d\langle \xi \rangle/d\tau$ in the order of magnitude. Substituting the usual expansion of φ as a superposition of the forward and backward waves $\varphi(\xi, \tau) = F_1(\xi - \Psi\tau) + F_2(\xi + \Psi\tau)$ into Eq. (3) and using Eq. (2), we obtain that the mean size of clusters in the system originally involving only nuclei increases with time according to the power law

$$\langle a \rangle = a_0 K \left(\frac{t}{t_i}\right)^Z. \tag{4}$$

The constants K and Z can be determined by invoking relationship (1). Expanding the increment of the mean size in a standard power series of Δt and ignoring the

second-order terms, from formulas (4) and (1), we have the following relationship for the determination of the K and Z constants at $\Delta t = t_i$:

$$Z^2 K^{2/Z} \sim \frac{\hbar t_i}{2m_0 a_0^2}\left(\frac{\langle a\rangle}{a_0}\right)^{\frac{2}{Z}-5}. \quad (5)$$

The quantity Z is determined using the condition $K \equiv$ const; i.e., the right-hand side of relationship (5) should not depend on $\langle a\rangle$. The specific values of the constants in formula (4) depend on the value of t_i, i.e., are determined by the mechanism of interaction between the objects in a closed system.

3. APPROXIMATE LAWS FOR GROWTH OF DIAMOND CRYSTALS

First, we consider the processes of forming the nuclei of the diamond crystal structure—the molecules with a cyclohexane carbon skeleton. When the initial structure breaks into the fragments containing three carbon atoms, the total time of nucleation t_{nf} is equal to the sum of the time t_{cf} of forming the cyclane carbon skeletons and the time t_{cu} of uniting these fragments into the molecule with the cyclohexane carbon skeleton. The benzene carbon skeleton and the graphite hexagon are considered the initial structures. It can be assumed that these structures fail owing to the "bending" of the chemical bond between two adjacent carbon atoms. Then, the time t_{cf} can be defined as the product of the period of bending vibrations and the mean number of vibrations required for the transformation of the vibrational spectrum of the benzene (or hexagon) carbon skeleton into the vibrational spectra of two molecules with the cyclane carbon skeleton

$$t_{cf} \sim \frac{2\pi\hbar}{k\theta_\nu^{(2)}}\exp\frac{E_1 - 2E_2}{kT}. \quad (6)$$

Here, k is the Boltzmann constant; $\theta_\nu^{(2)}$ is the characteristic temperature of the bending vibrations of chemical bonds between carbon atoms; and E_1 and E_2 are the mean thermal energies of molecules with the benzene (hexagon) and cyclane carbon skeletons, respectively. The time t_{cu} can be evaluated as the product of the period of stretching vibrations of carbon atoms in the cyclane skeleton and the mean number of vibrations required for the transformation of the vibrational spectra of two molecules with the cyclane carbon skeleton into the vibrational spectrum of the cyclohexane carbon skeleton

$$t_{cu} \sim \frac{2\pi\hbar}{k\theta_\nu^{(1)}}\exp\frac{E_3 - 2E_2}{kT}. \quad (7)$$

Here, $\theta_\nu^{(1)}$ is the characteristic temperature of the stretching vibrations of chemical bonds between carbon atoms, and E_3 is the mean thermal energy of the molecule with the cyclohexane carbon skeleton. The mean thermal energies E_i (i = 1, 2, and 3) are calculated from the following formula derived by the integration of the approximate relationship for the heat capacity of nonlinear polyatomic molecules [26]:

$$E_i = 3kT + kT\left\{\sum_{\nu=1}^{N}\frac{\theta_\nu^{(1)}/T}{\{\exp[\theta_\nu^{(1)}/T]\}-1} + \frac{(3M-6)-N}{N}\sum_{\nu=1}^{N}\frac{\theta_\nu^{(2)}/T}{\{\exp[\theta_\nu^{(2)}/T]\}-1}\right\}, \quad (8)$$

where $\theta_\nu^{(j)}$ (j = 1, 2) are the characteristic temperatures of the stretching and bending vibrations of chemical bonds of atoms in the molecule, respectively; M is the number of atoms in the molecule; and N is the number of bonds. By using the characteristic temperatures of single and double chemical bonds between carbon atoms [26] and taking the temperature of the explosive decomposition of the organic compound as T = 3500 K [7], formulas (6) and (7) and formulas (6) and (8) lead to the estimates $t_{cf} \approx (3.6\text{–}5.4) \times 10^{-13}$ s and $t_{cu} \approx 6.3 \times 10^{-13}$ s. Thus, the time of forming the diamond phase nucleus in the explosive processes is approximately equal to $t_{nf} = t_{cf} + t_{cu} \approx 10^{-12}$ s. Similar calculations for the static synthesis [1, 2] at $T \approx 2000$ K give $t_{nf} \approx 6 \times 10^{-13}$ s.

The molecules with the cyclohexane carbon skeleton can be also directly formed from hexagons as a result of the bending of the planar structures upon their collisions. The time of this transformation of the initial carbon structure can be determined as the product of the period of bending vibrations into the mean number of interactions necessary for the corresponding transformation of the vibrational spectrum

$$t_{\text{trans}} = \frac{2\pi\hbar}{k\vartheta_\nu^{(2)}}\exp\frac{E_3 - E_1}{kT}.$$

According to the estimates, $t_{\text{trans}} \approx 0.95 \times 10^{-13}$ s at T = 3500 K and $t_{\text{trans}} \approx 1.2 \times 10^{-1}$ s at $T \approx$2000 K.

Therefore, the characteristic times of forming the nuclei of the diamond crystal structure, i.e., the molecules with the cyclohexane carbon skeleton, vary in the order of magnitude from 10^{-13} to 10^{-12} s. These times are considerably shorter than the characteristic times of the dynamic and static syntheses of diamonds, which range from microseconds to days [1–17]. This makes it possible to describe the cluster growth within the proposed kinetic approach based on the representation of multiple processes of interaction between the objects in terms of the probability density wave in the cluster size space. According to the universally accepted concepts (see, for example, [27, 28]), we can separate two possible types of particle growth: (1) the low flux of nuclei

when each nucleus has time to occupy the most energetically favorable site at the particle surface before the onset of the effective interaction with the next nucleus and (2) the high flux of nuclei when they almost simultaneously interact with the particle.

At the low flux of nuclei, the time t_i is equal to the time t_s of nucleus diffusion over the cluster surface until the stable bonds are formed [12]

$$t_i \equiv t_s = \frac{2\pi\hbar}{k\theta_D}\exp\frac{E_w - E_0}{2kT}, \quad (9)$$

where E_w and E_0 are the specific energies of nuclei in the cluster bulk and the environment, respectively. In the case when the nuclei are the polyatomic objects with elements of the cluster crystal structure, the electronic terms in the difference $E_w - E_0$ cancel out. Therefore, in the expression for E_0, it is sufficient to include the terms determined by the vibrational spectrum of nuclei, i.e., to use formula (8). For solid-state clusters that exhibit a fractal character, we have [29]

$$E_w = M\left\{|\chi| + 3DkT(T/\theta_D)^D \int_0^{\theta_D/T} [x^D/\exp x - 1]dx\right\},$$
$$x = 2\pi\hbar\nu/kT. \quad (10)$$

Here, $|\chi| \approx k\theta_D$ is the energy of the ground vibrational lattice state (the energy of zero-point vibrations), D is the internal (dynamic) fractal dimension of the cluster, and ν is the frequency of atomic vibrations in its lattice. Since the Debye temperature of large-sized clusters ($\xi \gg 1$) weakly depends on the size and virtually coincides with the Debye temperature of a macroscopic object, t_s does not depend on $\langle a\rangle$. Then, from relationships (4) and (5), we obtain the approximate formula for an increase in the mean size of large clusters due to the capture of nuclei

$$\langle a\rangle \approx a_0\left(\frac{5}{2\sqrt{2}}\right)^{2/5}\left(\frac{t}{t_{un}^{cn}}\right)^{2/5},$$
$$t_{un}^{cn} = a_0\left(\frac{m_0 t_s}{\hbar}\right)^{1/2}, \quad (11)$$

where t_{un}^{cn} is the time unit for the low flux of nuclei at the cluster.

In the case of the high flux of nuclei and also in processes of interaction between the large-sized clusters, it is expedient to use the mean time of the phonon excitation of the object as the characteristic time scale t_i

$$t_i = \frac{2\langle a\rangle}{c_0}. \quad (12)$$

Here, c_0 is the effective velocity of propagation of vibrations in the cluster structure ("sound velocity"). From formulas (1), (4), (5), and (12) we obtain the approximate relationship for an increase in the mean size of large clusters due to their interactions with the high flux of nuclei and between each other

$$\langle a\rangle \approx a_0\left(\frac{3}{2}\right)^{1/3}\left(\frac{t}{t_{un}^{cl}}\right)^{1/3}, \quad t_{un}^{cl} = a_0\left(\frac{a_0 m_0}{\hbar c_0}\right)^{1/2}, \quad (13)$$

where t_{un}^{cl} is the time unit in the processes of interaction between large clusters.

Inserting the above expression for t_s and $m_0 = AMm_u$ (where A is the atomic weight and m_u is the atomic mass unit) into the parametric relationships (11) and (13) and writing the relationship for the sound velocity within the Debye approximation $c_0 \approx k\theta_D/\hbar(6\pi^2 n)^{1/3}$ (where n is the concentration of atoms in the crystal lattice), we derive the following formulas for growth of crystalline particles from nuclei—the polyatomic molecules:

$$\langle a\rangle \approx \left(\frac{25k\theta_D a_0^3}{16AMm_u\exp\frac{E_w - E_0}{2kT}}\right)^{1/5} t^{2/5}, \quad (14)$$

$$\langle a\rangle \approx \left(\frac{9k\theta_D a_0^3}{4(6\pi^2 n)^{1/3}AMm_u}\right)^{1/6} t^{1/3}. \quad (15)$$

Formula (14) represents the cluster growth at the low flux of nuclei, and formula (15) describes the cluster growth at a high flux of nuclei and upon interaction between the clusters.

Let us treat the interaction between the nanodiamonds in the closed system. In this case, the crystal structure of the nuclei (nanodiamonds) is identical to that of the particles formed by their coalescence. Then, relationship (9) leads to $t_s = 2\pi\hbar/k\theta_D$. Representing the nucleus mass as $m_0 \approx \pi/6\rho_0 a_0^3 = \pi/6Am_u n a_0^3$, expressing c_0 within the Debye approximation, and using expressions (11) and (13), it is possible to obtain the formulas describing an increase in the mean particle size

$$\langle a\rangle \approx \left(\frac{75k\theta_D}{8\pi Am_u n}\right)^{1/5} t^{2/5}, \quad (16)$$

$$\langle a\rangle \approx \left(\frac{27k\theta_D}{2\times 6^{1/3}\pi^{5/3}Am_u n^{4/3}}\right)^{1/6} t^{1/3}. \quad (17)$$

Relationship (16) corresponds to the low flux of nuclei when the mean size increases owing to the interaction of the "particle–nucleus" type, and expression (17) describes the case of the high flux of nuclei when the growth is determined by the interaction of the "particle–particle" type. The mean sizes of the synthesized crystals do not depend on the initial size of nuclei (nanoclusters). This implies that the system "forgets" the initial conditions, and the particles grow in accord with the dynamics of the macroscopic crystal lattice.

4. ESTIMATES OF DIAMOND SIZES AND DISCUSSION

According to the concepts of the conventional boundary between the "macrocosm and mesocosm" [24], relationship (1) is fulfilled up to object sizes of an order of 10^{-7} m. This gives grounds to attempt to apply the above-derived equations to analysis of the kinetics of formation of diamond crystals from different solid carbon forms.

Now, we consider the synthesis of diamonds in the detonation wave in a solid explosive. By ignoring the specific chemical nature of the explosive decomposition products, they will be treated as a continuous medium whose role reduces to the confinement of the studied crystalline structures together. The confinement time t_{conf} can be defined as the time of unloading wave propagation from the edge of an explosive charge to its axis (center): $t_{\text{conf}} = R/c_{\text{eff}}$, where R is the radius of the explosive charge, and c_{eff} is the effective sound velocity in the detonation products. The "Lagrange" layer of the shocked organic compound (i.e., the layer with a constant mass) is considered a closed system. The expansion of this layer is accompanied by the formation of crystalline diamond-like clusters due to the vibrational interactions between the objects [14]. The particles grow in the flow behind the shock wave front due to the processes of two types: the interactions between the clusters and the nuclei [formula (14)] and the interactions between the clusters [formula (15)]. After the capture of all the nuclei, the particle growth is described by relationship (15). According to the estimates made from formula (14), for the time of the chemical reactions in the detonation wave $t = 0.5 \times 10^{-6}$ s [7], the particles about 30 nm in size can be formed in the flow behind the front. This value is in reasonable agreement with the maximum size of ultradisperse diamonds obtained by the detonation synthesis [7–11]. As follows from the estimates made by formula (15), during the confinement time $t_{\text{conf}} \cong 50 \times 10^{-6}$ s, i.e., in the Taylor wave, the diamond-like particles of sizes as large as $\sim 10^{-7}$ m can grow in the detonation products of solid explosive charges 30 cm in diameter. This agrees with the experimental data on the scaling of explosive charge size [30].

Let us dwell on the shock-induced coalescence of the detonation nanodiamonds (prepared by "water" synthesis [30]) under weak dynamic loading [15, 21] with an amplitude of about 10 GPa (i.e., near the lower boundary of the diamond stability region in the phase diagram of carbon). Since the thickness of the amorphous carbon layer surrounding the nanodiamond is of an order of atomic distance [10, 11], the interaction between the diamond nanoclusters having the excited crystal lattices can bring about the formation of covalent bonds between outer atoms of crystalline "grains" in the touching particles. Because the compression pulse duration is short ($\tau \sim 10^{-5}$ s), it is reasonable to assume that the particles predominantly grow under metastable conditions for the diamond in the phase diagram of carbon [1]: at zero pressure and increased residual temperatures. The estimates obtained from formulas (16) and (17) demonstrate that, for the time of sample cooling $t \sim 10^2$ s (typical of experiments under consideration [17]), two subsystems of particles with mean sizes of 1.5×10^{-5} and 1.5×10^{-4} m are formed in the system. The results of calculations are in agreement with the experimental bimodal distributions [15].

In experiments on the shock-wave synthesis of diamonds from fullerites [4], the time t_{hp} of the heat wave propagation from the shock-heated powder to the surrounding matrix was estimated (by analogy with [17], within the linear heat conductivity approximation) to be equal to $\sim 10^{-2}$ s. It can be assumed that the carbon sample was rapidly cooled, and the diamond phase was quenched for time t_{hp}. The estimates obtained from relationships (16) and (17) at $t \sim 10^{-2}$ s show that the mean sizes of diamond particles are equal to about 4 and about 1 μm, respectively. These values coincide in the order of magnitude with the experimental data [4].

Finally, we analyze the static synthesis of diamonds. From formula (16), it follows that the "faster" mechanism of the attachment of small-sized nuclei to the large-sized particle provides a way of growing the diamond crystals with characteristic sizes from 0.3 to 2 mm for the time interval from 10 min to one day. The particles with these sizes in the order of magnitude are formed for the above times in high-pressure chambers under the conditions that correspond to the lower boundary of the diamonds stability region in the phase diagram of carbon [1]. In the static synthesis of diamonds from carbon nanotubes at $P = 5$ GPa and $T \cong 1670$ K [6], it was found that the maximum size of crystallites formed in a high-pressure chamber for 30 s is equal to 20–50 μm. The diamond crystals 150–200 μm in size were obtained in parallel experiments with the use of graphite. The latter values are in satisfactory agreement with the estimate made by formula (16), according to which the mean size for the given time is equal to about 100 μm. At the same time, the estimate from relationship (17) leads to a mean size of about 10 μm, which agrees in the order of magnitude with the sizes of diamonds prepared from nanotubes.

It is believed that the model proposed is also applicable to investigations into the growth kinetics of natural diamond crystals formed in the earth's cataclysms, for example, a meteorite impact. The estimates obtained from formula (17) for a slower process demonstrate that diamonds of sizes 1–10 cm can grow for 8×10^3–8×10^6 years. These times are substantially shorter than the age of the Earth, which is likely of an order of 10^9 years (see, for example, [31]). This suggests the pulsed (accidental) character of the formation and growth of natural diamonds.

A good agreement between the results of calculations performed in this work and the available experi-

mental data confirms the adequacy of the proposed model for the growth of diamond-like structures under loads excluding the formation of the liquid phase. All the foregoing corroborates the hypothesis on the decisive role of vibrational interactions between crystalline objects with the anomalously high Debye temperature in the dynamic and static syntheses of diamonds from different solid carbon forms such as organic compounds, nanodiamonds, fullerite, graphite, and nanotubes.

ACKNOWLEDGMENTS

This work was supported by the State Scientific and Technical Program "New Materials" (the Direction "Superhard Materials") of the Ministry of Science and Technology of the Russian Federation (1999).

REFERENCES

1. G. N. Bezrukov, in *Physical Encyclopedia: Diamond*, Ed. by A. M. Prokhorov (Bol'shaya Ross. Éntsiklopediya, Moscow, 1988), Vol. 1, p. 60.
2. G. N. Bezrukov, V. P. Butuzov, and M. I. Samoĭlovich, *Synthetic Diamond* (Nedra, Moscow, 1976).
3. E. Vlodarchik and R. Trebinski, Shock Waves **7** (4), 231 (1997).
4. O. G. Epanchintsev, A. S. Zubchenko, Yu. D. Tret'yakov, *et al.*, Dokl. Akad. Nauk **340** (2), 201 (1995).
5. Ma Yanzhang and Zon Guangtian, in *Proceedings of the Joint XV AIRAPT and XXXIII EHPRG International Conference, Warsaw, Poland, 1995* (World Scientific, Singapore, 1996), p. 702.
6. A. M. Germanskiĭ, G. A. Dyuzhev, D. V. Novikov, *et al.*, Pis'ma Zh. Tekh. Fiz. **25** (5), 18 (1999) [Tech. Phys. Lett. **25**, 174 (1999)].
7. V. M. Titov, V. F. Anisichkin, and I. Yu. Mal'kov, Fiz. Goreniya Vzryva **25** (3), 117 (1989).
8. A. I. Lyamkin, E. A. Petrov, A. P. Ershov, *et al.*, Dokl. Akad. Nauk SSSR **302** (3), 611 (1988) [Sov. Phys. Dokl. **33**, 705 (1988)].
9. A. L. Vereshchagin, G. V. Sakovich, P. M. Brylyakov, *et al.*, Dokl. Akad. Nauk SSSR **314** (4), 866 (1990) [Sov. Phys. Dokl. **35**, 851 (1990)].
10. M. V. Baĭdakova, A. Ya. Vul', V. I. Siklitskiĭ, and N. N. Faleev, Fiz. Tverd. Tela (S.-Peterburg) **40** (4), 776 (1998) [Phys. Solid State **40**, 715 (1998)].
11. A. E. Aleksenskiĭ, M. V. Baĭdakova, A. Ya. Vul', and V. I. Siklitskiĭ, Fiz. Tverd. Tela (S.-Peterburg) **41** (4), 740 (1999) [Phys. Solid State **41**, 668 (1999)].
12. É. É. Lin, Khim. Fiz. **12** (3), 299 (1993).
13. V. F. Anisichkin, Khim. Fiz. **12** (5), 605 (1993).
14. É. É. Lin, Khim. Fiz. **18** (11), 91 (1999).
15. É. É. Lin, S. A. Novikov, V. G. Kuropatkin, *et al.*, Fiz. Goreniya Vzryva **31** (5), 136 (1995).
16. D. S. Dolgushin, V. F. Anisichkin, and V. F. Komarov, Fiz. Goreniya Vzryva **35** (3), 143 (1999).
17. É. É. Lin, Khim. Fiz. **16** (12), 113 (1997).
18. I. V. Obreimov, in *Physical Encyclopedia*, Ed. by B. A. Vvedenskiĭ and B. M. Vul (Sov. Éntsiklopediya, Moscow, 1960), p. 41.
19. *Physical Quantities: A Handbook*, Ed. by I. S. Grigor'ev and E. Z. Meĭlikhov (Énergoatomizdat, Moscow, 1991).
20. B. A. Vyskubenko, É. É. Lin, and A. V. Sirenko, Fiz. Goreniya Vzryva **29** (1), 134 (1993).
21. V. I. Skokov, É. É. Lin, V. A. Medvedkin, and S. A. Novikov, Fiz. Goreniya Vzryva **34** (3), 105 (1998).
22. A. N. Malyshev, É. É. Lin, S. A. Novikov, *et al.*, Khim. Fiz. **19** (2), 74 (2000).
23. I. D. Morokhov, V. P. Petinov, L. P. Trusov, and V. F. Petrunin, Usp. Fiz. Nauk **133** (4), 653 (1981) [Sov. Phys. Usp. **24**, 295 (1981)].
24. B. B. Kadomtsev, Usp. Fiz. Nauk **164** (5), 449 (1994) [Phys. Usp. **37**, 425 (1994)].
25. V. P. Dmitriev, *Stochastic Mechanics* (Vysshaya Shkola, Moscow, 1990).
26. Tsyan' Syue-sen', in *Physical Mechanics* (Mir, Moscow, 1965; Peking, 1962), p. 198.
27. M. Vollmer, *Kinetik der Phasenbildung* (T. Steinkopf, Dresden, 1939; Nauka, Moscow, 1986).
28. I. V. Kazakova, V. F. Anisichkin, and G. V. Gadiyak, Khim. Fiz. **13** (3), 35 (1994).
29. T. S. Yakubov, Dokl. Akad. Nauk SSSR **310** (3), 145 (1990).
30. B. A. Vyskubenko, V. V. Danilenko, É. É. Lin, *et al.*, Fiz. Goreniya Vzryva **16** (12), 113 (1992).
31. A. V. Kozenko, in *Physical Encyclopedia*, Ed. by A. M. Prokhorov (Bol'shaya Ross. Éntsiklopediya, Moscow, 1990), Vol. 2, p. 78.

Translated by O. Borovik-Romanova

Physics of the Solid State, Vol. 42, No. 10, 2000, pp. 1952–1957. Translated from Fizika Tverdogo Tela, Vol. 42, No. 10, 2000, pp. 1899–1903.

FULLERENES AND ATOMIC CLUSTERS

Quantum Chemistry of Hydrogenation and Methylation of a Fullerene Molecule C_{60}

S. S. Moliver* and Yu. F. Biryulin**

** Ul'yanovsk State University, ul. L'va Tolstogo 42, Ul'yanovsk, 432700 Russia*

*** Ioffe Physicotechnical Institute, Politekhnicheskaya ul. 26, St. Petersburg, 194021 Russia*

e-mail: biryulin@nano.ioffe.rssi.ru

Received December 30, 1999; in final form, March 23, 2000

Abstract—The electronic structure of a fullerene molecule C_{60} is calculated in the case of its hydrogenation and methylation with a varying number (from 1 to 12) of the covalent bonds being formed. The results of quantum-chemical analysis are compared with the optical experimental data on films of synthesized fullerene-containing starlike polystyrenes with a varying number of polymer chains covalently bound with fullerene. The dependences of the optical spectra of hydrogenated and methylated fullerenes on the isomeric composition are studied by the ΔSCF method, taking polarization into account. The energies of formation of isomers are calculated and used for depicting the optical spectra of a real isomer mixture formed upon chemical synthesis. Isomers with highest symmetry have the lowest energy, and their binding energies differ insignificantly if the saturated bonds are arranged as uniformly as possible over the fullerene surface. The type of arrangement of saturated bonds is reflected in the polarization dependences. According to the experimental results, the energy of optical transitions in the series of isomers with the highest binding energy increases with the number of saturated fullerene bonds. *© 2000 MAIK "Nauka/Interperiodica".*

The discovery of fullerenes in 1985, the third allotropic modification of carbon [1], subsequent development of the method of preparing these materials in macroscopic quantities [2], and intensive studies of their chemical and physicochemical properties [3] have demonstrated the potentialities of C_{60} in creating a wide range of new fullerene-containing compounds [3–6]. The article by Kroto *et al.* [1] also aroused the interest of theoretical physicists in the problems of fullerenes, which led to publications in which various approximations of the methods of quantum chemistry were used to study the electronic structure of I_h–C_{60} and its isomers, anions, cations, etc. Calculations were carried out by semiempirical and *ab initio* methods [4], thus making it possible to estimate the variations in the energy structure of molecular orbitals (MO) of fullerene under the action of different-type chemical bonds.

In this communication, we present the results of analysis of the hydrogenation and methylation of a fullerene molecule for a varying number (from 1 to 12) of the covalent bonds being formed. Earlier, Ballenweg [7] obtained dihydrofullerene $C_{60}H_2$ by selective hydrogenation of C_{60} with zirconium, followed by hydrolysis. Theoretical estimation of all possible isomers of $C_{60}H_2$ showed that many of them are stable [8]. We chose the methylation reaction for C_{60} as an analog of the chemical synthesis of the fullerene-containing starlike polystyrenes [9, 10] under the assumption that the main influence on MOs and their energies is exerted by the nearest neighbor atoms of fullerene (or the nearest monomer link in the polymer chain).

The results of quantum-chemical computations carried out by us are compared with the experimental data obtained from optical studies of the synthesized fullerene-containing starlike polystyrenes with a varying number of polymer chains covalently bound with C_{60} [11]. A distinguishing feature of our investigations is that we have simulated not only molecules, but also molecular crystals, including doped crystals. The dependences of the optical spectra of hydrogenated and methylated fullerenes on the isomer composition are studied, taking polarization into account. When considering the energies of isomer formation, it is, in principle, possible to present the shape of the optical spectra of a real isomer mixture formed upon the chemical synthesis.

1. COMPUTATIONAL TECHNIQUE

We used a semiempirical quantum-chemical (INDO) program, which can be applied to closed (RHF) and open (ROHF) electron shells of molecules and crystals [12, 13]. The choice of parametrization was dictated by the available computational potential and the experience gained from computations of systems formed by Si and C atoms.

The Slater valence atomic orbitals of carbon were optimized from the properties (such as lattice constant, binding energy, bulk modulus, and valence band structure) of the diamond crystal, cubic silicon carbide, and

graphite. The optimization technique and the physical meaning of the parameters were described earlier [13]. The parameters have since been slightly refined and used to carry out a large number of computations of defects and surfaces with dangling bonds in systems composed of silicon and carbon atoms.

The energies of electron transitions were calculated in the non-self-consistent approximation known in quantum chemistry as ΔSCF [14], when the required state is constructed as a superposition of determinants formed by one-electron excitations of the self-consistent ground state. The molecular orbitals for the determinants of the excited states were specified in conformity with the selection rules for the isomer symmetry group in order to attain the highest degree of precision by eliminating from the Hamiltonian all matrix elements that are identically equal to zero, and to classify the excitation energy levels according to irreducible representations (for example, to determine the type of optical transition and its polarization). The computational limitations restricted the number of determinants used in computations to 600, which was found to be sufficient upon verifying the convergence by decreasing the number of determinants.

2. THE C_{60} MOLECULE AND SINGLY CHARGED IONS

The method used for specifying the coordinates of atoms ensures a high degree of accuracy: all the atoms are arranged on a sphere whose radius is calculated from two preset values r_5 and r_6 of the atomic spacing. The directions from the center to the atoms are also calculated so that the molecule has all the symmetry elements of the icosahedral point group I_h (Fig. 1a). Consequently, the orbital energies and MOs are obtained with correct degeneracy. The ground state C_{60}^0 does not have an open shell. The highest occupied MO (HOMO) h_u is fivefold degenerate, and the lowest unfilled MO (LUMO) t_{1u} is triply degenerate (its irreducible representation is used for transforming the vectors).

The minimum value of the total energy was used to determine two parameters for the size of the fullerene molecule, viz., the length r_5 of the bonds between the atoms forming 12 regular pentagons, and the length r_6 of the remaining bonds. The results agree well with the experimental data (given in parentheses with reference to the review from which they are taken):

$$r_5 = 2.945 \text{ au} = 1.56 \text{ Å } (1.44 \pm 0.01 \text{ Å } [15]),$$

$$r_6 = 2.845 \text{ au} = 1.51 \text{ Å } (1.39 \pm 0.01 \text{ Å } [15]).$$

The binding energy of the fullerene molecule was found to be equal to 5.6 eV/atom (7.0 [16] and 7.4 [17]). Note that the binding energies for other modifications of carbon for the same atomic orbitals were calculated by us earlier [13]: 7.4 eV/atom for diamond and 7.8 eV/atom for graphite. The error in determining the binding energy is inherent in the computations for molecules, because the parameters of atomic orbitals were fitted to reproduce the properties of the crystals [13], when the radius of summation of the exchange integrals should be confined to half the lattice constant of the quasi-molecular large unit cell (no such restrictions exist for molecules). However, this error does not affect the other results. In addition, one encounters a molecular face-centered cubic (fcc) fullerene crystal much more frequently in experiments. Its insignificant crystal field of symmetry T_h makes it possible to correctly take the exchange interaction into consideration for the chosen parametrization of atomic orbitals of carbon.

The intramolecular bond lengths obtained conform with the fullerene radius 7.209 au = 3.81 Å (3.55 [4, 16] and 3.42 Å [17]). A variation in this radius for a constant ratio of the bond lengths led to a value of about 500 cm^{-1} for the frequency of the totally symmetric vibrations (breathing mode), which agrees with the experimental data [4, 15].

The ΔSCF method was used to determine the energy of the dipole-allowed unpolarized optical transition, which was found to be 2.764 eV (this transition is associated with optical absorption at about 3 eV [15]). The main contribution to the transition comes from excitations of the type $h \longrightarrow t$; i.e., HOMO and adjoining fivefold degenerate MOs to triplet MOs, including LUMO. On the whole, the ΔSCF method gives the following picture of low-energy singlet electron excitations:

$$^1A_g \longrightarrow \begin{cases} {}^1T_{2g} = 2.220 \text{ eV} \\ {}^1T_{1g} = 2.714 \text{ eV} \\ {}^1T_{1u} = 2.764 \text{ eV}^* \\ {}^1G_g = 2.820 \text{ eV} \\ {}^1T_{2u} = 2.838 \text{ eV} \\ {}^1G_u = 2.969 \text{ eV}. \end{cases}$$

The asterisk marks the dipole-allowed unpolarized optical transition. It should be emphasized that these energies of intramolecular electron transitions correspond to measurements in the gaseous phase, even though they are close to the values for molecular crystals of fullerene or its solutions. The above-mentioned accuracy (a few meV) is required for comparing the excitation energies, but a rounding off is necessary for comparing the computed energy of an excitation with its experimental value. The experimental values for excitations to even states (g) are in the range of 2 eV [18].

Singly charged ions have open shells: a positive ion $(h_u)^9$ and a negative ion $(t_{1u})^1$. Their electronic structure is calculated by the restricted open shell Hartree–Fock method (ROHF) [12]. A comparison of their total ener-

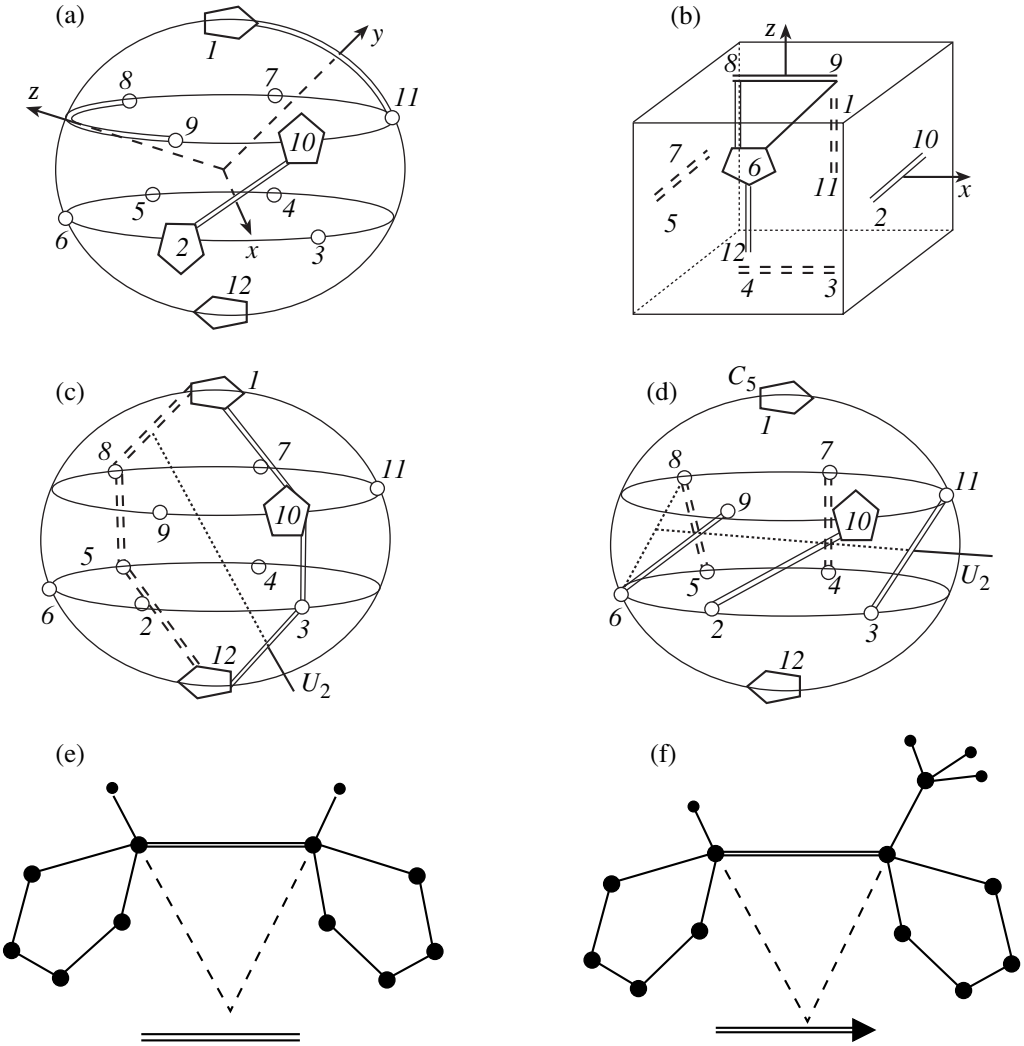

Fig. 1. (a) Structure of fullerene C_{60}. The atoms are grouped into twelve regular pentagons with side r_5, which are formed by a section of the icosahedron vertices. For clarity of vision, only a few pentagons are shown, and their relative size is reduced in comparison with their actual size. (b) The cubic aspect. The bold double bonds (cube) comprise the subgroup T_h. (c) The trigonal aspect. The bold double bonds (equator) encircle one of the threefold axes passing through the centers of the triangles (*2*–*6*–*9*) and (*4*–*7*–*11*). Dihedral axes of the U_2 type are preserved. (d) The pentagonal aspect. The bold double bonds (tropic) encircle one of the fivefold axes. Dihedral axes of the U_2 type are preserved. (e) Hydrogenation of a double bond. The carbon atoms are shown by larger dark circles than the hydrogen atoms. The conditional notation (below) is used for showing isomers formed as a result of *n*-fold hydrogenation: it replaces *n* double bonds on the fullerene diagram. (f) Methylation of a double bond. The conditional notation (below) is used for showing isomers formed as a result of *n*-fold methylation: it replaces *n* double bonds on the fullerene diagram. The arrow marks one of the two possible versions of bond saturation.

gies with the energy of a neutral molecule gives the ionization potential *IP* = 7.0 eV (7.61 [16] and 7.58 eV [17]) and the electron affinity *EA* = –0.01 eV (2.6–2.8 [4] and 2.65 eV [16, 17]). Agreement with the experiment is attained by the model described below for an fcc crystal with weak bonding between fullerene molecules. The negative charge of each electron introduced by the C_{60}^- ion was balanced by the positive correction of *e*/60 to the charge of each nucleus, so that the model is electrically neutral. The electron affinizy *EA* = +3.5 eV calculated by the ROHF technique agrees better with the experimental result.

3. THE PRIMITIVE FCC C_{60} CRYSTAL

The quasi-molecular large-unit-cell (LUC) method was used for carrying out computations for an fcc crystal with a single C_{60} molecule in the crystal basis. According to Fig. 1b, if the translation vectors are directed from the center of the cube to the midpoints of its edges, the model has an fcc Bravais lattice and the

highest possible crystal symmetry class T_h. The crystal class lowers to C_{3h} if all fullerenes in the crystal are turned identically around the [111] axis relative to the Bravais lattice. Naturally, such a rotation for a fixed value of the lattice constant changes the binding energy of the crystal (without regard for the kinetic energy of the nuclei), which was actually calculated in this work. In a natural fcc crystal, the thermal rotation of fullerene molecules (at a temperature above 262.1 K [19]) is not synchronized, and it is this random thermal movement that prevents the formation of strong covalent bonds. The covalent bonds are formed upon a decrease in temperature, but the unit cell contains several fullerene molecules. This makes it impossible for us to simulate the process, due to a lack of computational facilities. The synchronous rotation of all fullerene molecules in the crystal, which was simulated in this work, only partially reflects the effect of random thermal rotation which prevents molecules of the crystal from polymerizing at temperatures higher than the critical value.

Preliminary calculations show that the binding energy minimum of the crystal for rotation angles causing the greatest increase in the binding energy is obtained for an fcc lattice constant of about 15.4 Å (the experimental value is 14.2 Å). The binding energy of the fullerene molecule in an fcc crystal is found to be just 0.3 eV/C_{60}. Using the ΔSCF method, we obtained the following values for the singlet electron excitation (transition) energies in an fcc crystal (several of the lowest levels of the representation are indicated for the cases when they are lower than the lowest levels of other representations):

$$
{}^1A_g \longrightarrow \begin{cases}
{}^1T_g = 1.196, 3.351 \text{ eV} \\
{}^1T_u = 2.175, 3.288 \text{ eV}^* \\
{}^1A_u = 2.464, 3.610 \text{ eV} \\
{}^1A_g = 3.413, 3.433, 3.571 \text{ eV} \\
{}^1E_g = 3.632 \text{ eV} \\
{}^1E_u = 3.689 \text{ eV}.
\end{cases}
$$

The asterisk marks the dipole-allowed unpolarized optical transitions. Forward and backward photoemission spectroscopy of the crystal gives 2.3 ± 0.1 eV for the band gap, while Auger spectroscopy gives 1.6 ± 0.2 eV for the effective energy of Coulomb repulsion [20]. These experimental data agree completely with the theoretical values of the excitation energy, with allowance made for the error in the model used here with a single fullerene in the primitive unit cell, which only gives a state with zero wave vector. It is also confirmed that the energy of the allowed optical transition in the crystal is less than that in the gaseous phase.

Table 1. Properties of isomers of hydrogenated fullerene $C_{60}(HH)_n$

n	Symmetry	Arrangement	Q^1 (eV)	ΔE_π (eV)	ΔE_σ (eV)
2	D_{2h}	Cube	0.43		
3	D_3	Equator	0.40	2.460	2.637
	C_3	Cube	0.41	2.669	2.508
4	D_{2h}	"	0.39		
5		Cube-1	0.37		
	D_5	Tropic	–1.42		
6	T_h	Cube	0.36	2.804 (unpolarized)	
	D_{3d}	Equator	0.25	2.816	3.004

[1] Thermal effect per hydrogenated bond.

Table 2. Properties of isomers of methylated fullerene $C_{60}(CH_3H)_n$

n	Symmetry	Arrangement	Q^1 (eV)	ΔE_π (eV)	ΔE_σ (eV)
3	C_3	Cube I	2.174	2.605	2.502
		Equator	2.168	2.424	2.655
		Cube II	2.149	2.578	2.500
5		Cube-1	2.088		
	C_5	Tropic	2.039		
6	S_6	Cube	2.049	2.850	2.451
	C_3	"	2.044	2.900	2.609
	C_3	Equator	2.037	2.756	2.731
	S_6	"	1.936	2.640	2.661

[1] Thermal effect per methylated bond.

4. FULLERENE WITH HYDROGENATED AND METHYLATED BONDS

Simulation of the saturation of the double bond r_6 (Figs. 1e, 1f) was based on the following two premises:

(1) the saturated bonds are distributed as uniformly as possible over the fullerene surface;

(2) isomers with the highest symmetry have the lowest energy.

Two hydrogen atoms, which saturated the double bond in the fullerene molecule upon hydrogenation, were situated on the radius from the carbon atom (Fig. 1e) at a distance of 2.13 au (2.06 au according to the experimental data). This corresponds to the equilibrium of the methane molecule model using the parametrization of the atomic orbitals. The thermal effect of hydrogenation of one bond of the fullerene molecule is found to be equal to

$$C_{60} + H_2 \longrightarrow C_{60}HH + 0.44 \text{ eV}.$$

Subsequent hydrogenation occurs with a decrease in the thermal effect.

Hydrogen atoms of the methyl group are situated at a distance of 2.13 au from the carbon atoms, as in the computations for the case of hydrogenation. Methyl-group carbon was situated 2.85 au away from fullerene (Fig. 1f). The thermal effect of methylation of one bond of the fullerene molecule is found to be equal to

$$C_{60} + CH_4 \longrightarrow C_{60}(CH_3H) + 2.239 \text{ eV}.$$

Subsequent methylation is accompanied by a decrease in the thermal effect.

The binding energies compiled in Tables 1 and 2 confirm the premises (1) and (2) (the highest thermal effect corresponds to the lowest binding energy). Saturated bonds were arranged in two patterns, viz., "cube" and "equator." These arrangements are illustrated in Figs. 1b and 1c for n = 6: each double bond in these figures should be replaced by the segment (H–r_6–H) or the arrow (CH_3–r_6–H). Arrangements of the type cube-1 indicate saturation of five out of six bonds shown in Fig. 1b. Although this arrangement has a low symmetry, the saturated bonds correspond to the lowest density, which is realized, according to the computational data, in the most stable isomers for $n = 5$. As regards the "equator" arrangement, it has a high-symmetry alternative "tropic" (Fig. 1d) for $n = 5$, where the saturated bonds also encircle fullerene.

For $n = 3$, two "cubic" methylated isomers (called cube I and cube II) have the same symmetry, but the lower binding energy corresponds to the isomer cube II, in which the methyl groups have the largest separation (e.g., are situated above the carbon atoms of pentagons *2*, *8*, and *11* in Fig. 1b).

Summarizing the computational results, it can be assumed that, since the binding energies of high-symmetry isomers do not differ significantly, all isomers with relevant thermodynamic weights are present at the end of the chemical synthesis of fullerene-containing starlike organic molecules [9, 10]. This raises questions about identifying them by optical methods, which may be answered by using the ΔSCF method for the energies ΔE of allowed optical electron transitions (the values shown in Tables 1 and 2 do not claim to be precise absolute values and should be treated as dependences in the series of isomers with close electronic structure).

All of the transition energies correspond to excitations of the system of electrons belonging to the π shell of fullerene (HOMO), which is as if "clamped" in the regions where its double bonds are saturated. The type of arrangement of saturated bonds is reflected in the polarization dependences. The π-polarized transitions have a higher energy than the σ-polarized transitions in the "cube" arrangements, while the situation is reversed in the "equator" arrangements. The only exception is the isomer $n = 6$ with the symmetry C_3, in which methyl groups combine in pairs, i.e., one half of the pentagons in the equator is found to be doubly methylated, while the other half is doubly hydrogenated. In this case, the energy ΔE_π of the π-polarized transition is only slightly higher than the energy ΔE_σ of the σ-polarized transition.

Finally, it should be noted that, in accordance with the experimental results [11], the energy of optical transitions in a series of isomers with the highest binding energy increases with the number n of saturated fullerene bonds. However, in comparing the energies of optical transitions with the theoretical values (2.764 eV for an isolated C_{60} molecule and 2.175 eV for a molecular fcc crystal), as well as with the experimental values for a solution, it should be kept in mind that the solvent molecules probably exert a stronger influence on the highest occupied molecular orbitals of pure fullerene (HOMO) as compared to fullerene with starlike adjoint polymer molecules.

The most unusual among all the isomers for which computations were made is probably the one with five hydrogenated bonds that encircle a fullerene molecule (Fig. 1d). According to the results of our computations, the reaction of its synthesis is endothermic, and three states have close energies (±0.15 eV): one with a closed shell and two others with an open shell e^2, viz., the spin-triplet state $^3A_2$ and the spinless state ^1E which is subjected to the Jahn–Teller effect.

ACKNOWLEDGMENTS

This work was supported by the Russian Interdepartmental Scientific Research Program "Fullerenes and Atomic Clusters" (project no. 98076 "Polymer-2") and the Russian Foundation for Basic Research (project no. 98-02-03327).

REFERENCES

1. H. W. Kroto, J. R. Heath, S. C. O'Brien, *et al.*, Nature **318**, 162 (1985).
2. W. Kraetschmer, L. D. Lamb, K. Fostiropoulos, and D. R. Huffman, Nature **347**, 354 (1990).
3. M. E. Vol'pin, Vestn. Ross. Akad. Nauk **10**, 25 (1993).
4. V. I. Sokolov and I. V. Stankevich, Usp. Khim. **62** (5), 455 (1993).
5. W. Weltner and R. J. van Zee, Chem. Rev. **89**, 1713 (1991).
6. H. W. Kroto, A. W. Allaf, and S. P. Balm, Chem. Rev. **91**, 1213 (1991).
7. S. Ballenweg, ThD Univ. Heidelberg (1992).
8. N. Matsuzawa, D. A. Dixon, and T. Fukunaga, J. Phys. Chem. **96**, 7594 (1992).
9. V. N. Zgonnik, E. Yu. Melenevskaya, L. S. Litvinova, *et al.*, Vysokomol. Soedin., Ser. A **38**, 203 (1996).
10. V. N. Zgonnik, in *Proceedings of the 3rd International Workshop "Fullerenes and Atomic Clusters IWFAC'97," St. Petersburg, 1997.*

11. A. N. Aleshin, Yu. F. Biryulin, N. B. Mironkov, *et al.*, Fullerene Sci. Technol. **6** (3), 545 (1998).
12. S. S. Moliver, Fiz. Tverd. Tela (S.-Peterburg) **41** (3), 404 (1999) [Phys. Solid State **41**, 362 (1999)].
13. S. S. Moliver, Fiz. Tverd. Tela (S.-Peterburg) **38** (7), 2029 (1996) [Phys. Solid State **38**, 1119 (1996)].
14. R. McWeeny, *Methods of Molecular Quantum Mechanics* (Academic, London, 1989).
15. V. P. Belousov, I. M. Belousova, V. P. Budtov, *et al.*, Opt. Zh. **64** (12), 3 (1997).
16. A. F. Hebard, Annu. Rev. Mater. Sci. **23**, 159 (1993).
17. C. Monteca-Diego and E. Moran, An. Quim. **90**, 143 (1994).
18. K. Hansen, R. Müller, P. Brockhaus, *et al.*, Z. Phys. D **42**, 153 (1997).
19. Y. Miyazaki, M. Sorai, R. Lin, *et al.*, Chem. Phys. Lett. **305**, 293 (1999).
20. R. W. Lof, M. A. van Veenendaal, B. Koopmans, *et al.*, Phys. Rev. Lett. *68* (26), 3924 (1992).

Translated by N. Wadhwa

Physics of the Solid State, Vol. 42, No. 10, 2000, pp. 1958–1965. Translated from Fizika Tverdogo Tela, Vol. 42, No. 10, 2000, pp. 1904–1910.

FULLERENES AND ATOMIC CLUSTERS

Physical Properties and Elemental Composition of Starlike Fullerene-Containing Polystyrene Films

Yu. F. Biryulin*, V. M. Lebedev*, S. N. Mikov****, S. E. Orlov****, D. A. Sykmanov*, L. V. Sharonova*, and V. N. Zgonnik****

** Ioffe Physicotechnical Institute, Russian Academy of Sciences, Politekhnicheskaya ul. 26, St. Petersburg, 194021 Russia*
*** Institute of Macromolecular Compounds, Russian Academy of Sciences, Bol'shoi proezd 31, St. Petersburg, 199004 Russia*
**** Konstantinov Institute of Nuclear Physics, Russian Academy of Sciences, Gatchina, Leningradskaya oblast, 189350 Russia*
***** Ul'yanovsk State University, ul. L'va Tolstogo 42, Ul'yanovsk, 432700 Russia*
e-mail: biryulin@nano.ioffe.rssi.ru

Received December 30, 1999; in final form, March 27, 2000

Abstract—The elemental composition of starlike fullerene-containing polystyrene films has been determined by the Rutherford backscattering, ion x-ray spectrum analysis, and nuclear reaction method. The physical properties of the films are investigated by ellipsometric, photoluminescence, and dc electrical conductivity techniques. The complex refractive index of the films is equal to $1.7 - i(0.05–0.10)$. It is found that a maximum in the photoluminescence spectrum of the fullerene-containing polystyrene film is shifted toward the high-energy range as compared to that of the C_{60} film. The energy shift is directly proportional to the number N of polymer chains chemically bonded to the fullerene molecule and can be described by the empirical formula ΔE [eV] = $0.04N$. The electrical conductivity of the films increases proportionally with the molar concentration of C_{60}.

1. INTRODUCTION

The discovery of the third allotropic carbon form (other than diamond and graphite), namely, fullerene [1], gave impetus to the development of a new direction in polymer chemistry. Fullerene possesses a number of unique chemical properties [2], which, in particular, made it possible to synthesize starlike polymers whose structural element represents a macromolecule with a core in the form of a C_{60} molecule [3]. For example, the interaction of C_{60} with poly(styryl lithium) brought about the formation of starlike fullerene-containing polystyrene in which the number of polymer chains attached to the C_{60} molecule can reach six. The physical properties of these fullerene-containing polymers are still not clearly understood [4–7]. In the present work, we studied the elemental composition and background impurities of fullerene-containing polystyrene films and their physical properties by ellipsometric, photoluminescence, and dc electrical conductivity techniques.

Fullerene-containing polystyrenes (FPS) were synthesized according to the procedure described in [8]. The preparation of such polymers in the form of films was reported in [4]. These films are characterized by good adhesion with silicon, gallium arsenide, and glass, which were used as substrates. After a lapse of one year, the polymer films 100–200 nm thick did not peel from the given substrates and withstood repeated temperature changes from 300 to 77 K. The molecular and structural characteristics of fullerene-containing polystyrene films are listed in Table 1.

Since uncontrollable background impurities remaining in starlike polymers after the synthesis could considerably affect their physical properties, we investigated the elemental composition of the films by nuclear physical techniques such as Rutherford backscattering, ion x-ray spectrum analysis, and nuclear reaction method. The experiments were performed on an analytical complex for material research on the basis of an ÉSU-2 electrostatic accelerator at the Konstanti-

Table 1. Molecular structure and composition of fullerene-containing polystyrene films

Sample no.	Number of attached polymer chains	Molecular mass of chain	C_{60} concentration, mol %
1	1–2 PS	7000	0.7
2	1–2 PS*	7000	0.7
3	4 PS	2000	7
4	4 PS**	2000	7
5	6 PS	5000	0.5

Note: PS—polystyrene. * Fullerene-containing polystyrene molecules are linked via the $–Si(CH_3)_2–$ group. ** Fullerene-containing polystyrene molecules are linked via the $–CH_2–C_6H_4–CH_2–$ group.

nov Institute of Nuclear Physics, Russian Academy of Sciences (Gatchina) [9, 10].

The complex refractive indices of polymer films and their thicknesses were determined by ellipsometry with the use of a LÉF-3M ellipsometer and a He–Ne laser (wavelength, 632.8 nm) as a light source.

Photoluminescence of fullerene-containing polystyrene films was examined using an MDR-2 diffraction monochromator at temperatures of 300 and 77 K. The excitation was achieved with an argon laser at a wavelength of 488 nm.

The dc electrical conductivity was measured on a V7É-42 electrometer. The films were deposited onto the glass. Contacts were applied with the use of a silver contact agent.

2. ELEMENTAL COMPOSITION OF FULLERENE-CONTAINING POLYSTYRENE FILMS

The quantitative nuclear and physical investigations into the elemental composition were performed with fullerene-containing polystyrene films prepared on oxygen-containing (glass) and oxygen-free (gallium arsenide and silicon) substrates. In the latter case, the oxygen content determined in the films was also contributed by natural oxide formed at the surface of gallium arsenide and silicon wafers. The results of measurements are presented in Table 2. The experimental spectra obtained for one of samples (sample 4 in Table 1) by different methods to characterize the film composition are shown in Figs. 1–4.

The content of heavy elements (bromine and chlorine) with respect to carbon was determined by the Rutherford proton backscattering (E_p = 1 MeV) using the "step technique" [11]. Since the step height in the measured spectrum is proportional to the scattering cross-section and the number of atoms of a particular type in a film sample, the elemental composition can be determined from the measured ratio of step heights and the known Rutherford scattering cross-sections (194, 510, and 2160 mb/sr for C, Cl, and Br, respectively [12]). The number of carbon atoms per cubic centimeter was evaluated from the data on the composition of the studied films (Table 1).

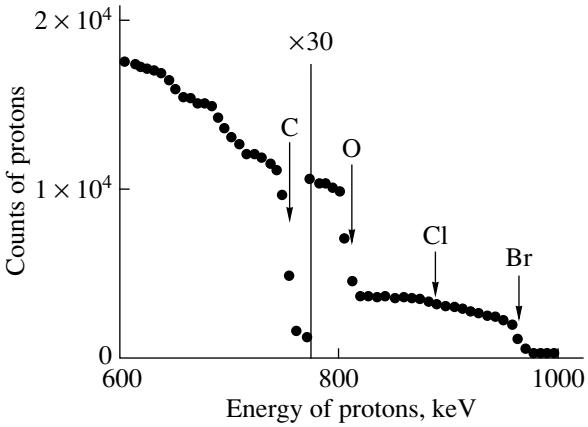

Fig. 1. Spectrum of protons (E_p = 1 MeV) scattered at angle θ = 135° from a fullerene-containing polystyrene film on the glass substrate (sample 4 in Tables 1, 2). Arrows indicate the maximum energies of protons scattered by elements involved in the film composition.

It should be noted that the mass resolution of this technique is insufficient for the identification of elements with atomic numbers more than 20 (Fig. 1). For this reason, the bromine content was determined using the characteristic x-ray radiation excited by protons (Fig. 2). In order to absorb soft quanta from the substrate, a Si(Li) detector was covered by a carbon absorber 80 mg/cm^2 thick.

The sensitivity of the Rutherford backscattering technique in the determination of bromine and chlorine

Table 2. Elemental composition of fullerene-containing polystyrene films

Sample no.	Film	Substrate	Element content in film, 10^{19} cm^{-3}			
			Br	Li	O	Cl
1	FPS	Glass	–	14	*	9.5
2	FPS	″	–	12	*	9.0
3	FPS	″	–	16	*	9.6
4	FPS	″	3.9	11	*	11
6	FPS 7×10^3	Si	–	9	180	<3
7	FPS 7×10^3	GaAs	–	8	240	<3
8	PS 4×10^3	Si	–	7	100	8.6
9	PS 100×10^3	Si	–	7	120	5.8
10	$C_{60} + C_{70}$	Si	–	–	410	–

Note: Molecular mass is given for films 6–9. Fullerene mixture $C_{60} + C_{70}$ was applied to the silicon substrate by the sublimation technique.
*Oxygen content was not determined. Numbering of samples 1–4 matches that in Table 1.

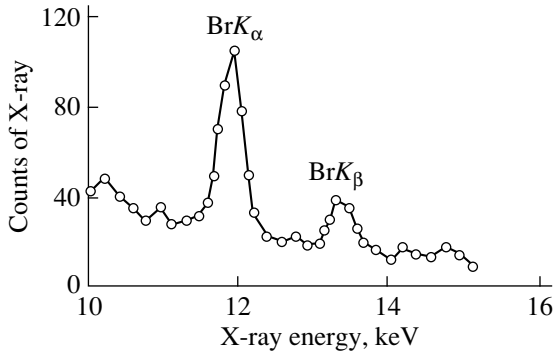

Fig. 2. X-ray fluorescence spectrum of the fullerene-containing polystyrene film on the glass substrate (sample 4 in Tables 1, 2). Proton energy E_p = 1 MeV.

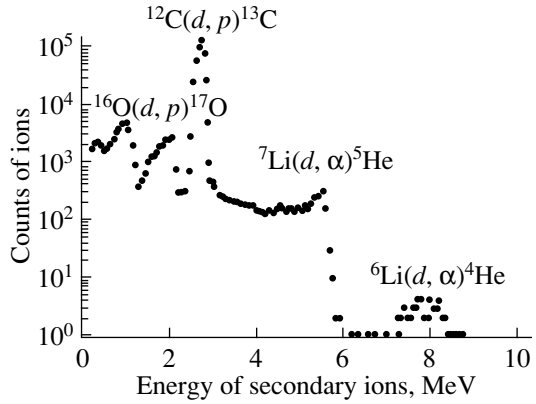

Fig. 3. Spectra of protons and α-particles formed by the (d, p) and (d, α) nuclear reactions under irradiation of fullerene-containing polystyrene film (sample 4 in Tables 1, 2) by deuterons with energy E_d = 1 MeV.

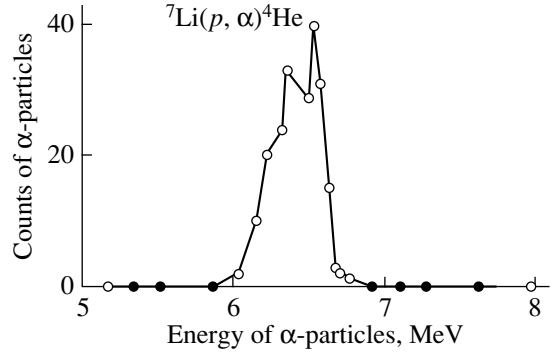

Fig. 4. Spectrum of the α-particles formed by the ^{7}Li(p, α)^{4}He nuclear reaction under bombardment of fullerene-containing polystyrene film (sample 4 in Tables 1, 2) by protons with energy E_p = 670 keV.

is equal to ~10^{-4} and ~5×10^{-4}, respectively. The absolute error is less than 5%.

Bromine at a level of $(3.9 \pm 0.3) \times 10^{19}$ at/cm^3 was found only in sample 4 (fullerene with four polystyrene chains and a molecular mass of 2000). Only in this case, LiBr was formed during the synthesis. No bromine was found in the other samples. An uncontrollable background chlorine impurity at a level of 10^{18}–10^{19} at/cm^3 could appear upon preparation and chemical treatment of substrates for the formation of fullerene-containing polystyrene films.

The content of light elements (lithium, carbon, and oxygen on oxygen-free substrates) was determined by the nuclear reaction method: (a) lithium from the reactions ^{7}Li(p, α)^{4}He for ^{7}Li at E_p = 670 keV (σ = 0.4 mb) and ^{6}Li(d, α)^{4}He for ^{6}Li at E_d = 1.0 MeV (σ = 4.5 mb), where E_d is the energy of accelerated deuterons; (b) carbon from the reaction ^{12}C(d, p)^{13}C at E_d = 1.0 MeV (σ = 30 mb); and (c) oxygen from the reaction ^{16}O(d, p_1)^{17}O at E_d = 0.9 MeV (σ = 4.5 mb).

The experimental spectra of sample 4 are displayed in Figs. 3 and 4. The α-particles were recorded with a surface barrier detector mounted at the angle θ = 135°. In order to prevent overload, the detector was covered by an aluminum absorber 11 μm thick, which passed α-particles and protons formed by nuclear reactions, but blocked the passage of elastically scattered ions of the beam.

By measuring the yield Y of reaction products and the number I_0 of ions impinged onto a target, the content n_a (atoms/cm^2) of atoms of a particular type in the sample can be determined from the known reaction cross-section σ and angular size Ω of the detector, that is,

$$n_a = Y/(I_0 \sigma \Omega k),$$

where k is the content of the measured isotope in a natural mixture.

For the ^{7}Li isotope, the sensitivity of the technique for determining lithium ranges up to 10^{-6}, and the error in determination is less than 10%, because, in this case, there are no other side nuclear reactions [12]. Lithium at a content of ~10^{20} at/cm^3 was observed in all the samples. This means that lithium is not completely removed from the solution of the prepared starlike fullerene-containing polystyrene after its synthesis from poly(styryl lithium) and fullerene solutions and partly remains (for example, in the form of LiOH and Li_2CO_3) in the starlike fullerene-containing polystyrene synthesized.

A comparison of the experimental data (Table 1) and the estimates made for the lithium content in the samples demonstrates that no less than 50% of lithium (in the form of salts) is retained in polymer samples as in a matrix (for the given technique of synthesizing the polymer).

For comparison, we investigated films of poly(styryl lithium) with different molecular masses (MM). Approximately the same amounts of lithium and chlorine were observed in these films. At the same time, it

is quite reasonable that only oxygen was found in a $C_{60} + C_{70}$ fullerene mixture deposited onto the silicon substrate by sublimation.

Therefore, it can be concluded that elements (lithium, bromine, oxygen, and chlorine) involved in the synthesis of starlike fullerene-containing polystyrene are partly retained in the prepared compound and can substantially affect its physical properties. It should be noted that the found oxygen can be contained in the deposited film and also in the surface layer of natural oxide that originally occurs on the substrate. The hydrogen content in the materials was not determined but was included in calculations from the data on the molecular structure of polymers (Table 1).

3. ELLIPSOMETRY

The ellipsometric investigations of starlike fullerene-containing polystyrene films allowed us to evaluate the film thicknesses and to determine the complex refractive index $\bar{N} = n - ik$ (where n is the refractive index, and k is the extinction coefficient).

The interaction between the initially polarized incident radiation and a sample induces additional polarization of reflected electromagnetic radiation. The parameters of such polarization are determined in the ellipsometric technique by measuring two ellipsometric angles ψ and Δ (see, for example, [13]). These angles and the complex reflectivities R_p and R_s for the light wave electric field vectors parallel and perpendicular to the incidence plane are related by the basic ellipsometric relationship $\rho \equiv R_p/R_s = \tan\Psi \exp i\Delta$. The experimental angles ψ and Δ contain integral information on the thicknesses and optical characteristics of all the surface layers that interact with radiation. The characteristics of the sample are determined from the ψ and Δ angles by computer simulation.

The complex refractive index for solid-state fullerene (one of the components of the studied samples) $\bar{N}_F = 2.13 - i0.05$ is known from [14]. As regards the refractive indices of the other components (polymer materials), our attempts to find the sufficiently reliable data in the literature failed. Hence, we studied pure (free from fullerene) polystyrene with molecular masses of 100 000 and 4000 on the Si, GaAs, and glass substrates. The complex refractive indices of the materials used for substrates at $\lambda = 632.8$ nm are as follows: $3.882 - i0.02$ for Si, $3.857 - i0.198$ for GaAs [15], and $1.52 - i0.00$ for glass (experimental data). According to the ellipsometric analysis, the semiconductor substrates are more preferable due to a larger optical contrast between the film and the substrate material; however, it is not universally possible to prepare continuous films on these substrates.

Our experimental data for polystyrene samples are shown in Fig. 5 (points on the ψ–Δ plane). A rather large scatter in the experimental points is associated with fluctuations in the thickness of polymer films, each characterized by a pronounced surface relief. For comparison with the experimental data, Fig. 5 also demonstrates the curves calculated within the "homogeneous dielectric film/gallium arsenide or silicon substrate" model for different refractive indices of the film, which reflect changes in the ellipsometric parameters with an increase in the film thickness. Despite a considerable scatter, the comparison of the experimental points and the calculated curves provides a means of evaluating the refractive index of polystyrene: $n = 1.5$–1.6 and 1.9–2.1 for molecular masses of 100 000 and 4000, respectively. As can be seen, the refractive index strongly depends on the molecular mass, which, first, seems to be reasonable, and, second, causes us to treat critically the optical constants presented for polymers in reference books.

Hereafter, the figures for pure and fullerene-containing polymers represent the data for the angle of incidence of the light beam $\varphi = 70°$. As a check, we carried out the measurements at other angles of incidence. These data agree with the results presented in this paper.

The ellipsometric measurements of fullerene-containing polymers were performed with samples in the form of films on glass substrates. In addition to the thickness nonuniformity, these films (unlike pure polymer films) exhibit a nonuniform distribution of fullerene, which leads to a further scatter in the experimental points. This scatter gives no way of characterizing the difference between the optical properties of different samples. Nonetheless, it is possible to reveal the main tendency. A comparison of the experimental results with the data calculated at the refractive index $n = 1.70$ is given in Fig. 6. This value is close to the refractive index for pure polystyrene with the appropriate molecular mass. The calculations with variations in

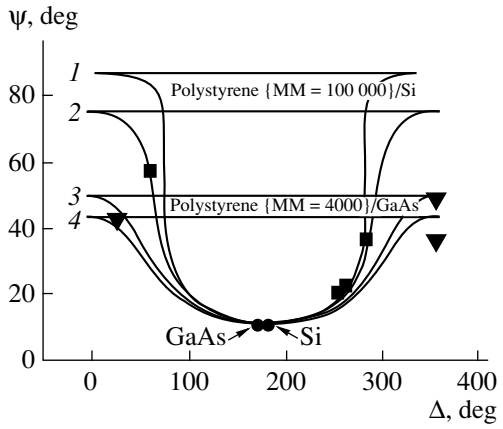

Fig. 5. (*1–4*) Experimental (points) and calculated (solid lines) ellipsometric parameters ψ and Δ for polystyrene films on the semiconductor substrate upon increase in the film thickness. $\varphi = 70°$. Refractive index n: (*1*) 1.5, (*2*) 1.6, (*3*) 1.9, and (*4*) 2.0. Extinction coefficient $k = 0$.

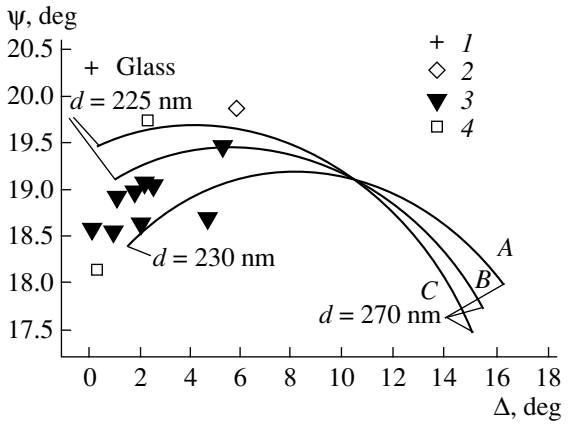

Fig. 6. Ellipsometric parameters for fullerene-containing polystyrene films on glass substrates: (*1*) substrate and (*2–4*) films with numbering matching that of samples in Table 1. φ = 70°. Solid lines *A*, *B*, and *C* refer to films with thickness ranging from 170 to 225 (230) nm and different complex refractive indices $\bar{N}$: (*A*) 1.70 – *i*0.10, (*B*) 1.70 – *i*0.07, and (*C*) 1.70 – *i*0.05.

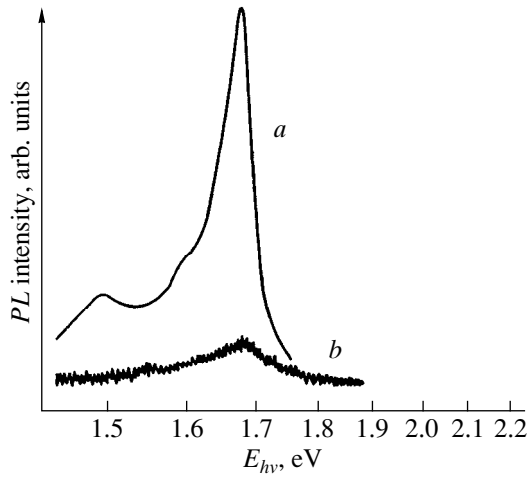

Fig. 7. Photoluminescence spectra of (*a*) C_{60} film on silicon and (*b*) film prepared from a solution of the C_{60}–polystyrene mechanical mixture in toluene. Temperature (K): (*a*) 77 and (*b*) 300.

the fitting parameters *n* and *k* indicate that a better agreement is achieved at nonzero extinction coefficient. It was found that the refractive index *n* is equal to 1.7, and the extinction coefficient *k* falls in the range 0.05–0.10.

4. PHOTOLUMINESCENCE

The experimental data on photoluminescence of starlike fullerene-containing polystyrene films were analyzed in comparison with the results obtained for a reference series of samples: C_{60} thin films and films prepared by dissolution of a mechanical mixture of fullerene and the polymer in toluene followed by evaporation of a solvent. The former (solid-state fullerene) films were deposited by sublimation from a fullerene-containing carbon black prepared according to the procedure described in [16]. In the latter films (mechanical mixtures), unlike starlike polymers, the chemical interaction between components (C_{60} and polystyrene) is absent.

The photoluminescence spectra of the reference samples at $T = 77$ and 300 K are shown in Fig. 7. The photoluminescence spectrum of the C_{60} thin film exhibits a main maximum at a photon energy of 1.69 eV. Two weak side shoulders are observed in the low-energy range (relative to the main peak) at 1.50 and 1.60 eV. Matus *et al.* [17] proved that the emission of an excited C_{60} molecule is described by a self-localized exciton polaron. The incident light with a photon energy higher than the energy of the forbidden transition h_u–t_{1u} excites the C_{60} molecule, thus forming the electron–hole pair. Excited electrons and holes cannot recombine through the energy gap, because the transition from the lowest unoccupied molecular orbital (LUMO) to the highest occupied molecular orbital (HOMO) is dipole-forbidden. The excited electrons and holes produce a local strain in the skeleton of the fullerene structure and, hence, become self-localized below the bottom of the conduction band and above the top of the valence band. The selection rules for this self-localized state are violated, and the radiative recombination becomes possible.

Friedman and Harigaya [18] explained this mechanism of photoluminescence in C_{60} in the framework of the model proposed by Heeger *et al.* [19], as applied to a single C_{60} molecule. The transfer of an electron from the h_u orbital to the t_{1u} orbital leads to the formation of the exciton polaron state and a distortion of the molecular structure, which resides in the fact that the lengths of two different carbon bonds in the equatorial ring of the C_{60} molecule become virtually identical.

Thus, we believe that the main peak at 1.69 eV in the photoluminescence spectrum of C_{60} is attributed to the recombination between the levels of the exciton polaron. Two peaks at 1.50 and 1.60 eV can be assigned to the phonon satellites of the main peak.

The main peak in the photoluminescence spectrum of a thin film consisting of the C_{60}–polystyrene mixture is also observed at 1.69 eV. It is reasonable that the intensity of this peak is weaker than that of the C_{60} film, because the fullerene content in the mixture with polystyrene is equal to at most 0.7 mol %. The absence of the energy shift indicates that fullerene and polystyrene do not interact in the film, as was expected for the mechanical mixture.

The photoluminescence spectra of fullerene-containing polystyrene films with different numbers of polystyrene chains attached to the C_{60} fullerene are depicted in Fig. 8. The maximum in the photoluminescence spectrum is shifted toward the high-energy range. The shift increases with an increase in the number of chains.

The dependence of the energy shift ΔE at a maximum of the photoluminescence spectrum on the number of polystyrene chains attached to the fullerene molecule is demonstrated in Fig. 9. As a first approximation, the energy shift is directly proportional to the number of attached polymer chains and can be described by the empirical formula $\Delta E = 0.04N$, where ΔE is expressed in electron-volts, and N is the number of attached polymer chains. The observed evolution of the photoluminescence spectrum indicates a strong intermolecular interaction.

Let us consider what happens to the C_{60} molecule as the polymer chains are attached. The transformation in the electronic structure of fullerene will be considered in terms of the covalent interaction between the C_{60} molecule and polymer chains. The mechanism for formation of starlike fullerene-containing polystyrene can be schematically represented as follows. Owing to the chemical activity of lithium at the end of a poly(styryl lithium) chain, one of two C=C double bonds in fullerene is broken. The polymer chain covalently adds to one end of the broken bond, and lithium adds to its other end. Upon termination of the reaction by water, lithium is replaced by hydrogen. Thus, upon formation of starlike polystyrene with the fullerene core, each act of the attachment of a polymer chain is accompanied by the formation of two new covalent bonds: the C–C bond with the polystyrene chain and the C–H bond at the other end of the broken double bond of fullerene.

First, we dwell on the least modified molecule C_{60}, namely, C_{60} with one or two attached polymer chains. In the case when the polymer chains are attached to the fullerene molecule, the distortion of its skeleton is similar to the polaron in polyacetylene; i.e., the difference between long and short carbon bonds along the equatorial line of the C_{60} sphere decreases. The structure of the energy levels is also changed. One energy level is split out upward from the HOMO, and the other energy level is split out downward from the LUMO. As a result, we observe the photoluminescence of these split levels.

A more complex reconstruction is observed for a strongly modified system when the C_{60} molecule attaches from four to six polymer chains. The symmetry of the strongly modified C_{60} molecule is considerably lowered. The Fermi level of the π electron subsystem shifts. All these transformations lead to an energy shift at the maximum in the photoluminescence spectrum.

The energy shift at a maximum of the photoluminescence spectrum toward the high-energy range with

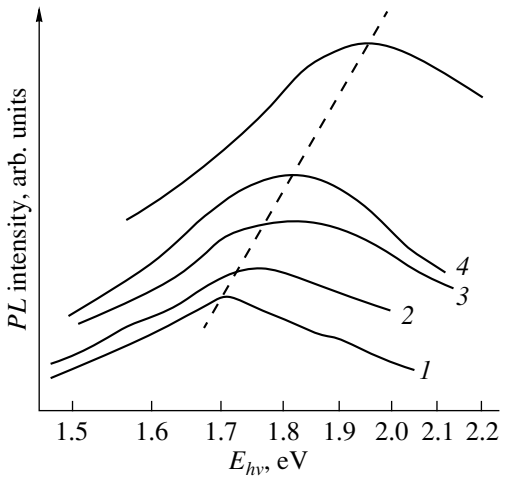

Fig. 8. Photoluminescence spectra of fullerene-containing polystyrene films with different numbers of attached polystyrene chains per single C_{60} molecule at 300 K. Numerals near the curves match the sample numbers in Table 1.

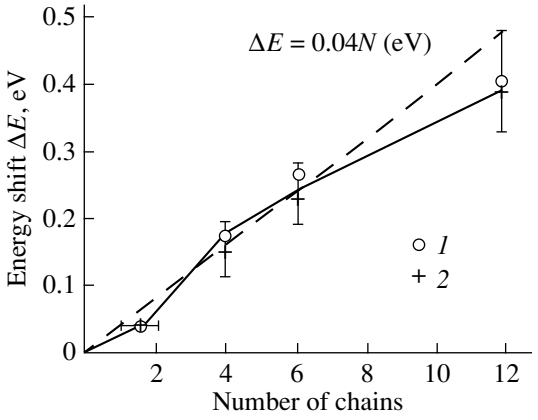

Fig. 9. Dependences of the energy shift at a maximum of the photoluminescence spectrum on the number of polystyrene chains attached to a single C_{60} molecule at temperatures of (*1*) 300 and (*2*) 77 K.

an increase in the number of the C–C chemical covalent bonds between fullerene and other fragments is additionally confirmed by the analysis of the photoluminescence spectra for films of a new chemical compound—the C_{60} fullerene with 12 covalently attached phenyl rings instead of polystyrene chains (Fig. 9). Despite a substantial change (the replacement of polystyrene chains by phenyl rings), the linear dependence of the change in the HOMO–LUMO energy gap on the number of attached fragments is retained. This suggests that the electronic structure of the C_{60} fullerene with different covalently attached groups is primarily affected not by the type of attached fragments (polymer or phenyl ring), but by the type of chemical bonds (in the given

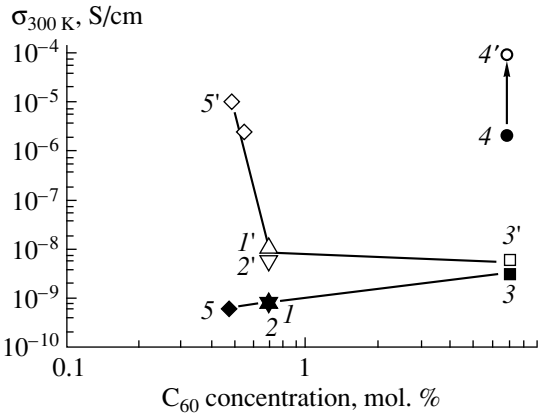

Fig. 10. Dependences of the electrical conductivity on the fullerene concentration in fullerene-containing polystyrene films (*1*–*5*) undoped and (*1*'–*5*') doped with iodine. Film *4* is doped with LiBr upon synthesis. Numerals near the points match the sample numbers in Table 1.

case, these are the C–C covalent bond with the fragment and the C–H bond at the other end of the broken bond in fullerene).

It is clear that the synthesis of fullerene with polymer chains, unlike the mechanical mixture of components, leads to the formation of a starlike compound in which chains are covalently attached to the fullerene molecule. In turn, this results in a shift of the maximum in the photoluminescence spectrum of the C_{60} fullerene toward the high-energy range with an increase in the number of attached polymer chains. To a first approximation, the shift is proportional to the number of the attached polymer chains and does not depend on their molecular mass.

5. ELECTRICAL CONDUCTIVITY

We studied the electrical conductivity of thin fullerene-containing polystyrene films with a fullerene concentration from 0.5 to 7 mol % and different numbers of polymer chains (from 1 to 6). It was found that, in fullerene-containing polystyrene films, an increase in the C_{60} concentration leads to an increase in the electrical conductivity from 6×10^{-10} to 3×10^{-9} Ω^{-1} cm^{-1} (Fig. 10). The conductivity of starlike polystyrene macromolecules (7 mol % C_{60}), which are linked though the $–CH_2–C_6H_4–CH_2$ groups upon synthesis and contain LiBr as an impurity, is considerably higher and reaches 2×10^{-6} Ω^{-1} cm^{-1} (Fig. 10, point *4*). As follows from the investigation of the current–voltage characteristics, the films exhibit a strong nonohmic behavior. It should be noted that the conductivity of fullerene-containing polystyrene films only weakly depends on the number of polymer chains.

In order to reveal the possibility of preparing the fullerene-containing polystyrene films with a lower resistivity and to elucidate the conductivity mechanism, several samples were doped in iodine vapors at room temperature for 24 h. The measurements of the electrical conductivity in fullerene-containing polystyrene films doped with iodine revealed that doping leads to a considerable increase in the conductivity up to 10^{-5} Ω^{-1} cm^{-1} for samples containing 0.5 mol % C_{60} and up to 10^{-8} Ω^{-1} cm^{-1} for samples with 0.7 mol % C_{60}. The conductivity of the samples doped during synthesis also increases up to 10^{-4} Ω^{-1} cm^{-1} after iodine doping (Fig. 10). A substantial increase in the linear portion of the current–voltage characteristics is observed for the fullerene-containing polystyrene samples doped with iodine at all fullerene concentrations. These observations can be explained by a combined effect of fullerene and iodine molecules in polystyrene. We assume that both fullerene and iodine in polystyrene polymers are acceptor impurities. The mechanism of charge carrier transfer can be described within the hopping conductivity model.

The results obtained in this study on the physical properties of fullerene-containing polystyrene films indicate that fullerene forming covalent bonds with polystyrene considerably affects these properties despite its low concentration compared to the polymer. Actually, according to the ellipsometric investigations, the fullerene-containing polystyrene films have a nonzero extinction coefficient. The covalent bonds are responsible for an increase in the HOMO–LUMO energy gap in the system of optical transitions in the C_{60} fullerene. Moreover, the electrical conductivity of fullerene-containing polystyrene films is four or five orders of magnitude higher than that of pure polystyrene and correlates with an increase in the fullerene concentration in the films.

ACKNOWLEDGMENTS

We are grateful to Ya. L. Kogan for supplying the $C_{60}(C_6H_5)_{12}$ film and A. N. Aleshin for measuring the electrical conductivity of fullerene-containing polystyrene films.

This work was supported by the State Scientific and Technical Program "Topical Directions in Physics of Condensed Matter," the Direction "Fullerenes and Atomic Clusters" (project no. 98076 "Polymer-2") and the Russian Foundation for Basic Research (project no. 98-02-03327).

REFERENCES

1. N. W. Kroto, J. R. Heath, S. C. O'Brien, *et al.*, Nature **318**, 162 (1985).
2. M. E. Vol'pin, Vestn. Ross. Akad. Nauk **10**, 25 (1993).
3. N. T. Samulsky, J. M. de Simone, M. O. Hunt, *et al.*, Chem. Mater. **4**, 1153 (1992).
4. A. N. Aleshin, Yu. F. Biryulin, L. V. Vinogradova, *et al.*, Pis'ma Zh. Tekh. Fiz. **21** (23), 64 (1995) [Tech. Phys. Lett. **21**, 979 (1995)].

5. C. E. Bunker, G. T. Lawson, and Ya-Ping Sun, Macromolecules **28**, 3744 (1995).
6. Ch. Wang, B. Pan, Sh. Fu, *et al.*, Macromol. Chem. Phys. **197**, 3783 (1996).
7. J. M. Janot, H. Eddaoudi, P. Seta, *et al.*, Chem. Phys. Lett. **302**, 103 (1999).
8. V. N. Zgonnik, E. Yu. Melenevskaya, L. S. Litvinova, *et al.*, Vysokomol. Soedin., Ser. A **38** (2), 203 (1996).
9. V. M. Lebedev, V. A. Smolin, and B. B. Tokarev, PNPI Research Report 1994–1995 (Gatchina, 1996), p. 292.
10. V. B. Andrienko, A. N. Dyumin, V. M. Kuz'min, and V. M. Lebedev, Preprint No. 872, LIYaF (Institute of Nuclear Physics, Leningrad, 1983).
11. W. K. Chu, J. W. Mayer, and M. A. Nicolet, *Backscattering Spectrometry* (Academic, New York, 1978).
12. *Ion Beam Handbook for Material Analysis*, Ed. by M. A. Mayer and E. Rimini (Academic, New York, 1977).
13. R. M. A. Azzam and N. M. Bashara, *Ellipsometry and Polarized Light* (North-Holland, Amsterdam, 1977; Mir, Moscow, 1981).
14. Yu. F. Biryulin, A. Ya. Vul', I. K. Ionova, *et al.*, Fiz. Tverd. Tela (S.-Peterburg) **37** (10), 3124 (1995) [Phys. Solid State **37**, 1722 (1995)].
15. D. E. Aspnes and A. A. Studna, Phys. Rev. B **27** (2), 985 (1983).
16. W. Kraetschmar, L. D. Lamb, K. Fostiropoulos, and D. R. Huffmann, Nature **347**, 354 (1990).
17. M. Matus, H. Kuzmany, and E. Sohment, Phys. Rev. Lett. **68**, 2822 (1992).
18. B. Friedman and K. Harigaya, Phys. Rev. B **47**, 3975 (1993).
19. A. J. Heeger, S. Kivelson, G. R. Schrieffer, and W. P. Su, Rev. Mod. Phys. **60**, 781 (1988).

Translated by O. Borovik-Romanova

Physics of the Solid State, Vol. 42, No. 10, 2000, pp. 1966–1971. Translated from Fizika Tverdogo Tela, Vol. 42, No. 10, 2000, pp. 1911–1916.

FULLERENES AND ATOMIC CLUSTERS

Electronic Structure Model of a Metal-Filled Carbon Nanotube

N. A. Poklonskiĭ, E. F. Kislyakov, G. G. Fedoruk, and S. A. Vyrko

Belarussian State University, ul. Leningradskaya 14, Minsk, 220050 Belarus

e-mail: Poklonski@phys.bsu.unibel.by

Received October 12, 1999; in final form, April 5, 2000

Abstract—Carbon monolayer nanotubes filled with K, Rb, and Cs atoms, in which every ten carbon atoms captures an electron from the doping atoms, are considered. It is assumed that a positive charge in the bulk of the nanotube and a negative charge on its surface are distributed uniformly so that the potential energy of a conduction electron inside the nanotube is proportional to the square of the distance to its center. The dependences of the Fermi quasi-momentum for conduction electrons inside the nanotube on their volume density and the tube radius are obtained in the one-electron approximation for an arbitrary number of subbands of transverse motion. The Landauer formula is used for calculating the dependence of the conductivity of the metallic subsystem of the nanotube on its radius. © *2000 MAIK "Nauka/Interperiodica".*

The carbon nanotubes discovered by Iijima [1] can serve as convenient model objects for studying low-dimensional structures. Among other things, a carbon nanotube filled with a metal can be used in the future for producing quantum wires. The formation of nanotubes with various diameters and their doping with various metals [2, 3] makes it possible to control the properties of quantum wires. For this reason, the construction of an electronic structure model of a metal-filled nanotube is an urgent problem. For example, Kepp and D'yachkov [4] calculated the electronic structure of a chain formed by individual atoms of a metal inside the nanotube. The interaction between conduction electrons of a metal and the surrounding carbon core of the nanotube was simulated by a two-dimensional cylindrical rectangular well with infinitely high walls. The origin of such a potential was not considered in [4].

In contrast to [4], we propose here a model taking into account the acceptor properties of the carbon core of the nanotube and leading to a more realistic form of the mean field inside the nanotube. We disregard the atomic structure of the metal inside the nanotube and confine our analysis to the "jellium" model for nanotubes with a sufficiently large radius. This assumption leads to simple analytical formulas for calculating the conduction electron spectrum for the metallic subsystem inside a nanotube. The conduction of the carbon core with excess electrons is not analyzed.

1. ATOMIC STRUCTURE OF MONOLAYER NANOTUBES

Let us consider a nanotube consisting of a single graphite layer. A graphite layer strip can be rolled into a cylindrical surface without discontinuities in many ways. According to Hamada *et al.* [5], each possibility is characterized by a certain chiral vector (n, m), which indicates the coordinates of the benzene ring (in units of the magnitude of the basal vector of the graphite layer) coinciding with the ring at the origin when the layer is rolled up to form a cylinder. Two types of nanotubes, viz., zigzag tubes with the chiral vector (n, 0) and those having an armchair configuration with the chiral vector (n, n), apart from the symmetry axis, possess a symmetry plane perpendicular to the nanotube axis. It is natural to assume that nanotubes in which the structure of hexagonal benzene rings is distorted to the minimum extent are most stable. In the case of linear carbon–carbon (C–C) bonds, none of the nanotubes can be regarded as exactly cylindrically (axially) symmetric. A nanotube with a zigzag configuration, for which two sides of each of the hexagons constituting it are parallel to the nanotube axis, is closest in shape to a cylindrically symmetric nanotube. In this paper, we will consider only zigzag-type nanotubes.

A nanotube cannot be designed in such a way that all the benzene rings constituting it are planar. There are two configurations of zigzag tubes for which the structure of a benzene ring is distorted to the least extent. These structures are depicted in Fig. 1 (the dashed lines denote the bending lines of the graphite plane). In Fig. 1a, all hexagons are identical and slightly bent along the diagonal, so that there are two types of nonequivalent C–C bonds. In Fig. 1b, half of the benzene rings constituting the nanotube are planar, and the other half are bent rings. The layers formed by these rings alternate along the length of the nanotube, so that there are three types of nonequivalent C–C bonds. The width of plane strips along the nanotube is twice that in Fig. 1a. The translation periods along the z axis of the nanotube in Figs. 1a and 1b are approximately identical and equal to $3a_0$, where a_0 is the average length of the C–C bond.

1063-7834/00/4210-1966$20.00

In order to find out which of the configurations considered above is more stable, detailed quantum-chemical calculations are required; to our knowledge, such calculations have not been made thus far. Usually, all C–C bonds on the surface of a nanotube are regarded in calculations as identical and equal in length to bonds in a plane graphite layer ($a_0 = 0.142$ nm). This approximation is reasonable for nanotubes with a sufficiently large radius. For definiteness, we consider the structure presented in Fig. 1a, whose shape is the closest to being cylindrical. In this case, the minimum radius $a_0\sqrt{3}/2$ corresponds to a nanotube with only three hexagons (six carbon atoms) in the perimeter, and the number of atoms in the unit cell is 12. An increase in the nanotube radius is observed when two carbon atoms are added to the unit cell, and the number of hexagons in the perimeter of the nanotube increases by unity.

2. FILLING OF NANOTUBES WITH K, Rb, AND Cs ATOMS

Nanotubes can be filled [6] either in the course of their preparation, or by opening the ends of empty tubes and their filling by using, for example, the capillarity effect. This effect is manifested when the surface tension of the filling material is ≤0.2 N/m. This condition is satisfied for K, Rb, and Cs melts. Their ionic radii according to Pauling are 0.133, 0.148, and 0.167 nm respectively [7]. The (12, 0) nanotube has a diameter approximately equal to 0.9 nm and can contain seven K ions in its cross-section (Fig. 2). According to Charlier and Issi [8], monolayer nanotubes have a diameter of 0.8–3 nm.

We consider a solitary nanotube whose radius R is substantially smaller than its length L. A detailed analysis of the atomic structure of a nanotube containing metals of alkali atoms is beyond the scope of this paper. It is only important for further analysis that even a nanotube with a diameter of at most 1 nm can be regarded as cylindrically symmetric to an admissible degree of accuracy. Such a nanotube is a simple and sufficiently realistic model of a quantum wire.

It is well known [9] that fullerene-like objects are acceptors of electrons. According to estimates [10], every ten carbon atoms in the nanotube captures an electron. We assume that, if the nanotube is filled (doped) with alkali metals, its surface traps their valence electrons, so that all vacant orbitals of the lateral surface of the nanotube are filled. This assumption is confirmed by the calculations [11] of a monatomic chain of potassium atoms inside the (7, 0) nanotube, which demonstrate the complete transfer of potassium valence electrons to the carbon core. As a result, the surface of the nanotube acquires a negative charge, while its interior has a positive charge. We assume that the negative charge is distributed uniformly over the surface of the nanotube. A carbon nanotube filled with a metal can serve as a simple model of a quantum wire

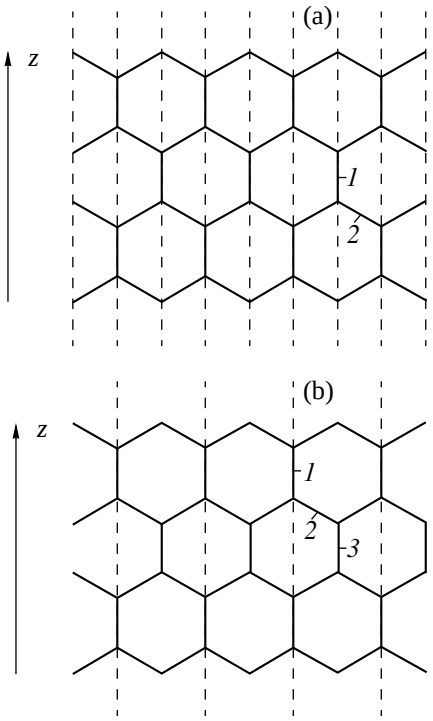

Fig. 1. Two possible atomic structures of a carbon nanotube of the zigzag type: z is the nanotube axis; dashed lines are the lines of bending of the graphite monolayer; and *1*, *2*, and *3* are nonequivalent carbon–carbon bonds.

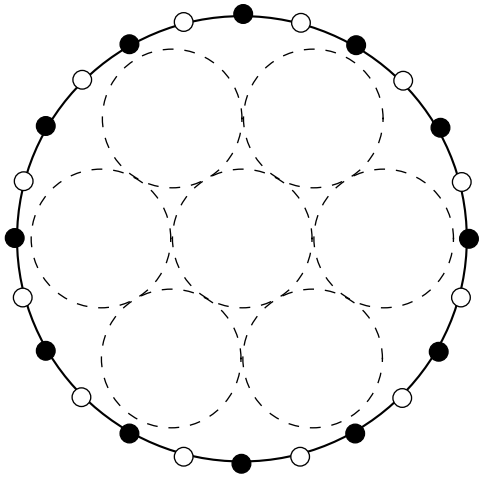

Fig. 2. Cross-section of the (12, 0) nanotube of diameter $2R \approx 0.9$ nm, filled with K atoms (dashed circles); dark and light circles indicate carbon atoms in the cross-sectional plane and at a distance $a_0/2$ from it (a_0 is the length of the C–C bond), respectively. Solid lines are projections of C–C bonds onto the plane of the figure (the length of a projection is $a_0\sqrt{3}/2$).

with a nonuniform distribution of positive and negative charges over its cross-section. The nanotube is electrically neutral as a whole, and, hence, the potential outside the tube is equal to zero. If we assume that the pos-

itive charge is uniformly distributed over the volume bounded by the surface of the nanotube, the potential energy of conduction electrons in the nanotube is a quadratic function of the distance $r < R$ to the center of the nanotube (see, for example, [12]):

$$U(r) = \begin{cases} e\alpha\left(\frac{r^2}{R^2} - 1\right), & r \le R \\ 0, & r > R, \end{cases} \quad (1)$$

where e is the magnitude of the electron charge, and α is the magnitude of the surface charge per unit length of a nanotube with radius $R \ll L$.

Since ionic cores of atoms of alkali metals are practically not polarized [13], we can assume that the relative permittivity inside the nanotube is equal to unity. The potential well depth $U(0) = -e\alpha$ is related to radius R of the nanotube through a simple expression following from the condition that ten carbon atoms capture one electron [10]. Then, α is equal to the number of carbon atoms per unit length of the nanotube, multiplied by e and divided by 10. If we disregard the difference between the length of the circle $2\pi R$ and the perimeter $2Rn\sin(\pi/n)$ of the n-gon which is inscribed in it and has carbon atoms at the vertices (Fig. 2), simple geometrical considerations give

$$\alpha = \frac{e\gamma}{10 \times 3a_0} \approx \frac{4\pi e}{15\sqrt{3}}\frac{R}{a_0^2}, \quad (2)$$

where $\gamma \approx 8\pi R/(a_0\sqrt{3})$ is the number of carbon atoms in an axisymmetric unit cell of the nanotube with the translation period $3a_0$.

It should be noted that the potential energy $U(r)$ is only the first approximation to the mean self-consistent field in which electrons move. It is meaningless to carry out the complete self-consistency procedure in the proposed simplified structural model of a doped nanotube. It is only clear that, in view of the axial symmetry of the system under investigation, the self-consistent potential should also possess this symmetry.

3. CONDUCTION ELECTRON IN A DOPED NANOTUBE

In the effective mass approximation, the Hamiltonian of an electron in the cylindrical reference frame (r, z, φ) has the form

$$\hat{H} = -\frac{\hbar^2}{2m_\perp}\left[\frac{1}{r}\frac{\partial}{\partial r}\left(r\frac{\partial}{\partial r}\right) + \frac{1}{r^2}\frac{\partial^2}{\partial\varphi^2}\right] - \frac{\hbar^2}{2m_\parallel}\frac{\partial^2}{\partial z^2} + U(r), \quad (3)$$

where $m_\perp$ and $m_\parallel$ are the transverse and longitudinal effective masses of the electron delocalized in a doped nanotube, and $U(r)$ is the potential energy of the electron at a distance r from the center of the nanotube in a direction perpendicular to the symmetry axis z. For 3D alkali metals, the effective masses of conduction electrons (in units of free electron mass m_0) are equal to 1.25 for K, 1.26 for Rb, and 1.43 for Cs [7]. Since the number of atoms in the nanotube cross-section is small, we can write $m_\perp \approx m_0$. The value of $m_\parallel$ is determined by the potential periodicity along the nanotube, which we will not analyze here, assuming that $m_\parallel \approx m_0$.

In the mean field approximation, the states of conduction electrons in a nanotube filled with a metal for $r < R$ can be determined from the solution of the Schrödinger equation with the potential energy (1). The distribution of electrons over energy levels is governed by the Pauli exclusion principle.

The operators of the quasi-momentum ($\hat{p}_z$) and angular momentum ($\hat{l}_z$) components of an electron along the z axis commute with each other and with Hamiltonian (3). Consequently, the eigenfunctions of these operators have the form [14]

$$\Psi_{nm_z p_z} = \frac{1}{\sqrt{4\pi^2\hbar}}\exp\left[i\left(\frac{p_z z}{\hbar} + m_z\varphi\right)\right]\Psi_{n|m_z|}(r), \quad (4)$$

where the wave function of the "longitudinal" motion of an electron is normalized to the δ-function of the quasi- momentum; $\Psi_{n|m_z|}(r)$ is the solution of the radial Schrödinger equation

$$\frac{\hbar^2}{2m_0}\left[-\frac{1}{r}\frac{d}{dr}\left(r\frac{d}{dr}\right) + \frac{m_z^2}{r^2}\right]\Psi_{n|m_z|} + U(r)\Psi_{n|m_z|} = E_{n|m_z|}\Psi_{n|m_z|}, \quad (5)$$

which determines the energy spectrum of the "transverse" motion $E_{n|m_z|}$ with the principal quantum number $n = 0, 1, 2, \ldots$ and the azimuthal number m_z.

The wave function (4) corresponds to the energy of an electron delocalized inside the nanotube

$$E_{n|m_z|p_z} = E_{n|m_z|} + \frac{p_z^2}{2m_0}, \quad (6)$$

where $E_{n|m_z|}$ is determined by the specific form of the potential energy $U(r)$.

Each energy level of the discrete spectrum $E_{n|m_z|}$ of the transverse motion can be put in correspondence with either one eigenfunction (at $m_z = 0$), or two eigenfunctions (at $m_z \neq 0$). If we have an accidental degeneracy, the multiplicity of degeneracy of the energy levels can also assume other values. The ground state is characterized by the quantum numbers $n = 0$ and $m_z = 0$ and is nondegenerate.

In the axisymmetric case, as well as for one dimension, there is always at least one energy level with $m_z = 0$. The number of discrete energy levels with $m_z \neq 0$ in a two-dimensional square well with a constant depth U and radius R is determined (see, for example, [14]) by the parameter $\xi = m_0 R^2 |U| \hbar^2$. For $\xi \ll 1$, there exists only one energy level with $n = 0$ and $m_z = 0$, whose energy is smaller than the well depth. The state with $n = 0$ and $|m_z| = 1$ appears at $\xi \geq 2.88$.

In order to estimate the number of discrete electron energy levels in the localizing potential (1), we use the parameter ξ, assuming that $U = U(0)$.

In accordance with relationship (2), the parameter ξ is approximately equal to 57 for a nanotube of diameter $2R = 1$ nm, the translation period $3a_0 = 0.426$ nm, and the well depth $U(0) = -e\alpha$; i.e., the well is quite deep, so it contains a large number of energy levels with $m_z \neq 0$. The condition for the existence of only one discrete energy level in a nanotube is satisfied for extremely thin nanotubes ($R \leq 0.2$ nm).

In the case of transverse motion of an electron in a parabolic potential well (1), the variables in the Schrödinger equation can also be separated in the Cartesian coordinates [14]

$$\left\{-\frac{\hbar^2}{2m_0}\left(\frac{\partial^2}{\partial x^2}+\frac{\partial^2}{\partial y^2}\right)-e\alpha\left(1-\frac{x^2+y^2}{R^2}\right)\right\} \times \Psi_{n_1}(x)\Psi_{n_2}(y) = E_{n_1+n_2}\Psi_{n_1}(x)\Psi_{n_2}(y), \quad (7)$$

and the spectrum $E_{n_1+n_2}$ of the transverse motion at the bottom of the localizing potential (see below) has the form of a harmonic oscillator spectrum

$$E_{n_1+n_2} = E_\nu = (\nu+1)\hbar\omega - e\alpha, \quad (8)$$

where $\omega = \sqrt{2e\alpha/(R^2 m_0)}$ is the frequency of zero-point oscillations of the electron, and $\nu = n_1 + n_2$ is the number of the oscillator level; $n_1, n_2 = 0, 1, 2, \ldots$.

According to Eqs. (7) and (8), the energy level E_ν with a given value of ν corresponds to the linearly independent eigenfunctions of a two-dimensional harmonic oscillator $\Psi_{n_1 n_2}(x, y) = \Psi_{n_1}(x)\Psi_{n_2}(y)$ at $n_1 = 0, 1, \ldots, \nu$, $n_2 = \nu, \nu-1, \ldots, 0$; i.e., this energy level of the oscillator is $(\nu+1)$-fold degenerate. The total energy of an electron in a state with the quantum number ν and with a quasi-momentum p_z is given by

$$E = E_\nu + p_z^2/2m_0. \quad (9)$$

For a finite-depth well with the potential energy (1), we should generally join the solutions of the Schrödinger equation at $r = R$ inside and outside the well. However, for the deep well, the lowest discrete energy levels change insignificantly as compared to the purely oscillator levels (8), and the spectrum remains virtually equidistant. Let us quantitatively estimate the number and the energies of the levels corresponding to a transverse motion in a monolayer doped nanotube with a diameter close to the minimum possible value. For example, at $2R = 1$ nm, the well depth $U(0) = -17.27$ eV, and the separation between the levels is $\hbar\omega = 3.24$ eV. This means that such a nanotube contains approximately five discrete oscillator levels E_ν. The first energy level is not degenerate and has the energy $E_{00} = -14$ eV. This corresponds to the wave function $\Psi_{00}(r) = (\pi b^2)^{-1/4}\exp(-r^2/(2b^2))$, where $b = \sqrt{\hbar/(m_0\omega)}$. The second level is doubly degenerate and has the energy $E_{01} = E_{10} = -10.8$ eV and two linearly independent wave functions $\Psi_{01}(x, y) \propto x\exp(-r^2/(2b^2))$ and $\Psi_{10}(x, y) \propto y\exp(-r^2/(2b^2))$. The third energy level is triply degenerate, and so on. It should be noted that the well depth $U(0)$ is directly proportional to the radius R of the nanotube, and the separation between the energy levels is proportional to $R^{-1/2}$; i.e., the number of energy levels is proportional to $R^{3/2}$.

4. DENSITY OF ONE-ELECTRON STATES AND CONDUCTIVITY

Now, we calculate the density $D(E)$ of quasi-one-dimensional states and the Fermi energy $E_F = p_F^2/(2m_0)$ of a nanotube on the basis of formula (9) for an oscillatorlike spectrum of transverse motion of a conduction electron in the nanotube at temperature $T \longrightarrow 0$.

If we have only one discrete energy level (one subband), the condition for determining the Fermi quasi-momentum p_F for a longitudinal motion of an electron in a nanotube of radius R and length L can be written [7] as $2p_F L/(\pi\hbar) = \pi R^2 L\rho$, where ρ is the density of conduction electrons. Then, the Fermi quasi-momentum for electrons located only in the first subband is determined by the formula

$$p_F = \frac{\pi^2\hbar\rho R^2}{2}, \quad (10)$$

so that the condition of filling only one subband ($E_F < \hbar\omega$) by electrons has the form

$$\pi^4\hbar^2\rho^2R^4/(8m_0) < \hbar\omega.$$

To estimate the orders of magnitude of the quantities, for the electron density ρ in the nanotube we choose the values corresponding to $3D$ metals [7]. Then, in the case of potassium ($\rho = 14$ nm^{-3}), the radius of a nanotube containing electrons only in one subband is $R \leq 0.38$ nm. For rubidium ($\rho = 11.5$ nm^{-3}) and cesium ($\rho = 9.1$ nm^{-3}), we have $R \leq 0.41$ and 0.46 nm, respectively. This means that, for nanotubes with $2R \geq 1$ nm, we are concerned only that the lowest energy levels for transverse motion are filled; for these levels, the difference between potential (1) and a purely oscillator potential can be ignored.

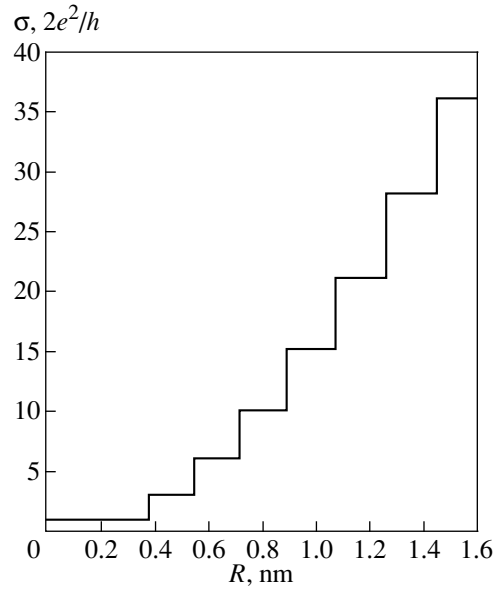

Fig. 3. Dependence of the conduction (in units of $2e^2/h$) of a nanotube filled with potassium atoms at the electron density $\rho = 14$ nm^{-3} on its radius R according to formula (13) for $T \longrightarrow 0$.

In view of the one-dimensional motion of electrons along the nanotube, their quasi-momenta in the first subband belong to the interval $[-p_F; p_F]$, and the Fermi surface degenerates into two isolated points $E_F(p_F)$ and $E_F(-p_F)$. For the Fermi level lying at the midpoint between the first and second levels for transverse motion, we have $E_F = p_F^2/(2m_0) = \hbar\omega/2$. In this case, the Fermi quasi-wave vector $k_F = p_F/\hbar$ at $R \approx 0.45$ nm is $k_F = 6.7$ nm^{-1}. At the same time, the maximum quasi-wave vector q for an acoustic phonon in a one-dimensional chain of carbon atoms with the translation period $3a_0 = 0.426$ nm is $q = \pi/3a_0 \approx 7.38$ nm^{-1}. Since $q < 2k_F$, the umklapp processes cannot be realized (at least, when $T \longrightarrow 0$ and electrons occupy only the first subband). As a result, the probability of inelastic scattering of electrons from acoustic phonons at low temperatures is small. For the same reason, the probability of electron–electron scattering is also low, which allows us to use the one-electron approximation to describe electronic states in the nanotube.

As the nanotube radius and/or the concentration of conduction electrons change, the electrons begin to occupy the second subband, the number of states increases by $2(p_F - \sqrt{2m_0\hbar\omega})L/(\pi\hbar)$, and the condition for determining the Fermi quasi-momentum takes the form $\pi^2\hbar\rho R^2/2 = p_F + 2(p_F - \sqrt{2m_0\hbar\omega})$, where the factor 2 on the right-hand side of the equality accounts for double degeneracy of the second oscillator level. Then, the Fermi quasi-momentum in the first subband with due regard for the occupation of two subbands by electrons is given by

$$p_F = \frac{\pi^2\hbar\rho R^2}{6} + \frac{2}{3}\sqrt{2m_0\hbar\omega}. \quad (11)$$

Generalizing the line of reasoning leading to formulas (10) and (11) to the case of an arbitrary number of subbands $N(R)$ occupied by electrons, we find that the $N(R)$ dependence and the Fermi quasi-momentum $p_F(R)$in the first subband on the nanotube radius R is determined from the following two equations:

$$p_F = \frac{\pi^2\hbar\rho R^2}{N(N+1)} + \frac{2\sqrt{2m_0\hbar\omega}}{N(N+1)}\sum_{j=0}^{N-1}(j+1)\sqrt{j},$$
$$\frac{p_F^2}{2m_0} = N\hbar\omega, \quad (12)$$

where $\omega^2 \approx 0.967e^2/(m_0 a_0^2 R)$, $a_0 = 0.142$ nm.

For instance, the radii of nanotubes filled with K, Rb, and Cs atoms, for which electrons are distributed among $N = 7$ subbands, were calculated from Eqs. (12) and found to be equal to 1.44, 1.58, and 1.75 nm, respectively.

The number of states for one subband with the quantum number ν in the energy interval dE is $D_\nu(E)dE = 4(\nu + 1)Ldp_z/(2\pi\hbar)$ where one value of E corresponds to two values of the quasi-momentum $\pm p_z$ (see, for example, [15]). Taking into account the fact that the total energy of an electron is $E = E_\nu + p_z^2/(2m_0)$, the density of one-electron states in the nanotube has the form

$$D(E) = L\frac{\sqrt{2m_0}}{\pi\hbar}\sum_{E_\nu < E}(\nu+1)(E - E_\nu)^{-1/2},$$

where $E_\nu = (\nu + 1)\hbar\omega - e\alpha$ is the energy of the discrete level ν for transverse motion.

According to the Landauer theory [16], the dc conductivity of the interior of a nanotube in units of the conductivity quantum $2e^2/h$ at $T \longrightarrow 0$ is equal to the number of open nondissipative channels of electron transfer. In our case, the number of open channels is equal to the number of subbands occupied by electrons with allowance made for the multiplicity of the degeneracy of the subband, which is equal to its number $N(R)$. The number of channels for electron transfer is $N(R)[N(R) + 1]/2$. Then, the conduction of a doped nanotube of radius R takes the form

$$\sigma(R) = \frac{2e^2}{h}\frac{N(R)[N(R)+1]}{2}, \quad (13)$$

where $N(R)$ is determined from Eq. (12).

The step curve describing the conduction dependence $\sigma(R)$ on the radius R of a nanotube filled with potassium (Fig. 3) reflects the discrete nature of $N(R)$.

Thus, we have proposed a model of the electronic structure of a solitary monolayer carbon nanotube filled with atoms of an alkali metal. The model is based on the approximation of noninteracting electrons and a parabolic localizing potential. The dependences of the density of states, the Fermi energy, and the number of occupied discrete levels for a transverse motion of electrons on the nanotube radius are determined. Numerical estimates are obtained for nanotubes filled with K, Rb, and Cs atoms. It is shown that the separation between energy levels in a nanotube with a radius approximately equal to 1 nm is of the order of a few electronvolts. A simple formula is derived for calculating the Fermi energy of the electronic system in a doped nanotube with an arbitrary number of occupied subbands in it. The Landauer formula is used to calculate the dependence of the dc conduction of a nanotube filled with potassium on its radius for $T \longrightarrow 0$.

In the proposed model, the dependences of the Fermi energy and the number of occupied energy subbands on the radius R and the density ρ of conduction electrons in the nanotube can be easily calculated. This makes it possible to analyze the phenomena of electron transport in doped nanotubes. A possible manifestation of conduction through the negatively charged carbon core of the nanotube can be included in the model as a parallel channel.

ACKNOWLEDGMENTS

This work was supported by the Belarussian Republic Foundation for Basic Research, grant no. F97-246.

REFERENCES

1. S. Iijima, Nature **354** (6348), 56 (1991).
2. A. V. Eletskiĭ, Usp. Fiz. Nauk **167** (9), 945 (1997) [Phys. Usp. **40**, 899 (1997)].
3. A. L. Ivanovskiĭ, Usp. Khim. **68** (2), 119 (1999).
4. O. M. Kepp and P. N. D'yachkov, Dokl. Akad. Nauk **365** (3), 365 (1999).
5. N. Hamada, S. Sawada, and A. Oshiyama, Phys. Rev. Lett. **68** (10), 1579 (1992).
6. J. Cook, J. Sloan, and M. L. H. Green, Fullerene Sci. Technol. **5** (4), 695 (1997).
7. C. Kittel, *Introduction to Solid State Physics* (Wiley, New York, 1995, 7th ed.; Nauka, Moscow, 1978).
8. J.-C. Charlier and J.-P. Issi, Appl. Phys. A **67** (1), 79 (1998).
9. R. C. Haddon, Philos. Trans. R. Soc. London **343** (1667), 53 (1993).
10. M. F. Lin and K. W.-K. Shung, Phys. Rev. B **52** (11), 8423 (1995).
11. Y. Miyamoto, A. Rubio, X. Blase, *et al.*, Phys. Rev. Lett. **74** (15), 2993 (1995).
12. V. V. Batygin and I. N. Toptygin, *Problems in Electrodynamics* (Nauka, Moscow, 1970; Academic, London, 1964).
13. A. Animalu, *Intermediate Quantum Theory of Crystalline Solids* (Prentice-Hall, Englewood Cliffs, 1977; Mir, Moscow, 1981).
14. V. M. Galitskiĭ, B. M. Karnakov, and V. I. Kogan, *Problems in Quantum Mechanics* (Nauka, Moscow, 1981).
15. P. Y. Yu and M. Cardona, *Fundamentals of Semiconductors: Physics and Materials Properties* (Springer-Verlag, Berlin, 1999).
16. R. Landauer, IBM J. Res. Dev. **32** (3), 306 (1988).

Translated by N. Wadhwa